Universitat de Girona

SYNTHESIS OF MOLECULAR NANOCAPSULES FOR SUPRAMOLECULAR HOST-GUEST CHEMISTRY AND ENZYME-LIKE CATALYSIS

Cristina GARCÍA SIMÓN

Dipòsit legal: Gi. 821-2015
http://hdl.handle.net/10803/289567

Universitat de Girona

DOCTORAL THESIS

SYNTHESIS OF MOLECULAR NANOCAPSULES FOR SUPRAMOLECULAR HOST-GUEST CHEMISTRY AND ENZYME-LIKE CATALYSIS

Cristina García Simón

2015

Doctoral programme in Chemistry

Supervised by: Dr. Xavi Ribas Salamaña and Dr. Miquel Costas Salgueiro

Tutor: Dr. Xavi Ribas Salamaña

This manuscript has been presented to opt for the doctoral degree from the University of Girona

Universitat de Girona

Dr. Xavi Ribas Salamaña and Dr. Miquel Costas Salgueiro, from Universitat de Girona, WE DECLARE:

That the thesis entitled “Synthesis of molecular nanocapsules for supramolecular host-guest chemistry and enzyme-like catalysis”, presented by Cristina García Simón to obtain a doctoral degree, has been completed under our supervision and meets the requirements to opt for an International Doctorate.

For all intents and purposes, we hereby sign this document.

Dr. Xavi Ribas Salamaña

Dr. Miquel Costas Salgueiro

Girona, February 18, 2015

A mis padres y hermana

FULL LIST OF PUBLICATIONS

This thesis is based on a compendium of the followed publications:

Chapter III

Self-Assembled Tetragonal Prismatic Molecular Cage Highly Selective for Anionic π Guests. C. García-Simón; M. Garcia-Borràs; L. Gómez; I. Garcia-Bosch; S. Osuna; M. Swart; J.M. Luis; C. Rovira; M. Almeida; I. Imaz; D. Maspoch; M. Costas; X. Ribas, *Chem. Eu. J.* **2013**, *19*, *4*,1445-1456. (Impact factor: 5.696, position 22/151 in Chemistry, multidisciplinary, 1st quartile)

Chapter IV

Sponge-like molecular cage for purification of fullerenes. C. García-Simón; M. Garcia-Borràs; L. Gómez; T. Parella; S. Osuna; J. Juanhuix; I. Imaz; D. Maspoch; M. Costas; X. Ribas *Nat. Commun*. 5:5557, **2014**, DOI: 10.1038/ncomms6557. (Impact factor: 10.742, position 3/55 in multidisciplinary sciences, 1st quartile)

Chapter V

Enantioselective hydroformylation by a Rh-catalyst entrapped in a supramolecular metallocage. C. García-Simón; R. Gramage-Doria; S. Raoufmoghaddam; T. Parella; M. Costas; X. Ribas and J. N.H.Reek. *J. Am. Chem. Soc.* **2015**, DOI: 10.1021/ja512637k. (Impact factor: 11.444, position 10/151 in Chemistry, multidisciplinary, 1st quartile).

All these papers have been published in journals that belong to the first quartile according to JCR.

LIST OF ABBREVIATIONS

AcO	Acetate
[C60]PCBM	Phenyl-C61-butyric acid methyl ester
2D	Bidimensional
3D	Three-dimensional
Å	Ångströms
acac	Acetylacetonate
AcFc	Acetylferrocene
AHF	Asymmetric Hydroformylation
BArF	Tetrakis[3,5-bis(trifluoromethyl)phenyl]borate
bpy	Bipyridine
cat	Catalyst
CD	Cyclodextrins
CF_3SO_3 or OTf	Trifluoromethanesulfonate (triflate)
CG	Gas Chromatography
CNT	Carbon nanotube
conv	Conversion
CPP	Cycloparaphenylenes
CTV	Cyclotriveraveratrylene
CV	Cyclic voltammetry
DBA	Directional-Bonding Approach
DBBA	Dimetallic Building Block Approach
DCM	Dichloromethane
DFT	Density Functional Theory
DMF	Dimethylformamide
DMSO	Dimethyl Sulfoxide
DOSY	Diffusion-ordered Spectroscopy
ee	Enantiomeric excess
eq	Equation
equiv	Equivalents
ESI-MS	ElectroSpray Ionization Mass Spectrometry
en	Ethylenediamine
FT-IR	Fourier Transform Infrared Spectroscpy
G	Guest
H	Host
h	Hour
HRMS	High Resolution Mass Spectrometry
K_{as}	Association constant
Kcal	Kilocalorie

L	Ligand
LMCT	Ligand to Metal Charge Transfer
M	Metal
Me	Methyl
min	Minutes
MMFF	Merck Molecular Force Field
MOF	Metal-Organic Framework
MPA	Molecular paneling approach
MW	Molecular weight
$N(CF_3SO_2)_2$ or NTf_2	Bis(trifluoromethanesulfonyl)imide (triflimide)
n.d.	Not-detected
NMR	Nucleat Magnetic Ressonance
p.	Page
PAHs	Polycyclic aromatic hydrocarbons
PBI	Perylene bisimide
PEt_3	Triethylphosphine
Ph	Phenyl
Porph	Porphyrin
ppm	Part per milion
py	Pyridine
Ref.	Reference
r.t.	Room temperature
SIA	Symmetry Interactional Approach
SubPc	Suphthalocyanine
T	Temperature
TBA	Tetrabutylammonium
TBAP	Tetrabutylammonium perchlorate
TCE	Trichloroethane
TEA	Triethylamine
TFA	Trifluoroacetic acid
TFE	Trifluoroethanol
THF	Tetrahydrofurane
TON	Turn Over Number
TPP	Tetraphenylporphyrin
TPyP	*meso*-substituted tetrapyriyl-porphyrin
TL	Toluene
TS	Transition State
TTF	Tetrathiafulvalene
UV-Vis	Ultraviolet-Visible spectroscopy
WLA	Weak Link Approach
XRD	X-ray diffraction data

LIST OF FIGURES

LIST OF TABLES

LIST OF SCHEMES

ACKNOWLEDGEMENTS

This work would not have been possible without the following collaborations:

- Serveis Tècnics de Recerca from Universitat de Girona for technical support.
- Dr. Josep M. Luis, Dr. Marcel Swart, Dr. Silvia Osuna and Marc Garcia Borràs from the Institut de Química Computacional i Catàlisi from Universitat de Girona for the DFT calculations.
- Dr. Daniel Maspoch, Dr. Inhar Imar and Dr. Jordi Juanhuix from Institut Català de Nanocència and ALBA synchrotron, for the XRD data.
- Dr. Teodor Parella from Universitat Autònoma de Barcelona for the support with the NMR data.
- Prof. Dr. Joost N.H. Reek from University of Amsterdam for hosting a scientific visit and the collaborative research in the hydroformylation studies.
- Prof. Dr. Pau Ballester from Institut Català d'Investigació Química (ICIQ) for the fluorescence mesurements.
- Generalitat de Catalunya for the PhD grant “Beques predoctorals per a la formació de personal investigador (FI- DGR 2012)”.
- Generalitat de Catalunya for the mobility grant “Beques per a estades de recerca a l’estranger (BE-DGR 2012)”.
- Europearn Research Foundation (ERC) for financial support through project ERC-20009-StG-239910 (M.C.).
- X.R. Icrea Acadèmia award 2010 (9111087).
- Dr. Christopher Whiteoak for English grammar corrections.

GRAPHICAL ABSTRACT

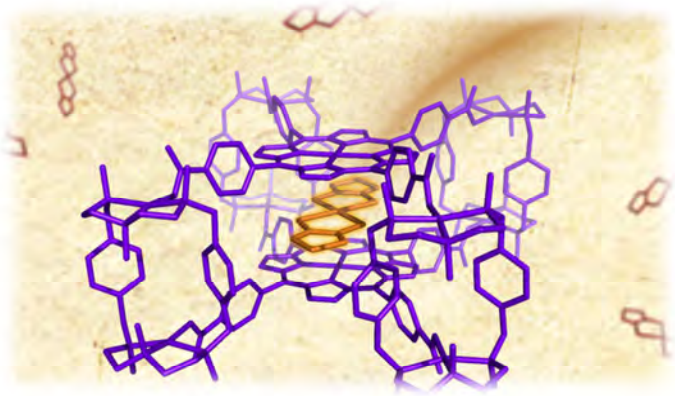

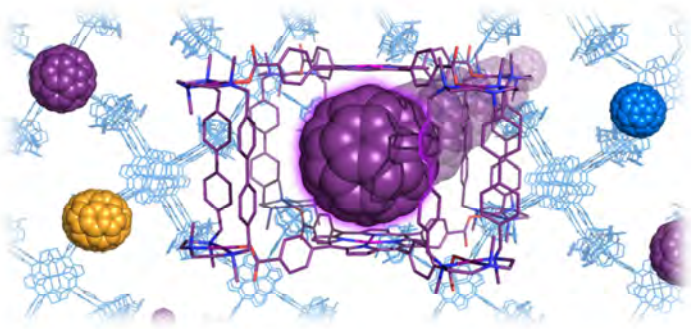

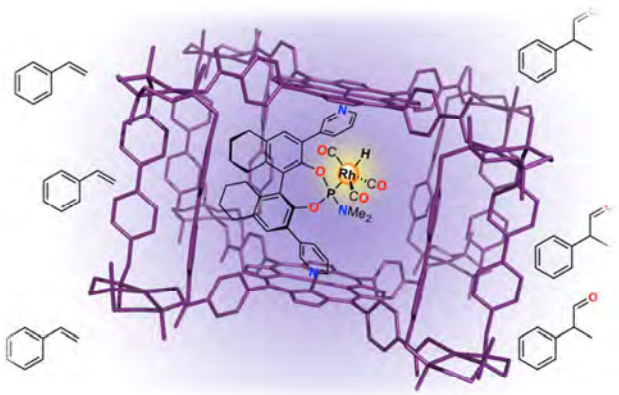

TABLE OF CONTENTS

SUMMARY

Supramolecular self-assembly directed by coordination bonds has led to the preparation of an increasing number of elegant and complex functional structures that approach nanoscopic dimension. The synthesis of 3D coordination capsule-like structures is of particular interest due to the multiple potential applications they offer, particularly for use in selective molecular recognition (host-guest chemistry), reactivity modulation (nanoreactors), molecular sensors or biological applications.

This thesis started with the preparation and characterization of two palladium(II)-based heaxaaza macrocyclic complexes of different sizes (**A** and **A'**). These diamagnetic compounds adopt a well-defined structure, in which each palladium(II) ion bears a labile coordination site available for binding to an external molecule. These complexes were used as building blocks ("molecular clips") in the preparation of higher ordered constructions through coordination bonds.

In the first part of the thesis the smaller molecular clip was used in the preparation of a 3D nanocapsule with $\mathbf{A}_4\mathbf{B}_2$ tetragonal prismatic geometry, where **B** corresponds to the tetraanionic form of 5,10,15,20-tetrakis(4-carboxyphenyl)porphyrin-Pd(II). Host-guest interactions between the nanocapsule and different guest molecules have been studied by means of NMR, UV-Vis, ESI-MS, and DOSY-2D experiments. The capsule displayed selectivity towards anionic, planar-shaped π-guests.

Afterwards, the larger molecular clip **A'** was used in the synthesis of a larger nanocapsule, $\mathbf{A'}_4\mathbf{C}_2$, where **C** corresponds to 5,10,15,20-tetrakis(4-carboxyphenyl)porphyrin-Zn(II). As a consequence of its wider inner cavity, the latter metallocapsule was able to encapsulate fullerenes in a rapid manner at room temperature, by simply soaking a solid sample of the capsule in a fullerene containing solution. The nanocage presents an adaptive structure which allows for encapsulation of fullerenes of varying size (C_{60}-C_{84}) with different affinities. Effectiveness for the selective separation of C_{60} from a mixture of fullerenes was demonstrated by using a straightforward washing protocol of a solid sample of fullerene containing capsule.

In the final part of this thesis, the confined inner cavity of the larger nanocapsule was also used to encapsulate a chiral monoligated rhodium catalyst, in order to explore its potential in asymmetric hydroformylation. The encapsulated catalyst gave among the highest selectivities in the asymmetric hydroformylation of styrene for a monoligated rhodium catalyst. The obtained results demonstrate a substantial increase of steroselectivity upon encapsulation of the catalyst, providing evidence of a selectivity-inducing effect of the secondary coordination sphere reminiscent of enzymatic active sites.

RESUM

L'autoacoblament supramolecular dirigit per enllaços de coordinació ha facilitat la preparació d'una gran varietat d'estructures químiques complexes i funcionals, que en alguns casos arriben a mides nanoscópiques. La síntesi de capsules de coordinació 3D rep un interès especial degut a la multitud d'aplicacions que aquestes ofereixen, destacant la seva aplicació en el reconeixement selectiu de molècules (química receptor-substrat), modulació de reactivitat (nanoreactors), sensors moleculars o les seves aplicacions biològiques.

Aquesta tesi doctoral va començar amb la preparació i caracterització de dos complexos hexaaza-macrocíclics de paladi(II) de diferents mides (**A** i **A'**). Aquest compostos diamagnètics adopten una estructura ben definida, en la que cada ió de Pd(II) manté una vacant de coordinació làbil que pot interaccionar amb una molècula externa. Aquests complexos es van utilitzar com a sintons moleculars ("clips moleculars") en la preparació d'agregats moleculars majors, mitjançant la formació d'enllaços de coordinació.

A la primera part de la tesi el clip molecular més petit es va utilitzar en la preparació d'una nanocàpsula 3D amb geometria tetragonal prismàtica y fórmula general $\mathbf{A}_2\mathbf{B}_2$, a on **B** correspon a 5,10,15,20-*tetrakis*(4-carboxifenil)porfirina de Pd(II). Tot seguit, es van investigar interaccions de tipus receptor-substrat entre la nanocàpsula i diferents substrats mitjançant tècniques de RMN, ESI-MS, UV-Vis i DOSY-2D. Es va comprovar que la nanocàpsula és altament selectiva per substrats plans, aniònics amb sistemes π.

Posteriorment, el clip molecular **A'** es va utilitzar en la preparació d'una nanocàpsula de mides superiors, $\mathbf{A'}_4\mathbf{C}_2$, a on **C** correspon a 5,10,15,20-*tetrakis*(4-carboxifenil)porfirina de Zn(II). Aquesta darrera nanocàpsula conté una cavitat interior més gran que li permet encapsular ful·lerens de manera ràpida i a temperatura ambient, simplement amarant una mostra sòlida de la nanocàpsula en una dissolució de ful·lerens. La nanocàpsula presenta una estructura adaptativa que li permet encapsular ful·lerens de diferents mides (C_{60}-C_{84}) amb diferents afinitats. A més, la nanocàpsula es va emprar amb èxit en la separació selectiva de C_{60} d'una barreja de ful·lerens utilitzant un senzill protocol experimental basat en rentats del sistema nanocàpsula-ful·lerè en estat sòlid.

Finalment, la cavitat interior de la nanocàpsula de majors dimensions també es va utilitzar per encapsular un catalitzador de rodi quiral monolligat, amb la finalitat d'explorar el seu potencial en reaccions d'hidroformilació asimètrica. El catalitzador encapsulat va donar alts valors de selectivitat, dels més alts que s'han observat per a un catalitzador de rodi monolligat. Els resultats obtinguts demostren que l'encapsulació del catalitzador incrementa notablement l'esteroselectivitat de la reacció, i indiquen que el confinament del catalitzador dins la caixa causa un efecte d'inducció de la selectivitat similar al que té lloc en els centres catalítics dels enzims.

RESUMEN

El autoacoplamiento supramolecular dirigido por enlaces de coordinación ha facilitado la preparación de una gran variedad de estructuras químicas complejas y funcionales, que en algunos casos alcanzan tamaños nanoscópicos. La síntesis de capsulas de coordinación 3D es especialmente interesante debido a las múltiples aplicaciones que estas estructuras ofrecen, destacando su aplicación en el reconocimiento selectivo de moléculas (química receptor-sustrato), modulación de reactividad (nanoreactores), sensores moleculares o sus aplicaciones biológicas.

Esta tesis doctoral empezó con la preparación y caracterización de dos complejos hexaaza-macrocíclicos de paladio(II) de diferentes tamaños (**A** y **A'**). Estos compuestos diamagnéticos adoptan una estructura bien definida, en la que cada ion de paladio(II) mantiene un vacante de coordinación lábil que puede interaccionar con una molécula externa. Estos complejos se utilizaron como subunidades moleculares ("clips moleculares") en la preparación de agregados moleculares de mayores dimensiones, mediante enlaces de coordinación.

En la primera parte de la tesis el clip molecular más pequeño se utilizó en la preparación de una nanocápsula 3D con geometría tetragonal prismática y fórmula general $\mathbf{A}_2\mathbf{B}_2$, donde **B** corresponde a 5,10,15,20-tetrakis(4-carboxifenil)porfirina de Pd(II). Seguidamente, se estudiaron interacciones tipo receptar-sustrato entre la nanocápsula y diferentes sustratos mediante técnicas de RMN, ESI-MS, UV-Vis y DOSY-2D. La nanocápsula mostró selectividad hacia sustratos aniónicos, planos con sistemas π.

Posteriormente, el clip molecular **A'** se utilizó en la síntesis de una nanocápsula de mayores dimensiones $\mathbf{A'}_4\mathbf{C}_2$, donde **C** corresponde a 5,10,15,20-tetrakis(4-carboxifenil)porfirina de Zn(II). Esta última nanocápsula posee una cavidad interior más grande que le permite encapsular fulerenos de manera rápida y a temperatura ambiente, simplemente empapando una muestra sólida de la nanocápsula en una disolución de fulerenos. La nanocápsula presenta una estructura adaptativa que le permite encapsular fulerenos de distintos tamaños (C_{60}-C_{84}) con diferentes afinidades. Además, la nanocáspsula se empleó con éxito en la separación selectiva de C_{60} de una mezcla de fulerenos usando un sencillo protocolo experimental basado en lavados del sistema nanocápsula-fulereno en estado sólido.

En la parte final de esta tesis, la cavidad interior de la nanocápsula de mayor tamaño también se usó para encapsular un catalizador de rodio quiral monoligado, con el fin de explorar su potencial en reacciones de hidroformilación asimétrica. El catalizador encapsulado mostró altos valores de selectividad, de los más altos hasta la fecha para un catalizador de rodio monoligado. Los resultados obtenidos demuestran que la encapsulación del catalizador incrementa notablemente la estereoselectividad de la reacción, e indican que el confinamiento

del catalizador en la caja causa un efecto de inducción de la selectividad similar al que tiene lugar en los centros catalíticos de las enzimas.

Chapter I.

General Introduction

I. GENERAL INTRODUCTION

I.1. Supramolecular chemistry: core concepts

Supramolecular chemistry was defined by one of its leading proponents, 1987 Nobel laureate Jean-Marie Lehn, as “chemistry beyond the molecule”. This area of chemistry is based upon molecular systems whose components are held together by weak and reversible intermolecular forces. This strategy makes it possible to construct highly complex functional chemical systems, by overcoming problems arising through traditional chemistry utilizing strong covalent bonds, which typically results in low yields as the complexity of the molecule increases. For these reasons the multidisciplinary area of supramolecular chemistry has undergone extraordinary development during the last decades.[1]

Weak non-covalent interactions such as hydrogen bonds, ion-ion interactions, ion-dipole, dipole-dipole, van der Waals forces, cation-π, π-π and closed shell interactions are used to hold the molecular building blocks together in order to form sophisticated supramolecular structures. Moreover, some interactions that possess a significant covalent bond component (e.g. coordination metal-ligand bonds) are also widely used. Although all these interactions are relatively weak when compared to strong covalent bonds, when they are used in a cooperative manner, highly stable supramolecular species can be constructed.

Self-assembly and host-guest chemistry are the two main fields into which supramolecular chemistry can be divided, with the difference between these two areas relating to size and shape of the interacting species. When the difference in size of the interacting molecules is not significant and they spontaneously interact to yield a higher ordered aggregate, this interaction is denominated self-assembly. On the other hand, when one molecule in the system is significantly larger than another, it is termed as a “host” and can wrap around the smaller molecule, the “guest” (host-guest interaction).[2,3]

I.1.1 Self-Assembly: programmed molecules

The basis of self-assembly is the spontaneous association of two or more molecules or ions through reversible intermolecular interactions to create a larger species (see Figure I.1). The molecules participating in the self-assembly process are programmed chemical entities, in other words, they contain complementary functionalities capable of driving the organization of matter over its spatial (structural) and temporal (dynamic) features.[4]

The lability of supramolecular interactions, which are responsible for a self-assembly process, gives rise to an inherent feature of supramolecular self-assembling systems: their ability to correct mistakes occurring during their synthesis and as a result permitting gradual evolution towards the most thermodynamically stable product (dynamic character). When different building blocks are mixed in order to obtain a supramolecule, more than one combination between these molecules is possible. Nevertheless, one possible combination will

be predominant due to a greater thermodynamic stability over the other species under specific reaction conditions. For this reason, these systems are considered to be thermodynamically selective.

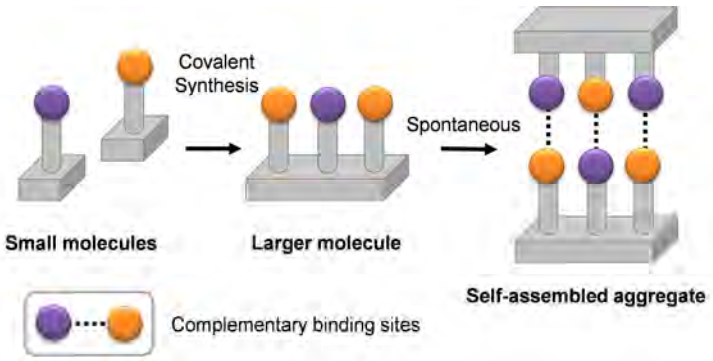

Figure I.1. Representation of the spontaneous self-assembly between complementary molecules (building-blocks) to give a self-assembled aggregate.

The success of the self-assembly process essentially lies in the precise design of the molecular building blocks. By programming the molecular moieties it is possible to control supramolecular output: self-organization by design. However the next step in supramolecular self-assembly is to reach self-organization by selection, which operates on dynamic constitutional diversity in response to either external or internal factors in order to obtain adaptive systems.[5–7]

Self-assembly is present in many natural systems. Nature has the ability to assemble relatively simple molecular precursors, using supramolecular interactions (e.g. hydrogen bonds or van der Waals interactions), into extremely complex biomolecules which are vital for life processes. The most highlighted example is the formation of the DNA double helix. The formation of this complex structure is a spontaneous and reversible process, capable of self-correcting any mistake during DNA synthesis. The process is always thermodynamically directed towards the most stable product, and against kinetic products.[8]

I.1.2 Host-guest Chemistry: molecular recognition

Host-guest chemistry is based on supramolecular recognition. The host molecule (receptor) is defined as a covalent or supramolecular molecule, possessing a central hole or cavity, which is able to accommodate a smaller molecule (guest or substrate) through a complexation event (see Figure I.2).[9]

The receptor and substrate molecules experience an attractive force between them, which leads to a stabilising binding free energy. Generally host-guest chemistry refers to the formation and stability of inclusion compounds in solution. However, there are some examples of solid host molecules, which are able to maintain their binding abilities towards a substrate both in the solid state and in solution.[10]

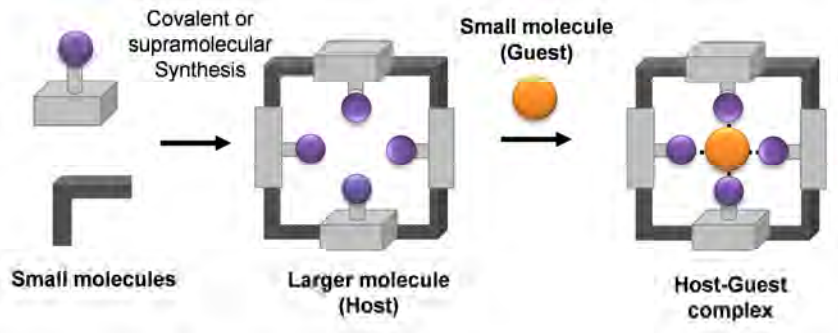

Figure I.2. Representation of the formation of a host molecule bearing an inner cavity, and the inclusion of a guest molecule into the receptor cavity giving a host-guest complex.

There are examples in which the guest molecule acts as a template, because it contains the required information to organize a collection of building blocks so that they can interact in a specific way. This strategy is commonly used in the synthesis of otherwise unstable supramolecules or supramolecular architectures with unusual topologies such as helicates. Anions are frequently used as template molecules.[11–13]

The association constant (K_{as}) or binding constant is the parameter which measures the thermodynamic stability of a host-guest adduct (see Equation I.1). A high value of the association constant corresponds to a high relative equilibrium concentration of the bound over the free substrate, and consequently a more stable host-guest adduct. Generally, binding constants can be measured by any experimental technique that can give information about the host-guest concentration ([H·G]) as a function of concentration of host ([H]) or guest ([G]). Among all the methodologies available for the determination of the K_{as}, NMR titration, UV-vis-titration, fluorescence titration and calorimetric titration are the most widely used.

$$\text{Host + Guest} \leftrightarrow \text{Host·Guest} \qquad K_{as} = \frac{[H \cdot G]}{[H] \cdot [G]} \qquad \text{(I.1)}$$

There are several factors to take into account for the design of the host molecule in order to obtain a highly stable host-guest adduct. Since supramolecular interactions are weak, it is necessary to synthesize a host that ensures as many as possible of these interactions are present to stabilise the guest inside. When two or more binding sites on a receptor cooperate to bind to a guest the phenomenon is known as cooperativity. Additionally it is essential that size and shape complementarity exists between the binding sites of the interacting species (preorganization). Finally, it is very important to consider that the interactions between a host and its guest are not isolated as a result of external influences. For instance, in real systems, guests are competing with surrounding solvent molecules. For binding to occur, many interactions between the receptor and solvent molecules must be broken, which has both enthalpic and entropic consequences.

The ultimate goal in the design of supramolecular receptors is the achievement of selectivity and reversibility. Selectivity is the preferential encapsulation of a guest over another.

In thermodynamic terms, it is the ratio of the binding constant for one guest over another. In the design of host molecules, the binding sites need to be tuned in order to target a specific guest. With regards to reversibility, it is understood as the possibility to liberate the sequestered guest. The guest exchange in-and-out of the host molecule can occur *via* (partial) dissociation of the receptor or by diffusion through the gate apertures (gating mechanism).[14]

I.2. Metal-ligand directed self-assembly

Nature is the source of inspiration for molecular architects who are working towards the construction of sophisticated and highly complex architectures using supramolecular interactions. Nevertheless, as the scale and complexity of target molecules increases, the assembly of small molecules into larger aggregates turns into an increasingly impeded process, and often low yielding. This is mainly due to the impossibility of fully controlling the directionality of the traditional weak supramolecular interactions mentioned previously in section I.1, such as electrostatic forces or van der Waals interactions. As a response to these limitations, coordination-driven self-assembly has emerged as a powerful tool to regain control over supramolecular synthesis. It facilitates the formation of large complex molecules, ranging from a few cubic Ångströms to in excess of a cubic nanometer.[15–17]

The strength of covalent coordination bonds is between that of a weak traditional supramolecular interaction and of a strong covalent bond. Metal-ligand interactions offer a high degree of directionality as a result of predictable metal-ion coordination geometries. In addition, the diversity of transition metal complexes and ligands available as building blocks makes this strategy very versatile, allowing the generation of multiple supramolecular structures.

Over the years different supramolecular synthetic approaches have been developed based on coordination bonds. The most widely used strategies are directional bonding, molecular panelling and symmetry interaction approaches, which will be described in further detail later. In addition, weak link and bimetallic building block approaches have also lead to complex coordination supramolecules and will be included as well.

The directional bonding approach (DBA),[18,19] also known as “Molecular library”, demands two major structural requirements: 1) complementary rigid precursors, with predefined angles and symmetry for the desired product to form and 2) the combination of the precursors in the appropriate ratios for the chosen outcome. Generally, the donor building blocks are rigid organic ligands that contain two or more binding sites bearing angular orientations between 0-180º. The acceptor moiety is a metal-containing subunit possessing coordination vacancies which are at a fixed angle with respect to each other and are suitable for binding the acceptor residue. The symmetry and binding positions available in the acceptor unit are responsible for the final shape of the target molecule (2D or 3D structure). On the other hand, the organic linker modulates the size of the aggregate.

In this context, the group of Ribas and Costas reported the synthesis of 2D and 3D coordination structures using the DBA based on macrocyclic copper(II) complexes which were used as metal-organic molecular clips, with a rigid conformation and two coordination vacancies (see Scheme I.1).[20–22] These copper molecular clips ([(**Cu-1**)$(H_2O)_2]^{4+}$ and [(**Cu-2**)$(CH_3CN)_4]^{4+}$) are capable of self-assembling with different di-, tri- and tetracarboxylate linkers to yield a library of differently sized 2D rectangles and helicates (Scheme I.1), and a 3D trigonal prismatic cage.

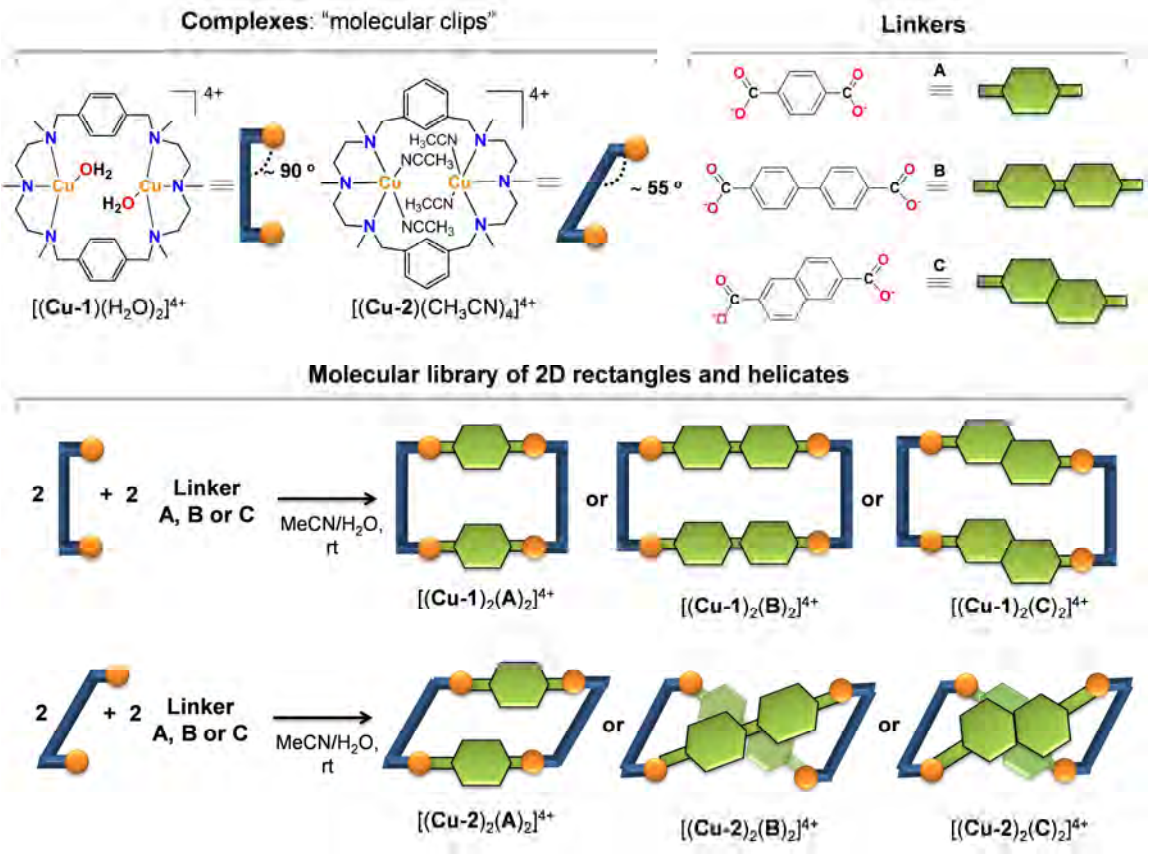

Scheme I.1. Schematic representation of **a)** hexaaza macrocyclic copper(II)-based complexes (molecular clips), **b)** dicarboxylate linkers of different sizes and **c)** reactions through the DBA to obtain the corresponding 2D molecular rectangles or helicates reported by Costas and Ribas.

The molecular panelling approach (MPA) is based on the synthesis of 3D supramolecules, starting from the corresponding 2D molecular components which make up the polyhedron. For example, a tetrahedral cage can be designed by using 4 triangular panels. By changing the number of panels used, a different structure can be generated. Commonly, palladium(II) or platinium(II) *cis*-capped ligands are used as metal nexus.[23–25] The position of the binding sites in the molecular panels is key to directing the final geometry of the resulting supramolecule.

Fujita designed different triangular molecular panels which were able to assemble into several 3D polyhedra.[26] Different numbers of panels have been described, containing coordination positions at distinct positions. When three equivalents of $(en)Pd(NO_3)_2$ (en = ethylenediamine) were mixed with two equivalents of panel **3** (Scheme I.2), the octahedral M_6L_4 capsule (**5**) was obtained.[27] Interestingly, when two equivalents of panel **4** were mixed with two equivalents of the palladium(II) salt, a M_6L_4 square pyramidal cone (**6**) was obtained instead.

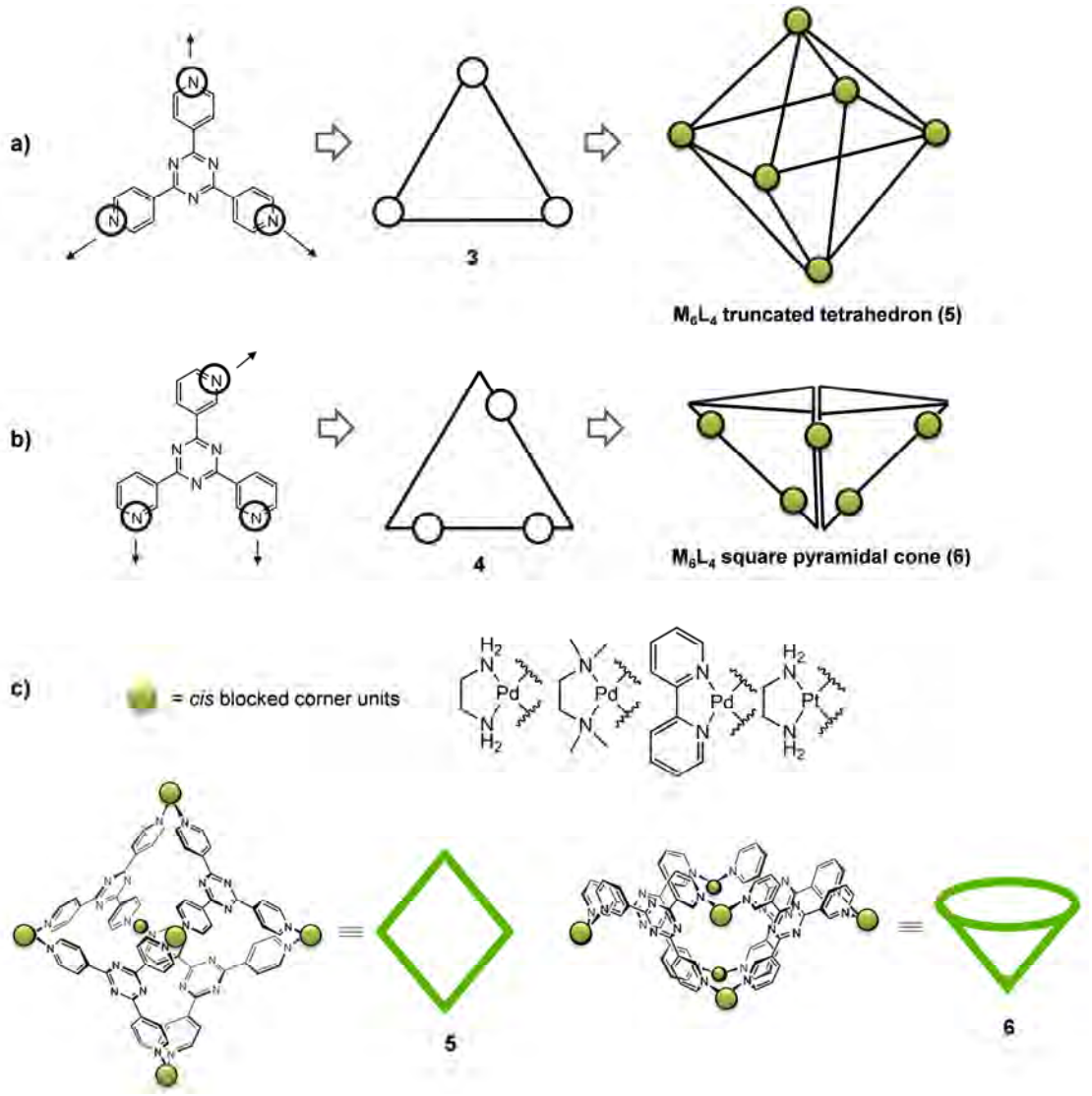

Scheme I.2. Representation of the assembly of **a)** a M_6L_4 truncated tetrahedron **5** and **b)** an M_6L_4 square-pyramidal cone **6** using triangular panels (**3** and **4** respectively). In **c)** the *cis*-capped palladium complexes used for the synthesis of Fujita's octahedral cage **5** and the bowl-shaped cage **6** making use of the molecular panelling approach.

In the symmetry interactional approach (SIA), multibranched chelating linkers with rigid and well defined geometries interact with naked main group or transition metal ions.[28] For this reason, there has to be a close geometric relationship between the ligand and the metal centre. The inherent symmetry of the coordination vacancies of the metal centres, along with the strong binding affinity of the chelating ligands, serves as the driving force in the assembly process.

The synthesis of M_4L_6 coordination assemblies based on this approach has been reported by Raymond.[29] The reported system comprises of four metal ions (M= silver(I), aluminium(III), indium(III), iron(III) or gallium(III)) located at the vertices of a tetrahedron. The metal centres are bridged by six *bis*-dentate catechol ligands, situated on the edges of the tetrahedron. This requires that the C_2 axes of the tetrahedron lie within the chelate plane at each of the metal centres. Additionally, the chelate vectors within the ligand must maintain an

angle of 70.6º (Scheme I.3). The *tris*-bidentate chelation of the metal atoms renders them chiral (Δ or Λ).

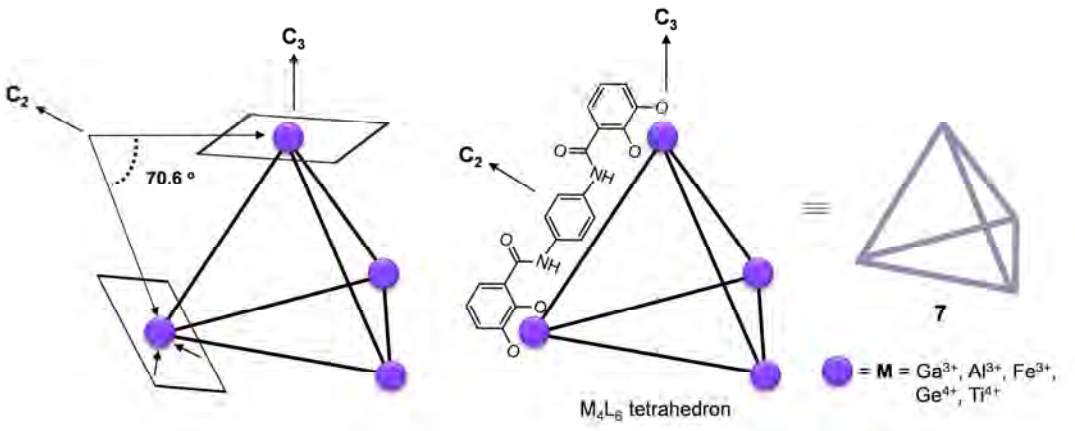

Scheme I.3. Design of a 3D M_4L_6 tetrahedral coordination cage (**7**) using the symmetry interaction approach, reported by Raymond.

The weak link approach (WLA) takes advantage of hemilabile ligands, which are used to coordinate transition metals in a bidentate fashion, in such a manner that one of the metal-ligand bonds is weaker than the other.[30] First a kinetic product is generated as a condensed intermediate, in which the bridging ligands are interacting (e.g. π-π interactions if the bridge is based on aromatic rings) (Scheme I.4 a). Subsequent addition of small molecules or metal ions with higher affinity towards the metal centre gives the thermodynamic open structure (Scheme I.4 b).[31] Flexible structures are obtained using this methodology.

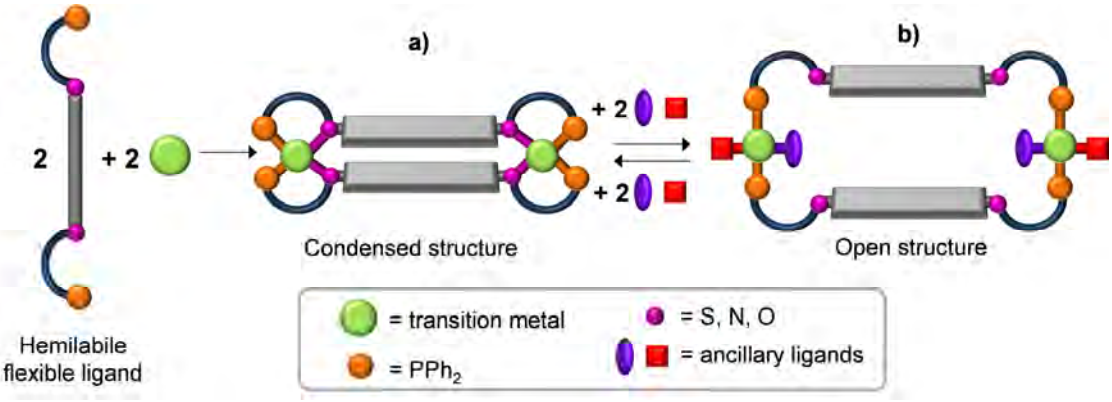

Scheme I.4. Illustration representing the different stages, and molecular species participating in the WLA.

In the dimetallic building block approach (DBBA), organic linkers interact with dimetallic units to form higher ordered aggregates.[32] The metal-metal bonded cationic subunits have one or more of the edges blocked by non-labile chelating N-donor ligands (Scheme I.5 a) and the remaining coordination sites are occupied by easily displaceable ligands. Polycarboxylic acid anions serve as the equatorial linkers, while polynitriles or polypyridyls are usually used as axial linkers. Two dimetallic units can interact by means of equatorial connectors (end-to-end

interaction, L_{eq}), by means of axial connectors (face-to-face interaction, L_{ax}), or by a combination of both spacers (Scheme I.5 b).

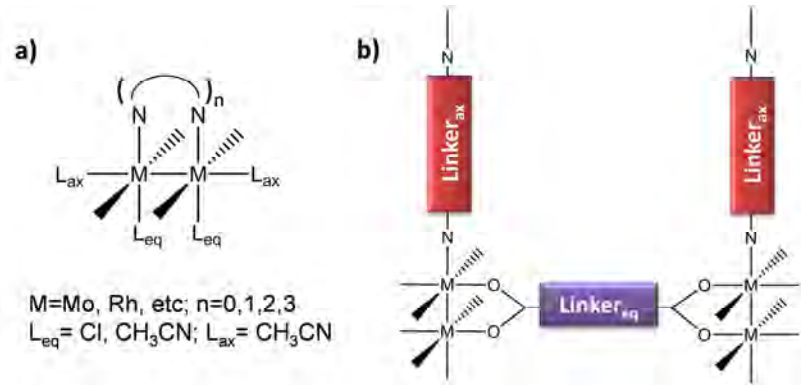

Scheme I.5. a) *Cis*-blocked dimetallic units used in the dimetallic building block approach. **b)** Schematic representation of the end-to-end (L_{eq}) and face-to-face (L_{ax}) modes of assembly.

These five mentioned strategies have been used to synthesize most of the reported coordination supramolecular structures (2D and 3D), which usually are highly symmetric and resemble Archimedean or Platonic solids in shape. However, apart from the metal-ligand interaction itself, there are other factors to consider which play a crucial role in the development of coordination supramolecules, such as the counter anions in charged species, labilization agents, guest templates or solvent interactions. In many cases these subtle secondary interactions are not fully understood. On the other hand, with the aim of constructing increasingly complex and functional structures, there is a great interest in the rational design of structures of lower symmetry.[33–35] For this purpose researchers have used heterotopic ligands,[36] different ligands around the metal centre (heteroleptic species)[37,38] or more than one metal centre (heterobimetallic assemblies).[39] In the next section, some interesting examples of 2D and 3D non-classical structures and the subtle effects responsible of their formation (giving special attention to the 3D molecular flasks and their applications) will be discussed.

I.2.1 Two-dimensional structures

The most common strategies for the development of coordination structures are generally based on a direct assembly process; by mixing the pre-programmed building blocks in the proper ratio the desired geometry is obtained. Nevertheless, depending on the building blocks used, it is possible that the desired product does not form in one step, and therefore the reaction conditions need to be tuned in order to obtain the desired species. In 2004, Hupp and Nguyen reported the synthesis of supramolecular loops and squares based on Salen-type ligands.[40,41] Salen complexes participate as selective catalysts, in a wide variety of chemical reactions such as olefin epoxidation.[42,43]

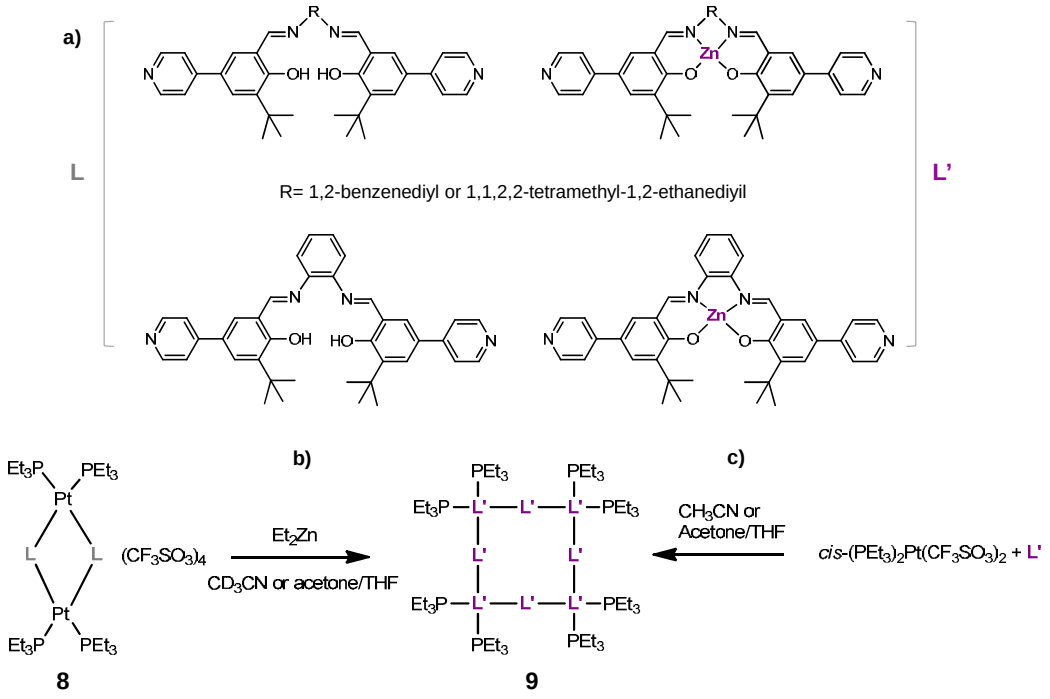

Scheme I.6. a) *Bis*-(pyridyl)-functionalized Salen ligands and their zinc(II) complexes (**L** and **L'**). Synthesis of the coordination square **9** from the corresponding dimetallic loop **8** by metallation of the free-base Salen moieties (**b**) or by reaction of the zinc(II) Salen complex (**L'**) and *cis*-$(PEt_3)_2Pt(CF_3SO_3)_2$.

To obtain the molecular square **9**, the authors mixed *cis*-$[(PEt_3)_2Pt(CF_3SO_3)_2]$ and the *bis*-(pyridyl)-functionalized Salen ligand, **L**, in a 1:1 molar ratio in acetonitrile. To their surprise, a metallic coordination loop (**8**) was obtained in whose ligands where slightly twisted and the metal centres partially strained. The formation of this smaller and more strained structure, over less constrained square species containing more assembling units, was reasoned by the fact that entropy is the factor predominating in the self-assembly process. Subsequent metalation of the free base Salphen ligand by adding a zinc(II) salt rigidified the ligand frameworks favouring the square formation. The square molecule **9** was also obtained by direct self-assembly, by using the zinc(II) metallo-Salen complexes (**L'**).

The vast majority of bidimensional supramolecular architectures reported have regular shapes, for example squares or rectangles. Nevertheless, it is also possible to obtain irregular

shapes. A relevant example was reported in 2009 by Schmittel that used a sophisticated self-sorting strategy to generate the first coordination trapezoid (**15_T**). A library of 3 bifunctional organic linkers (**10**, **11** and **12**) and two metal ions (zinc(II) and copper(I)) was used to obtain the trapezoid (see Scheme I.7).[44] In this example the organic ligands were carefully designed in order to favour the formation of the trapezoid (**15_T**) versus rectangles (**13_{RL}** and **14_{RS}**). Steric hindrance was also introduced in order to avoid the formation of homoleptic species. A self-sorting experiment was performed by first mixing ligands **11** and **12** with zinc(II) salts in acetonitrile at 60ºC for 2h. Afterwards copper(I) salts and ligand **10** were added, and the same reaction conditions were maintained for 8h. ESI-MS and ^{1}H-NMR experiments confirmed the quantitative formation of trapezoid (**15_T**). Considering the relative stability of the 3 coordination species **13_{RL}**, **14_{RS}** and **15_T**, the smaller rectangle was the most unstable. The interaction between ligand **11** and **12** is more favourable than the one between **10** and **12**, because the methoxy groups of **11** can coordinate to the zinc(II) ion and further stabilize its octahedral geometry. On the other hand, comparing **15_T** and **13_{RL}** structures, the different length of the ligands **10** and **11** caused a distortion of the geometry at the metal ions of **15_T** making it more unstable. The relative stability can be summarized as: **13_{RL}**>>**15_T** >**14_{RS}**, **13_{RL}** being the most stable structure. However, the final outcome of the reaction is not determined by the individual energy of a species, but instead by the total energy of the ensemble. Since the authors added the same amount of ligands **10** and **11**, the same amount of **13_{RL}** and **14_{RS}** was generated. **13_{RL}** and **14_{RS}** altogether are more unstable than **15_T**, as a result they dynamically rearrange into the trapezoid form (**15_T**) to gain stability.

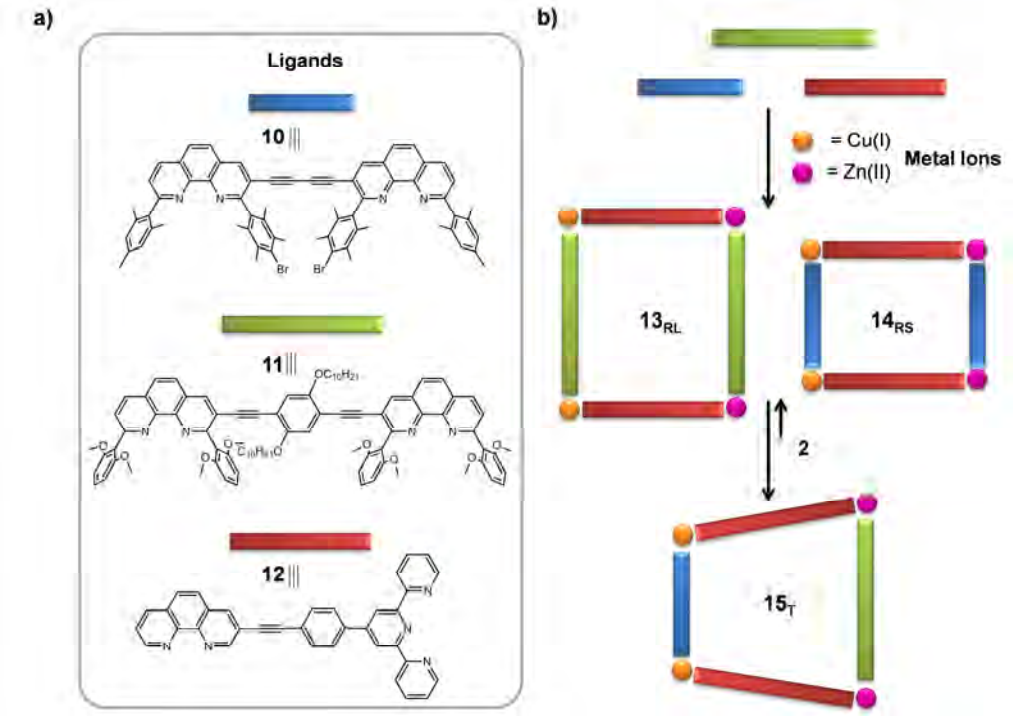

Scheme I.7. Ligands **10**, **11** and **12** (**a**) used for the preparation of the self-sorted supramolecular trapezoid **15_T** (**b**).

I.2.2 Three-dimensional polyhedra and cages

Three dimensional structures involve more sophisticated systems, in which many more building blocks can participate and consequently many more combinations are possible. As complexity increases, further factors can influence the assembly reaction.

Molecular spheres reflect the degree of complexity that metal-driven self-assembly has reached. In 2004 Fujita reported the synthesis of a 36-component sphere-like nanocapsule ($M_{12}L_{24}$, **17**).[45] The coordination sphere **17** was obtained by mixing the banana-shape ligand **16** with $Pd(NO_3)_2$ in DMSO at 70ºC for 4h (see Figure I.3). More recently, the same authors synthesized $M_{24}L_{48}$ giant coordination spheres **19**, containing 24 palladium(II) ions and 48 curved ligands (**18**a-c).[46] The ligands used were analogous to ligand **16**, only differing in the substitution of a sulphur atom by an oxygen atom. Surprisingly, such a small modification on the ligand caused an incommensurable difference at the molecular level. The spheres radii increased from 3.5 nm ($M_{12}L_{24}$) to 5 nm ($M_{24}L_{48}$). The difference in the output molecule was explained by the slight difference in the ligand bend angle. More interestingly, when the synthesis was performed by mixing $Pd(NO_3)_2$ with a 1:1 mixture of ligands **16** and **18**, the system self-organizes towards the exclusive formation of a $M_{24}L_{48}$ sphere and no mixtures of **17** and **19** were observed. By changing the **16**/**18** ratio it was possible to switch from sphere **19** to sphere **17**. Afterwards, a more robust sphere analogous to **17** was obtained by using platinum(II) ions as metal nexus, and using coordinating solvents such as 2,2,2-trifluoroethanol (TFE) to temporarily labilize the platinum(II)-pyridine coordination bond.[47]

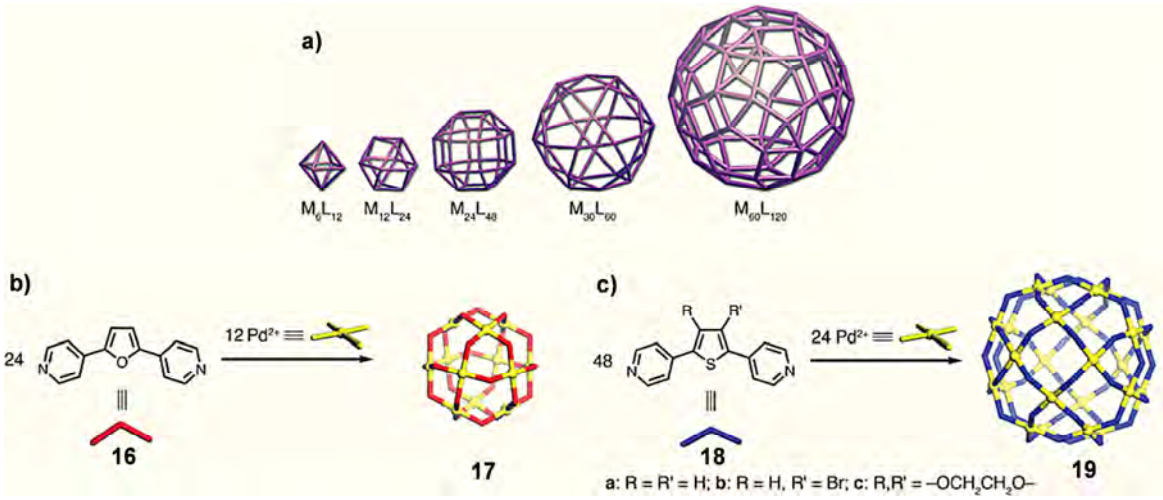

Figure I.3. a) Family of M_nL_{2n} polyhedra where the metals are located in the vertices and bridging ligands (**16** and **18**) on the edges. **b**) Self-assembly of $M_{12}L_{24}$ sphere **17** and **c**) Self-assembly of $M_{24}L_{48}$ sphere **19**. From [Ref. 46]. Reprinted with permission from AAAS.

There are supramolecular structures which are able to respond to external stimuli, for instance by changing their structure, this feature allows researchers to approach more complex biomolecular systems. In 2012 Nitschke reported the synthesis of a chemical system which was

able to structurally rearrange, upon interacting with an anionic species giving a tight binding pocket able to encapsulate a different anion (see Figure I.4).[48,49]

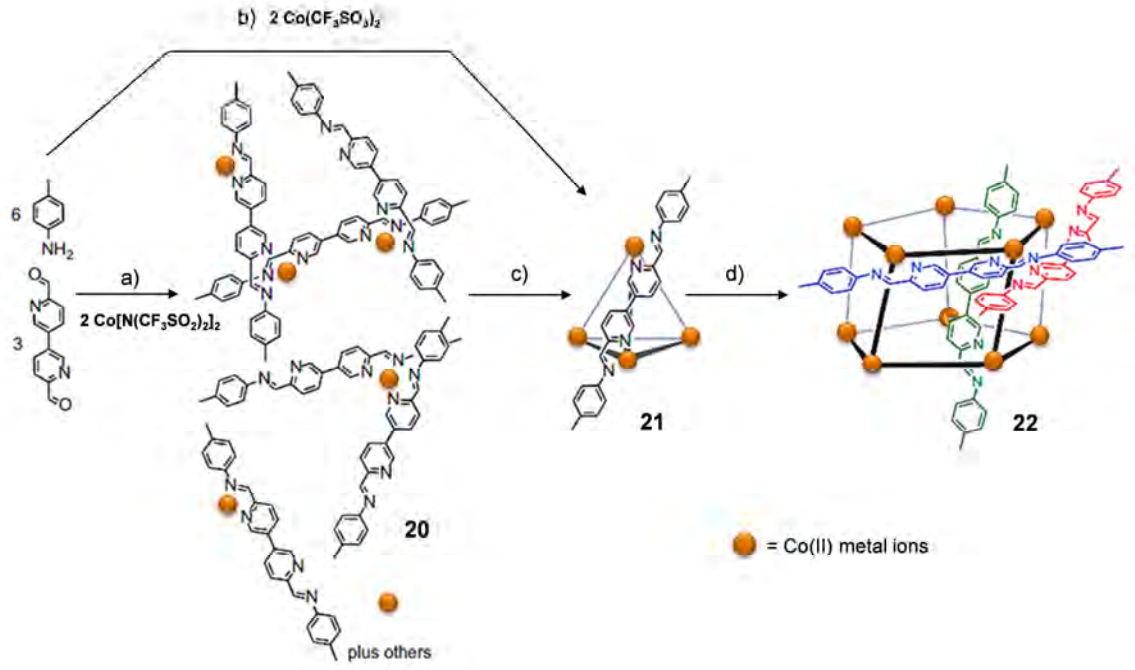

Figure I.4. States during the chemical system: 6,6'-diformyl-3,3'-bipyridine, *p*-Toluidine and cobalt(II)-triflimide react to form a complex dynamic library of interconverting coordination complexes (**a**). Tetrahedral **21** can be prepared either by direct subcomponent self-assembly (**b**) or though templation on the addition of triflate or hexafluorophosphate anions to dynamic library **20** (**c**). The addition of $LiClO_4$ to **20** or **21**, caused the quantitative conversion to a $Co_{10}L_5$ pentagonal prism **22**. Adapted by permission from Macmillan Publishers Ltd: [Nature Chemistry] (Ref. 48), copyright (2012).

When *p*-toluidine, 6,6'-diformyl-3,3'-bipyridine and cobalt(II) triflimide hydrate, ($Co[N(CF_3SO_2)_2]_2.H_2O$), were mixed in acetonitrile the dynamic library **20** was obtained. If cobalt(II) triflate hexahydrate, ($Co(CF_3SO_3)_2 \cdot 6H_2O$), was used, the tetrahedral nanocage **21** (Co_4L_6) was directly obtained. The triflate counterion acted as a template molecule and consequently as a driving force for the reorganization of the dynamic library (**20**).The addition of $NaCF_3SO_3$ to **20** resulted in the formation of **21**. When complexes **20** or cage **21** were reacted with $LiClO_4$, structure **22** was obtained. Barrel-like architecture **22** ($Co_{10}L_{15}$) comprises of two parallel CoL_5 pentagonal rings (slightly twisted), in which each cobalt atom of the ring is linked by an axial ligand. This connection between the upper and lower rings creates five potential anion binding pockets. A channel surrounded by the ligands and the ClO_4^- anions generate a sixth binding site, which is occupied by a chloride anion (from the medium). Three main factors favoured the formation of cage **22**: (1) each perchlorate anion is surrounded by four cobalt(II) ions, which leads to an electrostatic attraction and stabilization, (2) meridional coordination environment is more favourable than facial coordination for a high-spin *tris*(pyridylimine)cobalt(II) and (3) electron-poor pyridine units and electron-rich toluidine groups were closer in this structure, which facilitates the interaction between them and further stabilizes

the structure. This study shows how different anions play important template roles in the interconversion between species **20**, **21** and **22**. It is important to highlight that the cylindrical shape of **22** is a promising candidate to be used as a model for ion channels in membranes.

The introduction of building blocks bearing chemical functionalization into 3D coordination architectures is an attractive strategy to design functional structures. Recently Stang and co-workers reported the synthesis of rectangular-prismatic coordination cages of different sizes, which contain two *meso*-substituted tetrapyridyl-zinc(II)-porphyrins (Zn-**TPyP**) and dicarboxylate linkers that are held together by *cis*-capped platinum(II) complexes (see Scheme I.8).[50,51] The authors were interested in porphyrin molecules since they are related to the ubiquitous chlorophyll found in natural light-harvesting systems.[52,53] Porphyrins have been incorporated in multiple 3D supramolecular architectures for different fields applications (photosynthesis, molecular electronics, catalysis, *etc.*).[54]

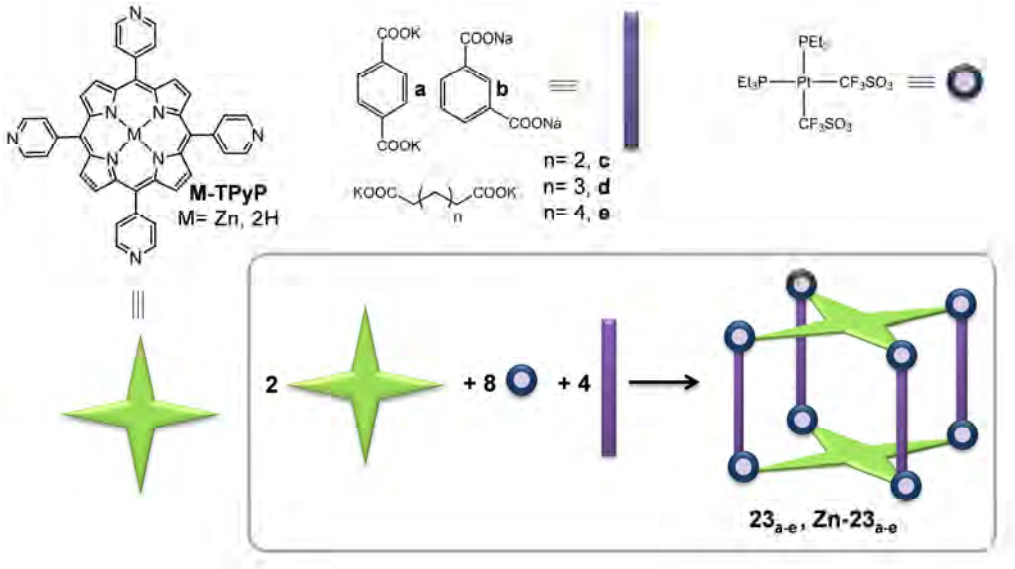

Scheme I.8. Self-assembly of the heteroleptic 3D tetragonal prism **23$_{a-e}$** (M=H) and **Zn-23**$_{a-e}$ (M=Zn).

The three-component self-assembly was performed in a mixture of solvents due to the different solubilities of the building blocks. After mixing the platinum(II) acceptor, with the ditopic carboxylate linker and Zn(II)-**TPyP**, in a 8:4:2 ratio for 1h at 65ºC, the heteroleptic capsules **23a-e** were formed as a sole reaction product. Energetically the heteroleptic species were more favoured than the homoleptic ones. The higher stability of the heteroleptic cage was rationalized by a charge separation phenomenon. One neutral pyridyl residue (donor) and a negative carboxylate group are coordinated to each platinum(II) centre, therefore the charges are separated and the electrostatic repulsion reduced.

I.2.3 Applications of coordination capsules

The development of three dimensional coordination architectures has drawn the attention of many chemists due to the multiple potential applications they can offer. Their isolated cavities create a unique environment and geometric constraint which can be selectively functionalized and thus provide different interactions from the bulk solution. The wide range of applications that 3D coordination capsules confer, can be classified in four main categories: molecular recognition, reactivity modulation, molecular sensors and biological applications. This thesis will mainly focus on the two first categories.

I.2.3.1. Molecular recognition

Molecular flasks can be designed in order to encapsulate a target molecule (selectivity), by means of host-guest interactions. Thus, depending on the size and chemical nature of the cavities, these supramolecular receptors will be able to selectively recognize compatible substrates.

One very interesting example is the use of coordination cages to encapsulate contaminant molecules. There are examples of nanocapsules able to selectively sequester polycyclic aromatic hydrocarbons (PAHs), which constitute an important group of environmental pollutants.[55,56] Strikingly, in 2011 Nitschke synthesized a coordination capsule able to encapsulate and store sulfur hexafluoride (SF_6), the most potent green-house gas known (Figure I.5).[57]

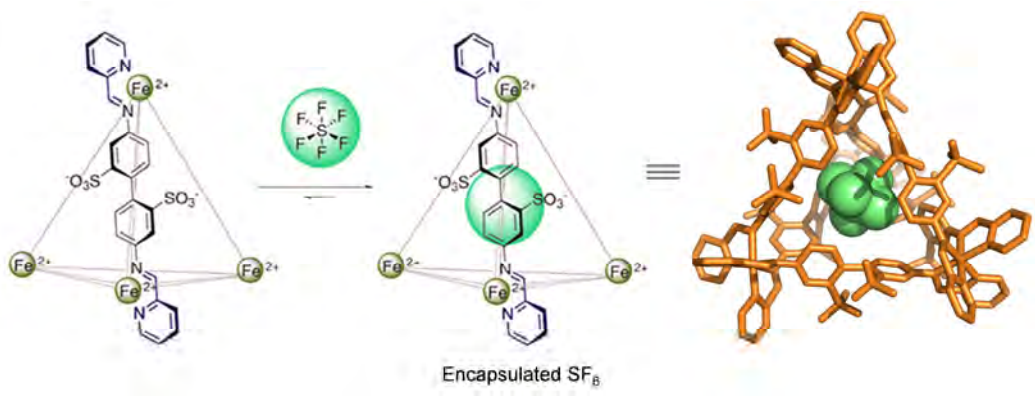

Figure I.5. Sequestration of SF_6 green-house gas. On the right representation of the ordered portion of the X-ray crystal structure of encapsulated SF_6. Adapted from {Ref. 57} with permission of The Royal Society of Chemistry.

The use of coordination cages for the encapsulation of anionic molecules is also interesting since many relevant biomolecules are anionic.[58] Nanocapsules can also be applied in the encapsulation of substrates with high economic value.[59] Interestingly, coordination cages permit the selective separation of specific molecules from mixtures of different species, taking advantage of different binding affinities. For example, capsules can be used to selectively separate fullerenes from mixtures containing differently sized fullerenes and carbon allotropes (Chapter I.3).

I.2.3.2. Reactivity modulation

Capsule-like receptors are able to modify the reactivity of the molecules they are hosting. There are coordination 3D cages able to stabilize highly reactive chemical species or unstable reaction intermediates,[60–63] as well as to suppress undesired reaction pathways.[64] In this context, Nitschke reported in 2009 the use of an iron(II) based tetrahedral container, which was able to encapsulate and stabilize, a single molecule of white phosphorus (P_4).[65] White phosphorus spontaneously combusts when it is exposed to air. The stabilization of the P_4 molecule achieved upon encapsulation is a result of the constraints applied by the confining capsule, which prevents the formation of the oxidized product which would be too large for the cavity. Moreover, the phosphorus could be released from the cage in a controlled fashion.

Supramolecular cages can also influence a chemical reaction just by providing an isolated cavity of particular size and shape. A number of stoichiometric organic reactions such as cycloadditions or olefin photodimerization have been performed inside 3D coordination cages.[66–68] Higher efficiencies in comparison to the analogous reactions performed in the bulk solution were observed, as well as different selectivities.

Most supramolecular cages have been designed in order to mimic the cavity features of active sites of natural enzymes; these cages can function as enzyme mimics to catalyze multiple reactions. In Chapter I.4, some relevant examples of coordination cages for enzyme-like catalysis will be discussed.

I.2.3.3. Molecular sensors

Several research groups have developed nanocapsules which can be used as molecular sensors. The host-guest interaction can be measured by a chemical or physical change on the receptor that in some cases can be easily observed. For instance, Fujita synthesized a Ru(II) based capsule that is able to encapsulate molecules of adamantane, which was used as a colorimetric sensor.[69] Whilst a solution of the empty cage is orange, inclusion of the guest molecule within the cage caused a colour change to red due to a change in the electronic properties of the cage. Another example was reported by Clever who synthesized a palladium(II) coordination cage which suffered structural rearrangement upon anion encapsulation, therefore acting as an anion sensor.[70] This structural change was proven to be useful for the uptake and release of anionic molecules. One further interesting example was reported by Stang who developed fluorescence sensors.[71] Trigonal-prismatic cages based on 1,3,5-tris(4-pyridyl ethenyl)benzene ligands and dinuclear ruthenium arene metallo-linkers were synthesized. The fluorescence emission of these electron-rich capsules was quenched upon addition of electron deficient nitroaromatic substrates.

I.2.3.4. Biological applications

The use of coordination capsules for biological and medical applications is a developing field of research.[72,73] Many research groups have become interested in the design of drug carriers. In these systems, a biologically active compound is confined within a capsule, in order

to protect it from the environment. Then the encapsulated molecule is carried to a specific location in the organism, where it can be liberated upon application of an external stimulus. One relevant example was reported by Therrien in 2010, in which spacious hexanuclear ruthenium(II)-prisms were used to strongly encapsulate $M(acac)_2$ complexes (acac = acetylacetonate and M= platinum or palladium) in water (Figure I.6).[74] The cytotoxic activity of these host-guest adducts was tested in ovarian cancer cells. The capsules allowed non-water soluble $M(acac)_2$ to be taken up by cancer cells. A different example was reported by Crowley concerning the synthesis of a discrete dipalladium(II) molecular cage able to encapsulate two molecules of *cis*-platin which is one of the most used drugs for cancer chemotherapy.[75] The cage was stimuli-responsive and was reversibly assembled-disassembled in order to release the encapsulated drugs.

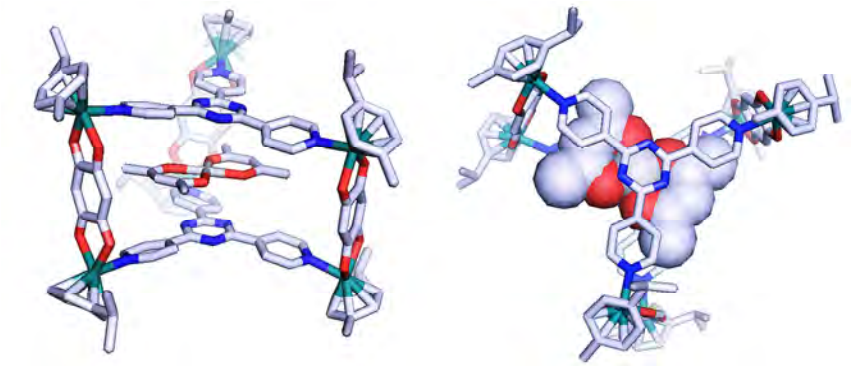

Figure I.6. Front and top view of the crystal structure of the encapsulated $Pt(acac)_2$ molecule reported by Therrien.

I.3. Host molecules for fullerene recognition

Several examples of molecular receptors, including three-dimensional nanocapsules, have been prepared in order to separate fullerenes in a selective manner (molecular recognition). The purification of fullerenes is essential to facilitate the exploitation of these molecules as will it be explained hereafter.

Fullerenes are the third most stable allotrope of carbon and in contrast to graphite or diamond, that are infinite extended arrays, fullerenes are spherical discrete molecules which contain a defined number of atoms. Consequently fullerenes are soluble in various organic solvents, an essential requirement for chemical manipulations. These spherical molecules were first observed experimentally by Kroto and Smalley in 1985.[76] The finding of fullerenes opened a gateway towards the discovery of other carbon nanoforms such as carbon nanotubes, graphene, nano onions, peapods, *etc*.

Fullerenes are highly symmetric molecules built up of fused pentagons and hexagons. The pentagon units are responsible for their curved shape. The smallest stable and most abundant fullerene is C_{60}, which has the shape of a soccer ball. The second most stable is C_{70} followed by higher fullerenes C_{74}, C_{76}, C_{78}, C_{80}, C_{82}, C_{84}, and so on.

The next breakthrough after the discovery of fullerenes was their production on a multi-gram scale by Krätschmer and Huffman, opening the fullerenes world towards potential chemical derivatization. Their method was based on the evaporation and recondensation of graphite using an arc-discharge method to give predominantly C_{60}, although C_{70} was also generated at levels of few per cent.[77] Nowadays fullerenes can be prepared on the ton scale.[78]

Fullerene structure is based on an extended π-system, containing carbon atoms with a sp^2 hybridation, and their reactivity is typical of an electron deficient olefin.[79,80] Fullerenes undergo a variety of chemical reactions, especially organic cycloadditions reactions that give stable and characterizable adducts. On one hand, exohedral functionalization of fullerenes (i.e. phenyl-C_{61}-butyric acid methyl ester (PCBM)) allows the acquisition of more soluble fullerenes and to combine the outstanding properties of fullerenes with the those from the functionalization molecules.[81,82] Additionally, fullerenes have been combined with other elements in their inner spaces giving rise to large families of endohedral fullerenes (fullerenes containing an atom, a cluster or a molecule in their inner cavity) such as $Sc_3N@C_{80}$.[83,84]

Fullerenes and their derivates present a wide range of applications highlighting their use in materials science (polymers,[85] thin films,[86] liquid cristals,[87,88] *etc*),[89] electroactive materials in solar cells,[90] superconductivity[91] and biological applications[92,93]. However, all these applications are limited in origin by the selective purification of fullerenes.

The crude product generated from the evaporation of graphite to obtain fullerenes, contains mixtures of fullerenes of different sizes, as well as other carbon allotropes such as carbon nanotubes and amorphous forms of carbon. The first examples reported for the

purification of fullerenes were based on controlled sublimation of the carbon soot.[94] Another common method to separate fullerenes from soot is by extraction with organic solvents.[95,96] Soxhlet extraction with toluene is the preferred extraction method. A different option is purification by crystallization which is inexpensive, although only gives moderate yields.[97] Currently, chromatographic techniques are predominantly used for the purification of fullerenes. Alumina,[98,99] graphite,[100,101] activated carbon,[102] polystyrene gel[103,104] or γ-cyclodextrines[105] have been used as stationary phases. In spite of the fact that efficient columns for the HPLC separation of fullerenes are available (COSMOSIL columns), most of the methods mentioned here require enormous amounts of solvent and can cause fullerene decomposition or irreversible absorption of fullerenes within the stationary phase. Furthermore, these methods are often tedious, energy and time-consuming, and generally, it is difficult to achieve high selectivities.

The use of molecular receptors for fullerene separation in solution has emerged as an attractive alternative since it allows potential selectivity, no specific equipment is required and ideally, recyclable hosts can be designed. Additionally, the encapsulation promotes the solubilisation and chemical modification of fullerenes. It also facilitates the selective extraction of higher fullerenes and their chiral resolution.[106]

In order to design a molecular receptor for the separation of fullerenes, the most important factor to take into account is the complementarity between the host and the fullerene (Chapter I.1.2). For this reason, the majority of molecular hosts for fullerenes described so far are based on extended π-systems because of their high affinity towards the spherical geometry of fullerenes. Another factor to consider when designing a fullerene receptor is the structural and electronic tunability of the container. This is an important feature that allows higher selectivity towards a specific fullerene to be reached for a particular higher-fullerene or an endohedral-fullerene. Finally, it is indispensable to design a system capable of liberating the sequestered fullerenes easily, in order to obtain reusable receptors and to recover the fullerene (reversible process).

Herein some examples of relevant fullerenes receptors will be described. In this Chapter the attention has been focused towards receptors having cage-like structures. Nevertheless, some examples in which the 3D cage structures are more diffuse, but are deemed interesting in the context of this thesis will also be discussed.

I.3.1 Fully organic cage-like receptors

Ringsdorf and Wennerström reported the first examples of molecular receptors for fullerenes in 1992, complexing fullerenes using aza-crown compounds and γ-cyclodextrins.[107,108] Since then, a number of fully organic receptors have been developed making use of different supramolecular or covalent strategies. For example, arene based receptors such as cyclodextrins (CD),[109] calixarenes[110–112] and cyclotriveratrylenes (CTV's)[113] have proven to be efficient receptors for fullerenes, especially when two or more of these units

are associated, through the formation of cage-like receptors (*vide infra*). There are also arene-based fullerene receptors such as cycloparaphenylenes or carbon nanotubes (CNTs), which give rise to peapod structures.[114–116] Another relevant example was reported by Martín who used π-extended derivates of tetrathiafulvalene (exTTF) to wrap around different fullerenes.[80,117–119] Multiple examples of fully organic fullerene receptors have been reported so far and as such an extensive account is beyond the purpose of this introduction. Herein attention will mainly focus on fully organic receptors having a cage-like structure.

With the aim of encapsulating fullerenes, Mendoza prepared a nanocapsule (**25**) by self-assembly, utilizing hydrogen bonding between two CTV (**24**) units that were modified with three high-affinity hydrogen-bonding units (1,1'-carbonyldiimidazole) (Scheme I.9). This nanocapsule presents affinity towards C_{60} (K_a (C_{60})= $1.82 \cdot 10^3$ M^{-1}) and C_{70} (K_a (C_{70})= $3.89 \cdot 10^4$ M^{-1}).[120] The higher affinity towards the C_{70} was rationalized through an improved hydrogen-bonding interaction among the CTV units giving rise to a more stable host-guest adduct. The addition of a few drops of trifluoroacetic acid (TFA) to a host-guest adduct in solution caused the hydrogen-bonded network to break and the fullerenes to precipitate. Interestingly, the host could be partially recycled (50% of the cage was lost after two cycles) and the fullerenes easily recovered. Moreover higher fullerenes (C_{76}-C_{84}) could also be extracted from fullerite, likely because of the flexibility and adjustability of the capsule around larger guests.[121]

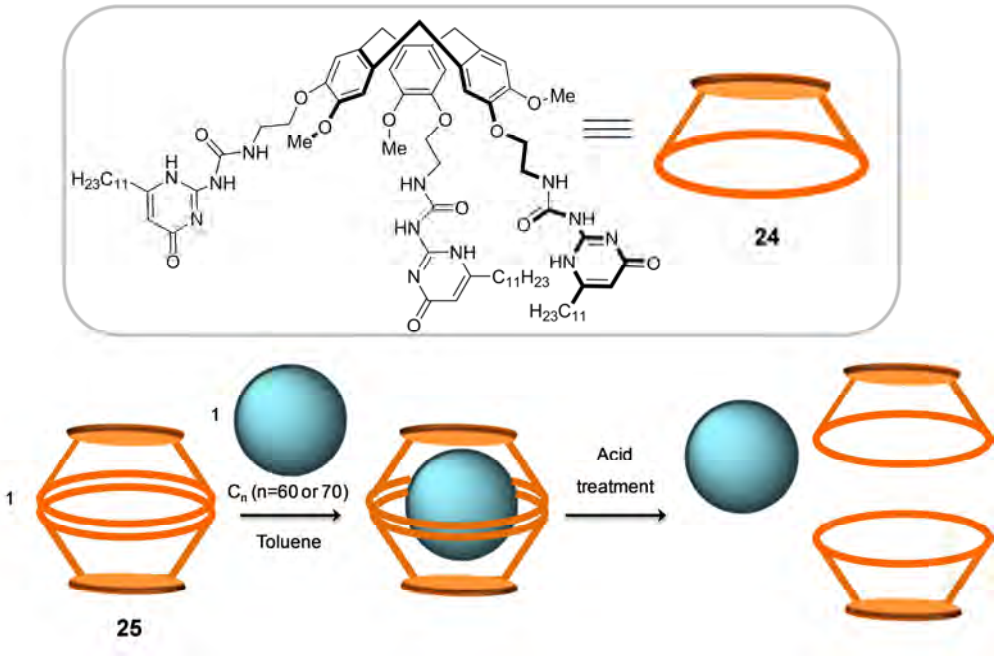

Scheme I.9. Top: CTV unit (**24**) used for the preparation of the supramolecular capsule **25** reported by Mendoza. Bottom: reaction scheme for the encapsulation and liberation of C_{60} and C_{70} fullerenes.

The suitability of dimeric CTV cage-like structures for fullerene separation was further exemplified by Chiu who synthesized a cage formed by two covalently linked CTV units (**26**) (Scheme I.10). Zig-zagging alkyl chains were chosen as spacers in order to minimize the energy cost of structural reorganization during the guest binding event. Notably, receptor **26** is

able to encapsulate C_{60} and C_{70} fullerenes at room temperature.[122] The cage favours the formation of the hemicarceplex bound to C_{70} in presence of C_{60} and therefore, the system was able to be applied in the isolation of C_{70} from fullerene extracts. To a solution of **26** in tetrachloroethane (TCE), fullerene extract was added and the mixture was heated to 313 K for 16h, thereafter host-guest adducts with the C_{70} fullerene were exclusively formed. Finally, to recover the encapsulated C_{70} the host-guest adducts were dissolved in toluene and the solution was heated to 303 K and after 12h the hemicarcerand precipitated as a solid and the toluene solution mainly contained C_{70} and residual C_{70}⊂hemicarceplex.

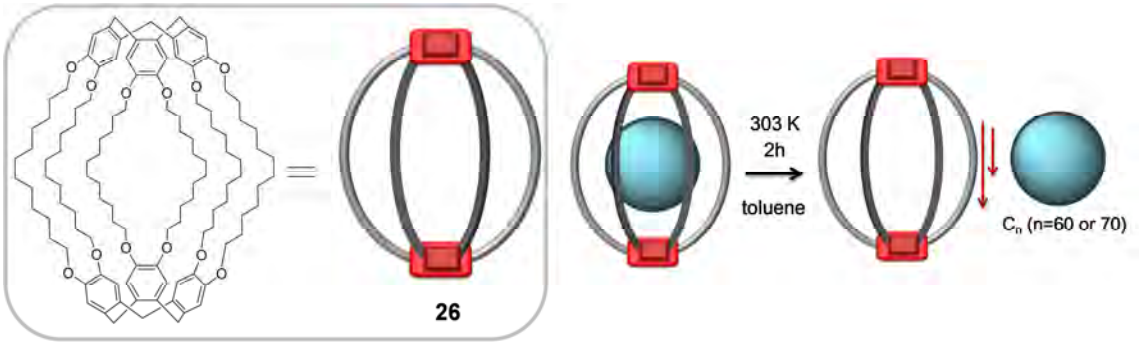

Scheme I.10. Chemical structure of the CTV-based molecular cage **26** reported by Chiu. Schematic representation of the dissociation of the fullerene caused by prolonged heating.

Very recently it was demonstrated that capsule **26** was also able to encapsulate $Sc_3N@C_{80}$ metallofullerene, under solvent-free conditions. $Sc_3N@C_{80}$ exhibits two structural isomers D_{5h} and I_h.[123] The lack of solubility of these higher fullerenes makes their isolation and characterization challenging tasks. Moreover, the lack of hydrogen atom presence in their structure prevents their study by ^{1}H-NMR. Consequently, ^{13}C-NMR, a less sensitive technique, is the most widely used technique for directly identifying the fullerene isomers. When $Sc_3N@C_{80}$ was sequestered inside cage **26**, its solubility in TCE was increased by approximately 50 times, which allowed for its characterization by ^{1}H NMR. However, the solubility was still too poor to permit its characterization by ^{13}C-NMR. The authors therefore decided to synthesise the more soluble cage **27** which contained three succinic diester linkages (Figure I.7). The enlarged cage **27** was able to encapsulate $Sc_3N@C_{80}$ and a crystal structure was obtained for the [$Sc_3N@C_{80}$]⊂**27** adduct, which confirmed the Russian doll (Matryoshka)-like multilayer structure. Remarkably, when $Sc_3N@C_{80}$ was encapsulated within cage **27**, its solubility in TCE was 200 times greater than that of the free endofullerene, allowing its characterization by ^{13}C-NMR. The ^{13}C-NMR spectrum corresponding to [$Sc_3N@C_{80}$]⊂**27** allowed for identification of the hemicarceplexes of both $Sc_3N@D_{5h}$-C_{80} and $Sc_3N@I_h$-C_{80} isomers, which appear in a 1:4 ratio respectively. Moreover, the ^{1}H-NMR spectrum also displays two set of signals of the aromatic carbon nuclei of the CTV units in the same 1:4 ratio.

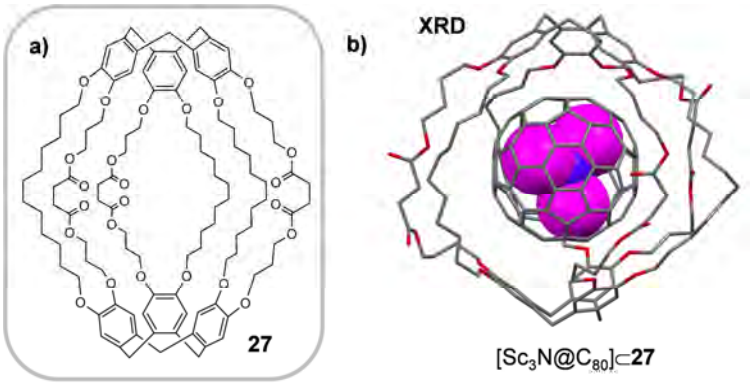

Figure I.7. a) Chemical structure of soluble hemicarceplex **27** and **b)** representation of the solid state structure of the $[Sc_3N@C_{80}]\subset$**27** host-guest adduct (hydrogens are omitted for clarity).

Another example of an organic covalent nanocapsule was reported by Zhang, who developed a shape persistent capsule containing non-metalated porphyrin units.[124] The rectangular prismatic cage (**29**) was synthesised *via* alkyne metathesis of two tetrasubstituted porphyrins (**28**). Interestingly, the cage forms 1:1 complexes with C_{60} and C_{70} fullerenes, when the cage is mixed with fullerenes in toluene at room temperature (Scheme I.11). It is well known that there is a favoured donor-acceptor interaction between porphyrins and fullerenes (*vide infra*). The rigidity of host **29** along with its combination of conjugated systems results in a cage with a higher affinity towards C_{70} ($K_a = 1.5 \cdot 10^8\ M^{-1}$) compared to C_{60} ($K_a = 1.4 \cdot 10^5\ M^{-1}$) and this is one of the highest association constants reported so far for a fully organic fullerene receptor. The significant difference in affinity of the cage towards C_{70} over C_{60} prompted the authors to investigate the separation of C_{70} from fullerene mixtures and to study the controlled liberation of the fullerene as well as recovery of the cage. Remarkably, fullerene association-dissociation was reversible and controlled by changing the pH of the media, which arises from the protonation-deprotonation of the porphyrin which caused the release of the fullerene. The authors optimized the isolation process in three steps: i) the cage is added to a C_{60}/C_{70} (10/1) solution in CS_2, and sonicated for 30 seconds; ii) then the host-guest adducts are collected in a chloroform solution, whereby upon addition of 100 equivalents of TFA to the chloroform solution, the fullerene molecules (mainly C_{70}) are released as a black precipitate and removed. Once a cycle of the isolation process was completed, the abundance of C_{70} increased from 9 mol% to 79 mol%. iii) in a final step the nanocapsule was recovered by the addition of 100 equivalents of triethylamine (TEA) to the remaining chloroform solution.

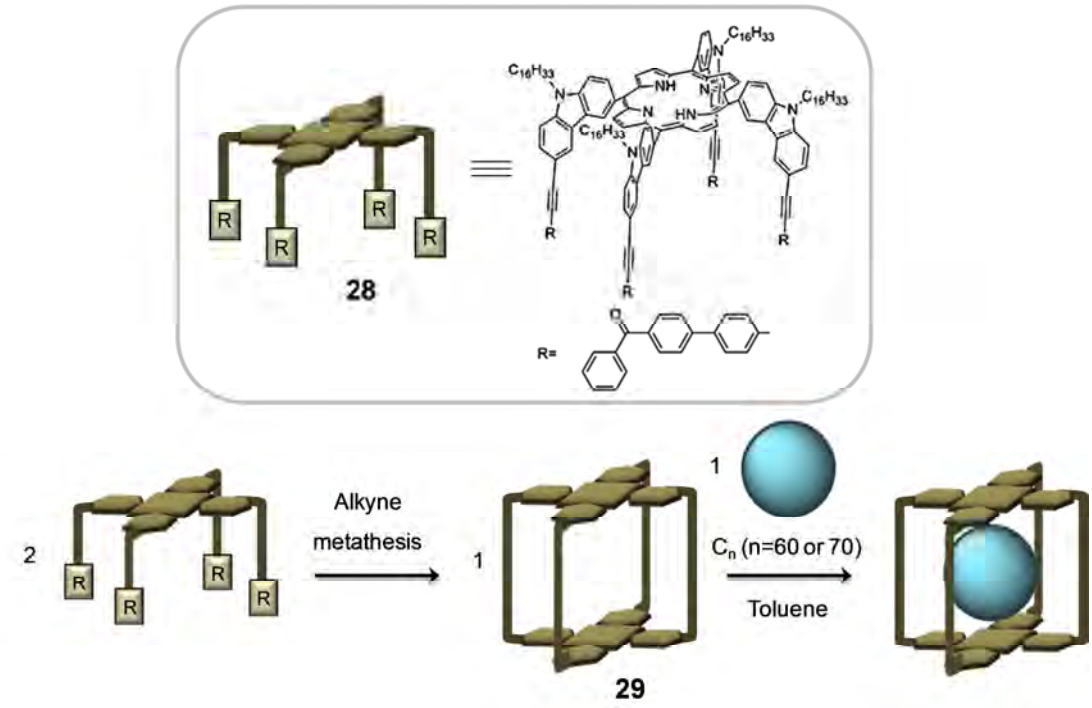

Scheme I.11. Top: tetra-substituted porphyrin (**28**), used for the preparation of covalent capsule **29** reported by Zhang. Bottom: schematic representation of the construction of capsule **29** by alkyne metathesis, and subsequent encapsulation of the fullerene.

I.3.2 Metal-containing cage-like hosts

I.3.2.1. Metalloporphyrin-based covalent receptors

Metalloporphyrins contain a large π-conjugated system, thus they tend to act as π-donor moieties. Conversely, fullerenes behave as π-acceptors and this electronic complementarity favours the interaction between these two molecules.[125] Nevertheless, this interaction is weak in solution and is difficult to visualize spectroscopically. For this reason, several examples of fullerene hosts containing two or more metalloporphyrin units have been reported in the literature, making attempts to enhance the strength of this fullerene-host interaction.[106]

One example of fullerene receptors bearing metalloporphyrins, was reported by Aida in 1999. The authors reported the synthesis of a covalent cyclic dimer of zinc(II) porphyrins (**30**) (Scheme I.12).[126] This cyclic host formed a highly stable 1:1 inclusion complex with C_{60} in benzene at room temperature ($K_a = 6.7 \cdot 10^5$ M^{-1}). When the inclusion complex was mixed with an equimolar amount of 4,4'-bipyridine (4,4'-bpy), the encapsulated C_{60} was released, leaving 1:1 adducts of zinc porphyrin coordinated to 4,4-bpy. Remarkably, in analogous experiments using C_{70} fullerene, an association constant 30 times larger than that of C_{60} (K_a (C_{70})~10^7 M^{-1}) was obtained. It appears that the C_{70} adopts a side-on conformation with respect to the two metalloporphyrin moieties in order to maximize the π-stacking interactions. With the intention to obtain more stable host-guest adducts, the authors modified the receptor structure by changing:

i) the porphyrin substituents, R, which could modify the π-basicity of the porphyrin or its conformation; ii) the linker parts (Z) in order to gain flexibility or rigidity (aliphatic or acetylenic chains); iii) the metal ions of the porphyrin moieties. It was observed that hydrogenated separators (Z) gave more flexible structures (**30$_a$** more flexible than **30$_c$**), and facilitated the host-guest interaction. Furthermore, when the porphyrin used contains a more concave conformation (i.e. β-pyrrole-substituted porphyrin, host **30$_b$**) the host-guest contact is improved. Finally it was observed that the metal ions which gave higher association constants are those belonging to group 9 of the periodic table. Strikingly, the rhodium(III) porphyrin dimer showed an affinity 100 times higher towards C_{60} and C_{70} than its zinc(II) analogue. [127] Further, in the case of the iridium(II) porphyrin cyclic dimer the association constant for C_{60} and C_{70} in benzene, was too large to be evaluated accurately ($K_a > 10^9$ M^{-1}). Studies in the solid state (XRD) and in solution (NMR), at low temperature, indicated that dynamic covalent bonds between the iridium(II) metal ions from the porphyrins and the π-electron-rich 6:6 junctions from the fullerenes were formed. This metal-fullerene interaction caused an ellipsoidal deformation of the C_{60} and an end-on orientation of C_{70} relative to the porphyrin units.[128] Finally, the authors successfully used the different binding ability of the hosts towards the fullerenes to perform the selective extraction of higher fullerenes (≥ C_{76}) from fullerene mixtures.[129,130]

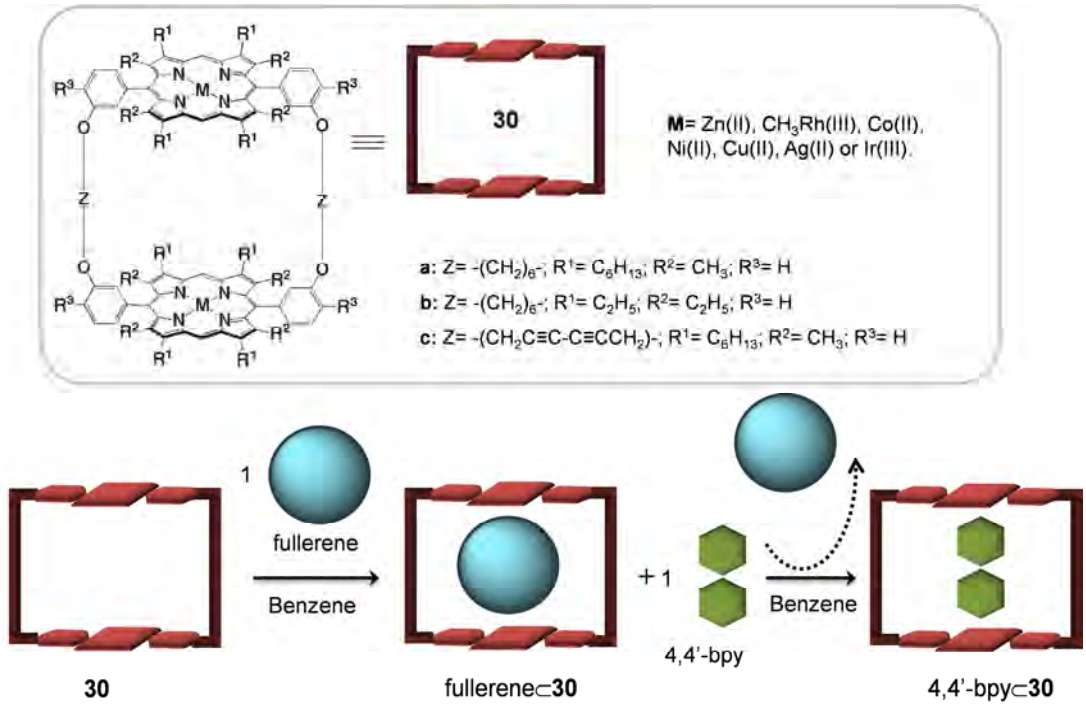

Scheme I.12. Top: molecular structure and formulae of metalloporphyrin dimer **30** reported by Aida. Bottom: schematic representation of the encapsulation of the fullerene and subsequent guest exchange with 4,4'-bpy.

The same authors further reported in 2011 the synthesis of a new cyclic receptor based on copper(II) or zinc(II) metalloporphyrins (**31$_{cyclo}$**), which could be transformed into the cubic-cage (**31$_{cage}$**) analogue by intramolecular ring-closing olefin metathesis (Scheme I.13).[131] Both structures were able to encapsulate La@C_{82} endofullerene in toluene at 25ºC (K_a ~10^6-10^7 M^{-1}).

The inclusion experiments using the cyclic receptors based on copper(II) paramagnetic porphyrins, showed ferromagnetic coupling with the paramagnetic La@C_{82} fullerene. However, a ferrimagnetic coupling was observed when the receptor was transformed into its cage analogue. This change in spin coupling was rationalized by the change in the geometry of the host-guest complex.

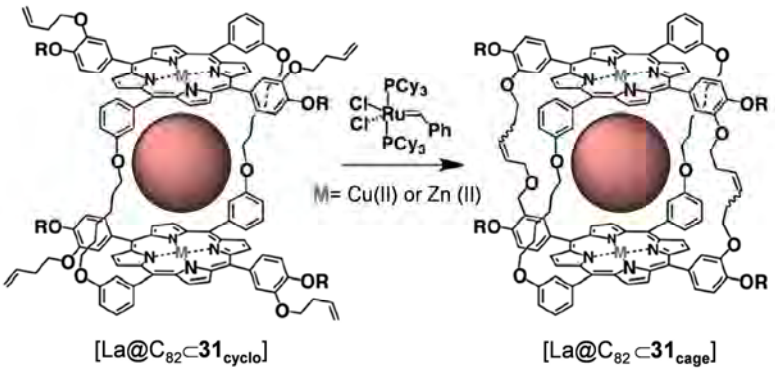

Scheme I.13. Representation of the molecular structure of [La@C_{82}]⊂**31**$_{cyclo}$ and [La@C_{82}]⊂**31**$_{cage}$, and their transformation by ring-close metathesis. Adapted with permission from (Ref. 131). Copyright (2011) American Chemical Society.

A different example of cyclic porphyrin dimers was investigated by Ballester. Cyclic covalent receptors were synthesized by dimerization of two non-*β*-pyrrole-substituted mono porphyrins, bearing four meso-aryl substituents (**32**) to give **33** (Figure I.8).[132] Subsequently, hydrogenation of **33** afforded the flexible cyclic dimer **34**. As Aida had observed previously in their receptors, the relative rigidity of the spacer units affected the shape and flexibility of the hosts and controlled their affinity towards different fullerene guests. Both receptors **33** and **34** form 1:1 host-guest adducts with C_{60} and C_{70} fullerenes at room temperature using toluene or dichloroethane as solvents. The more rigid receptor **33**, which bears fully unsaturated spacers (six carbon acetylenic chain), presented a relatively weak interaction with C_{70} ($K_{a(DCM)}$ ~ 10^4 M^{-1} and $K_{a(TL)}$ ~ 10^4 M^{-1}) fullerene and an unobservable interaction with C_{60} (K_a < 10^3 M^{-1}). On the other hand, the more flexible host **34**, containing fully saturated six-carbon linkers, forms more stable complexes with C_{60} ($K_{a(DCM)}$ ~ 10^4 M^{-1} and $K_{a(TL)}$ ~ 10^4 M^{-1}) and C_{70} ($K_{a(DCM)}$ ~10^5 M^{-1} and $K_{a(TL)}$ ~10^4 M^{-1}) due to better adaptability. The host-guest adducts with both **33** and **34** receptors, were also characterized in the solid state. In collaboration with Echegoyen the authors discovered that both dimers were also able to form inclusion complexes with $Sc_3N@C_{80}$ endofullerene (K_a ~ 10^5). For the first time, solid state structures were obtained for an endohedral fullerene bound to molecular *bis*-porphyrin receptors.[133]

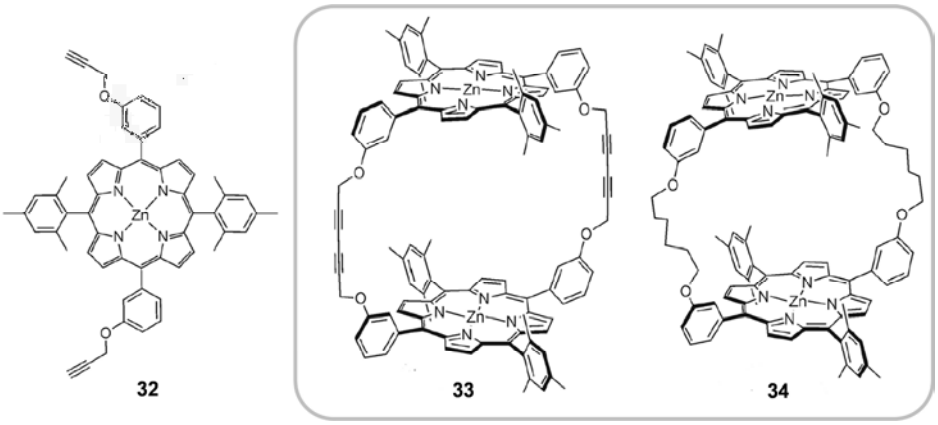

Figure I.8. Molecular structure of the substituted zinc(II) porphyrin **32** used by Ballester to prepare covalent dimers **33** and **34**. Reproduced in part from {Ref. 132} with permission of John Willey and Sons.

A different strategy was followed by Tani, who prepared a tubular structure able to encapsulate multiple fullerenes taking advantage of the rigidity of porphyrins (Scheme I.14). First, covalent cyclic nickel(II)-porphyrin dimers similar to those reported by Aida and Ballester were synthesized (bearing acetylenic chains **35**, or phenothiazine as spacers **36**). The porphyrins contained self-assembling pyridyl groups at opposite meso-positions. Afterwards, the cyclic dimers were linked by self-assembly of two kinds of cooperative non-covalent interactions: 1) a pair of complementarity C-N···N hydrogen-bonding interactions between the pyrrole β-CH and 2) π-π interactions between the pyridyl groups. The formation of 1:1 adducts between the porphyrin dimers and fullerenes C_{60} (K_a up to 10^6 M^{-1}) and C_{70} (K_a up to 10^7 M^{-1}) was confirmed in solution (toluene). In the solid state structure, the fullerene C_{60} was linearly arranged in the inner channel of the tubular structure.[134,135]

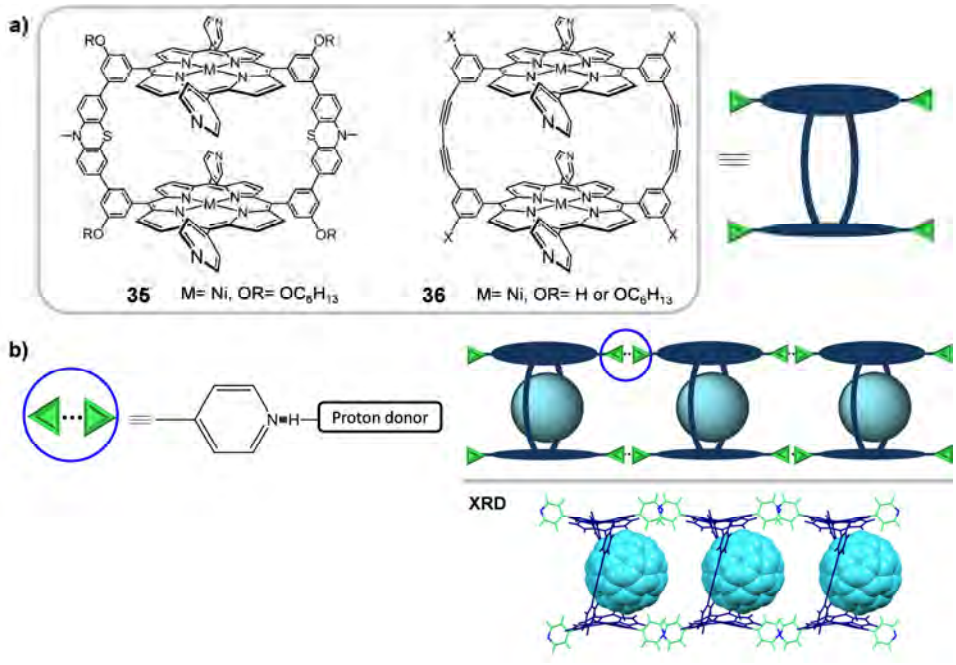

Scheme I.14. a) Chemical structures of cyclic porphyrin dimers **35** and **36**. **b**) Linear array of fullerenes within the self-assembled porphyrin nanotube (supramolecular peapod).

The association constant between fullerenes and porphyrins dramatically increased when using porphyrin dimers (*vide supra*) instead of a single porphyrin. In response, different research groups worked on the development of multiple-porphyrin systems with the aim of achieving even higher association constants.[136–138]

An interesting example was reported by Anderson who developed a cyclic porphyrin trimer which presented a high affinity for fullerenes (see Scheme I.15). The rigid cyclic porphyrin trimer (**37**) was synthesized by Sonogashira coupling of 3,4-iodophenethylamine and the alkyne-terminated linear porphyrin trimer. The linear porphyrin trimer was synthesized following a tedious synthetic protocol.[138] The trimeric receptor **37**, formed 1:1 host-guest adducts with C_{60} at room temperature in different organic solvents. The association constant for $C_{60}\subset$**37** in toluene was $(1.6\pm0.7)\cdot10^{6}$ M^{-1}. On the other hand, the inclusion compound with C_{70} was two orders of magnitude more stable than the one with C_{60} (K_a (C_{70})= $(1.6\pm0.7)\cdot10^{8}$ M^{-1}. The receptor also formed 1:1 adducts with higher fullerene C_{86} and La@C_{82} endofullerene, however, the adducts are too stable for the equilibrium constant to be calculated by UV-Vis or fluorescence titrations (K_a >10^{9} M^{-1}). The value obtained for the association constant between the cyclic trimer and C_{60} in toluene is slightly stronger than the ones obtained for zinc(II)-porphyrin dimers, indicating that the presence of the third porphyrin moiety has a positive effect on the affinity towards C_{60}. The effect of the third porphyrin is more relevant for C_{70} and higher fullerenes. The association constant of $C_{70}\subset$**37** is much higher than those reported for other zinc(II) porphyrin hosts and the association constant for $C_{86}\subset$**37** and La@$C_{82}\subset$**37** is still higher, therefore the larger size of the fullerene enables them to better interact with the three walls of the receptor, giving higher association constants.

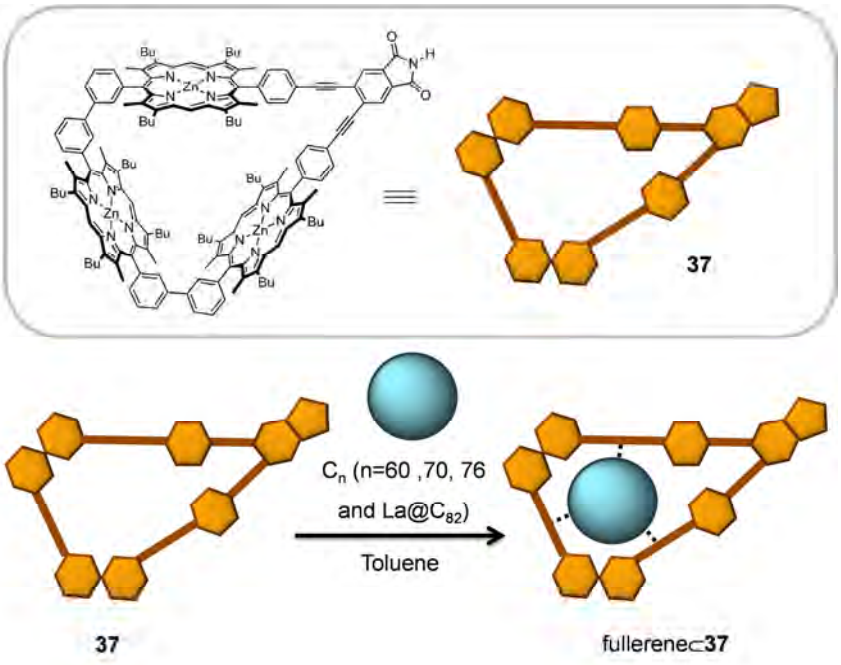

Scheme I.15. Top: Molecular structure and schematic representation of the cyclic porphyrin trimer synthesized by Anderson. Bottom: Representation of the inclusion of a fullerene within the receptor **37**.

With these results in hand Osuka, Shionokubo and Aratani further increased the number of porphyrin units in order to improve the fullerene-porphyrin interaction. The authors synthesized the nanobarrel **38** bearing four porphyrin units (Figure I.9 a), following a concise synthetic route. The addition of C_{60} to a solution of **38** in toluene, at room temperature, gave 1:1 inclusion adducts.[139] Unexpectedly, the association constant for C_{60}⊂**38** calculated from UV-vis titrations in toluene was $(5.3\pm0.1)\cdot10^5$ M^{-1}, which is certainly large, but slightly smaller than those reported for cyclic porphyrin dimers and Anderson's tetramer. The lower value for the association constant was rationalized by the high rigidity of this covalent receptor, which in this case is detrimental and certain flexibility could improve the porphyrin-C_{60} interaction. Nevertheless, the host-guest adduct structure was unambiguously confirmed by X-Ray diffraction studies (Figure I.9 b).

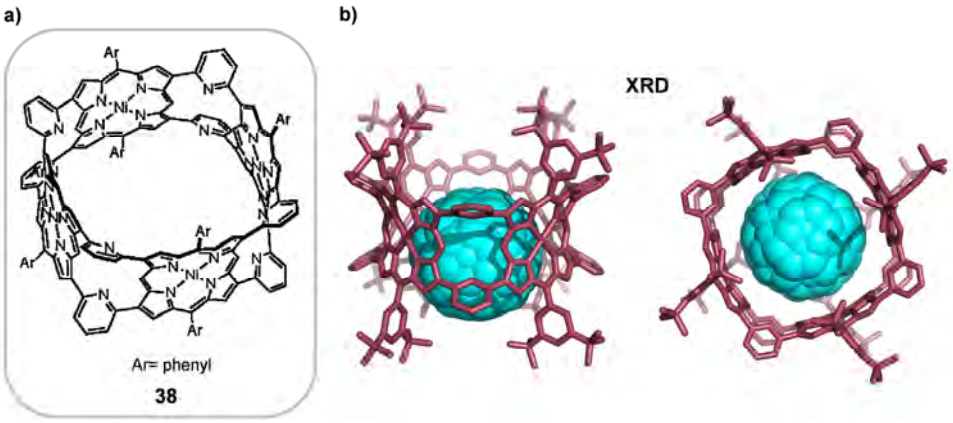

Figure I.9. a) Structure of nanobarrel **38**. **b)** Lateral and top view of the X-ray crystal structure of C_{60}⊂**38** (hydrogen atoms have been omitted for clarity).

I.3.2.2. Metalloporphyrin-based coordination capsules

It has been shown that when covalent-multiporphyrinc hosts are used to entrap fullerenes in solution, the association constants dramatically increase compared with the acyclic analogues. However, the covalent synthesis of these receptors is tedious, synthetically complex and often low yielding. Moreover, highly rigid structures are usually formed which in some cases can be detrimental for the host-guest interaction.[139] On the other hand, dimeric porphyrin hosts linked by hydrogens-bonds have also been reported in the literature, but the K_a values observed are usually smaller than those of their covalent analogues.[140] With these precedents, metal-ligand coordination receptors bearing porphyrins appear to be a promising alternative. The metal-ligand interaction allows the construction of fullerene host molecules in a straightforward manner, and permits the fine tuning of receptor features, such as its geometry or solubility. For these reasons, the attention of several research groups has been directed towards the use of the coordination-driven self-assembly approach to build complex architectures containing metalloporphyrins for the encapsulation of fullerenes and herein, some examples will be highlighted.

Schmittel reported in 2008 the synthesis of an heteroleptic structure ($M_6L_2L'_3$) prepared by self-assembly through copper(I) ions (Scheme I.16). The reaction between $[Cu(CH_3CN)_4]PF_6$, and ligands **39** (L) and **40** (L'), gave nanocapsule **41** which contains three zinc(II)-porphyrin units, along with some undesired oligomeric aggregates. Subsequent addition of C_{60} to the product mixture provided an extra driving force which shifted the reaction equilibrium towards complete formation of the desired 3D nanocapsule, which contained the fullerene within its cavity ($C_{60}\subset$**41**).[141] In this example, fullerene C_{60} is not just a guest molecule but it also acts as a template leading to a more stable host-guest complex and avoiding the formation of the undesired oligomers. Interestingly, the encapsulation of C_{60} into nanocapsule **41** leads to atypical protons shifts and splitting in the ^{1}H-NMR spectrum. These changes were rationalized by a lateral distortion of the host, resembling an accordion, in order to maximize its interaction with the substrate molecule, leading to a constricted prism which strongly interacts with the fullerene (adaptive structure).

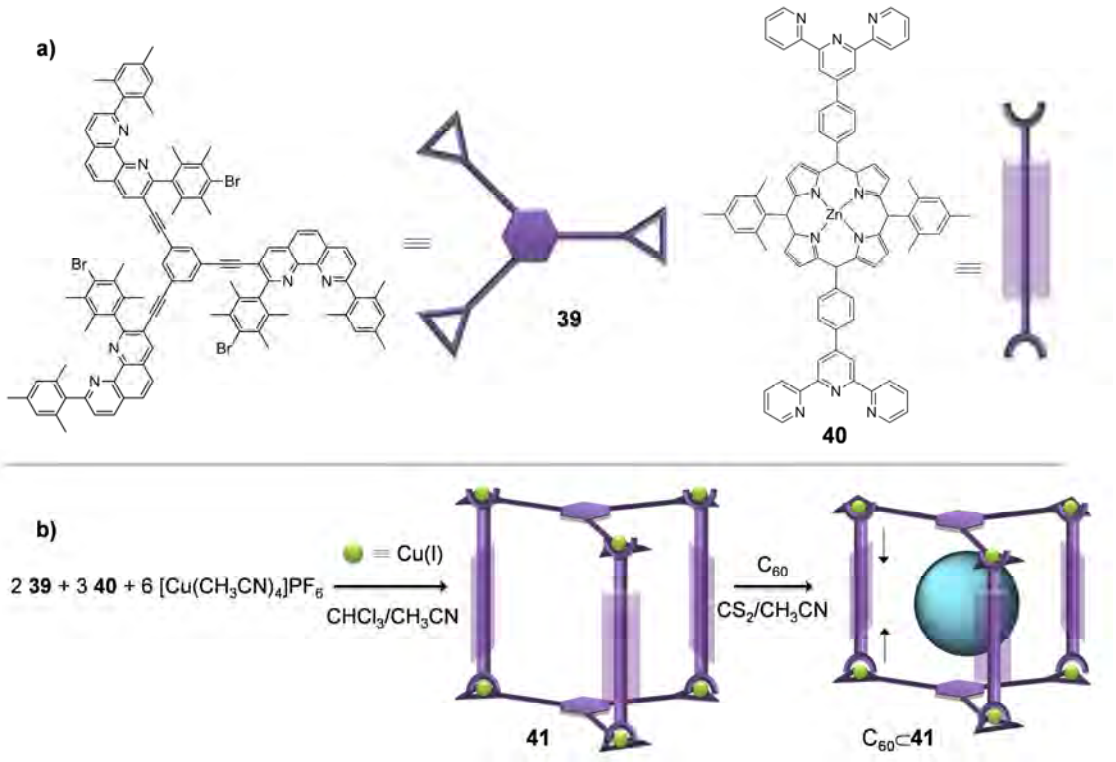

Scheme I.16. **a**) Ligands **39** and **40** used for **b**) the self-assembly of capsule **41**, which encapsulates C_{60} fullerene through its adaptive structure.

A similar strategy was used by Shionoya who reported another example of a metallocage in which the C_{60} fullerene acts as a template molecule, and helps to stabilize the desired product (see Scheme I.17).[142] To perform the metal-ligand directed self-assembly reaction the authors selected zinc(II), a metal centre with a versatile coordination sphere. Despite the variety of geometries that zinc(II) can adopt, by using coordinating counteranions and solvent molecules, and a proper template molecule (C_{60}), the authors were able to synthesize a discrete *tetra*-porphyrin structure ($[M_8L_4X_{16}]^{n+}$, where X =solvent molecule or *p*-

$CH_3C_6H_4SO_3^-$ (**42**)). Initially, the synthesis of cage **43** was attempted by mixing 4 equivalents of *tetrakis*-(bispyridyl)-porphyrin and 8 equivalents of Zn(*p*-$CH_3C_6H_4SO_3)_2$, in a 1:1 mixture of $CHCl_3$/MeOH. However, the major product of this reaction was a porphyrin trimer $[M_8\mathbf{42}_3X_{12}]^{n+}$, which was in equilibrium with the desired porphyrin tetramer $[M_8\mathbf{42}_4X_{16}]^{n+}$ (**43**). Finally, it was found that the addition of C_{60} was necessary to shift the equilibrium towards the formation of $C_{60}\subset$**43** adduct (75%). Single crystal X-ray diffraction analysis confirmed that $C_{60}\subset$**43**, is formed by four zinc(II) porphyrins wrapping around a single C_{60} molecule. The tetrameric barrel **43** was not formed when weakly-coordinating counterions were used (*i.e.* Zn$(CF_3SO_3)_2$). These results indicated that the *p*-$CH_3C_6H_4SO_3^-$ anions play a key role as capping ligands. Thus *p*-$CH_3C_6H_4SO_3^-$ molecules are able to moderate the coordination sphere of the zinc(II) anions and they control the self-assembly interaction between the metal ion and the ligands.

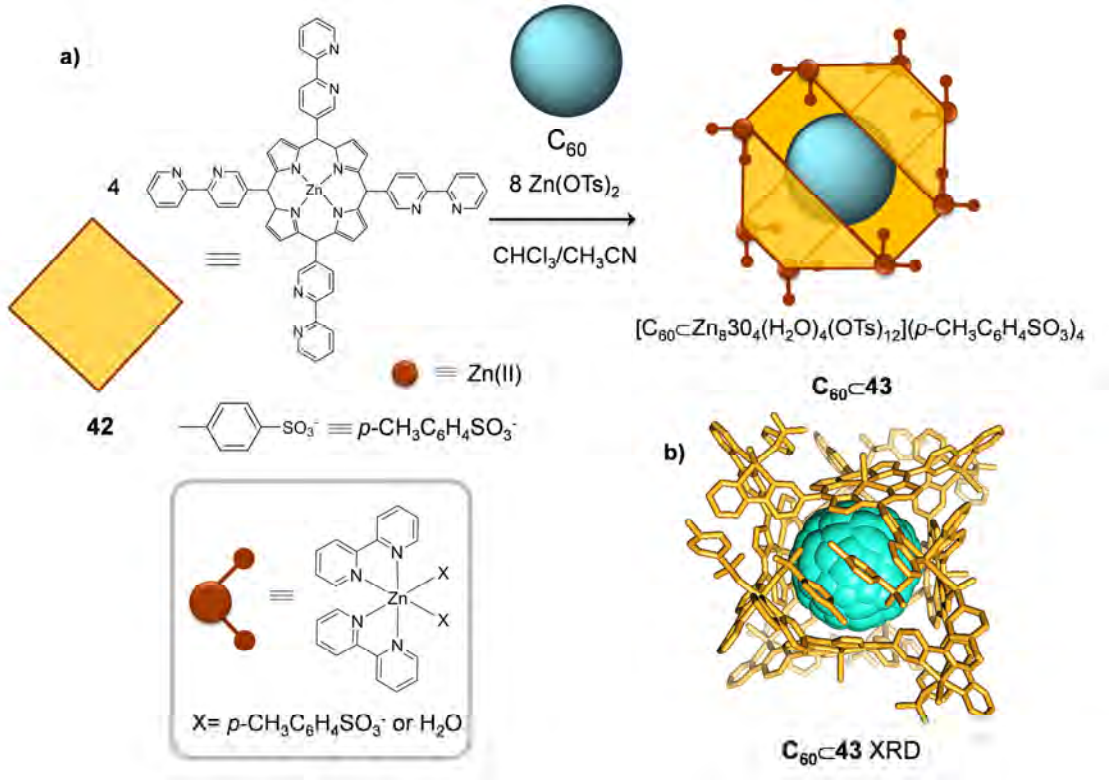

Scheme I.17. **a)** Building blocks used for the zinc(II) mediated self-assembly of porphyrin barrel complex $C_{60}\subset$**43**. **b)** X-ray crystal structure of complex $C_{60}\subset$**43** (hydrogen atoms are omitted for clarity).

Another example was reported by Nitschke in 2011 who synthesized a closed-face cubic metallo-cage containing six porphyrin units, which allowed for the isolation of the guest molecules from the bulk solution.[143] In this work the self-assembly reaction was exclusively controlled by the metal ions (iron(II)) and the geometry of the selected pyridine-based ligands. Cage **44** was obtained by reacting nickel(II) *tetrakis*-(4-aminophenyl)porphyrin, 2-formylpyridine and Fe$(CF_3SO_3)_2$ in DMF (Scheme I.18). The cage was obtained as a single product which was confirmed by NMR spectroscopy and ESI-MS. Crystals suitable for X-Ray diffraction were obtained and the crystallographic data revealed the cage to have an octahedral geometry, containing six porphyrins on its faces and eight iron(II) centres located at the corners (M_8L_6).

The volume of the inner cavity was 1340 Å^3, large enough to host large aromatic guests such as fullerenes.

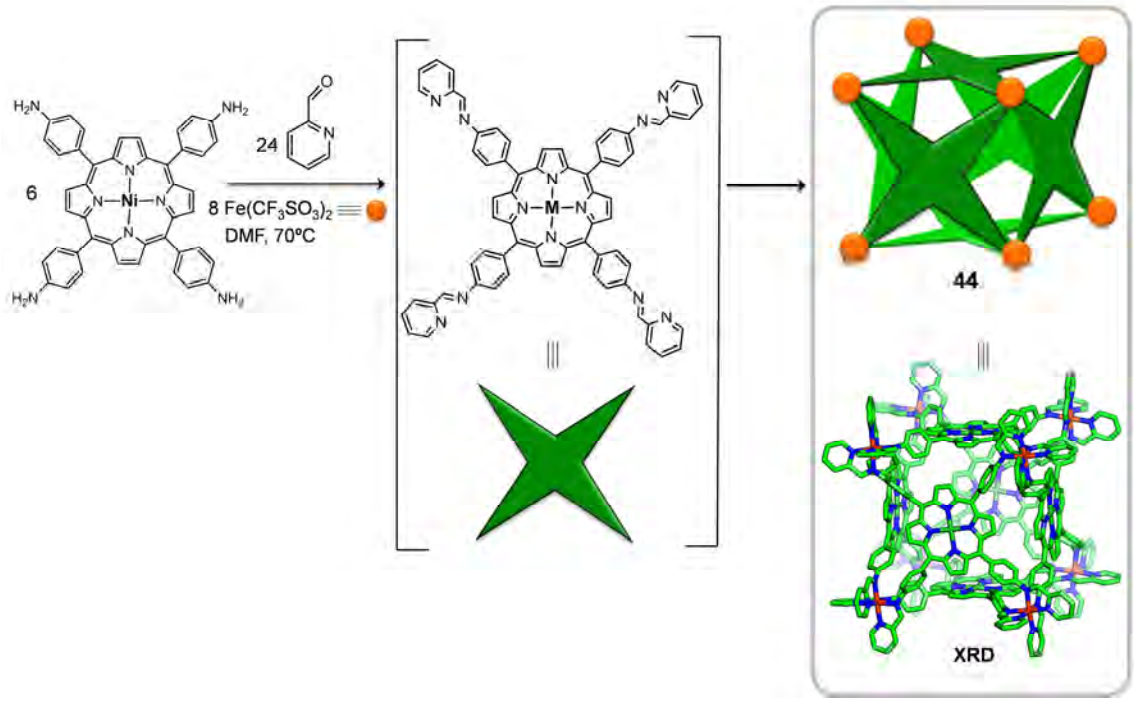

Scheme I.18. Schematic representation of the synthesis of cubic cage **44** through component self-assembly and its X-ray structure (hydrogens and anions are omitted for clarity).

The potential of cage **44** to encapsulate fullerenes was first explored with C_{60} fullerene. To a solution of **44** in DMF, were added 5 equivalents of C_{60} and the reaction was then heated at 70ºC for 5 days. The reaction resulted in a 35% conversion to C_{60}⊂**44** adduct ($K_a = 5.5 \cdot 10^3$ L mol^{-1}). In a further experiment 2 equivalents of C_{70} were added to a solution of the cage in DMF and full conversion to C_{70}⊂**44** adduct was obtained after stirring the reaction mixture for 3h at 70ºC. These experiments showed the higher affinity of **44** for C_{70} than for C_{60} which can be rationalized by the larger surface which facilitates a larger number of stabilizing π-π interactions (Scheme I.19). To further investigate these findings, an experiment in which 2 equivalents of C_{70} were added to a C_{60}⊂**44** solution, resulted in complete conversion towards C_{70}⊂**44** as confirmed by ESI-MS. These results encouraged the authors to investigate the discrimination between other fullerenes using fullerene soot as a source of a mixture of fullerenes. Nanocapsule **44** was mixed with fullerene soot, in a 1:10 weight ratio and after stirring the mixture for 12 h at 70ºC, neither **44** nor C_{60}⊂**44** compounds were observed in the ESI-MS spectrum. However, host-guest adducts with C_{70}, C_{76}, C_{78}, C_{82} and C_{84} fullerenes were observed. Although mass spectra are unable to provide quantitative information, comparable mass ionization behaviour was found for **44** and its fullerene adducts. Therefore from the ESI-MS experiments it was concluded that cage **44** displayed a higher affinity towards the higher fullerenes.

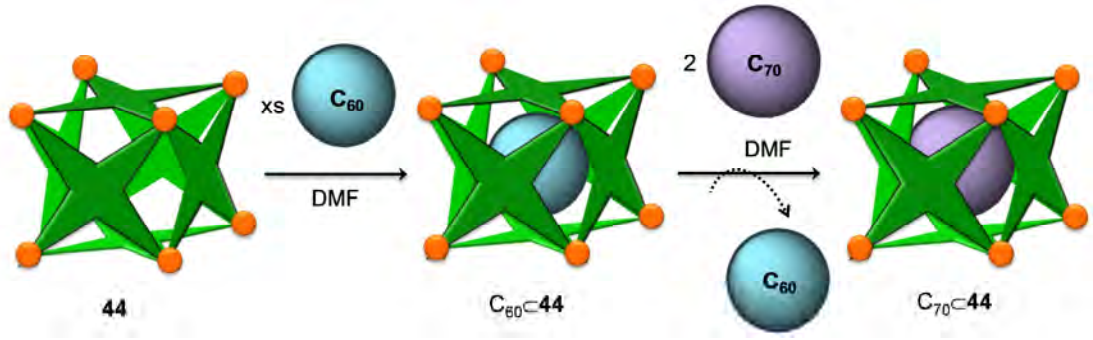

Scheme I.19. Hierarchy of the host-guest inclusion compounds with C_{60} and C_{70} fullerene with Nitschke's system. Nanocapsule **44** presents a higher affinity towards C_{70} than for C_{60}.

I.3.2.3. Coordination cage-like receptors containing π-extended moieties

Not only porphyrins but also other π-extended systems such as calixarenes and resorcinarenes have also been used as molecular building blocks in the preparation of coordination cages for the isolation of fullerenes.[144] Similarly to porphyrins, these species can also establish a donor-acceptor interaction with fullerenes.[145].

One of the first examples of a coordination cage-like receptor for fullerenes was reported in 1999 by Shinkai.[146] The authors targeted the synthesis of a dimeric calix[n]arene cage for fullerene inclusion, by self-assembly through coordination bonds. Calixar[3]arenes units substituted with 3 pyridine moieties were chosen and reacted with $[Pd^{II}(Ph_2PCH_2CH_2PPh_2)](CF_3SO_3)_2$ in a 2:3 ratio, to form the molecular cage **45** (Scheme I.20a). The nanocapsule forms 1:1 host-guest adducts with C_{60} fullerene at 25ºC in 1,2-dichloroethane (K_a ~50 M^{-1}). Afterwards it was discovered that the K_a for C_{60} was remarkably increased when lithium cations were bound to the ester lower rims of capsule **45**, giving a new complex **Li-45**.[147] In the **Li-45** capsule the phenyl groups are more flattened than those in **45**, in such a way that the three ethoxycarbonylmethoxy groups can interact with the bound lithium cation, improving the interaction between the fullerene and the calixarene walls (K_a ~ $2 \cdot 10^3$ M^{-1} in 1,2-dichloroethane at 25ºC). Moreover it was discovered that when the bigger sodium cation interacts with the esters pockets to give **Na-45**, the phenyl groups stand up, which tapers the cage structure and as a consequence the cage adopted an ellipsoidal shape which impeded the inclusion of the C_{60} fullerene (K_a ~ 5 M^{-1} in 1,2-dichloroethane at 25ºC) (Scheme I.20b). This modification of the cage shape and size, induced by cation binding presents a good strategy for the controlled binding and release of the encapsulated C_{60}.

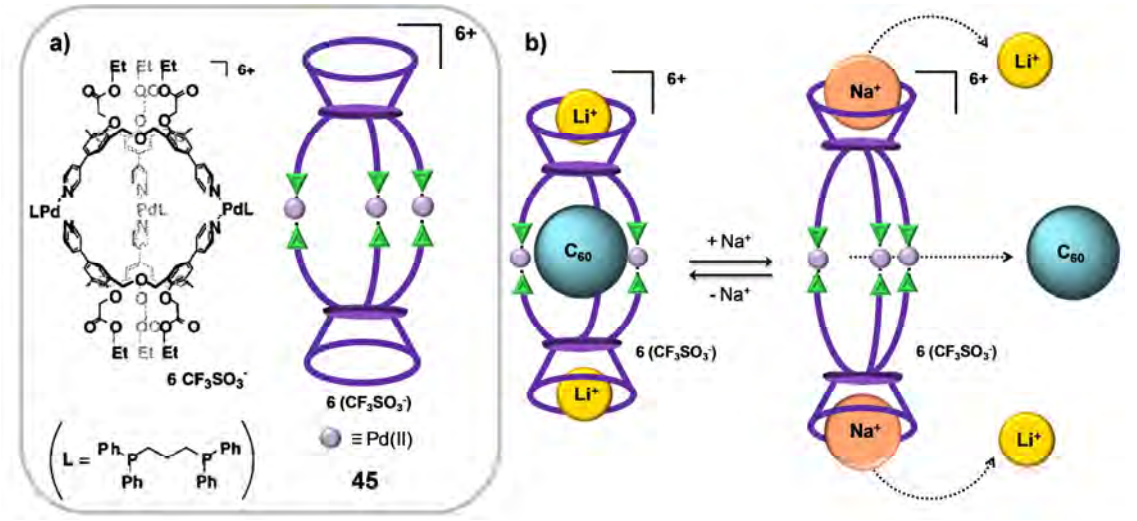

Scheme I.20. a) Chemical structure and schematic representation of the coordination cage **45** reported by Shinaki and co-workers. **b)** Flattening of the homoocalix[3]arene units induced by lithium cations, and release of C_{60} induced by the interaction with sodium cations.

Also taking advantage of the predictability and high directionality of the pyridine-N···Pd coordination bond, and using subphthalocyanine substituted with pyridines (**46**) as building blocks, Torres reported on the synthesis of a library of M_3L_2 metallic cages suitable for the encapsulation of fullerenes (Scheme I.21). Subhthalocyanines (SubPcs) have a concave geometry comprising of a 14 π-electron core able to interact with fullerenes. The synthesis of metallocages with a C_3 symmetry (**47$_{a-e}$**) was performed by mixing stoichiometric amounts of SubPc (**46**) and the corresponding palladium(II) or platinum(II) complex and stirring the solution in DCM under reflux. First a cage **47$_a$** containing ethylenediamine as a ligand and palladium(II) as the metal was reported. In solution the cage revealed the presence of two diastereoisomers which slowly exchange until reaching a thermodynamic equilibrium.[148,149] Cages **47$_{b-e}$** were prepared by self-assembly of palladium(II) or platinum(II) metal ions and phosphine ligands, in order to allow characterization by ^{31}P NMR. The host-guest adduct between capsule **47$_a$** and C_{60} was formed by adding 5 equivalents of the fullerene to a previously equilibrated solution of the host in acetone at room temperature. The formation of 1:1 (**47$_a$**⊂C_{60}) complex was confirmed by NMR and ESI-MS experiments. The encapsulation in acetone dramatically increases the solubility of the fullerene in this solvent, which makes the capsule of potential interest as a phase-transfer catalyst for C_{60}. Host-guest experiments with cages **47$_{b-e}$** under the same conditions (acetone, r.t.) also gave 1:1 host guest adducts with C_{60}, C_{70}, [60]PCBM and [70]PCBM fullerenes. These experiments were also performed following a fullerene template approach.[150] Initially, SubPc (**46**) was stirred with the fullerene for one hour and subsequently the metal complex was added. The association constants for [60]PCBM and [70]PCBM were calculated by monitoring changes in the NMR spectra. Unfortunately, for the palladium(II) cages the equilibrium was too fast and no significant shifts were observed upon addition of the fullerenes. For the platinum(II) analogues (**47$_{d-e}$**), the K_a for **47$_d$** was found to be $4.6\cdot10^4$ M^{-1} and $1.5\cdot10^5$ M^{-1} for ([60]PCBM and [70]PCBM) respectively and for **47$_e$** $3.2\cdot10^2$ M^{-1} and $2.2\cdot10^3$ M^{-1}

for ([60]PCBM and [70]PCBM) respectively. [70]PCBM forms more stable adducts with the capsules because its size is more appropriate for interaction with the cage.

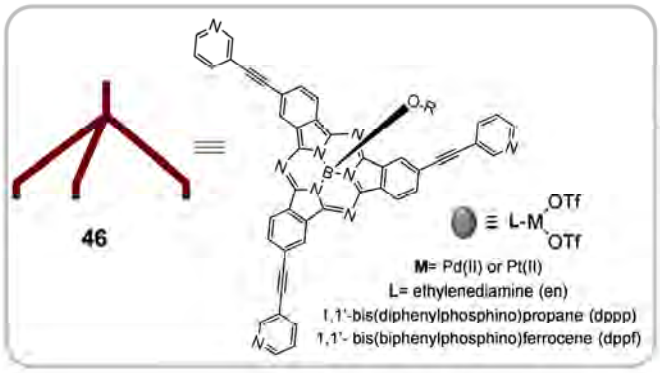

Host **47**	M	L	R
a	Pd	en	*o,m*-di-*tert*-butylphenyl
b	Pd	dppp	*p-tert*-butylphenyl
c	Pd	dppf	*p-tert*-butylphenyl
d	Pt	dppp	*p-tert*-butylphenyl
e	Pt	dppf	*p-tert*-butylphenyl

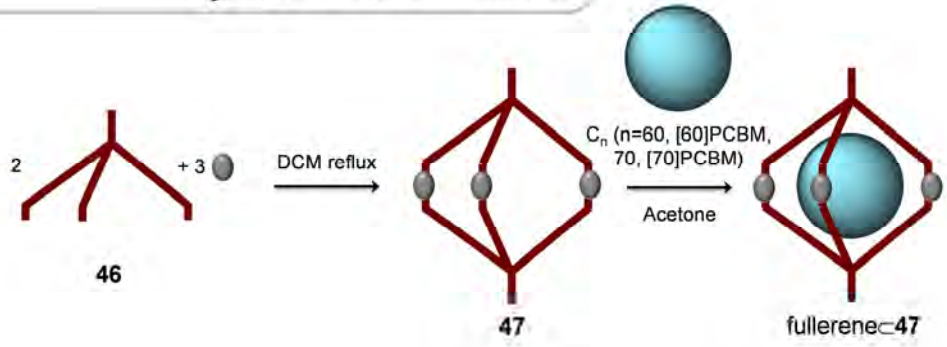

Scheme I.21. Representation of the self-assembly reaction between SubPc (**46**) and the corresponding metal complexes, to give the coordination cage **47**. Cages $\mathbf{47_{a\text{-}e}}$ encapsulate different fullerenes in acetone.

The versatility of pyridine-based ligands in coordination-driven self-assembly was further exemplified by Yoshizawa in 2013. The authors prepared fullerene receptors that are especially interesting not only because they can selectively entrap a specific fullerene in a mixture of fullerenes, but also the sequestered fullerene can be easily released by an external stimuli (light radiation or mercury(II) ions). This feature is particularly interesting from the point of view of practical purification of fullerenes.

The same authors reported in 2011 on the synthesis of a M_2L_4 cage (**49**), by self-assembly of ligand **48** and $Pd(NO_3)_2$ in DMSO at 100ºC.[151] A bipyridine curved ligand **48** bearing large aromatic panels (two anthracene molecules linked by *m*-phenylene) was designed in order to provide an aromatic shell that possess an enclosed cavity which can facilitate stronger host-guest interactions (Scheme I.22). Interestingly the cage cavity was large enough (~1 nm in diameter) for the encapsulation of large guest molecules. The reaction between cage **49** and an excess of C_{60} in acetonitrile at 80ºC for 3 h, gave 1:1 host-guests complexes. The palladium(II) based cage irreversibly binds C_{60} fullerene through π-stacking interactions. Remarkably, cage **49** showed selective molecular recognition abilities and could only encapsulate C_{60} of complementary shape and size, from a mixture of C_{60} and C_{70}.

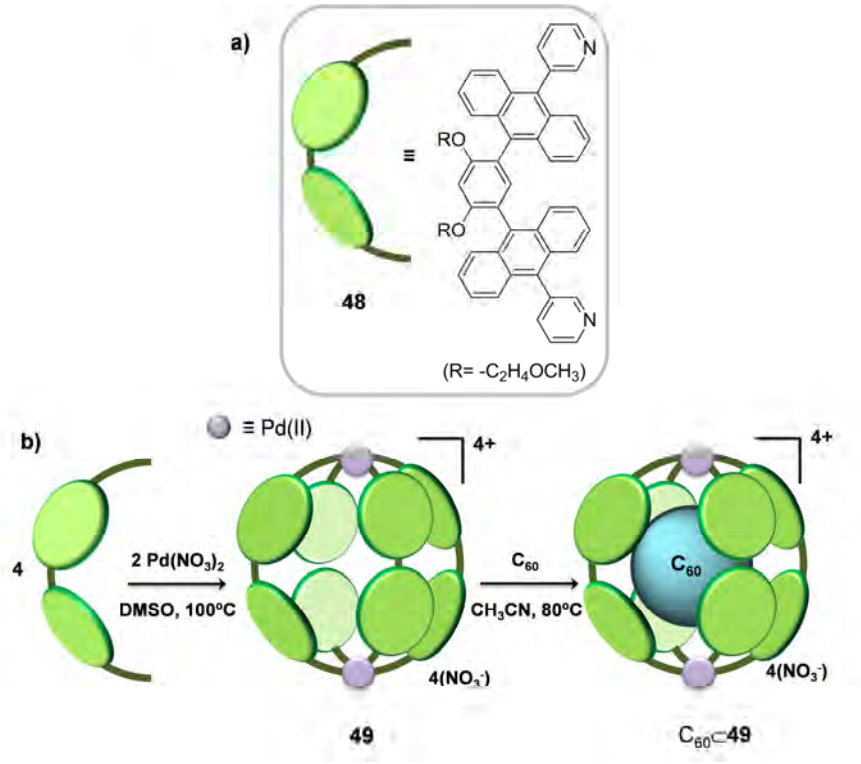

Scheme I.22. Chemical formula and schematic representation of ligand **48** (**a**) used for the self-assembly of cage **49** (**b**), reported by Yoshizawa which displays selectivity towards C_{60} fullerene.

With the aim of designing a reversible system, the same authors reported in 2013 on the synthesis of a tube-like fullerene receptor (**50**), using the same curved ligand (**48**) and silver(I) as metal for the coordination-driven self-assembly.[152] Strikingly, the encapsulated fullerenes were easily released by a non-invasive stimulus: light (Scheme I.23). The tubular capsule **50** was exclusively formed upon reaction of ligand **48** and $AgNO_3$, in presence of C_{60} fullerene in acetonitrile during 1 hour at room temperature in the dark, whereby the color of the solution changed from yellow to red-purple. The C_{60} plays the role of a template molecule and as a result 1:1 host-guest adducts were formed. Unlike palladium(II) ions, silver(I) adopted a linear geometry forming complexes with only two ligands (M_2L_2). Interestingly, when the red-purple solution containing C_{60}⊂**50** was irradiated with a 36W incandescent light (UV-vis irradiation, acetonitrile, room temperature) the solution turned yellow and a precipitate corresponding to C_{60} and metallic silver appeared. The released C_{60} was extracted with toluene and recovered as a brown solid (68%). Finally, UV-vis irradiation of the remaining yellow solution containing ligand **48** in the presence of C_{60} and $AgNO_3$, allowed recovery of the host-guest adduct C_{60}⊂**50** in a ~60% yield and again, selectivity towards C_{60} over C_{70} was observed. Moreover, thanks to its more open structure receptor **50** was also able to encapsulate and release different C_{60}-malonate and -indene derivatives.

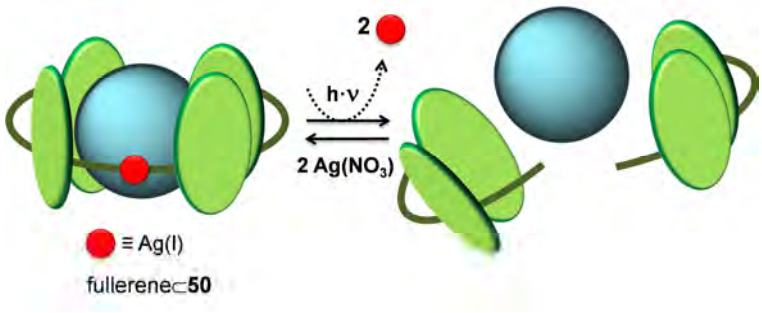

Scheme I.23. Representation of the sequestration and liberation of a fullerene, by using tubular structure **50**. The substrate uptake and release is modulated by the addition of metal ions which can be removed by photoirradiation.

Very recently, the same authors reported on the synthesis of a new cage **51** analogous to **49** in which mercury(II) metal ions were used as nexus.[153] This M_2L_4 capsule easily interconverts to a tube-like structure **52** (analogous to **50**) in response to modulation of the metal-to-ligand ratio (Scheme I.24), whereby this conformational change allowed the liberation of the bound fullerenes. When ligand **48** and $Hg(CF_3SO_3)_2$ were mixed in a 2:1 ratio in acetonitrile at room temperature for 5 min, nanocapsule **51** was obtained. On the other hand, if the curved ligand **48** and $Hg(CF_3SO_3)_2$ were mixed in a 1:1 molar ratio under similar conditions, receptor **52** was obtained. Both structures were fully characterized by means of NMR, ESI-MS and XRD. Fast interconversion between the cage-like structure **51** and the tube **52** was achieved by changing the metal-to-ligand ratio, by the addition of further equivalents of the ligand or the metal ion. When 2 equivalents of the mercury(II) salt were added to 1 equivalent of cage **51** (M_2L_4), the cage changed its conformation to give two units of tube **52** (M_2L_2), in 15 min at room temperature in acetonitrile. Additionally, tube **52** was quickly transformed to cage **51** by adding 2 equivalents of ligand **48** for each equivalent of tube. In spite of the fact that both receptors **51** and **52** possess large inner cavities with similar diameters (~1 nm) they present different affinities towards fullerenes. When a colourless solution of capsule **51** in acetonitrile was mixed in a 1:3 ratio with fullerene C_{60} at room temperature for 15 min, the solution turned blue-violet owing to the formation of C_{60}⊂**51** host-guest adduct. Cage **51** was also able to encapsulate C_{70}, however as it was observed for cage **49**, a better fit of C_{60} fullerene inside the cavity resulted in higher association constants than for C_{70} fullerene. Unexpectedly, tube **52** showed no affinity towards C_{60} or C_{70} and the authors reasoned that in the case of the analogous tube-like structure **50**, the fullerene⊂receptor interaction was possible due to the presence of Ag-π interactions. The authors subsequently took advantage of this different affinity to design a fullerene liberation procedure. All the fullerenes embedded in cage **51** were liberated upon the conformational transformation from the capsule to the tube **52**. When 2 equivalents of $Hg(CF_3SO_3)_2$ were added to a blue-violet solution of C_{60}⊂**51** in acetonitrile, the solution turned pale yellow, and a suspension of C_{60} was formed upon guest expulsion. The C_{60}, suspended as a brown solid, was recovered by centrifugation. Hence the conformational change and the fullerene liberation phenomenon could be detected by the naked eye on the

basis of the colour change. The encapsulation and liberation of C_{70} fullerene was successfully performed using the same reaction conditions.

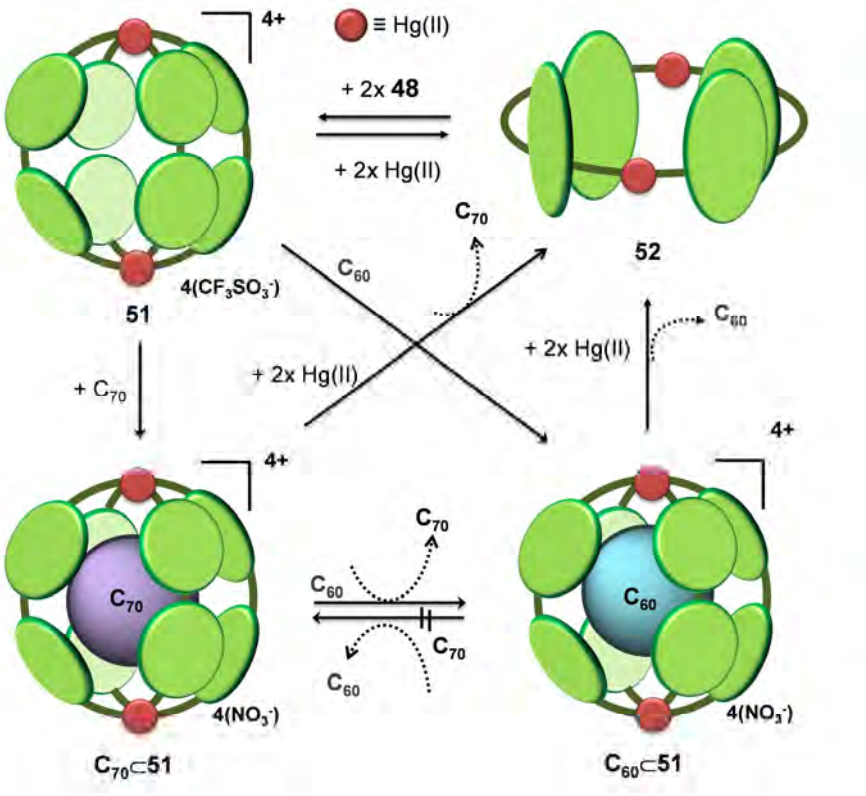

Scheme I.24. Schematic illustration of the host-guest interactions of cage **51** and tube **52** with fullerene guest (C_{60} and C_{70}) through metal-to-ligand structural transformations

First row transition metals, which are attractive from an environmental and economic point of view, have also been used as nexus between pyridine ligands to give cage-like receptors for fullerenes. Würthner used FeX_2 salts (X = BF_4^-, $CF_3SO_3^-$) to link perylene bisimide (PBI) dyes, containing 2,2'-bipyridine groups (**53**), in order to prepare a M_4L_6 tetrahedral structure **54** (Scheme I.25) which is one of the largest M_4L_6 tetrahedrons ever reported.[154] As a result of the known electronic interaction between C_{60} and the PBI units and considering the large volume of the cage cavity (~950-2150 $Å^3$), host-guest experiments were performed with this fullerene. Nancapsule **54** was reacted with an excess of C_{60} (1:10 ratio) in a $CDCl_3/CH_3CN$ mixture (9/1) and the reaction crude was heated to 70ºC overnight. Afterwards the solvents were removed and the remaining mixture was dissolved in CH_3CN and filtered to separate the excess of C_{60} that is insoluble in CH_3CN. The HRMS spectrum displayed peaks corresponding to **54**, C_{60}⊂**54** and 2·C_{60}⊂**54** host-guest adducts. Molecular force field (MMFF) geometry optimization of singly and doubly occupied host-guest complexes indicated that the fullerenes are preferentially located closer to the corners of the tetrahedral cage.

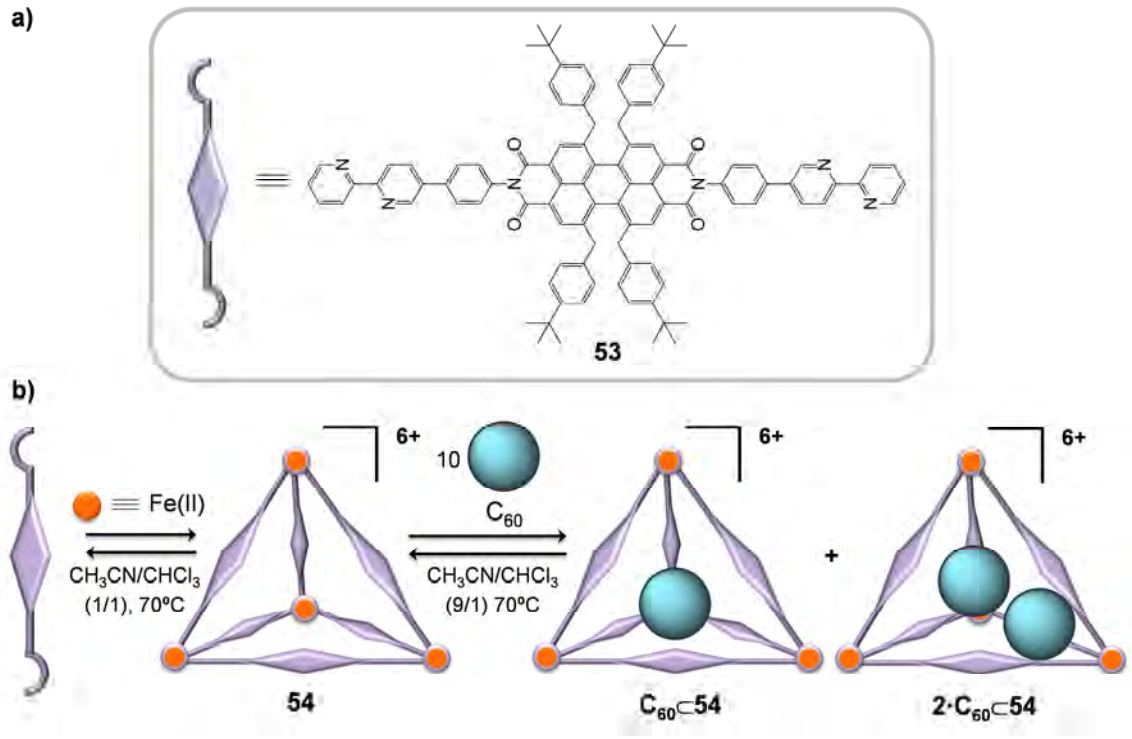

Scheme I.25. PBI-based ligand **53** used in the self-assembly of giant tetrahedral host **54** (**b**) which was able to accommodate one or two molecules of C_{60} fullerene.

Recently, Nitschke reported the synthesis of a M_6L_6 tetragonal cage by self-assembly of diamine 1,6-pyrene-based ligands (6 equiv.) with 2-formylpyridine (12 equiv.) and iron(II)triflimide (4 equiv.), where it was found that the resulting cage product consisted of a mixture of three diastereoisomers.[155] Interestingly, both fullerenes C_{60} and C_{70} were observed to form 1:1 host guest adducts with the tetrahedral cage, moreover the cage was able to adapt its structure when binding the fullerene, favouring the formation of the diastereoisomers best able to encapsulate the fullerene in order to maximize the cage-fullerene interaction.

A different strategy was used by Fujita who developed crystalline sponges for fullerene encapsulation using a different first row transition metal, cobalt(II). As mentioned in section I.2, Fujita reported the synthesis of multiple positively charged nano-vessels by self-assembly of rigid tridentate pyridine ligands through coordination with palladium(II) and platinum(II). The M_6L_4 octahedral flask **5** (Scheme I.2 in Chapter I.2) was proven to be able to create an isolated micro-environment with properties different from those in the bulk solution and allows small organic molecules to be confined.[156,157] The authors reported in 2010 on the synthesis of a crystalline coordination network, **55**, generated from an infinite array of octahedral M_6L_4 cages (M= $Co(NCS)_2$), $\mathbf{55_a}$, in which each metal corner is shared between two adjacent octahedra (Figure I.10).[158] The cage framework $\mathbf{55_a}$ resembles the octahedral cages previously reported with palladium(II) and platinum(II) ions (**5**, Scheme I.2). The crystalline structure of the Metal Organic Framework (MOF) revealed the presence of other types of cavities besides the M_6L_4 octahedral cage motifs. The interstitial void spaces between $\mathbf{55_a}$ moieties (63% of the total lattice volume), define alternating $M_{12}L_8$ ($\mathbf{55_b}$) and $M_{12}L_{24}$ ($\mathbf{55_c}$) cuboctahedral molecular cages,

that are analogous to the palladium(II)-based discrete nanocapsules previously reported.[159] Thus, crystalline infinite network **55** provides three distinct molecular cage environments (**55**$_{a\text{-}c}$).

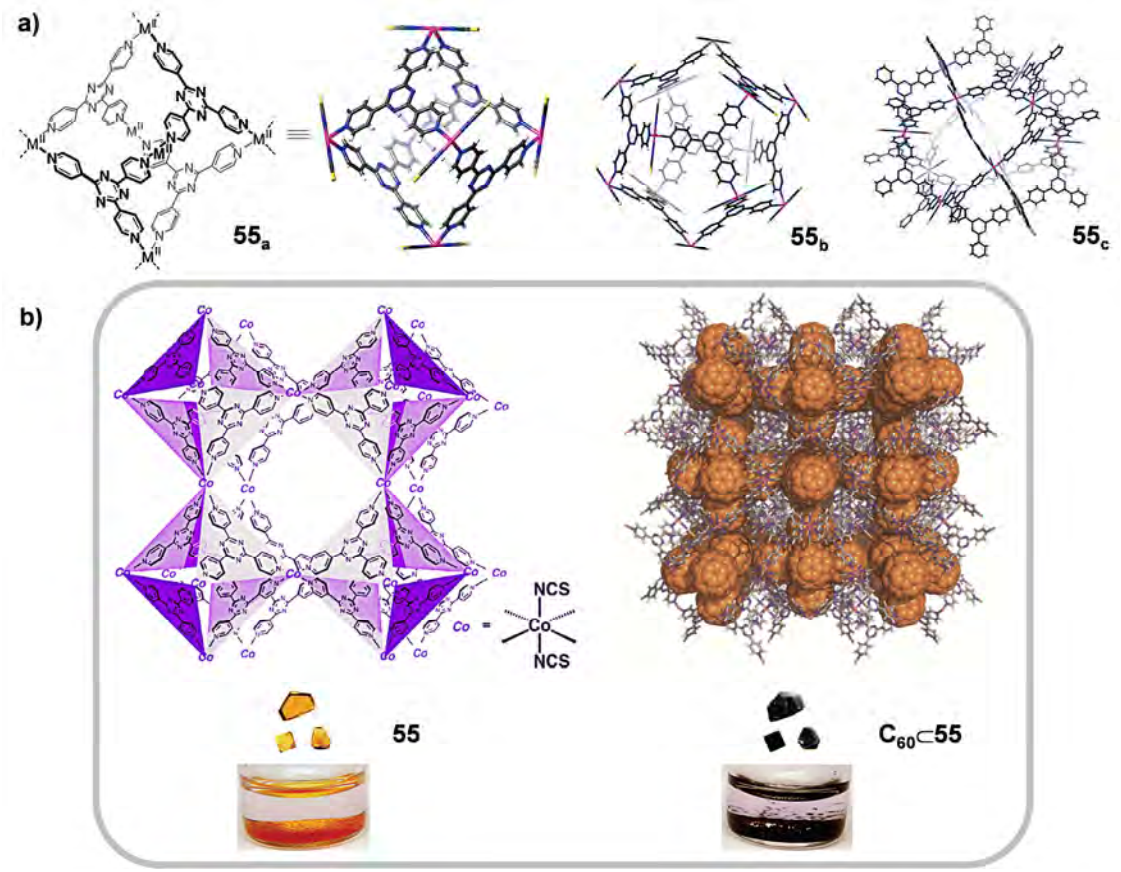

Figure I.10. a) Representation of the crystal structures of the three distinct polyhedral molecular cages in the infinite crystalline network **55**. **b)** Inclusion of C_{60} fullerene into the crystalline sponge **55,** and photographs of complex **55** before (yellow) and after (black) inclusion of C_{60} fullerene. Adapted by permission from Macmillan Publishers Ltd: [Nature Chemistry] (Ref. 158), copyright (2010).

The octahedral cage **55**$_a$ has a narrow window which allows the binding of small organic guests, i.e. tetrathiafulvalene (TTF), through solid-liquid host-guest recognition. On the other hand, the larger cuboctahedra **55**$_{b\text{-}c}$ are of an ideal size for the encapsulation of large aromatic guests such as fullerenes. To perform the encapsulation of fullerenes, a crystalline sample of MOF **55** was soaked in C_{60} fullerene containing toluene at 60ºC for a week. During this time the **55** yellow crystals turned black (Figure I.10 b). X-ray data was obtained for the inclusion compound and it was found that 35 wt% C_{60} fullerene was accommodated. An analogous experiment was performed using C_{70} fullerene and 34 wt% C_{70} was accommodated. The half-lives of the inclusion complexes C_{60}⊂**55** and C_{70}⊂**55** in toluene were found to be 15 and 25 days respectively. Cages **55**$_{b\text{-}c}$ displayed preferential encapsulation towards C_{70} than for C_{60} (C_{60}/C_{70}, 8/2 ratio). The cuboctahedral cages were also used to encapsulate fullerene soot, where interestingly the C_{70} content was enriched from 10% to 24%. Moreover, the cuboctahedral cages also showed preferential encapsulation of higher fullerenes from fullerene soot (C_{76}, C_{78}, C_{82} and C_{84}). The content of higher fullerenes relative to C_{60} increased ~3 times on inclusion.

In the same year, Fujita also reported the synthesis of a sphere-like molecular nanocapsules able to isolate fullerenes. The nanosphere **57** was synthesised by self-assembly of ligand **56** treated with $Pd(NO_3)_2$ in DMSO for 4h at 70ºC, resulting in a $M_{12}L_{24}$ cage (Scheme I.26). The sphere **57** contains 24 large aromatic coronene molecules concentrated inside, which behave as a "nanodroplet" able to host C_{60}. Confined C_{60}⊂**57** in DMSO is 30 times more soluble than in toluene.[160]

Scheme I.26. Self-assembly of $M_{12}L_{24}$ coordination sphere **57**, using $Pd(NO)_3$ and pendant coronene molecule **56** as molecular building blocks. Adapted with permission from (Ref. 160). Copyright (2010) American Chemical Society.

I.4. Supramolecular capsules for enzyme-like catalysis

Enzymes, catalysts of living organisms, efficiently mediate a wide range of biochemical reactions. Compared to man-made chemical catalysts, enzymes typically exhibit greater performance in terms of rate enhancement, capacity of regulation, reaction specificity and work under milder conditions. Moreover, effects such as substrate recognition, substrate preorganization near the catalytic centre, restricted substrate motion, stabilization of the transition state or intermediate, and desolvation of the substrate, also play a key role in enzymatic catalysis. Most of these effects are induced by the enzyme protein secondary structure. It is well known that the reaction medium influences chemical reactions. When a reaction takes place inside the enzyme cavity, the substrate and the transition state are protected from the bulk solution, which may induce a different reactivity. Although considerable progress in enzyme catalysis has been realized, there is still not a complete and profound comprehension, for example, of how enzymes display extraordinary catalytic efficiency or selectivity for a specific substrate due to its protein supramolecular structure.[161] Synthetic models which allow investigation and further understanding of the relationship between the supramolecular structure and catalytic features of enzymes are of interest.[162]

Supramolecular chemistry is a powerful tool for the development of nanosized reaction vessels, which may mimic the cavity-like structure of enzymes. As a result, several examples of supramolecular nanocapsules able to participate as catalysts in different chemical reactions (reactions performed by enzymes or more traditional transition metal catalysis) have been reported in the literature.[163–169] There are relevant examples of supramolecular nanoreactors based on classical supramolecular interactions (e.g. hydrogen bonds or π-π stacking) and based on coordination bonds and here special attention will be given to metallocages.

There are two different approaches for using supramolecular capsules as enzyme-like catalysts. On one hand, it is possible that the molecular cage contains a catalytic moiety in its structure and the cage therefore offers a confined environment around this catalytic moiety. Alternatively, the nanovessel can be designed without using a catalytic moiety and the isolated and restricted environment within the cage can modify the chemical activity.

I.4.1 Capsules for cavity directed catalysis

When a catalytic reaction is performed within a nanocapsule which does not contain a catalytic moiety, it can catalyze the reaction by proximity and/or preorganization of the substrate inside its cavity. Like an enzyme, a supramolecular capsule can stabilize the transition state (TS) of the reaction, lowering the activation energy barrier ($\Delta G^{\#}$). The stabilization of the transition state can be due to enthalpic stabilization, *via* non-covalent interactions between the TS and the surrounding, or it can be caused by entropic factors since the cage can preorganize the encapsulated substrates towards the TS. On the other hand, it is possible that the cage

does not modify the activation parameters, but the concentration of reagents inside its cavity is higher than in the bulk solution and the acceleration of the reaction is due to a higher effective concentration. Essentially, the reactions go from a bimolecular to an intramolecular reaction pathway.[170,171]

The specific geometry of the cage and the confined hydrophobic environment inside its cavity can facilitate the desolvation and isolation of the substrate, leading to different selectivities and reactivities. For example, if there is a competitive reaction between two molecules, the cage will favour the reaction with the molecule to which it has higher affinity, in terms of size and shape-selectivity, compared with the other substrate which does not effectively fit inside the cavity.

One of the most common problems that supramolecular chemists have to deal with when designing a nanoreactor is product inhibition, which can prevent catalytic performance. Product inhibition occurs when the capsule presents higher affinity towards the reaction products than for the substrate(s) and is mainly due to the fact that the product has multiple attractive interactions with the host or it is too large to leave the cavity. It is also common in bimolecular reactions in which two substrates replace a single product, a process entropically disfavoured.

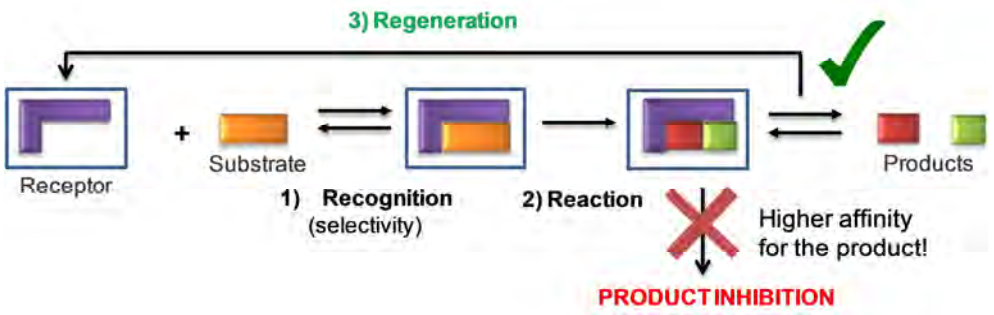

Figure I.11. Illustration of the different stages that take place in a reaction catalyzed by a molecular flask.

The first example of a supramolecular nanocage able to catalyze a chemical reaction was reported by Rebek in 1998. The authors synthesized a multiring ball-like cage structure (called softball), which exists as a hydrogen-bonded dimer in organic solvents (Scheme I.27 a). Cage **58** was proven to be efficient in the encapsulation of two smaller complementary molecules.[172,173] This ability stimulated researchers to utilize the cage as a microreactor for bimolecular reactions.

The Diels-Alder reaction between *p*-benzoquinone (**a**) and cyclohexadiene (**b**) within the softball was accelerated 200 times compared to the bulk solution. The rate enhancement was rationalized by the fact that the two substrates are in closer proximity within the capsule. The restricted environment within the cavity also forced the exclusive formation of the endo-isomer. However, effective turnover was prevented because of product inhibition (Scheme I.27 b) as a result of the product fitting perfectly within the capsule ($K_a > 10^5$ M^{-1}).[174,175]

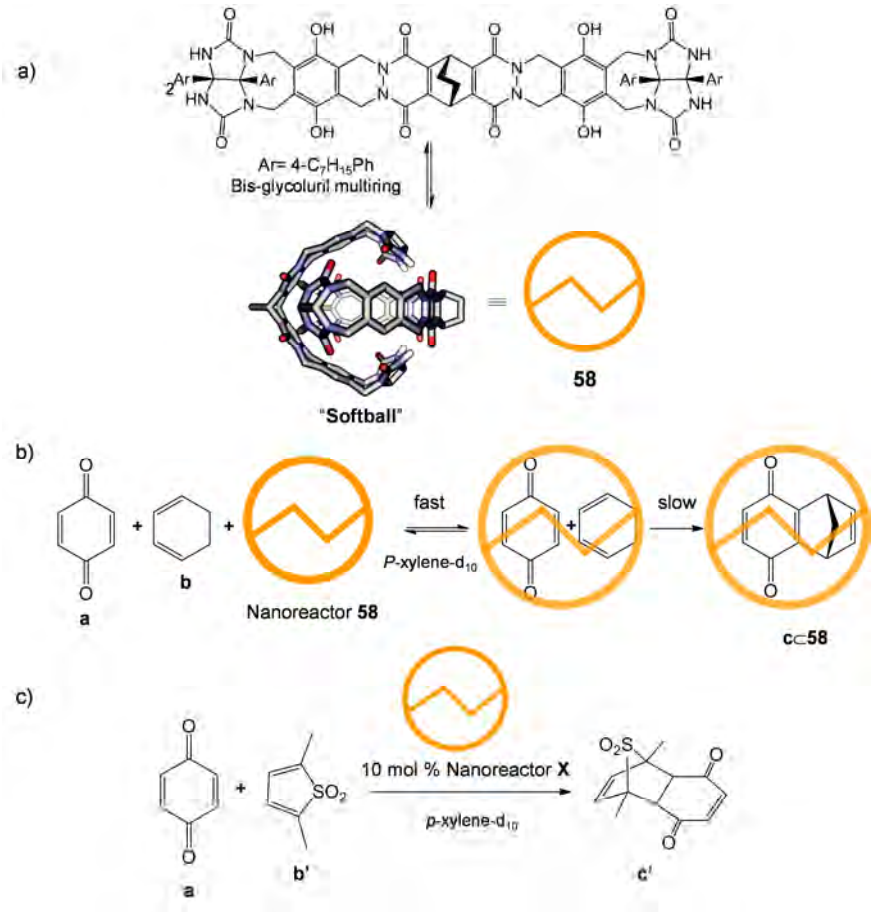

Scheme I.27. a) Representation dimeric supramolecular capsule reported by Rebek (**58**). **b)** Confined Diels-Alder reaction between **a** (*p*-benzoquinone) and **b** (cyclohexadiene) to give **c⊂58**. **c)** Cage catalysed Diels-Alder reaction between **a** and **b'** (thiophene dioxide derivate) to give product **c'**. Reproduced in part from {Ref. 176} with permission of The Royal Society of chemistry.

Product inhibition was suppressed by using a thiophene dioxide derivative (**b'**) as the diene in the cycloaddition with *p*-benzoquinone. In this case, the cage presented higher affinity towards the reagents than for the Diels-Alder product and the reaction became catalytic (Scheme I.27 c).The Diels-Alder adduct was formed in 75% yield over four days in the presence of the cage **58** (10 mol%), whilst only 17% conversion was obtained in its absence.[177]

Another example was reported by Fujita who used an octahedral cage (**5**) and a bowl-like complex (**6**) (Chapter I.2, Scheme I.2) as reaction vessels. These highly positive charged palladium structures (total charge +12) are able to encapsulate multiple organic molecules in water *via* hydrophobic effects, π-π and C-H-π interactions.[27,178] Different reactions have been improved in presence of these two coordination structures; however in most cases product inhibition precluded catalytic turnover.[179,180]

The Diels-Alder reaction coupling of anthracene and maleimides in water was studied in 2006 (Scheme I.28) and it was observed that when nanocapsule **5** was suspended in water along with 9-hydroxymethylanthracene (**d**) and N-cyclohexylmaleimide (**e**), both substrates were encapsulated. Afterwards, the solution was heated at 80ºC for 5 hours and the *syn* 1,4-Diels-

Alder adduct was exclusively obtained. The 1,4-Diels-Alder reaction was found to proceeded with various substrates.[181] In contrast, in absence of capsule **5**, the reaction gave the 9,10-Diels-Alder product. Due to the steric restrictions caused by the cage, the C=C bond of the N-cyclohexyl maleimide interacts poorly with the 9,10-position of the 9-hydroxymethyl anthracene molecule.

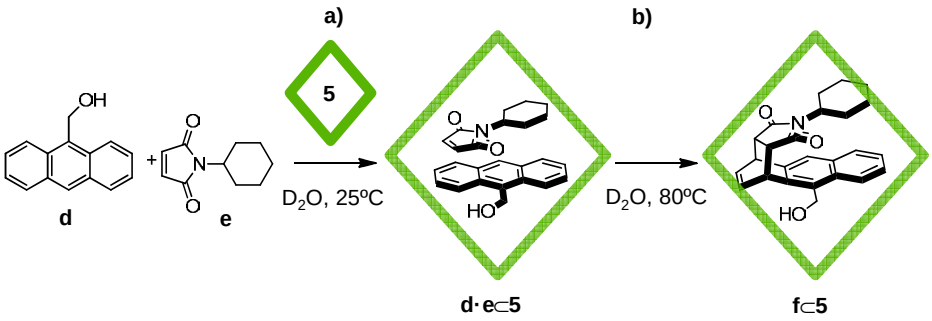

Scheme I.28. a) Selective encapsulation of the two reagents **d** and **e** within cage **5**. **b)** Diels-Alder reaction that leads to the *syn*-1,4-adduct **f** within nanovessel **5**.

Whereas **5** yielded high regioselectivity, open bowl-shape host **6** gave efficient catalytic turnover (Scheme I.29). Substrates **d** and N-phenylmaleimide (**e'**) were suspended in water and 10 mol % of bowl **6** was added, which was sufficient to quantitatively generate the 9,10-Diels-Alder product (yield: <99%, 5h at room temperature). In the absence of **6**, the reaction only gave 2% yield. Before the reaction takes place, the anthracene derivative molecule is stabilized inside **6**, through π-π or electrostatic interactions. Once the reaction is complete, the product molecule is bent at the 9,10-position, impeding π-π stacking interaction between the host and the guest and as a result the encapsulated product is destabilized and displaced by incoming reagents.

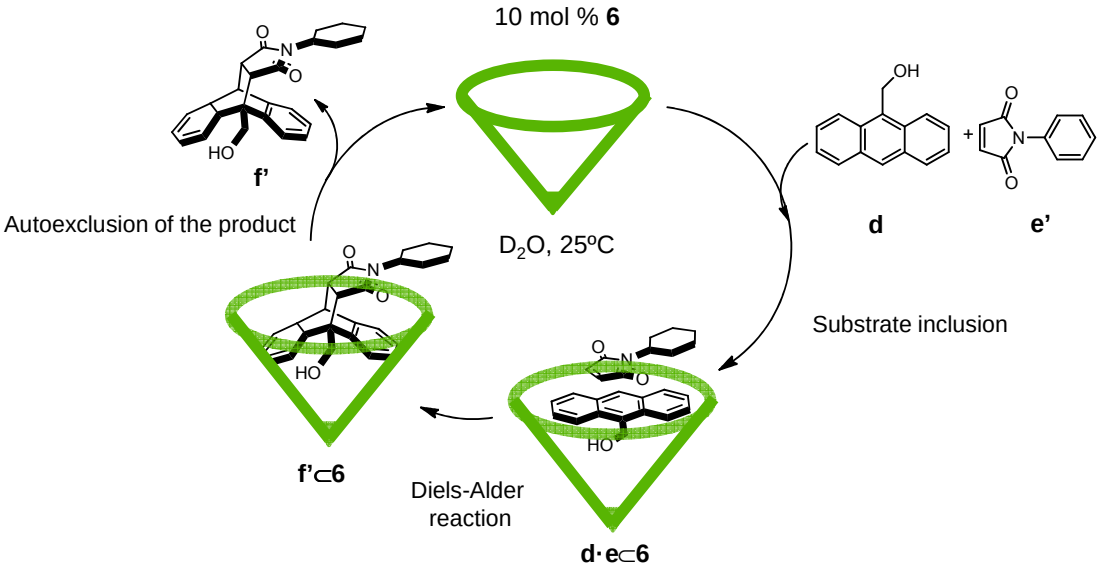

Scheme I.29. Representation of the Diels-Alder reaction between anthracene **d** and maleimide **e'** catalyzed by the bowl-like vessel **6**.

The opposite tendency was observed in the Knoevenagel condensation of aromatic aldehydes in water under mild conditions, where the reaction was highly efficient under catalytic amounts of cage **5**, but not when bowl **6** was used.[182]

The reaction was performed by mixing 2-naphthaldehyde (**g**), with Meldrum's acid (**h**) in water in the presence of cage **5** (1 mol%), and the reaction mixture was stirred during 6h at room temperature (Scheme I.30) and the condensation product was obtained in 96% yield. When **5** was not present, the reaction only provided trace amounts of the reaction product. The addition of the nucleophile to the encapsulated aldehyde to generate anionic intermediates is favoured inside the cationic cavity of cage **5** (12+ charged cage). The oxyanion is most effectively stabilized by the palladium(II) centres located at the vertices of cage **5** and less so by the closely arranged palladium centres of bowl **6**. Importantly, the condensation product poorly fits inside **5**, probably due to its large volume, so it can be spontaneously released from the cage favouring the catalytic process.

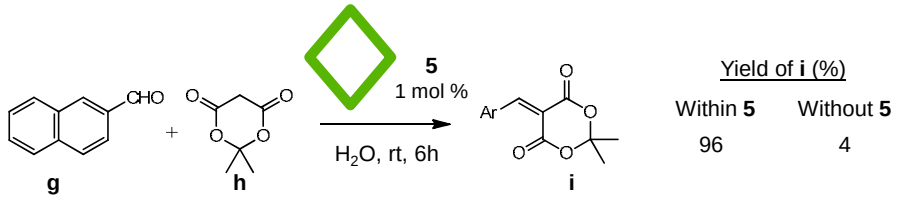

Scheme I.30. Knoevenagel condensation of a naphthalene derivate (**g**) and Meldrum's acid (**h**) catalysed by nanocapsule **5**.

The electrostatic analogue of Fujita's work was reported by Raymond and Bergman in 2007. The authors used the highly negatively charged cage **59** (M= Ga^{III} and L= N,N'-*bis*(2,3-dihydroxybenzoyl)-1,5-diaminonaphthalene)), bearing a hydrophobic cavity, to perform the normal acidic hydrolysis of orthoformate ($HC(OR)_3$) in basic solution (Scheme I.31).[183,184]

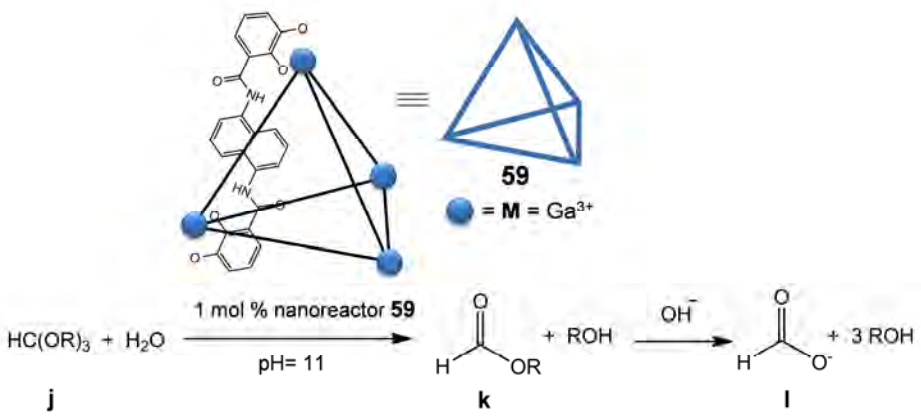

Scheme I.31. Hydrolysis of orthoformates catalysed by nanoreactor **59**.

Hydrolysis of orthoformate involves a protonated intermediate. Considering that the cage is anionic, it can thermodynamically stabilize protonated species small enough to fit inside its cavity. The cage exhibited size-selectivity and only orthoformates smaller than triphenyl

orthoformate (**j**, R = Ph_3) were hydrolyzed. Catalytic amounts of the coordination cage (1 mol%) in basic solution (pH 11, 22ºC) gave rapid hydrolysis of orthoformate (**j**) to the corresponding formate ester, HC(O)(OR) (**k**) and finally to formate, HCO_2^- (**l**). Product inhibition did not occur and the empty cage re-entered the catalytic cycle. The reaction rate was accelerated up to 890 times for triisopropyl orthoformate.

The same cage performed catalytic activity in different reactions such as the hydrolysis of acetal derivatives or unimolecular Aza-Cope rearrangement of alkyl ammonium cations.[185–187] The most significant rate enhancement was achieved for the Nazarov cyclization of 1,4-pentadien-ols. It was the first example of cage-like supramolecular catalysis that achieved a rate enhancement comparable to that observed in enzymatic systems.

The Nazarov cyclization of 1,4-pentadiene-ols (**m**) to give a cyclopentadiene (Cp, **n**) in water, or in mixed water/dimethyl sulfoxide, occurred at a rate up to $2.1 \cdot 10^6$ times higher than that of the uncatalyzed reaction (Scheme I.32). The unprecedented reaction acceleration was explained as a combination of: 1) preorganization of the encapsulated substrate, 2) stabilization of the transition state by constrictive binding and 3) an increase in the basicity of the of the encapsulated alcohol moiety. Product inhibition was observed during the reaction. To solve this problem the authors chemically transformed the product **n** into a poorer guest which can easily leave the cavity. Thus maleimide (**o**) was added to give a Diels-Alder adduct that is a noncompetitive guest (**p**).

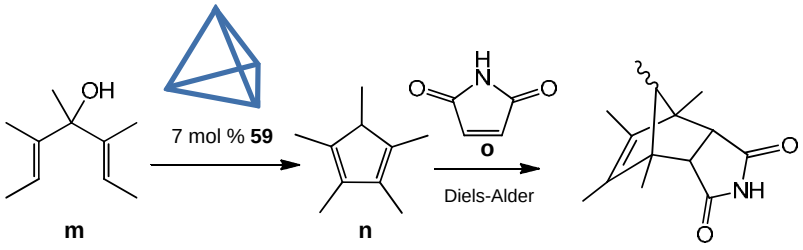

Scheme I.32. Nazarov cyclization of **m** within cage **59**. The obtained product **n** is immediately trapped with maleimide (**o**) to give a product **p** which is easily displaced from the cavity.

As was the case in the tetrahedral cluster **7** (Chapter I.2, Scheme I.3), cage **59** is chiral as a result of the *tris*-bidentate chelation of the metal atoms (Δ or Λ). The mechanical coupling between the metals through the rigid ligands results in the exclusive formation of the homochiral assemblies Δ,Δ,Δ,Δ and Λ, Λ, Λ, Λ (as racemic mixtures). A study in which the enantiopure form of their cage was tested as enantioselective catalyst in the Aza-Cope rearrangement of enamonium substrates has been reported (Table I.1).[188] When the reaction was performed with the enamonium tosylate **q**, in water at 50ºC for 2 h (20 mol% cage loading), a good enantioselectivity was obtained (Table I.1, Entry 1). However, when the reaction was performed at low temperature lower yields were obtained, but the enantioselectivity was improved (Table I.1, Entry 2). The enantioselectivity displayed was rationalized by the fact that the reactions take place inside a chiral confined space rather than specific interactions with a moiety on the substrate. The chiral metal centres produced good asymmetric induction in this rearrangement.

Table I.1. Asymmetric induction in the Aza-Cope rearrangement reactions, catalyzed by cage **59**.

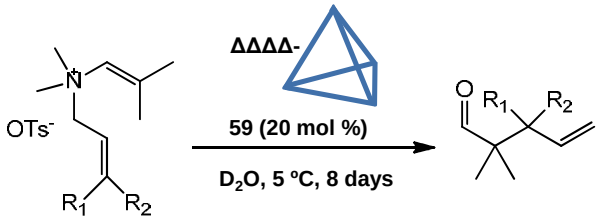

Entry	Substrate	R_1	R_2	Yield (%)[a]	*Ee*
1	**q$_f$**	H	iPr	74	60
2	**q$_f$**[b]	H	iPr	49	78

[a] Yields measured by ^{1}H-NMR spectroscopy using $CHCl_3$ as an internal standard.

Very recently the same authors reported on the use of a modified cage GaL_6^{12-} which also contains a well-defined hydrophobic cavity (**59$_{a\text{-}b}$**, Figure I.12). The new cage only differs from the previously mentioned example (**59**) in its exterior; it contains chiral amide functional groups. Modified cage **59** was proven to be a more efficient catalyst for enantioselective catalysis of a neutral guest in water, than the previously reported cage.[189] More interestingly, the new cage was capable of catalyzing the substitution reaction at a secondary benzylic carbon centre to give products with retention of absolute stereochemistry, whilst reaction of the same substrates in bulk solution gave the product with inversion of stereochemistry.[190]

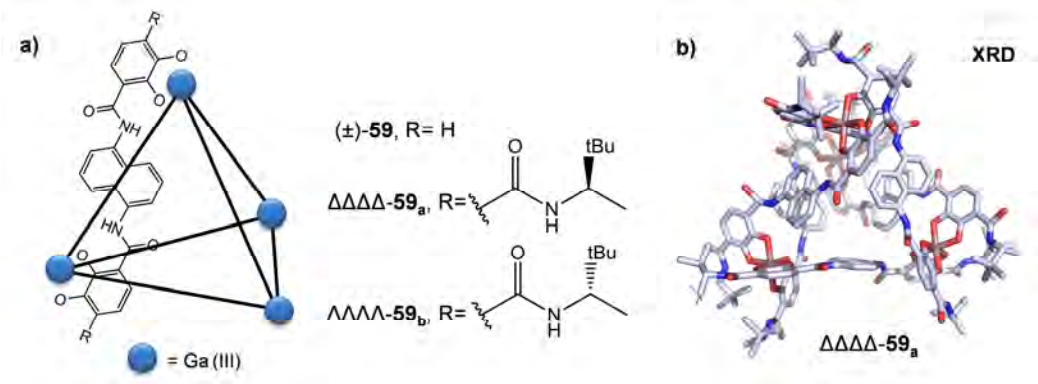

Figure I.12. a) Schematic representation of the Ga_4L_6 assemblies **59** and **59$_{a\text{-}b}$. b)** Representation of the XRD structure of ΔΔΔΔ-**59** (hydrogens have been omitted for clarity).

Another coordination nanoreactor was reported by Duan, who synthesized neutral Ce-based cages (**60$_{TTS}$**, **60$_{TBS}$** and **60$_{TNS}$**) of different sizes (Figure I.13). The tetrahedral cages bearing a well-defined cavity catalysed the cyanosilylation of aromatic aldehydes.[191] When the reaction was performed within cages **60$_{TTS}$** or **60$_{TBS}$**, conversions of up to 99% were obtained for 4-nitrobenzaldehyde (Table I.2, entry 1). However, only the **60$_{TBS}$** cage was able to catalyze the cyanosilylation of the larger 2-(anthracen-9-yl)acetaldehyde. To demonstrate that the reactions were taking place inside the nanoreactor, the authors synthesized cage **60$_{TNS}$**, which had smaller pores and inner cavity in spite of having a bigger structure (Table I.2, Entry 2). All the

reactions with the latter cage proceed with low conversions, suggesting that when using cages **60**$_{TTS}$ or **60**$_{TBS}$ the reactions occur inside their confined cavities.

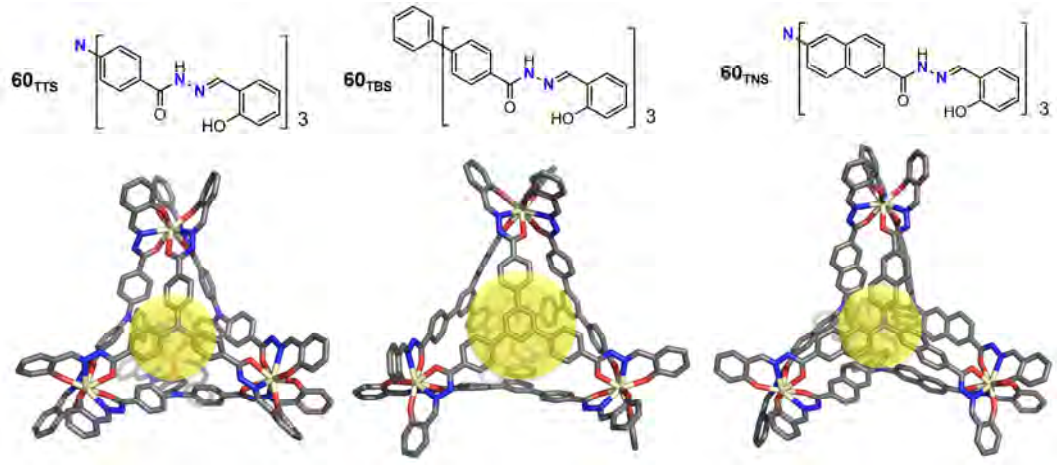

Figure I.13. Ligands of the Ce-based tetrahedral cages **60**$_{TTS}$, **60**$_{TBS}$ and **60**$_{TNS}$, and their crystal structures. The yellow spheres indicate the volume and the size of each cavity.

Table I.2. Conversions for the cyanosilylations of carbonyl substrates in the presence of **60**.[a]

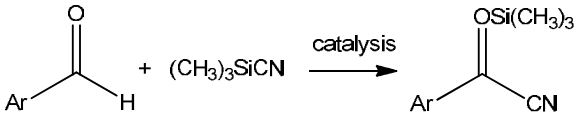

Substrate	**60**$_{TTS}$ (%)	**60**$_{TBS}$ (%)	**60**$_{TNS}$ (%)
4-nitrobenzaldehyde	99	99	30
2-(anthracene-9-yl)acetaldehyde	21	95	22

[a] Reaction conditions: homogeneous reaction, $(CH_3)_3SiCN$ (0.20 mM), aldehyde (0.08 mM), 60 (1.6 mM) at r.t. under N_2 for 1h in 2 mL of DMF/$CHCl_3$ (v/v=1/99) solution.

Interestingly, cage **60** incorporated moieties with luminescence emission and upon encapsulation of substrates, the emission was quenched. The bright emission of the cage molecules decreased during the catalytic process and afterwards it was gradually recovered. This luminescent response provided the possibility to monitor the catalytic process.

I.4.2 Capsules containing a catalytic moiety

When the nanoreactor contains a catalytically active species such as a transition metal, similar effects as those described above can be observed. The capsule can confine the reactants in close proximity within the catalytic centre, or it can also modify the energetic parameters. The catalytic cycle of the encapsulated catalyst can be different from the one obtained in the bulk solution and the rate determining step can change because of the changes in the activation parameters. The encapsulation of a catalyst can also alter its second coordination sphere, inducing new size-, shape-, and regio-selectivities. Moreover it can prevent catalyst decomposition, due to a higher stability of the sequestered catalytic species.

Tetrahedral nanocage **59** (Ga_4L_6) developed by Raymond and Bergman was also proven as an efficient receptor molecule for a variety of monocationic species including organometallic complexes and chiral guests (Scheme I.31).[192–195] Taking advantage of the fact that this nanocage can encapsulate transition metal complexes, the authors decided to use the coordination cage to isolate catalytically active species.

The sequestration of a rhodium catalyst for the isomerization of allylic alcohols was reported by the authors in 2007 (Scheme I.33).[196] First, $[(P(CH_3)_2Rh(COD)]^+$ catalyst precursor was encapsulated and subsequently the precursor was hydrogenated to give the catalytically active species $[(P(CH_3)_3)_2Rh(OD)_2^+ \subset Ga_4L_6]$. The restricted cavity of the cage (~300-500 $Å^3$), imposed substrate size and shape selectivity, and only small and linear allylic alcohols were isomerized. Additionally, the nanoreactor protected the catalyst against decomposition.

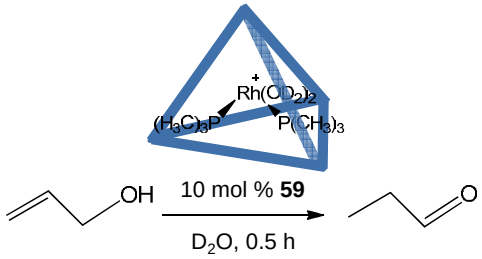

Scheme I.33. Catalytic isomerization of allylic alcohols by $[(PMe_3)_2Rh(OD_2)_2^+] \subset$ **59**.

Raymond, Bergman and Toste also reported the encapsulation of gold(I)-phosphine complexes for the intramolecular hydroalkoxylation of allenes (Scheme I.34).[197] First, host-guest experiments to encapsulate the $(CH_3)_3PAu^+$ complex inside the cage were performed. When the free catalyst ($(CH_3)_3PAu_3Br$) was added to a solution of allenyl alcohol **r** in water only 11% conversion was observed. However, when the allenyl alcohol **r** (40 eq) was added to a solution of $[(CH_3)_3PAu^+ \subset Ga_4L_6]^{11-}$, 48% conversion was observed after 48 h. To prove that the reaction was taking place inside the cavity of the cage, an analogous experiment was performed in presence of a blocking guest molecule, which strongly binds inside the cavity and only 11% conversion was obtained. When $[(CH_3)_3PAu^+ \subset Ga_4L_6]^{11-}$ was used in catalytic amounts, up to 67 TONs were achieved. Apparently the low rate observed in the background reaction was due to catalyst decomposition, which means that the capsule protects the catalysts against decomposition and enhances its lifetime leading to higher activities.

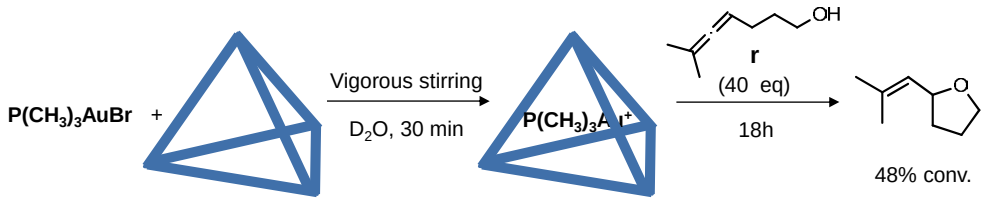

Scheme I.34. Hydroalkoxylation reaction catalysed by $(CH_3)_3PAu^+ \subset$ **59**.

In the examples previously mentioned in this section, the catalytic moiety is sequestered within the cavity by hydrophobic effects or weak supramolecular interactions (e.g. electrostatics). There are coordination capsules in which the catalytic moiety is bound directly to the supramolecular structure through coordination bonds. In the latter case, the catalytic moiety can be embedded in the supramolecular cage as a guest or it can be a template molecule. The most widely used catalytic moieties are Salen complexes and metalloporphyrins, due to the wide range of reactions in which they can participate and their rigid structure.[42,54]

In Chapter I.2.1 an example reported by Hupp and Nguyen, of a 2D coordination structure containing Salen complexes has been highlighted. A similar square structure based on rhenium(I) metal ions and zinc(II) and manganese(III)-porphyrins was also reported by the same group and this coordination square was shown to be a good catalyst for the epoxidation of olefins.[198]

The authors reported a more sophisticated rectangular cage for the epoxidation of olefins in 2008 (Scheme I.35).[199] Capsule **61** consists of four zinc(II)-porphyrin trimers and two tin(IV)-porphyrin dimers on the sides of the rectangle and one central manganese(III)-porphyrin dimer as a catalytic centre. As a result of introducing bulky chiral substituents to the tin(IV)-porphyrin dimer a chiral version of the capsule was obtained. Initially, experiments were carried out using the achiral structure and a competitive epoxidation reaction between *cis*-stilbene and more bulky *cis*-3,3',5,5'-tetra(*tert*-butyl)-stilbene was performed. The smaller olefin reacted 5.5 times faster, due to impeded access of the larger olefin to the metal centre, which was sterically hindered by the bulky carboxylate ligands on the tin(IV)-porphyrins and this is a good example of substrate-size based selectivity. On the other hand, when the chiral version of the cage **61** was used in the catalytic sulfoxidation of *p*-tolyl sulfide, *p*-tolyl sulfoxide was obtained with 12% *ee* (*ee*= enantiomeric excess). No enantioselectivity resulted when only free manganese(III)-porphyrin dimer was used, with or without the tin(IV)-porphyrin dimers. The enantioselectivity was proposed to originate from a through space interaction with the N-acetyl-D-phenylalanine ligands on the tin(IV)-porphyrins.

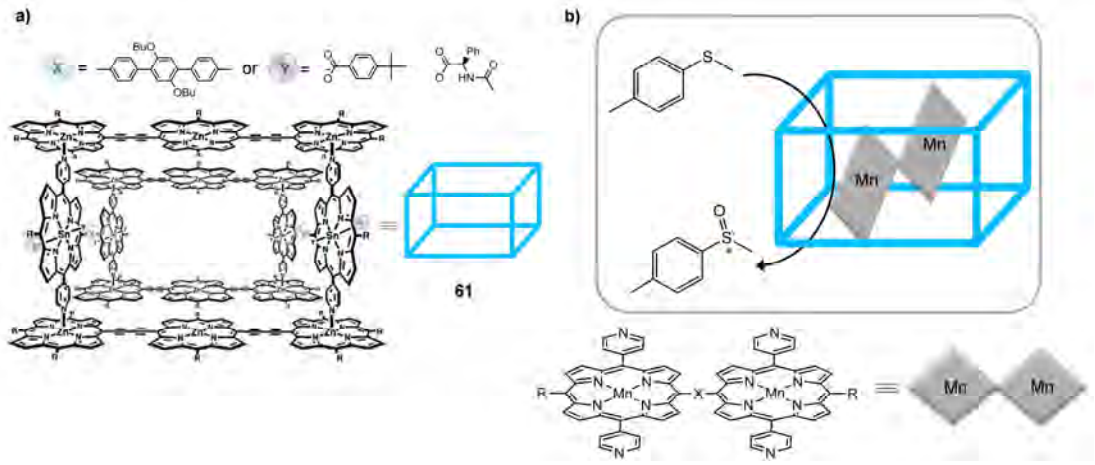

Scheme I.35. Supramolecular porphyrin-based rectangular nanocage **61** for the epoxidation of olefins and chiral sulfoxidation of thioesters.

Inspired by the self-assembled cubic cage reported by Nitschke and De Bruin designed an enlarged M_8L_6 cubic cage **62$_a$** capable to encapsulate metalated tetrapyridyl-metalloporphyrins (**TPyP**) as catalytic moieties (M= cobalt(III) or zinc(II)).[200] The cage has sufficient space for inclusion of additional organic substrates and allows catalytic turn over inside the supramolecular cavity (Scheme I.36). The catalytic performance of a metallo-radical catalyst upon encapsulation was evaluated. Initially, the cobalt(III)-porphyrin-catalyzed radical cyclopropanation of styrene (**s**) with ethyl diazoacetate (**t**) in DMF to give the corresponding cyclopropane (**u**) was studied. The results indicated that the 50% yield obtained with the encapsulated cobalt(III) porphyrin (Co(III)-**TPyP⊂62**), is substantially more active than free tetra(4-pyridyl)porphyrin catalyst Co(III)-**TPyP** (15% yield). The authors pointed to two major effects of encapsulation on the activity of the Co(III)-**TPyP**: 1) activation of the guest as a catalytically active species (prevents self-aggregation of the cobalt(III)-porphyrins *via* pyridine-cobalt coordination), and 2) it (sterically) delays unwanted radical-type side reactions (e.g. radical coupling). The cage was also active in Z-selective olefin synthesis using a disubstituted diazo compound as the substrate.

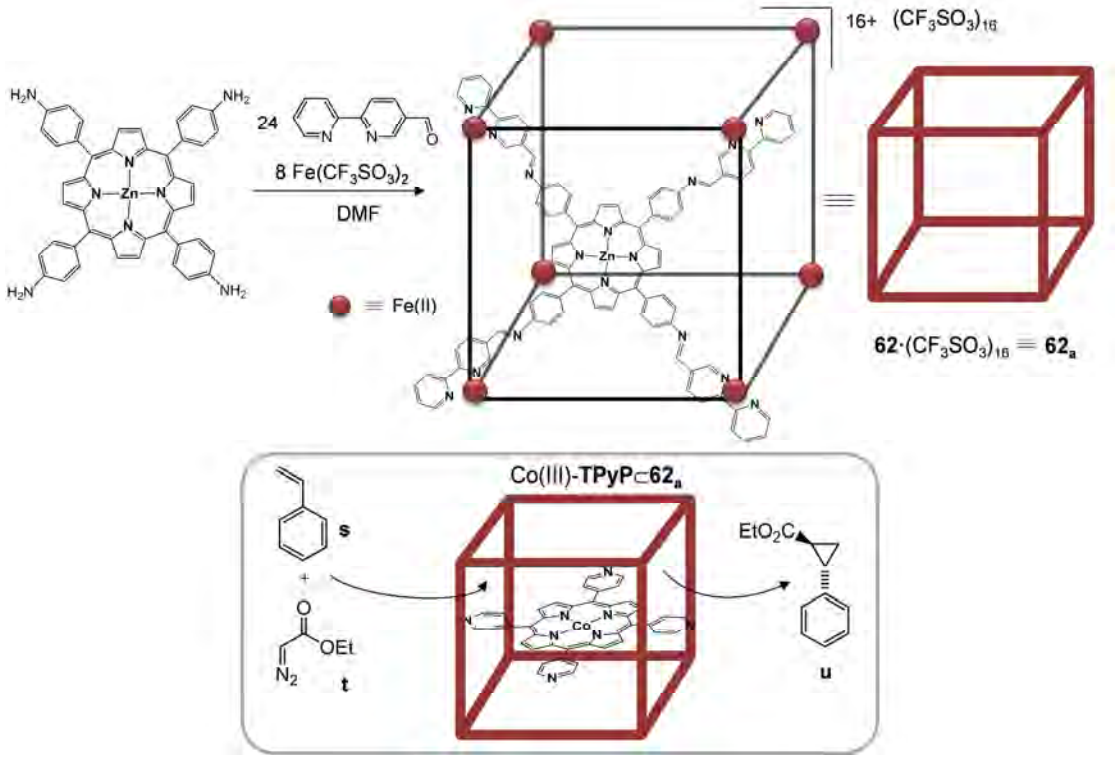

Scheme I.36. a) Schematic representation of the self-assembly of cubic cage **62$_a$**. **b**) Encapsulation of a cobalt(III)-pophyrin, and an example of the catalyzed cyclopropanation of styrene by Co(III)-**TPyP⊂62$_a$**.

All of the reactions performed using cage **62$_a$** were limited to DMF as solvent. Replacing $Fe(CF_3SO_3)_2$ by $Fe[N(CF_3SO_2)_2]_2$ resulted in a modified cage **62$_b$**, which was soluble in acetone, acetonitrile, DMF and mixtures of solvents such us water/acetonitrile. This new cage was also able to encapsulate zinc(II)- and cobalt(III)-tetra(4-pyridyl)porphyrin catalyst.[201] Afterwards, the ability of Co(III)-**TPyP⊂62$_b$** to catalyze the cyclopropanation of styrene with ethyl diazoacetate in

different solvents was explored. The authors discovered that the reactivity of Co(III)-**TPyP⊂62$_b$** was optimum using a 5:1 mixture of water and acetone furnishing a 43% yield, substantially more active than the free analogue (3% yield). Competition experiments between styrene and different styrene derivatives showed that the cage imposed size-selectivity towards the less bulky product (Scheme I.37). Nanocage Co(III)-**TPyP⊂62$_b$** exhibited size-selectivity favouring the cyclopropanation of small styrene and diazo substrates. This size-preference was explained by a slower migration of larger substrates through the pores of the cage compared to smaller substrates.

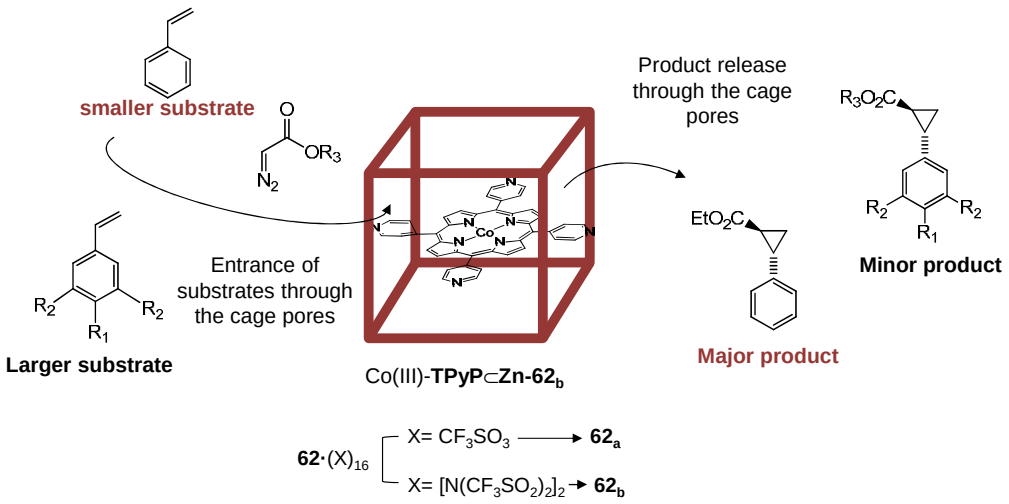

Scheme I.37. Representation of the proposed pore-size-controlled, size-selective transformation catalyzed by Co(III)-TPyP⊂**Zn-62$_b$**.

A different strategy was followed by Reek, defined by the author as the ligand-template approach. Bifunctional pyridyl-based templating ligands were used and either zinc(II)-porphyrin or zinc(II)-salphen groups in order to isolate the transition metal catalyst. This approach leads to versatile systems, in which the blocking ligands, the metal or the template ligands can be modified in order to fine-tune the product distribution from the reaction.

One of the template ligands chosen was the tetradentate *tris*-3-pyridylphosphine (PPy_3). The PPy_3 has three pyridyl positions (*meta*- or *para*-substituted, *m*-**63** and *p*-**63**, respectively) which can selectively bind to three zinc(II) blocking groups (Scheme I.38). Upon coordination, the porphyrin/Salphen groups create a hemispherical wraparound. The central phosphorous donor atom, from the template ligand, remains available for metal coordination. These templated structures were used as catalysts to study the hydroformylation of alkenes, using [Rh(acac)$(CO)_2$] as a catalyst precursor.[202,203]

The templated structures were reacted with Rh(acac)$(CO)_2$. Under syngas pressure (H_2/CO) and species similar to [Rh(CO)(acac)](**63**) are transformed to [$HRh(CO)_3$](**63**), which are the active species for the hydroformylation reaction. The hydroformylation of terminal alkenes was studied, from which linear or branched aldehydes can be obtained with the ratio of these products strongly depending on the catalyst used. The results showed that the templated

[Rh(acac)CO](*m*-**63**) catalyst is 10-fold more active than non-templated rhodium catalyst [$HRh(CO_2)_2$](*m*-**63**) with 1-octene and in addition, that the selectivity for the product is reversed. The supramolecular catalyst provided 63% of branched aldehyde compared to 26% observed for the non-encapsulated species. Conversely, when the [Rh(acac)CO](*p*-**63**) catalyst was used in the hydroformylation of 1-octene, the linear aldehyde was obtained as the major product in a similar fashion to that observed with the free rhodium catalyst, [$HRh(CO_2)_2$](*p*-**63**). In the case of the *meta*-catalyst, upon encapsulation, the rhodium(I) complex changes from containing two phosphines to only a single phosphine, which generally produces more branched aldehyde products along with higher reaction rates compared to the bisphosphine species. Part of these effects were attributed to the isolation of the catalytic species, as open cage analogues having only one phosphite coordinated to the rhodium are less active and produce less branched aldehyde. On the other hand, the more open structure of the *para*-catalyst allows the formation of bisphosphine complexes, as is the case of the non-encapsulated catalyst.

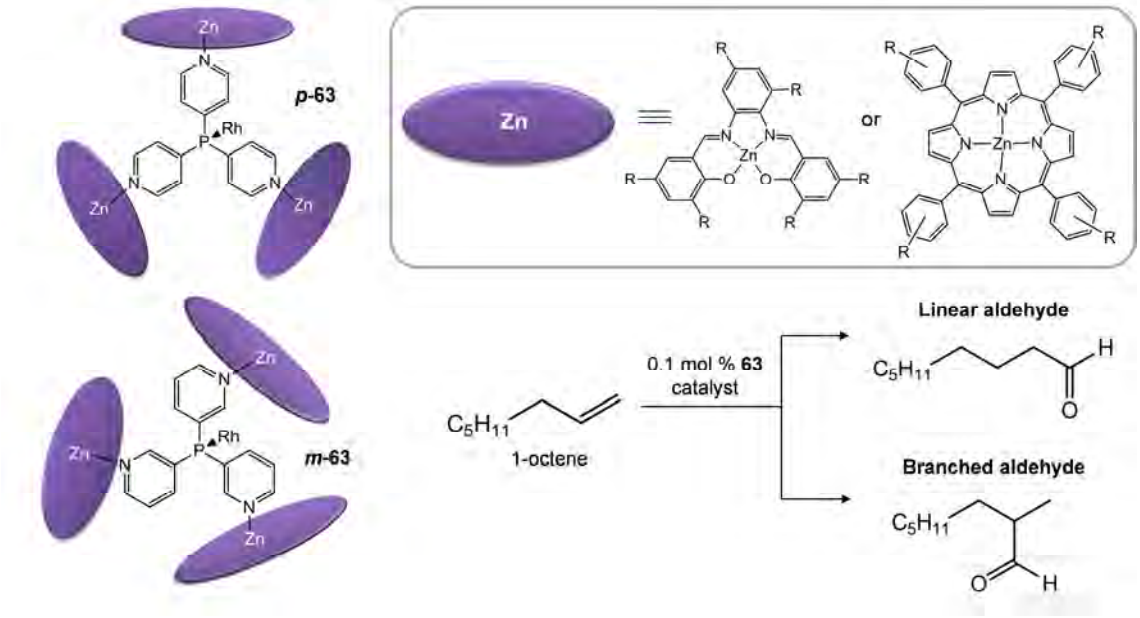

Scheme I.38. Templated nanoreactors *m*-**63** and *p*-**63** used as catalysts in the hydroformylation of 1-octene.

The hydroformylation of internal alkenes was also studied using these template systems. When [Rh(acac)CO](*m*-**63**) catalyst was used in the hydroformylation of 2-octene, 2-ethylheptanal was obtained in 88%, whilst the non-templated catalyst gave a near statistical mixture of 2-methyloctanal and 2-ethyl heptanal. This unprecedented regioselectivity in the hydroformylation of internal alkenes, was explained as a result of the steric restrictions imposed by the inner side of the templated structure.[204]

More recently Berthon-Gelloz and Reek reported on a mono-phosphoramidite ligand containing two *para*-pyridyl moieties (4-PyMonoPhos), as a new template for zinc(II)-tetraphenylporphyrines (Zn-**TPP**) yielding a new templated supramolecular catalyst for hydroformylation reactions (Scheme I.39).[205] High pressure ^{1}H and ^{13}P NMR experiments together with infrared spectroscopy, performed under hydroformylation conditions (H_2/CO),

indicated that in complex **64** the bulky phosphorammidite ligand occupies an axial position *trans* to the hydride. On the contrary, in the free catalyst the monoligated rhodium hydrido complexes are formed with the ligand in the equatorial plane, in *cis* orientation to the hydride. This unusual coordination mode in the encapsulated complex is facilitated by supramolecular control imparted from the Zn(II)-**TPP** units, and affects the catalytic performance in the asymmetric hydroformylation of internal alkenes. In the hydroformylation of 2-octene, the templated catalyst gave higher conversion (45%) and enantioselectivity (*ee* = 44%) than the free catalyst with only 12% conversion and 25% *ee*. These results illustrate the positive effect imparted from the isolated space in the supramolecular coordination assembly.

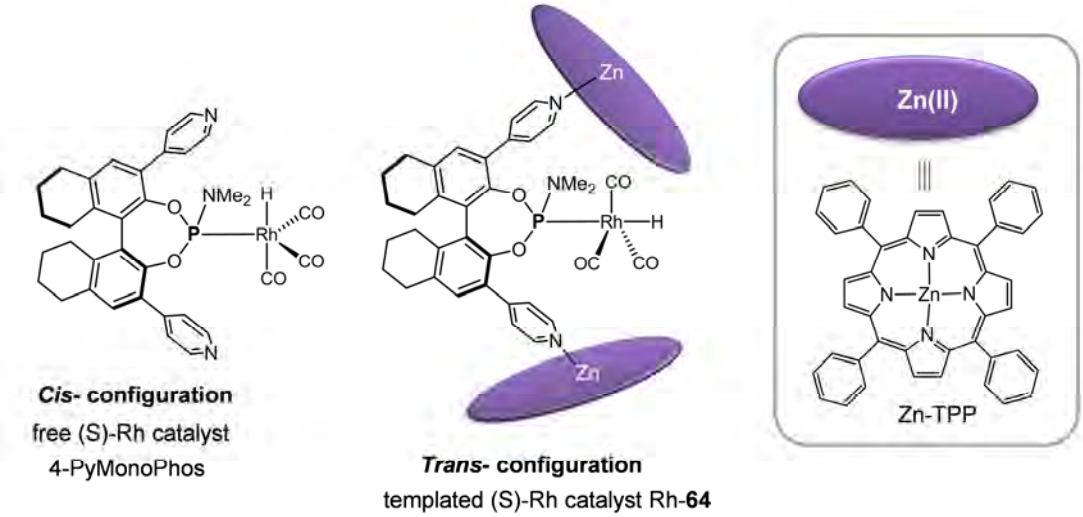

Scheme I.39. Rh-**64** supramolecular catalyst templated with a phosphoramidite chiral ligand.

Another example in which Reek illustrated the effects of catalyst confinement in hydroformylation was reported in 2012.[206] A chiral mono-phosphoramidite analogous to (4-PyMonoPhos), but containing *meta*-pyridyl moieties (3-PyMonoPhos), was used to assemble a supramolecular box together with *bis*-[zinc(II)-salphen] complexes (**65**, Scheme I.40). In this new structure the two phosphorus atoms are in close proximity, affording a self-assembled chiral bidentate ligand. The box was reacted with Rh(acac)$(CO)_2$ (Rh-**66**), and subsequently the catalytically active species were generated under syngas, and used in the hydroformylation of internal alkenes. When free monodentate ligand (S)-3-PyMonoPhos was used in the hydroformylation of *cis*- or *trans*-2-octene, both were converted to 2-methyloctanal preferentially. Upon fixation of the phosphoramidites into the box structure the regioselectivity was reversed, resulting in a modest preference for the innermost aldehyde (2-ethylheptanal), however, an increase in the enantioselectivity was observed. Using the supramolecular box-like **66** the ratio of the R enantiomers of 2-ethylheptanal obtained from *cis*-2-octene increased from 19% to 65%. The relevance of these results is best understood when compared with commercially available catalysts such as Chiraphite or (S,S)-DIOP, which gave ~20% of (*R*)-2-ethylheptenal. The substrate scope was then evaluated using different unfuctionalized alkenes,

and it was observed that the selectivities obtained for *cis*- and *trans*-2-octene were general for all 2-olefins.

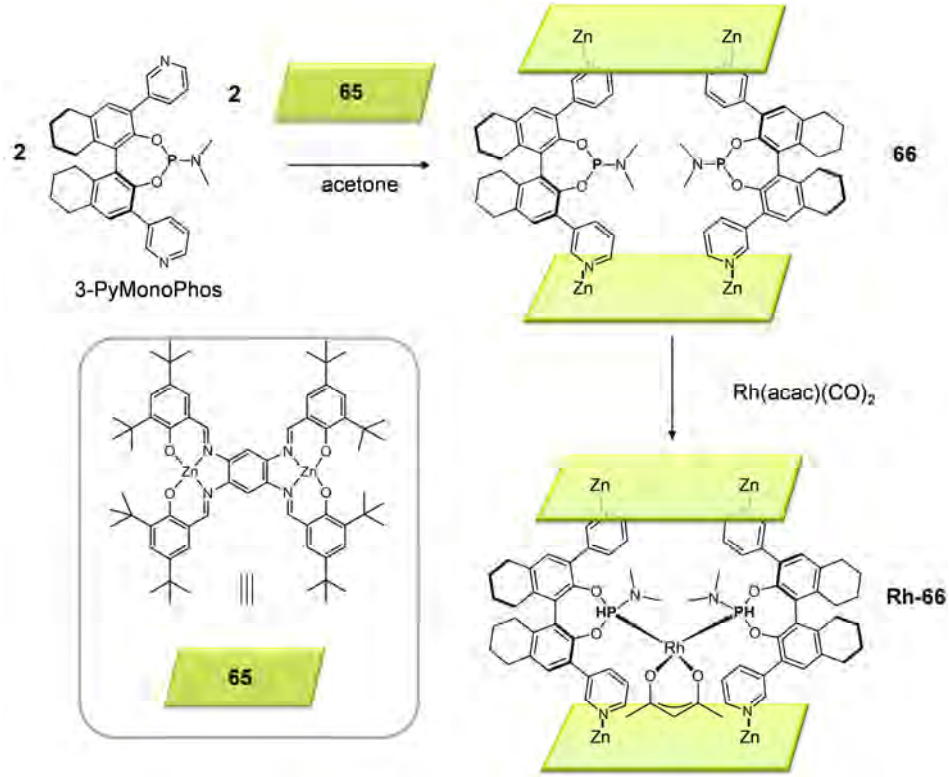

Scheme I.40. Assembly of the supramolecular box-like system **66** through self-assembly of (S)-3-PyMonoPhos ligand and bis[Zn(salphen)] **65**. Metalation of **66** gives Rh-**66** catalyst precursor.

Recently, Reek reported a self-assembly strategy to prepare nanosized molecular spheres, analogous to the previously described by Fujita, with an extremely high metal-complex concentration inside. At this high concentration the AuCl was reactive and showed high selectivity in intramolecular C-O and C-C bond forming ion reactions.[207] The $M_{12}L_{24}$ spherical cages were synthesized using two different ditopic ligands, one functionalized with a $[(aryl)_3PAuCl]$ linked with an aliphatic spacer (**67**) and a second one containing an acetate functional group (**68**) (Scheme I.41). After mixing **67** or **68** with $[Pd(CH_3CN)_4](CF_3SO_3)_2$ in a 24:12 ratio, the corresponding homoleptic spheres where obtained (**69** and **70**, Scheme I.41). The preparation of mixed spheres was also possible using different ratios of **67** and **68** in the presence of the palladium(II) salt. By modifying the **67**:**68** ratio, the local concentration of gold inside the nanosphere could be varied from 1.07 M (**67**:**68** ratio 24:0) to 0.05 M (**67**:**68** ratio 1:23). Afterwards, the authors explored the effect of local catalyst concentration inside the $[(\mathbf{67}_n\mathbf{68}_{24-n})Pd_{12}](CF_3SO_3)_{24}$ spheres, on the hydroalkoxylation of 2,2-diphenylpent-4-en-1-ol. This is a typical gold-mediated transformation in which either a five- or six-membered ring products can be obtained. The authors performed the reaction with different sets of spheres with Au(I) local concentration between 0.05-1.07 M, while the overall gold concentration was kept constant at 5 mM. The results indicated that the catalyst activity increased with the local concentration of gold inside the sphere and the five-membered ring product was selectively

formed. Sphere **69** gave the highest activity ([AuCl]=1.07M) and a turnover number (TON) of 67 was reached. It is also remarkably that free AuCl complexes did not show any conversion under these reaction conditions. The authors then repeated the same reaction using a less reactive substrate and by slight tuning the reaction conditions, excellent yields and selectivities were obtained. In a control experiment the reaction was performed under the same high concentrations (1.1 M) using Ph_3PAuCl or **67** separately and no conversion was observed. It suggested that not only the high concentration but other factors play a role in the activity and selectivity displayed in the reactions.

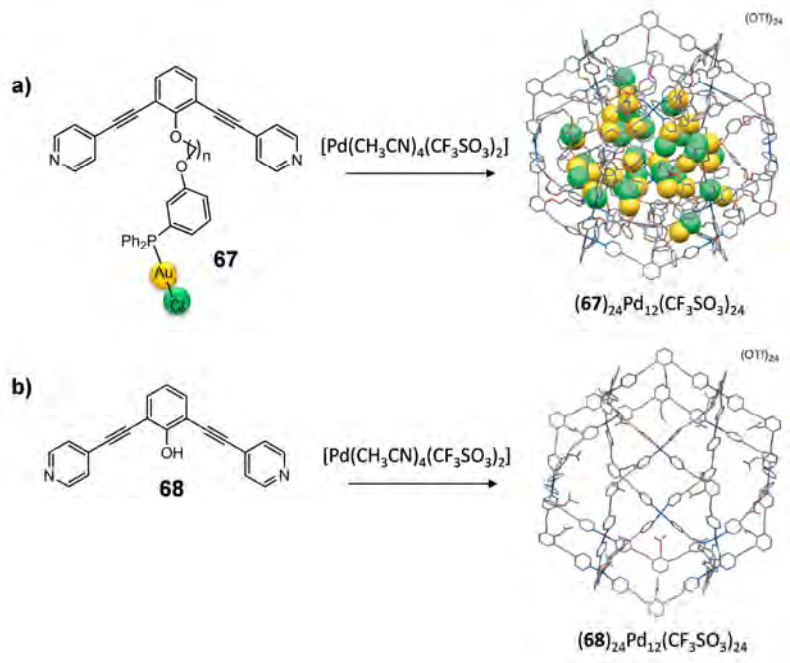

Scheme I.41. Building block **67** (**a**) and **68** (**b**) used for the preparation of the corresponding spheres **69** and **70**. PM3-Spartan-modeled coordination spheres. Reproduced in part with from {Ref. 207} with permission of John Willey and Sons.

I.5. References

(1) Lehn, J.-M. *Supramolecular Chemistry: concepts and perspectives*; Wiley-VCH: Weinheim, Germany, 1995.

(2) Steed, J.W; Turner, R.D; Wallace, K. *Core Concepts in Supramolecular Chemistry and Nanochemistry*; John Willey & Sons: Cichester, UK, 2007.

(3) Steed, J.W.; Atwood, J. L. *Supramolecular Chemistry*; John Willey & Sons, Ltd: UK, 2009.

(4) Hosseini, M. W. *Chem. Commun.* **2005**, 5825.

(5) Kramer, R.; Lehn, J.-M.; Bel, I. Le; Pasteur, U. L.; Marquis-rigault, A. *Proc. Natl. Acad. Sci. U. S. A.* **1993**, *90*, 5394.

(6) Lehn, J.-M. *Science* **2002**, *295*, 2400.

(7) Lehn, J.-M. *Chem. Soc. Rev.* **2007**, *36*, 151.

(8) McLaughlin, C. K.; Hamblin, G. D.; Sleiman, H. F. *Chem. Soc. Rev.* **2011**, *40*, 5647.

(9) Dodziuk, H. *Introduction to Supramolecular Chemistry*; Springer: USA, 2002.

(10) Henkelis, J. J.; Carruthers, C. J.; Chambers, S. E.; Clowes, R.; Cooper, A. I.; Fisher, J.; Hardie, M. J. *J. Am. Chem. Soc.* **2014**, *136*, 14393.

(11) Li, S.; Yan, H.; Wan, L.; Yang, H.; Northrop, B. H.; Stang, P. J. *J. Am. Chem. Soc.* **2007**, *129*, 9268.

(12) McKinlay, R. M.; Thallapally, P. K.; Cave, G. W. V; Atwood, J. L. *Angew. Chem. Int. Ed.* **2005**, *44*, 5733.

(13) Gimeno, N.; Vilar, R. *Coord. Chem. Rev.* **2006**, *250*, 3161.

(14) Pluth, M. D.; Raymond, K. N. *Chem. Soc. Rev.* **2007**, *36*, 161.

(15) Holliday, B. J.; Mirkin, C. A. *Angew. Chem. Int. Ed.* **2001**, *40*, 2022.

(16) Chakrabarty, R.; Mukherjee, P. S.; Stang, P. J. *Chem. Rev.* **2011**, *111*, 6810.

(17) Cook, T. R.; Zheng, Y.-R.; Stang, P. J. *Chem. Rev.* **2013**, *113*, 734.

(18) Leininger, S.; Olenyuk, B.; Stang, P. J. *Chem. Rev.* **2000**, *100*, 853.

(19) Seidel, S. R.; Stang, P. J. *Acc. Chem. Res.* **2002**, *35*, 972.

(20) Company, A.; Roques, N.; Güell, M.; Mugnaini, V.; Gómez, L.; Imaz, I.; Datcu, A.; Solà, M.; Luis, J. M.; Veciana, J.; Ribas, X.; Costas, M. *Dalton Trans.* **2008**, *3*, 1679.

(21) Company, A.; Gómez, L.; López Valbuena, J. M.; Mas-Ballesté, R.; Benet-Buchholz, J.; Llobet, A.; Costas, M. *Inorg. Chem.* **2006**, *45*, 2501.

(22) Gómez, L.; Company, A.; Fontrodona, X.; Ribas, X.; Costas, M. *Chem. Commun.* **2007**, 4410.

(23) Umemoto, K.; Yamaguchi, K.; Fujita, M. *J. Am. Chem. Soc.* **2000**, *122*, 7150.

(24) Fujita, M.; Umemoto, K.; Yoshizawa, M.; Fujita, N.; Kusukawa, T.; Biradha, K. *Chem. Commun.* **2001**, 509.

(25) Fujita, M.; Tominaga, M.; Hori, A.; Therrien, B. *Acc. Chem. Res.* **2005**, *38*, 369.

(26) Fujita, M.; Yu, S.-Y.; Kusukawa, T.; Funaki, H.; Ogura, K.; Yamaguchi, K. *Angew. Chem. Int. Ed.* **1998**, *37*, 2082.

(27) Fujita, M.; Oguro, D.; Miyazawa, M.; Oka, H.; Yamaguchi, K.; Ogura, K. *Nature* **1995**, *378*, 469.

(28) Caulder, D. L.; Raymond, K. N. *Acc. Chem. Res.* **1999**, *32*, 975.

(29) Caulder, D. L.; Brückner, C.; Powers, R. E.; König, S.; Parac, T. N.; Leary, J. a; Raymond, K. N. *J. Am. Chem. Soc.* **2001**, *123*, 8923.

(30) Farrell, J. R.; Mirkin, C. A.; Guzei, I. A.; Liable-sands, L. M.; Rheingold, A. L. *Angew. Chem. Int. Ed.* **1998**, *3*, 465.

(31) Masar, M. S.; Ovchinnikov, M. V; Mirkin, C. A.; Zakharov, L. N.; Rheingold, A. L. *Inorg. Chem.* **2003**, *42*, 6851.

(32) Cotton, F. A.; Lin, C.; Murillo, C. A. *Proc. Natl. Acad. Sci. U. S. A.* **2002**, *99*, 4810.

(33) Smulders, M. M. J.; Riddell, I. A.; Browne, C.; Nitschke, J. R. *Chem. Soc. Rev.* **2013**, *42*, 1728.

(34) Han, M.; Engelhard, D. M.; Clever, G. H. *Chem. Soc. Rev.* **2014**, *43*, 1848.

(35) Saha, M. L.; De, S.; Pramanik, S.; Schmittel, M. *Chem. Soc. Rev.* **2013**, *42*, 6860.

(36) Hiraoka, S.; Shiro, M.; Shionoya, M. *J. Am. Chem. Soc.* **2004**, *126*, 1214.

(37) Mirtschin, S.; Slabon-Turski, A.; Scopelliti, R.; Velders, A. H.; Severin, K. *J. Am. Chem. Soc.* **2010**, *132*, 14004.

(38) Chepelin, O.; Ujma, J.; Barran, P. E.; Lusby, P. J. *Angew. Chem. Int. Ed.* **2012**, *51*, 4194.

(39) Hiraoka, S.; Sakata, Y.; Shionoya, M. *J. Am. Chem. Soc.* **2008**, *130*, 10058.

(40) Splan, K. E.; Massari, A. M.; Morris, G. A.; Sun, S.-S.; Reina, E.; Nguyen, S. T.; Hupp, J. T. *Eur. J. Inorg. Chem.* **2003**, *2003*, 2348.

(41) Sun, S.-S.; Stern, C. L.; Nguyen, S. T.; Hupp, J. T. *J. Am. Chem. Soc.* **2004**, *126*, 6314.

(42) Canali, L.; Sherrington, D. C. *Chem. Soc. Rev.* **1999**, *28*, 85.

(43) Whiteoak, C. J.; Salassa, G.; Kleij, A. W. *Chem. Soc. Rev.* **2012**, *41*, 622.

(44) Mahata, K.; Schmittel, M. *J. Am. Chem. Soc.* **2009**, *131*, 16544.

(45) Tominaga, M.; Suzuki, K.; Kawano, M.; Kusukawa, T.; Ozeki, T.; Sakamoto, S.; Yamaguchi, K.; Fujita, M. *Angew. Chem. Int. Ed.* **2004**, *43*, 5621.

(46) Sun, Q.-F.; Iwasa, J.; Ogawa, D.; Ishido, Y.; Sato, S.; Ozeki, T.; Sei, Y.; Yamaguchi, K.; Fujita, M. *Science* **2010**, *328*, 1144.

(47) Fujita, D.; Takahashi, A.; Sato, S.; Fujita, M. *J. Am. Chem. Soc.* **2011**, *133*, 13317.

(48) Riddell, I. a; Smulders, M. M. J.; Clegg, J. K.; Hristova, Y. R.; Breiner, B.; Thoburn, J. D.; Nitschke, J. R. *Nat. Chem.* **2012**, *4*, 751.

(49) Riddell, I. a; Hristova, Y. R.; Clegg, J. K.; Wood, C. S.; Breiner, B.; Nitschke, J. R. *J. Am. Chem. Soc.* **2013**, *135*, 2723.

(50) Wang, M.; Zheng, Y.; Ghosh, K.; Stang, P. J. *J. Am. Chem. Soc.* **2010**, *132*, 6282.

(51) Shi, Y.; Sánchez-Molina, I.; Cao, C.; Cook, T. R.; Stang, P. J. *Proc. Natl. Acad. Sci. U. S. A.* **2014**, *111*, 9390.

(52) Wasielewski, M. R. *Acc. Chem. Res.* **2009**, *42*, 1910.

(53) Aratani, N.; Kim, D.; Osuka, A. *Acc. Chem. Res.* **2009**, *42*, 1922.

(54) Durot, S.; Taesch, J.; Heitz, V. *Chem. Rev.* **2014**, *114*, 8542.

(55) Han, Y.-F.; Lin, Y.-J.; Hor, T. S. A.; Jin, G.-X. *Organometallics* **2012**, *31*, 995.

(56) Therrien, B. *Eur. J. Inorg. Chem.* **2009**, *2009*, 2445.

(57) Riddell, I. a; Smulders, M. M. J.; Clegg, J. K.; Nitschke, J. R. *Chem. Commun.* **2011**, *47*, 457.

(58) Amouri, H.; Mimassi, L.; Rager, M. N.; Mann, B. E.; Guyard-Duhayon, C.; Raehm, L. *Angew. Chem. Int. Ed.* **2005**, *44*, 4543.

(59) Meng, W.; Clegg, J. K.; Nitschke, J. R. *Angew. Chem. Int. Ed.* **2012**, *51*, 1881.

(60) Ziegler, M.; Brumaghim, J. L.; Raymond, K. N. *Angew. Chem. Int. Ed.* **2000**, *112*, 4285.

(61) Brumaghim, J.; Michels, M.; Raymond, K. *Eur. J. Org. Chem* **2004**, *2004*, 4552.

(62) Dong, V. M.; Fiedler, D.; Carl, B.; Bergman, R. G.; Raymond, K. N. *J. Am. Chem. Soc.* **2006**, *128*, 14464.

(63) Yamashina, M.; Sei, Y.; Akita, M.; Yoshizawa, M. *Nat. Commun.* **2014**, *5*, 4662.

(64) Furusawa, T.; Kawano, M.; Fujita, M. *Angew. Chem. Int. Ed.* **2007**, *46*, 5717.

(65) Mal, P.; Breiner, B.; Rissanen, K.; Nitschke, J. R. *Science* **2009**, *324*, 1697.

(66) Nishioka, Y.; Yamaguchi, T.; Yoshizawa, M.; Fujita, M. *J. Am. Chem. Soc.* **2007**, *129*, 7000.

(67) Yoshizawa, M.; Takeyama, Y.; Kusukawa, T.; Fujita, M. *Angew. Chem. Int. Ed.* **2002**, *41*, 1347.

(68) Chen, J.; Rebek, J. *Org. Lett.* **2002**, *4*, 327.

(69) Yamashita, K.-I.; Kawano, M.; Fujita, M. *Chem. Commun.* **2007**, *1*, 4102.

(70) Han, M.; Michel, R.; He, B.; Chen, Y.-S.; Stalke, D.; John, M.; Clever, G. H. *Angew. Chem. Int. Ed.* **2013**, *52*, 1319.

(71) Wang, M.; Vajpayee, V.; Shanmugaraju, S.; Zheng, Y.-R.; Zhao, Z.; Kim, H.; Mukherjee, P. S.; Chi, K.-W.; Stang, P. J. *Inorg. Chem.* **2011**, *50*, 1506.

(72) Tashiro, S.; Tominaga, M.; Kawano, M.; Therrien, B.; Ozeki, T.; Fujita, M. *J. Am. Chem. Soc.* **2005**, *127*, 4546.

(73) Hatakeyama, Y.; Sawada, T.; Kawano, M.; Fujita, M. *Angew. Chem. Int. Ed.* **2009**, *48*, 8695.

(74) Therrien, B.; Süss-Fink, G.; Govindaswamy, P.; Renfrew, A. K.; Dyson, P. J. *Angew. Chem. Int. Ed.* **2008**, *47*, 3773.

(75) Lewis, J. E. M.; Gavey, E. L.; Cameron, S. a.; Crowley, J. D. *Chem. Sci.* **2012**, *3*, 778.

(76) Kroto, H. W.; Heath, J. R.; O'Brien, S. C.; Curl, R. F.; Smalley, R. E. *Nature* **1985**, *318*, 162.

(77) Krätschmer, W.; Lamb, L. D.; Fostiropoulos, K.; Huffman, D. R. *Nature* **1990**, *347*, 354.

(78) Hirch, A. and Brettreich, M. *Fullerenes: chemistry and reactions*; Wiley-VCH: Weinheim, Germany, 2005.

(79) Hirsch, A. *Nat. Mater.* **2010**, *9*, 868.

(80) Martín, N. *Chem. Commun.* **2006**, 2093.

(81) Śliwa, W. *Fuller. Sci. Technol.* **1995**, *3*, 243.

(82) Nakamura, Y.; Kato, S. *Chem. Rec.* **2011**, *11*, 77.

(83) Popov, A. A.; Yang, S.; Dunsch, L. *Chem. Rev.* **2013**, *113*, 5989.

(84) Cerón, M. R.; Li, F.-F.; Echegoyen, L. A. *J. Phys. Org. Chem.* **2014**, *27*, 258.

(85) Anderson, H. L.; Boudon, C.; Diederich, F.; Gisselbrecht, J.-P.; Gross, M.; Seiler, P. *Angew. Chem. Int. Ed.* **1994**, *33*, 1628.

(86) Arias, F.; Godínez, L. A.; Wilson, S. R.; Kaifer, A. E.; Echegoyen, L. *J. Am. Chem. Soc.* **1996**, *118*, 6086.

(87) Chuard, T.; Deschenaux, R. *Helv. Chim. Acta* **1996**, *79*, 736.

(88) Campidelli, S.; Brandmüller, T.; Hirsch, A.; Saez, I. M.; Goodby, J. W.; Deschenaux, R. *Chem. Commun.* **2006**, 4282.

(89) Prato, M. *J. Mater. Chem.* **1997**, *7*, 1097.

(90) Dennler, G.; Scharber, M. C.; Brabec, C. J. *Adv. Mater.* **2009**, *21*, 1323.

(91) Iwasa, Y. *Nature* **2010**, *466*, 191.

(92) Liu, G.-F.; Filipović, M.; Ivanović-Burmazović, I.; Beuerle, F.; Witte, P.; Hirsch, A. *Angew. Chem. Int. Ed.* **2008**, *47*, 3991.

(93) Friedman, S. H.; DeCamp, D. L.; Sijbesma, R. P.; Srdanov, G.; Wudl, F.; Kenyon, G. L. *J. Am. Chem. Soc.* **1993**, *115*, 6506.

(94) Yeretzian, C.; Wiley, J. B.; Holczer, K.; Su, T.; Nguyen, S.; Kaner, R. B.; Whetten, R. L. *J. Phys. Chem.* **1993**, *97*, 10097.

(95) Parker, D. H.; Chatterjee, K.; Wurz, P.; Lykke, K. R.; Pellin, M. J.; Stock, L. M.; Hemminger, J. C. *Carbon* **1992**, *30*, 1167.

(96) Ajie, H.; Alvarez, M. M.; Anz, S. J.; Beck, R. D.; Diederich, F.; Fostiropoulos, K.; Huffman, D. R.; Kraetschmer, W.; Rubin, Y.; et al., . *J. Phys. Chem.* **1990**, *94*, 8630.

(97) Doome, R. J.; Fonseca, A.; Richter, H.; Nagy, J. B.; Thiry, P. A.; Lucas, A. A. *J. Phys. Chem. Solids* **1997**, *58*, 1839.

(98) Taylor, R.; Hare, J. P.; Abdul-Sada, A. K.; Kroto, H. W. *J. Chem. Soc. Chem. Commun.* **1990**, 1423.

(99) Johnson, R. D.; Meijer, G.; Bethune, D. S. *J. Am. Chem. Soc.* **1990**, *112*, 8983.

(100) Kremenskaya, I. N.; Nudelman, M. A.; Shlyamina, I. G.; Shlyamin, V. I. *Mendeleev Commun.* **1993**, *3*, 9.

(101) Vassallo, A. M.; Palmisano, A. J.; Pang, L. S. K.; Wilson, M. A. *J. Chem. Soc. Chem. Commun.* **1992**, 60.

(102) Komatsu, N.; Ohe, T.; Matsushige, K. *Carbon* **2004**, *42*, 163.

(103) Gügel, A.; Becker, M.; Hammel, D.; Mindach, L.; Räder, J.; Simon, T.; Wagner, M.; Müllen, K. *Angew. Chem. Int. Ed.* **1992**, *31*, 644.

(104) Meier, M. S.; Selegue, J. P. *J. Org. Chem.* **1992**, *57*, 1924.

(105) Cabrera, K.; Wieland, G.; Schäfer, M. *J. Chromatogr. A* **1993**, *644*, 396.

(106) Canevet, D.; Pérez, E. M.; Martín, N. *Angew. Chem. Int. Ed.* **2011**, *50*, 9248.

(107) Effing, J.; Jonas, U.; Jullien, L.; Plesnivy, T.; Ringsdorf, H.; Diederich, F.; Thilgen, C.; Weinstein, D. *Angew. Chem. Int. Ed.* **1992**, *31*, 1599.

(108) Andersson, T.; Nilsson, K.; Sundahl, M.; Westman, G.; Wennerström, O. *J. Chem. Soc. Chem. Commun.* **1992**, 604.

(109) Liu, Y.; Wang, H.; Liang, P.; Zhang, H.-Y. *Angew. Chem. Int. Ed.* **2004**, *43*, 2690.

(110) Suzuki, T.; Nakashima, K.; Shinkai, S. *Chem. Lett.* **1994**, 699.

(111) Atwood, J. L.; Koutsantonis, G. A.; Raston, C. L. *Nature* **1994**, *368*, 229.

(112) Haino, T.; Fukunaga, C.; Fukazawa, Y. *Org. Lett.* **2006**, *8*, 3545.

(113) Yoshida, Z.; Takekuma, H.; Takekuma, S.; Matsubara, Y. *Angew. Chem. Int. Ed.* **1994**, *33*, 1597.

(114) Isobe, H.; Hitosugi, S.; Yamasaki, T.; Iizuka, R. *Chem. Sci.* **2013**, *4*, 1293.

(115) Miki, K.; Matsushita, T.; Inoue, Y.; Senda, Y.; Kowada, T.; Ohe, K. *Chem. Commun.* **2013**, *49*, 9092.

(116) Nakanishi, Y.; Omachi, H.; Matsuura, S.; Miyata, Y.; Kitaura, R.; Segawa, Y.; Itami, K.; Shinohara, H. *Angew. Chem. Int. Ed.* **2014**, *53*, 3102.

(117) Canevet, D.; Gallego, M.; Isla, H.; de Juan, A.; Pérez, E. M.; Martín, N. *J. Am. Chem. Soc.* **2011**, *133*, 3184.

(118) Huerta, E.; Isla, H.; Pérez, E. M.; Bo, C.; Martín, N.; de Mendoza, J. *J. Am. Chem. Soc.* **2010**, *132*, 5351.

(119) Grimm, B.; Santos, J.; Illescas, B. M.; Muñoz, A.; Guldi, D. M.; Martín, N. *J. Am. Chem. Soc.* **2010**, *132*, 17387.

(120) Huerta, E.; Metselaar, G. a; Fragoso, A.; Santos, E.; Bo, C.; de Mendoza, J. *Angew. Chem. Int. Ed.* **2007**, *46*, 202.

(121) Huerta, E.; Cequier, E.; de Mendoza, J. *Chem. Commun.* **2007**, 5016.

(122) Li, M.-J.; Huang, C.-H.; Lai, C.-C.; Chiu, S.-H. *Org. Lett.* **2012**, *14*, 6146.

(123) Ku, M.; Huang, S.-J.; Huang, S.; Liu, Y.; Lai, C.-C.; Peng, S.-M.; Chiu, S.-H. *Chem. Commun.* **2014**, *50*, 11709.

(124) Zhang, C.; Wang, Q.; Long, H.; Zhang, W. *J. Am. Chem. Soc.* **2011**, *133*, 20995.

(125) Wang, Y.-B.; Lin, Z. *J. Am. Chem. Soc.* **2003**, *125*, 6072.

(126) Tashiro, K.; Aida, T.; Zheng, J. *J. Am. Chem. Soc.* **1999**, *1*, 9477.

(127) Jian-Yu Zheng, Kentaro Tashiro, Yusuke Hirabayashi, Kazushi Kinbara, Kazuhiko Saigo, Takuzo Aida, S. S. and K. Y. *Angew. Chem. Int. Ed.* **2001**, *40*, 1857.

(128) Yanagisawa, M.; Tashiro, K.; Yamasaki, M.; Aida, T. *J. Am. Chem. Soc.* **2007**, *129*, 11912.

(129) Shoji, Y.; Tashiro, K.; Aida, T. *J. Am. Chem. Soc.* **2004**, *126*, 6570.

(130) Tashiro, K.; Aida, T. *Chem. Soc. Rev.* **2007**, *36*, 189.

(131) Hajjaj, F.; Tashiro, K.; Nikawa, H.; Mizorogi, N.; Akasaka, T.; Nagase, S.; Furukawa, K.; Kato, T.; Aida, T. *J. Am. Chem. Soc.* **2011**, *133*, 9290.

(132) Hernández-Eguía, L. P.; Escudero-Adán, E. C.; Pintre, I. C.; Ventura, B.; Flamigni, L.; Ballester, P. *Chem. Eur. J.* **2011**, *17*, 14564.

(133) Hernández-Eguía, L. P.; Escudero-Adán, E. C.; Pinzón, J. R.; Echegoyen, L.; Ballester, P. *J. Org. Chem.* **2011**, *76*, 3258.

(134) Nobukuni, H.; Shimazaki, Y.; Tani, F.; Naruta, Y. *Angew. Chem. Int. Ed.* **2007**, *46*, 8975.

(135) Sakaguchi, K.; Kamimura, T.; Uno, H.; Mori, S.; Ozako, S.; Nobukuni, H.; Ishida, M.; Tani, F. *J. Org. Chem.* **2014**, *79*, 2980.

(136) Kieran, A. L.; Pascu, S. I.; Jarrosson, T.; Sanders, J. K. M. *Chem. Commun.* **2005**, 1276.

(137) Mulholland, A. R.; Woodward, C. P.; Langford, S. J. *Chem. Commun.* **2011**, *47*, 1494.

(138) Gil-Ramírez, G.; Karlen, S. D.; Shundo, A.; Porfyrakis, K.; Ito, Y.; Briggs, G. A. D.; Morton, J. J. L.; Anderson, H. L. *Org. Lett.* **2010**, *12*, 3544.

(139) Song, J.; Aratani, N.; Shinokubo, H.; Osuka, A. *J. Am. Chem. Soc.* **2010**, *132*, 16356.

(140) Wu, Z.; Shao, X.; Li, C.; Hou, J.; Wang, K.; Jiang, X.; Li, Z. *J. Am. Chem. Soc.* **2005**, *127*, 17460.

(141) Schmittel, M.; He, B.; Mal, P. *Org. Lett.* **2008**, *10*, 2513.

(142) Nakamura, T.; Ube, H.; Miyake, R.; Shionoya, M. *J. Am. Chem. Soc.* **2013**, *135*, 18790.

(143) Meng, W.; Breiner, B.; Rissanen, K.; Thoburn, J. D.; Clegg, J. K.; Nitschke, J. R. *Angew. Chem. Int. Ed.* **2011**, *50*, 3479.

(144) Pirondini, L.; Bonifazi, D.; Cantadori, B.; Braiuca, P.; Campagnolo, M.; Zorzi, R. De; Geremia, S.; Diederich, F.; Dalcanale, E. *Tetrahedron* **2006**, *62*, 2008.

(145) Fox, O. D.; Wilkinson, E. J. S.; Beer, P. D.; Drew, M. G. B. *Chem. Commun.* **2000**, *6*, 391.

(146) Ikeda, A.; Yoshimura, M.; Udzu, H.; Fukuhara, C.; Shinkai, S. *J. Am. Chem. Soc.* **1999**, *121*, 4296.

(147) Ikeda, A.; Udzu, H.; Yoshimura, M.; Shinkai, S. *Tetrahedron* **2000**, *56*, 1825.

(148) Claessens, C. G.; Torres, T. *Chem. Commun.* **2004**, 1298.

(149) Claessens, C. G.; Torres, T. *J. Am. Chem. Soc.* **2002**, *124*, 14522.

(150) Sánchez-Molina, I.; Grimm, B.; Krick Calderon, R. M.; Claessens, C. G.; Guldi, D. M.; Torres, T. *J. Am. Chem. Soc.* **2013**, *135*, 10503.

(151) Kishi, N.; Li, Z.; Yoza, K.; Akita, M.; Yoshizawa, M. *J. Am. Chem. Soc.* **2011**, *133*, 11438.

(152) Kishi, N.; Akita, M.; Kamiya, M.; Hayashi, S.; Hsu, H.; Yoshizawa, M. *J. Am. Chem. Soc.* **2013**, *135*, 12976.

(153) Kishi, N.; Akita, M.; Yoshizawa, M. *Angew. Chem. Int. Ed.* **2014**, *53*, 3604.

(154) Mahata, K.; Frischmann, P. D.; Würthner, F. *J. Am. Chem. Soc.* **2013**, *135*, 15656.

(155) Ronson, T. K.; League, A. B.; Gagliardi, L.; Cramer, C. J.; Nitschke, J. R. *J. Am. Chem. Soc.* **2014**, *136*, 15615.

(156) Kusukawa, T.; Fujita, M. *J. Am. Chem. Soc.* **2002**, *124*, 13576.

(157) Yoshizawa, M.; Klosterman, J. K.; Fujita, M. *Angew. Chem. Int. Ed.* **2009**, *48*, 3418.

(158) Inokuma, Y.; Arai, T.; Fujita, M. *Nat. Chem.* **2010**, *2*, 780.

(159) Sato, S.; Iida, J.; Suzuki, K.; Kawano, M.; Ozeki, T.; Fujita, M. *Science* **2006**, *313*, 1273.

(160) Suzuki, K.; Takao, K.; Sato, S.; Fujita, M. *J. Am. Chem. Soc.* **2010**, *132*, 2544.

(161) Benkovic, S. J.; Hammes-Schiffer, S. *Science* **2003**, *301*, 1196.

(162) Dong, Z.; Luo, Q.; Liu, J. *Chem. Soc. Rev.* **2012**, *41*, 7890.

(163) Wiester, M. J.; Ulmann, P. a; Mirkin, C. a. *Angew. Chem. Int. Ed.* **2011**, *50*, 114.

(164) Amouri, H.; Desmarets, C.; Moussa, J. *Chem. Rev.* **2012**, *112*, 2015.

(165) Raynal, M.; Ballester, P.; Vidal-Ferran, A.; van Leeuwen, P. W. N. M. *Chem. Soc. Rev.* **2014**, *43*, 1734.

(166) Dydio, P.; Breuil, P.-A. R.; Reek, J. N. H. *Isr. J. Chem.* **2013**, *53*, 61.

(167) Wang, L.; Wang, G.-T.; Zhao, X.; Jiang, X.-K.; Li, Z.-T. *J. Org. Chem.* **2011**, *76*, 3531.

(168) Vriezema, D. M.; Comellas Aragonès, M.; Elemans, J. a a W.; Cornelissen, J. J. L. M.; Rowan, A. E.; Nolte, R. J. M. *Chem. Rev.* **2005**, *105*, 1445.

(169) Leenders, S. H. a M.; Gramage-Doria, R.; de Bruin, B.; Reek, J. N. H. *Chem. Soc. Rev.* **2014**, DOI:10.1039/c4cs00192c.

(170) Breiner, B.; Clegg, J. K.; Nitschke, J. R. *Chem. Sci.* **2011**, *2*, 51.

(171) Koblenz, T. S.; Wassenaar, J.; Reek, J. N. H. *Chem. Soc. Rev.* **2008**, *37*, 247.

(172) Meissner, R. S.; Rebek, J.; de Mendoza, J. *Science* **1995**, *270*, 1485.

(173) Kang, J.; Rebek, J. *Nature* **1996**, *382*, 239.

(174) Kang, J.; Rebek, J. *Nature* **1997**, *385*, 50.

(175) Kang, J.; Hilmersson, G.; Santamaría, J.; Rebek, J. *J. Am. Chem. Soc.* **1998**, *120*, 3650.

(176) Palmer, L. C.; Rebek, J. *Org. Biomol. Chem.* **2004**, *2*, 3051.

(177) Kang, J.; Santamaría, J.; Hilmersson, G.; Rebek, J. *J. Am. Chem. Soc.* **1998**, *120*, 7389.

(178) Yoshizawa, M.; Nakagawa, J.; Kumazawa, K.; Nagao, M.; Kawano, M.; Ozeki, T.; Fujita, M. *Angew. Chem. Int. Ed.* **2005**, *44*, 1810.

(179) Murase, T.; Horiuchi, S.; Fujita, M. *J. Am. Chem. Soc.* **2010**, *132*, 2866.

(180) Yoshizawa, M.; Takeyama, Y.; Okano, T.; Fujita, M. *J. Am. Chem. Soc.* **2003**, *125*, 3243.

(181) Yoshizawa, M.; Tamura, M.; Fujita, M. *Science* **2006**, *312*, 251.

(182) Murase, T.; Nishijima, Y.; Fujita, M. *J. Am. Chem. Soc.* **2012**, *134*, 162.

(183) Pluth, M. D.; Bergman, R. G.; Raymond, K. N. *Science* **2007**, *316*, 85.

(184) Pluth, M. D.; Bergman, R. G.; Raymond, K. N. *J. Am. Chem. Soc.* **2008**, *130*, 11423.

(185) Pluth, M. D.; Bergman, R. G.; Raymond, K. N. *J. Org. Chem.* **2009**, *74*, 58.

(186) Fiedler, D.; Bergman, R. G.; Raymond, K. N. *Angew. Chem. Int. Ed.* **2004**, *43*, 6748.

(187) Pluth, M. D.; Bergman, R. G.; Raymond, K. N. *Angew. Chem. Int. Ed.* **2007**, *46*, 8587.

(188) Brown, C. J.; Bergman, R. G.; Raymond, K. N. *J. Am. Chem. Soc.* **2009**, *131*, 17530.

(189) Zhao, C.; Sun, Q.-F.; Hart-Cooper, W. M.; Dipasquale, A. G.; Toste, F. D.; Bergman, R. G.; Raymond, K. N. *J. Am. Chem. Soc.* **2013**, *135*, 18802.

(190) Zhao, C.; Toste, F. D.; Raymond, K. N.; Bergman, R. G. *J. Am. Chem. Soc.* **2014**, *136*, 14409.

(191) Jiao, Y.; Wang, J.; Wu, P.; Zhao, L.; He, C.; Zhang, J.; Duan, C. *Chem. Eur. J.* **2014**, *20*, 2224.

(192) Parac, T. N.; Caulder, D. L.; Raymond, K. N. *J. Am. Chem. Soc.* **1998**, *120*, 8003.

(193) Fiedler, D.; Pagliero, D.; Brumaghim, J. L.; Bergman, R. G.; Raymond, K. N. *Inorg. Chem.* **2004**, *43*, 846.

(194) Fiedler, D.; Leung, D. H.; Bergman, R. G.; Raymond, K. N. *J. Am. Chem. Soc.* **2004**, *126*, 3674.

(195) Fiedler, D.; Leung, D. H.; Bergman, R. G.; Raymond, K. N. *Acc. Chem. Res.* **2005**, *38*, 349.

(196) Leung, D. H.; Bergman, R. G.; Raymond, K. N. *J. Am. Chem. Soc.* **2007**, *129*, 2746.

(197) Wang, Z. J.; Brown, C. J.; Bergman, R. G.; Raymond, K. N.; Toste, F. D. *J. Am. Chem. Soc.* **2011**, *133*, 7358.

(198) Merlau, M. L.; del Pilar Mejia, M.; Nguyen, S. T.; Hupp, J. T. *Angew. Chem. Int. Ed.* **2001**, *40*, 4239.

(199) Lee, S. J.; Cho, S.-H.; Mulfort, K. L.; Tiede, D. M.; Hupp, J. T.; Nguyen, S. T. *J. Am. Chem. Soc.* **2008**, *130*, 16828.

(200) Otte, M.; Kuijpers, P. F.; Troeppner, O.; Ivanović-Burmazović, I.; Reek, J. N. H.; de Bruin, B. *Chem. Eur. J.* **2013**, *19*, 10170.

(201) Otte, M.; Kuijpers, P. F.; Troeppner, O.; Ivanović-Burmazović, I.; Reek, J. N. H.; de Bruin, B. *Chem. Eur. J.* **2014**, *20*, 4880.

(202) Slagt, V. F.; Kamer, P. C. J.; van Leeuwen, P. W. N. M.; Reek, J. N. H. *J. Am. Chem. Soc.* **2004**, *126*, 1526.

(203) Kleij, A. W.; Lutz, M.; Spek, A. L.; van Leeuwen, P. W. N. M.; Reek, J. N. H. *Chem. Commun.* **2005**, 3661.

(204) Kuil, M.; Soltner, T.; van Leeuwen, P. W. N. M.; Reek, J. N. H. *J. Am. Chem. Soc.* **2006**, *128*, 11344.

(205) Bellini, R.; Chikkali, S. H.; Berthon-Gelloz, G.; Reek, J. N. H. *Angew. Chem. Int. Ed.* **2011**, *50*, 7342.

(206) Gadzikwa, T.; Bellini, R.; Dekker, H. L.; Reek, J. N. H. *J. Am. Chem. Soc.* **2012**, *134*, 2860.

(207) Gramage-Doria, R.; Hessels, J.; Leenders, S. H. a. M.; Tröppner, O.; Dürr, M.; Ivanović-Burmazović, I.; Reek, J. N. H. *Angew. Chem. Int. Ed.* **2014**, DOI:10.1002/anie.201406415.

Chapter II.

Objectives

II. OBJECTIVES

Coordination-driven supramolecular self-assembly has become a very powerful synthetic tool, to rationally and rapidly construct large and intricate chemical structures. Following this strategy, a variety of highly sophisticated 2D and 3D supramolecular structures have been reported. Some of these structures have been prepared to prove the capabilities of the rational design of self-assembly, whilst others were prepared with the aim of creating molecular receptors, sensors, transporters or reaction nanovessels.

In this context, this thesis will focus in the preparation of diamagnetic tetragonal prismatic 3D nanocapsules and on the investigation of some of their properties as supramolecular vessels. The preparation of diamagnetic macrocyclic complexes based on palladium(II), analogous to the copper-based ones previously developed in the group, will allow formation of species which can be characterized by NMR. The preparation of 3D tetragonal prismatic capsules will be realized through self-assembly of tetracarboxylated substituted metalloporphyrins and dipalladium macrocyclic complexes. Fine-tuning of the cage size will be targeted through modulation of the organic macrocyclic ligand dimensions in order to achieve cavities of different sizes. It can be envisioned that the void inner cavities of these nanocapsules and the affinity of guest molecules towards porphyrins, can be exploited in host-guest chemistry.

Molecular building blocks proposed for the self-assembly of the 3D diamagnetic cages

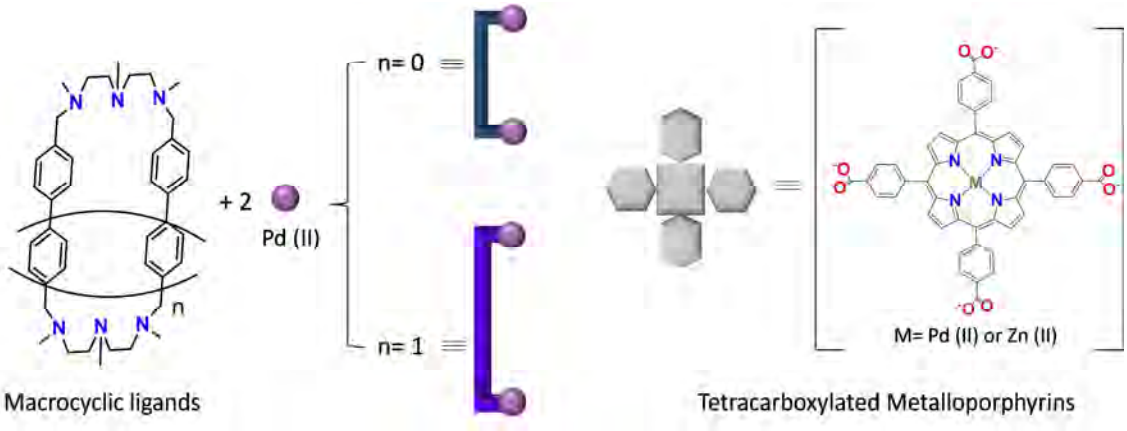

The first step of the thesis will concern the preparation of a diamagnetic 3D nanocapsule based on palladium(II) macrocylic ligands (n=0) and the investigation of its host-guest properties (**Chapter III**).

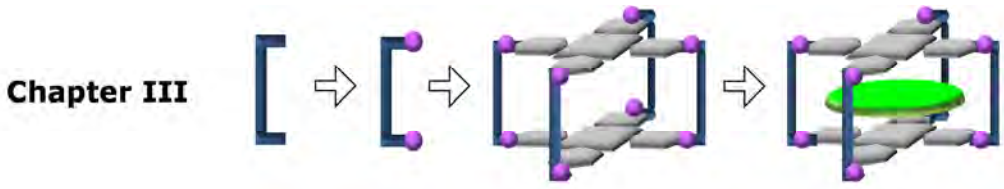

The second step will concentrate on enlarging the dimensions of the molecular clips (n=1) in order to obtain a larger cage, capable of encapsulating larger substrates such as fullerenes (**Chapter IV**).

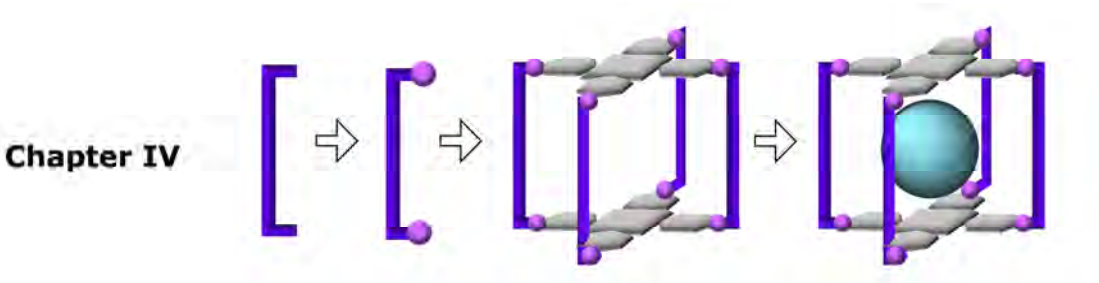

The 3D structure of enzymes is essential to their success in terms of high selectivity and high efficiency. In the last part of this dissertation (**Chapter V**), the confined inner cavity of the larger supramolecular nanocapsule will be used to attempt catalytic experiments, reminiscent of those taking place in enzymatic catalysis. As proof of concept, the performance of the system in the asymmetric hydroformylation (AHF) of alkenes will be studied. It is envisioned that these studies will provide evidence of catalytic activity modulated by the secondary coordination sphere, in this case by the supramolecular capsule.

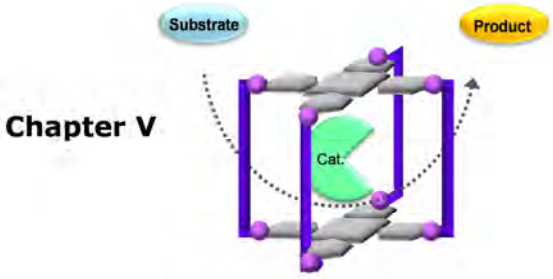

Chapter III.

Self-Assembled Tetragonal Prismatic Molecular Cage Highly Selective for Anionic π Guests

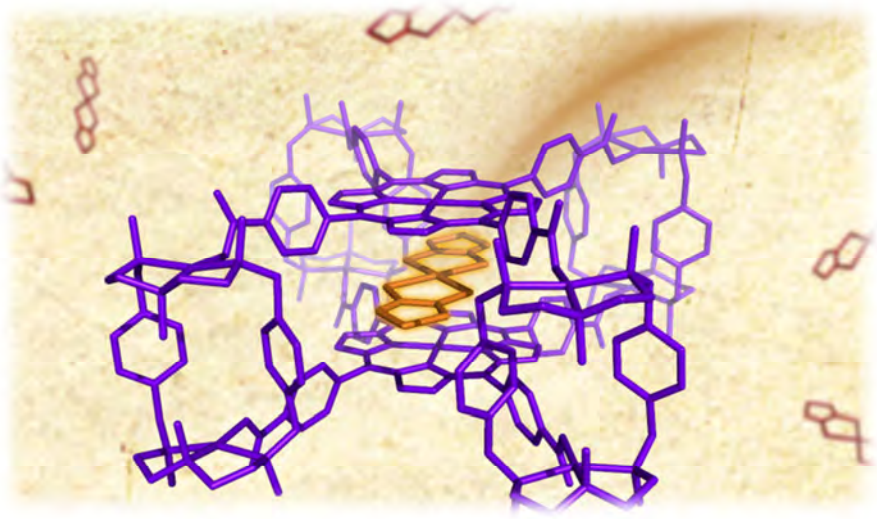

This chapter corresponds to the following publication:

C. García-Simón, M. Garcia-Borràs, L. Gómez, I. Garcia-Bosch, S. Osuna, M. Swart, J.M. Luis, C. Rovira, M. Almeida, I. Imaz, D. Maspoch, M. Costas* and X. Ribas*

Chem. Eu. J. **2013**, *19*, *4*, 1445-1456.

For this publication C.G.-S. synthetized and characterized **Pd-1b** molecular clip and **3**·$(CF_3SO_3)_8$ nanocapsule (L.G performed the ESI-MS experiments, T.P supervised the NMR experiments, I.I. and D.M. performed the XRD analysis). C.G.-S. also performed all the host-guest experiments with the bisthiolene complexes. Besides, C.G.-S. contributed in writing the manuscript and was involved in argumentations and discussions.

Cristina García-Simón,Marc Garcia-Borràs,Laura Gómez,Isaac Garcia-Bosch,Sílvia Osuna,Marcel Swart,Josep M. Luis,Concepció Rovira,Manuel Almeida,Inhar Imaz,Daniel Maspoch,Miquel Costas,Xavi Ribas (2012). "Self-Assembled Tetragonal Prismatic Molecular Cage Highly Selective for Anionic π Guests". *Chemistry: a European Journal, 19, 4,* 1445-1456

DOI: 10.1002/chem.201203376

http://onlinelibrary.wiley.com/doi/10.1002/chem.201203376/full

Article first published online: 4 DEC 2012

Abstract

The metal-directed supramolecular synthetic approach has paved the way for the development of functional nanosized molecules. In this work, we report the preparation of the new nanocapsule **3**·$(CF_3SO_3)_8$ with a A_4B_2 tetragonal prismatic geometry, where A corresponds to the dipalladium hexaazamacrocyclic complex **Pd-1**, and B corresponds to the tetraanionic form of palladium 5,10,15,20-tetrakis(4-carboxyphenyl)porphyrin (**2**). The large void space of the inner cavity and the supramolecular affinity for guest molecules towards porphyrin-based hosts converts this nanoscale molecular 3D structure into a good candidate for host–guest chemistry. The interaction between this nanocage and different guest molecules has been studied by means of NMR, UV/Vis, ESI-MS, and DOSY experiments, from which highly selective molecular recognition has been found for anionic, planar-shaped π guests with association constants (K_a) higher than $10^9\ M^{-1}$, in front of non-interacting aromatic neutral or cationic substrates. DFT theoretical calculations provided insights to further understand this strong interaction. Nanocage **3**·$(CF_3SO_3)_8$ can not only strongly host one single molecule of M(dithiolene)$_2$ complexes (M=Au, Pt, Pd, and Ni), but also can finely tune their optical and redox properties. The very simple synthesis of both the supramolecular cage and the building blocks represents a step forward for the development of polyfunctional supramolecular nanovessels, which offer multiple applications as sensors or nanoreactors.

Keywords:

cage compounds; density functional calculations; gold anionic guests; host–guest systems; self-assembly

Chapter IV.

Sponge-like molecular cage for purification of fullerenes

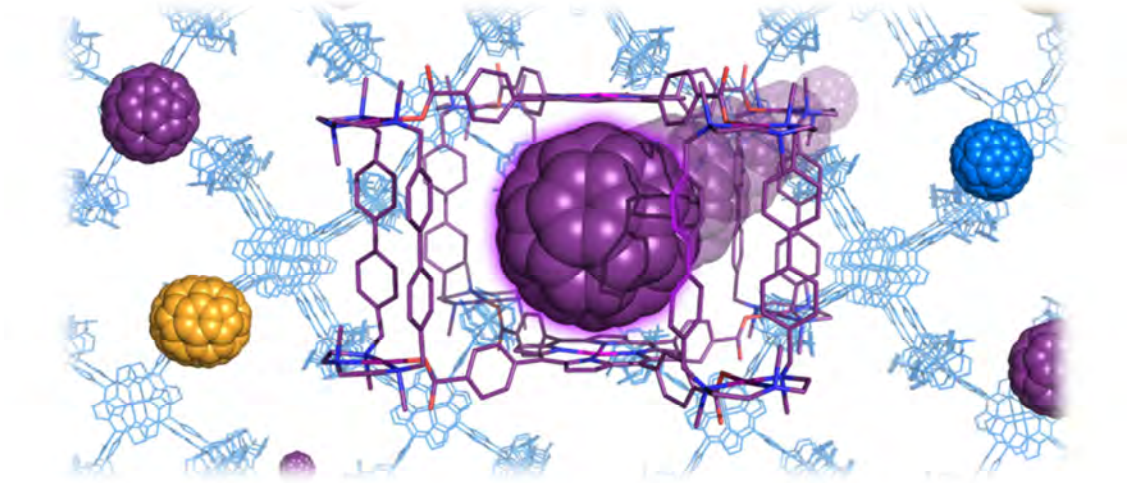

This chapter corresponds to the following publication:

C. García-Simón, M. Garcia-Borràs, L. Gómez, T. Parella, S. Osuna, J. Juanhuix, I. Imaz, D. Maspoch, M. Costas* and X. Ribas*

Nat.Commun., 5:5557, **2014**, DOI: 10.1038/ncomms6557

For this publication C.G.-S. performed all the experimental work and characterization (cage synthesis and fullerenes encapsulation/liberation experiments, L.G. supervised the HRMS experiments, I.I. and D.M. performed the XRD analysis). Besides, C.G.-S. contributed in writing the manuscript and was involved in argumentations and discussions.

nature COMMUNICATIONS

ARTICLE

Received 24 May 2014 | Accepted 13 Oct 2014 | Published 26 Nov 2014

DOI: 10.1038/ncomms6557

Sponge-like molecular cage for purification of fullerenes

Cristina García-Simón[1], Marc Garcia-Borràs[1], Laura Gómez[1,2], Teodor Parella[3], Sílvia Osuna[1], Jordi Juanhuix[4], Inhar Imaz[5], Daniel Maspoch[5,6], Miquel Costas[1] & Xavi Ribas[1]

Since fullerenes are available in macroscopic quantities from fullerene soot, large efforts have been geared toward designing efficient strategies to obtain highly pure fullerenes, which can be subsequently applied in multiple research fields. Here we present a supramolecular nanocage synthesized by metal-directed self-assembly, which encapsulates fullerenes of different sizes. Direct experimental evidence is provided for the 1:1 encapsulation of C_{60}, C_{70}, C_{76}, C_{78} and C_{84}, and solid state structures for the host–guest adducts with C_{60} and C_{70} have been obtained using X-ray synchrotron radiation. Furthermore, we design a washing-based strategy to exclusively extract pure C_{60} from a solid sample of cage charged with a mixture of fullerenes. These results showcase an attractive methodology to selectively extract C_{60} from fullerene mixtures, providing a platform to design tuned cages for selective extraction of higher fullerenes. The solid-phase fullerene encapsulation and liberation represent a twist in host–guest chemistry for molecular nanocage structures.

[1] Institut de Química Computacional i Catàlisi and Departament de Química, Universitat de Girona, Campus Montilivi, Girona, Catalonia 17071, Spain. [2] Serveis Tècnics de Recerca (STR), Universitat de Girona, Parc Cinetífic i Tecnològic, Girona, Catalonia 17003, Spain. [3] Servei de RMN and Departament de Química, Facultat de Ciències, Universitat Autònoma de Barcelona (UAB), Campus UAB, Bellaterra, Catalonia 08193, Spain. [4] ALBA Synchrotron, Cerdanyola del Vallès, Barcelona, Catalonia 08290, Spain. [5] Institut Català de Nanociència i Nanotecnologia, ICN2, Campus UAB, Bellaterra, Catalonia 08193, Spain. [6] Institució Catalana de Recerca i Estudis Avançats (ICREA), Pg. Lluís Companys 23, Barcelona, Catalonia 08010, Spain. Correspondence and requests for materials should be addressed to M.C. (email: miquel.costas@udg.edu) or to X.R. (email: xavi.ribas@udg.edu).

Fullerenes have a wide range of applications, highlighting their extensive use as electroactive materials in solar cells[1–3], and with continuously appearing new uses in medicine[4,5]. Any application, however, is limited in origin by tedious solid–liquid extractions (usually in toluene) and time-expensive chromatographic separations[6–15]. More recently, the host–guest chemistry of molecular containers has been explored to encapsulate fullerenes[16]. Still selectivity is usually difficult to achieve because fine modulation of the size of molecular cages to accommodate different fullerenes is challenging with the limitations of covalent synthesis[17]. Host platforms containing extended π-systems have been designed because of their affinity towards the sphere-like unsaturated structure of fullerenes. In this line, several covalent or supramolecular approaches pursued include: (a) macrocyclic arene-based receptors[18–24], (b) macrocyclic structures containing aromatic heterocycles[25–28], (c) π-extended TTF receptors[29–33] and (d) macrocyclic or jaw-like structures containing porphyrin moieties[17,34–45]. Interestingly, Fujita and co-workers reported the use of the empty channels of a metal–organic framework (MOF) for encapsulating fullerenes upon soaking MOF crystals in fullerene-containing toluene. This work is remarkable because it explores the ability of a solid crystalline structure to absorb fullerenes into its large pores by displacing solvent molecules[46].

On the other hand, focusing the interest on selective recovery of encapsulated fullerenes, several strategies have been applied to release the guest molecules as detailed in Fig. 1 (refs 17,28,39,45,47–50). In all reported examples, however, there is the need to expose the host to chemical or physical treatment to release the sequestered guests, which prevent its straightforward reusability either because it is blocked by a high-affinity secondary guest, or because the host cage is disassembled. In the case of Fujita's crystalline sponge strategy[46], the retention capability is high and half lives of inclusion complexes are over 15 days, thus release of fullerenes must be achieved by deconstructing MOF crystals by acid treatment.

Here we present a tetragonal prismatic supramolecular cage with a high affinity for the inclusion of fullerenes and a facile ability to release them by solvent washing of the solid inclusion compound. The cage, built by metal-directed self-assembly of two zinc porphyrin moieties and four molecular clips through Pd coordination bonds, encapsulates exclusively from C_{60} to C_{84} fullerenes, and C_{60} can be selectively released due to their different host affinities. Moreover, the tetragonal prismatic cage design endows four large entrances that enable an unprecedented example of inclusion and release of fullerenes within a molecular cage in the solid state, thus showing a sponge-like behaviour that allows for rapid purification of fullerene mixtures.

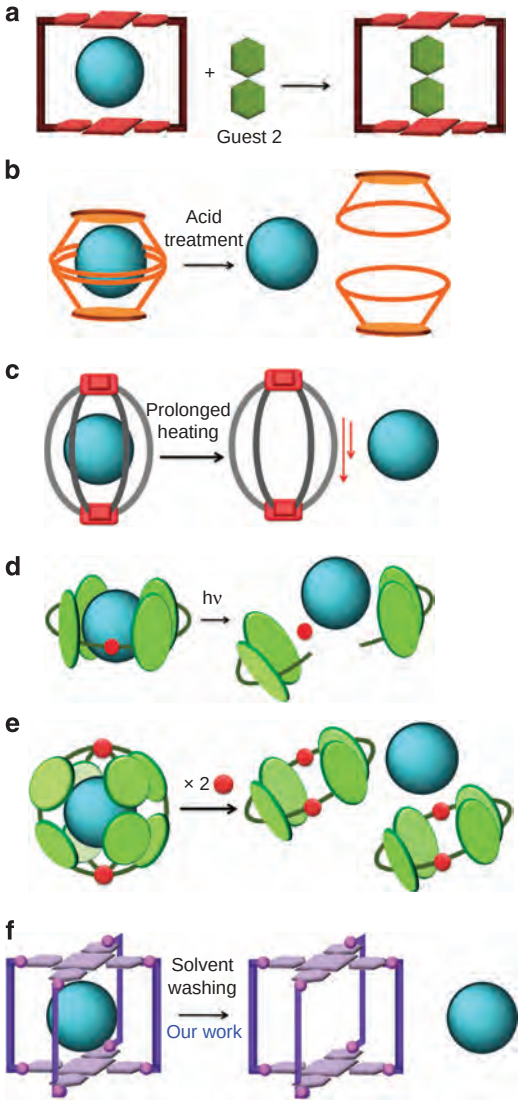

Figure 1 | Literature precedents for fullerene liberation from fullerene ⊂ host adducts. (**a**) Addition of secondary guests in a guest-exchange process[17,39,47], (**b**) acid or base treatment to provoke a structural rearrangement of the host[28], (**c**) prolonged heating to cause the precipitation of the host[48], (**d**) photoreduction of metal ions to disassemble metal-coordination-based supramolecular hosts[49], (**e**) by transforming the shape of the cage in response to an external stimulus[50] and (**f**) solid–liquid solvent washing strategy.

Results

Synthesis and characterization of $4\cdot(X)_8$ cages (X = CF_3SO_3 or BArF (BArF = tetrakis[3,5-bis(trifluoromethyl)phenyl]borate)). Three-dimensional tetragonal prismatic molecular cage $4\cdot(X)_8$ was synthesized by self assembly of a tetracarboxylate Zn^{II}-porphyrin and Pd^{II}-based macrocyclic synthons ((**Pd-1b**)$\cdot(AcO)_2(CF_3SO_3)_2$). $4\cdot(X)_8$ differs from the recently described cage $3\cdot(X')_8$ (X′ = ClO_4, CF_3SO_3) (ref. 51) in the aromatic part of the hexaaza macrocyclic ligands; $3\cdot(X')_8$ contained 1,4-substituted benzene rings that have been replaced by biphenyl rings in **1b**. As a result, the distance between metalloporphyrins is enlarged from 7.5 Å in $3\cdot(X')_8$ to 14.1 Å in $4\cdot(X)_8$ (Figs 2 and 3).

Cage $4\cdot(CF_3SO_3)_8$ was characterized in solution by electrospray ionization mass spectrometry (ESI-MS). However, the compound was poorly soluble in organic solvents. Improved solubility was exhibited by $4\cdot(BArF)_8$, which was isolated in 38% yield after anion exchange. The high resolution mass spectrometry (HRMS) spectrum of $4\cdot(BArF)_8$ shows ions corresponding to the cage with consecutive loss of counteranions, demonstrating its integrity in solution (Fig. 3a). Furthermore, full NMR characterization was performed for $4\cdot(BArF)_8$, showing that it has a D_{4h} symmetric structure in solution. Importantly, the diffusion-ordered spectroscopy nuclear magnetic resonance (DOSY NMR) experiment afforded a diffusion coefficient of $D = 3.1\times10^{-10}\,m^2\,s^{-1}$, indicating that the dimensions of 4^{8+} correspond to a hydrodynamic radius of 19.0 Å in solution, in line with the value estimated from crystallographic data (17.4 Å; see Supplementary Table 1). The dimensions of 4^{8+} derived from DOSY NMR are, as expected, larger than in tetragonal cage 3^{8+} (ref. 51).

Crystallographic data were obtained from $4\cdot(BArF)_8$ crystals at the XALOC beamline of the ALBA Synchrotron (Fig. 3b)[52]

using MD2M single-axis diffractometer (Maatel, France) and a Pilatus 6 M detector (Dectris, Switzerland). Due to its sensitivity to solvent loss, a crystal of $\mathbf{4}\cdot(BArF)_8$ was measured mounted in a thin glass capillary suspended in ether/dimethylformamide (DMF) (solution used to grow the crystal saturated with ether) and cryopreserved at 100 K. The crystal showed poor diffraction data with reflections of moderate intensity which were further degraded rapidly after 266 degrees oscillation (equivalent to 200 s of collection). This poor density and fast degradation (seen in all measured crystals, including both nanocages $\mathbf{4}^{8+}$ with encapsulated C_{60} and C_{70} *-vide infra-*) could be attributed to the high symmetry, solvent loss and severe motions of the solvents (volatile diethyl ether) and counteranions $BArF^-$ molecules in the large cavities of the crystal lattice (see additional comments to X-ray diffraction data in the Supplementary Discussion). All these reasons hampered a complete X-ray diffraction characterization, as counteranions could not be detected and located. Flash cooling the crystals at 100 K by mounting them in a capillary with cryoprotectants did not provide better crystallographic data. However, the correct structural solution for the cationic molecular cage $\mathbf{4}^{8+}$ was achieved. As expected, nanocage $\mathbf{4}^{8+}$ consists of two parallel tetracarboxylated Zn^{II}-porphyrins (distance between Zn^{II} centres at the porphyrin moieties = 14.1 Å) linked by four macrocyclic dinuclear Pd^{II} complexes. The four-carboxylate residues of each porphyrin are linked by means of η^1-O monodentate coordination to one Pd^{II} centre. Altogether, the overall structure is defined as a tetragonal prismatic cage taking the set of eight equivalent atoms of the carboxyphenyl moieties as vertices of the polyhedron, thus bearing D_{4h} symmetry.

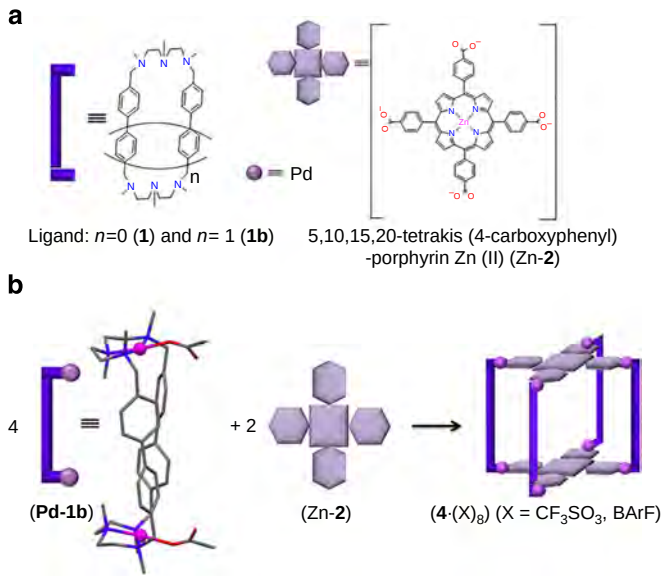

Figure 2 | Building blocks to obtain the tetragonal prismatic nanocage $\mathbf{4}\cdot\mathbf{(X)_8}$. (**a**) Building blocks used for (**b**) the self assembly of molecular clip **Pd-1b** and tetracarboxylated Zn-porphyrin (Zn-**2**) to form supramolecular nanocages $\mathbf{4}\cdot(X)_8$ ($X = CF_3SO_3$, BArF), (X-ray diffraction of **Pd-1b** shows one acetate anion coordinated to each Pd centre, and omits the two triflate counteranions for clarity).

Fullerene encapsulation. The large void volume of the cage (approximately able to encapsulate a spherical guest of up to 696 $Å^3$) and the known affinity of zinc-porphyrins for fullerenes[17], prompted us to explore the capability of $\mathbf{4}\cdot(BArF)_8$ to act as a host for fullerenes. Fast inclusion of C_{60} occurred during the mixing of a solution of $\mathbf{4}\cdot(BArF)_8$ in acetonitrile with C_{60} in toluene in a 1:1 molar ratio (Fig. 4). Job plot analysis of ultraviolet–visible (UV–vis) titration data indicated the formation of a 1:1 adduct $C_{60}\subset\mathbf{4}\cdot(BArF)_8$ with a high association constant of $K_a = 2.8\ (\pm 0.6)\cdot 10^7\ M^{-1}$ ($\log K_a = 7.44 \pm 0.1$). The association constant was further confirmed by fluorescence titrations ($\log K_a$ (fluorescence) $= 7.47 \pm 0.03$) (see Supplementary Fig. 1). In addition, a HRMS of this mixture showed exclusively the peaks corresponding to $C_{60}\subset\mathbf{4}\cdot(BArF)_8$. Crystals were grown by diethyl ether diffusion over a toluene/acetonitrile (4/1) solution of $C_{60}\subset\mathbf{4}\cdot(BArF)_8$ (isolated yield = 70%). The ^{1}H-NMR spectra in CD_3CN revealed that several aromatic C–H signals had shifted from the spectrum of the empty cage, indicating the inclusion of fullerene in the cage. DOSY NMR experiments afforded a similar hydrodynamic radius for $C_{60}\subset\mathbf{4}\cdot(BArF)_8$ when compared with that of the empty cage (see Supplementary Table 1), demonstrating that the molecular entity had not changed in size upon addition of the fullerene. Crystals of $C_{60}\subset\mathbf{4}\cdot(BArF)_8$ were also found to be extremely sensitive to solvent loss, therefore we resorted to low temperature X-ray diffraction analysis at the same synchrotron beamline in thin glass capillaries (flash cooling the crystals at 100 K by mounting them in a capillary with cryoprotectants did not afford better diffraction data). As was the case with $\mathbf{4}\cdot(BArF)_8$, a consistent crystallographic solution of

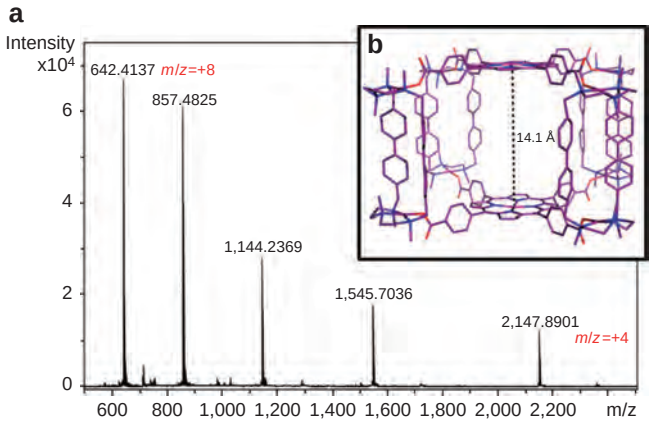

Figure 3 | Characterization of $\mathbf{4}\cdot\mathbf{(BArF)_8}$. (**a**) HRMS of $\mathbf{4}\cdot(BArF)_8$. (**b**) Representation of $\mathbf{4}^{8+}$ extracted from X-ray diffraction data.

the cationic molecular cage was achieved. The studies showed the presence of a spherical electron density at the centre of the cage that fitted nicely to a disordered entrapped C_{60} molecule (Fig. 4). Detection of this C_{60} molecule compared with the failure to locate counteranions and solvent guest molecules can be tentatively attributed to its lower mobility inside the cage. Moreover, the computed structure of the host–guest complex $C_{60} \subset \mathbf{4} \cdot (Cl)_8$ using state-of-the-art DFT methods showed nice agreement with crystallographic data (Fig. 4; all atoms were calculated at density functional theory (DFT) level). DFT calculations indicated that different orientations of C_{60} inside the host are accessible (see Supplementary Table 2), thus accounting for the disordered fullerene molecule found in the crystallographic structure.

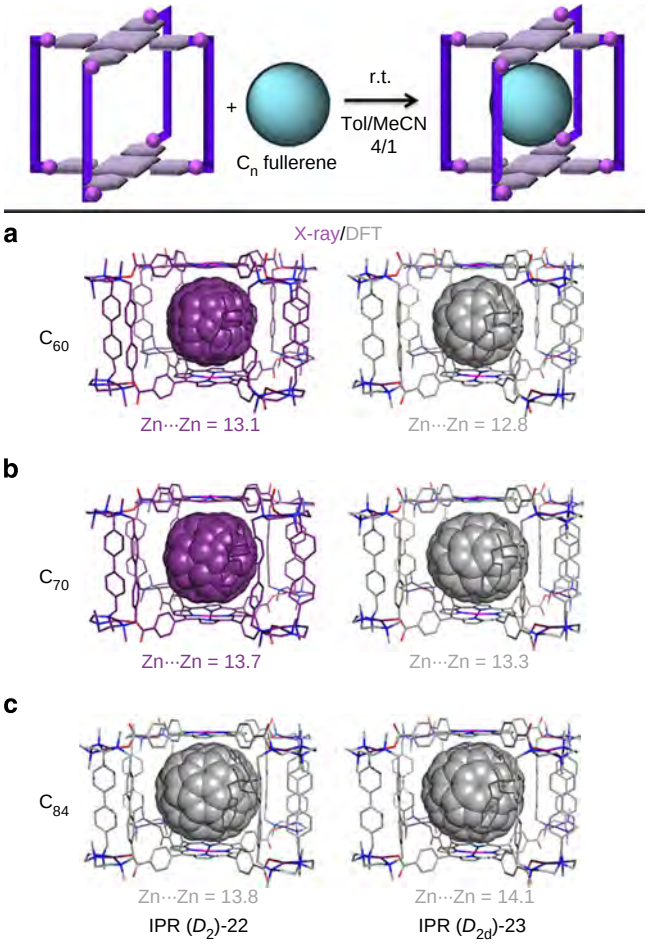

Figure 4 | X-ray diffraction and DFT analysis of fullerene host–guest compounds. Crystallographic data (purple) and DFT structures (grey) for cationic fullerene inclusion compounds (**a**) $C_{60} \subset \mathbf{4}^{8+}$ and (**b**) $C_{70} \subset \mathbf{4}^{8+}$; and (**c**) DFT calculation for $C_{84} \subset \mathbf{4}^{8+}$ isomers IPR (D_2)-22 and IPR (D_{2d})-23 (Zn · · · Zn distances in Å). r.t., room temperature.

We then explored the encapsulation of C_{70} with $\mathbf{4} \cdot (BArF)_8$ following an equivalent procedure as for C_{60} (Fig. 4). $C_{70} \subset \mathbf{4} \cdot (BArF)_8$ was instantaneously obtained upon mixing host and guest in a 1:1 ratio. UV–vis titration, ^{1}H-NMR and HRMS showed a very favourable association and stability of the inclusion complex in solution. Due to the high affinity of the cage towards the C_{70}, we were unable to obtain an association constant using UV–vis titrations; we therefore resorted to flurorescence titrations and we obtained $\log K_a = 8.6 \pm 0.3\ M^{-1}$ (see Supplementary Fig. 2), which is roughly 10-fold higher than for C_{60}. DOSY NMR spectrum also indicated the same diffusion coefficient as for $C_{60} \subset \mathbf{4} \cdot (BArF)_8$ and $\mathbf{4} \cdot (BArF)_8$, thus suggesting that C_{70} is also occupying the inner space of the cage with no substantial volume modification of the whole cage. Crystals were grown by diethyl ether diffusion and measured under synchrotron radiation. Similar problems of location of counteranions and rapid loss of crystallinity were encountered, but yet the data collected allowed identifying the structure of the cationic molecular cage including an ellipsoid-shaped electron density at the centre of the cage that fits nicely to a disordered C_{70} molecule, finding the semi-major axis parallel to the porphyrin planes (Fig. 4). DFT calculations indeed indicate that this arrangement is $\sim 6\ kcal \cdot mol^{-1}$ more stable than the perpendicular alignment. As observed in the case of C_{60}, different orientations of the C_{70} molecule with the semi-major axis parallel to the porphyrin planes are accessible, thus indicating that the fullerene moiety can easily rotate (see Supplementary Table 3). The DFT-optimized $C_{70} \subset \mathbf{4} \cdot (Cl)_8$ structure also showed nice agreement with crystallographic data (Fig. 4; all atoms were calculated at DFT level).

Comparison of crystallographic data for $\mathbf{4} \cdot (BArF)_8$, $C_{60} \subset \mathbf{4} \cdot (BArF)_8$ and $C_{70} \subset \mathbf{4} \cdot (BArF)_8$ shows that porphyrin–porphyrin interdistance is maximized (14.1 Å) when guest molecule is absent, whereas the inclusion of C_{70} compressed this distance down to 13.7 Å and inclusion of C_{60} further shrinks it to 13.1 Å (Table 1). DFT-optimized structures are in line with the observed experimental trends. Therefore, the sum of structural and computational information shows an important degree of adaptability or 'breathing' of the cage by maximizing the porphyrin–fullerene interaction (see Supplementary Fig. 3).

Given the large void space of the cage $\mathbf{4} \cdot (BArF)_8$, we explored the limits of encapsulation of higher fullerenes and chemically modified fullerenes. To that end, we selected the larger C_{84} and

Table 1 | Structural data.

		Crystallographic data	DFT data
$C_{60} \subset \mathbf{4}^{8+}$	Zn · · · Zn (in Å)	13.1	12.8
	C20-C20′-C20″-C45 (torsion angle (°))	−175.7	−173.5
$C_{70} \subset \mathbf{4}^{8+}$	Zn · · · Zn	13.7	13.3
	C20-C20′-C20″-C45	−176.3	−175.7
$C_{84} \subset \mathbf{4}^{8+}$	Zn · · · Zn	—	13.8
((D_2)-22)	C20-C20′-C20″-C45	—	−177.0
$C_{84} \subset \mathbf{4}^{8+}$	Zn · · · Zn	—	14.1
((D_{2d})-23)	C20-C20′-C20″-C45	—	−177.6
$\mathbf{4}^{8+}$	Zn · · · Zn	14.1	11.8
	C20-C20′-C20″-C45	−178.9	−169.4

DFT, density functional theory.
Relevant experimental and theoretical structural data for $C_{60} \subset \mathbf{4}^{8+}$, $C_{70} \subset \mathbf{4}^{8+}$, $C_{84} \subset \mathbf{4}^{8+}$ and $\mathbf{4}^{8+}$ (see Supplementary Fig. 6 for details on the torsion angle measurement).

[60]PCBM ([6,6]-phenyl-C_{61}-butyric acid methyl ester). Both of them were encapsulated in a 1:1 fashion forming $C_{84} \subset \mathbf{4} \cdot (BArF)_8$ and [60]PCBM $\subset \mathbf{4} \cdot (BArF)_8$, as indicated by HRMS. The extremely low solubility of C_{84} precluded NMR and UV–vis host–guest studies. On the other hand, HRMS for [60]PCBM $\subset \mathbf{4} \cdot (BArF)_8$ also indicated a clean 1:1 adduct and did not show desymmetrization of the ^{1}H-NMR signals, suggesting that the inner space is large enough to allow free rotation of the anisotropic [60]PCBM. Moreover, model $C_{84} \subset \mathbf{4} \cdot (Cl)_8$ species were optimized at a DFT level, selecting the two most abundant isomers ((D_2)-22 and (D_{2d})-23 IPR (Isolated-Pentagon-Rule) isomers, see Fig. 4 and Supplementary Figs 4 and 5). The computational investigation of C_{84} encapsulation inside the host indicated that the porphyrin–porphyrin interdistance is elongated $\sim$0.5 Å with respect to $C_{70} \subset \mathbf{4} \cdot (Cl)_8$. This value is similar to the porphyrin–porphyrin distance found for the empty nanostructure, indicating that there exists a good fit between C_{84} and the cavity of the host cage. $\mathbf{4} \cdot (BArF)_8$ is thus capable of unusually facile encapsulation of C_{60}, C_{70}, C_{84} and [60]PCBM.

Relative affinity for the most abundant and accessible C_{60} with respect to C_{70} was also explored in a HRMS study; one equivalent of $\mathbf{4} \cdot (BArF)_8$ was mixed with one equivalent of C_{60} and one equivalent of C_{70} in a 4:1 toluene:acetonitrile solvent mixture. HRMS of the resulting solution showed a preferential encapsulation of C_{70} with a 9:1 peak intensity ratio for $C_{70} \subset \mathbf{4} \cdot (BArF)_8$ versus $C_{60} \subset \mathbf{4} \cdot (BArF)_8$. On the other hand, when one equivalent of $\mathbf{4} \cdot (BArF)_8$ is combined with 10 equivalents of C_{60} and one equivalent of C_{70}, two equally intense signals are found for $C_{60} \subset \mathbf{4} \cdot (BArF)_8$ and $C_{70} \subset \mathbf{4} \cdot (BArF)_8$. Finally, a mixture of one equivalent of $\mathbf{4} \cdot (BArF)_8$ with one equivalent of C_{60} and nine equivalents of C_{70} completely excludes the noticeable encapsulation of C_{60} and $C_{70} \subset \mathbf{4} \cdot (BArF)_8$ is exclusively observed by HRMS. Substoichiometric additions of C_{60} and C_{70} confirmed the same MS ionization behaviour of free host, host-C_{60} and host-C_{70} compounds, meaning that the relative intensity of the peaks corresponding to host-C_{60} and host-C_{70} with the same charge reproduce their relative concentration in solution. An estimation of the affinity to the host for the two fullerenes could then be extracted from this analysis, revealing that C_{70} bears a nine-fold higher affinity for $\mathbf{4} \cdot (BArF)_8$ than C_{60}, in agreement with the 10-fold difference in association constants found by fluorescence spectroscopy studies. These results are rationalized by a higher degree of π-interactions with C_{70} due to its ellipsoid shape (see Supplementary Figs 7–10). This is confirmed by DFT calculations, which indicate a more favourable porphyrin–fullerene interaction for C_{70} fullerene molecule (see Supplementary Fig. 11 and Supplementary Tables 3 and 4). These results are consistent with the X-ray diffraction data in which $C_{70} \subset \mathbf{4} \cdot (BArF)_8$ presents a less-strained cage conformation, closer to its form as empty cage $\mathbf{4} \cdot (BArF)_8$, while the more distorted cage in case of $C_{60} \subset \mathbf{4} \cdot (BArF)_8$ gives a less stable adduct.

The inclusion of fullerenes in $\mathbf{4} \cdot (BArF)_8$ is also observed by using fullerene extract (SES Research, C_{60} 70%, C_{70} 28%, higher fullerenes 2%). HRMS of the inclusion compounds formed upon mixing $\mathbf{4} \cdot (BArF)_8$ with fullerene extract (1:3 molar ratio, assuming that all fullerenes are C_{60}) in a mixture of toluene/acetonitrile (4/1) exhibited the ion peaks corresponding to $C_{60} \subset \mathbf{4} \cdot (BArF)_8$, $C_{70} \subset \mathbf{4} \cdot (BArF)_8$ and $C_{84} \subset \mathbf{4} \cdot (BArF)_8$ as the main signals, although minor ion peaks corresponding to $C_{76} \subset \mathbf{4} \cdot (BArF)_8$ and $C_{78} \subset \mathbf{4} \cdot (BArF)_8$ were also observed. The $C_{60} \subset \mathbf{4}/C_{70} \subset \mathbf{4}$ and $C_{70} \subset \mathbf{4}/C_{84} \subset \mathbf{4}$ ratios derived from the relative intensity of the ion peaks are 0.72 and 12.8, respectively. However, when using different excesses of fullerene, enrichment of the proportion of higher fullerenes caged was observed. Thus, for 1:12 cage:fullerene extract molar ratios, mass spectra affords $C_{60} \subset \mathbf{4}/C_{70} \subset \mathbf{4}$ and $C_{70} \subset \mathbf{4}/C_{84} \subset \mathbf{4}$ ratios of 0.18 and 11.3, respectively, whereas larger excess (1:60 weight ratio) afforded $C_{60} \subset \mathbf{4}/C_{70} \subset \mathbf{4}$ and $C_{70} \subset \mathbf{4}/C_{84} \subset \mathbf{4}$ ratios of 0.05 and 6.7, respectively (see Supplementary Fig. 12). Therefore, the initial 30% content of C_{70} and higher fullerenes is remarkably improved to $>$96% after a single extraction with $\mathbf{4} \cdot (BArF)_8$.

On the other hand, when fullerene soot (Aldrich, C_{60} 5.3%, C_{70} 1.54%, higher fullerenes 0.14%, the rest being other forms of carbon) is suspended in toluene and reacted with $\mathbf{4} \cdot (BArF)_8$ (1:12 cage:soot weight ratio; final solvent mixture toluene/acetonitrile 4/1), similar ratios of encapsulation as for fullerene extract were found (see Supplementary Fig. 13).

The versatility of the cage is further exemplified by the fact that encapsulation of fullerenes can be performed by soaking $\mathbf{4} \cdot (BArF)_8$ as a solid (grain size: 3.1 ± 3.0 µm; median: 2.2 µm; Supplementary Fig. 14)[53] in a C_{70}-containing toluene solution, thus being the first example of solid-phase fullerene encapsulation for a supramolecular cage (to our knowledge, a single similar precedent using a MOF was reported by Fujita and co-workers)[46]. This observation discards partial cage disassembly during the host–guest event, and agrees with a guest encapsulation occurring by fullerene entrance through the four apertures of the cage; the dimensions of the apertures are large enough to envision the mobility of fullerene molecules through them. Moreover, we could also modify the selectivity toward higher fullerenes, using solid $\mathbf{4} \cdot (BArF)_8$ and fullerene extract dissolved in toluene by changing the fullerene extract ratio used (see Supplementary Figs 15–16). These results prompted us to investigate the encapsulation of C_{70} dissolved in toluene and insoluble $\mathbf{4} \cdot (CF_3SO_3)_8$ as solvent-evacuated crystals. After 5–10 min, complete inclusion was obtained forming $C_{70} \subset \mathbf{4} \cdot (CF_3SO_3)_8$, as ascertained by HRMS (Supplementary Fig. 17).

Discussion

Once the inclusion of fullerenes (from C_{60} to C_{84}) was thoroughly studied, we sought to find a straightforward experimental protocol to liberate the different fullerenes in a selective manner. Taking advantage of the fact that fullerenes are encapsulated in the solid state, we charged solid $\mathbf{4} \cdot (BArF)_8$ nanocapsule (0.33 µmols) together with Celite in a short column. Subsequently, a 1.4 mM solution of C_{60} was passed through the column seven times, and total encapsulation was confirmed by HRMS. Afterwards, the extraction of C_{60} from the solid sample of $C_{60} \subset \mathbf{4} \cdot (BArF)_8$ charged in the column was performed by consecutive washings with 1,2-dichlorobenzene/CS_2 (1/1 v/v mixture). This solvent mixture fulfills the requirements of a very high solubility of fullerenes and very low solubility of either $C_{60} \subset \mathbf{4} \cdot (BArF)_8$ or $\mathbf{4} \cdot (BArF)_8$. We were delighted to observe that washing with 5×1 ml of the 1,2-dichlorobenzene/CS_2 mixture was sufficient to liberate all encapsulated C_{60} (see Fig. 1f). On the other hand, the solid remaining in the filtration column was found to be $\mathbf{4} \cdot (BArF)_8$, which was ready to be filled again with C_{60}. The solid fullerene encapsulation–extraction protocol was repeated up to five cycles (see flow chart in Supplementary Fig. 18). After these cycles, 91% of $\mathbf{4} \cdot (BArF)_8$ was recovered from the column by washing with acetonitrile (Fig. 5a). To the best of our knowledge, this is the first example of the use of orthogonal solubility of the host and fullerene for the extraction of fullerenes (only the reverse adsorption of fullerenes by soaking a MOF crystal in fullerene-containing toluene was reported by Fujita and co-workers)[46].

The same protocol was attempted for the inclusion of a mixture of fullerenes (fullerene extract). However, ineffective mixing at the column between the solid $\mathbf{4} \cdot (BArF)_8$ and the toluene solution containing fullerene extract afforded inhomogeneous distribution of fullerenes among the solid. We therefore

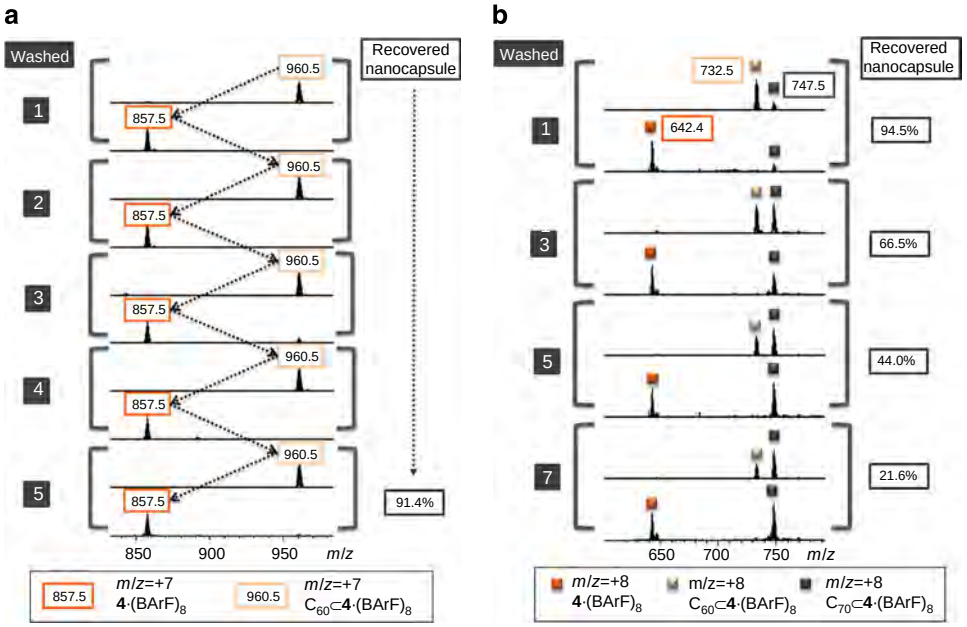

Figure 5 | Solid state extraction of fullerenes from $4\cdot(BArF)_8$. HRMS monitoring of the C_{60} extraction washing-protocol using (**a**) pure C_{60} encapsulated in $\mathbf{4}\cdot(BArF)_8$ in the solid phase and (**b**) fullerene extract encapsulated in $\mathbf{4}\cdot(BArF)_8$.

decided to improve the encapsulation step by re-dissolving the empty cage in CH_3CN and performing the encapsulation of fullerene extract in solution (1:1 molar ratio). Subsequently, the fullerene-containing cage was precipitated out by the addition of diethyl ether and the filled cage reintroduced in the column (see Supplementary Fig. 19). At the first cycle, $C_{60}\subset\mathbf{4}/C_{70}\subset\mathbf{4}$ ratio was 4.0 (by HRMS), and only C_{60} was released after washing the solid inclusion compound with 1,2-dichlorobenzene/CS_2 (1/1 v/v mixture). After repeating the inclusion and liberation sequence up to seven cycles (Fig. 5b), the cage was enriched with C_{70} at each cycle and was finally saturated of mainly C_{70} and C_{84} (an $\sim$10% mass loss was observed after each cycle due to the experimental setup). The maximum extraction capacity was calculated as 1 mol of C_{60} per mol of cage $\mathbf{4}\cdot(BArF)_8$, and a 61% of the expected C_{60} was recovered (quantified by UV–vis). Overall, this experiment demonstrates that the simple and fast selective C_{60} purification from a mixture of fullerenes is feasible by using cage $\mathbf{4}\cdot(BArF)_8$ and our solvent-washing protocol[54].

Regarding the recovery of higher fullerenes (mainly C_{70} and C_{84}) trapped in the saturated sample of $\mathbf{4}\cdot(BArF)_8$ after multiple encapsulation/liberation cycles, we tested other solvent mixtures but no significant liberation of higher fullerenes was achieved. Therefore, we resorted to triflic acid (10 equivalents) treatment (in toluene) of C_{70} and $C_{84}\subset\mathbf{4}\cdot(BArF)_8$ in the solid state to disassemble the cage and rapid release of the mixture of higher fullerenes into toluene solution. Further partial reassembly of cage $\mathbf{4}\cdot(CF_3SO_3)_8$ upon base (NEt_3) neutralization and reflux in DMF occurred, as ascertained by HRMS (see Supplementary Fig. 20).

To sum up, we have designed the new molecular cage $\mathbf{4}\cdot(BArF)_8$ that encapsulates fullerenes (from C_{60} to C_{84}) in a fast manner at room temperature. At the core of the adaptability of the cages to bind substrates that differ substantially in size is the remarkable ability to modulate the size of the cavities by alteration of porphyrin–porphyrin distances. This molecular 'breathing' ability of the cages relies on the substantial degree of flexibility of metal-coordination (Pd-carboxylate) bonds in the clips that hold the supramolecular structure. Full spectroscopic and spectrometric characterization of the host and host–guest compounds is reported. In addition, a sponge-like behaviour has been proven for $\mathbf{4}\cdot(BArF)_8$ for the selective purification of C_{60} from a mixture of fullerenes. This study provides fundamental results regarding the ability of the described tetragonal nanocage to encapsulate and liberate fullerenes, and paves the way to study the performance of newly designed cages (varying the nature of metalloporphyrin moieties, decorating the apertures of the cage, changing Pd cations at the molecular clips by first-row transition metals, and so on) to finely tune the selectivity for higher fullerenes or endohedral fullerenes. Here we demonstrate for the first time that the encapsulation event can occur by soaking the molecular nanocage in the solid state in a fullerene-containing toluene solution. Moreover, the liberation of C_{60} is also achieved by applying solvent-washing protocols to the host–guest complex in the solid state. We envision these findings may spark supramolecular host-guest research in the solid phase in cages bearing apertures for guest entrance.

Methods

Materials and instrumentation. Reagents and solvents used were commercially available reagent quality unless indicated otherwise. Ligand H2pp (see Supplementary Fig. 21) was synthesized according to published procedures[55]. NMR data concerning product identity were collected on Bruker 400 MHz AVANCE spectrometers in $CDCl_3$ or CD_3CN, and calibrated relative to the residual protons of the solvent. ESI-MS experiments were collected and analysed on both a Bruker Daltonics Esquire 6000 spectrometer and a Bruker MicroTOF-Q-II, using acetonitrile or DMF as the mobile phase. UV–vis spectroscopy was performed on an Agilent 8452 UV–vis spectrophotometer with 1 cm quartz cell, equipped with a temperature control cryostat from Unisoku Scientific Instruments (Japan), using a toluene/acetonitrile 9/1 (v/v) mixture as solvent. Fluorescence measurements were performed in a Spectrofluorimeter Fluorolog Horiba Jobin Yvon.

Synthesis and characterization of 1b ligand. 0.66 g of H2pp (1.2 mmols) are added to a 100 ml flask and mixed with: 10 ml of formaldehyde, 8 ml of formic acid and 10 ml of water. The resulting mixture is heated to reflux during 12 h. After this time, the reaction mixture is cooled to room temperature and the solvent removed under reduced pressure. Then 25 ml of NaOH 30% are added. The product is extracted with $CHCl_3$ (3×25 ml). Organic phases are combined, dried with anhydrous $MgSO_4$ and filtered. The remaining solution is dried under vacuum, and the obtained product purified by recrystallization with acetone. (Yield: 51.8%). ^{1}H-NMR (400 MHz, $CDCl_3$) δ p.p.m.: 7.39 (d, $J=8.24$ Hz, 8H, arom), 7.29 (d, $J=8.24$ Hz, 8H, arom), 3.47 (s, 8H, CH_2), 2.57–2.49 (m, 16H, CH_2), 2.28 (s, 6H, CH_3), 2.22 (s, 12H, CH_3). ^{13}C-NMR (75 MHz, CD_3CN) δ p.p.m.: 139.5 (arom),

137.9 (arom), 129.5 (arom), 126.7 (arom), 62.3 (–CH_2– benzylic), 54.8 (–CH_2–), 54.4 (–CH_2–), 43.6 (N–CH_3), 42.9 (N–CH_3). Fourier transform infrared (spectroscopy) ν (cm^{-1}): 1,462 (C–N st), 1,650–2,000, 2,780 (C–H st, sp^3), 2,935 (arC–H st), 2,967 (C–H st, sp^2). ESI-MS (*m/z*): calculated 647.9 and found 647.4 ($\{Me2pp + H\}^{+}$). For NMR and ESI-MS analysis of **1b**, see Supplementary Figs 21–25.

Synthesis and characterization of 1b•$(AcO)_2(CF_3SO_3)_2$ molecular clip. In a round-bottom flask, 0.08 g of **1b** ligand (0.125 mmols), 0.058 g of $Pd(AcO)_2$ (0.250 mmols) and 25 ml of anhydrous CH_3CN were mixed. The mixture is heated to reflux temperature, under nitrogen atmosphere for 18 h. After this time, the reaction mixture is cooled down to room temperature. Subsequently, an excess of $NaCF_3SO_3$ salt is added (0.525 mmols) and the mixture is stirred vigorously for 6 h. The reaction mixture is concentrated to a volume of 2–3 ml under reduced pressure, filtered through Celite and recrystallized under slow diethyl ether diffusion. Yellow crystalline solid is obtained. (Yield: 90.1%). ^{1}H-NMR (400 MHz, CD_3CN) δ p.p.m.: 8.37 (d, $J=8$ Hz, 10.5 H, arom), 8.15 (d, $J=8$ Hz, 8 H, arom), 7.94 (d, $J=8$ Hz, 2.5 H, arom), 4.06 (d, $J=13$ Hz, 5.25 H, –CH_2–), 3.62 (m, 5.26 H, –CH_2–), 3.33 (s, 11.9 H, N–CH_3), 3.31 (s, 3.6 H, N–CH_3), 3.25 (m, 5.25 H, –CH_2-), 3.11 (d, $J=13$ Hz, 5.17 H, –CH_2–), 2.38 (d, $J=14$ Hz, 5.0 H, –CH_2–), 2.30 (d, 5.2 H, –CH_2–), 2.07 (s, 5.9 H, AcO), 2.05 (s, 1.8 H, AcO), 1.50 (s, 1.8 H, N–CH_3), 1.41 (s, 6.0 H, N–CH_3). ^{13}C-NMR (100 MHz, CD_3CN) δ p.p.m.: 178.7 (C=O, AcO), 142.2 (arom), 141.03 (arom), 133.8 (arom), 133.6 (arom), 128.5 (arom), 128.1 (arom), 65.6 (–CH_2–), 65.4 (–CH_2–), 61.0 (–CH_2–), 60.8 (–CH_2–), 59.0 (–CH_2–), 58.9 (–CH_2–), 50.8 (N–CH_3), 43.9 (N–CH_3), 43.5 (N–CH_3), 24.2 (–CH_3, AcO), 24.1 (–CH_3, AcO). HRMS (*m/z*): calculated 1,127.259 and found 1,127.257 ($\{[Pd\text{-}\mathbf{1b}\cdot(AcO)_2](CF_3SO_3)_1\}^{1+}$), calculated 489.154 and found 489.153 ($\{[Pd\text{-}\mathbf{1b}\cdot(AcO)_2]\}^{2+}$). For NMR, IR and ESI-MS analysis of the **Pd-1b**$\cdot(AcO)_2(CF_3SO_3)_2$ compound, see Supplementary Figs 26–32.

Synthesis of 4$\cdot(BArF)_8$ molecular cage. 10.56 mg of 5,10,15,20-tetrakis(4-carboxyphenyl)porphyrin-Zn^{II} (**2**, 0.01 mmols) are weighed in a 10 ml flask, then 1 ml of DMF is added. Then, 10 µl of triethylenetriamine dissolved in 0.5 ml of DMF are added to the porphyrin solution. Finally 30 mg of **Pd-1b**$\cdot(AcO)_2(CF_3SO_3)_2$ (0.02 mmols) complex dissolved in 2.5 ml of DMF are added to the mixture. The solution obtained is heated to 105 °C under reflux for 16 h. After the reaction time, the mixture is cooled to room temperature, filtered through Celite and recrystallized by diethyl ether diffusion. The $\mathbf{4}\cdot(CF_3SO_3)_8$ crystalline solid obtained (extremely low solubility prevented NMR characterization; however, high sensibility of HRMS analysis allowed its mass spectrometry characterization, see Supplementary Fig. 33) is suspended in 12 ml of DCM, an excess of NaBArF salt is added (1 to 10 equivalents) and the mixture is stirred vigorously for 16 h. The reaction mixture is filtered. The product is obtained by precipitation with diethyl ether. The purple powder is washed several times with diethyl ether to remove the excess of NaBArF. (Yield: 38.3%). ^{1}H-NMR (400 MHz, CD_3CN) δ p.p.m.: 8.60 (dd, 8H, arom-porph), 8.58 (s, 16H, pyrrole ring), 8.35 (dd, $J=8$ Hz, 8H, arom-porph), 8.30 (d, $J=8.5$ Hz, 32H, arom-clip), 8.15 (d, $J=8.5$ Hz, 32H, arom-clip), 8.10 (dd, $J=8$ Hz, 8H, arom-porph), 7.98 (dd, $J=8$ Hz, 8H, arom-porph), 7.68 (m, 96H, NaBArF), 4.07 (d, $J=13$ Hz, 16H, –CH_2–), 3.70 (m, 16H, –CH_2–), 3.60 (s, 48H, N–CH_3), 3.38 (m, 16H, –CH_2–), 3.15 (d, $J=13$ Hz, 16H, –CH_2–), 2.49 (dd, $J=13.5$, 16H, –CH_2–), 2.39 (dd, $J=13.5$, 16H, –CH_2–), 1.58 (s, 24H, N–CH_3). ^{13}C-NMR (100 MHz, CD_3CN) δ p.p.m.: 206.7 (BArF), 166.0 (DMF), 160.4 (BArF), 148.8 (pyrrole ring), 140.4 (arom-clip), 134.6 (BArF), 133.8 (arom-porph), 133.1 (arom-clip), 133.1 (arom-porph), 129.7 (pyrrole ring), 127.1 (arom-clip), 127.1 (arom-porph), 116.6 (BArF), 64.7 (–CH_2–), 60.2 (–CH_2–), 59.1 (–CH_2–), 51.6 (NCH_3), 42.6 (NCH_3). HRMS (*m/z*): calculated 2,147.893 and found 2,147.893 ($\{\mathbf{4}\cdot(BArF)_4\}^{4+}$); calculated 1,545.701 and found 1,545.702 ($\{\mathbf{4}\cdot(BArF)_3\}^{5+}$), calculated 1,144.239 and found 1,144.242 ($\{\mathbf{4}\cdot(BArF)_2\}^{6+}$); calculated 857.481 and found 857.483 ($\{\mathbf{4}\cdot(BArF)\}^{7+}$); calculated 642.413 and found 642.414 ($\{\mathbf{4}\cdot(BArF)\}^{8+}$). For NMR and HRMS analysis of the 4$\cdot(BArF)_8$ compound, see Supplementary Figs 34–40.

Preparation and characterization of the fullerene adducts. Preparation of $C_{60}\subset\mathbf{4}\cdot(BArF)_8$: 2.5 mg of 4$\cdot(BArF)_8$ nanocapsule (0.2 µmols, 1 equivalent) were dissolved in 100 µl of CH_3CN. Then one equivalent of C_{60} dissolved in 400 µl of toluene was added to the cage solution. The mixture was stirred at room temperature for 5 min. The mixture is filtered and recrystallized by diethyl ether diffusion. ^{1}H-NMR (400 MHz, CD_3CN) δ p.p.m.: 8.64 (dd, 8H, arom-porph), 8.55 (s, 16H, pyrrole ring), 8.35 (dd, $J=8$ Hz, 8H, arom-porph), 8.30 (d, $J=8.5$ Hz, 32H, arom-clip), 8.14 (d, $J=8.5$ Hz, 32H, arom-clip), 8.04 (dd, $J=8$ Hz, 8H, arom-porph), 7.99 (dd, $J=8$ Hz, 8H, arom-porph), 7.68 (m, 96H, NaBArF), 4.07 (d, $J=13$ Hz, 16H, –CH_2–), 3.70 (m, 16H, –CH_2–), 3.60 (s, 48H, N–CH_3), 3.38 (m, 16H, –CH_2–), 3.15 (d, $J=13$ Hz, 16H, –CH_2–), 2.49 (dd, $J=13.5$, 16H, –CH_2–), 2.39 (dd, $J=13.5$, 16H, –CH_2–), 1.58 (s, 24H, N–CH_3). HRMS (*m/z*): calculated 2,328.143 and found 2,328.144 ($\{C_{60}\subset\mathbf{4}\cdot(BArF)_4\}^{4+}$); calculated 1,689.901 and found 1,689.902 ($\{C_{60}\subset\mathbf{4}\cdot(BArF)_3\}^{5+}$), calculated 1,264.406 and found 1,264.408 ($\{C_{60}\subset\mathbf{4}\cdot(BArF)_2\}^{6+}$); calculated 960.339 and found 960.341 ($\{C_{60}\subset\mathbf{4}\cdot(BArF)\}^{7+}$); calculated 732.413 and found 732.415 ($\{C_{60}\subset\mathbf{4}\cdot(BArF)\}^{8+}$).

Preparation of $C_{70}\subset\mathbf{4}\cdot(BArF)_8$: 2.5 mg of 4$\cdot(BArF)_8$ nanocapsule (0.2 µmols, one equivalent) was dissolved in 100 µl of CH_3CN. Then one equivalent of C_{70} dissolved in 400 µl of toluene was added to the cage solution. The mixture was stirred at room temperature for 5 min. The mixture is filtered and recrystallized by diethyl ether diffusion. ^{1}H-NMR (400 MHz, CD_3CN) δ p.p.m.: 8.66 (dd, $J=8$ Hz, 8H, arom-porph), 8.48 (s, 16H, pyrrole ring), 8.33 (dd, 8H, arom-porph), 8.33 (d, J = 8.5 Hz, 32H, arom-clip), 8.18 (d, $J=8.5$ Hz, 32H, arom-clip), 8.00 (m, $J=8$ Hz, 8H, arom-porph), 7.97 (m, $J=8$ Hz, 8H, arom-porph), 7.68 (m, 137H, NaBArF), 4.09 (d, $J=13$ Hz, 16H, –CH_2–), 3.70 (m, 16H, –CH_2–), 3.60 (s, 48H, N–CH_3), 3.38 (m, 16H, –CH_2–), 3.15 (d, $J=13$ Hz, 16H, –CH_2–), 2.49 (dd, $J=13.5$, 16H, –CH_2–), 2.39 (dd, $J=13.5$, 16H, –CH_2–), 1.59 (s, 24H, N–CH_3). HRMS (*m/z*): calculated 2,358.143 and found 2,358.141 ($\{C_{70}\subset\mathbf{4}\cdot(BArF)_4\}^{4+}$); calculated 1,713.901 and found 1,713.900 ($\{C_{70}\subset\mathbf{4}\cdot(BArF)_3\}^{5+}$), calculated 1,284.406 and found 1,284.409 ($\{C_{70}\subset\mathbf{4}\cdot(BArF)_2\}^{6+}$); calculated 977.624 and found 977.625 ($\{C_{70}\subset\mathbf{4}\cdot(BArF)\}^{7+}$); calculated 747.413 and found 747.413 ($\{C_{70}\subset\mathbf{4}\cdot(BArF)\}^{8+}$).

Preparation of $[C_{60}]PCBM\subset\mathbf{4}\cdot(BArF)_8$: 2.5 mg of 4$\cdot(BArF)_8$ nanocapsule (0.2 µmols, one equivalent) were dissolved in 100 µl of CH_3CN. Then one equivalent of $[C_{60}]$PCBM dissolved in 400 µl of toluene was added to the cage solution. The mixture was stirred at room temperature for 5 min. The mixture is filtered and recrystallized by diethyl ether diffusion. ^{1}H-NMR (400 MHz, CD_3CN) δ p.p.m.: 8.60 (dd, $J=8.0$ Hz, 8H, arom-porph), 8.50 (s, 16H, pyrrole ring), 8.35 (dd, $J=8.0$ Hz, 8H, arom-porph), 8.32 (d, $J=8.5$ Hz, 32H, arom-clip), 8.13 (d, $J=8.5$ Hz, 32H, arom-clip), 7.99 (m, $J=8$ Hz, 8H, arom-porph), 7.92 (m, $J=8$ Hz, 8H, arom-porph), 142 (m, 96H, NaBArF), 4.09 (d, $J=13$ Hz, 16H, –CH_2–), 3.67 (m, 16H, –CH_2–), 3.60 (s, 48H, N–CH_3), 3.38 (m, 16H, –CH_2–), 3.15 (d, $J=13$ Hz, 16H, –CH_2–), 2.49 (dd, $J=13.5$, 16H, –CH_2–), 2.40 (dd, $J=13.5$, 16H, –CH_2–), 1.59 (s, 24H, N–CH_3). HRMS (*m/z*): calculated 2,375.668 and found 2,375.667 ($\{[C_{60}]PCBM\subset\mathbf{4}\cdot(BArF)_4\}^{4+}$); calculated 1,727.921 and found 1,727.923 ($\{[C_{60}]PCBM\subset\mathbf{4}\cdot(BArF)_3\}^{5+}$), calculated 1,296.089 and found 1,296.088 ($\{[C_{60}]PCBM\subset\mathbf{4}\cdot(BArF)_2\}^{6+}$); calculated 987.639 and found 987.636 ($\{[C_{60}]PCBM\subset\mathbf{4}\cdot(BArF)\}^{7+}$); calculated 756.175 and found 756.173 ($\{[C_{60}]PCBM\subset\mathbf{4}\cdot(BArF)\}^{8+}$).

For NMR and HRMS analysis of the host–guest adducts, see Supplementary Figs 41–55.

General procedures for UV–vis and fluorescence titrations. Host–guest interactions in solution were studied by UV–vis and fluorescence spectroscopy. The UV–vis titration experiments between 4$\cdot(BArF)_8$ (4.32×10^{-7} M) and the different fullerenes tested (1.39×10^{-5} M) were performed by using toluene/acetonitrile (9/1) as solvent. The cage concentration was kept constant. The C_{60} (3.46×10^{-6} M) titration was repeated using a constant concentration of 4$\cdot(BArF)_8$ of 1.08×10^{-7} M. A magnetic stir bar and 2 ml of nanocapsule solution were added to the cuvette, then it was inserted into the spectrometer and the stirrer activated and the substrate added. The stoichiometry of the complexes was studied using the method of continuous variations. Solutions of nanocapsule 4$\cdot(BArF)_8$ and fullerenes (4.32×10^{-7} M) in toluene/acetonitrile (9/1) were mixed at different ratios. All the experiments were carried out at 22 °C. The fluorescence titration for C_{60} was performed under the same conditions of the UV–vis titration. C_{70} fluorescence titration experiment was performed using a 1.08×10^{-8} M solution of 4$\cdot(BArF)_8$ and 3.46×10^{-7} M solution of C_{70}. A 9/1 mixture of toluene/acetonitrile was used as solvent and the cage concentration was kept constant.

The data obtained from the UV–vis and the fluorescence spectrophotometric titrations were analysed using the software Origin Pro 8 and SPECFIT 3.0 from Spectrum Software Associates, Marlborough, MA, U.S.A. (SpecSoft@compuserve.com), which uses a global system with expanded factor analysis and Marquardt least-squares minimization to obtain globally optimized parameters. For UV–vis titrations of the host–guest adducts, see Supplementary Figs 56–60.

Diffusion-ordered NMR spectroscopy experiments. Diffusion-ordered NMR experiments (DOSY NMR) of **Pd-1b**$\cdot(AcO)_2(CF_3SO_3)_2$, 4$\cdot(BArF)_8$, $C_{60}\subset\mathbf{4}\cdot(BArF)_8$ and $C_{70}\subset\mathbf{4}\cdot(BArF)_8$, allow the determination of the translational self-diffusion coefficients (*D*) for these species in acetonitrile solution. Making use of the Stokes–Einstein equation (equation 1), the hydrodynamic radii (r_H) for the diffused species can be calculated from the *D* value (see obtained values on Supplementary Table 1).

$$D=\frac{k\cdot T}{6\cdot\pi\cdot\eta\cdot r_H} \quad (1)$$

where k is the Boltzmann constant, *T* is the temperature, and η is the viscosity of the solvent (η (CH_3CN) = 0.35 mPa s) (ref. 56).

The DOSY spectra were acquired using the LEDBP pulse sequence using 16 transients and eight dummy scans, at 298 K. The diffusion time *D* was 150 ms and the total diffusion-encoding gradient duration (*d*) was 1.1 ms. Sixteen values of diffusion-encoding gradient were used, varying from approximately 1 to 50 G cm^{-1} in equal steps of gradient squared. Data were acquired and processed using the automated 'dosy' and 'dosy2d' macros incorporated into the TOPSPIN v2.1 software package (Bruker Biospin, Rheinstetten, Germany). For DOSY-NMR experiments of the host–guest adducts, see Supplementary Figs 61–64.

X-ray diffraction studies details. Crystallographic data for **Pd-1b•**$(AcO)_2$ $(CF_3SO_3)_2$ were collected using Bruker-AXS SMART-APEXII CCD diffractometer (MoK_α, $\lambda = 0.71073$ Å). Indexing was performed using APEX2 (Difference Vectors method). Data integration and reduction were performed using SaintPlus 6.01. Absorption correction was performed by multi-scan method implemented in SADABS. The structure was solved using SHELXS-97 and refined using SHELXL-97 contained in SHELXTL program. All hydrogen atoms were placed using a riding model. Their positions were constrained relative to their parent atom using the appropriate HFIX command in SHELXL-97. See Supplementary Data 2.

Crystallographic data for $\mathbf{4}\cdot(BArF)_8$, $C_{60}\subset\mathbf{4}\cdot(BArF)_8$ and $C_{70}\subset\mathbf{4}\cdot(BArF)_8$ samples were collected at the XALOC beamline of the ALBA synchrotron at 100 K using a MD2M single-axis diffractometer (Maatel, France) and a Pilatus 6 M detector (Dectris, Switzerland). Due to their sensitivity to solvent loss, crystals of the three complexes were mounted in thin glass capillaries and cryopreserved at 100 K. Single crystals were introduced into the capillary suspended in a small volume of ether/DMF (solution used to grow the crystal saturated with ether). The data sets were collected on omega single-axis scans with 1-s per frame exposures at $\lambda = 0.82656$ Å. The crystals were diffracting at a moderate resolution (2.3 Å) (see Supplementary Fig. 67) and showed degradation due to radiation damage, as seen from the intensities and resolution of the reflections after 266 (for $\mathbf{4}\cdot(BArF)_8$; see Supplementary Fig. 67), 220 (for $C_{60}\subset\mathbf{4}\cdot(BArF)_8$; see Supplementary Fig. 67) and 178 ($C_{70}\subset\mathbf{4}\cdot(BArF)_8$; see Supplementary Fig. 67) images. This poor density and fast degradation is attributed to the high symmetry, solvent loss and severe motions of the solvents (volatile ether) and counteranion molecules (BArF) in the large cavities of the crystal lattice. The three structures were solved by charge flipping method using the code Superflip[57] and refined by the full matrix least-squares based of F^2 using SHELX97 (ref. 58). Although the limited quality of the data (Supplementary Table 5) did not allow locating the counteranions and solvent molecules in the unit cell, the atomic positions of the atoms composing the cage and disordered C_{60} and C_{70} could be determined. For the same reasons, the atoms have been refined only isotropically. We provide, as additional data sets, preliminary CIF files extracted from partial refinement X-ray diffraction data, see Supplementary Data 3–5. For X-ray diffraction data of $\mathbf{4}\cdot(BArF)_8$, $C_{60}\subset\mathbf{4}\cdot(BArF)_8$ and $C_{70}\subset\mathbf{4}\cdot(BArF)_8$, see Supplementary Figs 65–69.

Computational details. All DFT calculations were performed using the ADF 2010 program. The molecular orbitals were expanded in an uncontracted set of Slater-type orbitals of double-ζ (DZ), and double-ζ (DZP) and triple-ζ (TZP) quality that contained diffuse functions and one set of polarization functions. The Frozen core approximation was used along the self-consistent field procedure. Scalar relativistic corrections have been included self consistently by using the zeroth order approximation. Energies and gradients were calculated by using the local density approximation (Slater exchange) with non-local corrections for exchange (Becke88) and correlation (Lee–Yang–Parr) included self consistently (that is, BLYP functional). Solvent effects (acetonitrile) were included through the use of COSMO approach. All structures were optimized using the QUILD program, which functions as a wrapper around the ADF program. QUILD uses improved geometry-optimization techniques, such as adapted delocalized coordinates and specially constructed model Hessians. When necessary, Cl^- counteranions have been used instead of $BArF^-$ for reducing computational complexity. See the Supplementary Discussion 1 for a detailed description and corresponding references. For DFT structures of $\mathbf{4}\cdot(BArF)_8$ and its host–guest adducts, see Supplementary Figs 70–72 and Supplementary Data 1.

References

1. Giacalone, F. & Martín, N. Fullerene polymers: synthesis and properties. *Chem. Rev.* **106,** 5136–5190 (2006).
2. Dennler, G., Scharber, M. C. & Brabec, C. J. Polymer-fullerene bulk-heterojunction solar cells. *Adv. Mater.* **21,** 1323–1338 (2009).
3. Anthopoulos, T. D. *et al.* Air-stable n-channel organic transistors based on a soluble C84 fullerene derivative. *Adv. Mater.* **18,** 1679–1684 (2006).
4. Norton, S. K., Conrad, D. H. & Kepley, C. L. *J. Immunol.* **182,** 140–148 (2009).
5. Ryan, J. J. *et al.* Fullerene nanomaterials inhibit the allergic response. *J. Immunol.* **179,** 665–672 (2007).
6. Parker, D. H. *et al.* Fullerenes and giant fullerenes: Synthesis, separation, and mass spectrometric characterization. *Carbon N. Y.* **30,** 1167–1182 (1992).
7. Khemani, K. C., Prato, M. & Wudl, F. A simple Soxhlet chromatographic method for the isolation of pure fullerenes C60 and C70. *J. Org. Chem.* **57,** 3254–3256 (1992).
8. Scrivens, W. A., Bedworth, P. V. & Tour, J. M. Purification of gram quantities of C60. A new inexpensive and facile method. *J. Am. Chem. Soc.* **114,** 7917–7919 (1992).
9. Isaacs, L., Wehrsig, A. & Diederich, F. Improved Purification of C60 and Formation of σ- and π-Homoaromatic methano-bridged fullerenes by reaction with alkyl diazoacetates. *Helv. Chim. Acta* **76,** 1231–1250 (1993).
10. Hirsch, A. & Brettreich, M. *Fullerenes, Chemistry and Reactions* (Wiley-VCH, 2005).
11. Yeretzian, C. *et al.* Partial separation of fullerenes by gradient sublimation. *J. Phys. Chem.* **97,** 10097–10101 (1993).
12. Bhyrappa, P., Penicaud, A., Kawamoto, M. & Reed, C. A. Improved chromatographic separation and purification of C60 and C70 fullerenes. *J. Chem. Soc. Chem. Commun.* **13,** 936–937 (1992).
13. Arias, F. *et al.* Kinetic effects in the electrochemistry of fullerene derivatives at very negative potentials. *J. Am. Chem. Soc.* **116,** 6388–6394 (1994).
14. Xiao, J. & Meyerhoff, M. E. High-performance liquid chromatography of C60, C70, and higher fullerenes on tetraphenylporphyrin-silica stationary phases using strong mobile phase solvents. *J. Chromatogr. A* **715,** 19–29 (1995).
15. Komatsu, N., Ohe, T. & Matsushige, K. A highly improved method for purification of fullerenes applicable to large-scale production. *Carbon N. Y.* **42,** 163–167 (2004).
16. Canevet, D., Pérez, E. M. & Martín, N. Wraparound hosts for fullerenes: tailored macrocycles and cages. *Angew. Chem. Int. Ed.* **50,** 9248–9259 (2011).
17. Tashiro, K. & Aida, T. Metalloporphyrin hosts for supramolecular chemistry of fullerenes. *Chem. Soc. Rev.* **36,** 189–197 (2007).
18. Atwood, J. L., Koutsantonis, G. A. & Raston, C. L. Purification of C60 and C70 by selective complexation with calixarenes. *Nature* **368,** 229–231 (1994).
19. Matsubara, H. *et al.* Supramolecular inclusion complexes of fullerenes using cyclotriveratrylene derivatives with aromatic pendants. *Chem. Lett.* **27,** 923–924 (1998).
20. Kawase, T., Tanaka, K., Shiono, N., Seirai, Y. & Oda, M. Onion-type complexation based on carbon nanorings and a buckminsterfullerene. *Angew. Chem. Int. Ed.* **43,** 1722–1724 (2004).
21. Tian, X.-H. & Chen, C.-F. Triptycene-derived calix[6]arenes: synthesis, structures, and their complexation with fullerenes C60 and C70. *Chem. Eur. J.* **16,** 8072–8079 (2010).
22. Suzuki, K., Takao, K., Sato, S. & Fujita, M. Coronene nanophase within coordination spheres: increased solubility of C60. *J. Am. Chem. Soc.* **132,** 2544–2545 (2010).
23. Haino, T., Fukunaga, C. & Fukazawa, Y. A new calix[5]arene-based container: selective extraction of higher fullerenes. *Org. Lett.* **8,** 3545–3548 (2006).
24. Mahata, K., Frischmann, P. D. & Würthner, F. Giant electroactive M4L6 tetrahedral host self-assembled with Fe(II) vertices and perylene bisimide dye edges. *J. Am. Chem. Soc.* **135,** 15656–15661 (2013).
25. Wang, M.-X., Zhang, X.-H. & Zheng, Q.-Y. Synthesis, structure, and [60]fullerene complexation properties of azacalix[m]arene[n]pyridines. *Angew. Chem. Int. Ed.* **43,** 838–842 (2004).
26. Hu, S.-Z. & Chen, C.-F. Triptycene-derived oxacalixarene with expanded cavity: synthesis, structure and its complexation with fullerenes C60 and C70. *Chem. Commun.* **46,** 4199–4201 (2010).
27. Pirondini, L. *et al.* Inclusion of methano[60]fullerene derivatives in cavitand-based coordination cages. *Tetrahedron* **62,** 2008–2015 (2006).
28. Huerta, E. *et al.* Selective binding and easy separation of C70 by nanoscale self-assembled capsules. *Angew. Chem. Int. Ed.* **46,** 202–205 (2007).
29. Isla, H. *et al.* A bis-exTTF macrocyclic receptor that associates C60 with micromolar affinity. *J. Am. Chem. Soc.* **132,** 1772–1773 (2010).
30. Pérez, E. M., Sánchez, L., Fernández, G. & Martín, N. exTTF as a building block for fullerene receptors. Unexpected solvent-dependent positive homotropic cooperativity. *J. Am. Chem. Soc.* **128,** 7172–7173 (2006).
31. Canevet, D. *et al.* Macrocyclic hosts for fullerenes: extreme changes in binding abilities with small structural variations. *J. Am. Chem. Soc.* **133,** 3184–3190 (2011).
32. Huerta, E. *et al.* Tripodal exTTF-CTV hosts for fullerenes. *J. Am. Chem. Soc.* **132,** 5351–5353 (2010).
33. Goeb, S. *et al.* A BPTTF-based self-assembled electron-donating triangle capable of C60 binding. *Chem. Commun.* **48,** 3106–3108 (2012).
34. Gil-Ramírez, G. N. *et al.* A cyclic porphyrin trimer as a receptor for fullerenes. *Org. Lett* **12,** 3544–3547 (2010).
35. Song, J., Aratani, N., Shinokubo, H. & Osuka, A. A porphyrin nanobarrel that encapsulates C60. *J. Am. Chem. Soc.* **132,** 16356–16357 (2010).
36. Mulholland, A. R., Woodward, C. P. & Langford, S. J. Fullerene-templated synthesis of a cyclic porphyrin trimer using olefin metathesis. *Chem. Commun.* **47,** 1494–1496 (2011).
37. Nobukuni, H. *et al.* Supramolecular structures and photoelectronic properties of the inclusion complex of a cyclic free-base porphyrin dimer and C60. *Chem. Eur. J.* **16,** 11611–11623 (2010).
38. Schmittel, M., He, B. & Mal, P. Supramolecular multicomponent self-assembly of shape-adaptive nanoprisms: wrapping up C60 with three porphyrin units. *Org. Lett.* **10,** 2513–2516 (2008).
39. Meng, W. *et al.* A self-assembled M8L6 cubic cage that selectively encapsulates large aromatic guests. *Angew. Chem. Int. Ed.* **50,** 3479–3483 (2011).
40. Giguere, J.-B. & Morin, J.-F. New strapped porphyrins as hosts for fullerenes: synthesis and complexation study. *Org. Biomol. Chem.* **10,** 1047–1051 (2012).
41. Hernández-Eguía, L. P. *et al.* Supramolecular inclusion complexes of two cyclic zinc bisporphyrins with C60 and C70: structural, thermodynamic, and photophysical characterization. *Chem. Eur. J.* **17,** 14564–14577 (2011).

42. Sun, D., Tham, F. S., Reed, C. A., Chaker, L. & Boyd, P. D. W. Supramolecular fullerene-porphyrin chemistry. fullerene complexation by metalated 'jaws porphyrin' hosts. *J. Am. Chem. Soc.* **124,** 6604–6612 (2002).
43. Nakamura, T., Ube, H., Miyake, R. & Shionoya, M. A C60-templated tetrameric porphyrin barrel complex via zinc-mediated self-assembly utilizing labile capping ligands. *J. Am. Chem. Soc.* **135,** 18790–18793 (2013).
44. Boyd, P. D. W. & Reed, C. A. Fullerene − porphyrin constructs. *Acc. Chem. Res.* **38,** 235–242 (2004).
45. Zhang, C., Wang, Q., Long, H. & Zhang, W. A highly C70 selective shape-persistent rectangular prism constructed through one-step alkyne metathesis. *J. Am. Chem. Soc.* **133,** 20995–21001 (2011).
46. Inokuma, Y., Arai, T. & Fujita, M. Networked molecular cages as crystalline sponges for fullerenes and other guests. *Nat. Chem.* **2,** 780–783 (2010).
47. Shoji, Y., Tashiro, K. & Aida, T. Selective extraction of higher fullerenes using cyclic dimers of zinc porphyrins. *J. Am. Chem. Soc.* **126,** 6570–6571 (2004).
48. Li, M.-J., Huang, C.-H., Lai, C.-C. & Chiu, S.-H. Hemicarceplex formation with a cyclotriveratrylene-based molecular cage allows isolation of high-purity ($\geq$99.0%) C70 directly from fullerene extracts. *Org. Lett.* **14,** 6146–6149 (2012).
49. Kishi, N. *et al.* Facile catch and release of fullerenes using a photoresponsive molecular tube. *J. Am. Chem. Soc.* **135,** 12976–12979 (2013).
50. Kishi, N., Akita, M. & Yoshizawa, M. Selective host–guest interactions of a transformable coordination capsule/tube with fullerenes. *Angew. Chem. Int. Ed.* **53,** 3604–3607 (2014).
51. García-Simón, C. *et al.* Self-assembled tetragonal prismatic molecular cage highly selective for anionic π guests. *Chem. Eur. J.* **19,** 1445–1456 (2013).
52. Juanhuix, J. *et al.* Developments in optics and performance at BL13-XALOC, the macromolecular crystallography beamline at the Alba Synchrotron. *J. Synchrotron Rad.* **21,** 679–689 (2014).
53. Jiang, S. *et al.* Porous organic molecular solids by dynamic covalent scrambling. *Nat. Commun.* **2,** 207 (2011).
54. Ribas, X., Costas, M., García-Simón, C., Company, A. & Gómez, L. Nanocápsulas moleculares para la separación selectiva de fullerenos. *Patent P201430315* (2014).
55. Marcotte, N. & Taglietti, A. Transition-metal-based chemosensing ensembles: ATP sensing in physiological conditions. *Supramol. Chem.* **15,** 617–625 (2003).
56. Ribas, X. *et al.* Stepwise construction of oligomeric 1,2-diselenolene platinum(IV) complexes. *Angew. Chem. Int. Ed.* **43,** 4049–4052 (2004).
57. Palatinus, L. & Chapuis, G. SUPERFLIP—a computer program for the solution of crystal structures by charge flipping in arbitrary dimensions. *J. Appl. Crystallogr.* **40,** 786–790 (2007).
58. Sheldrick, G. A short history of SHELX. *Acta Crystallogr.* **A64,** 112–122 (2008).

Acknowledgements

This work was supported by grants from the European Research Council (Starting Grant Projects ERC-2011-StG-277801 and ERC-2009-StG-239910), the Spanish MICINN (CTQ2012-37420-C02-01/BQU, CTQ2012-32436, CTQ2011-23156/BQU, CTQ2011-25086/BQU, Consolider-Ingenio CSD2010-00065, INNPLANTA project INP-2011-0059-PCT-420000-ACT1, MAT2012-30994, a RyC contract to I.I., a JdC contract JCI-2012-14438 and CIG (FP7-PEOPLE-2013-CIG-630978) to S.O. and a PhD grant AP2010-2517 to M.G.B.) and the Generalitat de Catalunya (2009SGR637 and a PhD grant to C.G.S.). We thank Dr J.M. Luis and Professor M. Swart for fruitful discussions on DFT calculations, Dr C. Whiteoak for English grammar corrections, and Professor P. Ballester for providing us access to fluorescence spectroscopy measurements. X.R. and M.C. also thank ICREA-Acadèmia awards. Computational resources from Barcelona Supercomputing Center (Centro Nacional de Supercomputación) are acknowledged.

Author contributions

C.G.-S. performed all the experimental work (cage synthesis and fullerene encapsulation/liberation experiments); M.G.-B. and S.O. performed the theoretical calculations; T.P. supervised the NMR studies; L.G. assisted in designing and performing the mass spectrometry studies; J.J., I.I. and D.M. performed and supervised all the crystallographic experiments at ALBA synchrotron; M.C. and X.R. designed and directed the project, and wrote the paper.

Additional information

Accession codes: Supplementary crystallographic data for compounds $C_{60} \subset \mathbf{4} \cdot (BArF)_8$, $C_{70} \subset \mathbf{4} \cdot (BArF)_8$, $\mathbf{4} \cdot (BArF)_8$ and (**Pd-1b**) $\cdot (AcO)_2(CF_3SO_3)_2$ have been deposited at the Cambridge Crystallographic Data Centre under accession numbers CCDC 1027668–1027671, respectively. These data can be obtained free of charge at http://www.ccdc.cam.ac.uk/data_request/cif. Reprints and permissions information is available at www.nature.com/reprints. Readers are welcome to comment on the online version of the paper.

Supplementary Information accompanies this paper at http://www.nature.com/naturecommunications

Competing financial interests: The authors declare no competing financial interests.

Reprints and permission information is available online at http://npg.nature.com/reprintsandpermissions/

How to cite this article: García-Simón, C. *et al.* Sponge-like molecular cage for purification of fullerenes. *Nat. Commun.* 5:5557 doi: 10.1038/ncomms6557 (2014).

Chapter V.

Enantioselective hydroformylation by a Rh-catalyst entrapped in a supramolecular cage

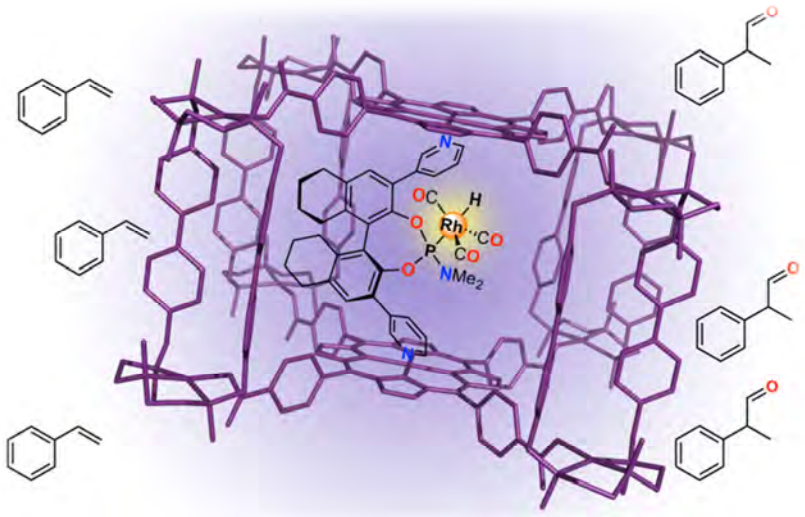

This chapter corresponds to the following manuscript:

C. García-Simón, R. Gramage-Doria, S. Raoufmoghaddam, T. Parella, M. Costas*, X. Ribas* and J. N.H.Reek*

J. Am. Chem. Soc., **2015**, DOI: 10.1021/ja512637k

For this publication C.G.-S. synthetized **4**·$(BArF)_8$ nanocapsule, performed the host guest experiments and the catalytic hydroformylation experiments (T.P supervised the NMR experiments and R.G.-D. supervised the host-guest experiments with **α** and the hydroformylation reactions, S.R. performed hydroformylation experiments involving ligands **γ** and **δ** and the molecular modelling calculations). Besides, C.G.-S. contributed in writing the manuscript and was involved in argumentations and discussions.

Cristina García-Simón, Rafael Gramage-Doria, Saeed Raoufmoghaddam, Teodor Parella, Miquel Costas, Xavi Ribas, and Joost N. H. Reek (2015).”Enantioselective Hydroformylation by a Rh-Catalyst Entrapped in a Supramolecular Metallocage”. *Journal of the American Chemical Society*. 137, 7, 2680-2687

DOI: 10.1021/ja512637k

http://pubs.acs.org/doi/abs/10.1021/ja512637k

Publication Date (Web): January 29, 2015

Abstract

Regio- and enantioselective hydroformylation of styrenes is attained upon embedding a chiral Rh complex in a nonchiral supramolecular cage formed from coordination-driven self-assembly of macrocyclic dipalladium complexes and tetracarboxylate zinc porphyrins. The resulting supramolecular catalyst converts styrene derivatives into aldehyde products with much higher chiral induction in comparison to the nonencapsulated Rh catalyst. Spectroscopic analysis shows that encapsulation does not change the electronic properties of the catalyst nor its first coordination sphere. Instead, enhanced enantioselectivity is rationalized by the modification of the second coordination sphere occurring upon catalyst inclusion inside the cage, being one of the few examples in achieving an enantioselective outcome via indirect through-space control of the chirality around the catalyst center. This effect resembles those taking place in enzymatic sites, where structural constraints imposed by the enzyme cavity can impart stereoselectivities that cannot be attained in bulk. These results are a showcase for the future development of asymmetric catalysis by using size-tunable supramolecular capsules.

Chapter VI.

Results and Discussion

VI. RESULTS AND DISCUSSION

The field of supramolecular self-assembly has opened up new routes towards the preparation of highly sophisticated molecular architectures. However, as the complexity of the supramolecular structures increases, self-assembly between the molecular subunits often turns into an increasingly unpredictable process. This is mostly a result of the lack of control during the self-assembly process. Coordination-driven self-assembly, which is based on the use of metal-ligand coordination bonds, permits an increased control during the synthesis thanks to the high degree of directionality of the M-L bond and the predictability of the metal ion coordination environment (Chapter I.2).

Hexaaza macrocyclic di-copper(II) complexes, previously reported by the QBIS-CAT group, can be considered as molecular clips, because they adopt a rigid conformation where each of the copper ions has a coordination vacancy, in relative parallel orientation (Table VI.1, entries a and g). These metal complexes are capable of self-assembling through a DBA (Directional Bonding Approach) with different rigid di- and tricarboxylate linkers to furnish an extended library of 2D rectangles and helicates of different sizes and also functionalized 3D capsules (Scheme I.1 in Chapter I.2 and Table VI.1).

In 2006 the synthesis of molecular rectangles synthesized through 2+2 self-assembly of [(**Cu-1**)$(H_2O)_2$]$(CF_3SO_3)_4$ or [(**Cu-2**)$(CH_3CN)_4$]$(CF_3SO_3)_4$ molecular clips and terephthalic acid (**A**) as linker was reported.[1] The tetranuclear coordination rectangles were characterized by single-crystal X-ray diffraction (XRD) analysis providing definitive proof of their structure (Table VI.1, entries b and h). Moreover, ESI-MS experiments confirmed that their structure was maintained in solution. Following these studies, it was reported that larger rectangles were obtained by mixing the *para*-substituted macrocyclic complex clip ([(**Cu-1**)$(H_2O)_2]^{4+}$) and enlarged dicarboxylic linkers, biphenyl-4,4'-dicarboxylic acid (**B**) and 2,6-naphthalenedicarboxylic acid (**C**) (Table VI.1, entries c-d). Instead, the reaction between the *meta*-substituted arene based clip ([(**Cu-2**)$(CH_3CN)_4]^{4+}$) with linkers **A** or **B** gave double-stranded helicates (Scheme I.1 in Chapter I.2 and Table VI.1, entries i-j). All these larger 2D structures were also characterized by XRD and by ESI-MS analyses in solution.[2]

The next step forward was the evolution from 2D to 3D trigonal prisms with the use of tricarboxylate linkers. Trigonal prismatic (and antiprismatic) cages were obtained by one pot reactions of ligand **1**, a copper(II) salt and 1,3,5-*tris*-(4-carboxyphenyl)benzene (**BTB**), tricarboxylate polychlorotriphenylmethane (**αH-PTMTC**) or tricarboxylate polychlorotriphenylmethyl radical (**PTMTC**) at room temperature.[3] Analytical evidence for the molecular composition of the 3D supramolecular structures was obtained by ESI-MS and the XRD structure of the cage bearing **BTB** units was obtained (Table VI.1, entry e). Additionally, the nature of the tricarboxylate linkers conferred fluorescent or magnetic properties to these cages; thereby an important step towards the development of polyfunctional structures was achieved.

The molecular clips ([(**Cu-1**)$(H_2O)_2$]$^{4+}$ and [(**Cu-2**)$(CH_3CN)_4$]$^{4+}$) used for the preparation of all the structures in Table VI.1 are based on copper(II) and therefore paramagnetic nature of the resulting species precludes their characterization by NMR and limits the possibility to further investigate their properties in solution.

This thesis is focused on the preparation of dipalladium(II) hexaaza macrocyclic complexes ([(**Pd-1**)$(AcO)_2$]$(X)_2$, X=CF_3SO_3, AcO) which are analogous to [(**Cu-1**)$(H_2O)_2$]$(CF_3SO_3)_4$ previously reported. The diamagnetic nature of these molecules enables characterization by standard NMR methods (Scheme VI.1). Also, palladium(II) typically forms stable compounds that present a well-defined square planar geometries in contrast to copper(II) which can adopt different geometries. With these precedents in mind, it was expected that palladium(II)-based coordination structures will be more predictable and stable than those previously prepared with copper(II).

The reaction of the molecular clip [(**Pd-1**)$(AcO)_2$]$^{2+}$ with tetracarboxylated metalloporphyrins (**M-Porph**), resulted in the formation of a 3D coordination tetragonal prismatic cage of general formula [(**Pd-1**)$_4$(**M-Porph**)$_2$]$^{8+}$. The diamagnetic nature of the new capsule facilitated the investigation of its host-guest properties in solution by means of NMR studies. Remarkably, the size of the dipalladium molecular clip could be tuned in order to obtain larger dipalladium-macrocycles which leaded to a larger cage with a wider inner cavity. The larger cage was not only interesting because it permitted the sequestration of larger substrates, but also because it allowed encapsulation of a catalytic moiety, creating an isolated environment reminiscent of the active site present in enzymes.

Table VI.1. Library of the molecular clips, and 2D and 3D coordination structures previously reported (**A**= *p*-terephthalalic acid, **B**= biphenyl-4,4'-dicarboxylic acid, **C**= 2,6-naphthalenedicarboxylic acid, **BTB**= (1,3,5-*tris*-(4-carboxyphenyl)benzene)).

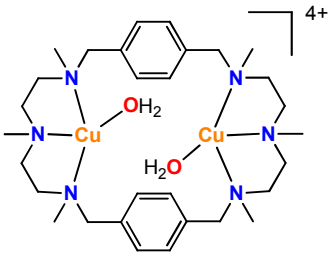

a) [(**Cu-1**)$(H_2O)_2$]$^{4+}$

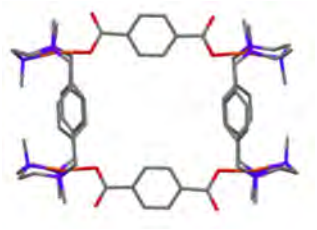

b) [(**Cu-1**)$_2$(**A**)$_2$]$^{4+}$

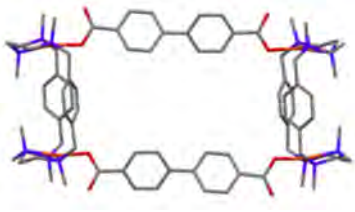

c) [(**Cu-1**)$_2$(**B**)$_2$]$^{4+}$

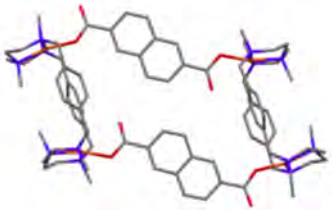

d) [(**Cu-1**)$_2$(**C**)$_2$]$^{4+}$

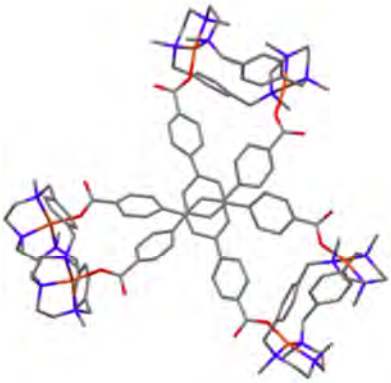

e) [(**Cu-1**)$_3$(**BTB**)$_2$]$^{6+}$

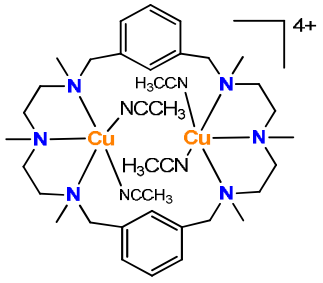

g) [(**Cu-2**)$(CH_3CN)_4$]$^{4+}$

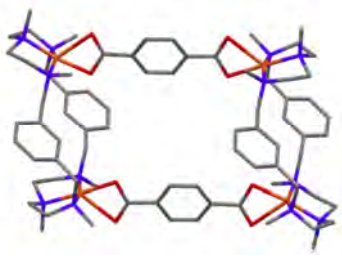

h) [(**Cu-2**)$_2$(**A**)$_2$]$^{4+}$

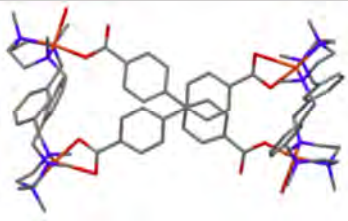

i) [(**Cu-2**)$_2$(**B**)$_2$]$^{4+}$

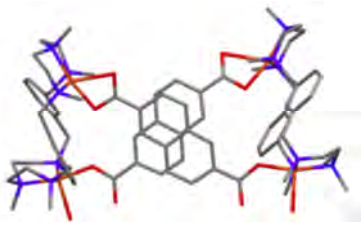

j) [(**Cu-2**)$_2$(**C**)$_2$]$^{4+}$

VI.1. Self-assembled tetragonal prismatic molecular cage highly selective for anionic π-guests

This section corresponds to the contents of the manuscript by García-Simón et al. *Chem. Eur. J*, **2013**, *19*, 1445-1456, which can be found in **Chapter III** of this thesis.

VI.1.1 Synthesis and characterization of 3·$(CF_3SO_3)_8$ nanocapsule

The synthesis of the diamagnetic molecular clip [(**Pd-1**)$(AcO)_2$]$(X)_2$ (X= CF_3SO_3, AcO) was similar to that previously described for [(**Cu-1**)$(H_2O)_2$]$(CF_3SO_3)_4$. The reaction of previously described hexaazamacrocyclic ligand **1** with $Pd(AcO)_2$ in refluxing CH_3CN, furnished complex [(**Pd-1**)$(AcO)_2$]$(AcO)_2$ as an intense yellow crystalline solid in 87% yield (Scheme VI.1).[4,5] The molecular clip [(**Pd-1**)$(AcO)_2$]$(AcO)_2$ was fully characterized in solution by means of NMR and ESI-MS.

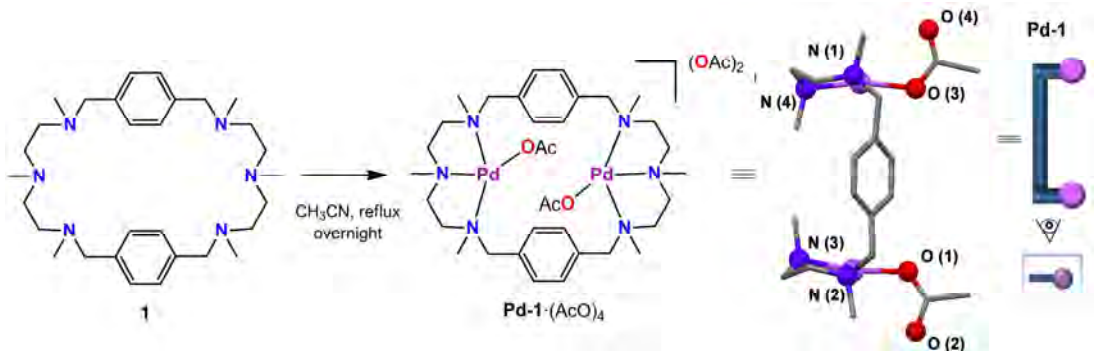

Scheme VI.1. Synthesis of the [(**Pd-1**)$(AcO)_2$]$(AcO)_2$ molecular clip and crystal structure of the macrocyclic compound [(**Pd-1**)$(AcO)_2$]$^{2+}$ (H atoms are omitted for clarity).

Crystals suitable for single X-ray diffraction structure for [(**Pd-1**)$(AcO)_2$]$(AcO)_2$ were obtained by slow diffusion of ether over a solution of the palladium molecular clip in acetonitrile. The palladium(II) ions (d^8) adopt a tetracoordinated slightly distorted square-planar geometry formed through coordination to three N atoms of the macrocyclic ligand **1** and one O atom from the carboxylate group, which coordinates in a monodentate fashion. The coordination planes of the two palladium(II) atoms approximately parallel, with Pd-O vectors oriented in the same direction. The rigidity of this complex, which is maintained in solution, is the key for the success of this molecular clip in the construction of 3D supramolecular structures (Scheme VI.1)

Nanocapsule **3**·$(CF_3SO_3)_8$ was easily prepared by reaction of 2 equivalents of the *in situ* prepared $HNEt_3^+$ salt of the commercially available tetracarboxylate linker 5,10,15,20-*tetrakis*(4-carboxyphenyl)-porphyrin-Pd(II) (**Porph-Pd**) and four equivalents of [(**Pd-1**)$(AcO)_2$]$(CF_3SO_3)_2$ (obtained from [(**Pd-1**)$(AcO)_2$]$(AcO)_2$ to which an excess of $NaCF_3SO_3$ had been previously added) molecular clip, in DMF at 105ºC. After stirring for 16 h, the solution was filtered, and capsule **3**·$(CF_3SO_3)_8$ was obtained as a red crystalline solid upon slow diffusion of diethyl ether.

X-ray diffraction analysis required the use of synchrotron radiation since the crystals were very unstable towards loss of solvent and due to weak crystal diffractions. Nevertheless, the XRD data confirmed that nanocapsule **3**·$(CF_3SO_3)_8$ consists of two parallel tetracarboxylate porphyrins (Pd···Pd distance of 7.49 Å) connected by four macrocyclic dinuclear palladium(II) complexes (Scheme VI.2). Each porphyrin carboxylate residue is linked by means of η^1-O monodentate coordination to one palladium(II) centre. The metal centre presents a slightly distorted square-planar geometry as was also observed in the 2D and 3D structures based on copper(II) previously reported.[1–3] The capsule resembles a cube and presents a D_{4h} symmetrywith 8 palladium(II) ions located at the corners. The cage is highly positively charged (8+) and all the counteraions were located outside of the inner cavity.

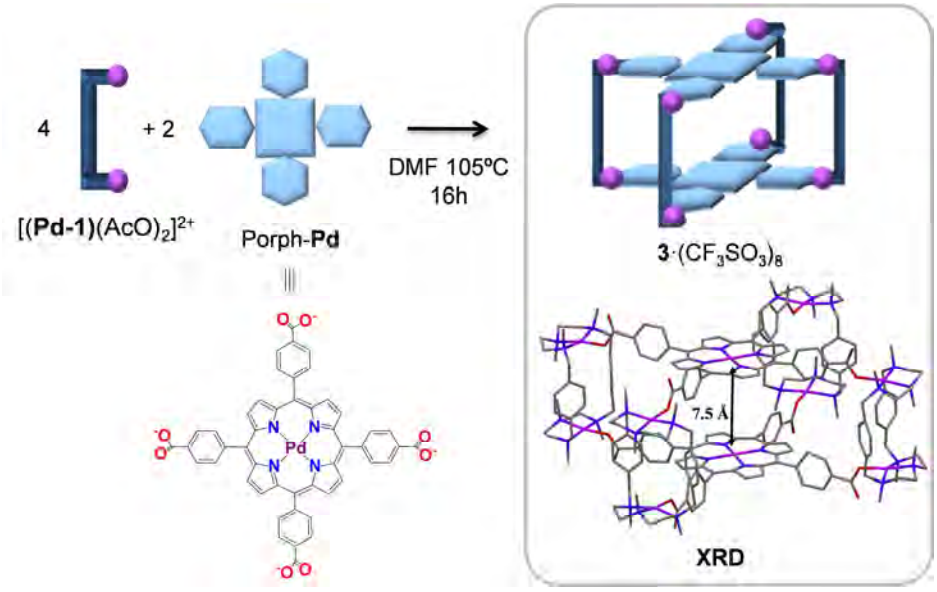

Scheme VI.2. Schematic representation of the building blocks used in the synthesis of tetragonal-prismatic nanocapsule (**3**·$(CF_3SO_3)_8$) and its XRD structure (hydrogen atoms have been omitted for clarity).

NMR experiments corroborated that the structure of **3**·$(CF_3SO_3)_8$ is retained in solution and through the use of 2D NMR methods, COSY and NOESY experiments, it was possible to fully assign all the proton signals. ESI-MS experiments in CH_3CN provided further evidence of the molecular composition of the nanocapsule in solution. The results indicated that this architecture retains its integrity in solution, as peaks corresponding to (**Pd-1**)$^{4+}$ complex were not observed; therefore cage **3**·$(CF_3SO_3)_8$ remains intact even at the low concentrations employed in the ESI-MS analyses. (Figure VI.1).

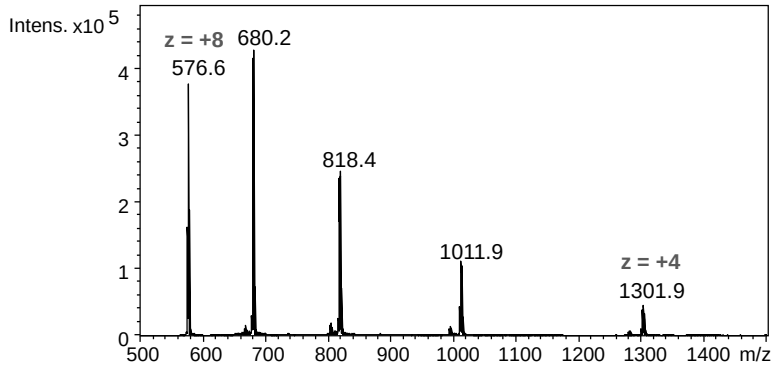

Figure VI.1. ESI-MS spectra of **3**·$(CF_3SO_3)_8$ nanocapsule. Experimental conditions: 100 μM in CH_3CN, recorded using a Bruker MicroTOF-Q-II exact mass spectrometer.

VI.1.2 Host-Guest experiments

The obtained results indicated that the cage contains a wide inner cavity, which prompted the study of the characteristics and properties of this molecular receptor, in order to determine the kind of substrates that could be suitable guests by means of host-guest experiments. Chemical characteristics of capsule $\mathbf{3}^{8+}$ were predicted by carefully analysing its structure which contains two metallo-porphyrins that are π-electron donor moieties; hence it was proposed that it may establish π-π interactions with suitable substrates. The lateral molecular palladium(II) clips contain aromatic rings and they can also potentially act as electron donor units, as well as establishing hydrogen-bonding or π-π interactions.[6,7] Square-planar palladium(II) centres from porphyrin moieties may also present weak interactions at their axial coordination vacancies. Additionally, the capsule is highly positively charged (+8), consequently it is plausible that it may be a suitable host for anionic substrates. With all these considerations in hand, an initial set of possible substrates was selected in order to perform different host-guest experiments (Table VI.2).

Preliminary host-guest studies of all substrates in Table VI.2 were performed by means of UV-Vis monitoring of the changes observed at the Soret band of the porphyrin moieties. However, only one of the eight selected substrates was found to display an interaction with the capsule. In the case of complex TBA[Au(tdas)$_2$] (**I,** TBA= tetrabutylammonium),[8] the significant changes observed in the Soret band were attributed to host-guest supramolecular interactions.

Table VI.2. Organic compounds and coordination complexes initially explored as guests for nanocacapsule **3**·$(CF_3SO_3)_8$.

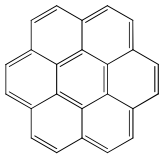 Coronene	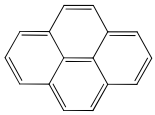 Pyrene
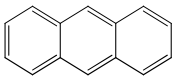 Anthracene	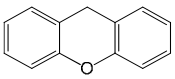 Xanthene
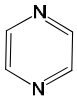 Pyrazine	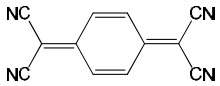 TCNQ
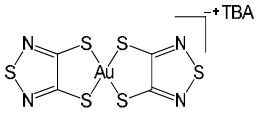 TBA[Au(tdas)$_2$] (I)	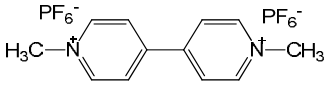 Paraquat

When substrate **I** was added to a CH_3CN solution of **3**·$(CF_3SO_3)_8$, the intensity of the Soret band notably decreased. A bathochromic shift of the band was observed, exhibiting two isosbestic points (Figure VI.2 a). The expected 1:1 stoichiometry, suggested by the presence of the isosbestic points, was confirmed through continuous variation plots (Job plots).

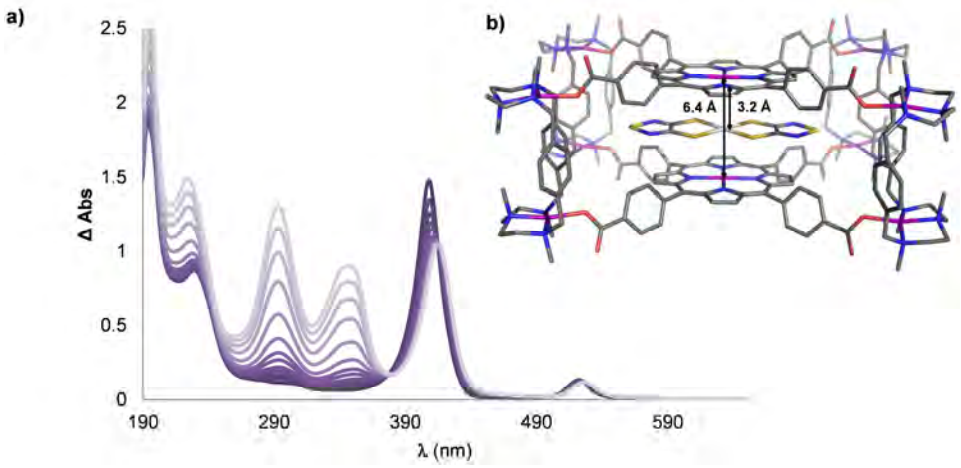

Figure VI.2. a) UV-Vis monitoring of the titration of nanocapsule **3**·$(CF_3SO_3)_8$ with substrate **I**. Fixed total concentration ($3.5\cdot10^{-6}$ M) of nanocapsule in CH_3CN. **b)** DFT-optimized structure of **I**⊂**3**·$(CF_3SO_3)_7$.

Through an initial estimation using an approximate graphical method, the data from the UV-Vis titration for substrate **I** and **3**·$(CF_3SO_3)_8$ gave a value of ~$4\cdot10^9$ M^{-1}. More recently the experiment was revisited and repeated by maintaining a fixed host concentration ($3.5\cdot10^{-6}$ M) during the titration and a more precise mathematical treatment of the data (Origin) was used

and the binding constant of **3**·$(CF_3SO_3)_8$ towards **I** in CH_3CN at room temperature was found to be $K_a = 1.1 (\pm 0.1)\cdot 10^6$ M^{-1} ($\log K_a = 6.02 \pm 0.04$) which remains indicative of a strong host-guest interaction.

Additional support for the 1:1 host-guest interaction was provided by ^{1}H-NMR and ESI-MS. Although compound **I** does not contain protons in its structure, by carefully analysing the ^{1}H-NMR spectra it could be observed that the signals belonging to the phenyl and pyrrole rings from the porphyrins were shifted upon inclusion of substrate **I**, particularly the protons which are closest to the pyrrole rings.

Crystals of the **I**⊂**3**·$(CF_3SO_3)_7$ adduct suitable for single crystal X-ray crystallography studies were obtained by slow diffusion of ether into a concentrated CH_3CN solution of the host-guest adduct, although unfortunately extreme sensitivity to solvent loss precluded their determination. In order to gain insight in the interaction between guest **I** and the nanocapsule, DFT calculations were performed and the calculated DFT structure for complex **I**⊂**3**·$(Cl)_7$ (Cl^- was used for model counterions) clearly showed that a planar substrate **I** is located in the middle of the cage cavity, in a triple-decker fashion (Figure VI.2 b). The Au(substrate **I**)…Pd(Porph) distance is 3.19 Å which likely corresponds to a strong π-π interaction between the porphyrin moieties and the planar π-guest substrate. Remarkably, the Au···Pd distance is shorter than the sum of the van der Waals radii (3.29 Å), which suggested some degree of metal bonding.[9] The shortened porphyrin-porphyrin distance upon guest inclusion, also suggested that the cage is able to adapt its structure towards guest inclusion through a breathing ability. The DFT optimized structure also showed that the phenyl rings from the porphyrin moieties and from the molecular palladium(II) clips were twisted after inclusion of **I**. This observation is in good agreement with the shifts observed in the ^{1}H-NMR spectra of **I**⊂**3**·$(CF_3SO_3)_7$.

VI.1.3 Expanding the scope of anionic-guests.

Once the inclusion of substrate **I** was thoroughly investigated, other anionic substrates such us linear N_3^-, SCN^-, or planar NO_3^-, or $AuCl_4^-$ were tested as guest molecules using **3**·$(CF_3SO_3)_8$. UV-Vis experiments indicated no interaction with any of these new substrates, which is in alignment with the XRD data which showed that no ClO_4^- anions were located inside of the capsule cavity. It was therefore clear that other requisites need to be fulfilled to find a suitable guest for cage **3**·$(CF_3SO_3)_8$, such as the existence of a planar structure and a delocalized π-system. Consequently, different *bis*-dithiolene complexes similar to **I** were tested (Table VI.3).[10–13]

Table VI.3. Planar *bis*-dithiolene-type metal complexes tested as guests for **3**·$(CF_3SO_3)_8$. *All complexes as TBA salts.

I	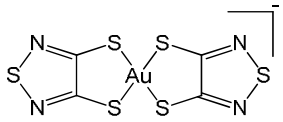 TBA[Au(tdas)$_2$]	VI	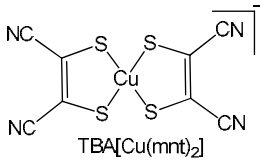 TBA[Cu(mnt)$_2$]
II	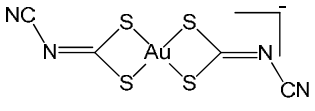 TBA[Au(cdc)$_2$]	VII	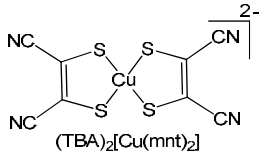 (TBA)$_2$[Cu(mnt)$_2$]
III	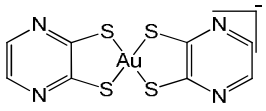 TBA[Au(pdt)$_2$]	VIII	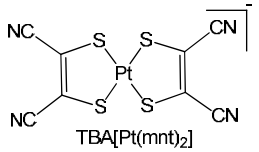 TBA[Pt(mnt)$_2$]
IV	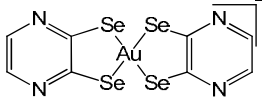 TBA[Au(pds)$_2$]	IX	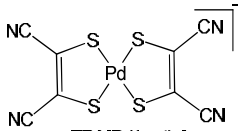 TBA[Pd(mnt)$_2$]
V	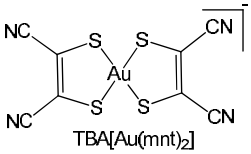 TBA[Au(mnt)$_2$]	X	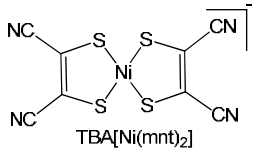 TBA[Ni(mnt)$_2$]

The potential interaction between nanocapsule **3**·$(CF_3SO_3)_8$ and substrates shown in Table VI.3 was first studied by means of UV-Vis experiments. For substrates **II**, **V**, **VIII**, **IX** and **X**, changes in the Soret band equivalent to the ones observed for substrate **I** occurred. Again, this is indicative of a 1:1 host-guest interaction that was further confirmed by a Job plot analysis. Further evidence for the 1:1 host guest interaction was given by ESI-MS experiments. Moreover, proton signals from **3**·$(CF_3SO_3)_8$ were shifted upon inclusion of substrates **II** or **V**, following the same trend observed for substrate **I**. Interestingly, when the sequestration of paramagnetic substrates **VIII**, **IX** or **X** was studied by ^{1}H-NMR, it was observed that the signals belonging to the aromatic protons of the capsule suffered a severe broadening, especially those orientated towards the inner space of the cage. Indeed, a blank experiment using a bulky paramagnetic substrate unable to fit into the capsule (*bis*(2-aminomethyl-6-phenylpyridine)Cu(II)]$(CF_3SO_3)_2$) did not cause any significant broadening of the signals, indicating that changes observed upon titration with **VIII**, **IX** or **X** are most likely due to sequestering of the substrate.

For all the substrates in Table VI.3 which were proven to interact with the nanocapsule, the association constant was higher than for substrate **I** (K_a = ~ 10^6). Complete conversion towards the encapsulated complex, was achieved just by adding 1 equivalent of the substrate, indicating a high affinity and precluding the direct determination of the association constant under the UV-Vis conditions used for substrate TBA[Au(tdas)]$_2$ (**I**). Therefore, competition

experiments were performed in order to find out if it was possible to exchange sequestered guests **II**, **V**, **VIII**, **IX** and **X** with substrate **I**. Notably, when 1 equivalent of substrates **II**, **V** or **VIII-X**, were added to a solution of **3**·$(CF_3SO_3)_8$ in acetonitrile, the Soret band drastically decreased. However, subsequent addition of an increasing number of equivalents of **I** did not cause any other change on the UV-Vis spectrum (Figure VI.3 a), indicating that the association with these substrates is stronger and no interchange of substrates followed (Annex, Supp. Info. Chapter III, Figure S24). On the contrary, substrate **I** was displaced after the addition of substrates **II**, **V** or **VIII-X** (Figure VI.3 b) as was reflected in the changes to the Soret band.

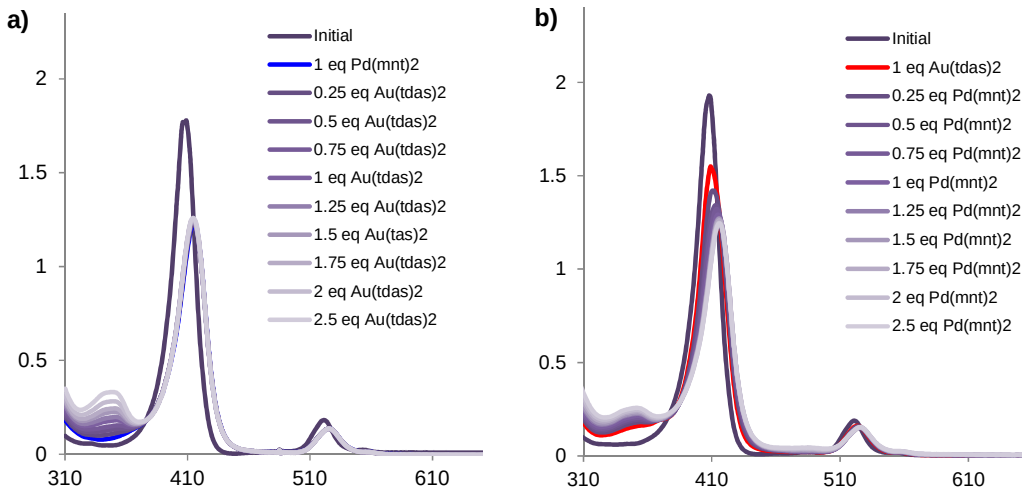

Figure VI.3. UV-Vis monitoring of the titrations of **3**·$(CF_3SO_3)_8$ nanocapsule ($3.8 \cdot 10^{-6}$ M in acetonitrile) with substrates **I** and **IX**: **a)** initially 1 equivalent of substrate **IX** was added to the capsule solution and subsequently up to 2.5 equivalents of substrate **I** were added, and **b)** initially 1 equivalent of substrate **I** was added to the capsule solution, subsequently up to 2.5 equivalents of substrate **IX** were added.

Unexpectedly, substrates **III** and **IV** which are similar to substrate **I**, did not fit inside capsule **3**·$(CF_3SO_3)_8$. The absence of interaction was rationalized by two main reasons; on one hand, the heteroatoms located on the extremes of the substrates (**I**, **II** and **V**), could play a key role in weak but additive interactions between the guest and the capsule's molecular clips, whilst on the other hand, substrates **III** and **IV** present a higher degree of aromaticity due to their pyrazine units. It has been reported previously that aromaticity can be a drawback for an efficient π-π interaction,[14] which could be the cause of the exclusion of guests **III** and **IV** from the cage cavity.

Addition of copper based substrates **VI** and **VII**, to a solution of the capsule caused its precipitation, suggesting that decomposition of the cage may occur, however the degradation process is not yet understood.

VI.1.4 Tuning the optical and redox properties of the guest molecules.

During the UV-Vis titration of **3**·$(CF_3SO_3)_8$ with complex **X** it was observed that the absorption band at ~860 nm, which originates from a ligand to metal charge transition (LMCT),[15] was quenched when the capsule and the substrate were mixed in a 1:1 molar ratio. When an excess of the substrate was added to the receptor the band increased again, indicating that the excess of guest remained outside of the nanocapsule (Figure VI.4 a). The quenching effect was attributed to the formation of the **X**⊂**3**·$(CF_3SO_3)_7$ host-guest adduct in which the π-π interactions between the porphyrin planes and the guest molecule affect the LMCT band at 860 nm. The same quenching effect was observed for substrates **VIII** and **IX** (Annex, Supp. Info. Chapter III, Figure S26 and S30).

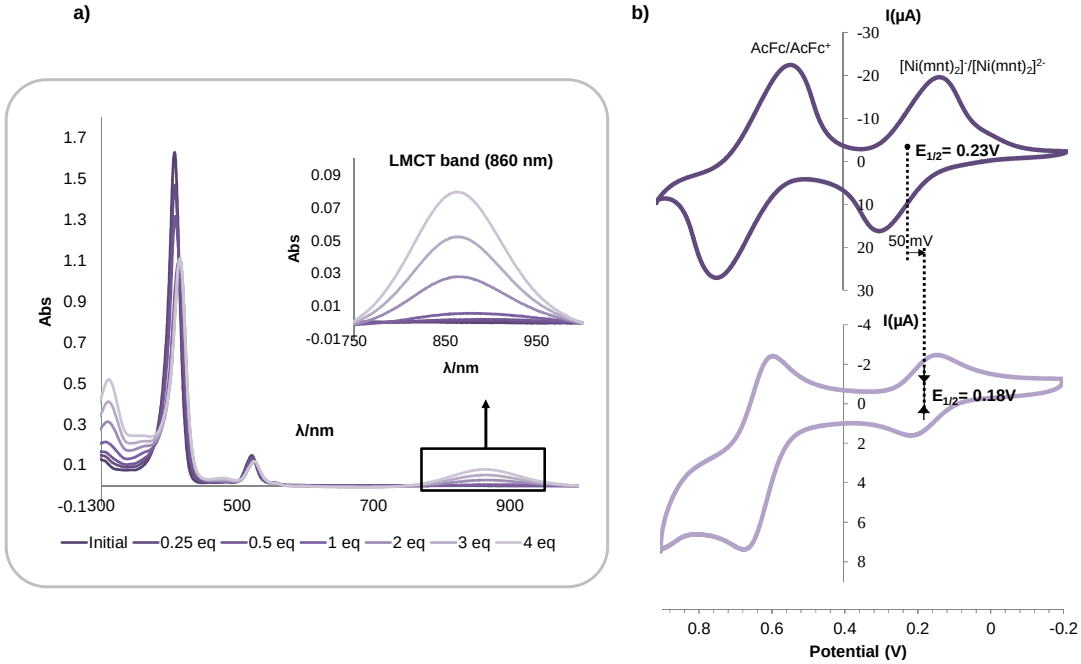

Figure VI.4. a) UV-Vis monitoring of the titration of **3**·$(CF_3SO_3)_8$ nanocapsule with TBA[Ni(mnt)$_2$] (**X**). Additions up to 4 eq. of **X** to a $3.8 \cdot 10^{-6}$ M solution of **3**·$(CF_3SO_3)_8$ in CH_3CN and **b)** Cyclic voltammetry spectrum of a 3.4 mM solution of **X** (top) and a 0.25 mM solution of nanocapsule **3**·$(CF_3SO_3)_8$ with 0.5 equivalents of **X** (bottom). Conditions: scan rate=0.1 V/s, [TBAP]=0.1 M, CH_3CN, using a saturated calomel electrode and AcFc/AcFc$^+$ as internal reference.

Encapsulation also altered the redox properties of the *di*-bisthiolene complexes, which are known to undergo multiple, reversible, one-electron redox reactions.[16,17] Cyclic voltammetry (CV) experiments of the empty cage, free substrates (**VIII**, **IX** and **X**) and **VIII**⊂**3**·$(CF_3SO_3)_7$, **IX**⊂**3**·$(CF_3SO_3)_7$ and **X**⊂**3**·$(CF_3SO_3)_7$ adducts were performed (acetylferrocene (AcFc) was used as internal reference). Remarkably, it was observed that the $[Ni(mnt)_2]^-/[Ni(mnt)_2]^{2-}$ couple in the CV spectrum belonging to **X**⊂**3**·$(CF_3SO_3)_7$ was shifted from 0.23V to 0.18V, in comparison with free **X**. No changes were observed in the wave belonging to AcFc, which did not interact with the nanocapsule. This shift to lower potential can be explained by a partial stabilization of the

monocationic form of the substrate inside the cubic cage. Furthermore, it was also observed that the intensity of the redox wave belonging to $[Ni(mnt)_2]^-/[Ni(mnt)_2]^{2-}$ was notably quenched with respect to the intensity of the $AcFc/AcFc^+$ pair, suggesting that the $[Ni(mnt)_2]^-/[Ni(mnt)_2]^{2-}$ redox potential is significantly altered upon forming the host-guest complex $\{\mathbf{X}\subset\mathbf{3}\}^{7+}$, while the acetylferrocene redox couple remains unaltered (Figure VI.4 b). The same experimental trend was observed for substrates **VIII** and **IX** (Annex, Supp. Info. Chapter III, Figure S27 and S31).

VI.1.5 Host-guest adducts volume estimation

By means of DOSY-NMR experiments and the Stokes-Einstein equation,[18–20] it was possible to obtain a value for the hydrodynamic ratio (r_H) of capsule $\mathbf{3}\cdot(CF_3SO_3)_8$ and $\mathbf{I}\subset\mathbf{3}\cdot(CF_3SO_3)_7$ adduct which was found to be 16.0 Å in both cases (diffusion coefficient (D) = $3.3\cdot10^{-10}$ m^2 s^{-1}). The r_H obtained for the empty capsule is in reasonable agreement with the radii based on the X-ray structure. The fact that the same value of r_H for $\mathbf{I}\subset\mathbf{3}\cdot(CF_3SO_3)_7$ and $\mathbf{3}\cdot(CF_3SO_3)_8$ species was obtained further supports the encapsulation of the substrate within the cage inner cavity.

CV experiments were performed in which substoichiometric amounts of substrates **VIII**, **IX** or **X** were added to a solution of capsule $\mathbf{3}\cdot(CF_3SO_3)_8$, and the measurements were repeated at different scan rates. The results allowed measurement of the diffusion coefficient (D) of the host-guest complexes formed by using the Randles-Sevick equation. Values of between 3.3 and $6.3\cdot10^{-10}$ m^2/s were obtained, which are in good agreement with the value obtained from the DOSY-NMR experiment for $\mathbf{I}\subset\mathbf{3}\cdot(CF_3SO_3)_7$ adduct.

In summary, in Chapter III a tetragonal prismatic coordination capsule has been synthesized by self-assembly of palladium(II) molecular clips and palladium(II)-tetracarboxylateporphyrins. The diamagnetic capsule was fully characterized by ^{1}H-NMR, DOSY, UV-Vis, HRMS and XRD experiments. The capsule has been proven to be highly selective for the encapsulation of flat, anionic π-guests. It has been shown that different metal *bis*-dithiolene-type complexes present strong interactions with the capsule, even though subtle changes on the substrate structure can condition the interaction. More interestingly, the host-guest interaction altered the optical and redox properties of the substrates. These results represent a step forward in the development of polyfunctional nano-vessels (sensors, nanoreactors, etc.). Moreover, this study encouraged the modification of the cage structure, by size-tuning of the palladium(II) molecular clips and by changing the metals of the porphyrins, in order to entrap larger substrates and induce different reactivities.

VI.2. Sponge-like molecular cage for purification of fullerenes

This section mainly corresponds to the contents of the manuscript by García-Simón et al. *Nat.Commun.*, 5:5557, **2014**, DOI: 10.1038/ncomms6557, which can be found in **Chapter IV** of this thesis.

VI.2.1 Synthesis and characterization of 4·(BArF)$_8$ nanocapsule

Once capsule **3**·$(CF_3SO_3)_8$ was fully characterized and its host-guest properties were studied, the second goal was the synthesis of a larger capsule, with an inner cavity capable of hosting fullerenes, molecules with exceptional properties (Chapter I.3).

To obtain a bigger capsule the hexaazamacrocyclic ligand (**1**) was enlarged by incorporating a second phenyl ring in the aromatic part of its structure to give ligand **1b** (Scheme VI.3). Biphenyl 4,4'-dicarbaldehyde was used as precursor for the synthesis of the ligand instead of terephthaldehyde. [(**Pd-1b**)$(AcO)_2$]$(CF_3SO_3)_2$ was obtained following the same experimental protocol used for [(**Pd-1**)$(AcO)_2$]$(CF_3SO_3)_2$ and the new diamagnetic molecular clip was fully characterized by means of ^{1}H-NMR, DOSY-NMR, ESI-MS and XRD.

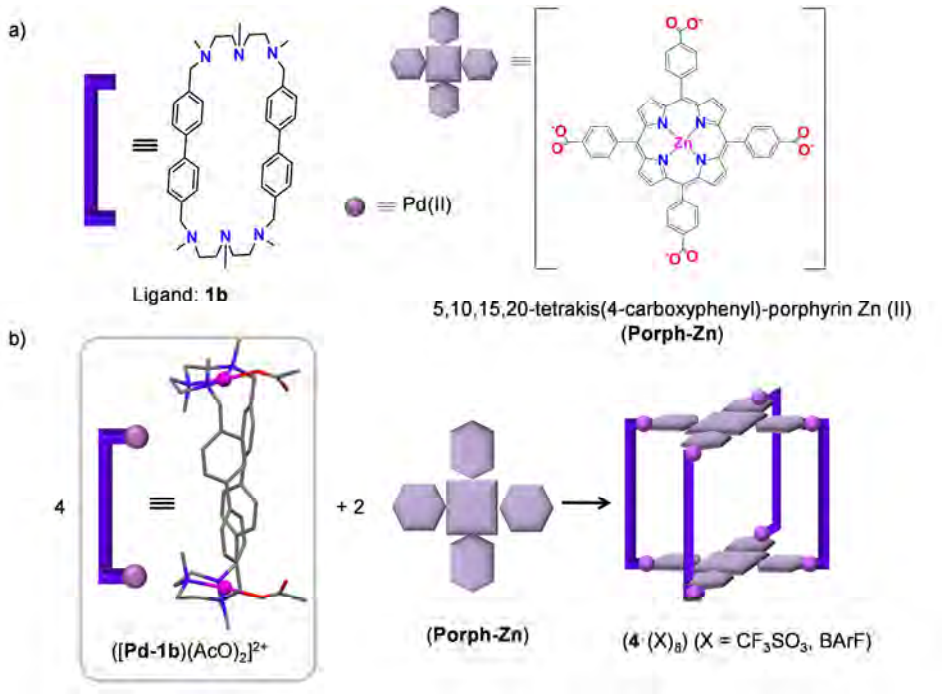

Scheme VI.3. a) Building blocks used to obtain the tetragonal prismatic nanocapsule **4**·$(X)_8$. **b)** Self-assembly of molecular clip (**Pd-1b**)$^{4+}$ and tetracarboxylated Zn-porphyrin (**Porph-Zn**) led to supramolecular nanocapsules **4**·$(X)_8$ (X = CF_3SO_3, BArF). XRD of [(**Pd-1**)$(AcO)_2$]$^{2+}$shows the acetate anion coordinated to each Pd centre, and omits the two triflate counteranions for clarity.

The reaction of four equivalents of molecular clip [(**Pd-1**)$(AcO)_2$]$(CF_3SO_3)_2$ and 2 equivalents of zinc(II)-porphyrin (**Porph-Zn**) gave capsule **4**·$(CF_3SO_3)_8$, which was characterized in solution by ESI-MS. However, this capsule was poorly soluble in most organic solvents. In order to improve solubility triflate anions were exchanged for *tetrakis*-[3,5-*bis*(trifluoromethyl)phenyl]boron anions (BArF), and a more soluble **4**·$(BArF)_8$ structure was obtained. Nanocapsule **4**·$(BArF)_8$ was fully characterized by NMR, HRMS and DOSY-2D experiments (Annex, Supp. Info. Chapter IV, Figure S35-40 and S62). Moreover, preliminary X-ray diffraction data of the cationic form of the capsule ($\mathbf{4}^{8+}$) was obtained at the Alba synchrotron which confirmed that the cage consists of two parallel zinc(II)-porphyrins linked by four dinuclear palladium(II) macrocyclic complexes. Analogously to cage **3**·$(CF_3SO_3)_8$, each of the four carboxylate moieties from the porphyrins were coordinated in a η^1-O monodentate fashion to the palladium(II) centres belonging to the molecular clips. The cage presented a tetragonal prismatic geometry (D_{4h}), in which the porphyrin-porphyrin distance was enlarged from 7.5 Å in **3**·$(CF_3SO_3)_8$ to 14.1 Å in **4**·$(BArF)_8$ (Figure VI.5) (Annex, Supp. Info. Chapter IV, Figure S66).

VI.2.2 Fullerene encapsulation

Due to its wide inner cavity and the known affinity of zinc(II)-porphyrins towards fullerenes, capsule **4**·$(BArF)_8$ was proposed as a good candidate for the sequestration of these sphere-like substrates. Gratifyingly, rapid inclusion occurred after mixing a solution of C_{60} or C_{70} fullerenes in toluene, with a solution of the nanocapsule in acetonitrile, in a 1:1 molar ratio at room temperature. The C_{60}⊂**4**·$(BArF)_8$ and C_{70}⊂**4**·$(BArF)_8$ host-guest adducts were studied by means of NMR, DOSY-NMR, HRMS and UV-Vis experiments and all these experiments clearly indicated the formation of 1:1 host-guest adducts. The data obtained from the UV-Vis titrations gave a value of $3.2(\pm0.6)\cdot10^7$ M^{-1} (log K_a = 7.44±0.10) for the association constant of the C_{60}⊂**4**·$(BArF)_8$ adduct, whilst the association constant was even higher for C_{70}⊂**4**·$(BArF)_8$, which prevented the calculation of the K_a by using this technique, thus fluorescence titrations were necessary. The fluorescence titrations further confirmed the association constant for C_{60}⊂**4**·$(BArF)_8$ (log K_a = 7.51 ± 0.01 M^{-1}), and log K_a = 8.6 ± 0.3 M^{-1} was obtained for C_{70}⊂**4**·$(BArF)_8$ which was roughly 10-fold higher than for C_{60}.

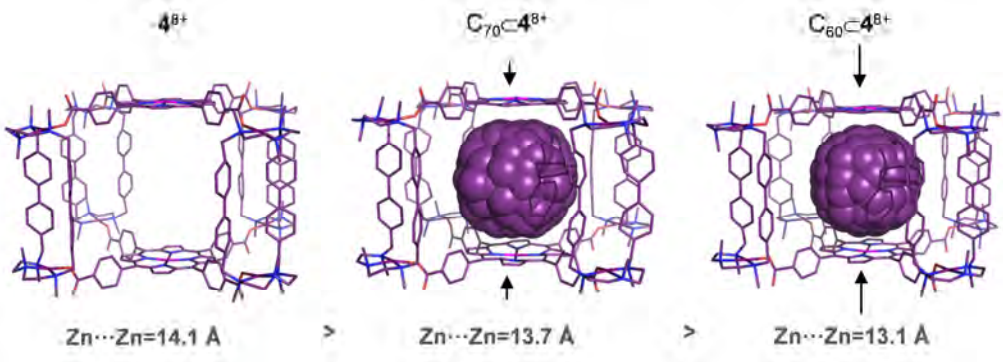

Figure VI.5. Crystallographic data for cationic capsule $\mathbf{4}^{8+}$ (left) and fullerene inclusion compounds C_{70}⊂$\mathbf{4}^{8+}$ (middle) and C_{60}⊂$\mathbf{4}^{8+}$(right). In all structures hydrogens have been omitted for clarity.

Again structural data for the cationic form of the host-guest adducts, $C_{60}\subset\mathbf{4}^{8+}$ and $C_{70}\subset\mathbf{4}^{8+}$, was obtained by synchrotron radiation. In addition to the structure of the cage, the data showed the presence of a spherical (C_{60}) or ellipsoid (C_{70}) electron density at the centre of the capsule which fitted nicely with a distorted fullerene molecule. Interestingly, comparison of the crystallographic data of the empty capsule $\mathbf{4}^{8+}$, $C_{60}\subset\mathbf{4}^{8+}$ and $C_{70}\subset\mathbf{4}^{8+}$ adducts showed that the **Porph-Zn**···**Porph-Zn** distance is maximized when the guest molecules are absent. The distance is compressed upon inclusion of C_{70} fullerene and it shrinks further after inclusion of C_{60} fullerene (Figure VI.5). This experimental trend, which was reproduced by state-of-the-art DFT calculations, indicates that the cage has the ability to adapt its structure upon guest encapsulation. The breathing ability might come from the flexible nature of the coordination bond between the carboxylate residues of the zinc(II)-porphyrins and the palladium(II) ions from the lateral molecular clips.

Considering the large void volume of the $\mathbf{4}\cdot(BArF)_8$ nanocapsule, the possibility to encapsulate the more bulky [60]PCBM ([6,6]-phenyl-C_{61}-butyric acid methyl ester) derivate and higher fullerene C_{84} was evaluated. NMR, UV-Vis and HRMS experiments indicated that 1:1 host-guest adducts were obtained with both substrates.

The relative binding affinity of nanocapsule $\mathbf{4}\cdot(BArF)_8$ towards the most abundant C_{60} and C_{70} fullerenes was further explored by means of HRMS competition experiments. In agreement with the value of the association constant obtained from the fluorescence titration, a ~9-fold higher affinity for C_{70} than for C_{60} was observed in these HRMS experiments (Annex, Supp. Info. Chapter IV, Figure S7-10). The higher affinity of the nanocapsule towards C_{70} fullerenes was explained by a higher degree of π-interactions due to their ellipsoidal shape (since they are positioned with the semi-major axis parallel to the porphyrin planes). The higher stability of the $C_{70}\subset\mathbf{4}\cdot(BArF)_8$ is also in agreement with the XRD data in which the C_{70} adduct presented a less strained conformation, closer to its form as an empty cage, while the more distorted and compressed structure of C_{60} gave a less stable adduct.

Fast inclusion was also observed when fullerene mixtures, fullerene extract (C_{60} 70%, C_{70} 28%, higher fullerenes 2%) or fullerene soot (C_{60} 53%, C_{70} 1.54%, higher fullerenes 0.14%), were used. The mixtures of fullerenes were mixed with nanocapsule $\mathbf{4}\cdot(BArF)_8$ in a toluene/CH_3CN mixture (1/1 (*v*/*v*)) at room temperature and host-guest adducts with the most abundant fullerenes, C_{60} and C_{70}, were observed, as well as inclusion compounds of higher ordered fullerenes such us C_{76}, C_{78} and C_{84} (Figure VI.6).

More interestingly, the encapsulation can be performed by only soaking a solid sample of the capsule in fullerene containing toluene. Nanocapsule $\mathbf{4}\cdot(BArF)_8$ was suspended as a solid in a solution of C_{70} in toluene and after stirring for 5-10 minutes at room temperature, full encapsulation was confirmed by HRMS (no peaks belonging to the empty cage remained). This example of solid-liquid encapsulation is similar to the one reported by Fujita in which a MOF crystal was used in the solid state to sequester fullerenes (Chapter I.3).[21] These results encouraged the investigation into the possibility of using insoluble capsule $\mathbf{4}\cdot(CF_3SO_3)_8$ to

entrap fullerenes in the solid state. When solid **4**·$(CF_3SO_3)_8$ was stirred for 5-10 min in a C_{70} solution in toluene, complete formation of C_{70}⊂**4**·$(CF_3SO_3)_8$ was obtained as ascertained by HRMS. All these results suggest that the fullerene enters $\mathbf{4}^{8+}$ through one of the four big lateral apertures of the capsule, which are large enough to allow easy mobility of the fullerenes through them.

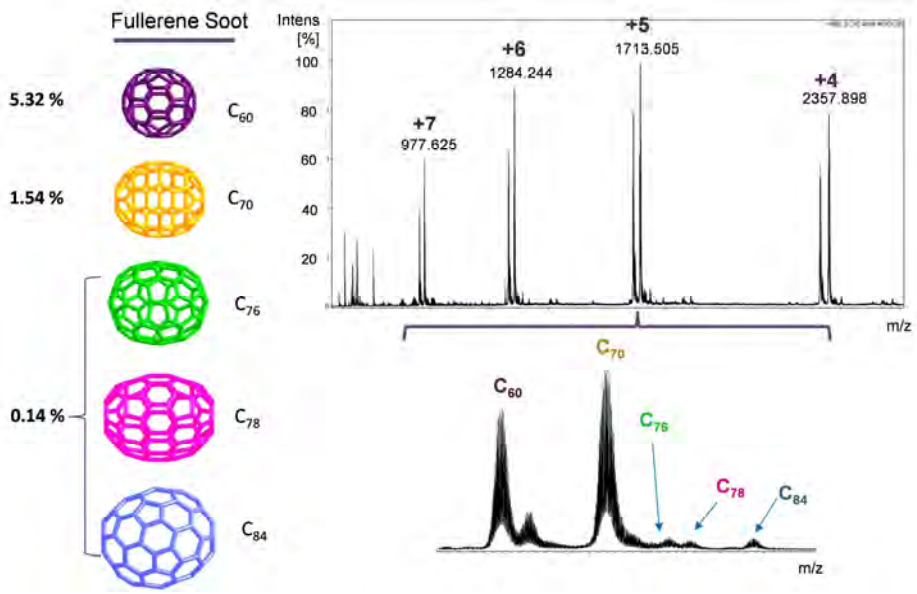

Figure VI.6. ESI-MS spectrum of fullerene soot⊂**4**·$(BArF)_8$ host-guest complex. Experimental conditions: 100 μM in Toluene/CH_3CN (4/1), recorded using a Bruker MicroTOF-Q-II exact mass spectrometer.

VI.2.3 Fullerene release

Once the encapsulation of the fullerenes had been carefully studied, a straightforward experimental protocol to liberate the sequestered fullerenes in a selective manner was attempted.

The encapsulation-liberation process was first explored for C_{60} fullerene. Taking advantage of the fact that the fullerene encapsulation can be performed in the solid state, first a solid sample of **4**·$(BArF)_8$ was charged in a small column of Celite® (Figure VI.7 a). Then a solution of C_{60} in toluene was passed through the column until full encapsulation was confirmed by HRMS (Figure VI.7 b). Afterwards, the liberation of C_{60} was achieved by consecutive washings of the solid sample of C_{60}⊂**4**·$(BArF)_8$ retained on the column, with a mixture of 1,2-dichlorobenzene/carbon disulfide (1/1 v/v mixture) (Figure VI.7 c). This solvent mixture fulfilled the requirements of both a high solubility for the fullerene and a low solubility for the **4**·$(BArF)_8$ receptor and C_{60}⊂**4**·$(BArF)_8$ adduct. Washing the solid containing the fullerene five times with the chosen solvent mixture (~1.3 mL/mg), was sufficient to liberate all of the encapsulated C_{60} as confirmed by HRMS. The solid remaining on the column was pure empty capsule **4**·$(BArF)_8$, which was ready to be filled again with C_{60}. The solid-liquid encapsulation-liberation protocol was repeated up to 5 times and finally the capsule which was retained on the column was recovered (91%) by dissolving it in acetonitrile (Figure VI.7 d and Figure VI.8 a).

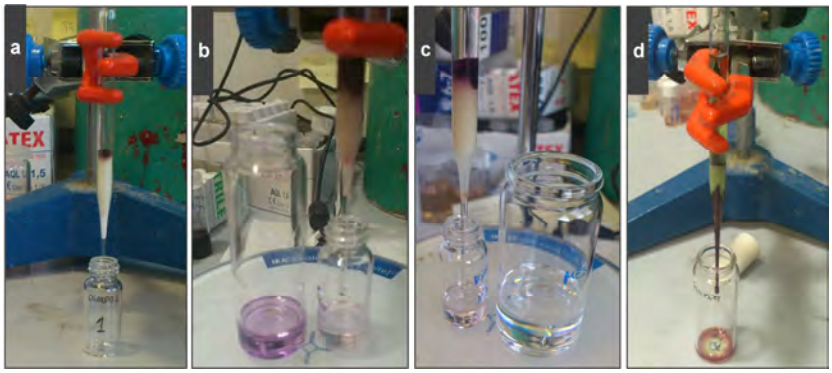

Figure VI.7. Images of the experimental protocol used for the solid-liquid encapsulation and liberation of C_{60} fullerene from solid nanocapsule **4**·$(BArF)_8$.

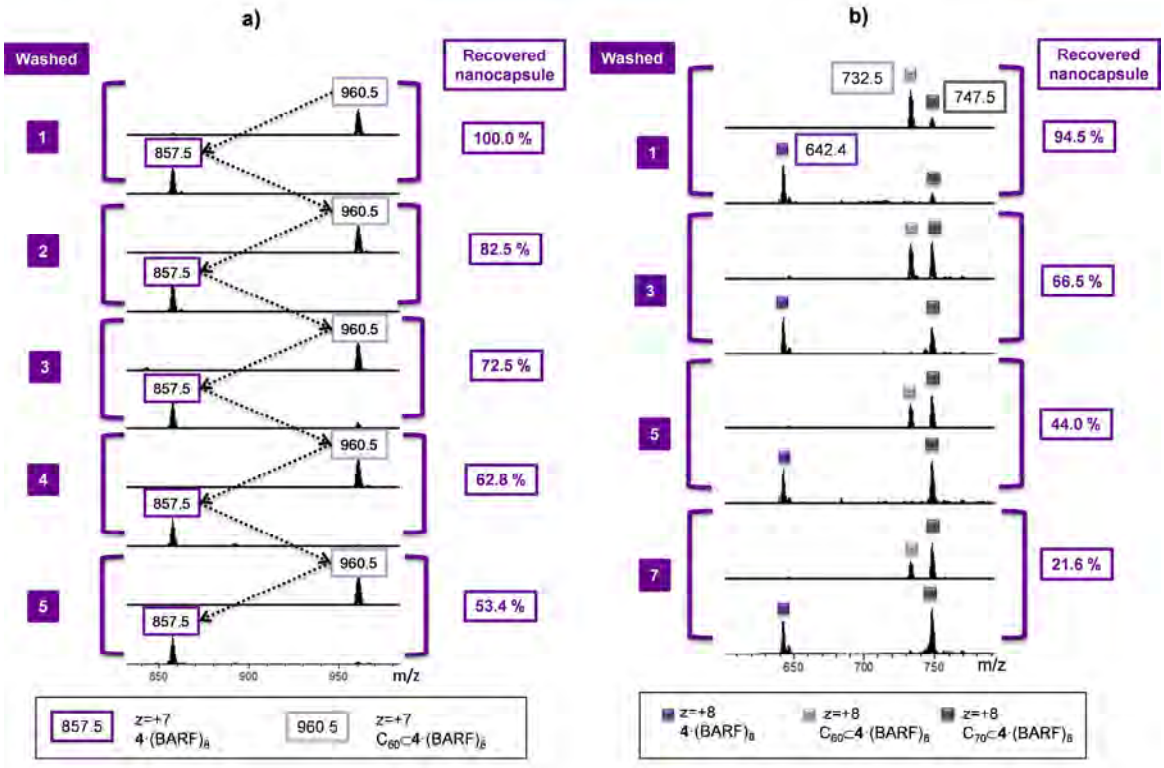

Figure VI.8. Solid state extraction of fullerenes from **4**·$(BArF)_8$. HRMS monitoring of the C_{60} extraction washing-protocol using **a)** pure C_{60} encapsulated in **4**·$(BArF)_8$ in the solid phase and **b)** fullerene extract encapsulated in **4**·$(BArF)_8$.

To summarize, in Chapter IV, palladium(II)-based molecular clips were enlarged allowing for the realization of a larger cage with an increased inner cavity. The new metallocage which contained zinc(II) porphyrins as linkers, was able to encapsulate fullerenes in a fast manner at room temperature, by simply soaking a solid sample of the cage in a solution containing fullerenes. Interestingly, the nanocapsule presented an adaptive structure (breathing ability) which allowed encapsulating fullerenes of varying size (C_{60}-C_{84}) with different affinities, without the need for modifying its structure. Effectiveness for the selective separation of C_{60} from fullerene mixtures has been demonstrated using a straightforward solid-washing protocol.

VI.3. Enantioselective hydroformylation by a Rh-catalyst entrapped in a supramolecular cage.

This section mainly corresponds to the contents of the manuscript by García-Simón et al., *JACS,* **2015**, DOI: 10.1021/ja512637k, which can be found in **Chapter V** of this thesis.

The work reported in this chapter was carried out in collaboration with the group of Prof. J.N.H. Reek of the University of Amsterdam.

VI.3.1 Encapsulation experiments

The extraordinary efficiency and selectivity displayed by enzymes is related to their 3D structure which provides the ideal active site cavity for enzymatic catalysis to take place. A profound comprehension of how the enzyme pocket affects its catalytic performance is still required and supramolecular nanocapsules bearing confined inner cavities have potential to be a powerful tool for mimicking and further understanding enzymatic catalysis (Chapter I.4).

In this chapter nanocapsule **4**·$(BArF)_8$ (Scheme VI.3) is used to encapsulate a transition metal-based catalyst in order to modulate its activity and enantioselectivity *via* effects induced by the secondary coordination sphere. It was envisioned that the confined inner cavity of **4**·$(BArF)_8$, in analogy to enzyme pockets, can impose spatial constraints which can modify and limit the substrate's trajectories and orientations, leading to different selectivity.

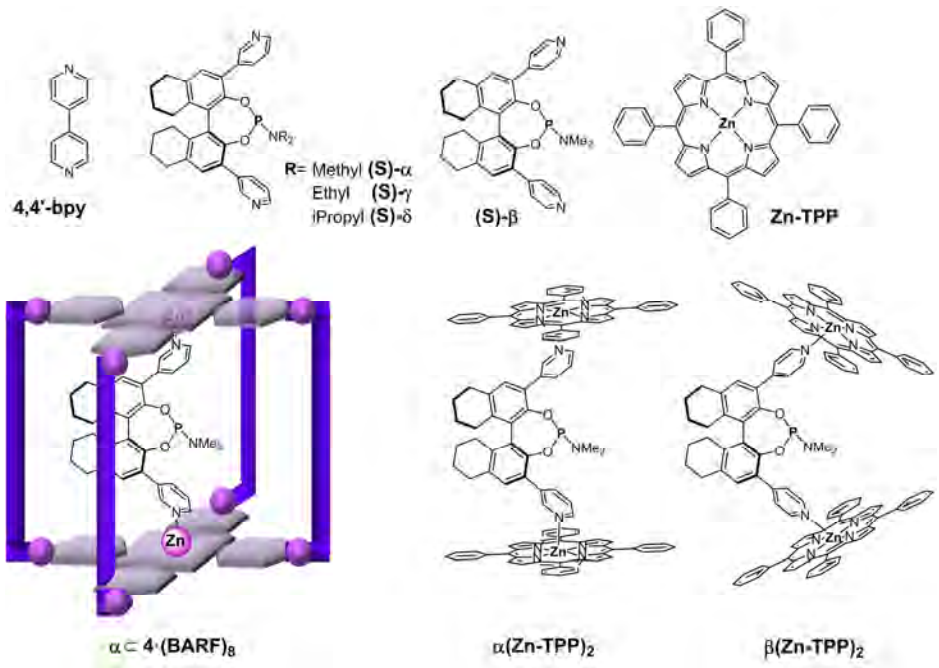

Scheme VI.4. Zn^{II}-template (**Zn-TPP**) and mono-phosphoramidite ligands (**α**, **β, γ, δ**) used in this study. Structure of host-guest **α**⊂**4**·$(BArF)_8$ cage structure and templated systems **α**(**Zn-TPP**)$_2$ and **β**(**Zn-TPP**)$_2$.

It was envisioned that tetragonal prismatic nanocapsule **4**·$(BArF)_8$ would be able to accommodate pyridine based ligands, since it is known that zinc-porphyrins can coordinate

pyridine moieties.[22–25] Moreover, the structural flexibility observed in the encapsulation of fullerenes of different sizes (Zn···Zn distance ~11-14 Å) might also allow for accommodation of ligands of different sizes.

In order to see if the larger capsule was able to encapsulate a ligand through Zn···N coordination, **4,4'-bpy** was used as substrate (Scheme VI.4). The UV-Vis titration in a toluene/CH_3CN (9/1) mixture, showed a clear interaction with a 1:1 stoichiometry and the formation of the **4,4'-bpy**⊂**4**·$(BArF)_8$ adduct was further confirmed by HRMS and NMR experiments (Annex, Supp. Info. Chapter V, Figure S1-9).

Once the possibility of accommodating a pyridine based ligand was proven, the encapsulation of the phosphoramidite ligands (S)-**α** and (S)-**β**, previously described by Reek was attempted with the aim of *in situ* preparation of the Rh catalyst for asymmetric hydroformylation (AHF) reactions. As mentioned in Chapter I.4, Reek demonstrated that the template ligand approach allowed for the realizations of highly reactive monoligated Rh species, moreover the confined environment allowed control of the regioselectivity through effects of the second coordination sphere.[26–29] In the case of chiral **β**(**Zn-TPP**)$_2$ template, its corresponding Rh species generally led to good activity, but low or moderate enantioselectivities.[30,31] In this thesis the full encapsulation of the chiral ligand within cage **4**·$(BArF)_8$ was envisioned to further transfer the chirality around its confined cavity while maintaining its efficiency.

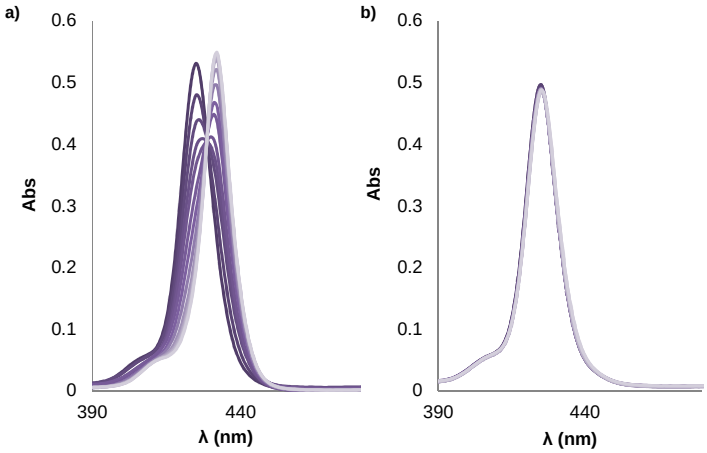

Figure VI.9. UV-Vis monitoring of the titration of **4**·$(BArF)_8$ nanocapsule with **a)** ligand **α** and **b)** ligand **β**, at a fixed total concentration ($4.32 \cdot 10^{-7}$ M) of nanocapsule **4**·$(BArF)_8$ in Toluene/CH_3CN (9/1).

It was anticipated that the pyridine-pyridine distance in **α** (~ 11.3 Å) was suitable to fit inside capsule **4**·$(BArF)_8$, whilst ligand **β** which contains pyridine groups substituted in the *para* position would not match. As expected, the changes observed during the UV-Vis titration of ligand **α** and the capsule were in agreement with the formation of a 1:1 adduct (Figure VI.9 a). UV-Vis data indicated an association constant of $3.56 \cdot 10^6$ M^{-1} for the **α**⊂**4**·$(BArF)_8$ host-guest complex. The ^{1}H-NMR experiments showed that **α** encapsulation caused a broadening of the signals belonging to the cage due to the loss of symmetry, and the aromatic protons signals belonging to the ligand were shifted upfield in agreement with pyridine-zinc(II)

coordination(Annex, Supp. Info. Chapter V, Figure S12-17).[32–34] The ^{31}P-NMR spectra revealed that the **α⊂4**·$(BArF)_8$ phosphorus signal was similar to the one corresponding to free **α**, suggesting that the phosphorous remains accessible for coordination to the metal centre (Annex, Supp. Info. Chapter V, Figure S18). On the other hand, as was also anticipated, ligand **β** was not encapsulated within **4**·$(BArF)_8$ and no changes were observed by UV-Vis titration (Figure VI.9 b).

VI.3.2 Catalyst formation

The rhodium catalyst precursor was formed *in situ* by addition of 1 equivalent of $[Rh(acac)(CO)_2]$ to a solution of **α⊂4**·$(BArF)_8$ in a mixture of deuterated toluene/CH_3CN (v/v, 2.5/1) and confirmed by ^{1}H-NMR, ^{31}P-NMR and IR experiments. ^{31}P-NMR displayed a doublet centred at δ = 147 ppm ($^1J_{P\text{-}Rh}$= 260 Hz), consistent with P···Rh coordination and indicating the formation of monoligated species (Figure VI.10). Additionally, the carbonyl vibration band (ν= 1995 cm^{-1}) belonging to [Rh(acac)CO-**α⊂4**·$(BArF)_8$] was detected by IR spectroscopy.

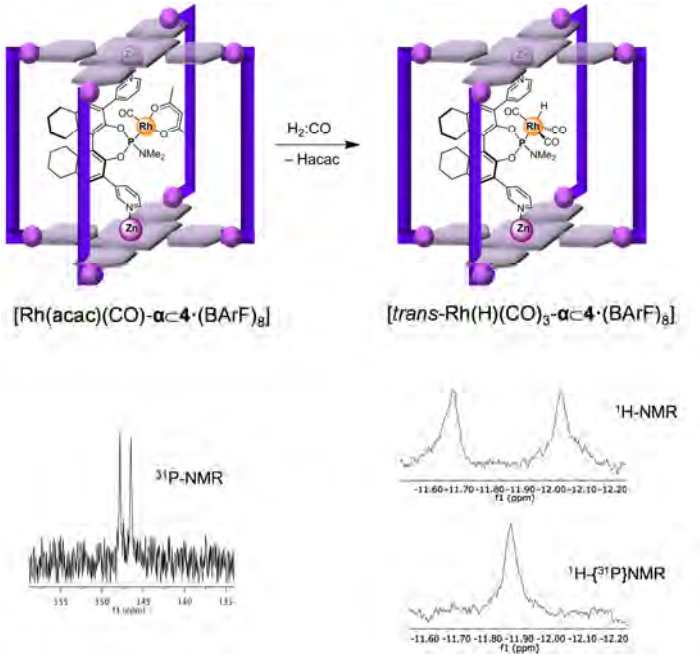

Figure VI.10. High Pressure (HP) ^{31}P and ^{1}H NMR spectra of [Rh(acac)(CO)-**α⊂4**·$(BArF)_8$] and *trans*-[$Rh(H)(CO)_3$-**α⊂4**·$(BArF)_8$].

Under 5 bar of *syngas*, the catalyst precursor was transformed into [*trans*-$Rh(H)(CO)_3$-**α⊂4**·$(BArF)_8$] species, analogous to the previously reported [*trans*-$Rh(H)(CO)_3$-**β**(**Zn-TPP**)$_2$] species (Chapter I.4.2). High pressure (HP) ^{1}H-NMR of [*trans*-$Rh(H)(CO)_3$-**α⊂4**·$(BArF)_8$] displayed a double doublet in the hydride region, centred at -11.7 ppm, suggesting that encapsulated **α⊂4**·$(BArF)_8$ was monoligated to the rhodium hydride complex. On the other hand, the large phosphorus coupling ($J_{H\text{-}P}$= 175.5 Hz, $J_{H\text{-}Rh}$ was poorly resolved) indicates that in the rhodium complex the phosphorus donor atom is located *trans* to the hydride.[25,31]

Additionally, the ^{1}H-{^{31}P}-NMR spectrum displayed a peak around -11.9 ppm ratifying the large coupling between the hydride and the phosphorous.

VI.3.3 Application of the encapsulated ligands in AHF

Catalyst performance of the *trans*-complexes based on encapsulated ligand **α**⊂**4**·$(BArF)_8$ and **β**(**Zn-TPP**)$_2$ template, as well as control experiments with free **α** ligand and the rhodium acetylacetonate were investigated for the AHF of styrene (Table VI.4). The catalyst loading was kept at $2\cdot10^{-4}$ mol %, and an excess of ligand⊂capsule was used in all experiments in order to prevent the formation of ligand-free rhodium species.

Taula VI.4. Asymmetric hydroformylation of styrene using encapsulated or ligand-templated rhodium-catalysts.[a]

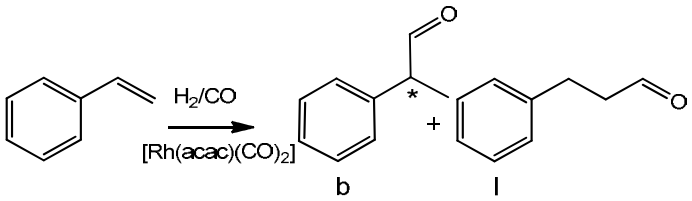

Entry	Ligand	b/l[d]	*ee* (%)[e]	TON
1	**α**⊂**4**·$(BArF)_8$	99/1	**74 (R)**	**797**
2	-	*n.d.*[f]	*n.d.*[f]	<1
3	**α**	99/1	<1	342
4	**α(Zn-TPP)$_2$**	99/1	9(R)	363
5	**4**·$(BArF)_8$	99/1	<1	300
6[b]	**α**⊂**4**·$(BArF)_8$	99/1	65 (R)	1600
7[c]	**α**⊂**4**·$(BArF)_8$	99/1	70 (R)	339
8[c]	-	*n.d.*[f]	*n.d.*[f]	<1
9[c]	**α**	99/1	8 (R)	197
10[c]	**α(Zn-TPP)$_2$**	99/1	16 (R)	215
11	**γ**⊂**4**·$(BArF)_8$	99/1	**79 (R)**	**308**
12	**γ**	99/1	7 (R)	136
13	**δ**⊂**4**·$(BArF)_8$	99/1	**77 (R)**	**104**
14	**δ**	99/1	6 (R)	41

[a] Reagents and conditions: [Rh]= 33 μM in toluene/CH_3CN (4/1), ligand⊂capsule/[Rh(acac)$(CO)_2$]=5, alkene/[Rh(acac)$(CO)_2$]=5000, rt, 20 bar, 96 h. Rh Complex: [Rh(acac)$(CO)_2$]. [b] The catalytically active species is generated under 20 bar of syngas, 16h, 40ºC. Subsequently styrene was added and the reaction was performed at room temperature, 20 bar syngas, 96h. [c] [Rh]= 33 μM in toluene/CH_3CN (2/3), room temperature, 20 bar syngas, 96 h. [d] Ratio of branched and linear aldehyde. [e] Enantiomeric ratio determined by chiral GC analysis (Supelco BETA DEX 225). [f] *n.d.*= not-detected.

Remarkably, encapsulated ligand **α**⊂4·$(BArF)_8$ gave higher activities and selectivities than free **α** (Table VI.4, entries 1 and 3). More interestingly, is the fact that the encapsulated catalyst also gave a higher turnover number (TON) than its template analogue and the selectivity was improved in the case of **α**⊂**4**·$(BArF)_8$ (up to 74 % *ee*) in comparison with **β**(**Zn-TPP**)$_2$ (9% *ee*) (Table VI.4 entries 1 and 4). To date, the encapsulated catalyst gives amongst the highest selectivities reported for a monophosphoramidite monoligated complex.[35] Afterwards, in order to fine tune the supramolecular assemblies and to improve the activity and

selectivity of **α**⊂**4**·$(BArF)_8$ based catalyst, new ligands **γ** (R=Et) and **δ** (R=*i*Pr) were synthesized and isolated within the capsule cavity to give **γ**⊂**4**·$(BArF)_8$ and **δ**⊂**4**·$(BArF)_8$ (Scheme VI.4). When encapsulated ligands **γ** or **δ** were used in the catalysis, the TON and enantioselectivity were higher than for their free analogues. However, in comparison with **α**⊂**4**·$(BArF)_8$ their enantioselectivity was slightly increased, yet the efficiency drastically decreased (Table VI.4, entries 1, 11 and 13). Therefore, **α**⊂**4**·$(BArF)_8$ based supramolecular catalyst afforded the best compromise in terms of *ee* and TON among this new family of encapsulated rhodium-catalysts for AHF.

Table VI.5. Asymmetric hydroformylation of styrene derivatives using rhodium-catalysts based on **α**⊂**4**·$(BArF)_8$ cage structure and ligand-templated system **α**(**Zn-TPP**)$_2$.[a]

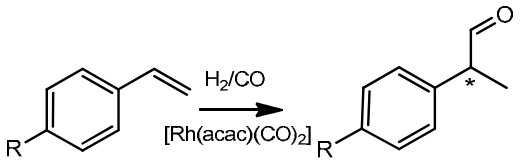

Entry	R	Ligand	b/l[b]	*ee* (%)[c]	TON
1	H	**α**⊂**4**·$(BArF)_8$	99/1	**74 (R)**	**797**
2	H	-	*n.d.*[d]	*n.d.*[d]	<1
3	H	**α**	99/1	<1	342
4	H	**α**(**Zn-TPP**)$_2$	99/1	**9(R)**	**363**
5	Cl	**α**⊂**4**·$(BArF)_8$	80/20	**58(R)**	**761**
6	Cl	-	*n.d.*[d]	*n.d.*[d]	<1
7	Cl	**α**	91/9	<1	180
8	Cl	**α**(**Zn-TPP**)$_2$	91/9	11 (R)	577
9	CH_3	**α**⊂**4**·$(BArF)_8$	91/1	**61(R)**	**1564**
10	CH_3	-	*n.d.*[d]	*n.d.*[d]	<1
11	CH_3	**α**	91/9	<1	140
12	CH_3	**α**(**Zn-TPP**)$_2$	91/9	12(R)	482
13	OCH_3	**α**⊂**4**·$(BArF)_8$	91/9	**69(R)**	**1125**
14	OCH_3	-	99/1	<1	180
15	OCH_3	**α**	99/1	<1.	168
16	OCH_3	**α**(**Zn-TPP**)$_2$	97/3	<1	340
17	^{t}Bu	**α**⊂**4**·$(BArF)_8$	99/1	**48(R)**	**1042**
18	^{t}Bu	-	99/1	<1	107
19	^{t}Bu	**α**	99/1	<1	180
20	^{t}Bu	**α**(**Zn-TPP**)$_2$	97/3	31(R)	361

[a] Reagents and conditions: [Rh]= 33 μM in toluene/CH_3CN (4/1), ligand⊂capsule/[Rh(acac)$(CO)_2$]= 5, alkene/[Rh(acac)$(CO)_2$]= 5000, room temperature, 20 bar syngas, 96 h. Rh Complex: [Rh(acac)$(CO)_2$]. [b] Ratio of branched and linear aldehyde. [c] Enantiomeric ratio determined by chiral GC analysis (Supelco BETA DEX 225). [d] *n.d.*= not-detected.

The encouraging results obtained in the AHF of styrene prompted the expansion of the substrate scope of **α**⊂**4**·$(BArF)_8$ and the catalytic performance of the encapsulated catalyst was further evaluated using different *para*-substituted styrene derivates (Table VI.5). In all cases the TON's and the enantioselectivities were higher when **α** was encapsulated, which confirmed the benefits of catalyst encapsulation. The efficiency and enantioselectivity was also improved with

respect to the template analogue. Generally, the *ee*'s are below 12% for **α**(**Zn-TPP**)$_2$ (Table VI.5 entries 4, 8, 12 and 16) and above 48% for **α**⊂**4**·(BArF)$_8$ (Table VI.5 entries 1, 5, 9 and 13). In the case of the most bulky substrate (R = ^{t}Bu), the effect of encapsulation is less significant (Table VI.5 entries 17 and 20). In comparison with styrene the *ee* was lower for all its derivates, whilst the regioselectivity depended to some extent on the substituent of the styrene. The selectivity towards the branched aldehyde was maintained when R = ^{t}Bu (Table VI.5 entry 17), whilst for R = CH_3 and OCH_3 the branched/linear ratio was 91/9 (Table VI.5 entries 9 and 13) and it was still lower (branched/linear = 80/20) for R = Cl (Table VI.5 entry 5).

Table VI.6. Asymmetric hydroformylation of *p*-, *m*- and *o*-methoxystyrene using rhodium-catalysts based on **α**⊂**4**·(BArF)$_8$ cage structure and templated system **α**(**Zn-TPP**)$_2$.[a]

Entry	Ligand	b/l[c]	*ee* (%)[d]	TON
	para-methoxystyrene			
1	**α**⊂**4**·(BArF)$_8$	91/9	**69(R)**	**1125**
2	-	99/1	<1	180
3	**α**	99/1	<1	168
4	**α**(**Zn-TPP**)$_2$	97/3	<1	340
	meta-methoxystyrene			
5	**α**⊂**4**·(BArF)$_8$	99/1	**56**	**519**
6	-	*n.d.*[d]	*n.d.*[d].	<1
7	**α**	99/1	<1	113
8	**α**(**Zn-TPP**)$_2$	99/1	<1	180
	ortho-methoxystyrene			
9	**α**⊂**4**·(BArF)$_8$	99/1	**47**	**127**
10	-	*n.d.*[d]	*n.d.*[d].	<1
11	**α**	99/1	<1	109
12	**α**(**Zn-TPP**)$_2$	99/1	<1	245

[a] Reagents and conditions: [Rh]= 0.033 mM in toluene/CH_3CN (4/1), ligand⊂capsule/[Rh(acac)(CO)$_2$]= 5, alkene/[Rh(acac)(CO)$_2$]= 5000, room temperature, 20 bar syngas, 96 h. Rh Complex: [Rh(acac)(CO)$_2$]. [b] Ratio of branched and linear aldehyde. [c] Enantiomeric ratio determined by chiral GC analysis (Supelco BETA DEX 225). [d] *n.d.*= not-detected.

α⊂**4**·(BArF)$_8$ and **α**(**Zn-TPP**)$_2$ are electronically similar, therefore the selectivity enhancement observed in the previous catalytic experiments might be induced by the steric restrictions imposed within the nanocapsule cavity. To further investigate the effect of steric effects, catalytic experiments with *ortho*-, *meta*- and *para*-substituted methoxy-styrene were performed. As can be observed in Table VI.6, in all cases the enantioselectivity is notably enhanced upon catalyst confinement. Moreover the *ee* values achieved are higher than the ones obtained with the **α**(**Zn-TPP**)$_2$ template, again supporting the important effect of catalyst confinement in the AHF reaction. For *p*-methoxystyrene, the highest TON value was reached when the encapsulated catalyst was used (Table VI.6 entries 1 and 4). Nevertheless, for *o*-methoxystyrene the TON was higher when **α**(**Zn-TPP**)$_2$ template was used as catalyst (Table VI.6 entries 9 and 12). Since *ortho*- and *para*-methoxystyrene can be considered to have electronically equivalent olefinic sites, the significant difference in TON can be attributed to steric restrictions imposed by the confined cavity of **4**·(BArF)$_8$, which may limit substrate approach to the metal catalytic centre, or product release.

Table VI.7. Asymmetric hydroformylation of styrene at different rhodium-catalyst concentrations.[a]

Entry	Cat.	[Rh] (μM)	b/l[b]	*ee* (%)[c]	TON
1	**α⊂4**·$(BArF)_8$	147	98/2	**71**	**193**
2	-		96/4	<1	128
3	**α**		98/2	3	180
4	**α(Zn-TPP)$_2$**		97/3	**15**	**183**
5	**α⊂4**·$(BArF)_8$	33	97/3	**68**	**158**
6	-		91/9	<1	39
7	**α**		97/3	3	176
8	**α(Zn-TPP)$_2$**		97/3	16	99
9	**α⊂4**·$(BArF)_8$	6	99/1	74	29
10	-		-	*n.d*[d]	0
11	**α**		99/1	<1	33
12	**α(Zn-TPP)$_2$**		99/1	<1	31
13	**α⊂4**·$(BArF)_8$	1	-	*n.d*[d]	<1
14	-		-	*n.d*[d]	<1
15	**α**		-	*n.d*[d]	<1
16	**α(Zn-TPP)$_2$**		-	+*n.d*[d]	<1

[a] Reagents and conditions: toluene/CH_3CN (4/1), ligand⊂capsule/[Rh(acac)$(CO)_2$]=5, alkene/[Rh(acac)$(CO)_2$]=200, room temperature, 20 bar syngas, 96 h. Rh Complex: [Rh(acac)$(CO)_2$]. [b] Ratio of branched and linear aldehyde. [c] Enantiomeric ratio determined by chiral GC analysis (Supelco BETA DEX 225).[d] *n.d.*= not-detected.

From UV-Vis titrations it was determined that the association constant for **α⊂4**·$(BArF)_8$ adduct ($3.56 \cdot 10^6$ M^{-1}) was much higher than for the **α**(**Zn-TPP**)$_2$ template ($1 \cdot 10^3$ M^{-1}). From these results it was envisioned that **α⊂4**·$(BArF)_8$ based catalyst could work under a wider range of concentrations than **α**(**Zn-TPP**)$_2$ based catalyst. To explore this, catalytic experiments were performed at different catalyst concentrations (from 1 μM to 147 μM). As would be expected when the catalyst loading was decreased, the efficiency dropped. However, the enantioselectivity remained high (~70%) when the encapsulated catalyst was used at concentrations ≥ 6 μM. On the contrary, the catalyst based on template **α**(**Zn-TPP**)$_2$ gave products in a racemic form when the concentration was ≤33 μM. These results, are consistent with the more robust structure of **α⊂4**·$(BArF)_8$ compared with **α**(**Zn-TPP**)$_2$.

In conclusion, in Chapter V the larger biphenyl based nanocapsule has been used to isolate a rhodium(I)-based hydroformylation catalyst with the aim of mimicking the effects produced by the confined pocket in which enzymatic reactions take place. The encapsulated catalyst exhibited higher activities and selectivities in the AHF of styrene than its free analogue, and are amongst the highest selectivities for a monoligated rhodium catalyst reported thus far. These results demonstrate the positive effect of the second coordination sphere in the catalytic performance occurring at the confined transition metal site.

VI.4. References

(1) Company, A.; Gómez, L.; López Valbuena, J. M.; Mas-Ballesté, R.; Benet-Buchholz, J.; Llobet, A.; Costas, M. *Inorg. Chem.* **2006**, *45*, 2501.

(2) Gómez, L.; Company, A.; Fontrodona, X.; Ribas, X.; Costas, M. *Chem. Commun.* **2007**, 4410.

(3) Company, A.; Roques, N.; Güell, M.; Mugnaini, V.; Gómez, L.; Imaz, I.; Datcu, A.; Solà, M.; Luis, J. M.; Veciana, J.; Ribas, X.; Costas, M. *Dalton Trans.* **2008**, *3*, 1679.

(4) Clifford, T.; Danby, A. M.; Lightfoot, P.; Richens, D. T.; Hay, R. W. *J. Chem. Soc. Dalt. Trans.* **2001**, 240.

(5) Costas, M.; Xifra, R.; Llobet, A.; Solà, M.; Robles, J.; Parella, T.; Stoeckli-Evans, H.; Neuburger, M. *Inorg. Chem.* **2003**, *42*, 4456.

(6) Yoshizawa, M.; Nakagawa, J.; Kumazawa, K.; Nagao, M.; Kawano, M.; Ozeki, T.; Fujita, M. *Angew. Chem. Int. Ed.* **2005**, *44*, 1810.

(7) Ono, K.; Yoshizawa, M.; Kato, T.; Watanabe, K.; Fujita, M. *Angew. Chem. Int. Ed.* **2007**, *46*, 1803.

(8) Simão, D.; Alves, H.; Santos, I. C.; Gama, V.; Almeida, M. *Inorg. Chem. Commun.* **2003**, *6*, 565.

(9) Bondi, A. *J. Phys. Chem.* **1964**, *68*, 441.

(10) Sarangi, R.; DeBeer George, S.; Rudd, D. J.; Szilagyi, R. K.; Ribas, X.; Rovira, C.; Almeida, M.; Hodgson, K. O.; Hedman, B.; Solomon, E. I. *J. Am. Chem. Soc.* **2007**, *129*, 2316.

(11) Ribas, X.; Mas-Torrent, M.; Rovira, C.; Veciana, J.; Dias, J. C.; Alves, H.; Lopes, E. B.; Almeida, M.; Wurst, K. *Polyhedron* **2003**, *22*, 2415.

(12) Dias, J. C.; Ribas, X.; Morgado, J.; Seiça, J.; Lopes, E. B.; Santos, I. C.; Henriques, R. T.; Almeida, M.; Wurst, K.; Foury-Leylekian, P.; Canadell, E.; Vidal-Gancedo, J.; Veciana, J.; Rovira, C. *J. Mater. Chem.* **2005**, *15*, 3187.

(13) Uruichi, M.; Yakushi, K.; Yamashita, Y.; Qin, J. *J. Mater. Chem.* **1998**, *8*, 141.

(14) Wheeler, S. E. *Acc. Chem. Res.* **2013**, *46*, 1029.

(15) Shupack, S. I.; Billig, E.; Clark, R. J. H.; Williams, R.; Gray, H. B. *J. Am. Chem. Soc.* **1964**, *86*, 4594.

(16) Wang, K.; Stiefel, E. I. *Science* **2001**, *291*, 106.

(17) Geiger, W. E.; Barrière, F.; LeSuer, R. J.; Trupia, S. *Inorg. Chem.* **2001**, *40*, 2472.

(18) Giuseppone, N.; Schmitt, J.-L.; Allouche, L.; Lehn, J.-M. *Angew. Chem. Int. Ed.* **2008**, *47*, 2235.

(19) Megyes, T.; Jude, H.; Grósz, T.; Bakó, I.; Radnai, T.; Tárkányi, G.; Pálinkás, G.; Stang, P. J. *J. Am. Chem. Soc.* **2005**, *127*, 10731.

(20) Morris, K. F.; Johnson, C. S. *J. Am. Chem. Soc.* **1992**, *114*, 3139.

(21) Inokuma, Y.; Arai, T.; Fujita, M. *Nat. Chem.* **2010**, *2*, 780.

(22) Tashiro, K.; Aida, T.; Zheng, J.-Y.; Kinbara, K.; Saigo, K.; Sakamoto, S.; Yamaguchi, K. *J. Am. Chem. Soc.* **1999**, *121*, 9477.

(23) O'Sullivan, M. C.; Sprafke, J. K.; Kondratuk, D. V; Rinfray, C.; Claridge, T. D. W.; Saywell, A.; Blunt, M. O.; O'Shea, J. N.; Beton, P. H.; Malfois, M.; Anderson, H. L. *Nature* **2011**, *469*, 72.

(24) Besset, T.; Norman, D. W.; Reek, J. N. H. *Adv. Synth. Catal.* **2013**, *355*, 348.

(25) Bellini, R.; Reek, J. N. H. *Chem. Eur. J.* **2012**, *18*, 7091.

(26) Slagt, V. F.; Reek, J. N. H.; Kamer, P. C. J.; van Leeuwen, P. W. N. M. *Angew. Chem. Int. Ed.* **2001**, *113*, 4401.

(27) Slagt, V. F.; Kamer, P. C. J.; van Leeuwen, P. W. N. M.; Reek, J. N. H. *J. Am. Chem. Soc.* **2004**, *126*, 1526.

(28) Kuil, M.; Soltner, T.; van Leeuwen, P. W. N. M.; Reek, J. N. H. *J. Am. Chem. Soc.* **2006**, *128*, 11344.

(29) Bocokić, V.; Kalkan, A.; Lutz, M.; Spek, A. L.; Gryko, D. T.; Reek, J. N. H. *Nat. Commun.* **2013**, *4*, 2670.

(30) Bellini, R.; Reek, J. N. H. *Chem. Eur. J.* **2012**, *18*, 13510.

(31) Bellini, R.; Chikkali, S. H.; Berthon-Gelloz, G.; Reek, J. N. H. *Angew. Chem. Int. Ed.* **2011**, *50*, 7342.

(32) Stulz, E.; Ng, Y.; Scott, S. M.; Sanders, J. K. M. *Chem. Commun.* **2002**, *1*, 524.

(33) Sawada, T.; Yoshizawa, M.; Sato, S.; Fujita, M. *Nat. Chem* **2009**, *1*, 53.

(34) Kim, H.; Redman, J. E.; Nakash, M.; Feeder, N.; Teat, S. J.; Sanders, J. K. M. *Inorg. Chem.* **1999**, *38*, 5178.

(35) Jouffroy, M.; Gramage-Doria, R.; Armspach, D.; Sémeril, D.; Oberhauser, W.; Matt, D.; Toupet, L. *Angew. Chem. Int. Ed.* **2014**, *53*, 3937.

Chapter VII.

General Conclusions

VII. GENERAL CONCLUSIONS

Bimetallic palladium(II)-based hexaaza-macrocyclic complexes differing in the size of the macrocycle ((**Pd-1**)$^{4+}$ and (**Pd-1b**)$^{4+}$) have been synthesized and fully characterized by NMR, HRMS, UV-Vis and XRD analysis. These diamagnetic compounds exhibit a rigid structure where each of the palladium ions has a vacant coordination site available for binding to an external molecule. The shape of the complexes is reminiscent of a molecular clip, suitable for the rational preparation of higher ordered 3D coordination supramolecular structures.

In **Chapter III**, the tetragonal prismatic nanocapsule **3**·$(CF_3SO_3)_8$ has been synthesized by reaction of molecular clip (**Pd-1**)$^{4+}$ with 5,10,15,20-*tetrakis*(4-carboxyphenyl)porphyrin–Pd(II) in a 4:2 molar ratio. In contrast to the copper(II)-based structures previously by described by Costas and Ribas, **3**·$(CF_3SO_3)_8$ could be successfully characterized by NMR as a result of its diamagnetic nature. The large inner cavity of this 3D structure led to the proposal that the nanocapsule may have potential as a receptor molecule in host-guest experiments. Selective recognition has been found for anionic, planar-shaped π-guests, ahead of non-interacting aromatic, neutral or cationic substrates. The host-guest interaction between the nanocapsule and different substrates has been investigated by means of 1D and 2D NMR, UV-Vis, ESI-MS experiments. It was further shown that different *bis*-dithiolene-type transition-metal complexes exhibited a strong interaction, although subtle changes in the structure of the substrate were critical for efficient recognition. Finally it has been demonstrated that redox and optical properties of guest molecules can be tuned upon encapsulation. These results are envisioned as a step forward towards the development of functional supramolecular nanovessels, which may offer multiple applications as chemical sensors or nanoreactors.

In **Chapter IV**, the reaction of 4 equivalents of the larger molecular clip, (**Pd-1b**)$^{4+}$, with 2 equivalents of 5,10,15,20-*tetrakis*(4-carboxyphenyl)porphyrin–Zn(II) was found to result in the formation of a bigger tetragonal prismatic nanocapsule, **4**·$(BArF)_8$. The larger nanocapsule has been demonstrated to be capable of encapsulating fullerenes in an efficient manner at room temperature. Remarkably, **4**·$(BArF)_8$ has been shown to be competent for the encapsulation of fullerenes which substantially differ in size (from C_{60} to C_{84}). Differently sized fullerenes were found to be encapsulated with different binding affinities without requiring modification of the structure of the host and therefore **4**·$(BArF)_8$ can be considered to have an adaptive structure. The fullerene adducts have been fully characterized by NMR, HRMS and UV-Vis analysis and for the C_{60} and C_{70} adducts preliminary XRD data has been obtained. Fullerene encapsulation has been achieved using a simple procedure involving the soaking of a solid sample of the nanocapsule in a toluene solution of the fullerene. Finally, a washing-based strategy that allowed separating highly pure C_{60} from a solid sample of cage charged with a mixture of fullerenes was designed. These results showcase an attractive methodology to selectively extract C_{60} from fullerene mixtures and provide a platform to design tuned capsules for the selective separation of higher fullerenes or endofullerenes.

Finally in **Chapter V**, a chiral monoligated Rh complex that has been previously proven active in the asymmetric hydroformylation (AHF) of olefins was embedded within nanocapsule **4**·$(BArF)_8$. The rhodium catalyst is based on a phosphoramidite ligand containing pyridine groups that can coordinate to the zinc(II)-porphyrin moieties of the capsule. The catalytic experiments performed have demonstrated a substantial increase of stereoselectivity upon encapsulation of the catalyst. The increased chiral induction was rationalized by modification of the secondary coordination sphere, a phenomena reminiscent of enzymatic active sites. Moreover, the encapsulated Rh-**L**⊂**4**·$(BArF)_8$ catalyst (**L**= phosphoramidite ligand) exhibited regio and stereoselectivities that are among the highest described in the asymmetric hydroformylation of styrenes with a monoligated rhodium catalyst. The robustness of the capsule has also been proven since the catalyst maintained activity even under high dilution conditions. The high affinity of zinc(II)-porphyrins for pyridine-containing ligands and the possibility to modify the apertures of the cage provide strong indications of potential future development of these cage structures in asymmetric catalysis.

Annex.

Supporting Information

Supporting Information Chapter III

SELF-ASSEMBLED TETRAGONAL PRISMATIC MOLECULAR CAGE HIGHLY SELECTIVE FOR ANIONIC π-GUESTS

Table of Contents

All the supplementary data including optimized xyz cartesian coordinates for all DFT structures can obtained from: http://onlinelibrary.wiley.com/doi/10.1002/chem.201203376/suppinfo.

*CCDC-900502 (**Pd-1**)·$(AcO)_4$), 900512 ((**Pd-1**)·$(CF_3CO_2)_4$), and 900503 (**3**·$(ClO_4)_8$) contain the supplementary crystallographic data for this paper. These data can be obtained from The Cambridge Crystallographic Data Centre: www.ccdc.cam.ac.uk/data_request/cif.*

1. Supplementary methods

1.1. Materials and methods

Reagents and solvents used were commercially available reagent quality unless indicated otherwise. Ligand **1** was synthesized following previously reported procedures.[1]

1.2. Instrumentation

NMR data concerning product identity were collected on Bruker 400 MHz AVANCE spectrometers in CD_3CN and calibrated relative to the residual protons of the solvent. ESI-MS experiments were collected and analyzed on both a Bruker Daltonics Esquire 6000 spectrometer and a Bruker MicroTOF-Q-II, using acetonitrile or DMF as the mobile phase. UV-Vis spectroscopy was performed on an Agilent 8452 UV-vis spectrophotometer with 1 cm quartz cell, equipped with a temperature control cryostat from Unisoku Scientific Instruments, Japan. Cyclic voltammetry (CV) experiments were performed in an IJ-Cambria HI-660 potentiostat using a three electrode cell. Glassy carbon disk electrodes (3mm diameter) from BAS were used as working electrode, platinium wire was used as auxiliary and SCE electrode as the reference.

1.3. Synthesis and characterization of dinuclear Pd^{II} molecular clip Pd-1

Synthesis (Pd-1). Pd-1·$(AcO)_4$: Ligand **1** (0.06 g, 0.12 mmols, ligand **1** is synthesized following publication procedures)[19], $Pd(COOCH_3)_2$ (0.054 g, 0.24 mmols) and anhydrous CH_3CN (20 mL) were mixed in a round bottom flask. The mixture is refluxed, under nitrogen atmosphere, during 18h. The solvent of the obtained solution is concentrated to a volume of 2 mL, filtered through Celite© and recrystallized under slow diethyl ether diffusion. A yellow crystalline solid corresponding to **Pd-1**·$(AcO)_4$ is obtained in good yield (88.6%).^{1}H-NMR (400 MHz, CD_3CN) δ ppm: 9.42 (s, 4H, arom), 7.38 (s, 4H, arom), 4.01 (d, J=12.5 Hz, 4H, -CH_2-), 3.73 (m, 4H, -CH_2-), 3.38 (s, 12 H, N-CH_3), 3.32 (m, 4H, -CH_2-), 3.08 (d, J=12.5 Hz, 4H, -CH_2-), 2.45 (dd, J= 4.0, 14.0 Hz, 4H, -CH2-), 2.29 (dd, J=4.0, 13.5 Hz, 4H, -CH_2-), 2.05 (s, 6H, $COOCH_3$), 1.65 (s, 6H, AcO), 1.44 (s, 6H, N-CH_3). ESI-MS (m/z): 885.2 ({1-Pd·$(COOCH_3)_3$}$^{1+}$), 412.6 ({{1-Pd·$(COOCH_3)_2$}$^{2+}$).

Pd-1·$(AcO)_2(CF_3SO_3)_2$: **Pd-1**·$(AcO)_2(CF_3SO_3)_2$ is obtained from **Pd-1**·$(AcO)_4$. **Pd-1**·$(AcO)_4$ (0.1 g, 0.11 mmols) was dissolved in CH_3CN (30 mL). An excess of $NaCF_3SO_3$ salt was added (1 to 4.2 equivalents) and the mixture was stirred vigorously during 4 h. The reaction mixture was concentrated to a volume of 2 mL under reduced pressure, filtered through Celite© and recrystallized under slow diethyl ether diffusion. Yellow crystalline solid is obtained. (Yield: 90.5 %).^{1}H-NMR (400 MHz, CD_3CN) δ ppm: 9.42 (s, 4H, arom), 7.38 (s, 4H, arom), 4.00 (d, J=12.5 Hz, 4H, -CH_2-), 3.62 (m, 4H, -CH_2-), 3.36 (s, 12 H, N-CH_3), 3.35 (m, 4H, -CH_2-), 3.09 (d, J=12.5 Hz, 4H, -CH_2-), 2.45 (dd, J=4.0, 14.0 Hz, 4H, -CH_2-), 2.30 (dd, J=4.0, 13.5 Hz, 4H, -CH_2-), 2.05

(s, 6H, AcO), 1.44 (s, 6H, N-CH_3). ESI-MS (m/z): 975.2 ({**1**·$(COOCH_3)_2(CF_3SO_3)$}$^{1+}$), 412.0 ({**1**·$(COOCH_3)_2$}$^{2+}$).

1.4. Synthesis and characterization of the tetragonal prismatic cage 3·$(CF_3SO_3)_8$.

5,10,15,20-Tetrakis(4-carboxyphenyl)porphyrin-Pd^{II} (**2**, 7.96 mg, 0.01 mmols) was weighed in a 10 ml flask, then DMF (1 mL) was added. 5 µl of triethylenetriamine dissolved in 0.5 mL of DMF was added to the porphyrin solution. Finally **Pd-1**·$(AcO)_2(CF_3SO_3)_2$ (20 mg, 0.02 mmols) complex dissolved in DMF (2.5 mL) were added to the mixture. The solution obtained is heated to 105ºC under reflux, during 16 h. After the reaction time, the mixture is cooled to room temperature, filtered through Celite© and recrystallized by diethyl ether diffusion. (Yield: 93.2%).^{1}H-NMR (400 MHz, CD_3CN) δ ppm: 9.49 (s, 16 H, arom-clip), 8.74 (dd, J=1.6, 8.0 Hz, 8H, arom-porph), 8.36 (s, 16H, pyrrole ring), 8.24 (dd, J=1.6, 8.0 Hz, arom-porph), 8.14 (dd, J=1.6, 8.0 Hz, arom-porph),7.62 (s, 16 H, arom-clip), 4.08 (d, J=13.0 Hz, 16 H, -CH_2-), 3.76 (m, 16H, -CH_2-), 3.63 (s, 48 H, N-CH_3), 3.53 (m, 16 H, -CH_2-), 3.22 (d, J=13.0 Hz, 16 H, -CH_2-), 2.61 (d, J=13.5 Hz, 16 H, -CH_2-), 2.46 (d, J=13.5 Hz, 16 H, -CH_2-), 1.73 (s, 24 H, N-CH_3). ESI-MS (m/z): 2750.8 ({**3**·$(CF_3SO_3)_6$}$^{2+}$), 1785.9 ({**3**·$(CF_3SO_3)_5$}$^{3+}$), 1301.9 ({**3**·$(CF_3SO_3)_4$}$^{4+}$), 1011.9 ({**3**·$(CF_3SO_3)_3$}$^{5+}$), 818.4 ({**3**·$(CF_3SO_3)_2$}$^{6+}$), 680.2 ({**3**·(CF_3SO_3)}$^{7+}$), 576.6 ({**3**}$^{8+}$).

1.5. General procedure for UV-Vis titrations

Host-guest interactions in solution were studied by UV-Vis spectroscopy. The stoichiometry of the complexes was studied using the methos of Continuous Variations. Solutions of nanocapsule **3**·$(CF_3SO_3)_8$ ($3.75\cdot10^{-6}$ M) and of the different substrates tested ($1\cdot10^{-4}$ M) were prepared using CH_3CN as solvent. A magnetic stirr and 2 ml of nanocapsule solution were added to the cuvette, then it was inserted into the spectrometer and the stirrer activated. The titration (all the experiments were carried out at 22 ºC) to determine the host:guest complex stoichiometry was initiated by adding different ratios of guest solution, in order to add an increasing number of substrate equivalents. In case of the exchange experiments, first 1 equivalent of **II**-**X** substrate was added to the nanocapsule solution on the cuvette, and then some equivalents of substrate **I** were added in order to observe if it could displace the encapsulated one. The reaction progress was monitored by measuring the change in absorbance at 408 nm (Soret band) of **3**·$(CF_3SO_3)_8$. In case of subtrates **VIII**, **IX** and **X,** low energy LMCT bands were also monitored.

1.6. General procedure for electrochemical experiments.

Using a standard three-electrode configuration with one-compartment cell, CV spectra were recorded using glassy carbon working electrode treated by means of a sequence of polishing with MicroPolish Powder (0.05 micron) interspersed by washings with purified water. A saturated calomel electrode (SCE) was used as the reference one, and a Pt wire as auxiliary electrode. All glassware for electrochemistry was dried at room temperature before use. All cyclic voltamperometries were conducted at room temperature, 22 ºC, under nitrogen

atmosphere, using anhydrous acetonitrile as solvent, acetylferrocene as internal reference and 0.1 M Bu_4NPF_6 as supporting electrolyte. We focused our studies on the $[Ni(mnt)_2]^-/[Ni(mnt)_2]^{2-}$ couple, thus measured at the -0.2 to 1 V range. To a 0.25 mM solution of **3**·CF_3SO_3 we added different equivalents of **XIII**, **IX** or **X** subtrates, using a 3.4 mM solution that contained 1:1 equimolar fraction of substrate and acetylferrocene. Diffusion coefficients of host:guest **VIII@3**, **IX@3** and **X@3** compounds were measured by means of the Randles-Sevick equation.

1.7. Diffusion-Ordered NMR spectroscopy experiments

Diffusion-Ordered NMR experiments (DOSY NMR) of Pd·**1**, **3**·$(CF_3SO_3)_8$ and **I@3**·$(CF_3SO_3)_7$ allow the determination of the translational self-diffusion coefficients (*D*) for these species in acetonitrile solution. Making use of the Stokes-Einstein equation (SEq.1), the hydrodynamic radii (r_h) for the diffused species can be calculated from the *D* value (see obtained values on Table 5, main text).

$$D = \frac{k \cdot T}{6 \cdot \pi \cdot \eta \cdot r_H} \qquad \text{(SEq.1)}$$

where k is the Boltzmann constant, T is the temperature, and η is the viscosity of the solvent (η (CH_3CN) = 0.35 mPa s).[2]

1.8. Computational calculations

All calculations have been performed using the Amsterdam Density Functional program (ADF, version 2010.01)[3,4] and the QUILD program.[5] The BLYP functional[6,7] was used including dispersion corrections[8] with double-ζ (DZ) and triple-ζ (TZP) basis sets. Solvent effects were included through the use of COSMO.[9,10,11] The dispersion effects were computed using the approach of Grimme and coworkers.[12]

1.8.1. DFT cartesian coordinates

In the file SI_xyz.doc we present the optimized Cartesian coordinates of the following compounds: $Au(tdas)_2^-$ (**I**), $Au(pdt)_2^-$ (**III**), $Au(mnt)_2^-$(**V**), **Pd-1**·$(AcO)_4$, **3**·$(Cl)_8$, **I@3**·$(Cl)_7$ calculated at BLYP-D3/DZ(COSMO:MeCN) level of theory. Also included are the simplified model structures using two Pd-based porphyrins sandwiching either **I** or a triflate anion, i.e. Pd-Por{**I**}Pd-Por and Pd-Por{triflate$^-$}Pd-Por.

1.8.2. Aromaticity evaluation

The aromatic indexes are the most reliable method to evaluate the aromaticity of different molecules. Different types of aromaticity indexes exist to describe the local aromaticity of molecules: magnetic, geometric, and electronic.[13,14] Due to the presence of the Au in small four or five atoms rings the magnetic indexes are discarded. Electronic indexes, based on the electronic density of the complexes, are computationally very expensive and out of our range

because of the heavy Au atom.[15] And finally, the most common geometric aromaticity index, the harmonic oscillator model of aromaticity (HOMA), cannot be used here because it has not been parameterized for the treatment of Au-S nor S-N bonds. Nevertheless, we have compared the local aromaticity of $Au(tdas)_2^-$ (**I**), $Au(pdt)_2^-$ (**III**), $Au(mnt)_2^-$(**V**), by analyzing the optimized bond lengths of the DFT geometries obtained at BLYP-D3/DZ-(COSMO:MeCN) level of theory (See Figure S39). This comparison is enough for a qualitative ordering of the molecules as function of their aromaticity.

We first focus on the 5-membered rings with a Au atom. Au–S and S–C bond lengths are very similar for the three molecules (differences smaller than 0.14 Å). The only important difference is found for the C–C bond lengths, which is shorter for the $Au(mnt)_2^-$ (**V**), molecule. A shorter C–C bond length indicates a double bond character that implies a higher electron localization of the π system on this bond, reducing the delocalization, and that is, the aromaticity of the ring. Thus, only taking into account the 5-membered rings where Au is present, one can conclude that $Au(tdas)_2^-$(**I**), $Au(pdt)_2^-$ (**III**) are more aromatic than $Au(mnt)_2^-$ (**IV**),. Furthermore, $Au(tdas)_2^-$ (**I**), and $Au(pdt)_2^-$ (**III**) molecules have two extra external rings that could increase the aromaticity of these molecules (6-membered rings for the $Au(tdas)_2^-$ (**I**), and a 5-membered ring for the $Au(pdt)_2^-$). It is known that the aromatic optimal bond length for the C-C, C-N and C-S are 1.388, 1.334 and 1.677 Å,[16] respectively. Although an S-N aromatic optimal bond length is not parameterized, there exists several examples of molecules that exhibit large local aromaticity and include S-N bonds of 1.669 Å.[17] Then, by comparing the bond lengths of $Au(pdt)_2^-$(**III**) with aromatic (optimal) references, one can see that differences are quite small (differences smaller than 0.03 Å), which means that $Au(pdt)_2^-$ (**III**) molecule 6-membered rings exhibit large aromaticity. On the other hand, although $Au(tdas)_2^-$ (**I**) C-C and C-N bonds have reasonable lengths in order to present good electron delocalization, the S-N bonds are too large in comparison to the aromatic optimal S-N bond length. The bond distance of $Au(tdas)_2$ (**I**) S-N bonds correspond to single bond character that does not allow for a correct electron delocalization on the ring, making them non-aromatic. Thus, we can conclude that the most aromatic molecule of the three Au complexes is clearly $Au(pdt)_2^-$ (**III**).

1.8.3. Computational model for Host-Guest systems.

We propose a theoretical model system for the π-stacked system of the host-guest structure. The model consists in considering only the two metallo-porphyrins with the guest molecule between them. We have computed the equilibrium geometries of this computational model using as a guest the $Au(tdas)_2^-$ (**I**) and the triflate at the BLYP-D3/DZ-(COSMO:MeCN) level of theory (see Figures S41 and S42). For the $Au(tdas)_2^-$ (**I**) case, the distance between the Pd-Au atoms is 3.28 Å, while for the DFT equilibrium geometry of the entire host-guest complex it is 3.19 Å. This small difference in Pd-Au distances indicates that the size of the **3** cage is optimal for a maximum interaction between $Au(tdas)_2^-$ (**I**) and the two porphyrins. Thus, the **3** cage has the perfect size to host $Au(tdas)_2^-$(**I**).

We have also studied the inclusion of a $CF_3SO_3^-$ triflate anion inside the **3** cage. A single point calculation of triflate@**3** host-guest system indicates a strongly endothermic interaction (ΔE=+61.3 kcal/mol). We tried to optimize the geometry of triflate@**3**, but the repulsion between the host and the guest was so large than the optimization was not possible due to problematic SCF convergence. Therefore, we investigated the triflate interaction with the cage using our model system. As it can be seen in Figure S42, the triflate anion induces a very large distortion of the (parallel) positions of the porphyrins, whose relative orientation does not match at all with their relative position in cage **3**. Thus, both the single point triflate@**3** calculation and the triflate@model optimization clearly show that the shape and size of the **3** cage does not allow the inclusion of a triflate molecule inside.

1.9. X-ray Diffraction studies

X-ray single-crystal diffraction data for **3**·$(ClO_4)_8$ were collected on the BM16 Spanish line of ESRF synchrotron in Grenoble. These measurements was performed on a single-crystal of **3**·$(ClO_4)_8$ sealed into a capillary due to its high instability (spontaneous loss of crystallinity) in air. The H atoms have been included in theoretical positions but not refined. The low max value is due to the data collections that have been performed in the BM16 line with only a phi scan. The structure was solved by direct methods using the program SHELXS-97. Due to the high beam sensitivity, and consequently the poor diffraction data, some atoms (O5 and O59) of perchlorate anions positions have been fixed. The high R2 value is due to the very poor diffraction data. The refinement and all further calculations were carried out using SHELXL-97.[18] Empirical absorption corrections were applied in both cases with SCALEPACK.[19]

Additionally, crystals of complexes **Pd-1**·$(AcO)_4$ and **Pd-1**·$(CF_3CO_2)_4$ were grown from slow diffusion of ethyl ether in a CH_3CN solution of the compound and crystals of complexes $\mathbf{1_{Cl}}$ and $\mathbf{1_{Br}}$ were grown from slow diffusion of ethyl ether in a DMF solution of the compound. Both were used for low temperature (180(2) K) X-ray structure determination. The measurement was carried out on a *BRUKER SMART APEX CCD* diffractometer using graphite-monochromated Mo $K\alpha$ radiation (λ = 0.71073 Å) from an x-Ray Tube. Crystal data is found in Tables S6. Programs used: data collection, Smart version 5.631 (Bruker AXS 1997-02); data reduction, Saint + version 6.36A (Bruker AXS 2001); absorption correction, SADABS version 2.10 (Bruker AXS 2001). Structure solution and refinement was done using SHELXTL Version 6.14 (Bruker AXS 2000-2003). The structure was solved by direct methods and refined by full-matrix least-squares methods on F^2. The non-hydrogen atoms were refined anisotropically.

Crystal data for **Pd-1**·$(AcO)_4$, **Pd-1**·$(CF_3CO_2)_4$ and **3**·$(ClO_4)_8$ were deposited as CCDC references 900502, 900512 and 900503, respectively, which contain the supplementary crystallographic data for each compound. These data can be obtained free of charge from CCDC via www.ccdc.cam.ac.uk/data_request/cif.

2. Supplementary Figures

Figure S1. NMR spectrum of **Pd-1** molecular clip: a) ^{1}H-NMR(CD_3CN, 298 K, 400 MHz), b) COSY-NMR (CD_3CN, 298 K, 400 MHz), c) NOESY-NMR (CD_3CN, 298 K, 400 MHz), d) ^{13}C-NMR (CD_3CN, 298 K, 100 MHz) and e) HSCQed (CD_3CN, 298 K, 400 MHz).

a)

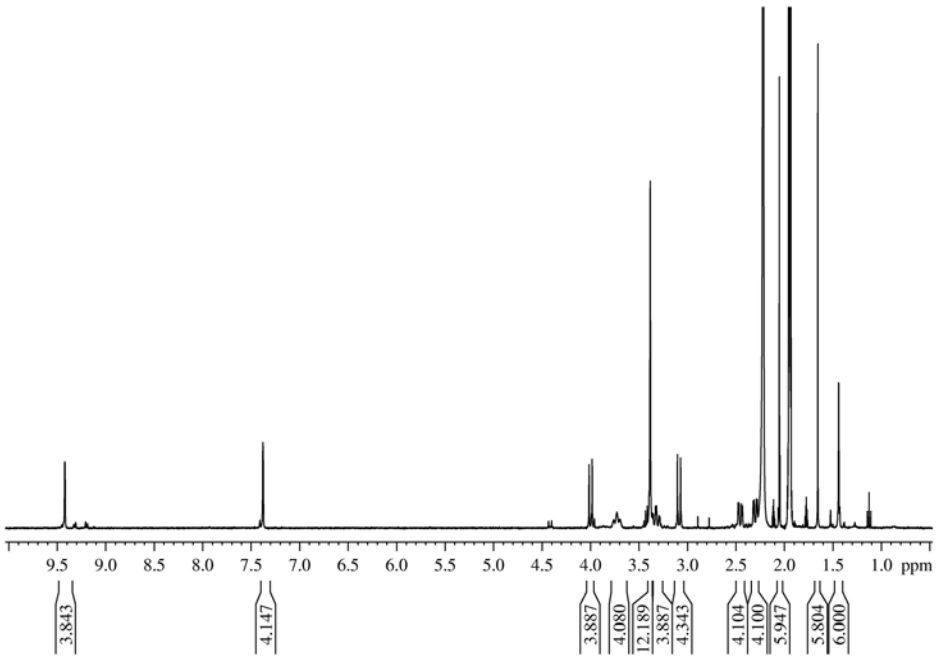

b)

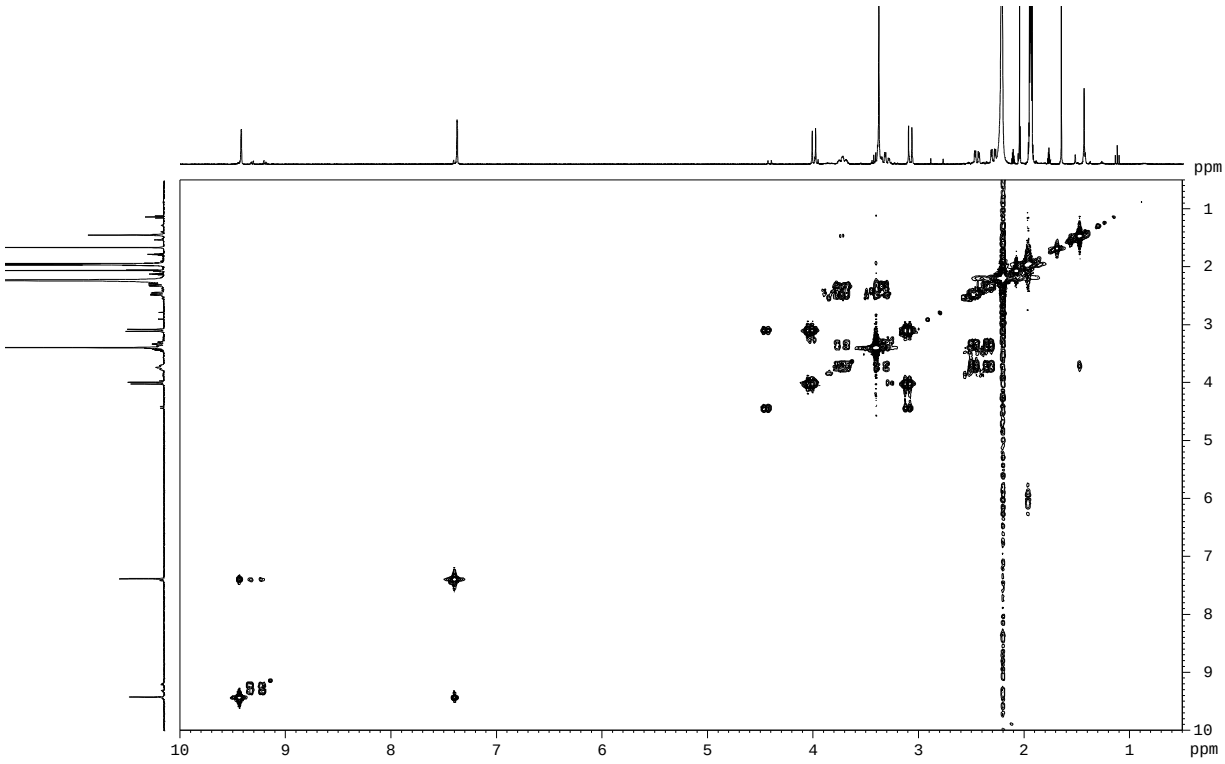
ppm
1
2
3
4
5
6
7
8
9
10
10
9
8
7
6
5
4
3
2
1
ppm

c)

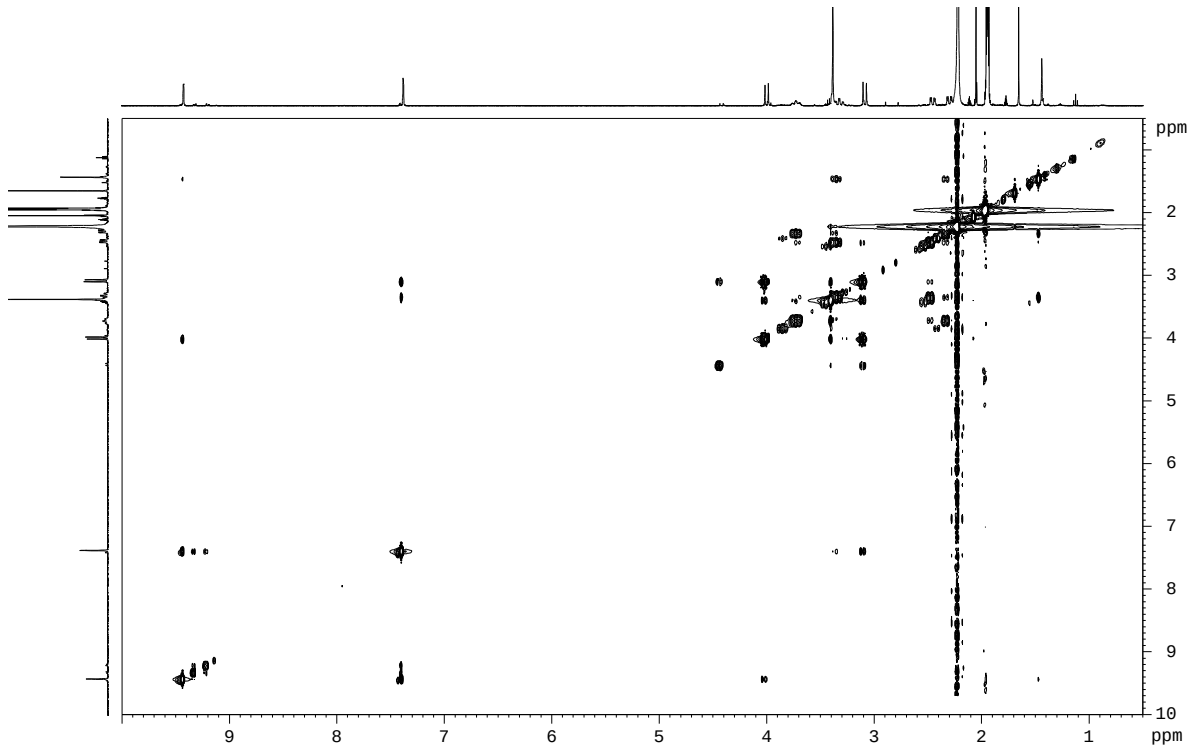
ppm
2
3
4
5
6
7
8
9
10
9
8
7
6
5
4
3
2
1
ppm

d)

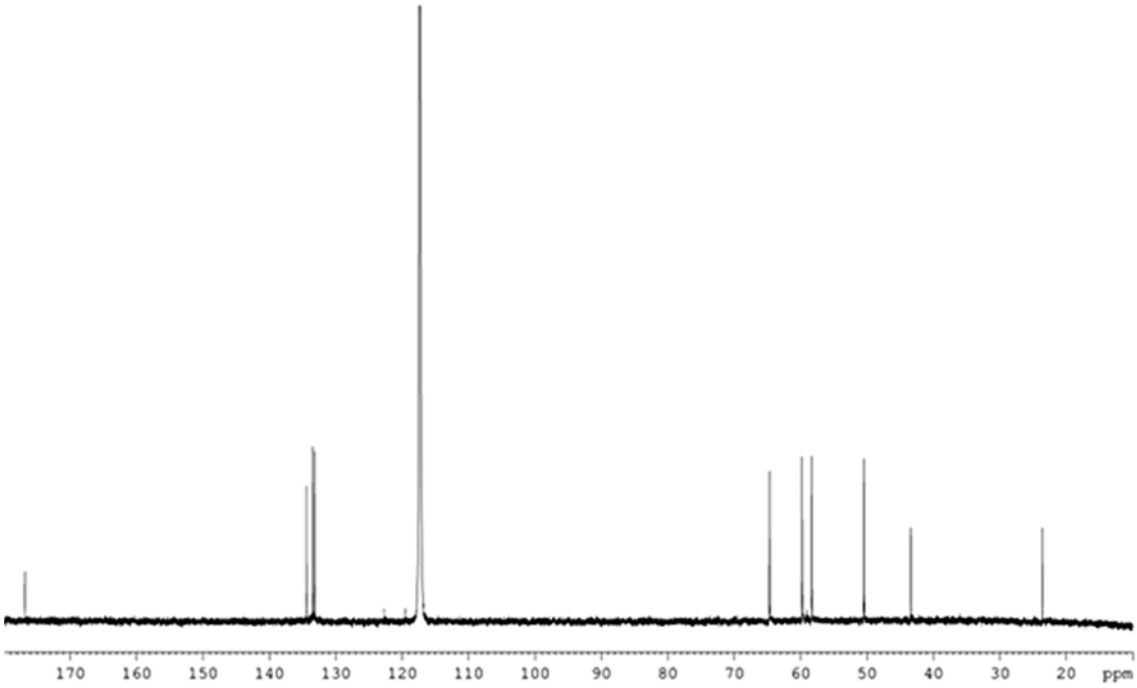
170 160 150 140 130 120 110 100 90 80 70 60 50 40 30 20 ppm

e)

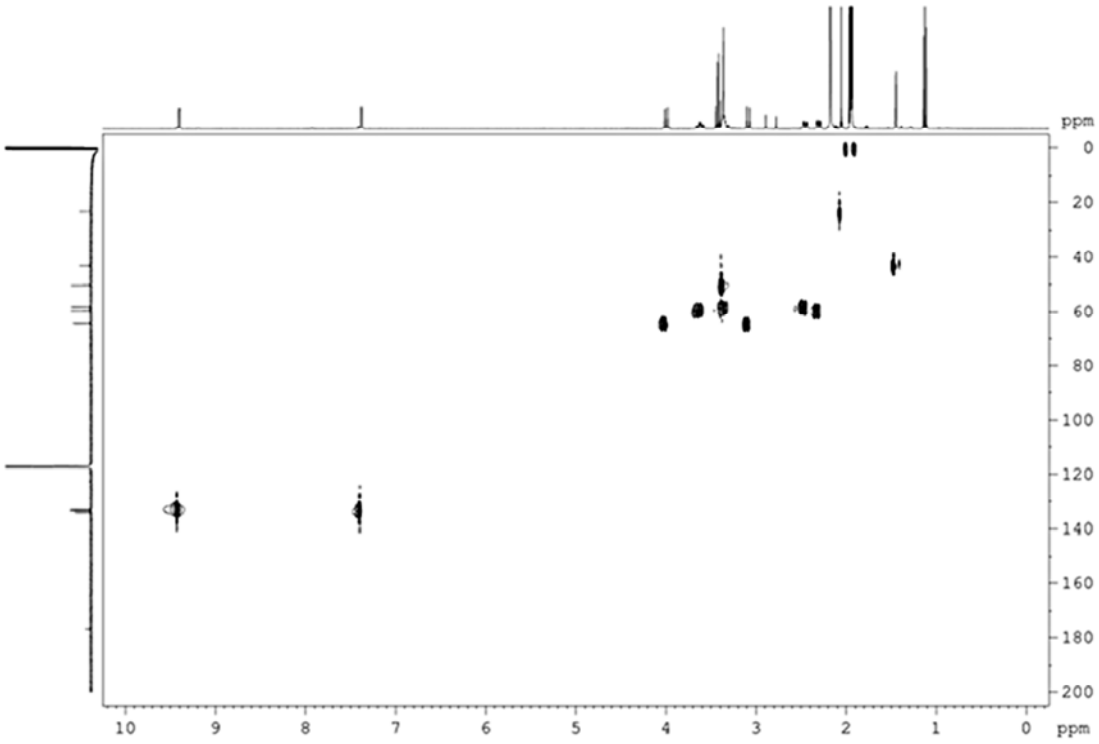
ppm
0
20
40
60
80
100
120
140
160
180
200
10 9 8 7 6 5 4 3 2 1 0 ppm

Figure S2. ESI-MS spectra of complex **Pd-1**·$(AcO)_4$. Simulated spectra of each peak are showed in red. Experimental conditions: 100 μM in CH_3CN.

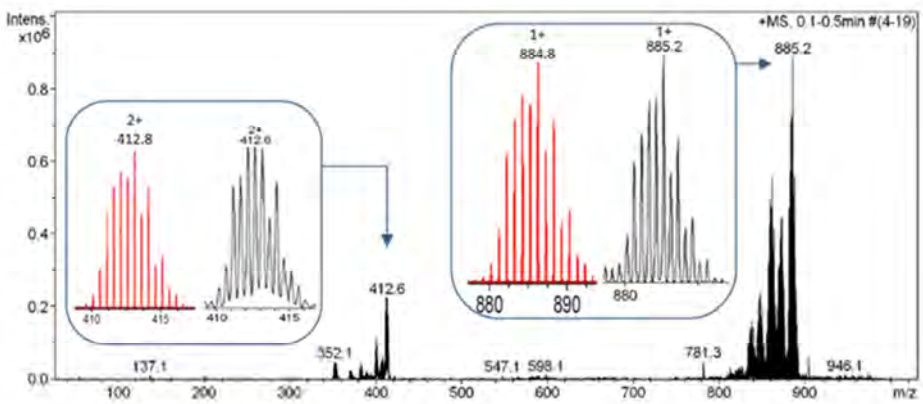

Figure S3. NMR spectrum of **3**·$(CF_3SO_3)_8$: a) ^{1}H-NMR(CD_3CN, 298 K, 400 MHz), b) COSY-NMR (CD_3CN, 298 K, 400 MHz) and c) NOESY-NMR (CD_3CN, 298 K, 400 MHz).

a)

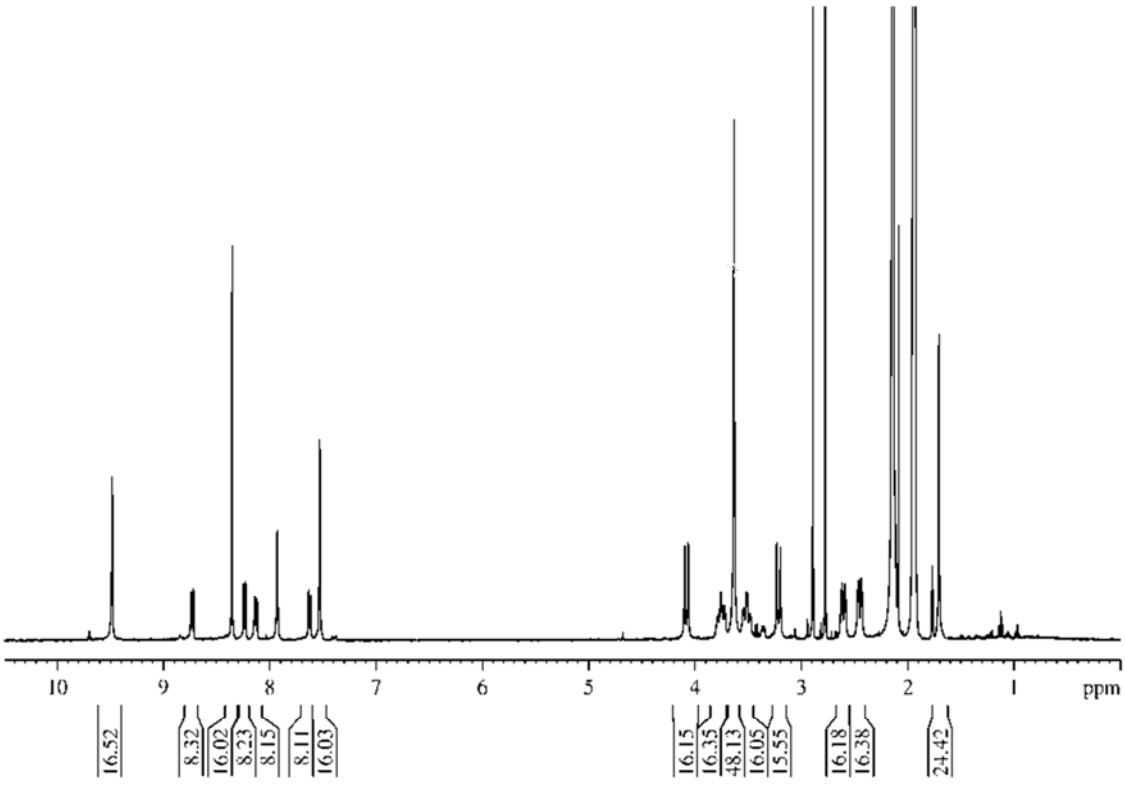

b)

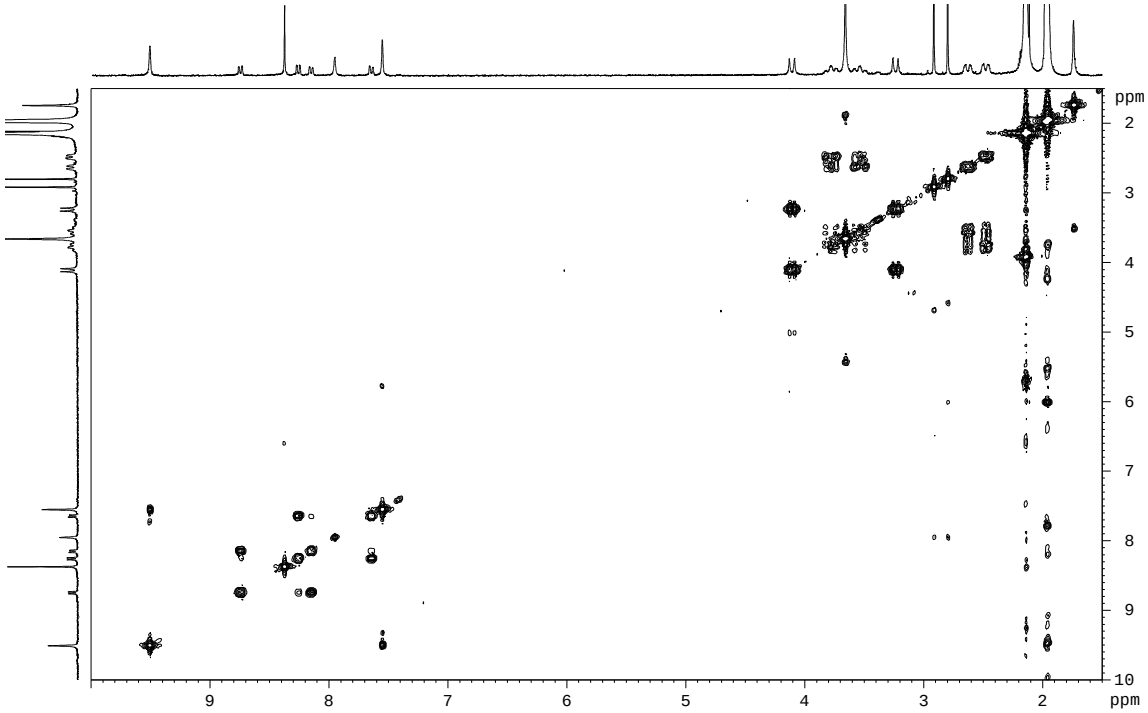
ppm
2
3
4
5
6
7
8
9
10
9
8
7
6
5
4
3
2
ppm

c)

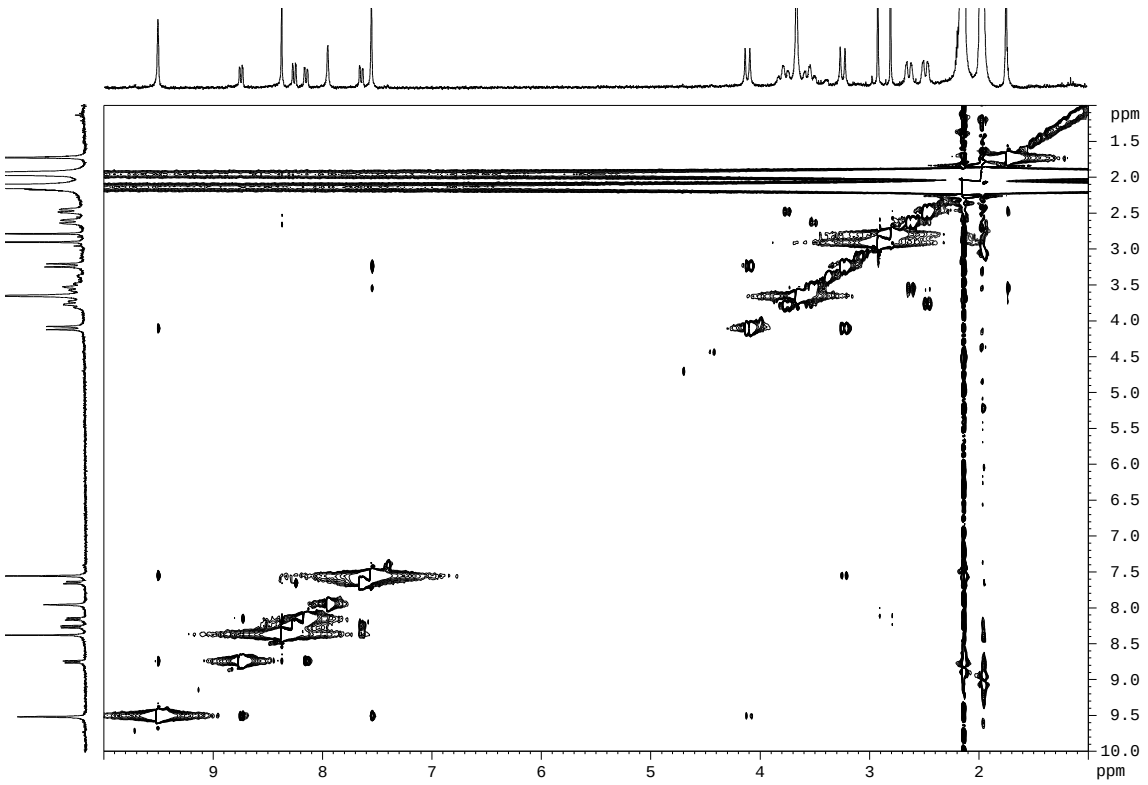
ppm
1.5
2.0
2.5
3.0
3.5
4.0
4.5
5.0
5.5
6.0
6.5
7.0
7.5
8.0
8.5
9.0
9.5
10.0
9
8
7
6
5
4
3
2
ppm

Figure S4. ESI-MS spectra of **3**·$(CF_3SO_3)_8$ nanocapsule. Simulated spectra of selected peaks are showed in red. Experimental conditions: 100 μM in CH_3CN, registered with a Bruker MicroTOF-Q-II exact mass spectrometer.

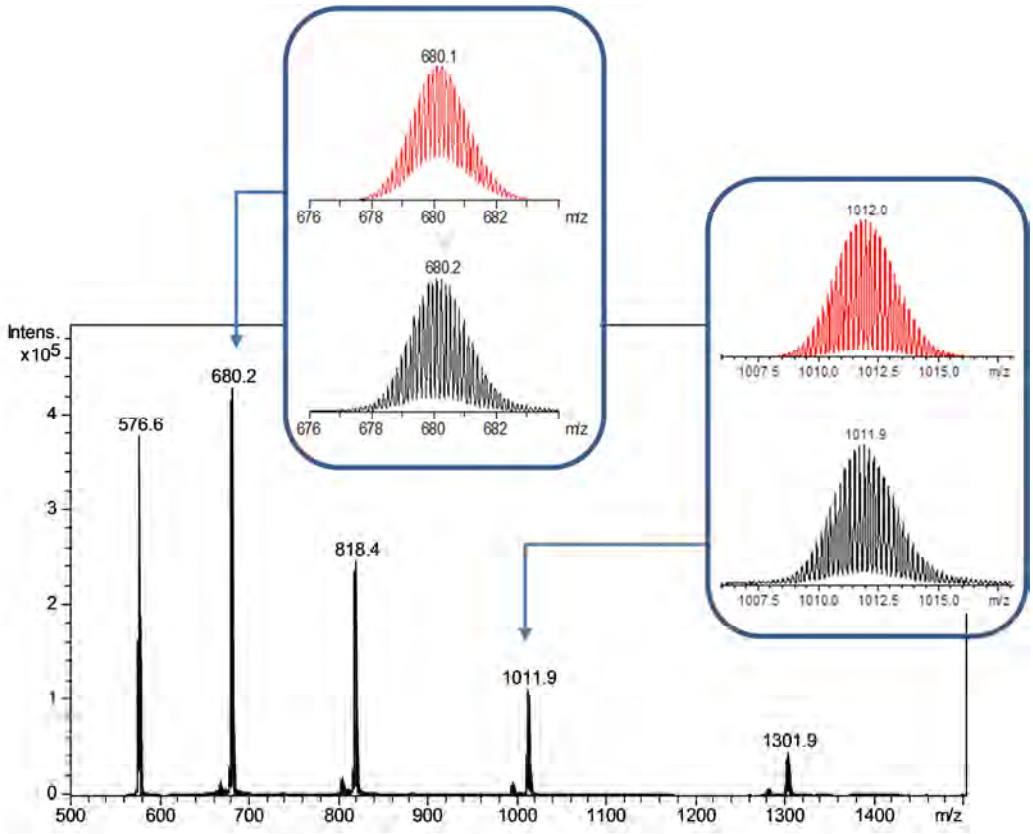

Figure S5. UV-Vis spectrum of a $3.75 \cdot 10^{-6}$ M solution of **3**·$(CF_3SO_3)_8$ nanocapsule in CH_3CN.

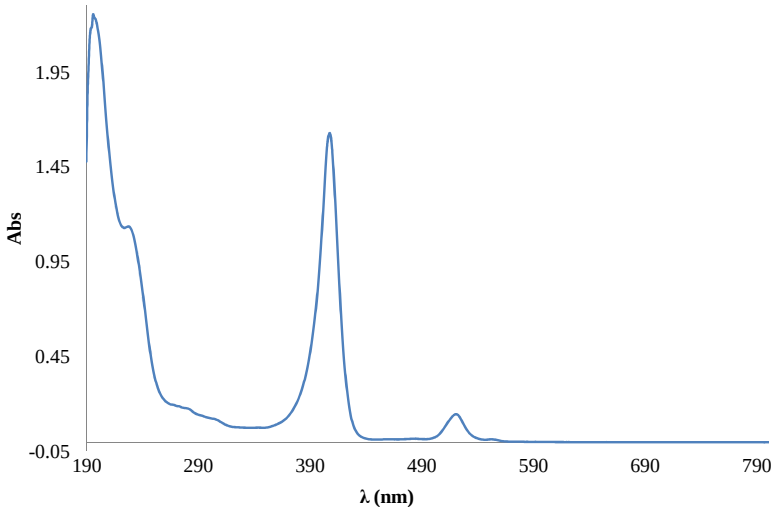

Figure S6. In blue ^{1}H-NMR spectrum of free nanocage **3**·$(CF_3SO_3)_8$ (top). In black ^{1}H-NMR spectrum of host-guest complex **I**@**3**·$(CF_3SO_3)_7$ (bottom) (CD_3CN, 295 K, 400 MHz).

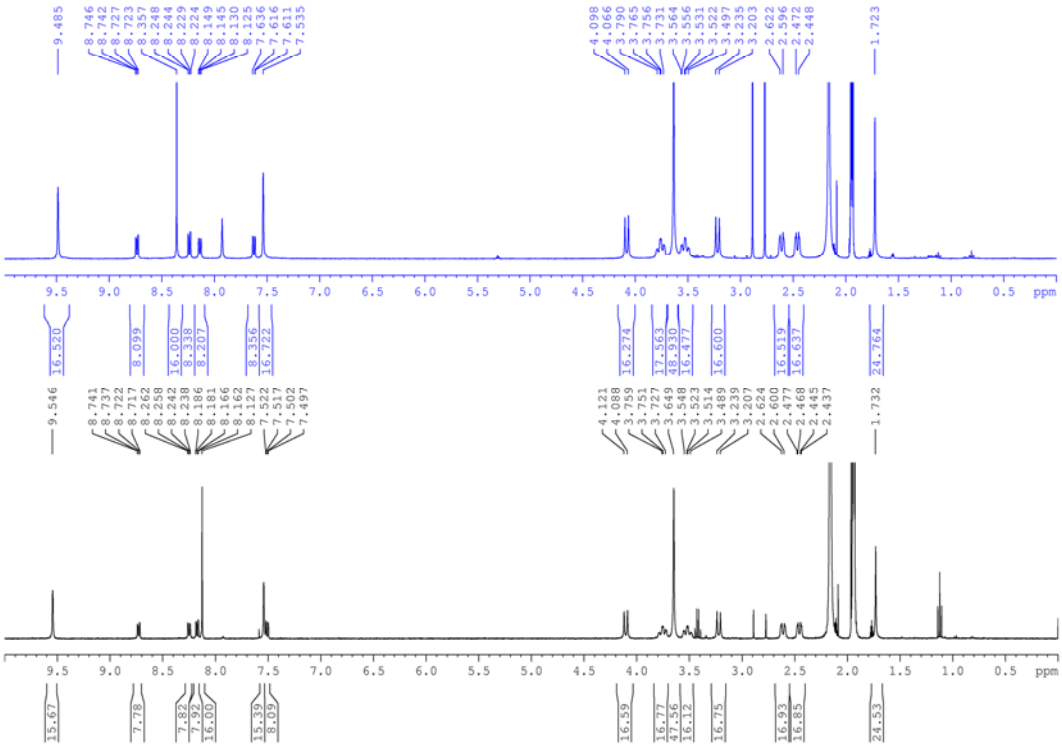

Figure S7. UV-vis monitoring of the titration of **3**·$(CF_3SO_3)_8$ nanocapsule with TBA[Au(tdas)$_2$]. Additions up to 20 eq. of TBA[Au(tdas)$_2$] (**I**) to a 3.75·10^{-6} mM solution of **3**·$(CF_3SO_3)_8$ in CH_3CN.

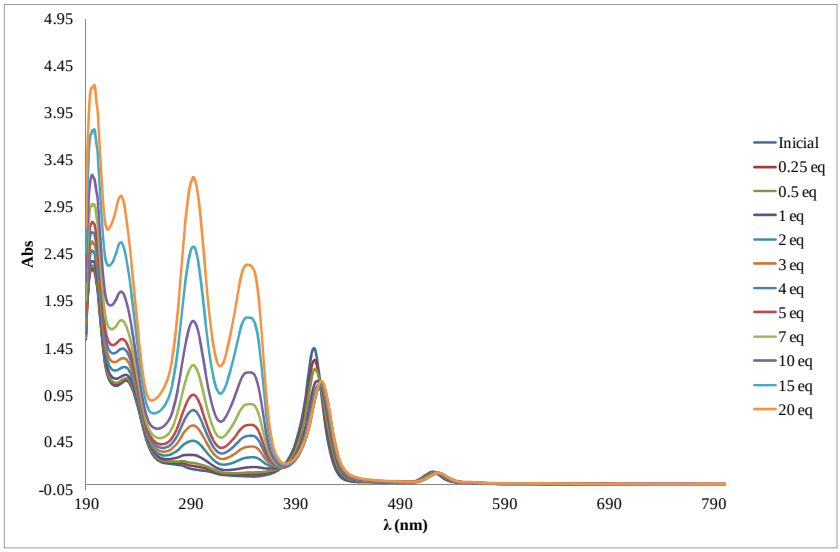

Figure S8. The association constant (K_a) of the **I@3**·$(CF_3SO_3)_7$ host-guest complex was obtained from the graphical representation of SEq. 2:

$$log\left[\frac{A-A_o}{A_F-A}\right] = n \cdot log[Guest] + logK_a \qquad \text{(SEq.2)}$$

Where A is the absorbance for a determined guest concentration, A_o is the absorbance at the beginning of the reaction, A_F the absorbance at the end of the reaction, and n the stoichiometry of the guest.

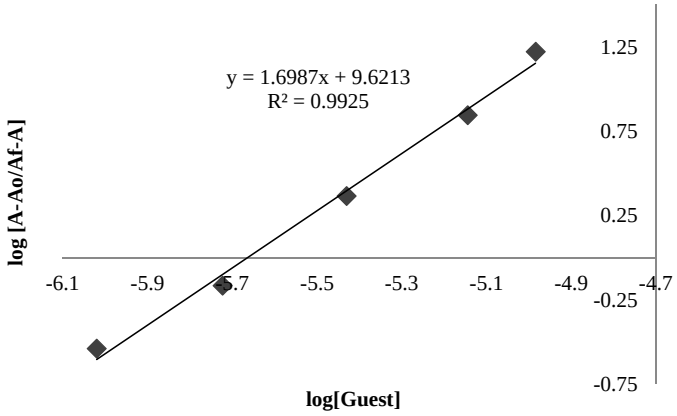

The obtained value for $logK_a$=9.62 (K_a value is $4.16 \cdot 10^9$ M^{-1}). With the K_a value the Gibbs free energy can be calculated with equation SEq. 3:

$$\Delta G^0 = -RTlnK_a \qquad \text{(SEq.3)}$$

A value of ΔG^0 = -54.3 KJ/mol is obtained, and it is consistent with a highly favourable host-guest interaction.

Figure S9. ESI-MS spectra of **I@3**·$(CF_3SO_3)_7$ host-guest complex. Simulated spectra of selected peaks are showed in colour red. Experimental conditions: 100 μM in CH_3CN, registered with a Bruker MicroTOF-Q-II exact mass spectrometer.

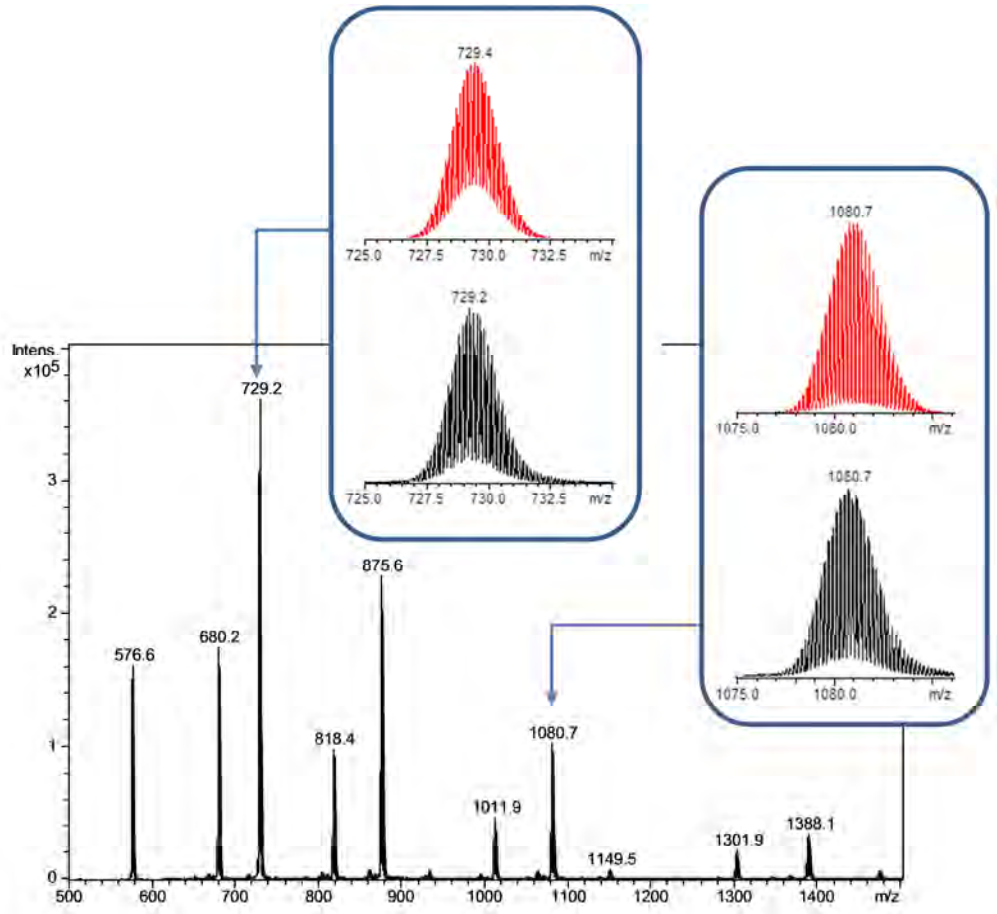

Figure S10. DOSY NMR experiments of complex **Pd-1**, affording a diffusion coefficient (*D*) of $D=10^{-9.085}$ m^2 s^{-1} ($D_{CD3CN}= 10^{-8.460}$ m^2 s^{-1}).

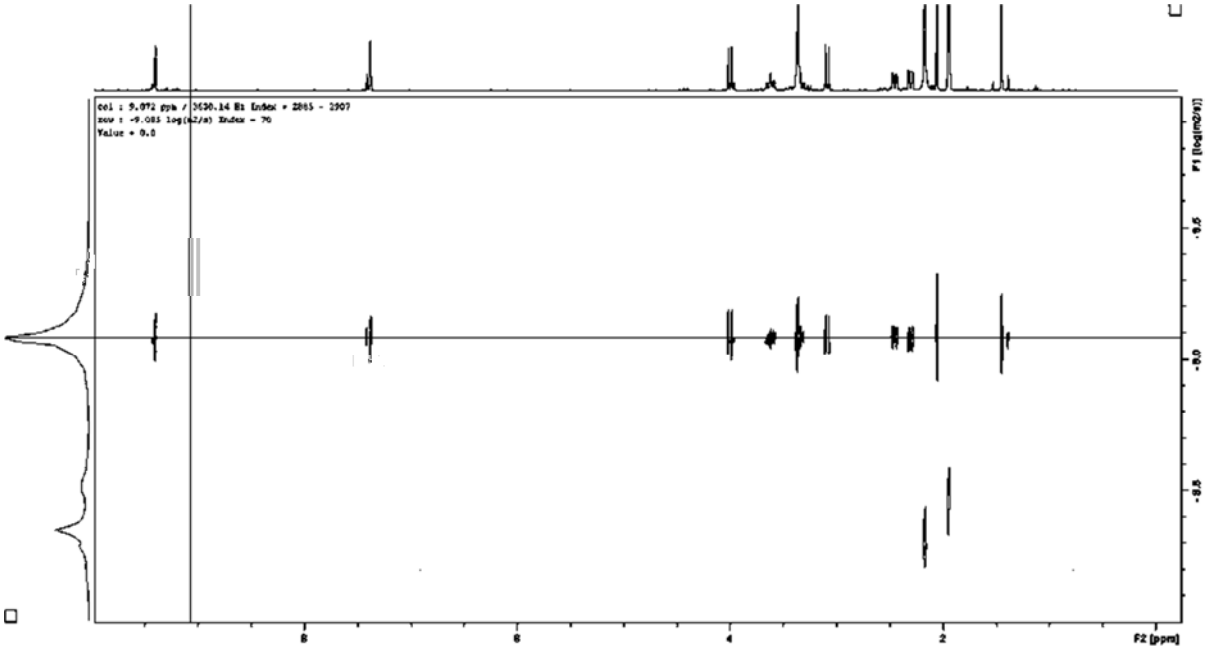

Figure S11. DOSY NMR experiments of nanocapsule **3**·$(CF_3SO_3)_8$, affording a diffusion coefficient (*D*) of $D=10^{-9.479}$ m^2 s^{-1} ($D_{CD3CN}= 10^{-8.488}$ m^2 s^{-1}).

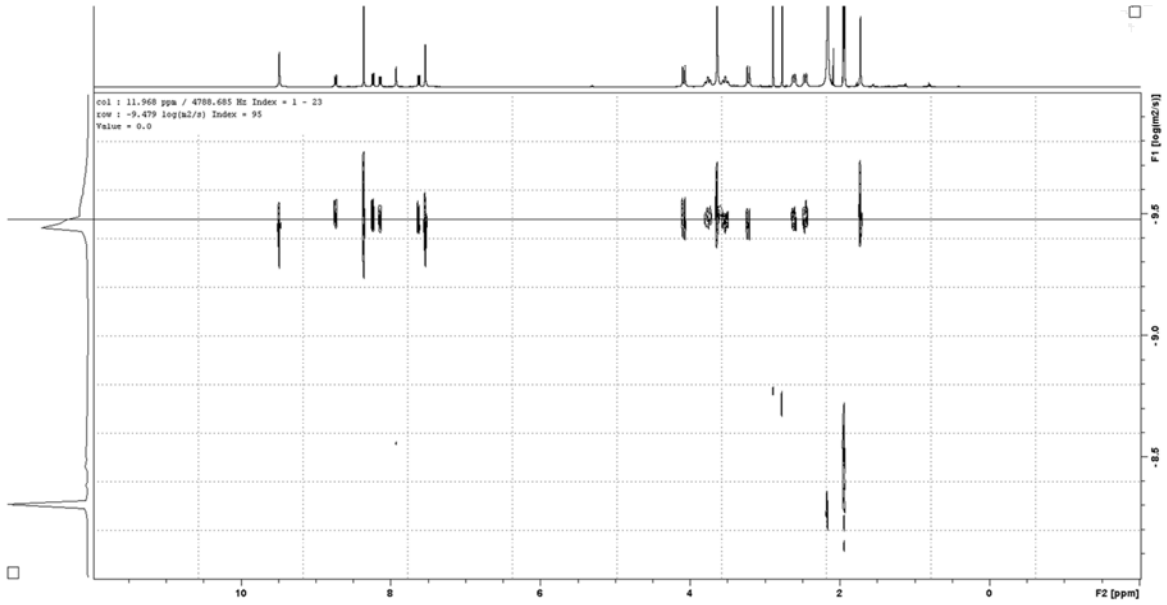

Figure S12. DOSY NMR experiments of **I@3**·$(CF_3SO_3)_7$ host-guest complex, affording a diffusion coefficient (*D*) of $D=10^{-9.476}$ m^2 s^{-1} ($D_{CD3CN}=10^{-8.425}$ m^2 s^{-1}).

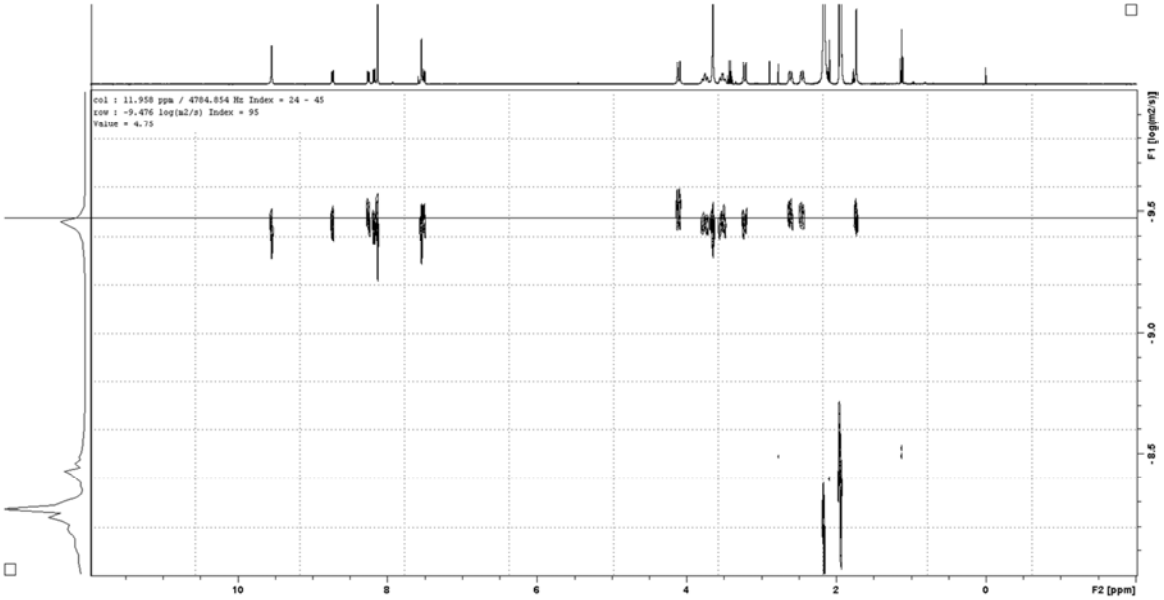

Figure S13. ^{1}H-NMR spectrum of free nanocage **3**·$(CF_3SO_3)_8$ (top). In dark blue ^{1}H-NMR spectrum of host-guest complex between this nanocage and $[Au(cdc)_2]^-$ (**II**) complex (bottom) (CD_3CN, 295 K, 400 MHz).

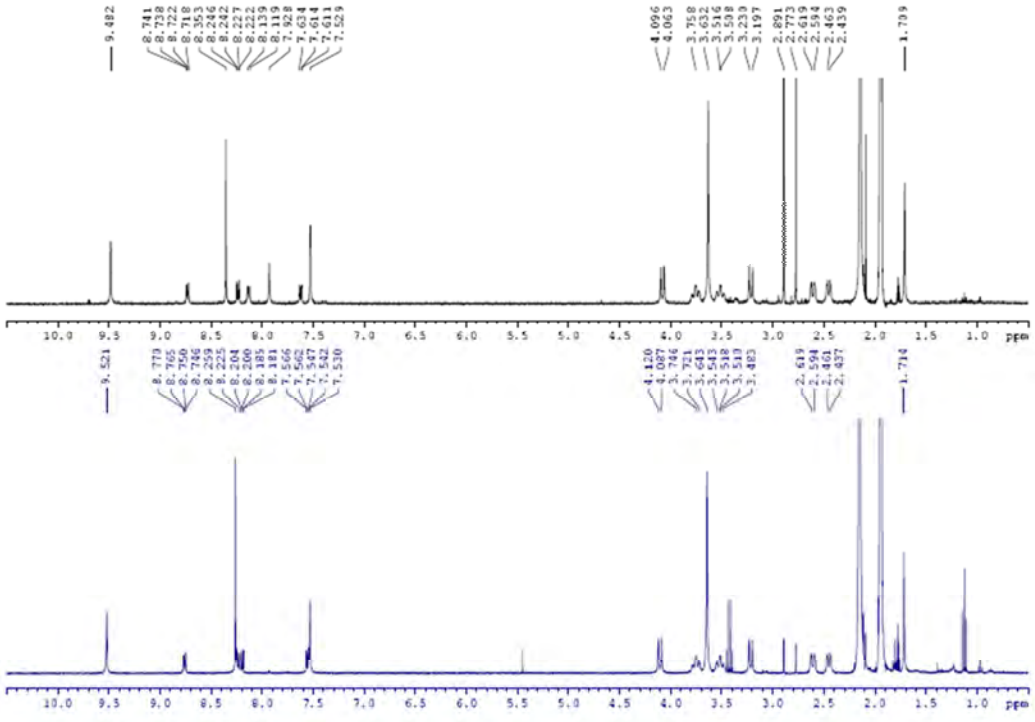

Figure S14. In black ^{1}H-NMR spectrum of free nanocage **3**·$(CF_3SO_3)_8$ (top). In dark blue ^{1}H-NMR spectrum of host-guest complex between this nanocage and $[Au(mnt)_2]^-$ (**V**) complex (bottom) (CD_3CN, 295 K, 400 MHz).

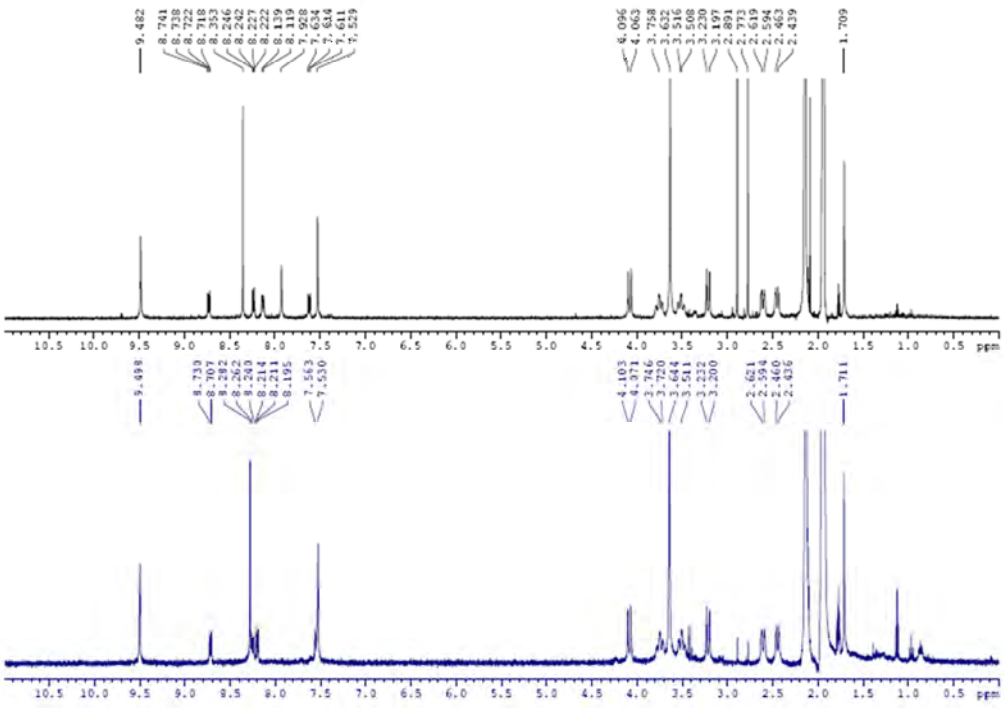

Figure S15. In black ^{1}H-NMR spectrum of free nanocage **3**·$(CF_3SO_3)_8$ (top). In dark blue ^{1}H-NMR spectrum of host-guest complex between this nanocage and $[Pt(mnt)_2]^-$ (**VIII**) complex (bottom) (CD_3CN, 295 K, 400 MHz).

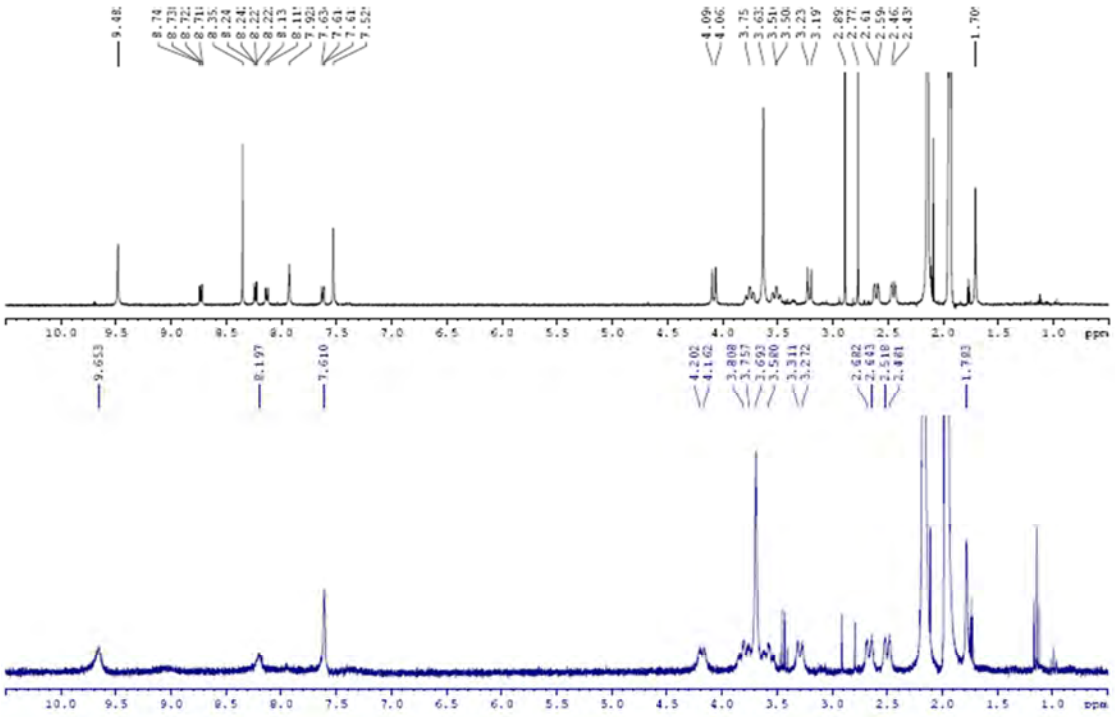

Figure S16. In black ^{1}H-NMR spectrum of free nanocage **3**·$(CF_3SO_3)_8$ (top). In dark blue ^{1}H-NMR spectrum of host-guest complex between this nanocage and $[Pd(mnt)_2]^-$ (**IX**) complex (bottom) (CD_3CN, 295 K, 400 MHz).

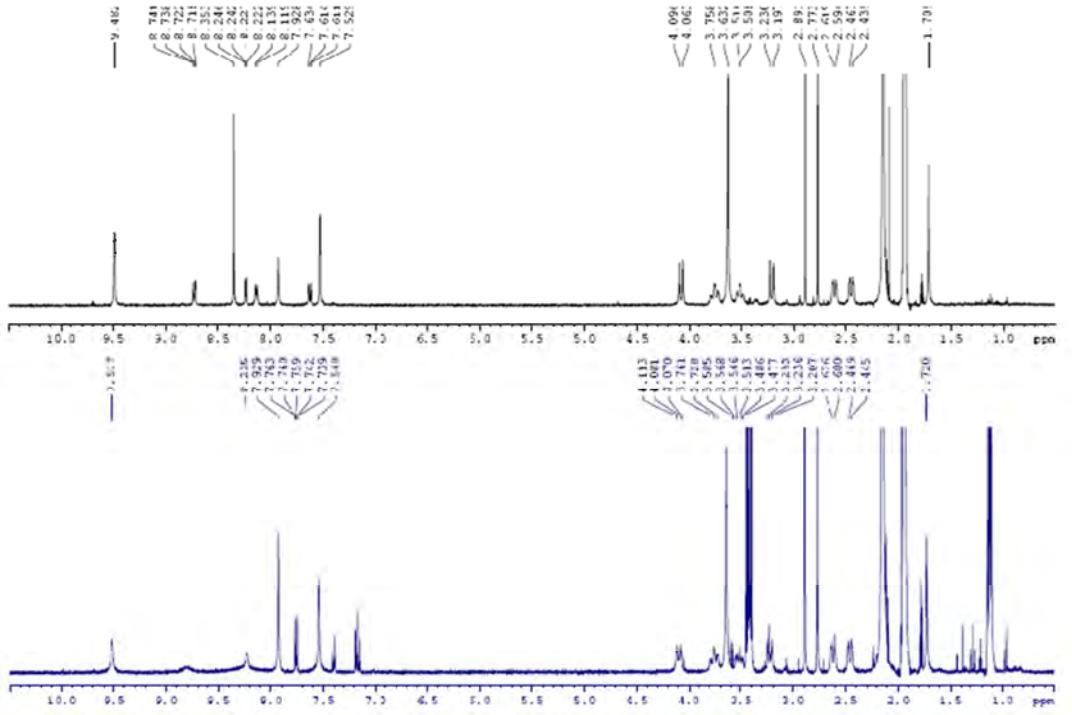

Figure S17. In black ^{1}H-NMR spectrum of free nanocage **3**·$(CF_3SO_3)_8$ (top). In dark blue ^{1}H-NMR spectrum of host-guest complex between this nanocage and $[Ni(mnt)_2]^-$ (**X**) complex (bottom) (CD_3CN, 295 K, 400 MHz).

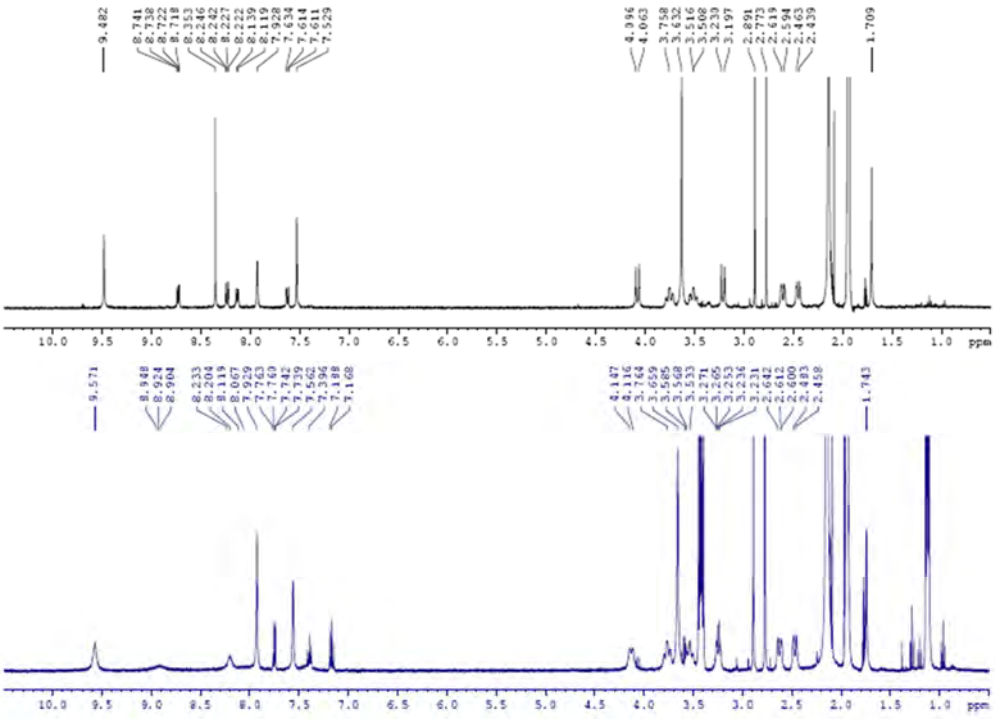

Figure S18. In black ^{1}H-NMR spectrum of free nanocage **3**·$(CF_3SO_3)_8$ (top). In dark blue ^{1}H-NMR spectrum of host-guest complex between this nanocage and paramagnetic (S= 1/2) [bis(2-aminomethyl-6-phenylpyridine)Cu^{II}]$(CF_3SO_3)_2$ complex (bottom) (CD_3CN, 295 K, 400 MHz).

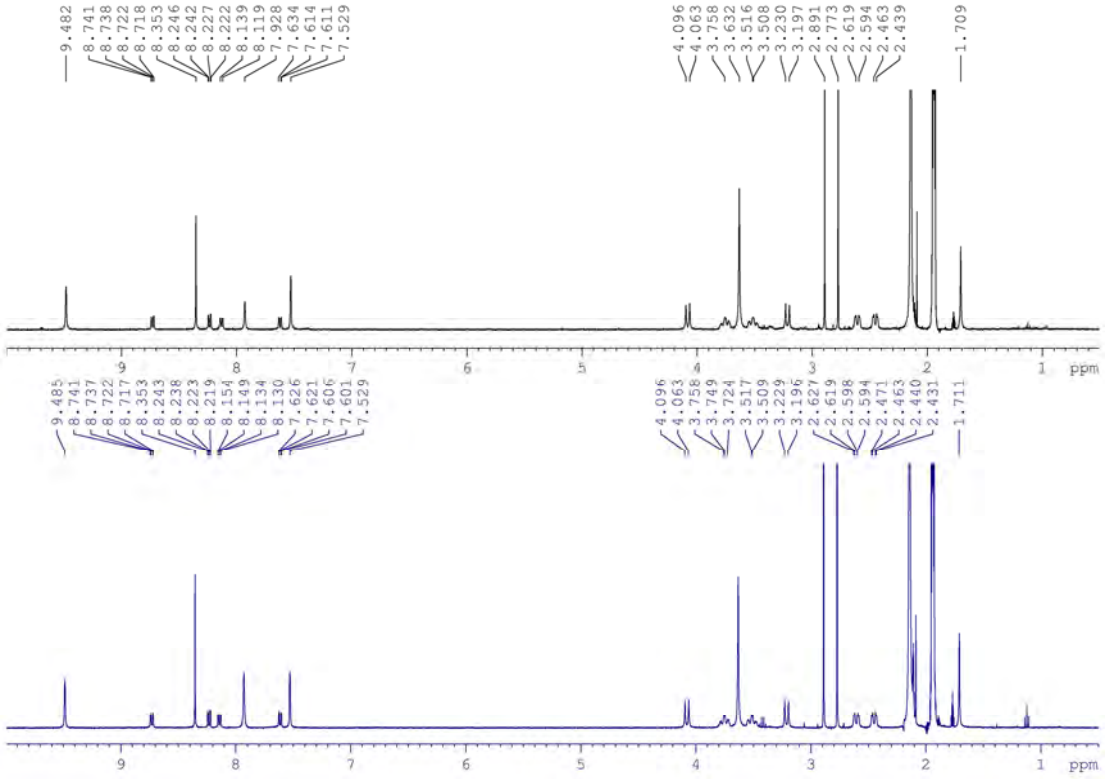

Figure S19. ESI-MS spectra of **II@3**·$(CF_3SO_3)_7$ host-guest complex. Experimental conditions: 100 μM in CH_3CN.

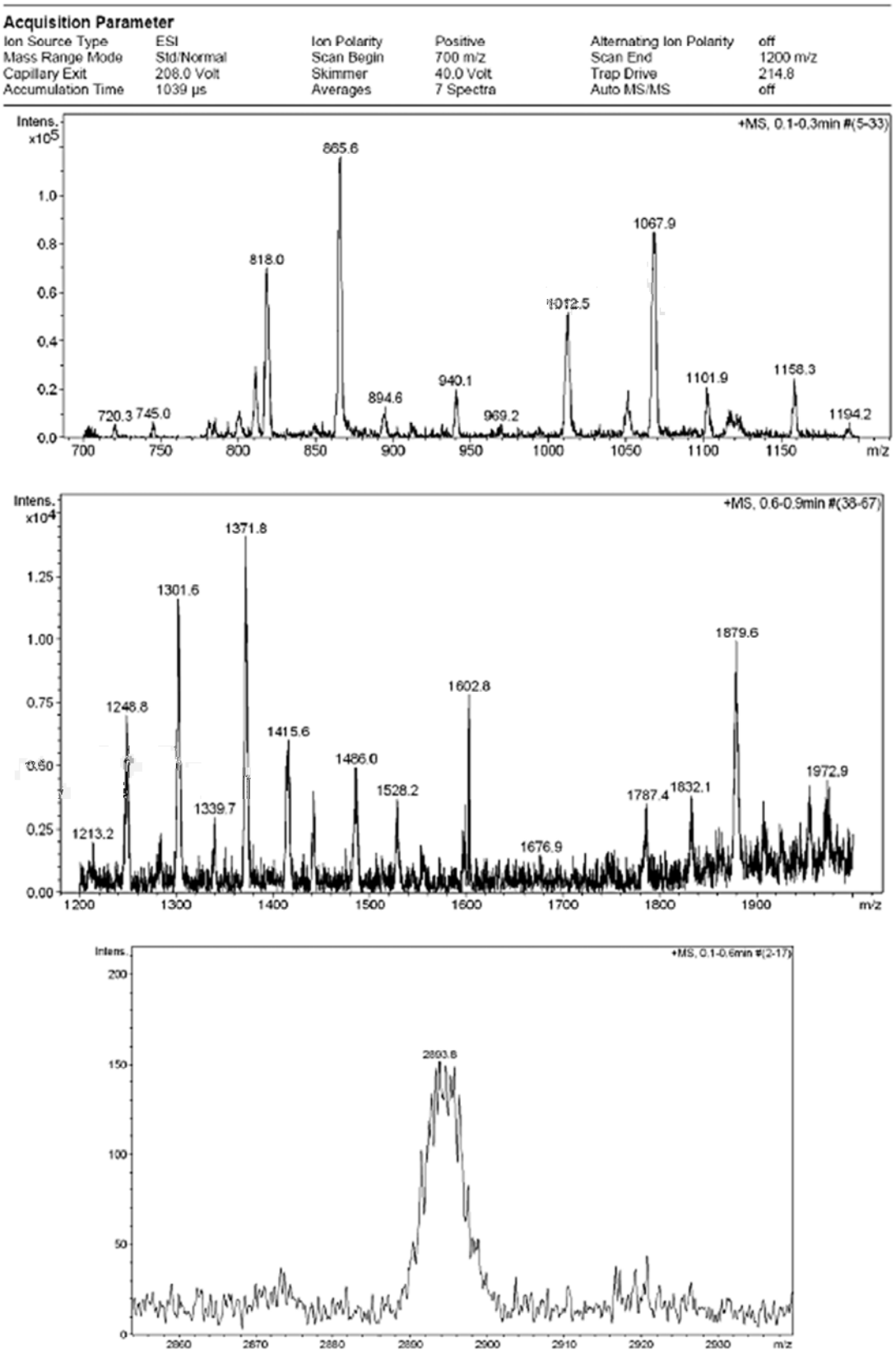

Figure S20. ESI-MS spectra of **V@3**·$(CF_3SO_3)_7$ host-guest complex. Experimental conditions: 100 μM in CH_3CN.

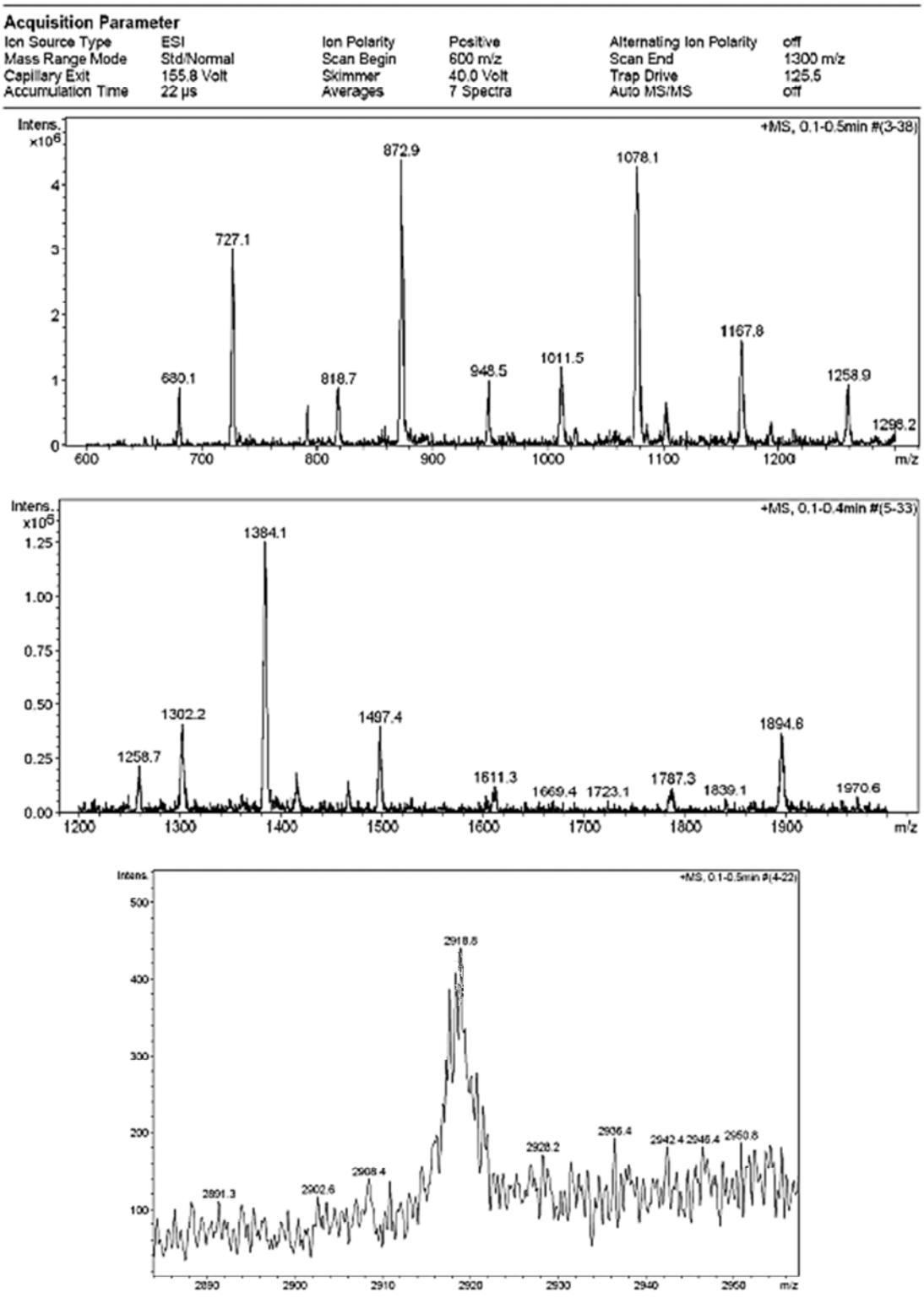

Figure S21. ESI-MS spectra of **VIII@3**·$(CF_3SO_3)_7$ host-guest complex. Experimental conditions: 100 μM in CH_3CN.

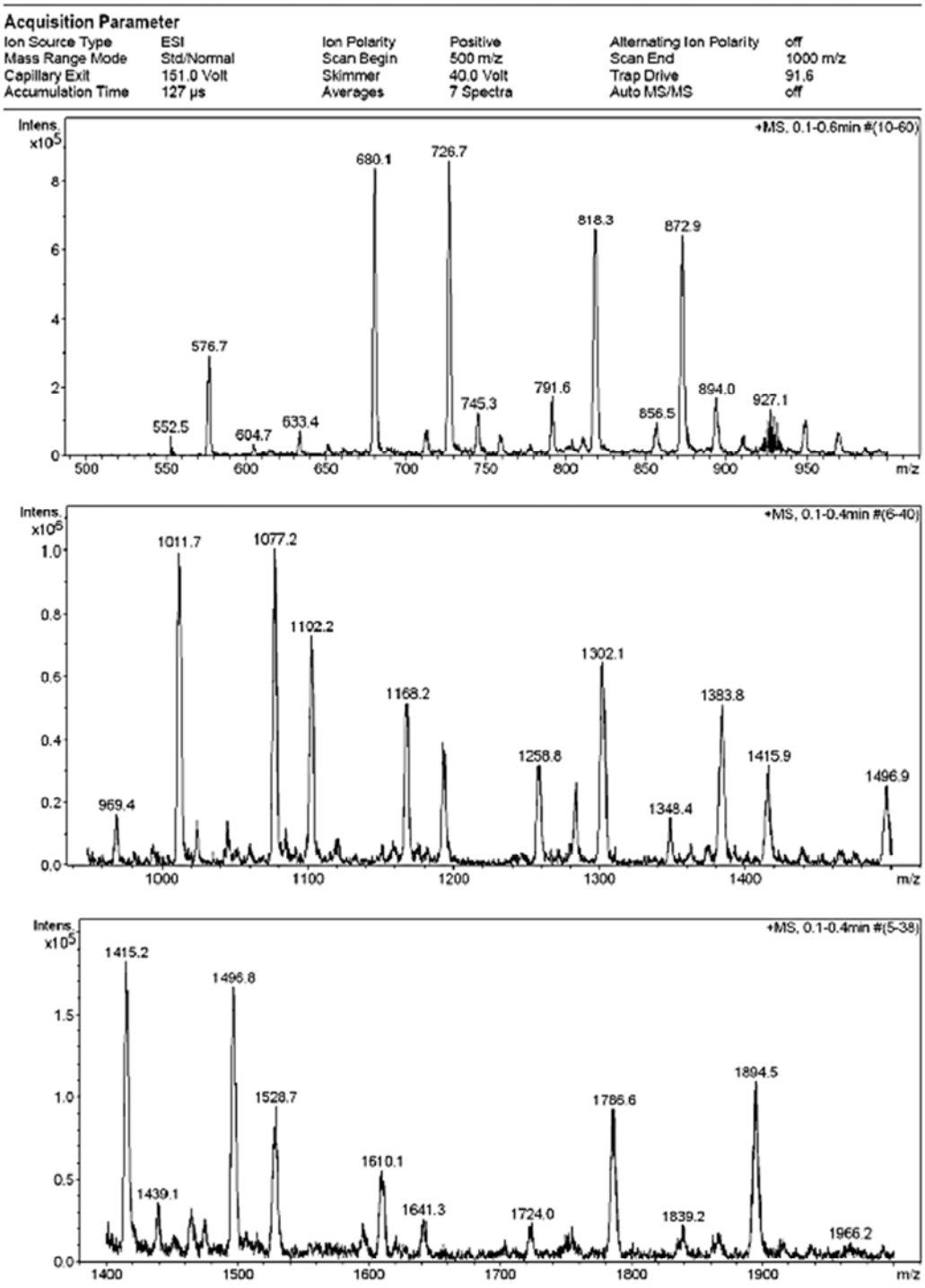

Figure S22. ESI-MS spectra of **IX@3**·$(CF_3SO_3)_7$ host-guest complex. Experimental conditions: 100 μM in CH_3CN.

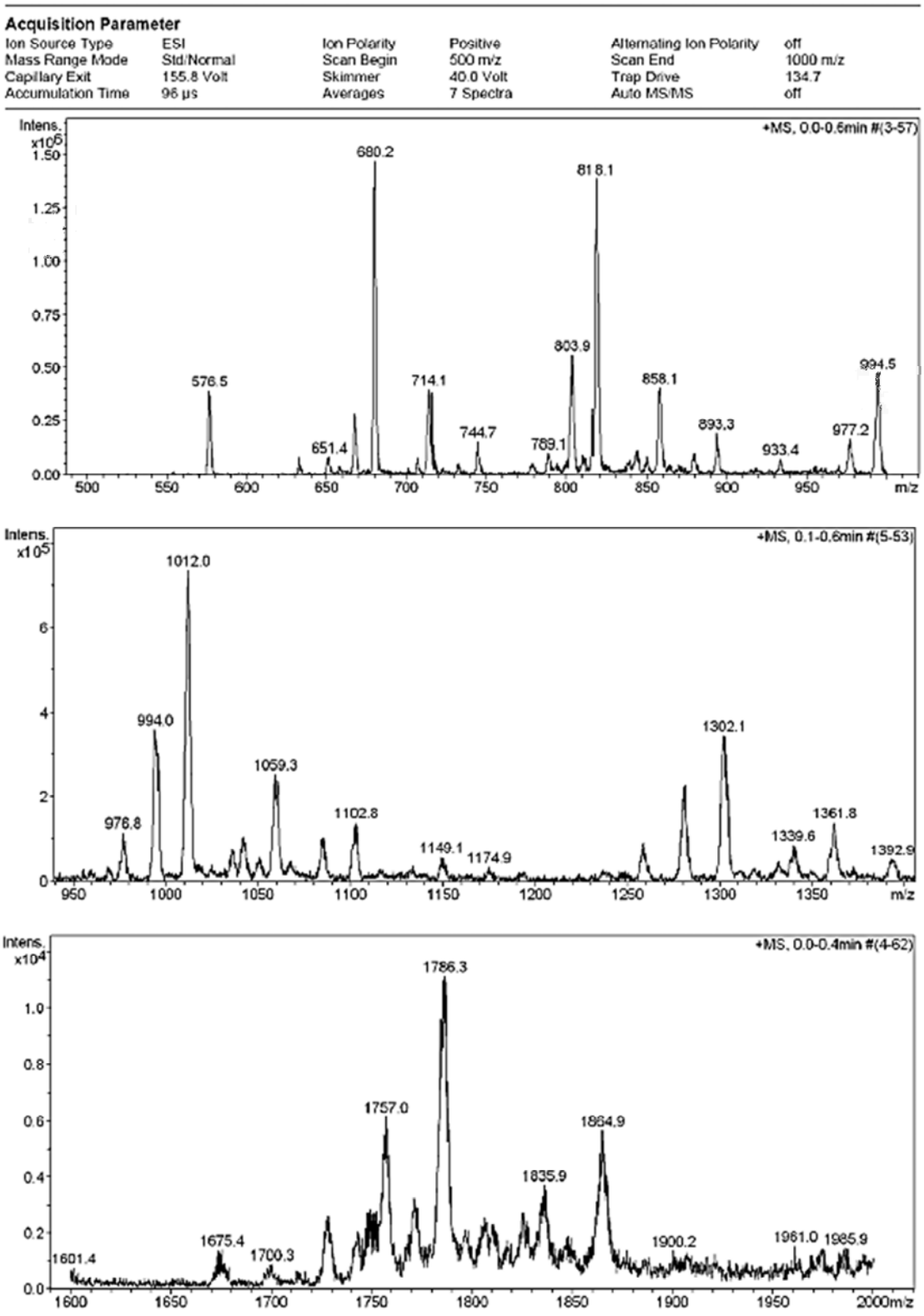

Figure S23. ESI-MS spectra of **X**@**3**·$(CF_3SO_3)_7$ host-guest complex. Experimental conditions: 100 μM in CH_3CN.

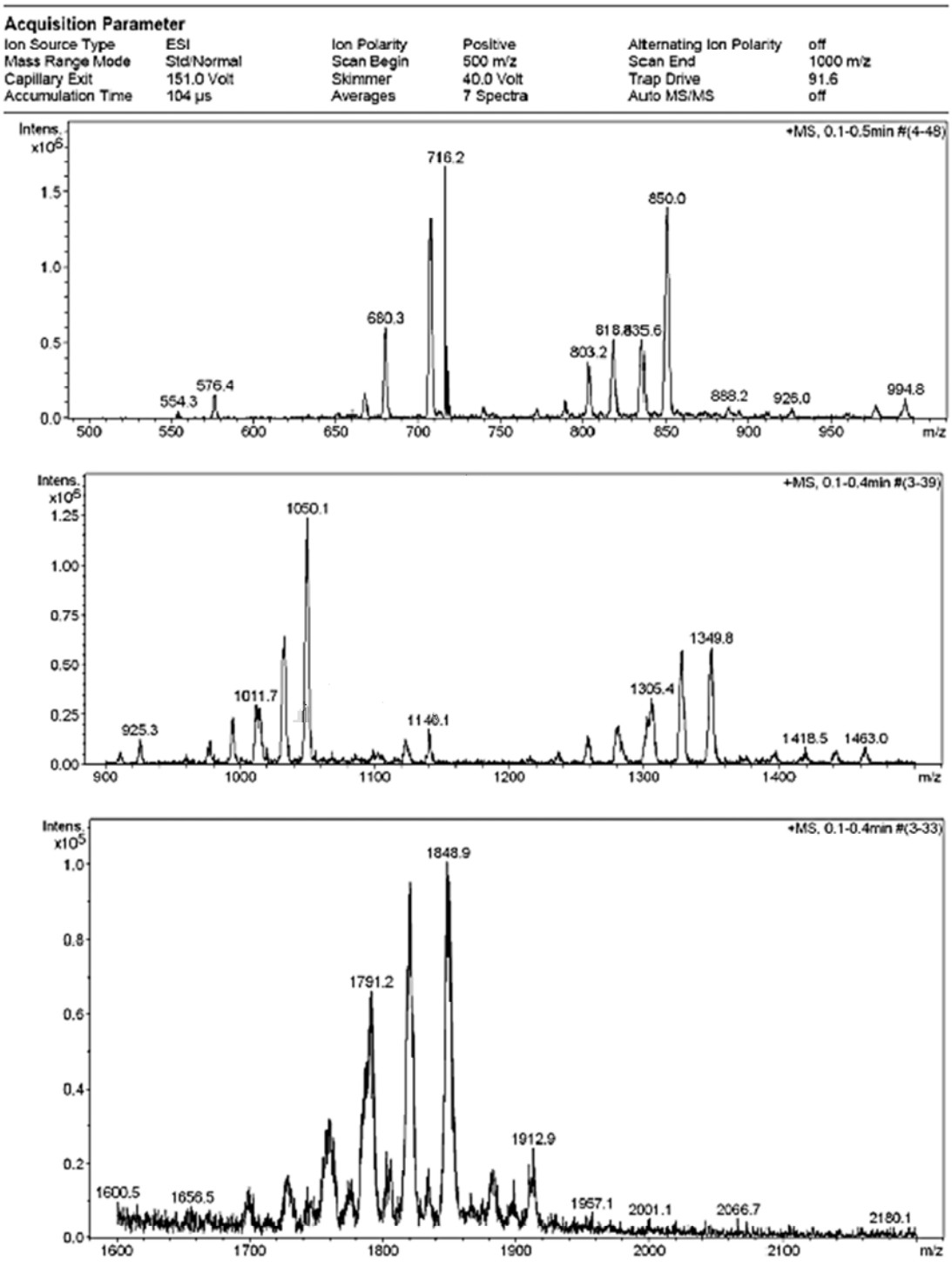

Figure S24. UV-Vis spectra of the exchange experiments between different bis-dithiolene complexes (see. Table 6, main text) and complex **I**. To 2 ml of a $3.75 \cdot 10^{-6}$ M solution of nanocapsule **3**$\cdot(CF_3SO_3)_8$, 1 equivalent of M(dithiolene)$_2$ complex (**II**, **V**, **VIII**, **IX** o **X**) was added. Then an increasing number of equivalents of substrate **I** were added to the mixture in order to evaluate its capacity to displace the already encapsulated guest. As shown in the figures (a-e) below, no more changes were produced on the Soret band (≈408 nm) when 5 equivalents of substrate **I** were added, showing that the association between the nanocapsule and the other substrates is stronger.

a) Competition: **I** vs **II**.

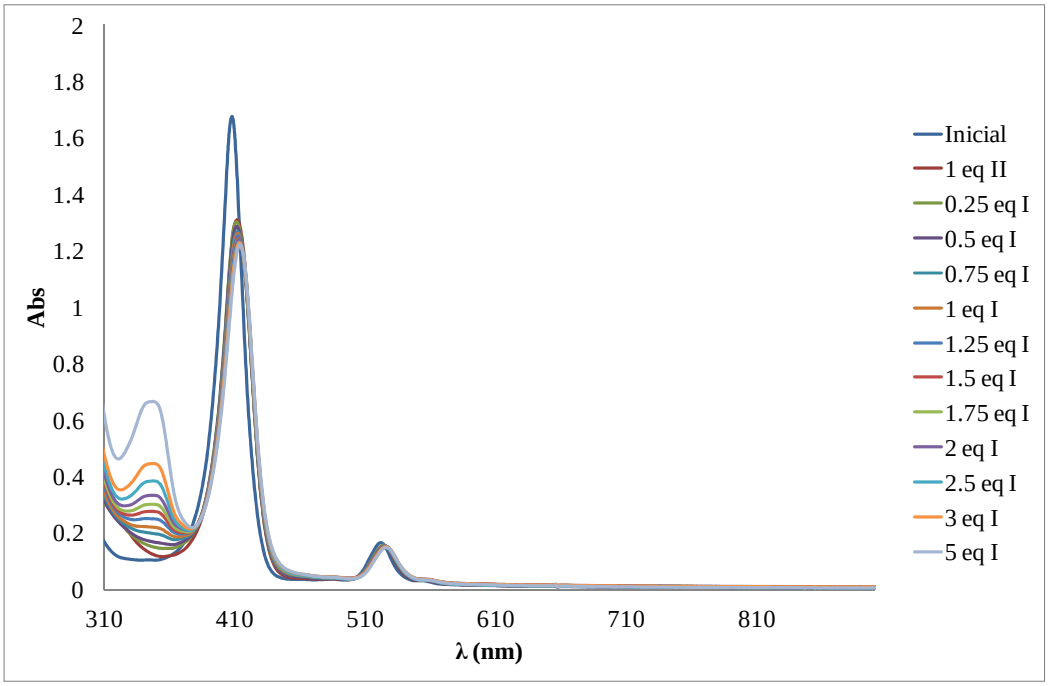

b) Competition: **I** vs **V**.

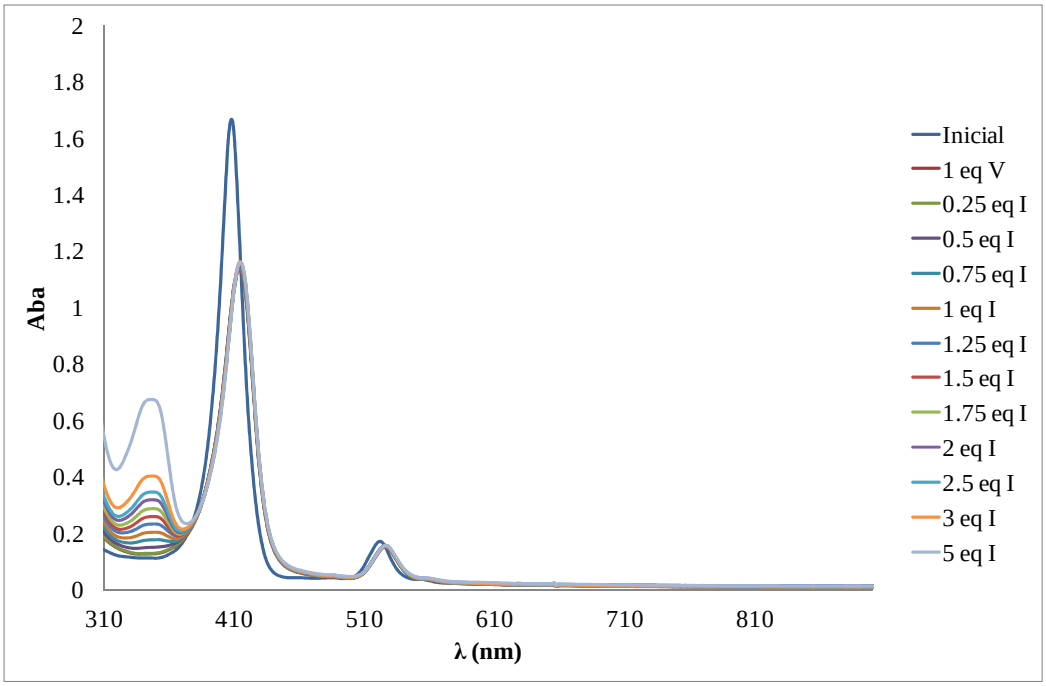

c) Competition: **I** vs **VIII**.

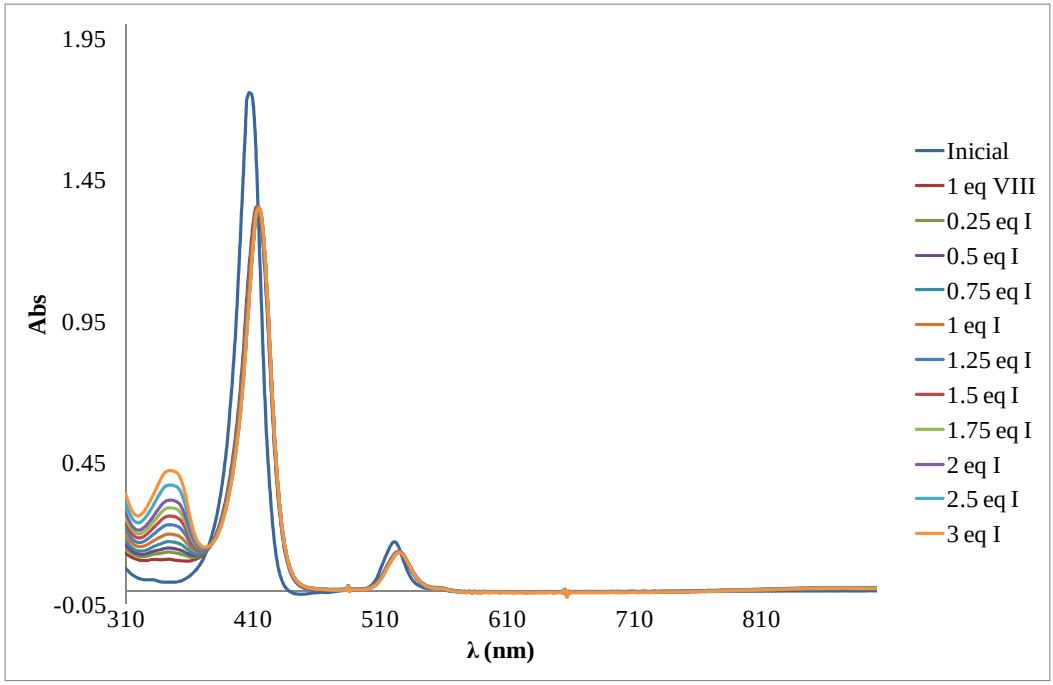

d) Competition: **I** vs **IX**.

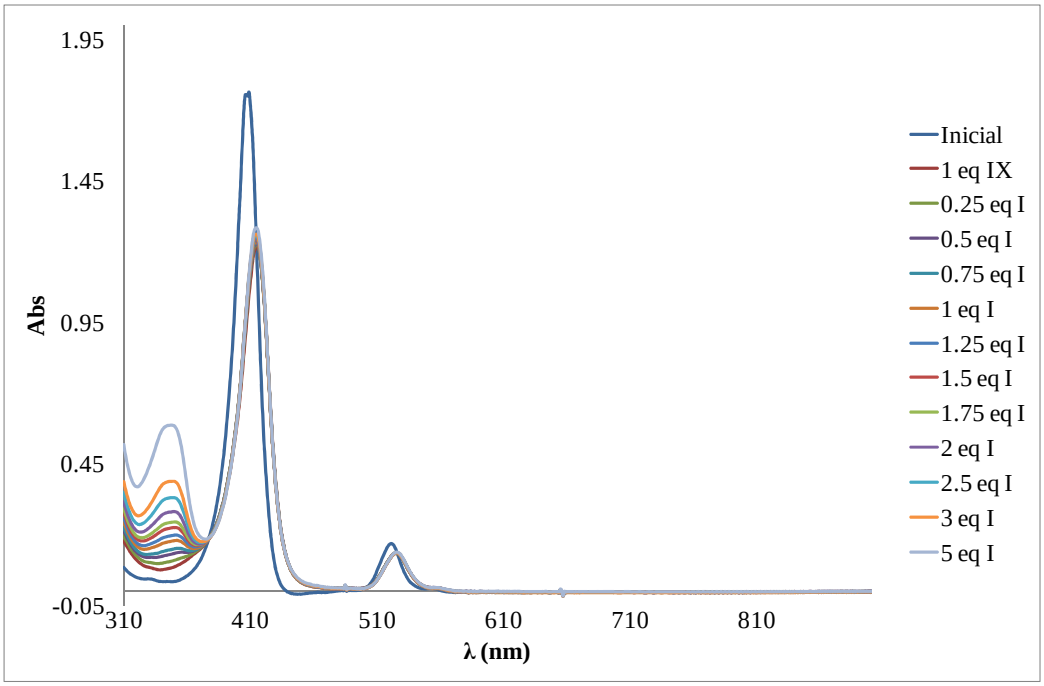

e) Competition: **I** vs **X**.

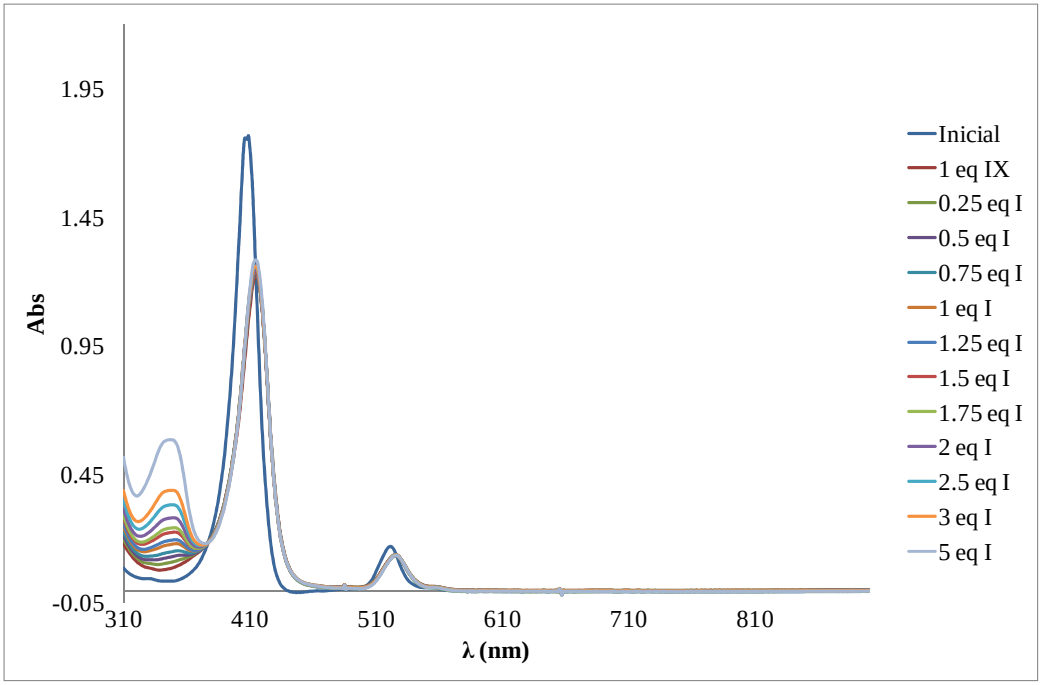

Figure S25. Job's plot, to obtain the stoichiometry for the host-guest complex of the nanocage **3**·$(CF_3SO_3)_8$ and the complexes showing encapsulation (**I**, **II**, **V**, **VII**, **IX**, **X**). As can be observed on the figures, in all cases x has a value arround 0.5, indicating that the host-guest complexes have a 1:1 stoichiometry (n≈1).

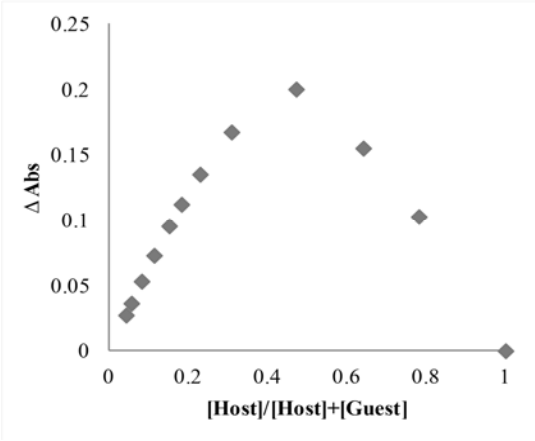

I@**3**·$(CF_3SO_3)_7$

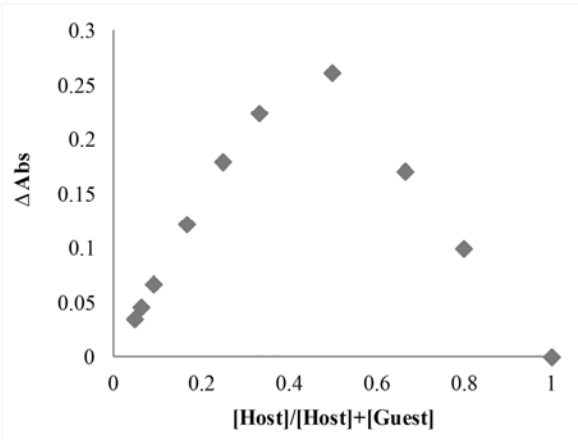

II@**3**·$(CF_3SO_3)_7$

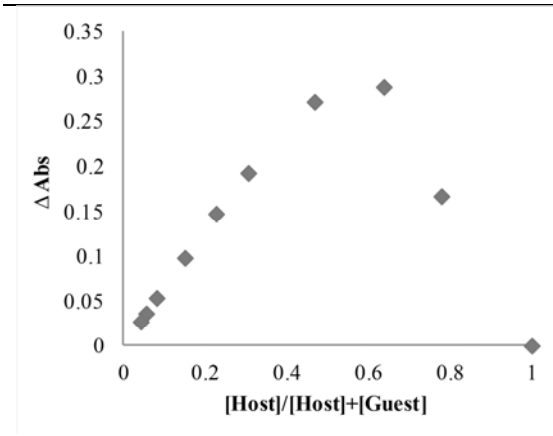

V@**3**·$(CF_3SO_3)_7$

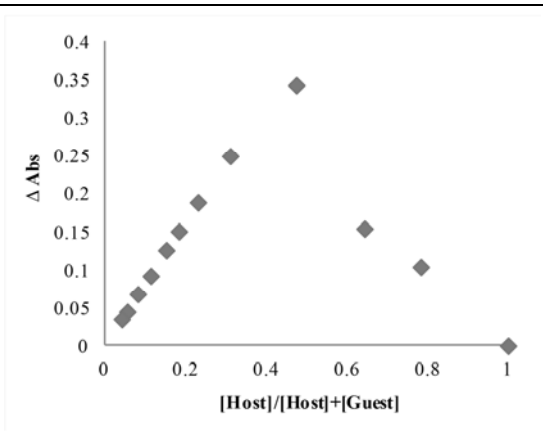

VIII@**3**·$(CF_3SO_3)_7$

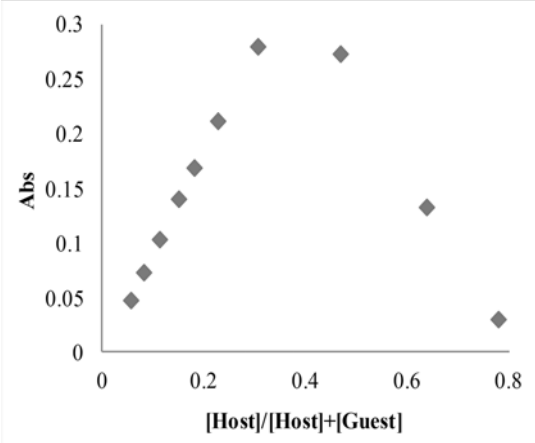

IX@**3**·$(CF_3SO_3)_7$

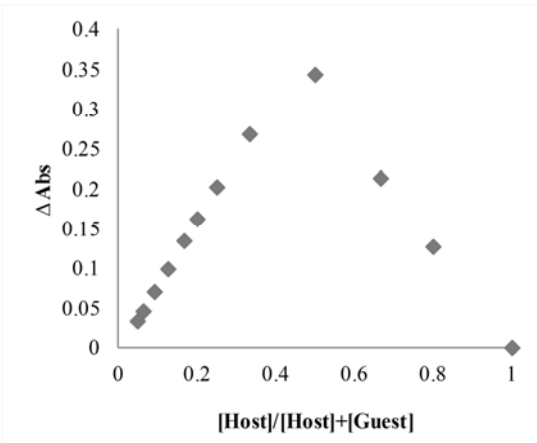

X@**3**·$(CF_3SO_3)_7$

Figure S26. a) UV-Vis monitoring of the titration of **3**·$(CF_3SO_3)_8$ nanocapsule with TBA[Pt(mnt)$_2$] (**VIII**). Additions up to 4 eq. of **VIII** to a $3.77 \cdot 10^{-3}$ mM solution of **3**·$(CF_3SO_3)_8$ in CH_3CN. b) Plot for comparison of the variation of the Soret band absorbance at 408 nm and the normalized variation of the absorbance of **VIII** (at 850 nm) during different additions of substrate.

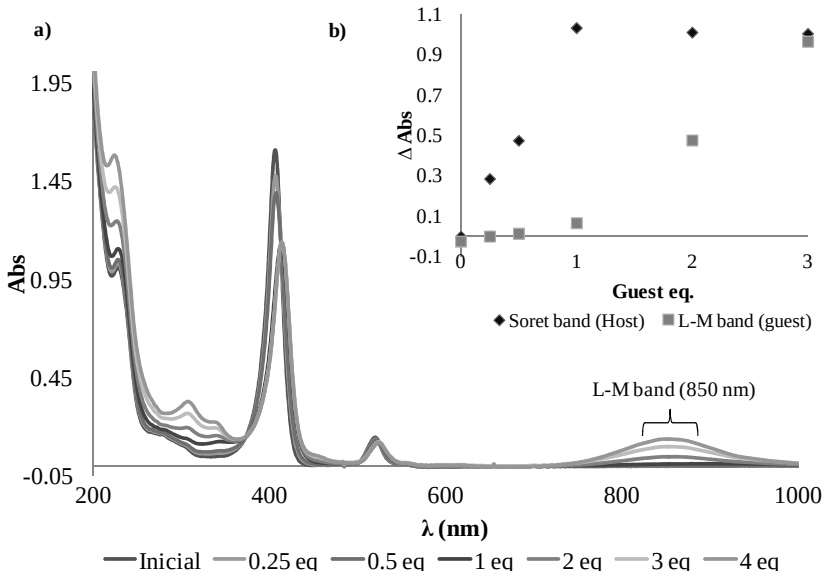

Figure S27. Cyclic voltammetry of a) a 3.4 mM solution of TBA[Pt(mnt)$_2$] (**VIII**) and b) a 0.25 mM solution of nanocapsule **3** with 0.5 equivalents of **VIII**. Conditions: scan rate=0.1 V/s, [TBAP]=0.1 M, CH_3CN, using a saturated calomel electrode and AcFc/AcFc$^+$ as internal reference.

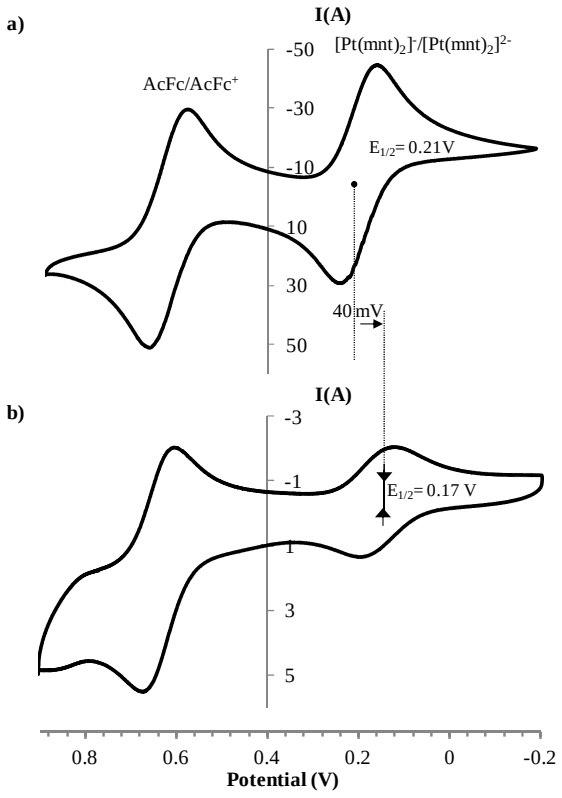

Figure S28. CV involving 1 equivalent of nanocapsule **3** and 0.5 equivalents of substrate **VIII** and acetylferrocene at different scan rates. Conditions: scan rate=0.5 V/s, 0.3 V/s, 0.2 V/s, 0.1 V/s, 0.08 V/s, 0.05 V/s and 0.03 V/s; [TBAP]=0.1 M, CH_3CN, using a saturated calomel electrode and $AcFc/AcFc^+$ as internal reference.

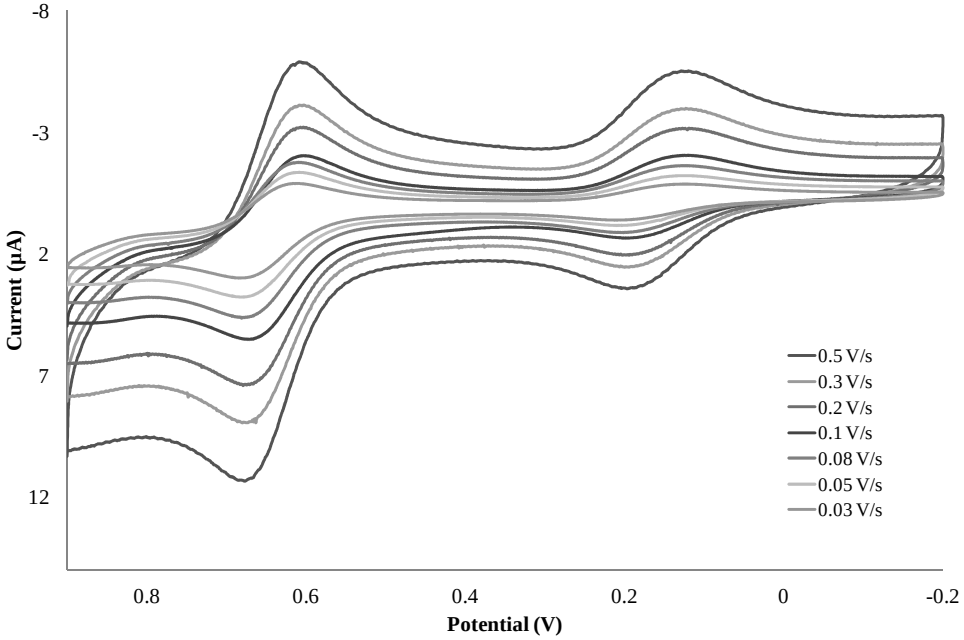

Figure S29.

The peak current for a reversible system is described by the Randles-Sevick equation:

$$i_p = (2.69 \cdot 10^5) n^{3/2} A D^{1/2} C \Upsilon^{1/2} \quad \text{(SEq.4)}$$

where i_p is peak current (A), n is electron stoichiometry, A is electrode area (cm2), D is diffusion coefficient (cm2/s), C is concentration, and Υ is scan rate (V/s).**¡Error! Marcador no definido.**

To find the diffusion coeficient, polarograms at different scan rates were done, in order to stablish a linear correlation between the peak current (i_p) and the scan rate ($\Upsilon^{0.5}$). We obtain the following equation:

$$i_p = k \cdot \Upsilon^{1/2} \quad \text{(SEq.5)}$$

where k is the linear regresion slope of i_p vs. $\Upsilon^{0.5}$ plot, and allow us to find the D value, taking into account SEq.4.

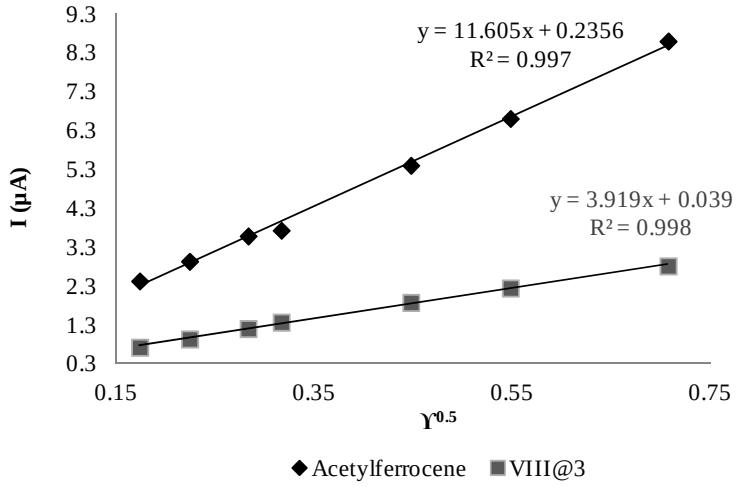

The CV expermiment of 1 equivalent of nanocapsule **3** and 0.5 equivalents of TBA[Pt(mnt)$_2$] (**VIII**) and acetylferrocene at different scan rates (See Figure **S27**), allowed us to obtain a value the diffusion coefficient (D) of the host-guest complex formed. A value of D= 3.35·10^{-10} m^2/s was obtained for **VIII@3**·(CF$_3$SO$_3$)$_7$, which is in strong agreement with the value obtained from the DOSY-NMR experiments carried out with substrate **I.** On the other hand a D=2.82·10^{-9} m^2/s was obtained for acetylferrocene, a value that is in agreement with the previously reported values for ferrocene under the same conditions.[20,21]

Figure S30. a) UV-Vis monitoring of the titration of **3**·$(CF_3SO_3)_8$ nanocapsule with TBA[Pd(mnt)$_2$] (**IX**). Additions up to 4 eq. of **IX** to a $3.77 \cdot 10^{-3}$ mM solution of **3**·$(CF_3SO_3)_8$ in CH_3CN. b) Plot for comparison of the variation of the Soret band absorbance at 408 nm and the normalized variation of the absorbance of **IX** (at 1090 nm) during different additions of substrate.

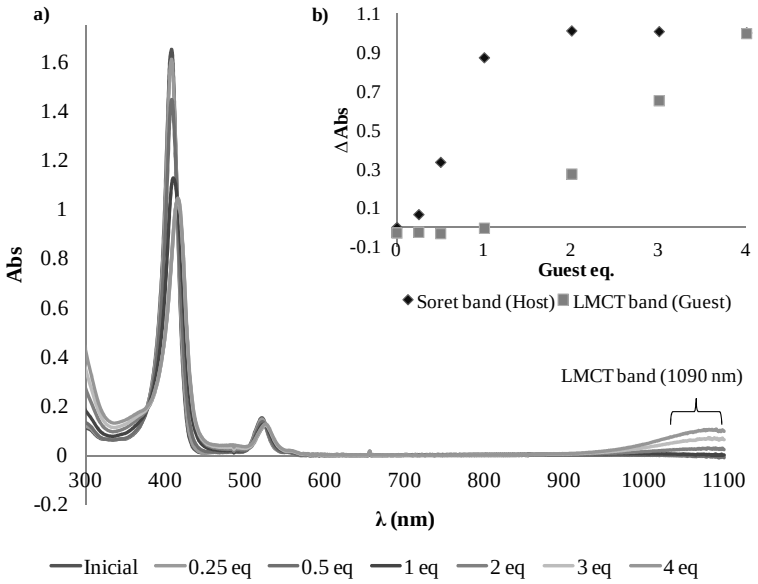

Figure S31. Cyclic voltammetry of a) a 3.4 mM solution of TBA[Pd(mnt)$_2$] (**IX**) and b) a 0.25 mM solution of nanocapsule **3** with 0.5 equivalents of **IX**. Conditions: scan rate=0.1 V/s, [TBAP]=0.1 M, CH_3CN, using a saturated calomel electrode and AcFc/AcFc$^+$ as internal reference.

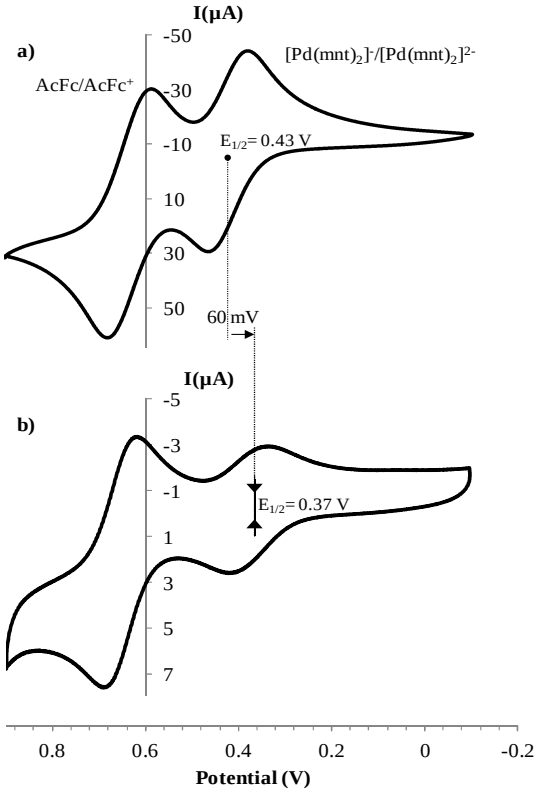

Figure S32. CV involving 1 equivalent of nanocapsule **3** and 0.5 equivalents of substrate **IX** and acetylferrocene at different scan rates. Conditions: scan rates=0.5 V/s, 0.3 V/s, 0.2 V/s, 0.1 V/s, 0.08 V/s, 0.05 V/s and 0.03 V/s; [TBAP]=0.1 M, CH_3CN, using a saturated calomel electrode and $AcFc/AcFc^+$ as internal reference.

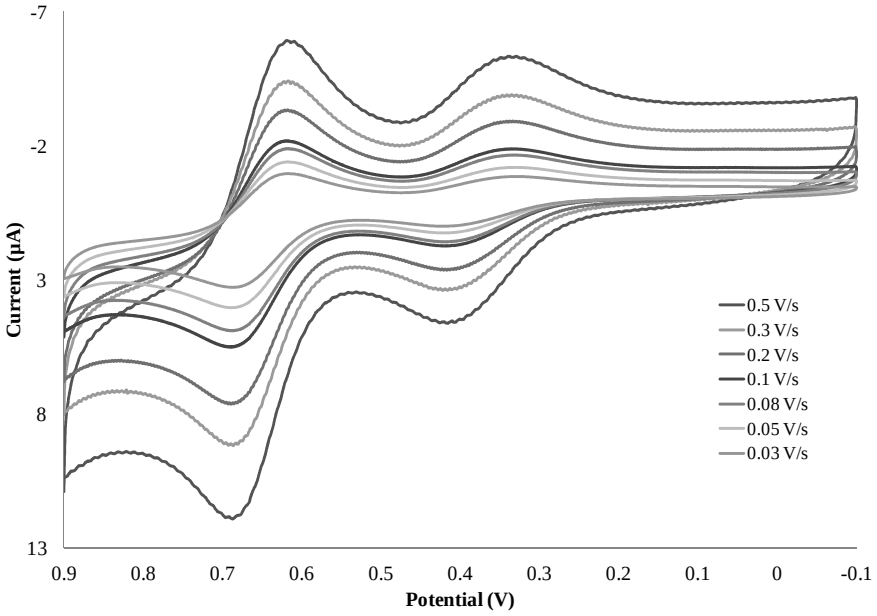

Figure S33. Following the procedure shown in Figure **S28** the CV expermiment of 1 equivalent of nanocapsule **3** and 0.5 equivalents of $TBA[Pd(mnt)_2]$ (**IX**) and acetylferrocene at different scan rates (See Figure **S31**), allowed us to obtain a value the diffusion coefficient (*D*) of the host-guest complex formed. A value of $D= 6.34\cdot10^{-10}$ m^2/s was obtained for **IX@3**$\cdot(CF_3SO_3)_7$, which is in strong agreement with the value obtained from the DOSY-NMR experiments carried out with substrate **I.** On the other hand a $D=2.72\cdot10^{-9}$ m^2/s was obtained for acetylferrocene.

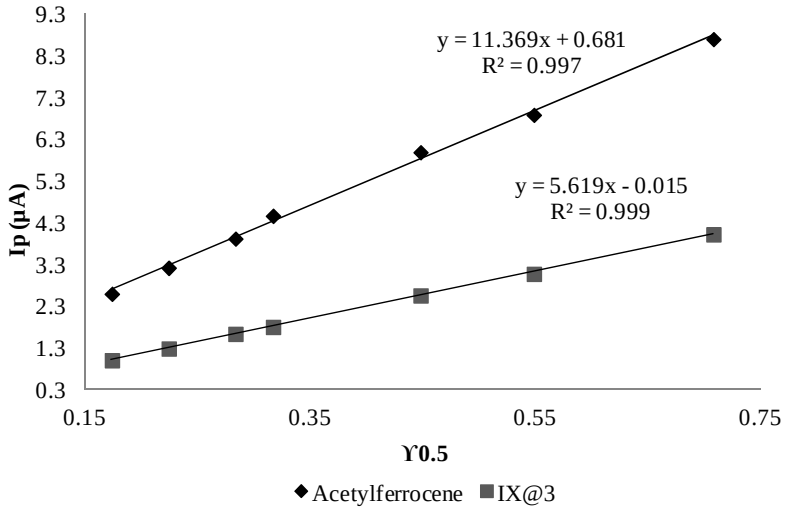

Figure S34. a) UV-Vis monitoring of the titration of **3**·$(CF_3SO_3)_8$ nanocapsule with TBA[Ni(mnt)$_2$] (**X**). Additions up to 4 eq. of **X** to a 3.77·10^{-3} mM solution of **3**·$(CF_3SO_3)_8$ in CH_3CN. b) Plot for comparison of the variation of the Soret band absorbance at 408 nm and the normalized variation of the absorbance of **X** (at 860 nm) during different additions of substrate.

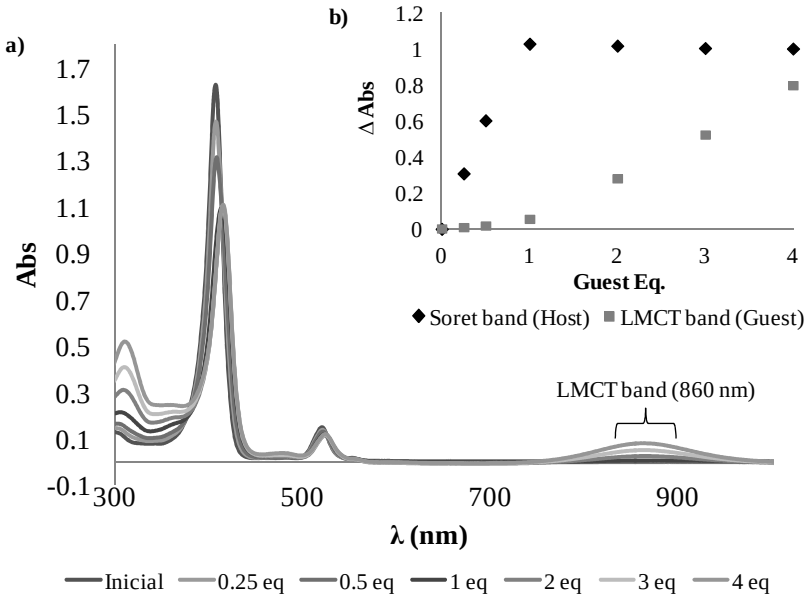

Figure S35. Cyclic voltammetry of a) a 3.4 mM solution of TBA[Ni(mnt)$_2$] (**X**) and b) a 0.25 mM solution of nanocapsule **3** with 0.5 equivalents of **X**. Conditions: scan rate=0.1 V/s, [TBAP]=0.1 M, CH_3CN, using a saturated calomel electrode and AcFc/AcFc$^+$ as internal reference.

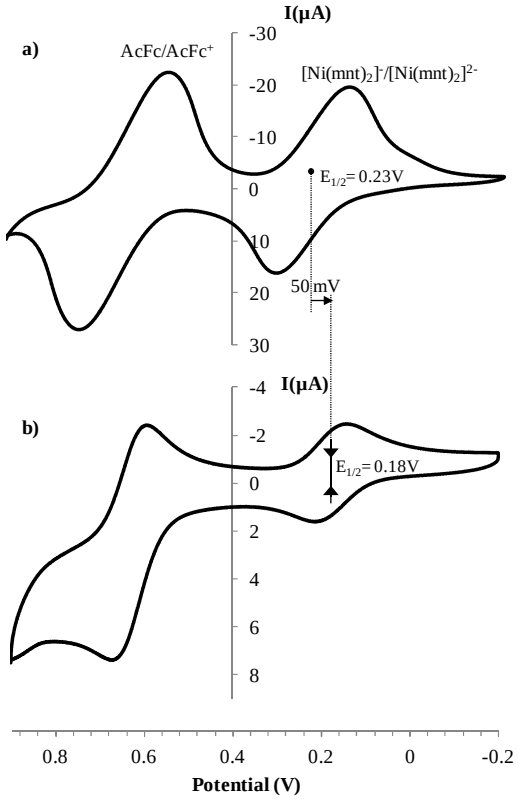

Figure S36. Cyclic voltammetry of a) a 3.4 mM solution of TBA[Ni(mnt)$_2$] (**X**) and b) a 0.25 mM solution of nanocapsule **3** with 0.5 equivalents of **X**. Conditions: scan rate=0.1 V/s, [TBAP]=0.1 M, CH_3CN, using a saturated calomel electrode and AcFc/AcFc$^+$ as internal reference.

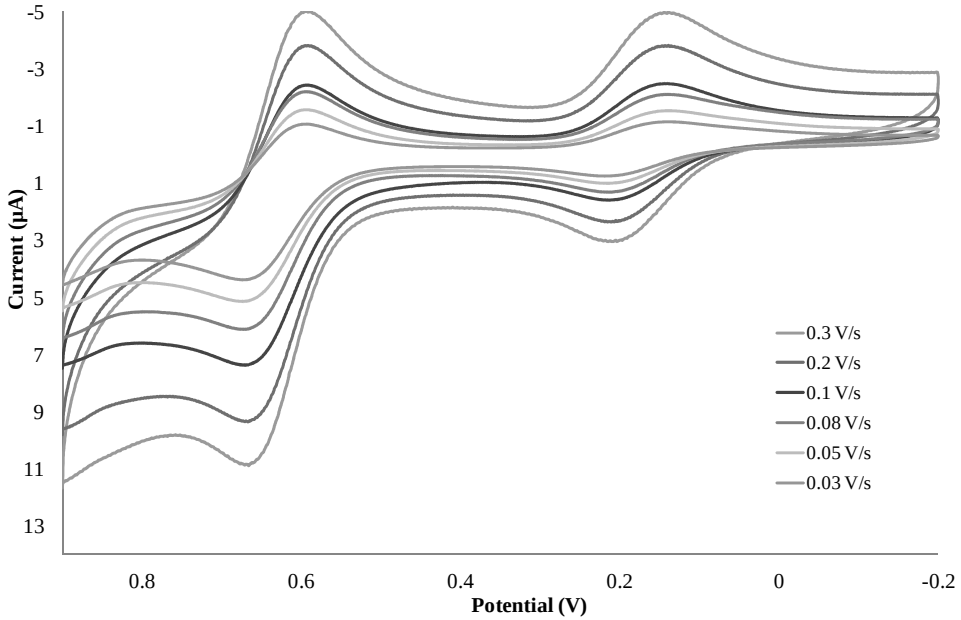

Figure S37. Following the procedure shown in figure **S28** the CV expermiment of 1 equivalent of nanocapsule **3** and 0.5 equivalents of TBA[Ni(mnt)$_2$] and acetylferrocene at different scan rates (See Figure S35), allowed us to obtain a value the diffusion coefficient (*D*) of the host-guest complex formed. A value of $D= 5.24\cdot10^{-10}$ m^2/s was obtained for **X@3**$\cdot(CF_3SO_3)_7$, which is in strong agreement with the value obtained from the DOSY-NMR experiments carried out with substrate **I.** On the other hand a $D=3.50\cdot10^{-9}$ m^2/s was obtained for acetylferrocene.

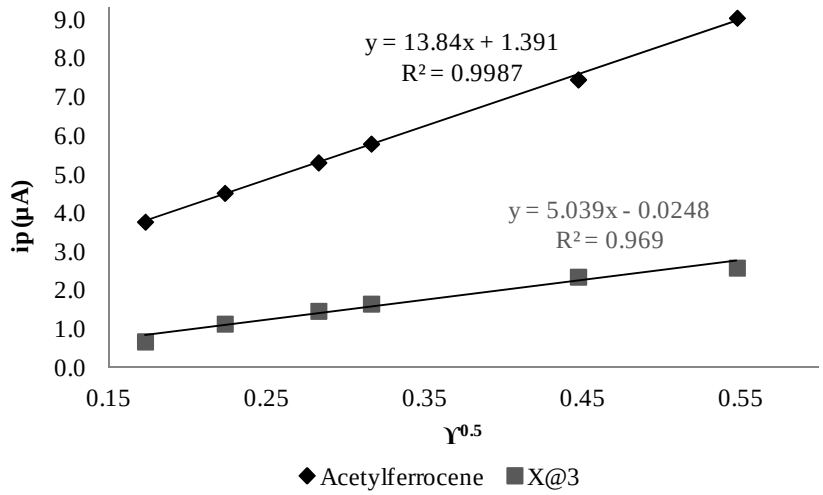

Figure S38: Comparison for **Pd-1**·$(AcO)_4$ between its X-ray structure and the DFT BLYP-D3/DZ-(COSMO:MeCN) geometry where the solvent (acetonitrile) was included through a dielectric continuum model (COSMO). The DFT geometry has been optimized taking as a starting point the X-ray structure. In this figure we present superimposed the X-ray (magenta) and DFT (green) optimized structures. The differences between both geometries are very small, which indicates that the structures obtained from XRD analyses are retained in solution.

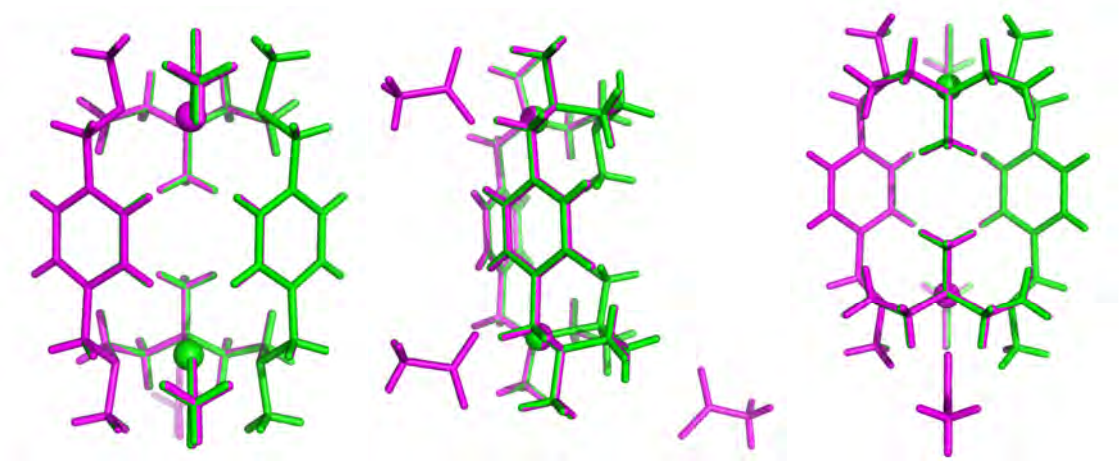

Figure S39: BLYP-D3/DZ-(COSMO:MeCN) optimized geometries of $Au(tdas)_2^-$ (**I**), $Au(pdt)_2^-$ (**III**), $Au(mnt)_2^-$(**V**). The ring bond distances (Å) for the three studied molecules are represented:

$Au(tdas)_2^-$ (**I**):

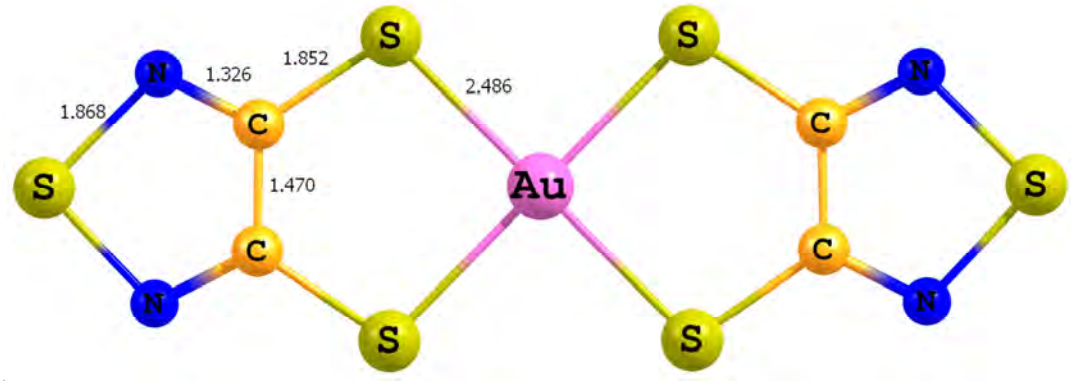

$Au(pdt)_2^-$ (**III**)

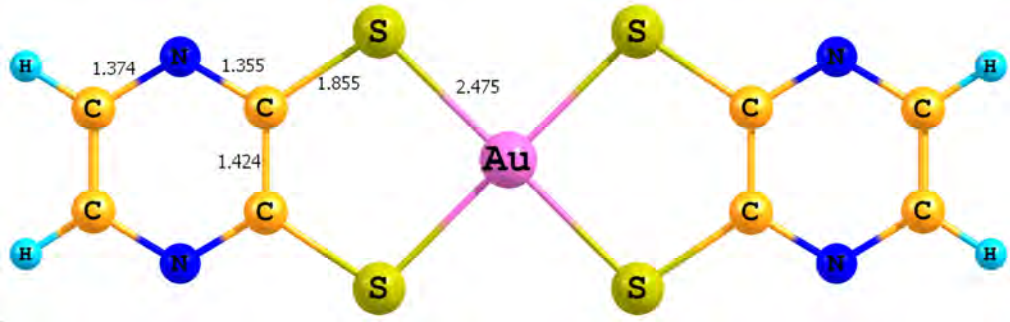

$Au(mnt)_2^-$ (**V**):

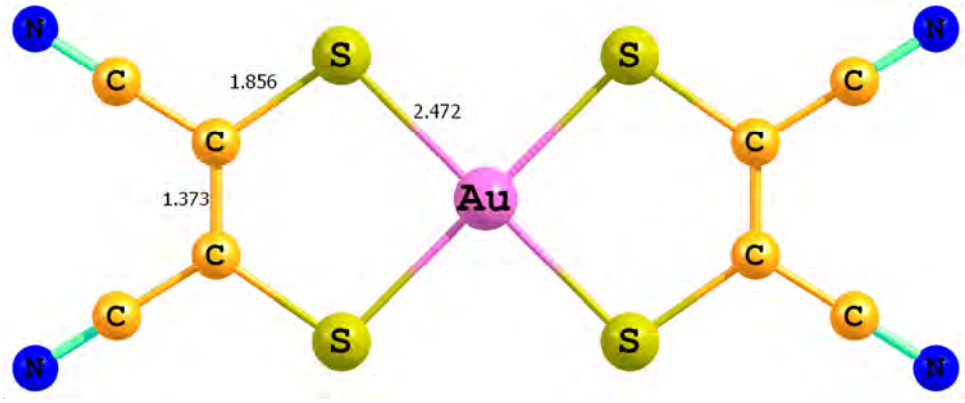

Figure S40: BLYP-D3/DZ-(COSMO:MeCN) optimized geometry of **3**·$(Cl)_8$, and selected M-M distances. The comparison with its X-Ray structure presented in Figure 3 of the main text show that the differences between both geometries are small (less than 0.7 Å for the Pd-Pd porphyrin and less than 0.8 Å for the Pd-Pd macrocycles), indicating that the 3D structure obtained from XRD analyses is well-reproduced computationally (including solvent effects), thus suggests retention of the structure in solution.

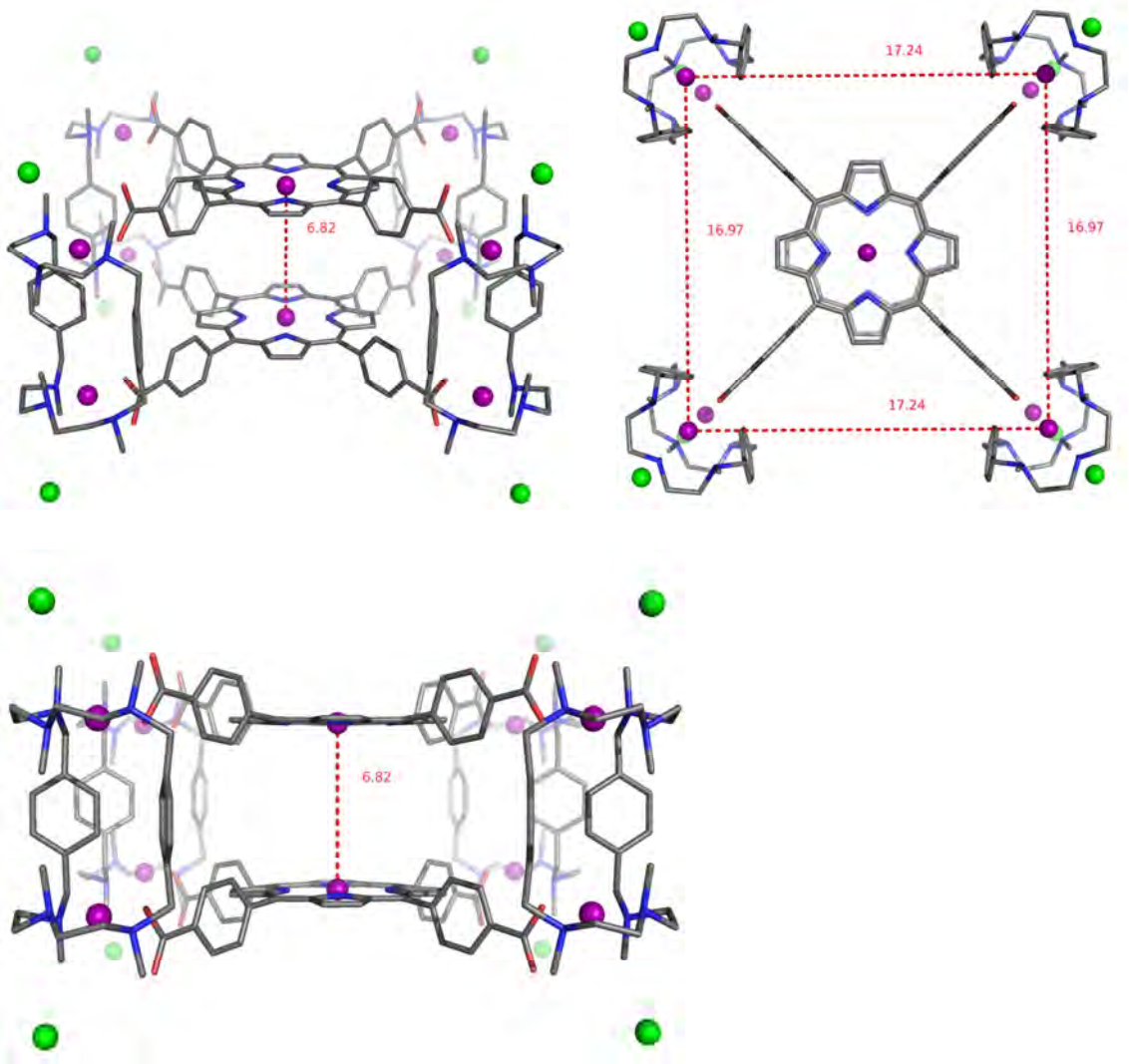

Figure S41: BLYP-D3/DZ-(COSMO:MeCN) optimized geometries of the π-π stacked model system using $Au(tdas)_2^-$ (**I**) as guest, Pd-Por{**I**}Pd-Por. The Pd-Au distance (Å) is represented.

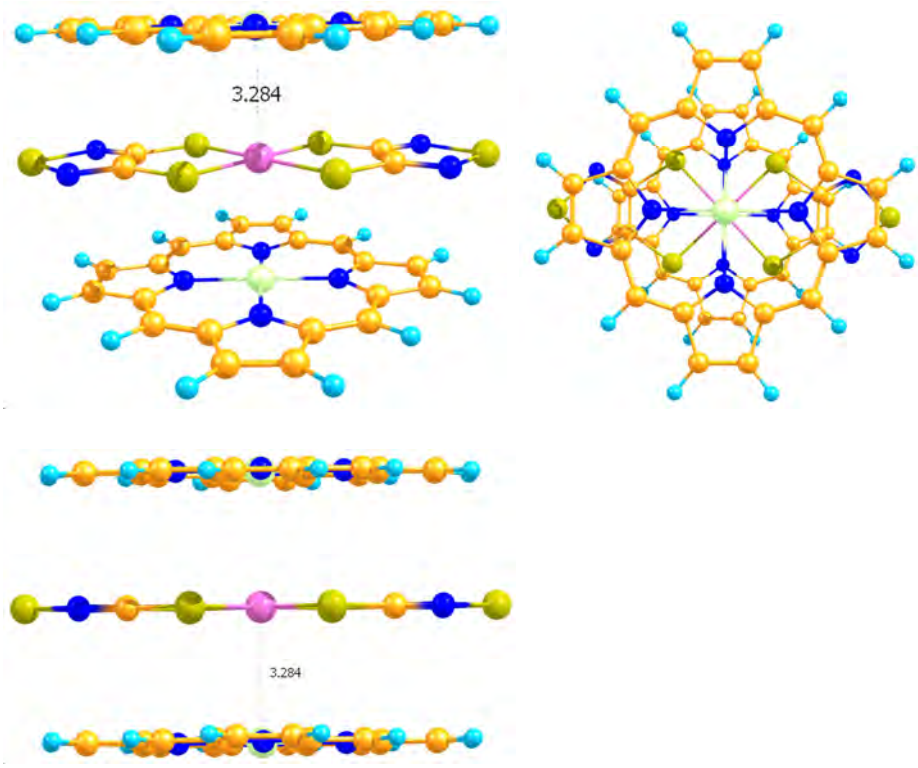

Figure S42: BLYP-D3/DZ-(COSMO:MeCN) optimized geometries of the π-π stacked model system using triflate anion as guest, Pd-Por{triflate$^-$}Pd-Por.

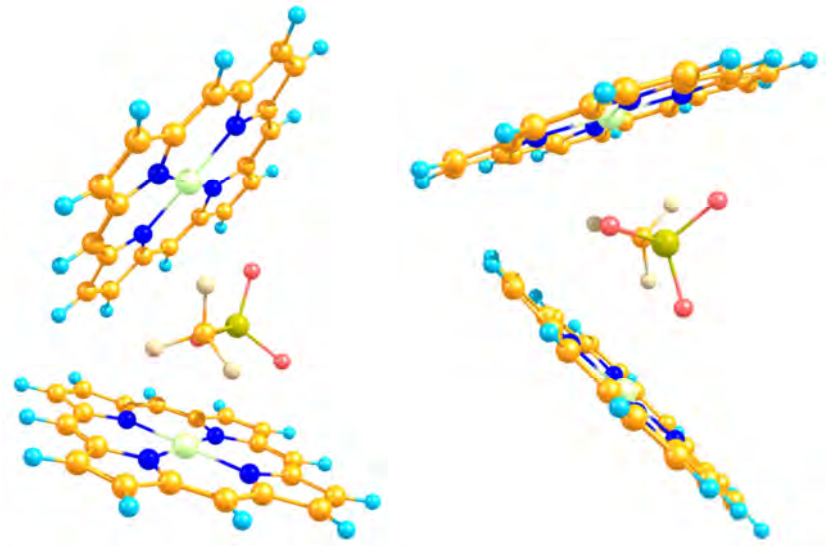

Figure S43. Crystal structure of macrocyclic compound **Pd-1**·$(CF_3COO)_4$. (H atoms and solvent molecules are omitted for clarity).

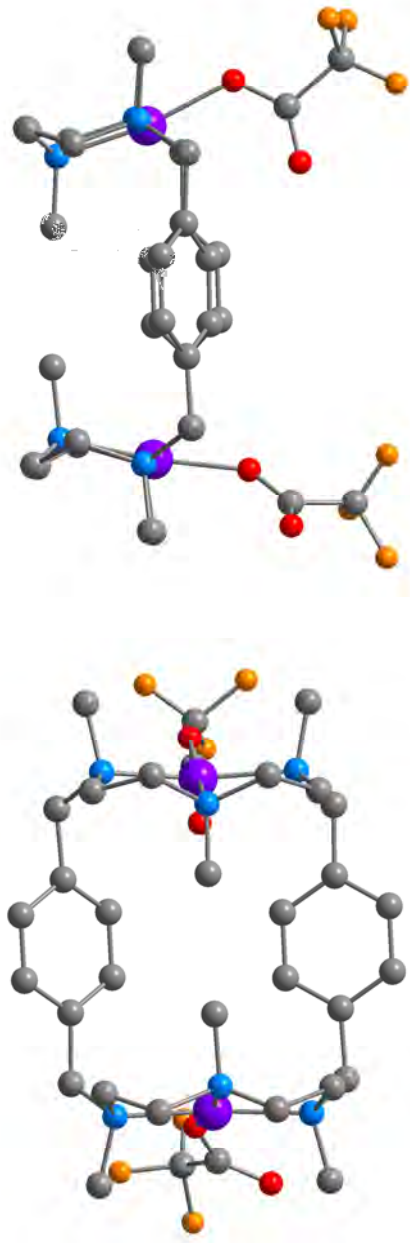

3. Supplementary Tables

Table S1. ESI-MS peaks of complex **II@3**·$(CF_3SO_3)_7$ from a 1:1 host:guest mixture. Experimental conditions: 100µM in CH_3CN.

	m/z Calculated	m/z Obtained
{**II@3**·$(CF_3SO_3)_5$}$^{2+}$	2893.7	2893.8
{**II@3**·$(CF_3SO_3)_4$}$^{3+}$	1879.4	1879.6
{**II@3**·$(CF_3SO_3)_3$}$^{4+}$	1372.3	1371.8
{**II@3**·$(CF_3SO_3)_2$}$^{5+}$	1068.0	1067.9
{**II@3**·(CF_3SO_3)}$^{6+}$	875.8	865.6
{**II@3**}$^{7+}$	729.4	729.1
{**3**·$(CF_3SO_3)_5$}$^{3+}$	1786.0	1785.3
{**3**·$(CF_3SO_3)_4$}$^{4+}$	1302.2	1301.8
{**3**·$(CF_3SO_3)_3$}$^{5+}$	1011.9	1012.5
{**3**·$(CF_3SO_3)_2$}$^{6+}$	818.5	818.0

Table S2. ESI-MS peaks of complex **V@3**·$(CF_3SO_3)_7$ from a 1:1 host:guest mixture. Experimental conditions: 100µM in CH_3CN.

	m/z Calculated	m/z Obtained
{**V@3**·$(CF_3SO_3)_4$}$^{3+}$	1895.4	1894.6
{**V@3**·$(CF_3SO_3)_3$}$^{4+}$	1384.3	1384.1
{**V@3**·$(CF_3SO_3)_2$}$^{5+}$	1077.6	1078.1
{**V@3**·(CF_3SO_3)}$^{6+}$	873.2	872.9
{**V@3**}$^{7+}$	727.1	727.1
{**3**·$(CF_3SO_3)_5$}$^{3+}$	1786.0	1787.3
{**3**·$(CF_3SO_3)_4$}$^{4+}$	1302.2	1302.2
{**3**·$(CF_3SO_3)_3$}$^{5+}$	1011.9	1011.5
{**3**·$(CF_3SO_3)_2$}$^{6+}$	818.5	818.7
{**3**·(CF_3SO_3)}$^{7+}$	680.2	680.1

Table S3. ESI-MS peaks of complex **VIII@3**·$(CF_3SO_3)_7$ from a 1:1 host:guest mixture. Experimental conditions: 100µM in CH_3CN.

	m/z Calculated	m/z Obtained
{**VIII@3**·$(CF_3SO_3)_4$}$^{3+}$	1894.8	1894.5
{**VIII@3**·$(CF_3SO_3)_3$}$^{4+}$	1383.8	1383.8
{**VIII@3**·$(CF_3SO_3)_2$}$^{5+}$	1077.2	1077.2
{**VIII@3**·(CF_3SO_3)}$^{6+}$	872.9	872.9
{**VIII@3**}$^{7+}$	726.8	726.7
{**3**·$(CF_3SO_3)_5$}$^{3+}$	1786.0	1786.6
{**3**·$(CF_3SO_3)_4$}$^{4+}$	1302.2	1302.1
{**3**·$(CF_3SO_3)_3$}$^{5+}$	1011.9	1011.7
{**3**·$(CF_3SO_3)_2$}$^{6+}$	818.5	818.3
{**3**·(CF_3SO_3)}$^{7+}$	680.2	680.1
{**3**}$^{8+}$	576.6	576.5

Table S4. ESI-MS peaks of complex **IX@3**·$(CF_3SO_3)_7$ from a 1:1 host:guest mixture. Experimental conditions: 100µM in CH_3CN.

	m/z Calculated	m/z Obtained
{**IX@3**·$(CF_3SO_3)_4$}$^{3+}$	1865.2	1864.9
{**IX@3**·$(CF_3SO_3)_3$}$^{4+}$	1361.7	1361.8
{**IX@3**·$(CF_3SO_3)_2$}$^{5+}$	1059.5	1059.3
{**IX@3**·(CF_3SO_3)}$^{6+}$	858.1	858.1
{**IX@3**}$^{7+}$	714.2	714.1
{**3**·$(CF_3SO_3)_5$}$^{3+}$	1786.0	1786.3
{**3**·$(CF_3SO_3)_4$}$^{4+}$	1302.2	1302.1
{**3**·$(CF_3SO_3)_3$}$^{5+}$	1011.9	1012.0
{**3**·$(CF_3SO_3)_2$}$^{6+}$	818.5	818.1
{**3**·(CF_3SO_3)}$^{7+}$	680.2	680.2
{**3**}$^{8+}$	576.6	576.5

Table S5. ESI-MS peaks of complex **X@3**·$(CF_3SO_3)_7$ from a 1:1 host:guest mixture. Experimental conditions: 100µM in CH_3CN.

	m/z Calculated	**m/z Obtained**
{**X@3**·$(CF_3SO_3)_4$}$^{3+}$	1849.3	1849.9
{**X@3**·$(CF_3SO_3)_3$}$^{4+}$	1349.7	1349.8
{**X@3**·$(CF_3SO_3)_2$}$^{5+}$	1050.0	1050.1
{**X@3**·(CF_3SO_3)}$^{6+}$	850.1	850.0
{**X@3**}$^{7+}$	707.4	707.5
{**3**·$(CF_3SO_3)_3$}$^{5+}$	1011.9	1011.7
{**3**·$(CF_3SO_3)_2$}$^{6+}$	818.5	818.4
{**3**·(CF_3SO_3)}$^{7+}$	680.2	680.3
{**3**}$^{8+}$	576.6	576.4

Table S6. Crystal Data and Structure Refinement for **Pd-1**·$(CF_3COO)_4$

	Pd-1·$(CF_3COO)_4$
Formula	$C_{34}\ H_{50}\ F_6\ N_6\ O_4\ Pd_2$,, $2(C_2\ F_3\ O_2)$
fw	1259.76
cryst system	Monoclinic
space group	P21/c
a (Å)	13.2030(13)
b (Å)	15.7306(15)
c (Å)	25-043(13)
α (deg)	90.00
β (deg)	99.046(14)
Y (deg)	90.00
V (Å^3)	5136(8)
Z	4
*D*c (g cm-3)	1.629
T (K)	180(2) K
λ (Mo KR) (Å)	0.71073
μ (mm-1)	0.803
2*Θ* max (deg)	28.28
reflns collected	77649
independent reflns	12019
	(*R*int= 0.1394)
parameters	768
GOF on F^2	1.093
R/R_w	R1 = 0.049, wR2 = 0.1409

4. Supplementary References

(1) (a) Menif, R.; Martell, A. E.; Squattrito, P. J.; Clearfield, A., Inorg. Chem. 1990, 29, 4723-4729. (b) A. Company et al., Inorg. Chem. 2006, 45, 2501–2508.

(2) X. Ribas, J.C. Dias, J. Morgado, K. Wurst, M. Almeida, T. Parella, J. Veciana, C. Rovira, Angew. Chem. Int. Ed. Engl. 2004, 43, 4049-4052.

(3) E.J. Baerends, ADF2010.01, SCM, Amsterdam, The Netherlands.

(4) G. te Velde, F. M. Bickelhaupt, E. J. Baerends, C. Fonseca Guerra, S. J. A. Van Gisbergen, J. G. Snijders, T. Ziegler, J. Comput. Chem. 2001, 22, 931-967

(5) M. Swart, F. M. Bickelhaupt, J. Comput. Chem. 2008, 29, 724-734.

(6) A. D. Becke, Phys. Rev. A 1988, 38, 3098-3100

(7) C. Lee, W. Yang, R. G. Parr, Phys. Rev. B 1988, 37, 785-789

(8) S. Grimme, J. Antony, S. Ehrlich, H. Krieg, J. Chem. Phys. 2010, 132, 154104

(9) A. Klamt, G. Schüürmann, J. Chem. Soc. Perkin Trans. 2 1993, 799-805

(10) C. C. Pye, T. Ziegler, Theoret. Chem. Acc. 1999, 101, 396-408

(11) M. Swart, E. Rösler, F. M. Bickelhaupt, Eur. J. Inorg. Chem. 2007, 3646-3654

(12) Grimme, J. Antony, S. Ehrlich, H. Krieg, J. Chem. Phys. 2010, 132, 154104

(13) F. Feixas, E. Matito, J. Poater, M. Solà, J. Comput. Chem. 2008, 29, 1543–1554

(14) F. Feixas, M. Solà, M. Swart, Can. J. Chem. 2009, 87, 1063-1073

(15) Feixas F., Jiménez-Halla J.O.C., Matito E., Poater J., Solà M., Polish J. Chem. 2007, 81, 783-797

(16) T. M. Krygowski, J. Chem. Inf. Comput. Sci. 1993, 33, 70

(17) Y. Jung, T. Heine, P. v. R. Schleyer, M. Head-Gordon, J. Am. Chem. Soc., 2004, 126, 3132–3138

(18) G. M. Sheldrick, SHELXL-97, Program for refinement of crystal structures, University of Göttingen, Germany, 1997

(19) Z. Otwinowski; W. Minor, Methods Enzymol., 1997, 276, 307.

(20) P.T. Kissinger, W.R. Heineman; J. Chem. Edu. 1983, 9, 702-706.

(21) Y. Wang, E.I. Rogers, R.G. Compton; J. Electroanal. Chem. 2010, 1, 15-19.0

Supporting Information Chapter IV

SPONGE-LIKE MOLECULAR CAGE FOR PURIFICATION OF FULLERENES

Table of Contents

All the supplementary data including optimized xyz cartesian coordinates for all DFT structures and CIF files of the corresponding crystal structures can be obtained from:

http://www.nature.com/ncomms/2014/141126/ncomms6557/full/ncomms6557.html

Supplementary Figures

Supplementary Figure 1. Fluorescence titration between nanocapsule 4·(BArF)$_8$ and C_{60}. a) Corrected emission spectrum for the titration between cage **4**·(BArF)$_8$ ($1.08 \cdot 10^{-7}$ M) and **C_{60}** fullerene ($4.36 \cdot 10^{-6}$ M). Excitation at 431 nm. b) Fit of the experimental data at 603 nm and 655 nm to the calculated theoretical binding curve for the binding model (only the host and the host-guest adduct give emission).

a)

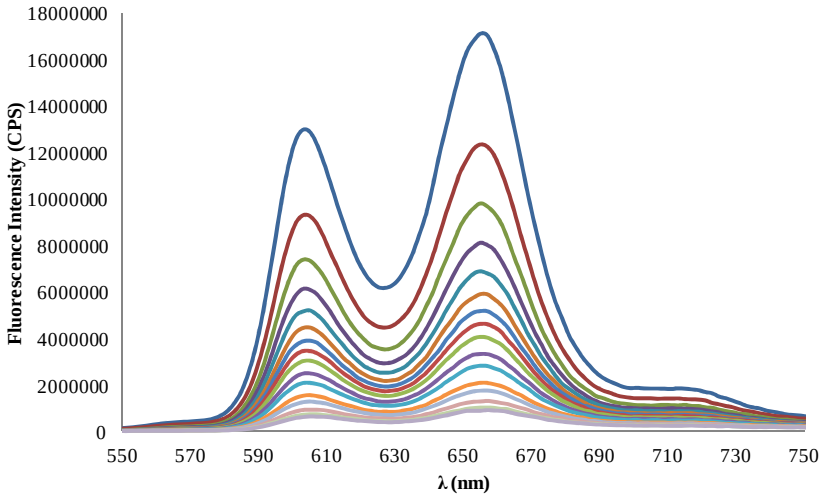

b)

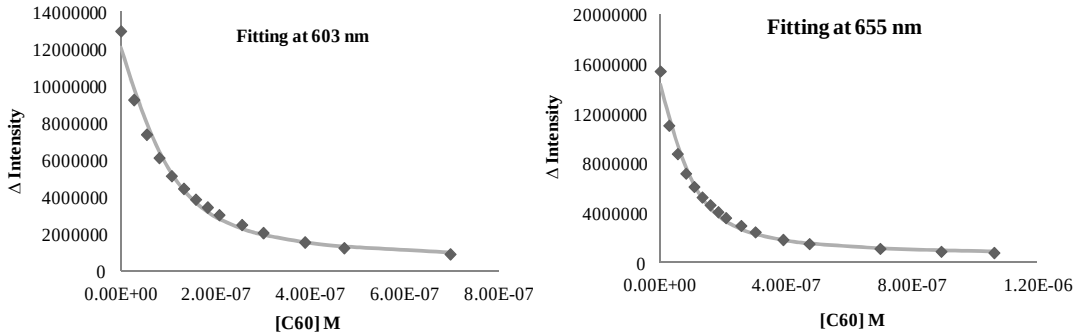

Supplementary Figure 2. Fluorescence titration between nanocapsule 4·(BArF)$_8$ and C$_{70}$. a) Corrected emission spectrum for the titration between cage **4**·(BArF)$_8$ ($1.08 \cdot 10^{-8}$ M) and **C$_{70}$** fullerene ($4.36 \cdot 10^{-7}$ M). Excitation at 431 nm. b) Fit of the experimental data at 611 nm and 657 nm to the calculated theoretical binding curve for the binding model (only the host and the host-guest adduct give emission).

a)

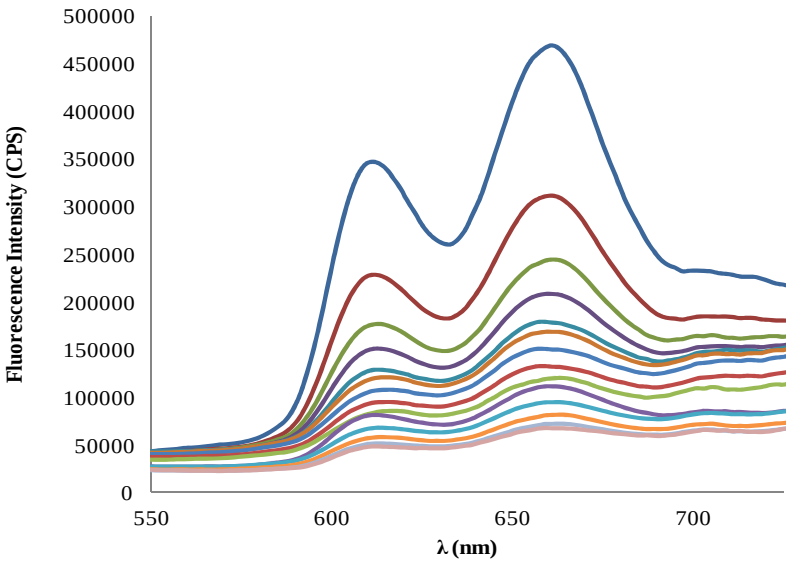

b)

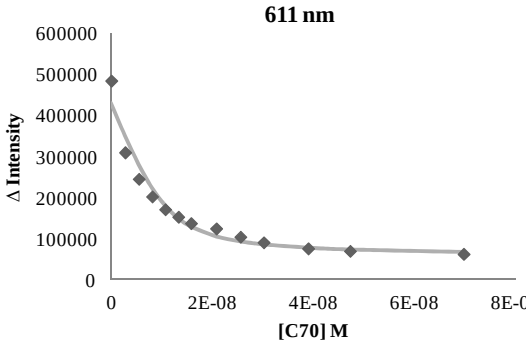

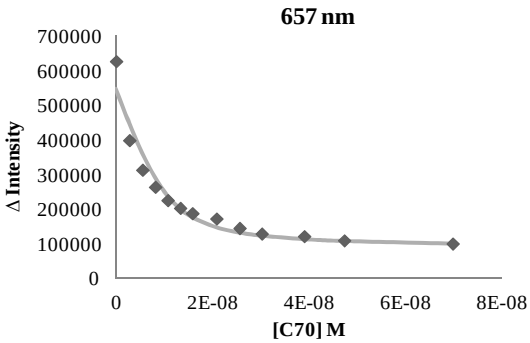

Supplementary Figure 3. Superposition between DFT optimized structures for $C_{60}\subset 4\cdot(Cl)_8$ $C_{70}\subset 4\cdot(Cl)_8$, and $C_{84}\subset 4\cdot(Cl)_8$ - (IPR (D_2)-22) systems and X-Ray structure of empty $4\cdot(BArF)_8$. All distances are given in Å. Cl, H atoms and fullerene structures are omitted for clarity.

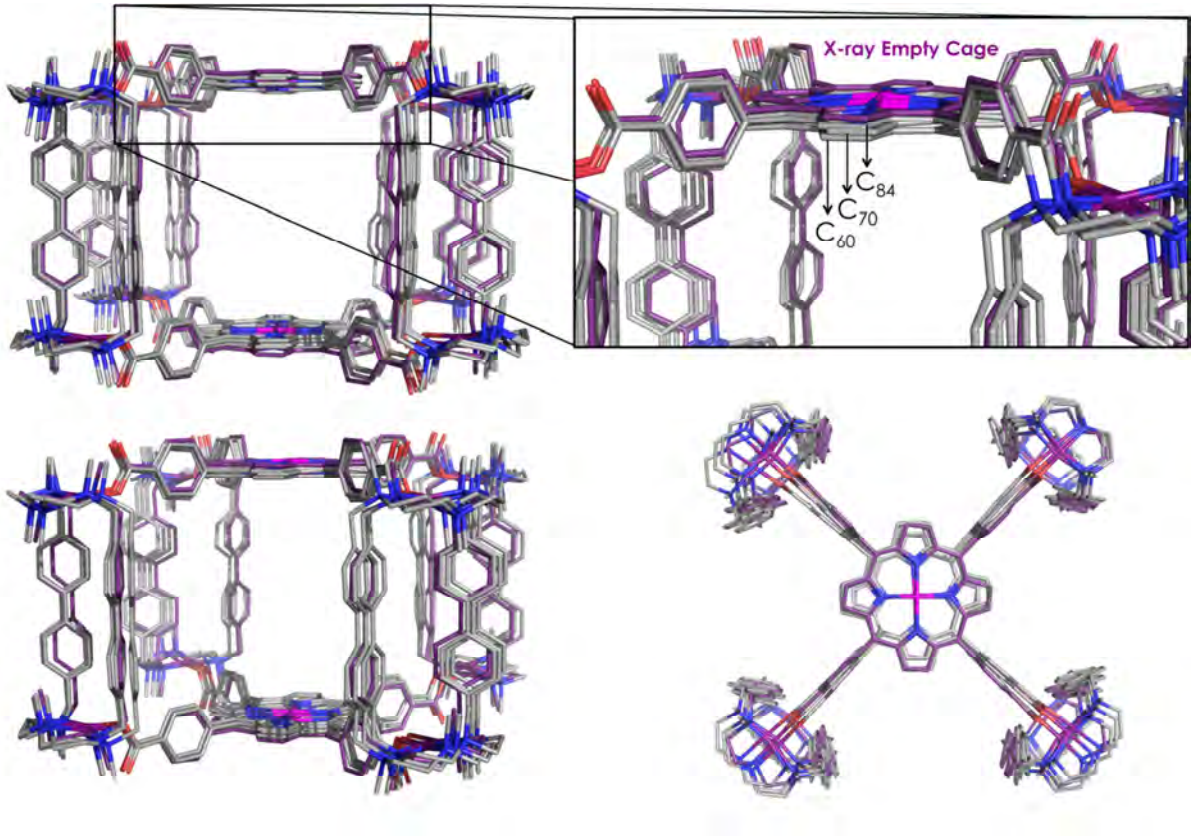

Supplementary Figure 4. C_{84}⊂4·$(Cl)_8$ (IPR (D_2)-22)) DFT optimized structure. All distances are given in Å. Cl and H atoms are omitted for clarity.

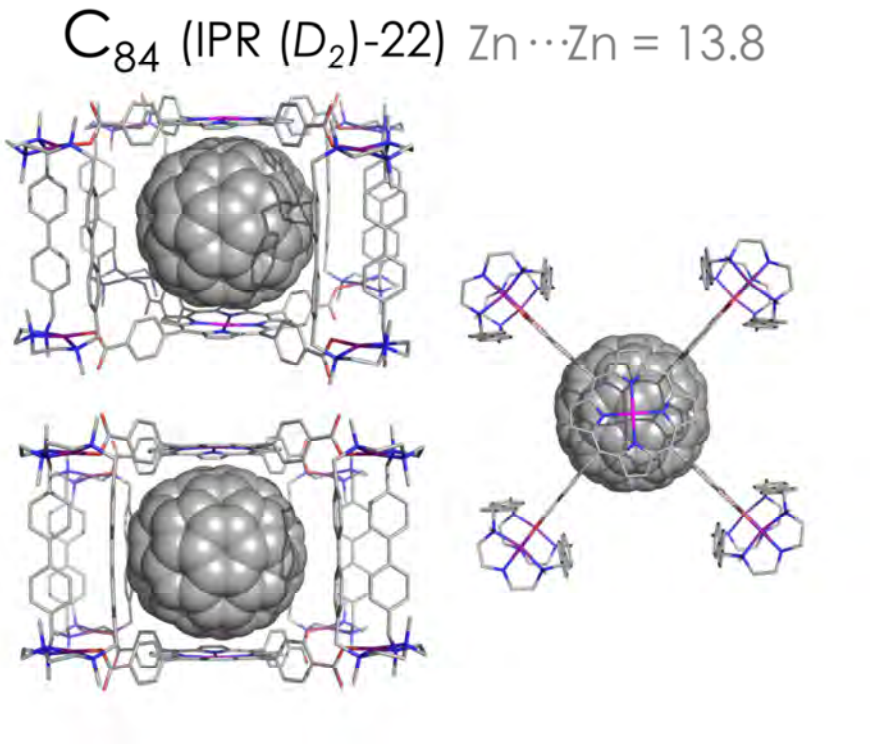

Supplementary Figure 5. C_{84}⊂4·$(Cl)_8$ (IPR (D_{2d})-23)) DFT optimized structure. All distances are given in Å. Cl and H atoms are omitted for clarity.

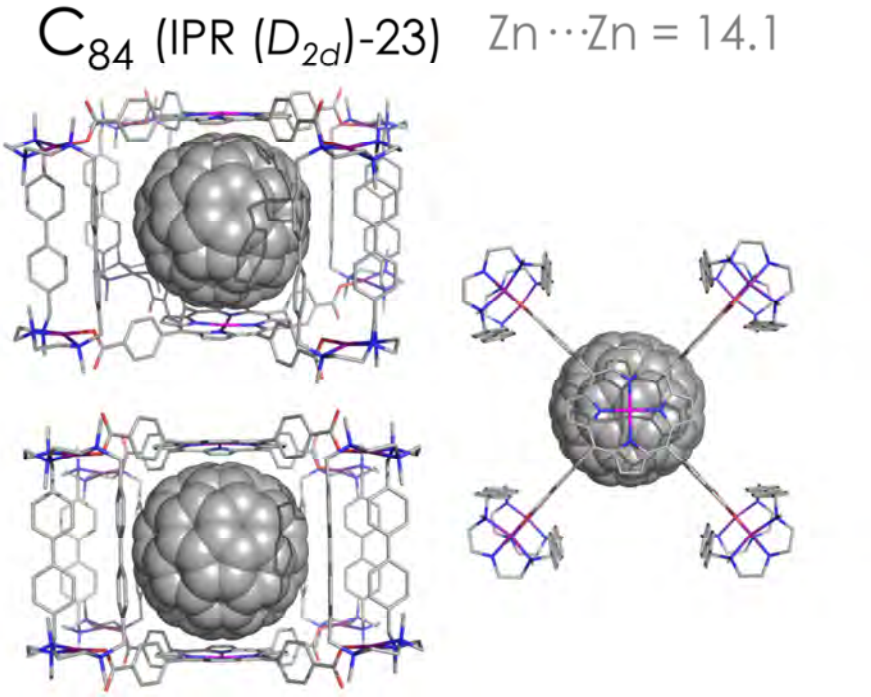

Supplementary Figure 6.Torsion angles measured for: a) X-Ray **4·(**BArF)$_8$ ∠(C20-C20'-C20''-C45) = -178.85 º, b) X-Ray **C$_{60}$⊂4·(**BArF)$_8$ ∠(C20-C20'-C20''-C45) = -175.73 º, c) X-Ray **C$_{70}$⊂4·(**BArF)$_8$ ∠(C20-C20'-C20''-C45) = -176.28 º.H atoms are omitted for clarity:

a)

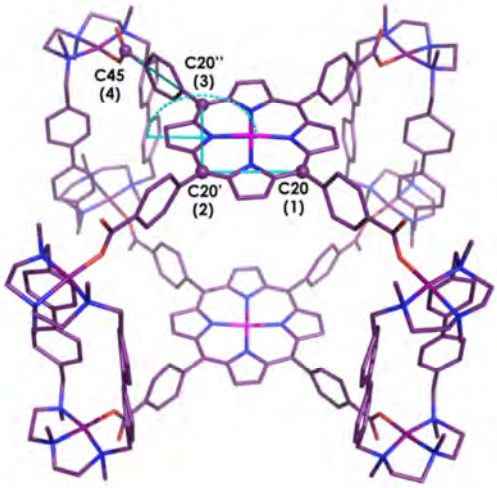

b)

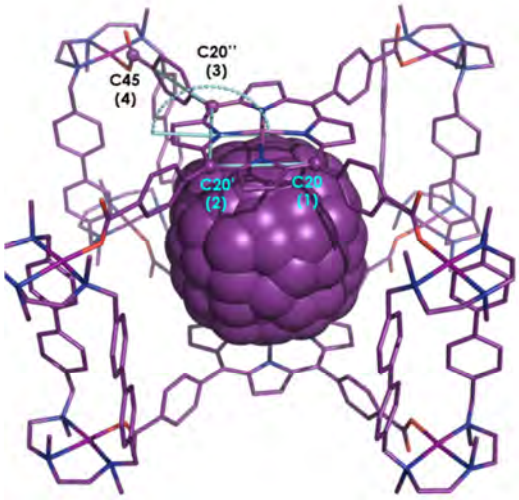

c)

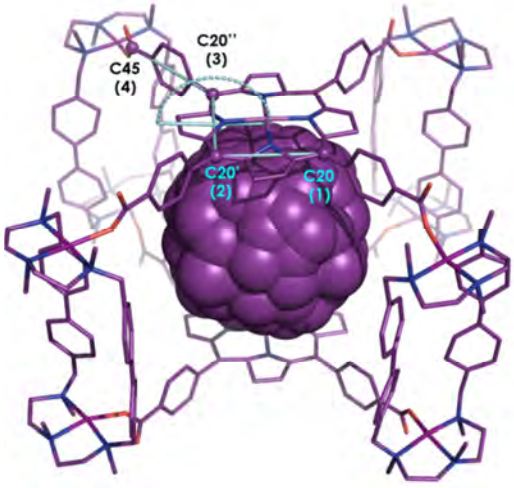

Supplementary Figure 7. HRMS spectrum of the mixture of 4·(BArF)$_8$ with 1 eq. of C_{60} and 1 eq. of C_{70}. Experimental conditions: 100 µM in Toluene/acetonitrile (4/1), registered with a Bruker MicroTOF-Q-II exact mass spectrometer.

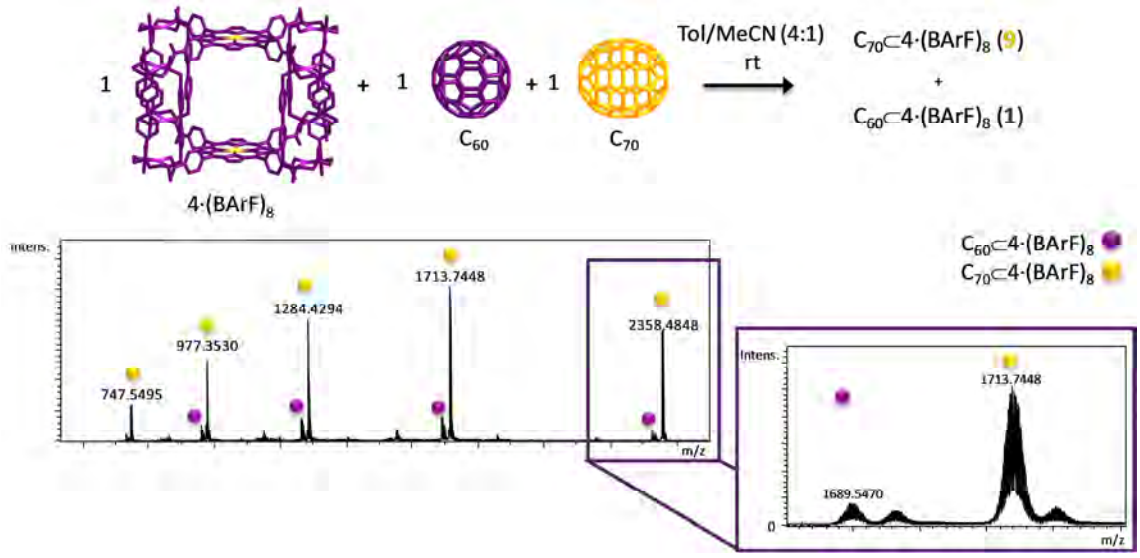

Supplementary Figure 8. HRMS spectrum of the mixture of 4·(BArF)$_8$ with 0.4 eq. of C_{60} and 0.4 eq. of C_{70}. Experimental conditions: 100 µM in Toluene/CH_3CN (4/1), registered with a Bruker MicroTOF-Q-II exact mass spectrometer.

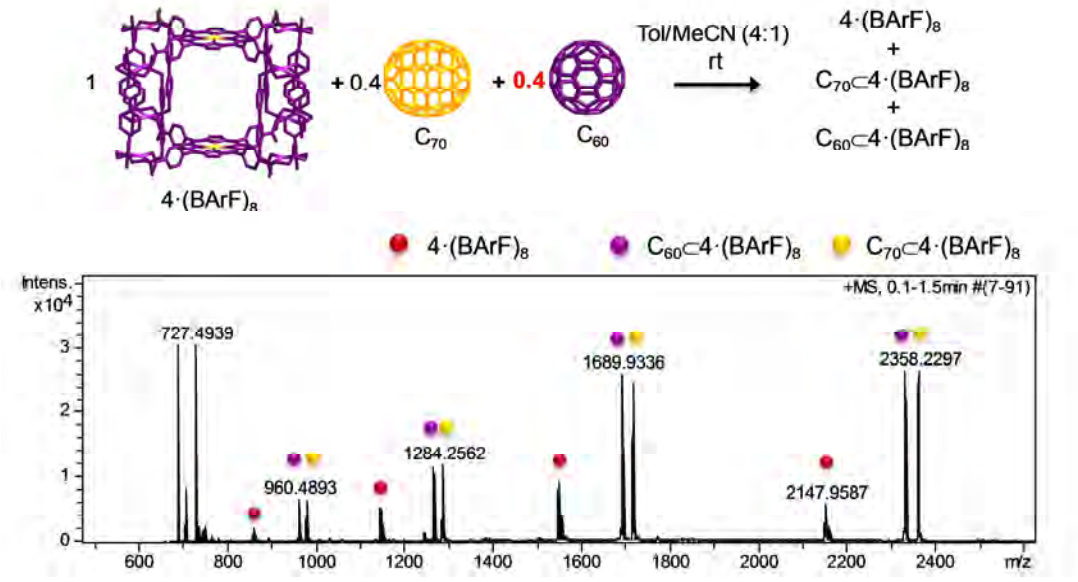

Supplementary Figure 9. HRMS spectrum of the mixture of 4·(BArF)$_8$ with 1 eq. of C$_{60}$ and 9 eq. of C$_{70}$. Experimental conditions: 100 μM in Toluene/CH_3CN (4/1), registered with a Bruker MicroTOF-Q-II exact mass spectrometer.

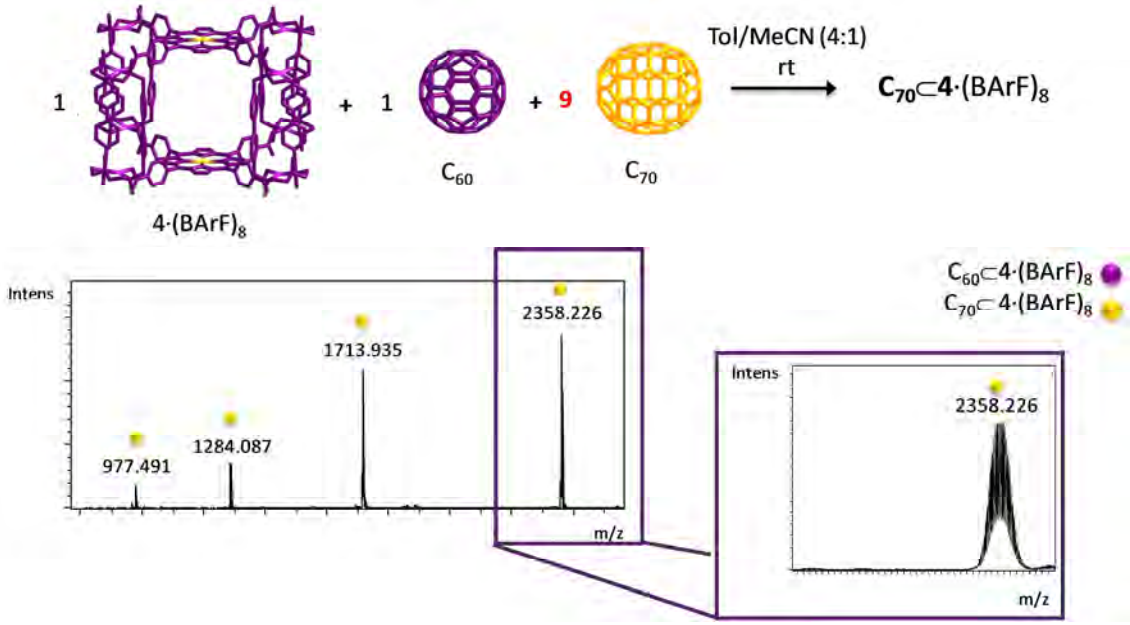

Supplementary Figure 10. HRMS spectrum of the mixture of 4·(BArF)$_8$ with 1 eq. of C$_{70}$ and 10 eq. of C$_{60}$. Experimental conditions: 100 μM in Toluene/CH_3CN (4/1), registered with a Bruker MicroTOF-Q-II exact mass spectrometer.

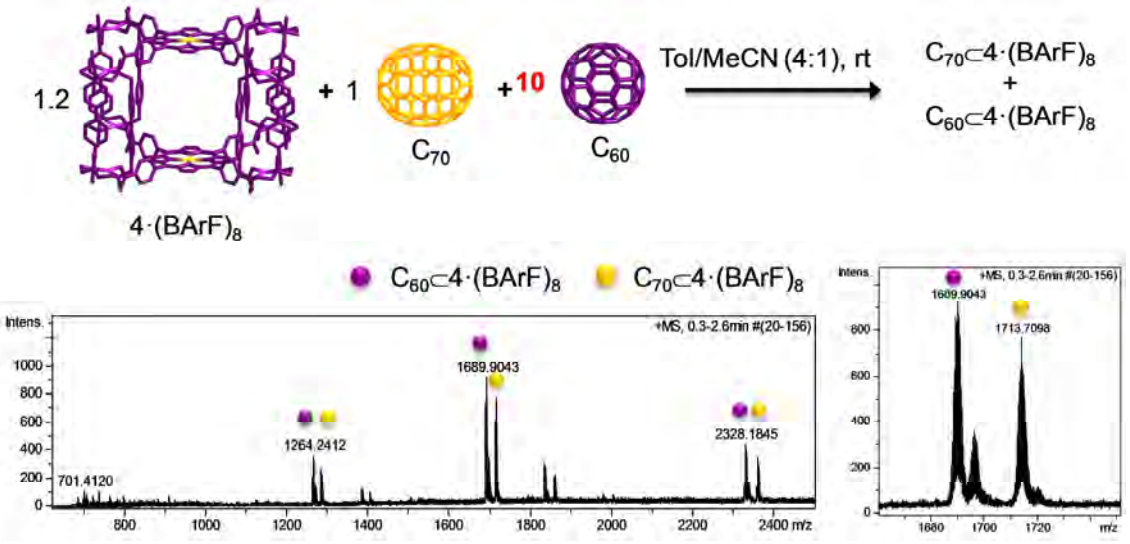

Supplementary Figure 11. DFT porphyrin-fullerene interaction analysis: Non-Covalent Interaction (NCI) analysis. ***a)*** and ***b)*** Representation of the gradient isosurfaces (s = 0.3 a.u.) using a RGB scale according to the sign(λ_2) over the range -0.07 to 0.07 a.u.. ***c)*** s(ρ) plot of the promolecular density in -0.2 to 0.2 range. ***d)*** s(ρ) plot of the promolecular density in -0.012 to 0.012 range. The peaks that appear at low densities (ρ), correspond to the different non-covalent interactions. All the peaks with lower values than 0.01 a.u., correspond to weak dispersion interactions, represented by the green color in the isosurface (a) and b)) representations. The larger number of peaks in this region, the larger the dispersion interaction is. Thus, focusing on the last d) superposition between C_{60} (in green) and C_{70} (in red) reduced gradients, we can see that dispersion interactions are much larger in the C_{70}-porphyrin dimer case. The increase of the π-π stacking interaction when going from C_{60} to C_{70} is clearly observed.Moreover, it has recently been reported that there exists a correlation between the binding energy of the stacked molecules and low gradient peaks density values.[19] As a consequence, the shift of the C_{60} *ca*. -0.004 a.u. NCI peak associated with the C···C dispersion interaction towards bigger density values for the C_{70} system (*ca*. -0.005) is indicative of the larger π-π stacking interaction (see superimposed reduced densities in d)).All these observations are in agreement with the computed interaction energies (see Table S5) for both systems, being the C_{70} model 1.5 kcal/mol more stable than C_{60} one because of the larger π-π stacking interaction. This is in line with the experimental observations for the entire supramolecular system

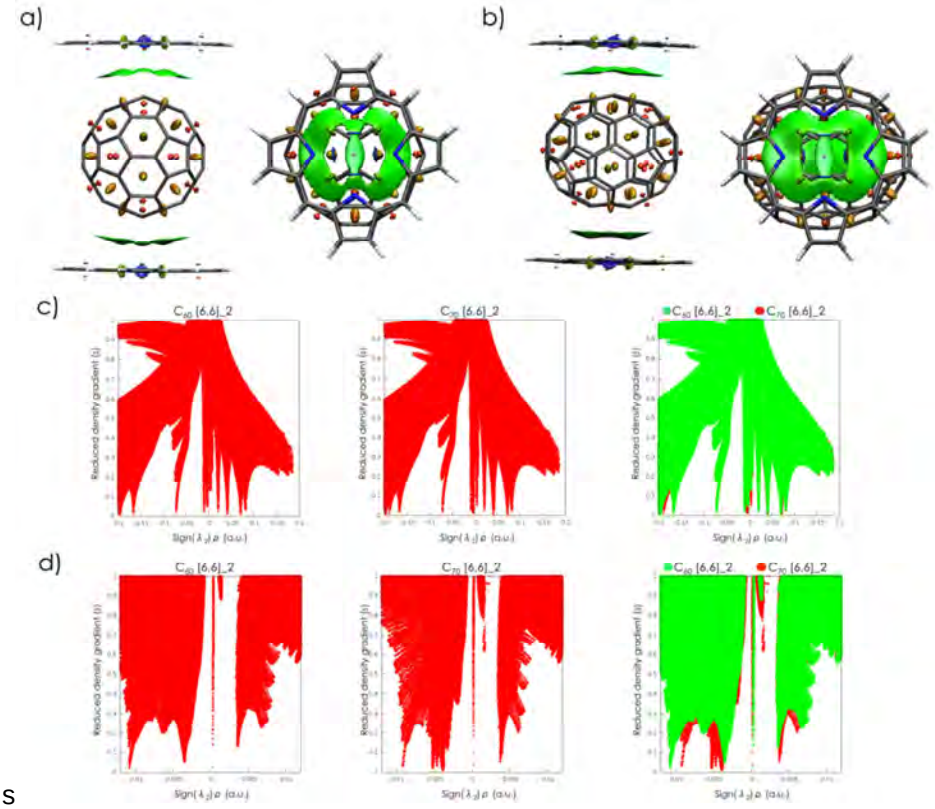

S

Supplementary Figure 12. Spectra of different fullerene adducts obtained from fullerene extract ion a tolunene/acetonitrile (4/1) mixture at r.t. different **4**·$(BArF)_8$/Fullerene Extract ratios were used. Experimental conditions: 100 μM in CH_3CN, registered with a Bruker MicroTOF-Q-II exact mass spectrometer.

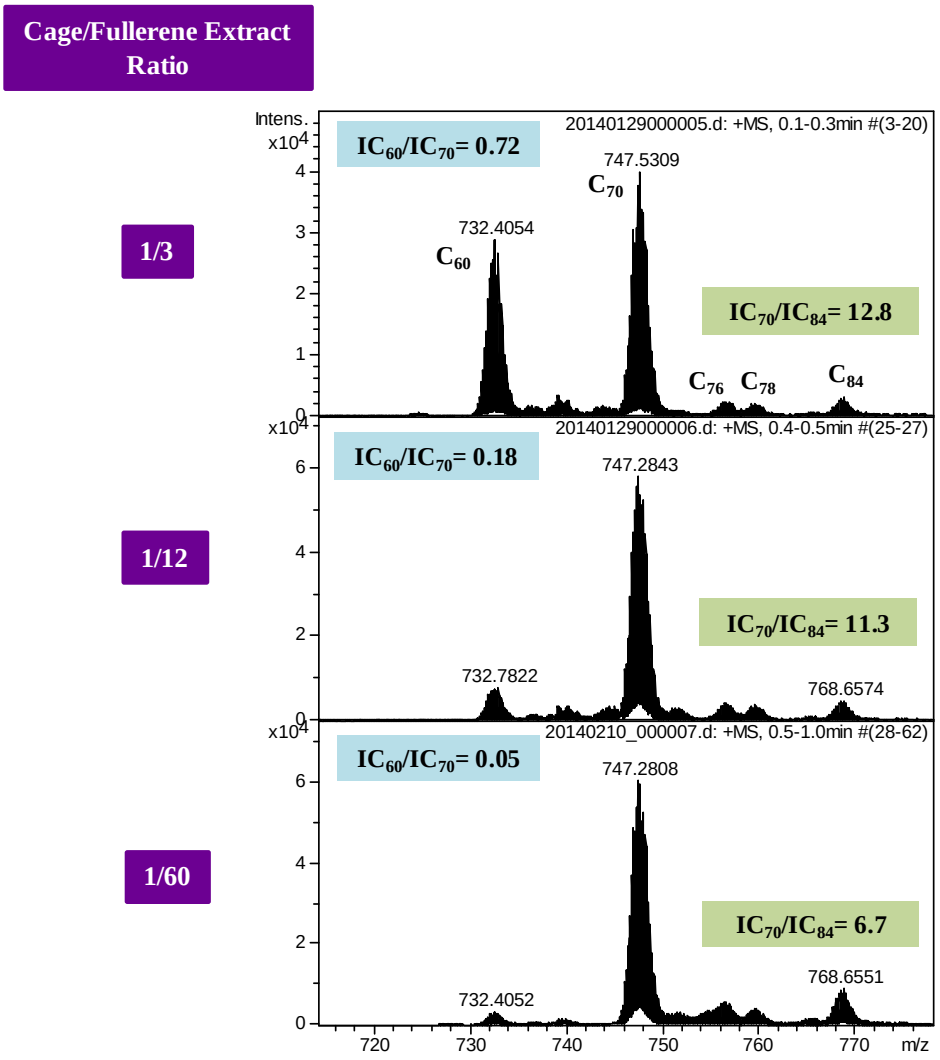

Supplementary Figure 13. ESI-MS spectrum of fullerene soot⊂4·(BArF)$_8$ host-guest complex. Calculated peaks are showed in colour red. Experimental conditions: 100 μM in Toluene/CH_3CN (4/1), registered with a Bruker MicroTOF-Q-II exact mass spectrometer.

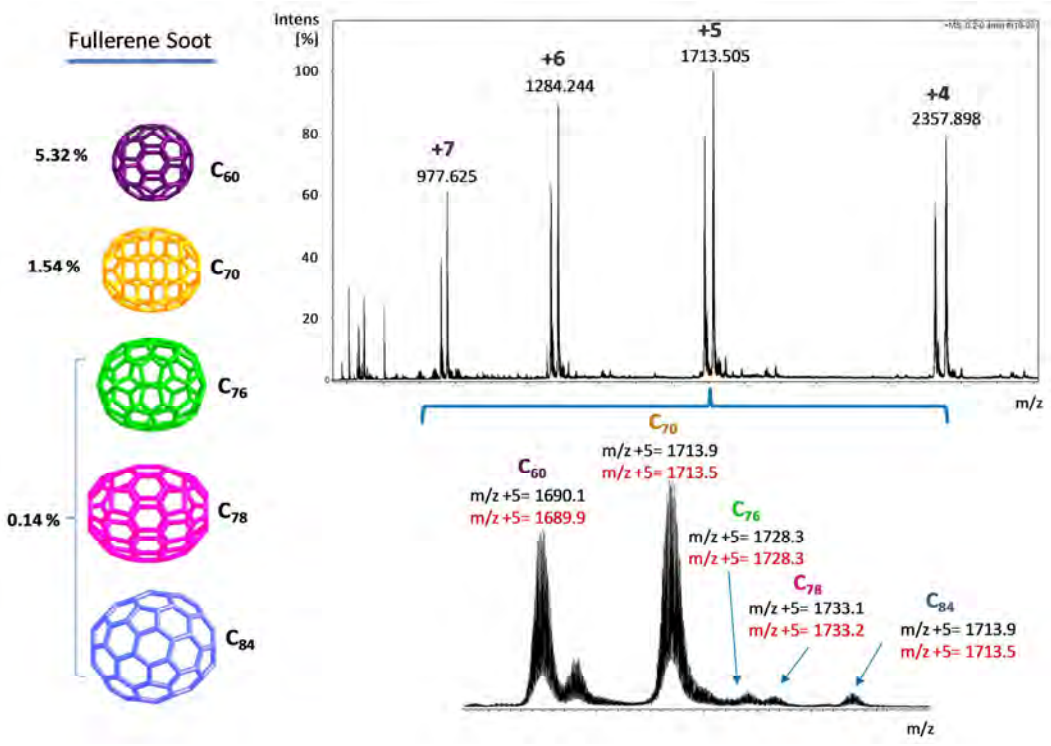

Supplementary Figure 14. Grain size study. Grain size distribution and representative FESEM image of **4**·(BArF)$_8$ powder.

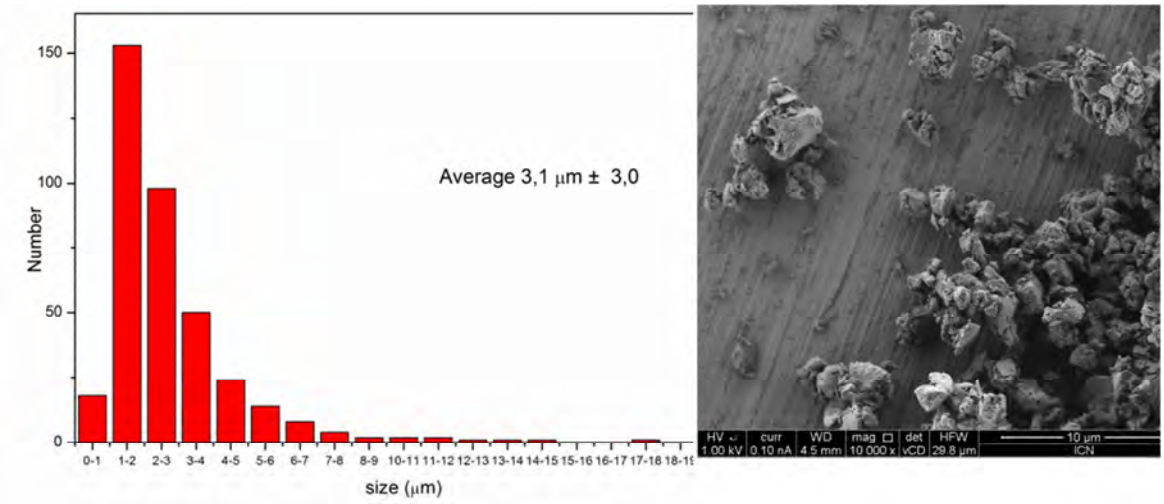

Supplementary Figure 15. HRMS spectrum of C_{70}⊂4·$(BArF)_8$ host-guest complex, formed using 4·$(BArF)_8$ as a solid and C_{70} dissolved in toluene. Experimental conditions: 100 μM in CH_3CN, registered with a Bruker MicroTOF-Q-II exact mass spectrometer.

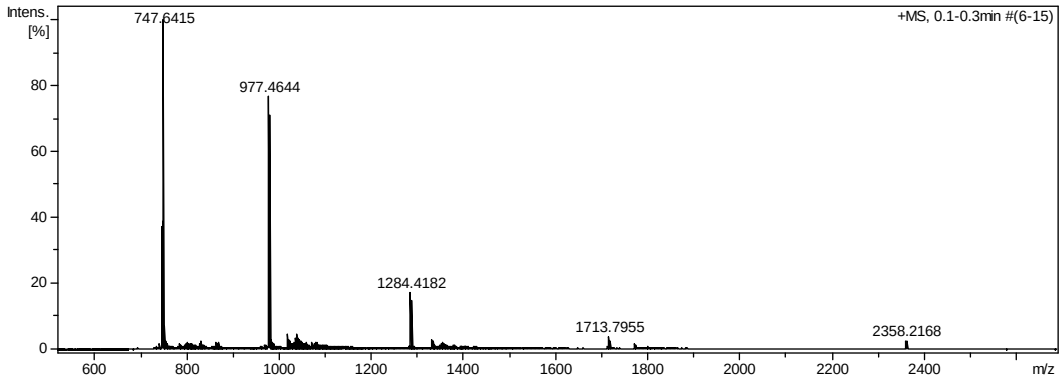

Supplementary Figure 16. HRMS spectra of different fullerene adducts obtained from fullerene extract in toluene, and 4·$(BArF)_8$ in the solid state. Different **4**·$(BArF)_8$/Fullerene Extract ratios were used. Experimental conditions: 100 μM in CH_3CN, registered with a Bruker MicroTOF-Q-II exact mass spectrometer.

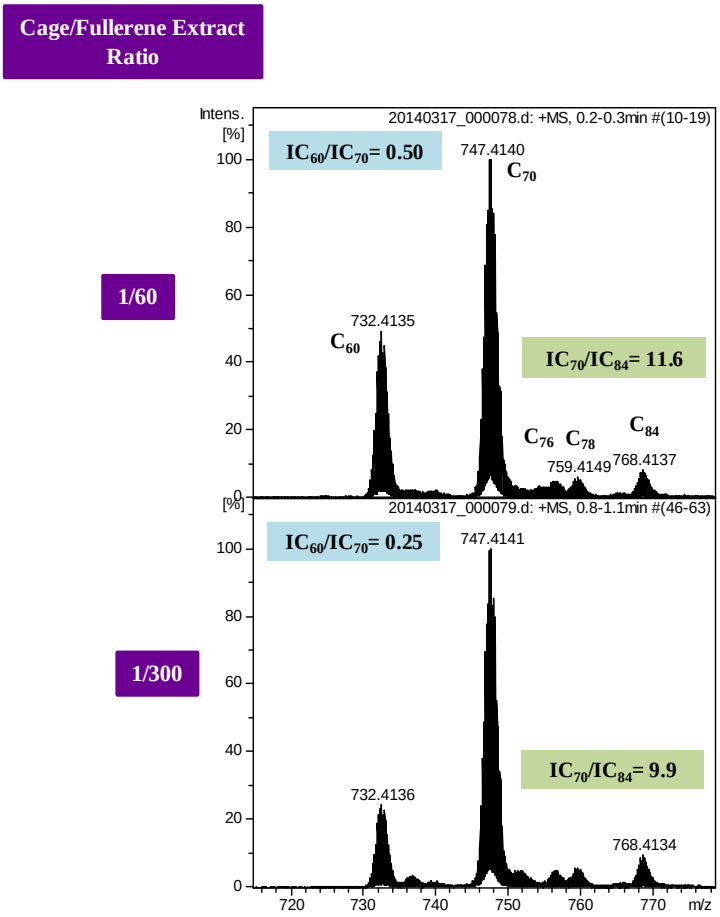

Supplementary Figure 17. HRMS spectrum of $C_{70}\subset 4\cdot(CF_3SO_3)_8$ host-guest complex, formed using $4\cdot(CF_3SO_3)_8$ as a solid and C_{70} dissolved in toluene. Experimental conditions: 100 μM in CH_3CN, registered with a Bruker MicroTOF-Q-II exact mass spectrometer.

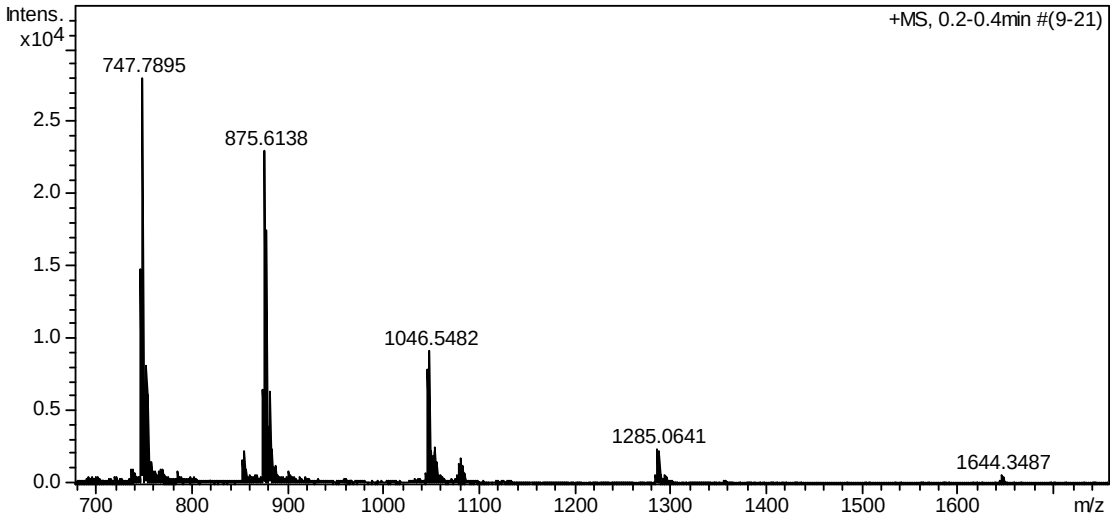

Supplementary Figure 18. Flow chart for the C_{60} extraction. Experimental protocol for the C_{60} extraction from **4**·$(BArF)_8$.

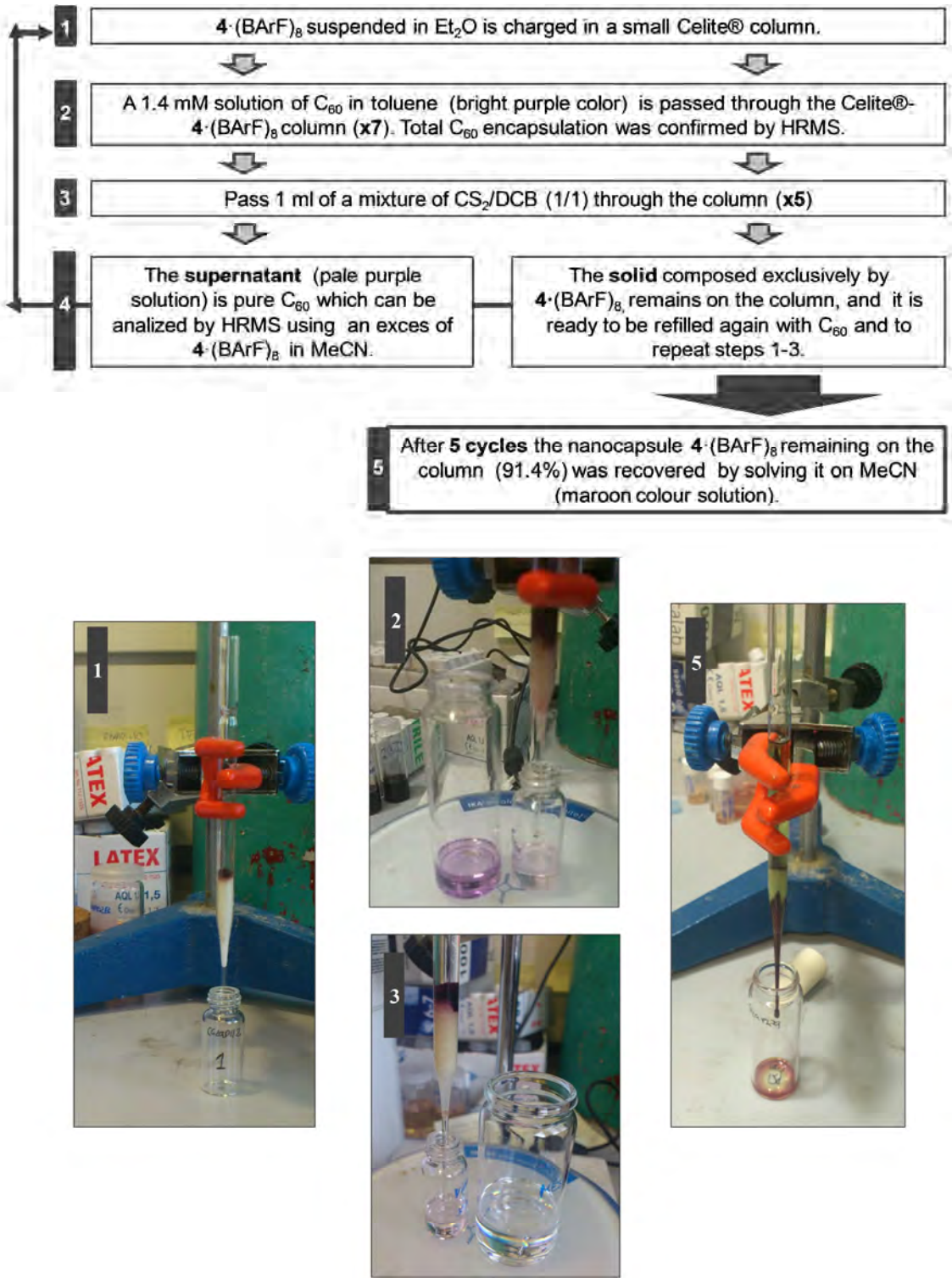

Supplementary Figure 19. Flow chart for the Fullerene-Extract extraction. Experimental protocol for the Fullerenen-Extract extraction from **4**·$(BArF)_8$.

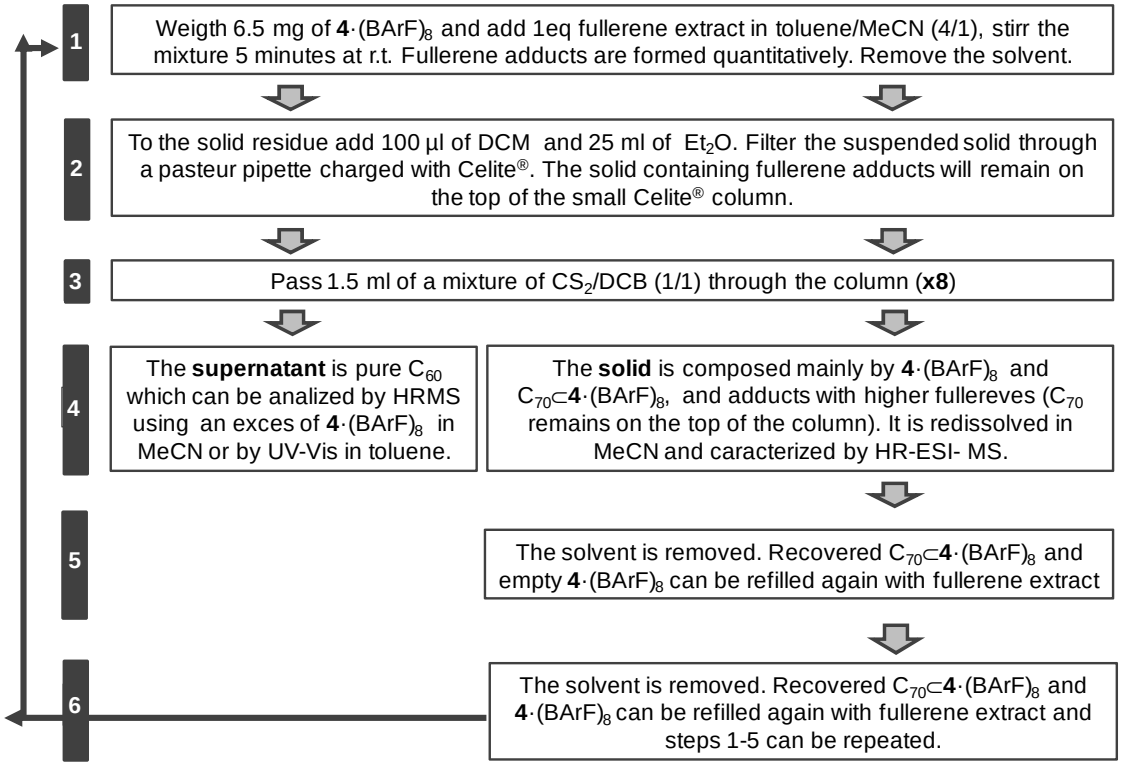

Supplementary Figure 20. Acid/base treatment of 4·$(CF_3SO_3)_8$. HRMS of the decomposition (10 eq of triflic acid)-reconstruction (NEt_3) of nanocage **4**·$(CF_3SO_3)_8$ to liberate pure C_{70}.

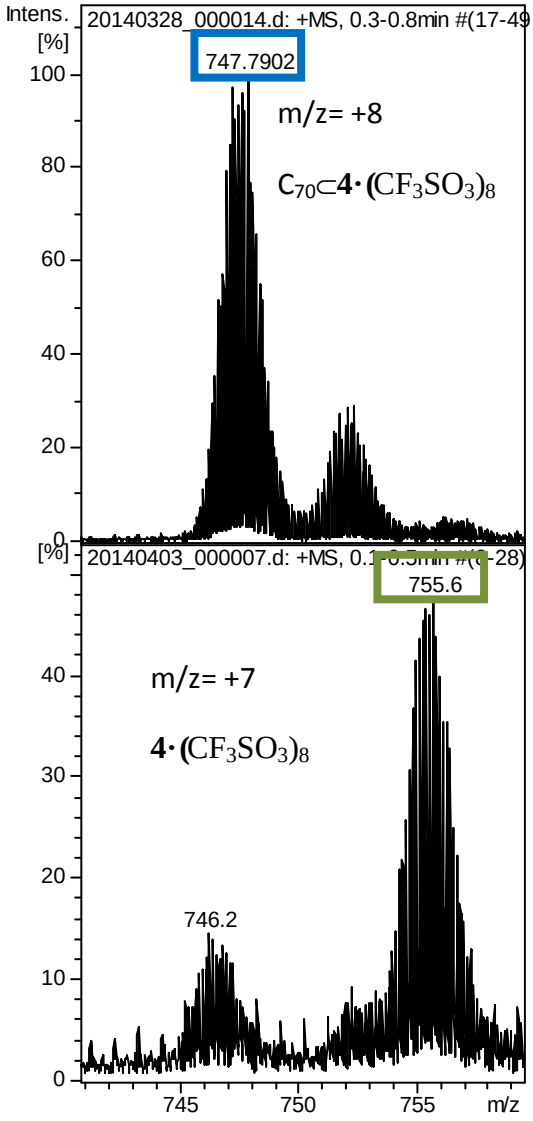

Supplementary Figure 21. Synthesis of 1b ligand. Schematich representation for the synthesis of Me2pp (**1b**) ligand.

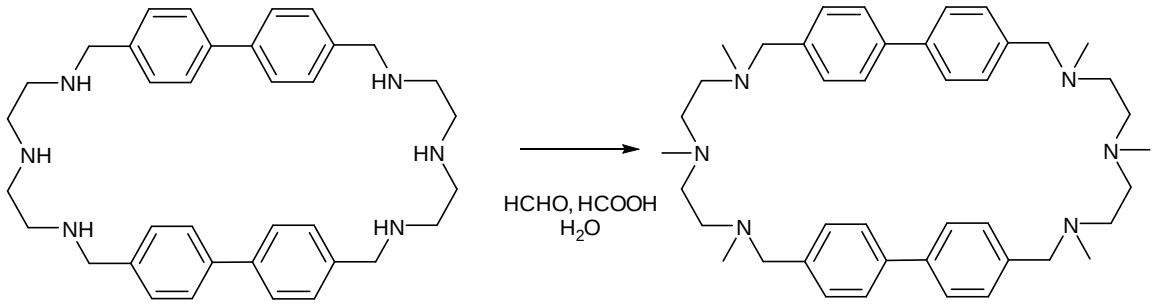

H2pp Me2pp (**1b**)

Supplementary Figure 22. ^{1}H-NMR of Me2pp (1b) macrocycle. Experiment performed in $CDCl_3$ at 298 K (400 MHz)

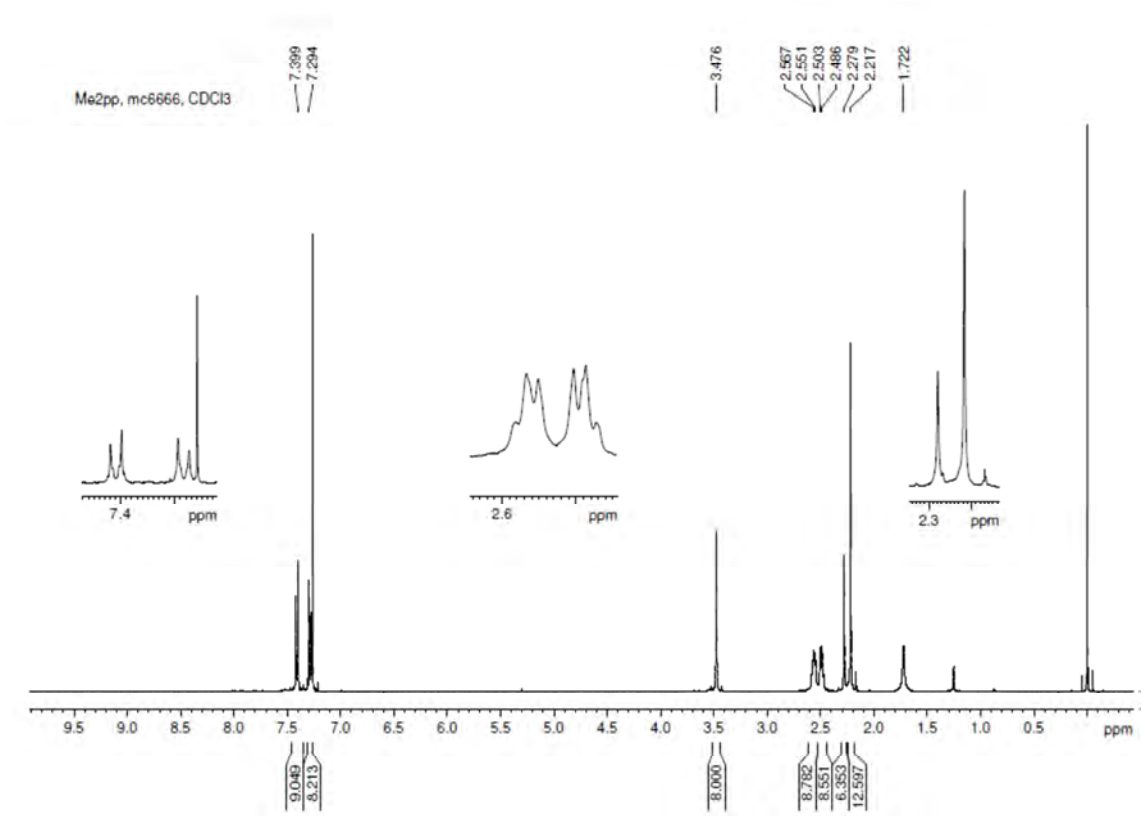

Supplementary Figure 23. ^{13}C-NMR of Me2pp (1b) macrocycle. Experiment performed in $CDCl_3$ at 298 K (100 MHz)

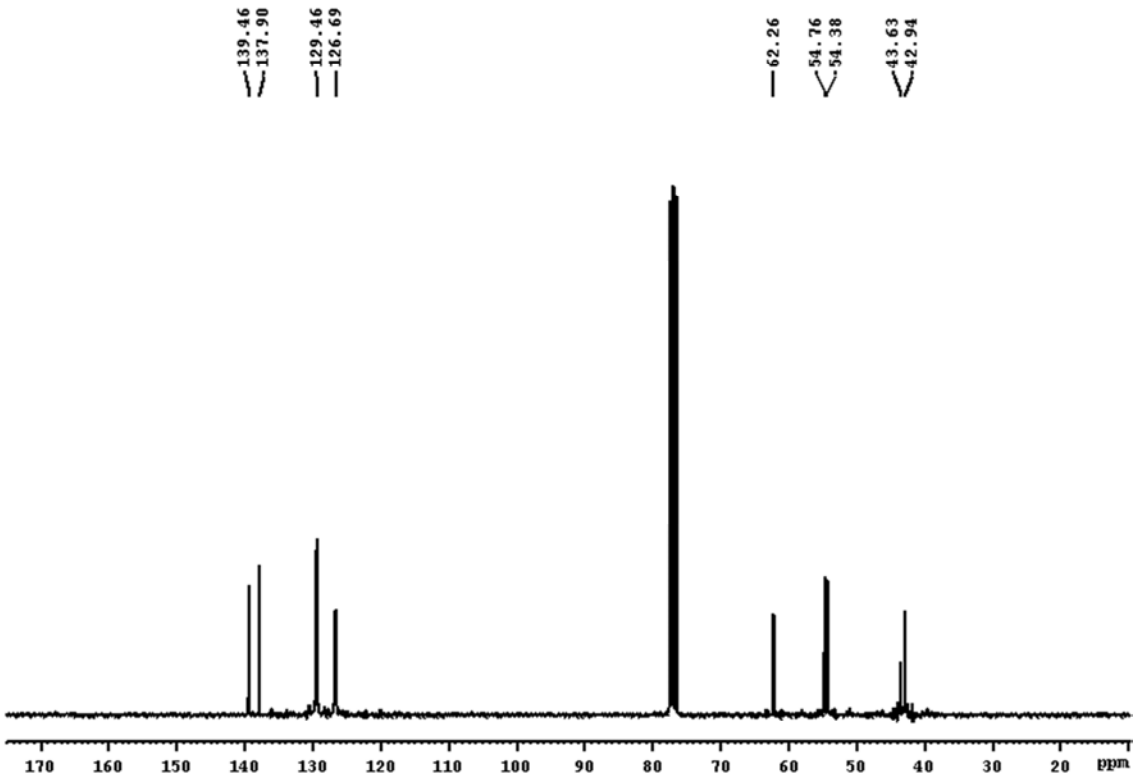

Supplementary Figure 24. IR of Me2pp (1b) macrocycle. 2 mg of the solid sample were used.

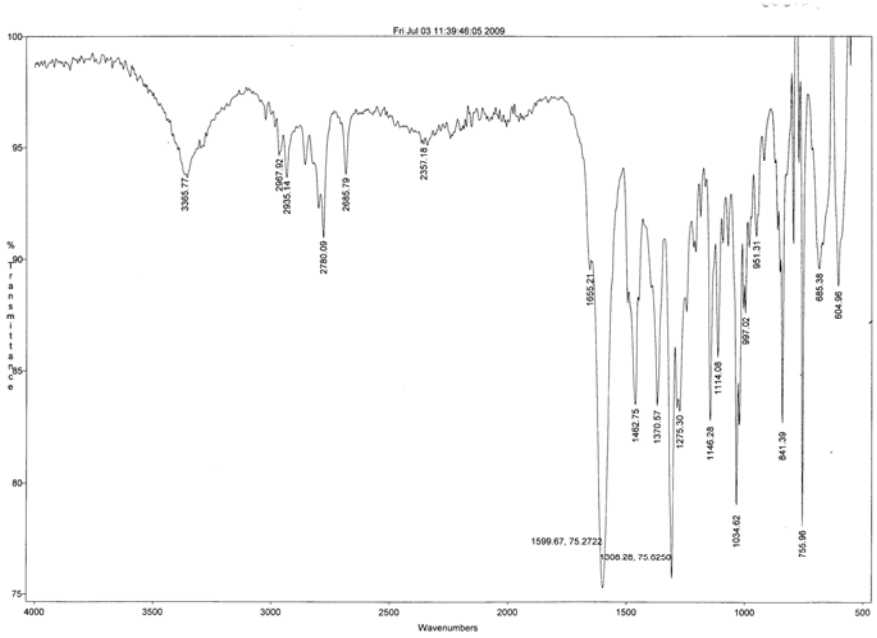

Supplementary Figure 25. ESI-MS spectra of Me2pp (1b) macrocycle. Experimental conditions: 100 μM in CH_3CN.

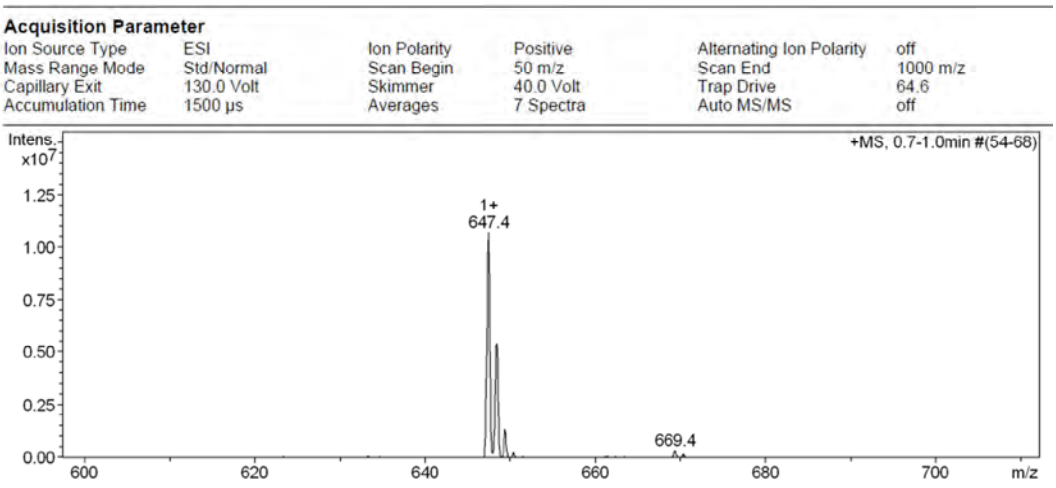

Supplementary Figure 26. ^{1}H-NMR spectrum of Pd-1b·$(OAc)_2(CF_3SO_3)_2$ molecular clip. Experiment performed in CD_3CN at 298 K (400 MHz). ((*)= conformational isomer, 3.33/1 ratio).

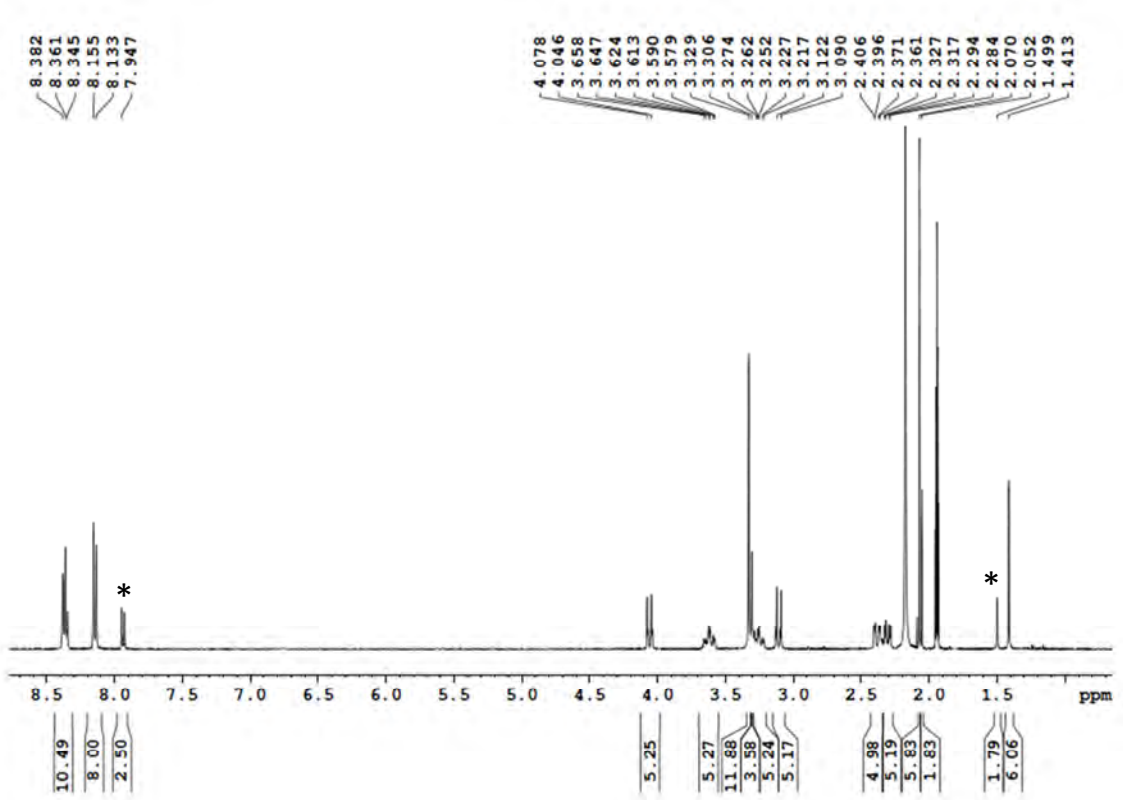

Supplementary Figure 27. ^{13}C-NMR spectrum of Pd-1b·$(OAc)_2(CF_3SO_3)_2$ molecular clip. Experiment performed in CD_3CN at 298 K (100 MHz).

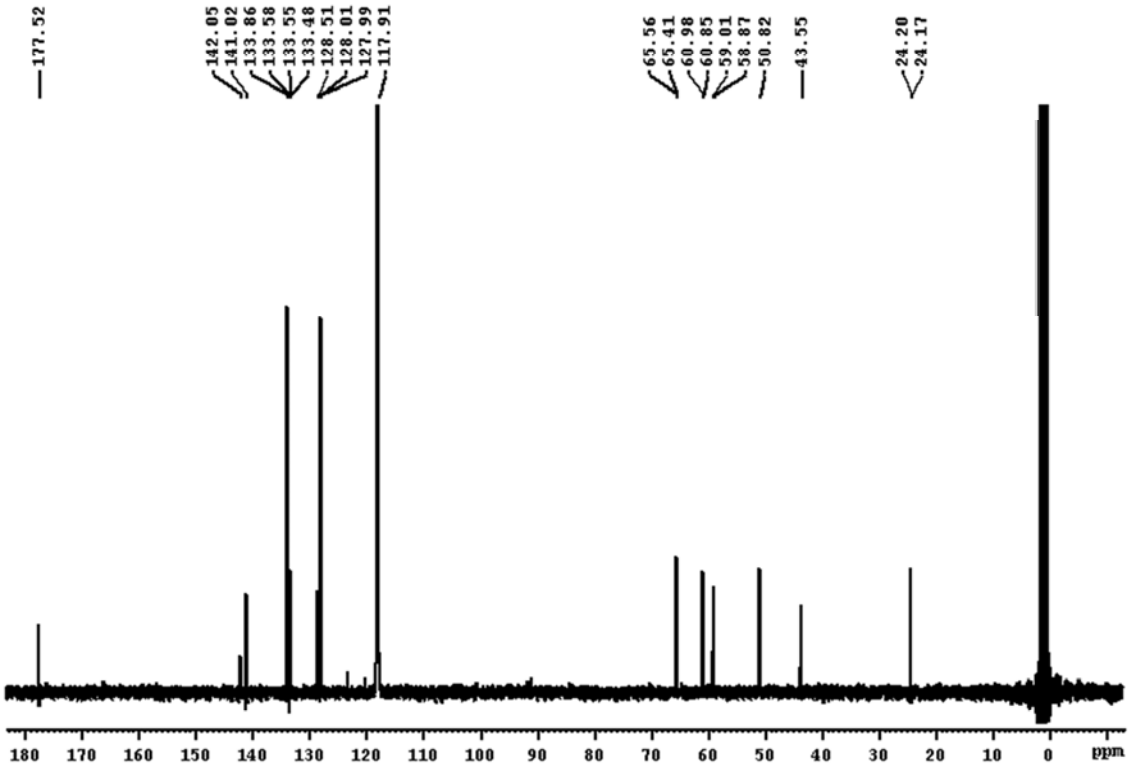

Supplementary Figure 28. COSY spectrum of Pd-1b·$(OAc)_2(CF_3SO_3)_2$ molecular clip. Experiment performed in CD_3CN at 298 K (400 MHz).

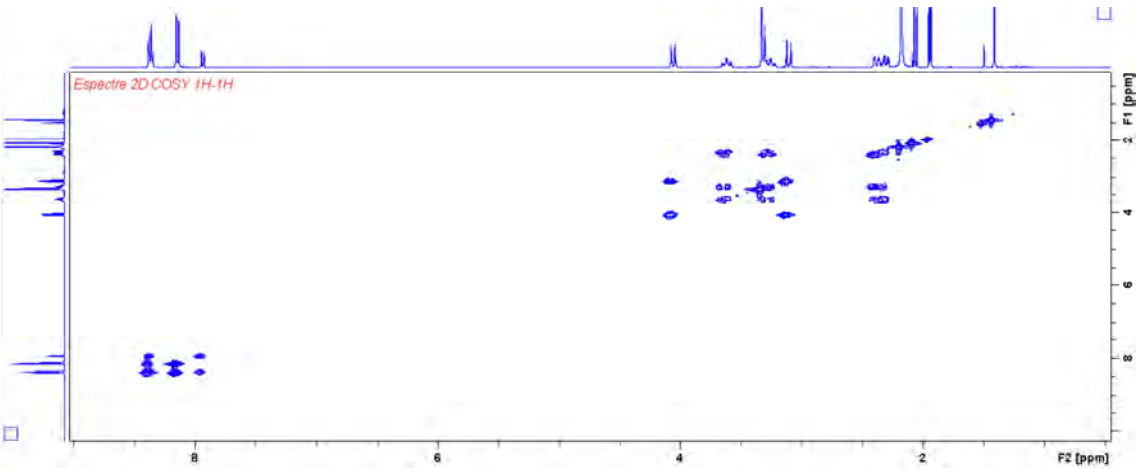

Supplementary Figure 29. NOESY spectrum of Pd-1b·$(OAc)_2(CF_3SO_3)_2$ molecular clip. Experiment performed in CD_3CN at 298 K (400 MHz).

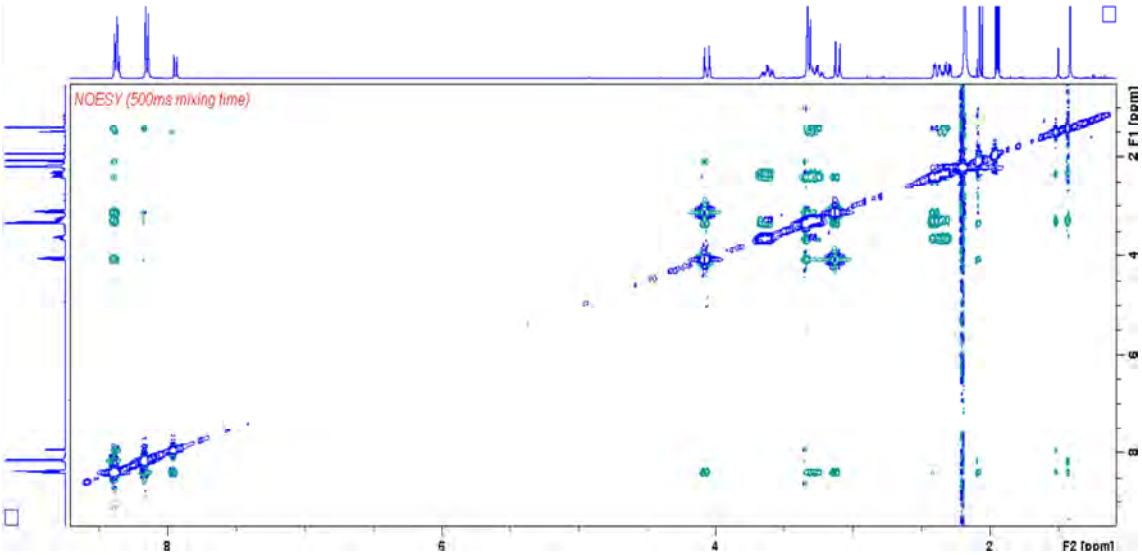

Supplementary Figure 30. Multiplicity-edited HSQC spectrum of Pd-1b·$(OAc)_2(CF_3SO_3)_2$ molecular clip. Experiment performed in CD_3CN at 298 K (400 MHz).

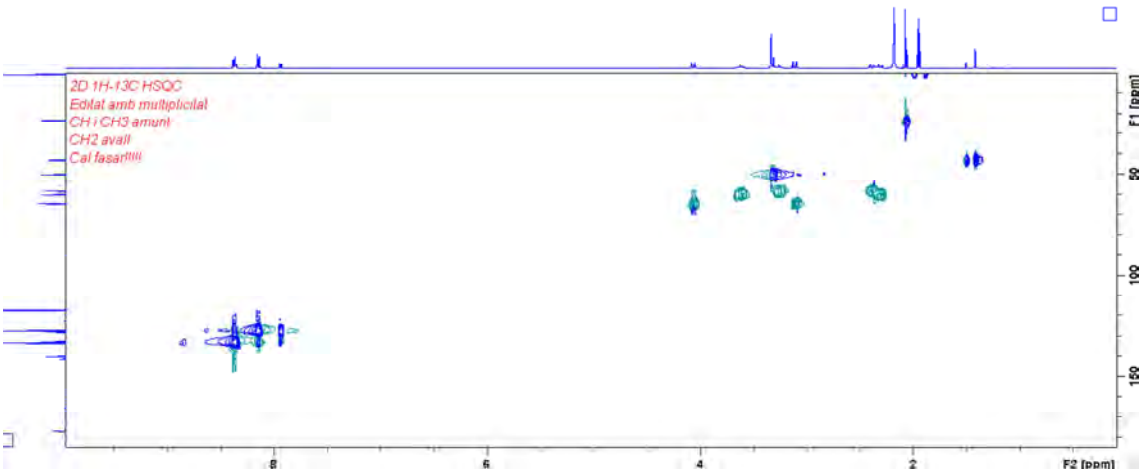

Supplementary Figure 31. HMBC spectrum of Pd-1b·$(OAc)_2(CF_3SO_3)_2$ molecular clip. Experiment performed in CD_3CN at 298 K (400 MHz).

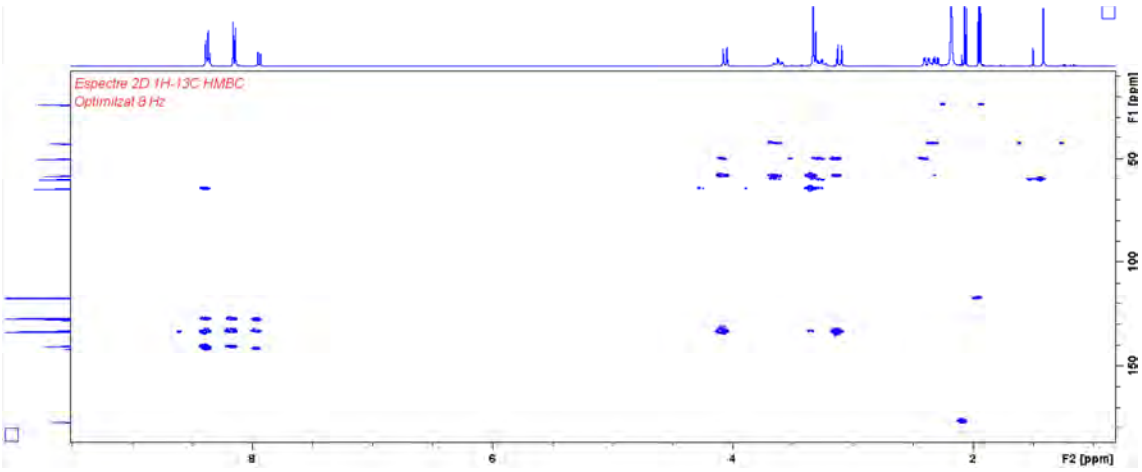

Supplementary Figure 32. HRMS of Pd-1b·$(AcO)_2(CF_3SO_3)_2$ molecular clip. Simulated spectra of selected peaks are showed in red. Experimental conditions: 100 μM in CH_3CN, registered with a Bruker MicroTOF-Q-II exact mass spectrometer.

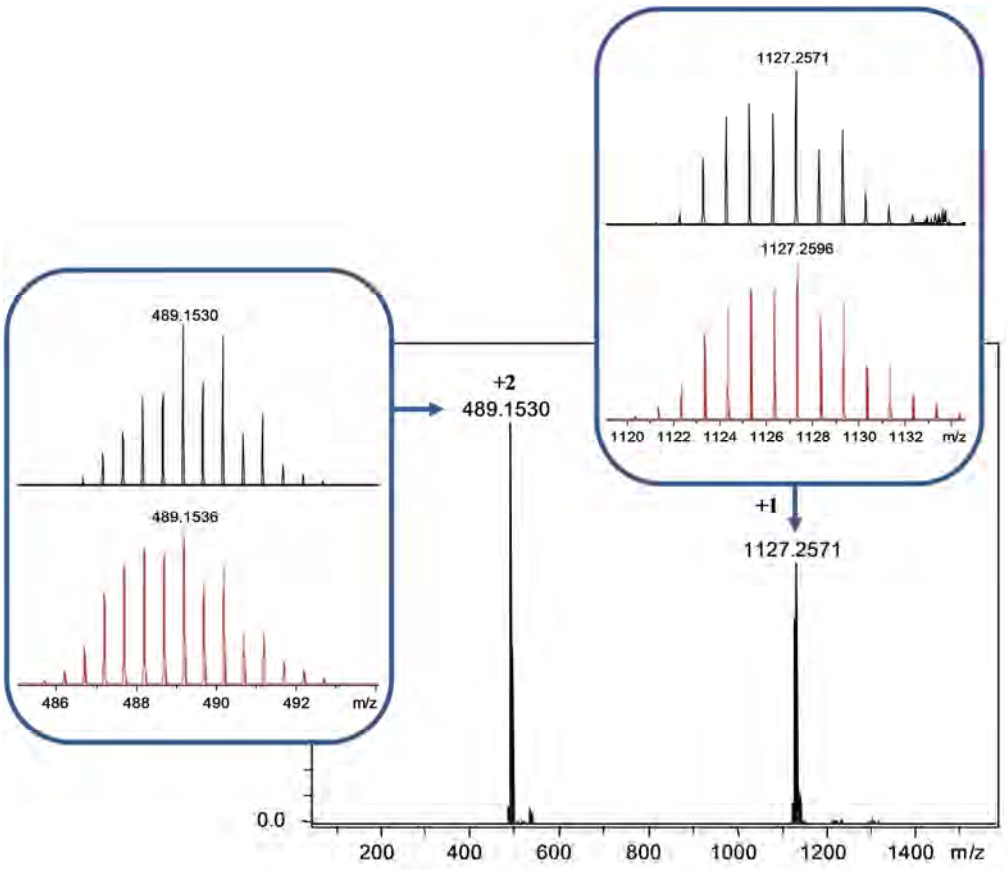

Supplementary Figure 33. ESI-MS spectrum of complex 4·$(CF_3SO_3)_8$ molecular cage. Experimental conditions: 100 μM in DMF.

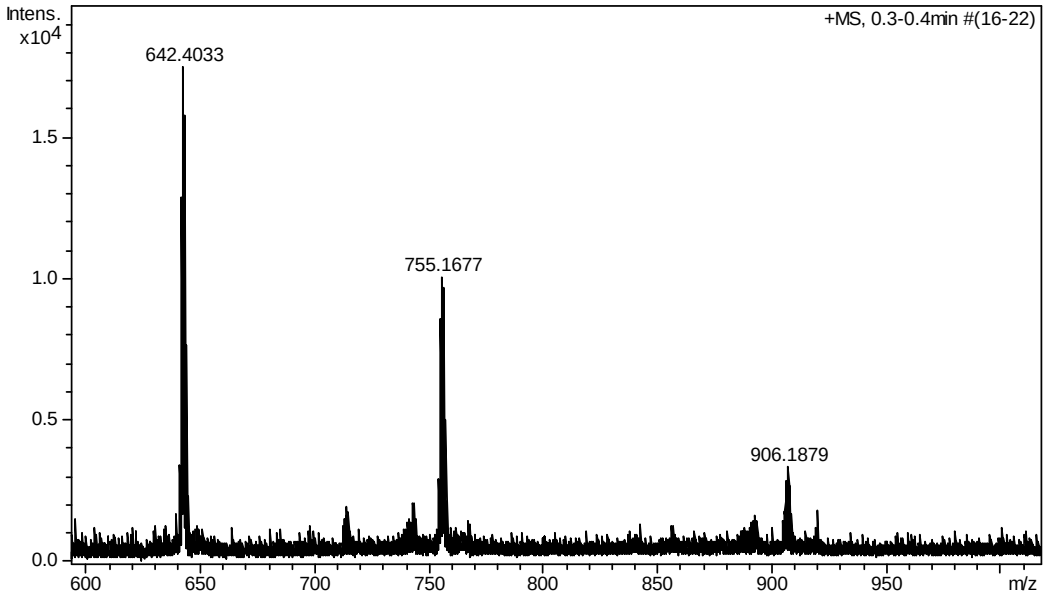

Supplementary Figure 34. HRMS spectrum of 4·$(BArF)_8$ nanocapsule. Simulated spectra of selected peaks are showed in red. Experimental conditions: 100 μM in CH_3CN, registered with a Bruker MicroTOF-Q-II exact mass spectrometer.

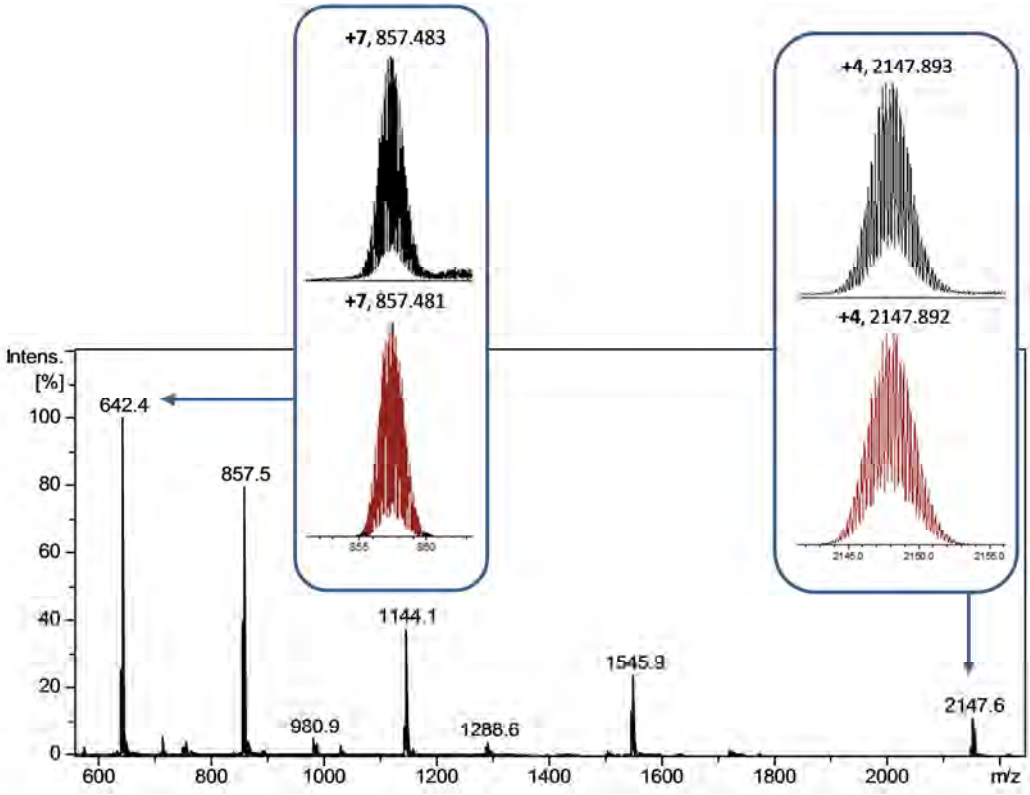

Supplementary Figure 35. ^{1}H-NMR spectrum of 4·(BArF)$_8$ molecular cage. Experiment performed in CD_3CN at 298 K (400 MHz). A slight excess of BArF anions is present; all signals belonging to solvent residues have been assigned.

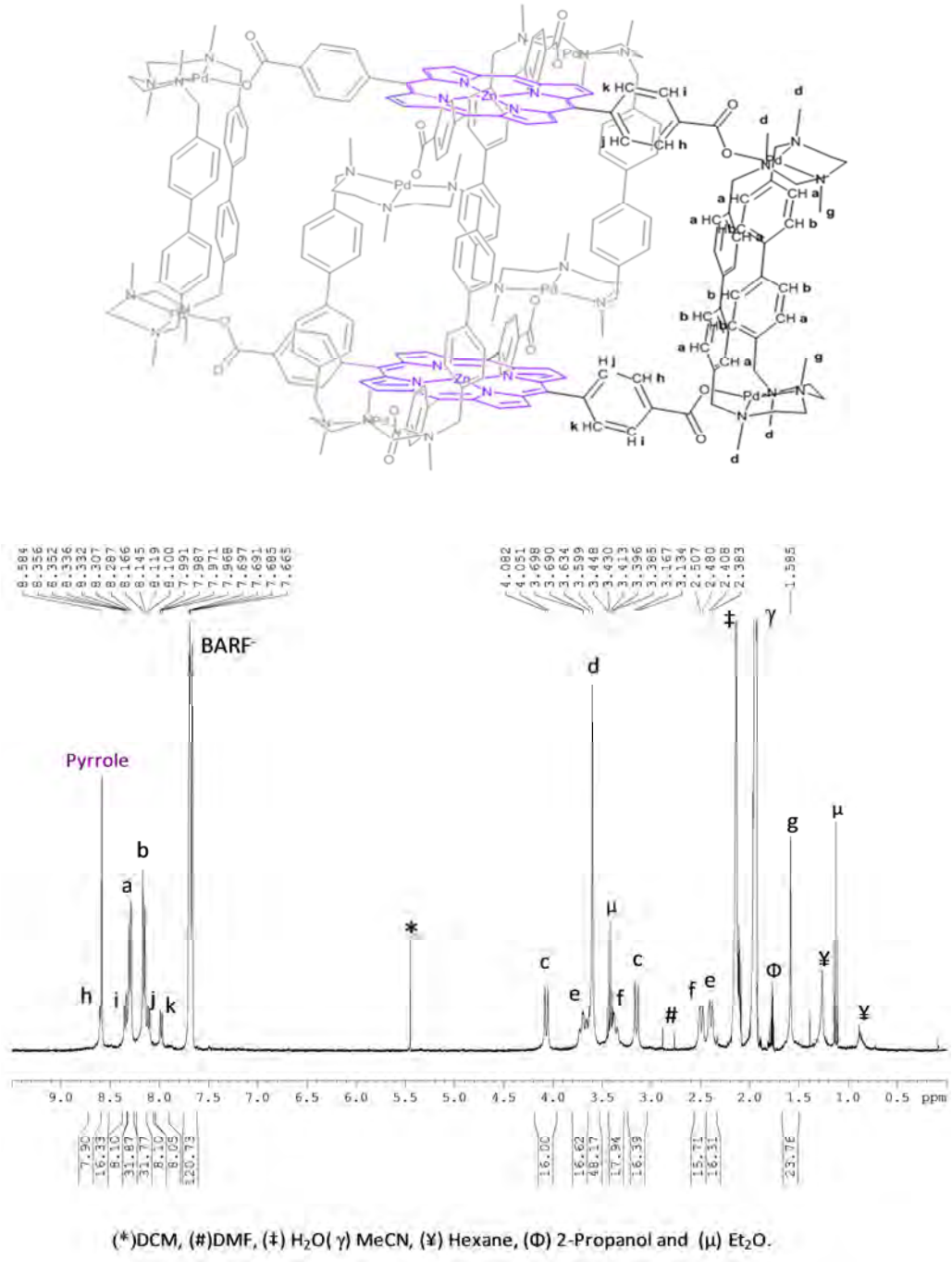

Supplementary Figure 36. COSY spectrum of 4·(BArF)$_8$ molecular cage. Experiment performed in CD_3CN at 298 K (400 MHz).

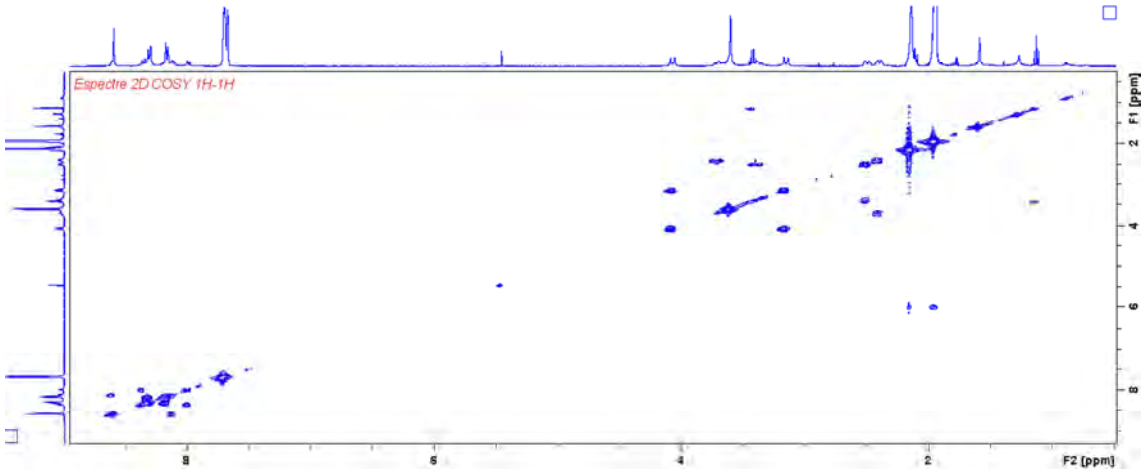

Supplementary Figure 37. NOESY spectrum of 4·(BArF)$_8$ molecular cage. Experiment performed in CD_3CN at 298 K (400 MHz).

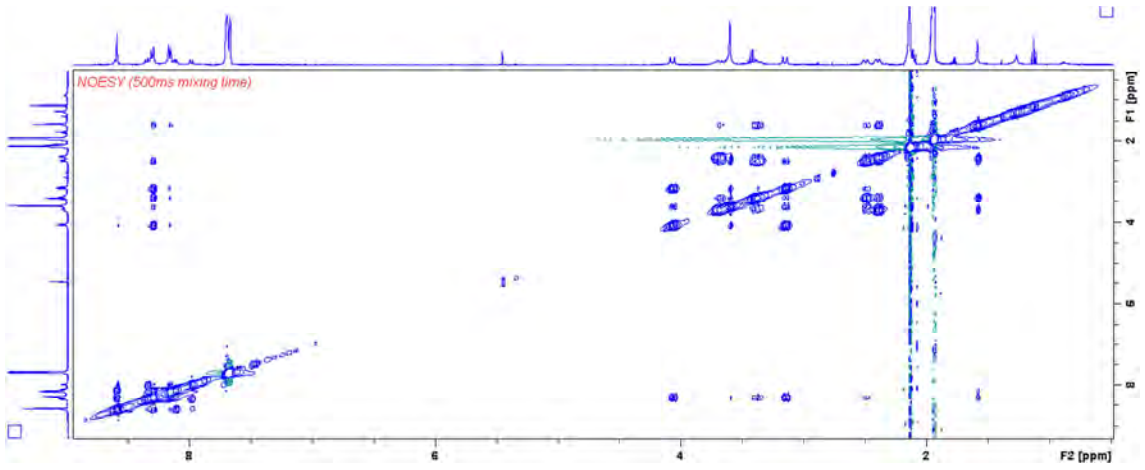

Supplementary Figure 38. Multiplicity-edited HSQC spectrum of 4·(BArF)$_8$ molecular cage. Experiment performed in CD_3CN at 298 K (400 MHz).

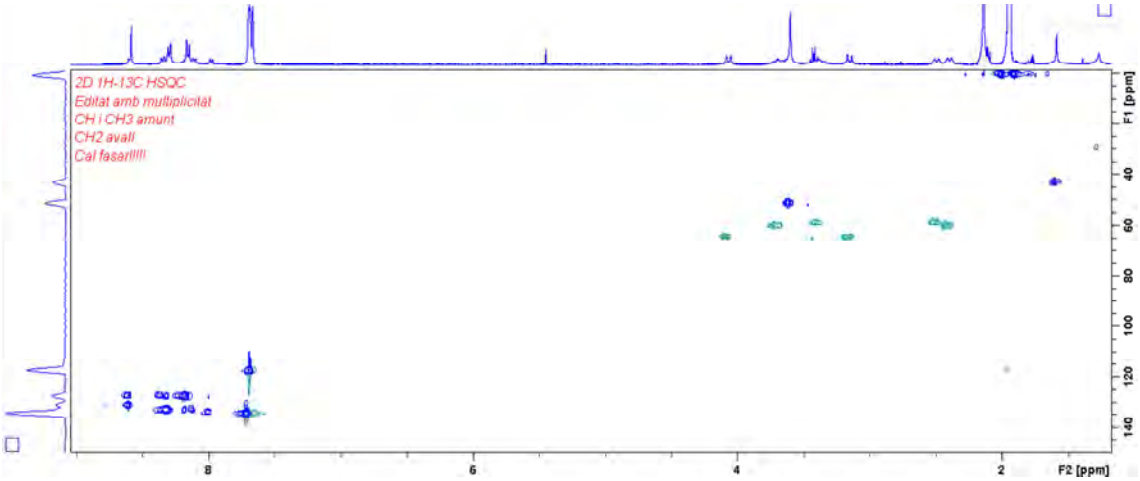

Supplementary Figure 39. HMBC spectrum of 4·(BArF)$_8$ molecular cage. Experiment performed in CD_3CN at 298 K (400 MHz).

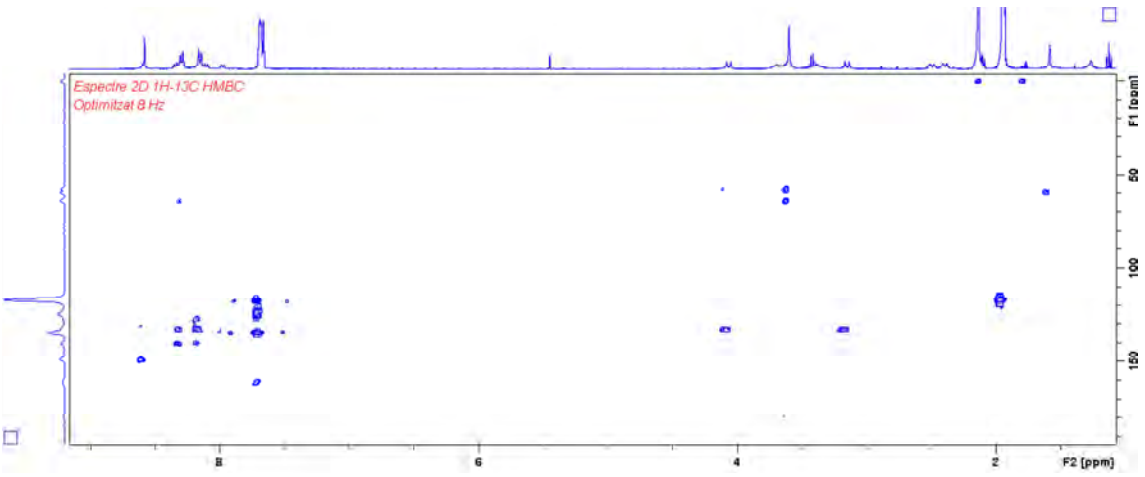

Supplementary Figure 40. UV-Vis spectrum of 4·(BArF)$_8$ nanocapsule. $4.32 \cdot 10^{-7}$ M solution of **4·(**BArF)$_8$ in Toluene/CH_3CN (9/1).

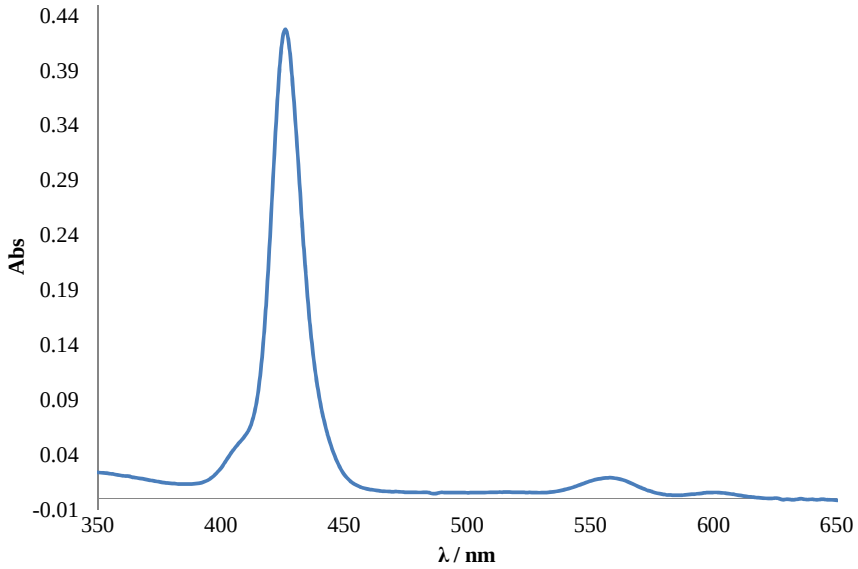

Supplementary Figure 41. HRMS spectrum of C_{60}⊂4·(BArF)$_8$ host-guest complex. Simulated spectra of selected peaks are showed in colour red. Experimental conditions: 100 μM in Toluene/CH_3CN (4/1), registered with a Bruker MicroTOF-Q-II exact mass spectrometer.

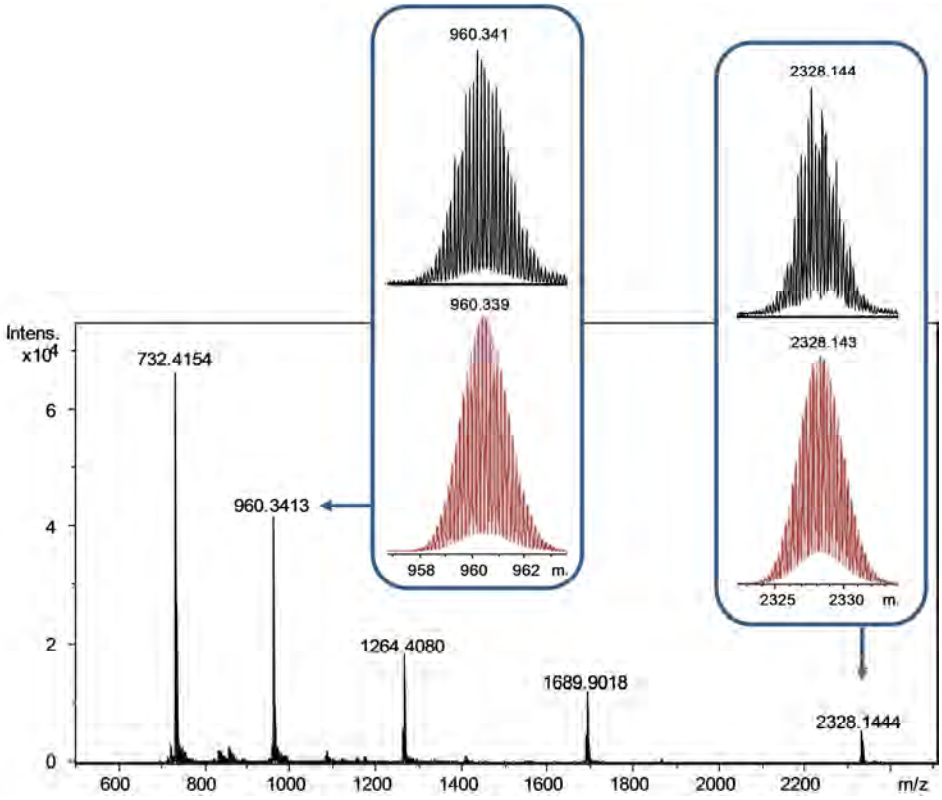

Supplementary Figure 42. ^{1}H-NMR spectrum of $C_{60}\subset$4·$(BArF)_8$ adduct. Experiment performed in CD_3CN at 298 K (400 MHz).

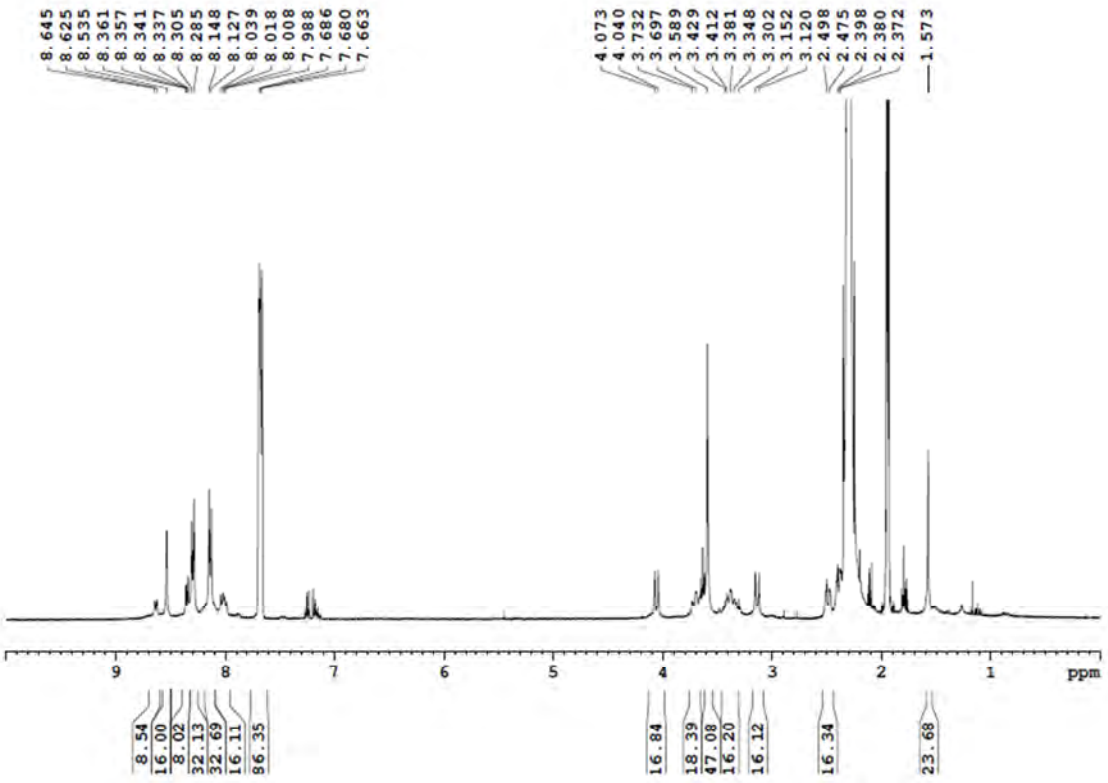

Supplementary Figure 43. COSY spectrum of $C_{60}\subset$4·$(BArF)_8$ adduct. Experiment performed in CD_3CN at 298 K (400 MHz).

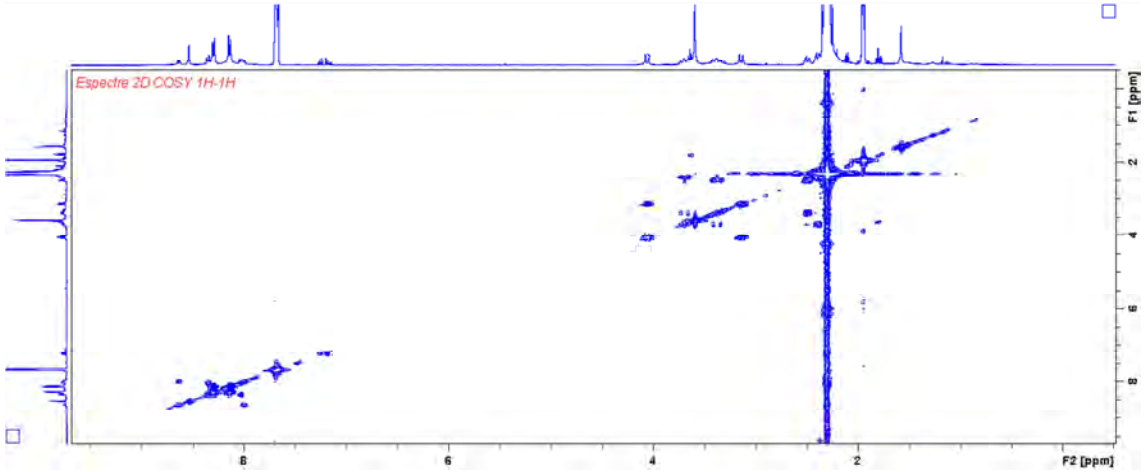

Supplementary Figure 44. NOESY spectrum of $C_{60}\subset$4·$(BArF)_8$ adduct. Experiment performed in CD_3CN at 298 K (400 MHz).

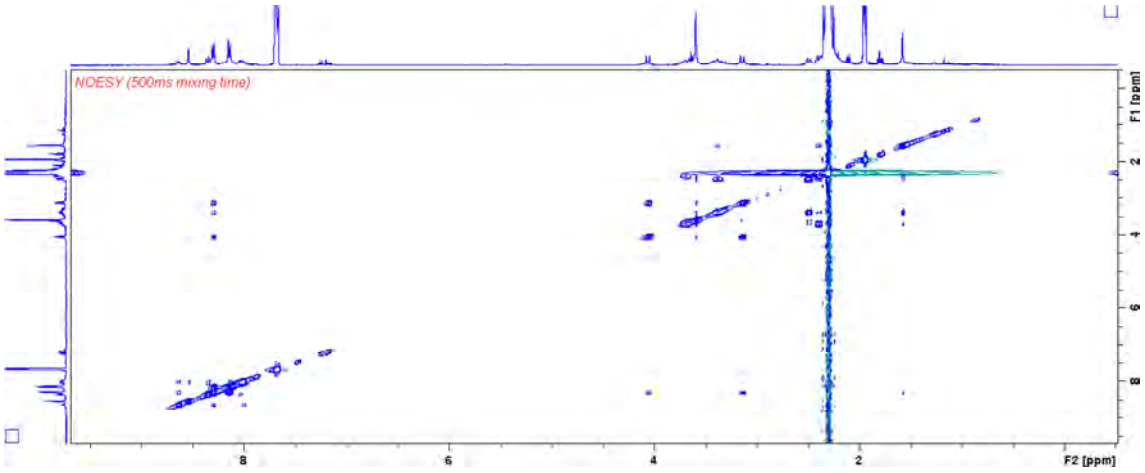

Supplementary Figure 45. Multiplicity-edited HSQC spectrum of $C_{60}\subset$4·$(BArF)_8$ adduct. Experiment performed in CD_3CN at 298 K (400 MHz).

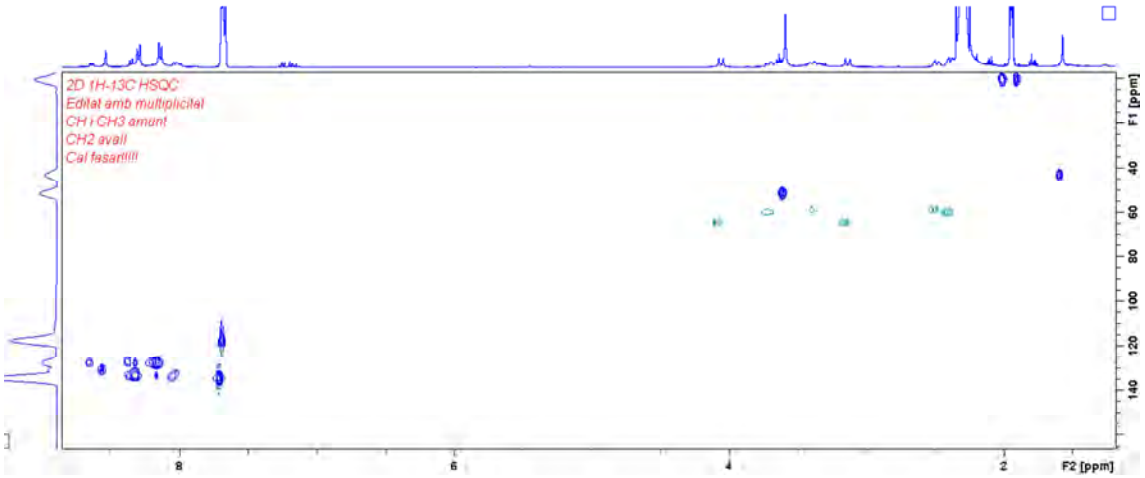

Supplementary Figure 46. ^{1}H-NMR spectra of (top) free nanocage 4·(BArF)$_8$ and (bottom) host-guest complex C_{60}⊂4·(BArF)$_8$. Experiment performed in CD_3CN at 298 K (400 MHz).

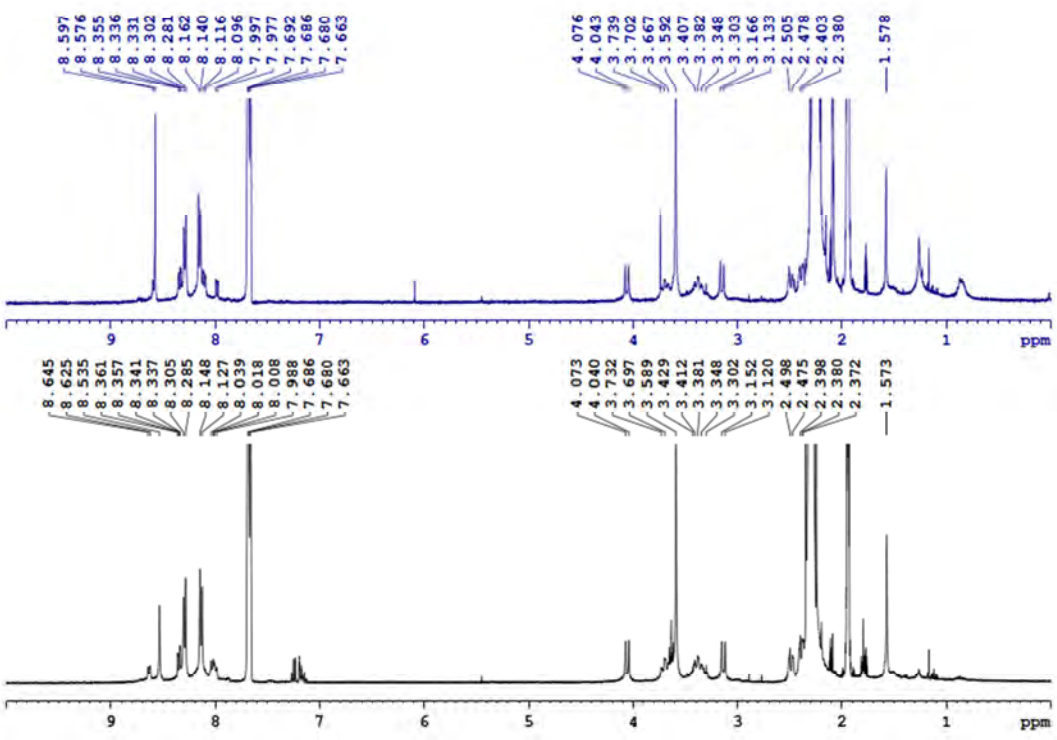

Supplementary Figure 47. ^{1}H-NMR spectrum of C_{70}⊂4·(BArF)$_8$ adduct. Experiment performed in CD_3CN at 298 K (400 MHz).

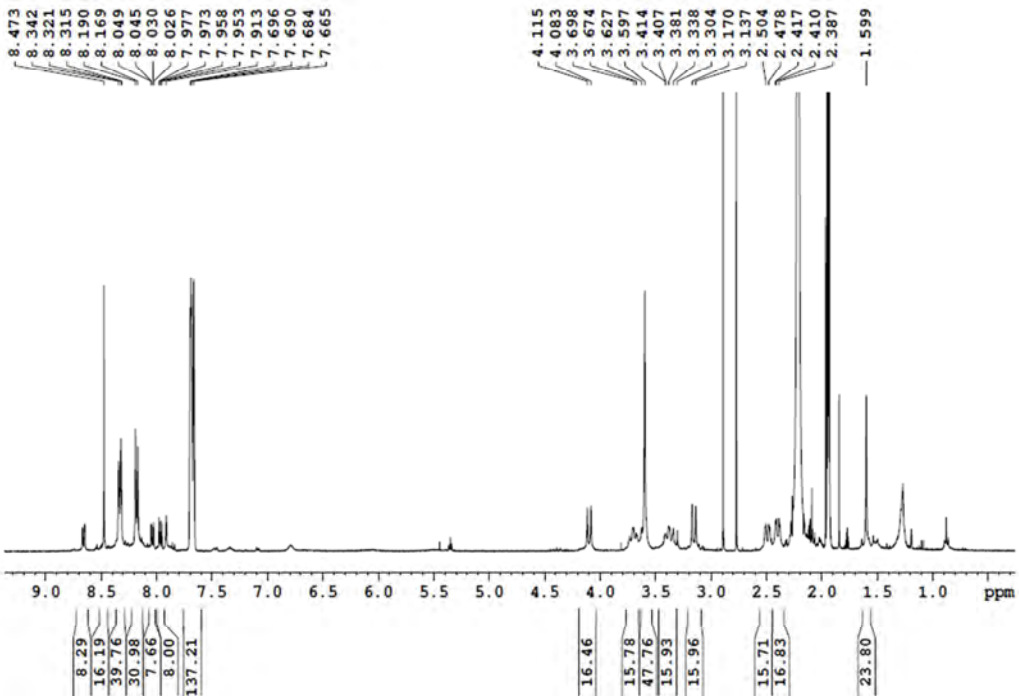

Supplementary Figure 48. COSY spectrum of C_{70}⊂4·$(BArF)_8$ adduct. Experiment performed in CD_3CN at 298 K (400 MHz).

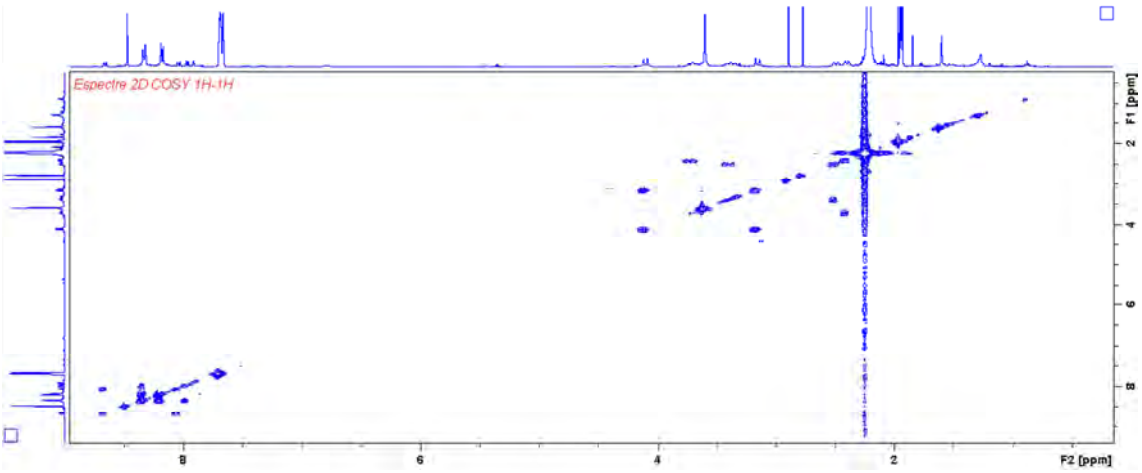

Supplementary Figure 49. NOESY spectrum of C_{70}⊂4·$(BArF)_8$ adduct. Experiment performed in CD_3CN at 298 K (400 MHz).

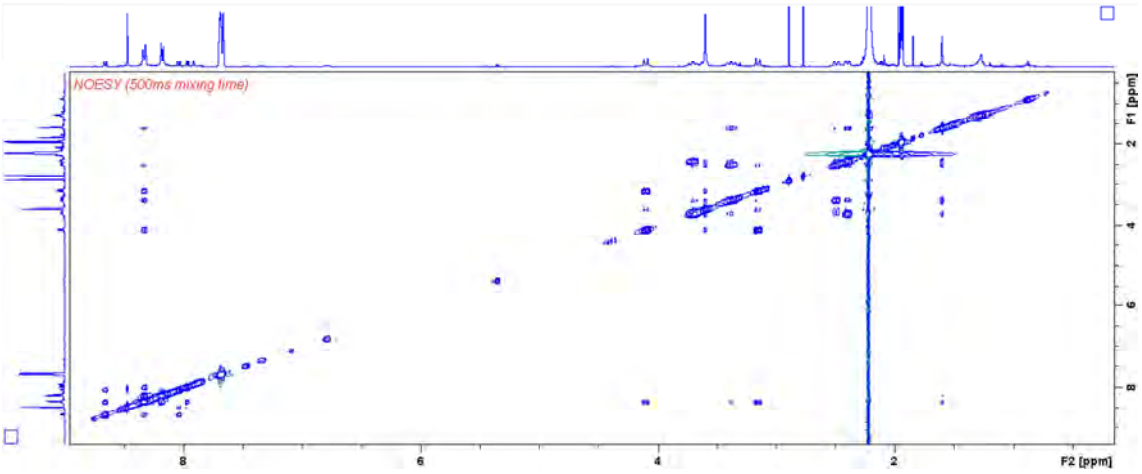

Supplementary Figure 50. Multiplicity-edited HSQC spectrum of C_{70}⊂4·$(BArF)_8$ adduct. Experiment performed in CD_3CN at 298 K (400 MHz).

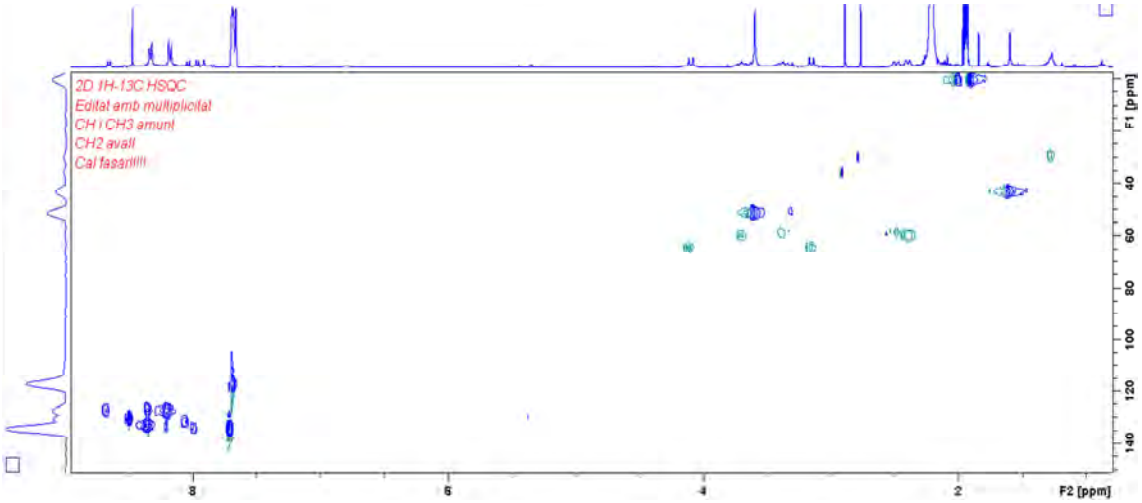

Supplementary Figure 51. ^{1}H-NMR spectraof (top) free nanocage 4·$(BArF)_8$ and (bottom) of host-guest complex C_{70}⊂4·$(BArF)_8$. Experiments performed in CD_3CN at 298 K (400 MHz).

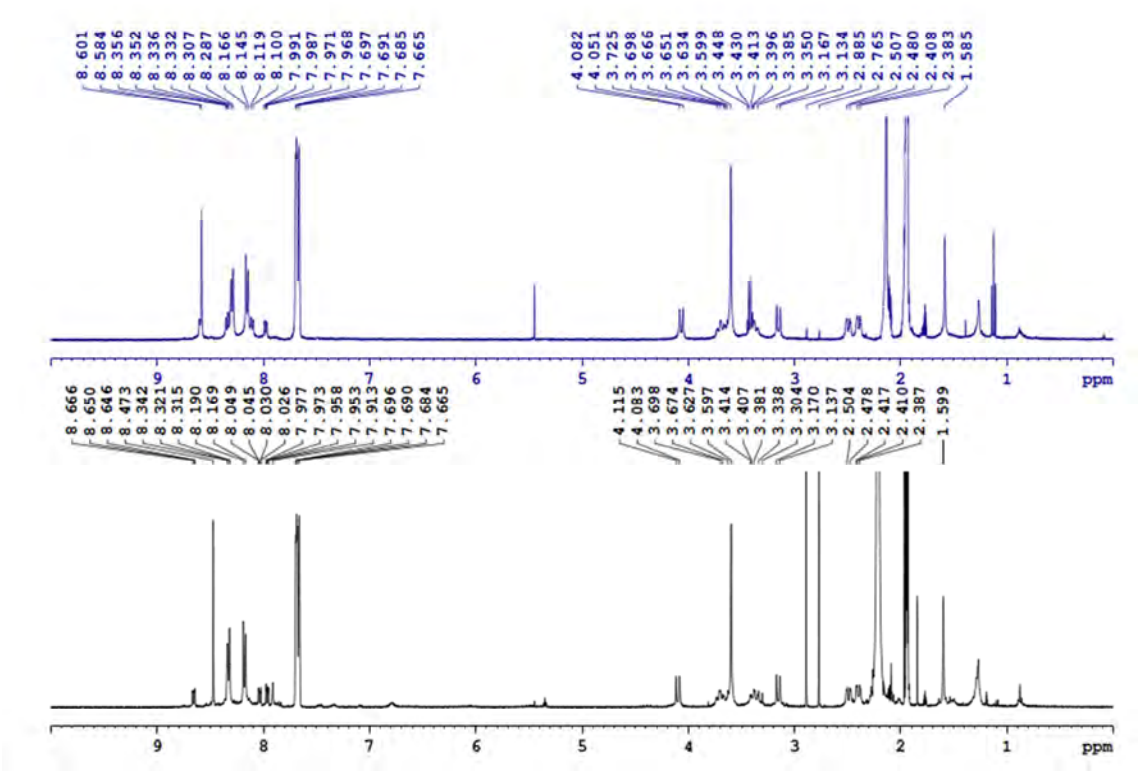

Supplementary Figure 52. HRMS spectrum of C_{70}⊂4·$(BArF)_8$ host-guest complex. Simulated spectra of selected peaks are showed in colour red. Experimental conditions: 100 μM in Toluene/CH_3CN (4/1), registered with a Bruker MicroTOF-Q-II exact mass spectrometer.

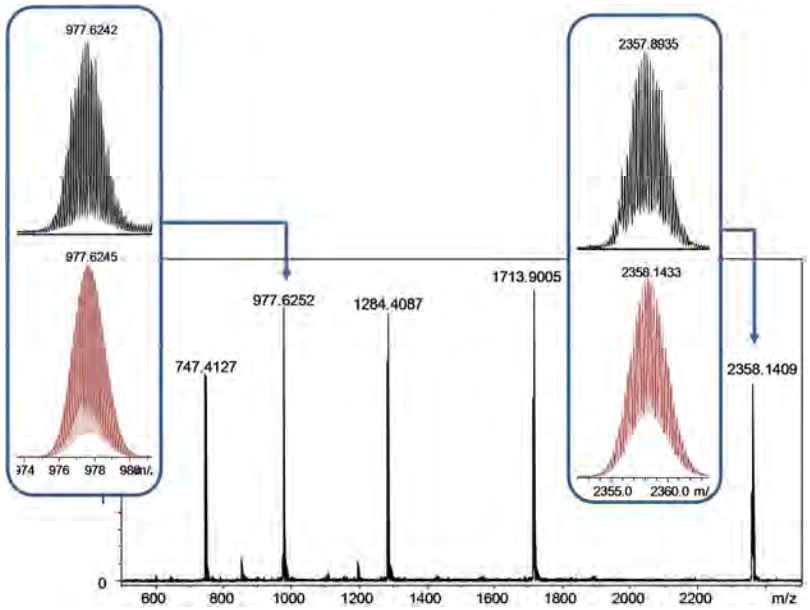

Supplementary Figure 53. ^{1}H-NMR spectraof (top) free nanocage 4·$(BArF)_8$ and (bottom) of host-guest complex [60]PCBM⊂4·$(BArF)_8$ (bottom). Experiments performed in CD_3CN at 298 K (400 MHz).

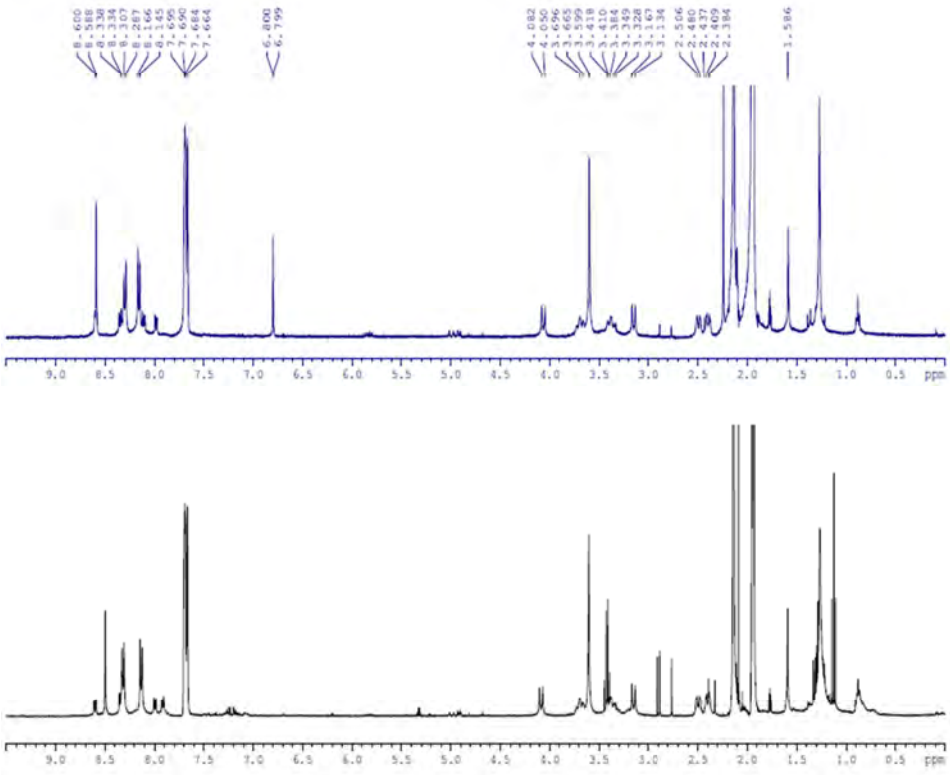

Supplementary Figure 54. HRMS spectrum of [60]PCBM⊂4·(BArF)$_8$ host-guest complex. Simulated spectra of selected peaks are showed in colour red. Experimental conditions: 100 μM in toluene/acetonitrile (4/1), registered with a Bruker MicroTOF-Q-II exact mass spectrometer.

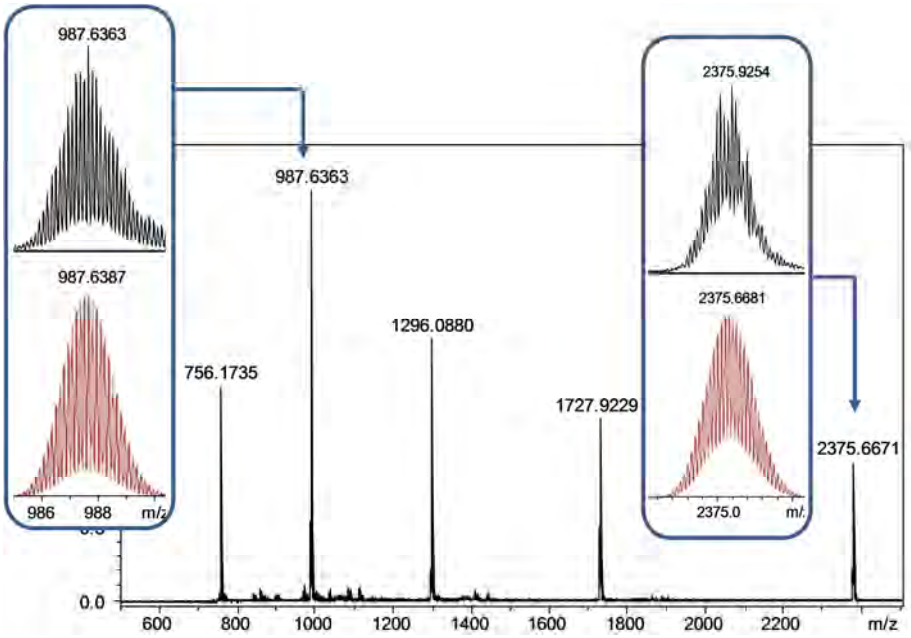

Supplementary Figure 55. HRMS spectrum of C_{84}⊂4·(BArF)$_8$ host-guest complex. Peaks belonging to **C_{84}⊂4·(**BArF)$_8$ are framed in green (* empty molecular cage signals). Experimental conditions: 100 μM in toluene/acetonitrile (4/1), registered with a Bruker MicroTOF-Q-II exact mass spectrometer.

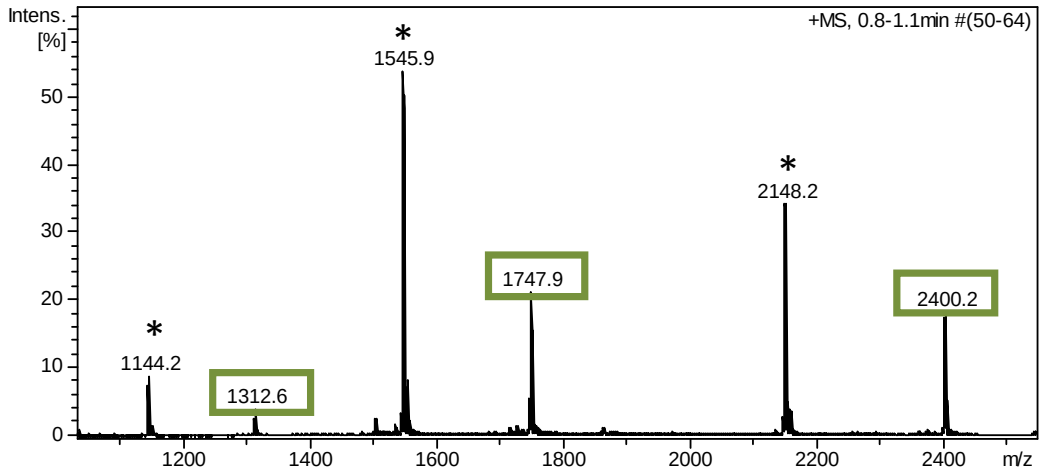

Supplementary Figure 56. UV-Vis monitoring of the titration of 4·(BArF)$_8$ nanocapsule with fullerene C_{60}. Fixed total concentration ($4.32 \cdot 10^{-7}$ M)) of nanocapsule in Toluene/Acetonitrile (9/1). Inset: Absorbance variation at 432 nm Soret band vs. different equivalents of added substrate.

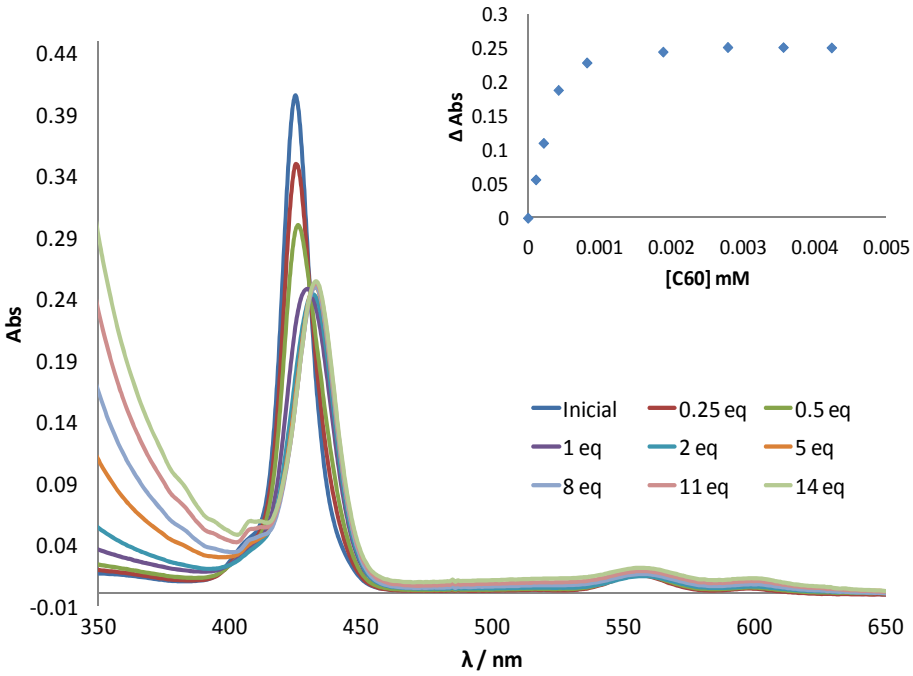

Supplementary Figure 57. UV-Vis monitoring of the titration of 4·(BArF)$_8$ nanocapsule with fullerene C_{60}. Fixed total concentration ($1.08 \cdot 10^{-7}$ M) of nanocapsule in toluene/acetonitrile (9/1).

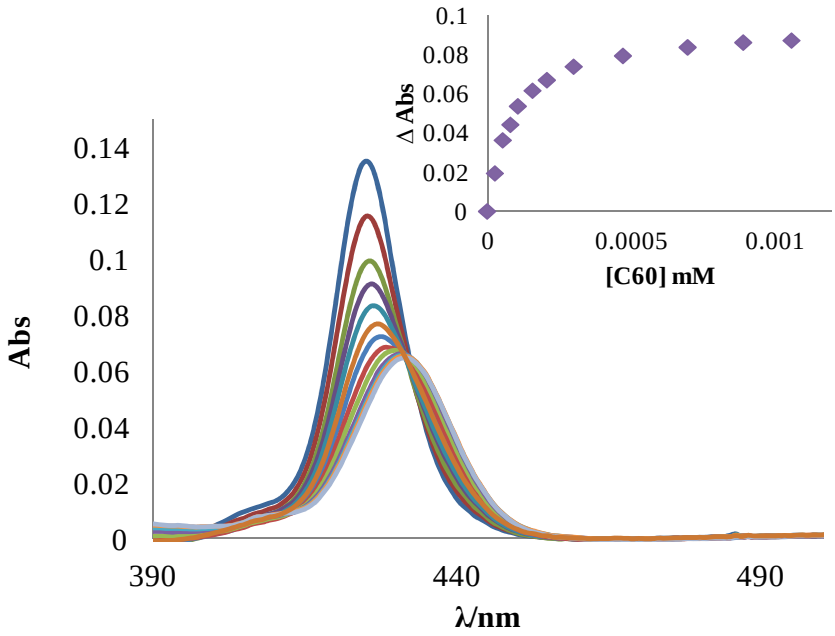

Supplementary Figure 58. Job's plot, to obtain the stoichiometry for the host-guest complex of the nanocage 4·$(BArF)_8$, and C_{60} and C_{70} fullerenes. As can be observed on the figures, in all cases *x* has a value arround 0.5, indicating that the host-guest complexes have a 1:1 stoichiometry (n≈1).

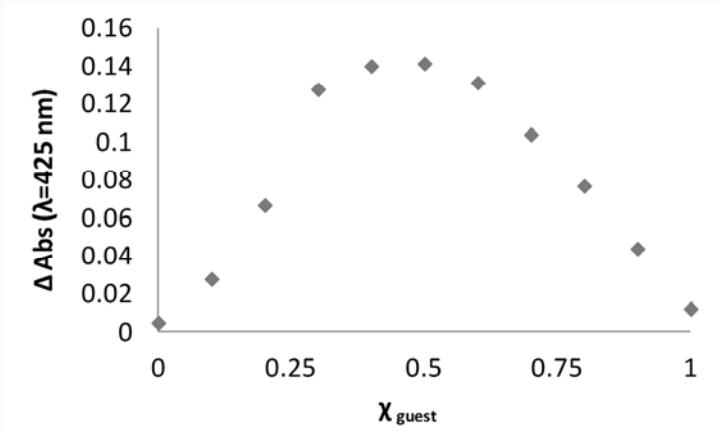

C_{60}⊂4·$(BArF)_8$

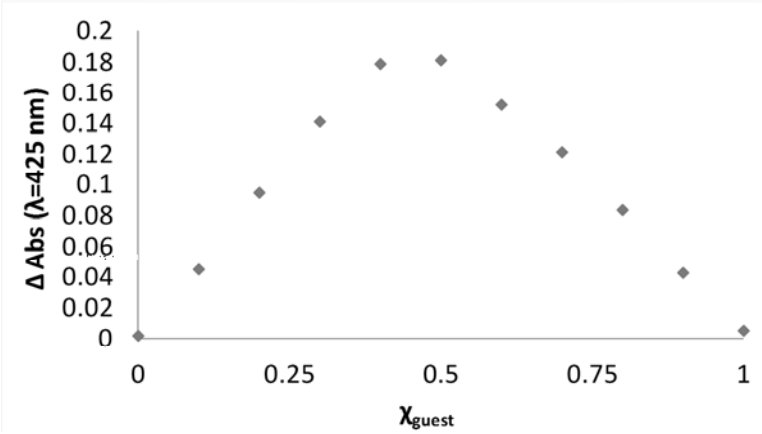

C_{70}⊂4·$(BArF)_8$

Supplementary Figure 59. UV-Vis monitoring of the titration of 4·$(BArF)_8$ nanocapsule with fullerene C_{70}. Fixed totlal concentration ($4.32 \cdot 10^{-7}$ M)) of nanocapsule in Toluene/Acetonitrile (9/1). Inset: Absorbance variation at 432 nm Soret band vs. different equivalents of added substrate.

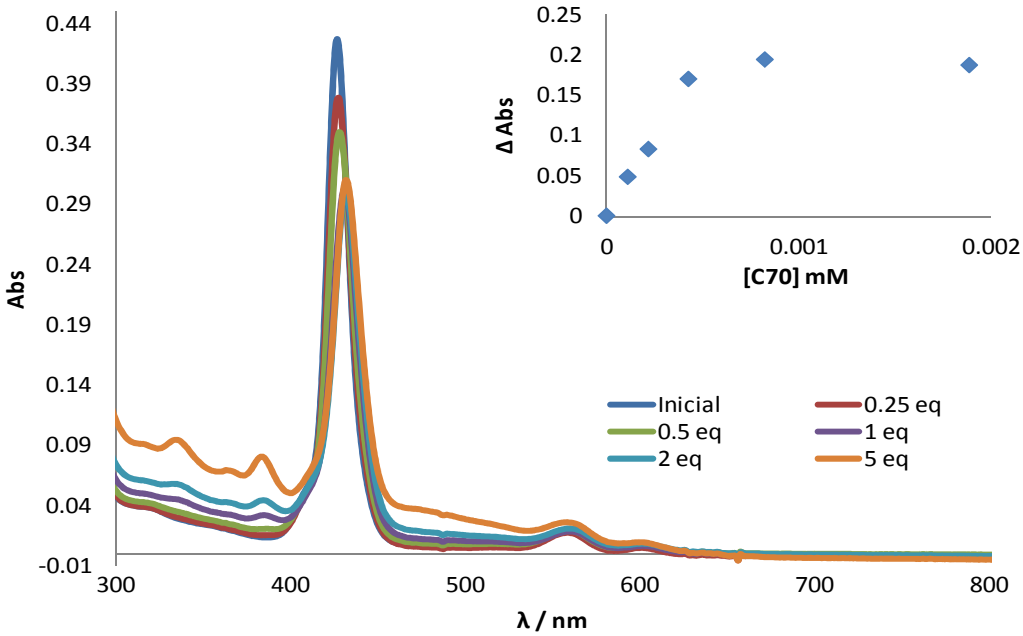

Supplementary Figure 60. UV-Vis monitoring of the titration of 4·$(BArF)_8$ nanocapsule with fullerene [60]PCBM. Fixed total concentration ($4.32 \cdot 10^{-7}$ M)) of nanocapsule in toluene/acetonitrile (9/1).

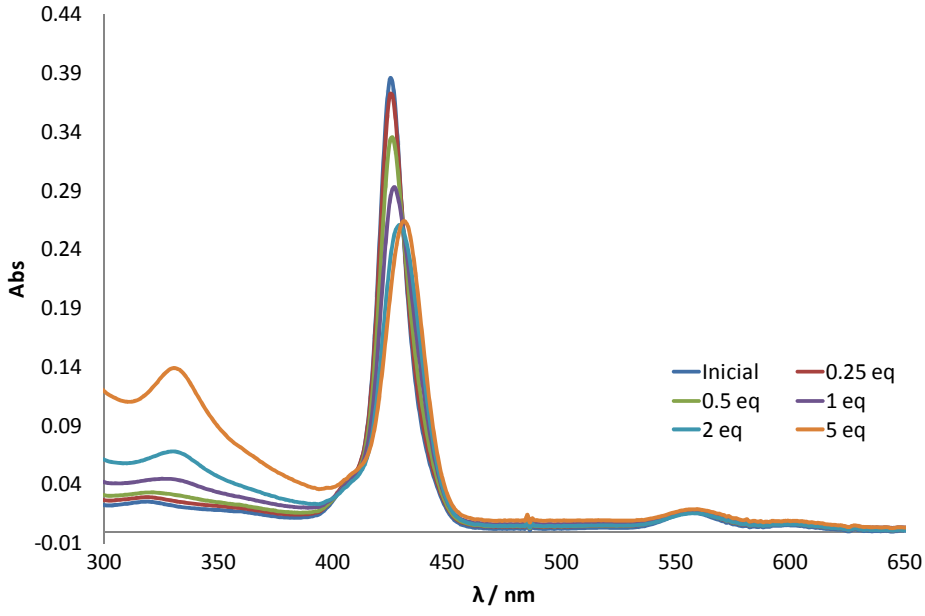

Supplementary Figure 61. DOSY NMR spectrum of molecular clip Pd-1b·$(AcO)_2(CF_3SO_3)_2$. Affording a diffusion coefficient (*D*) of $D=10^{-9.136}$ m^2 s^{-1} ($D_{CD3CN}= 10^{-8.400}$ m^2 s^{-1}).

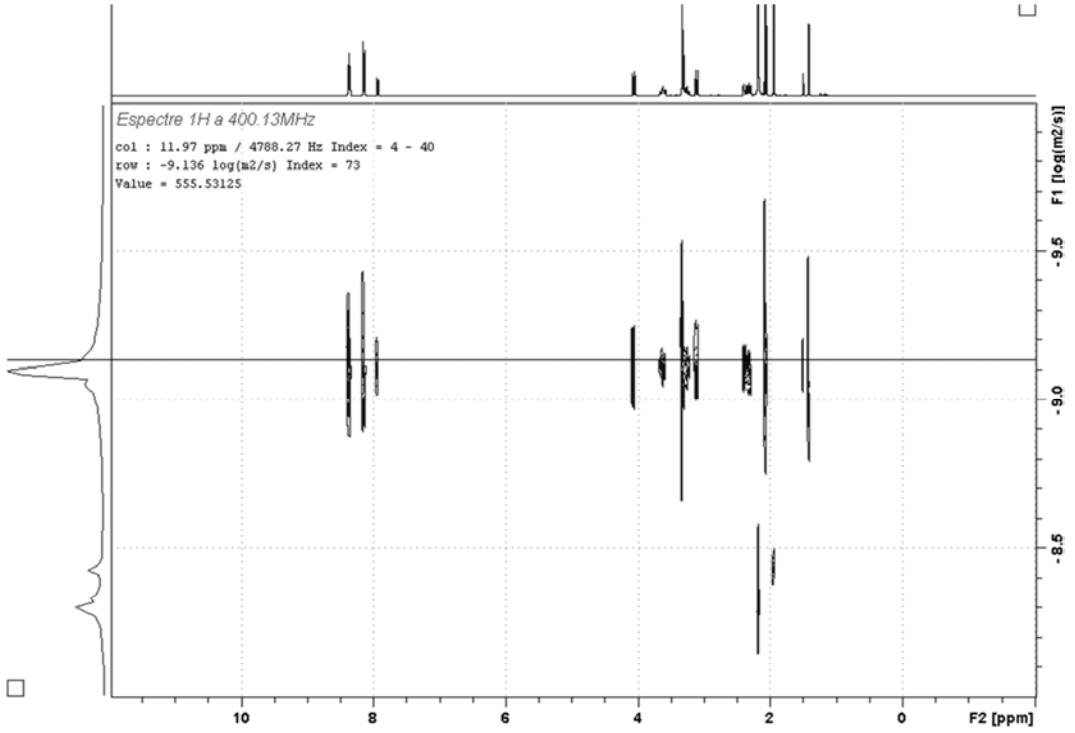

Supplementary Figure 62. DOSY NMR spectrum of nanocage 4·$(BArF)_8$. Affording a diffusion coefficient (*D*) of $D=10^{-9.514}$ m^2 s^{-1} ($D_{CD3CN}= 10^{-8.432}$ m^2 s^{-1}).

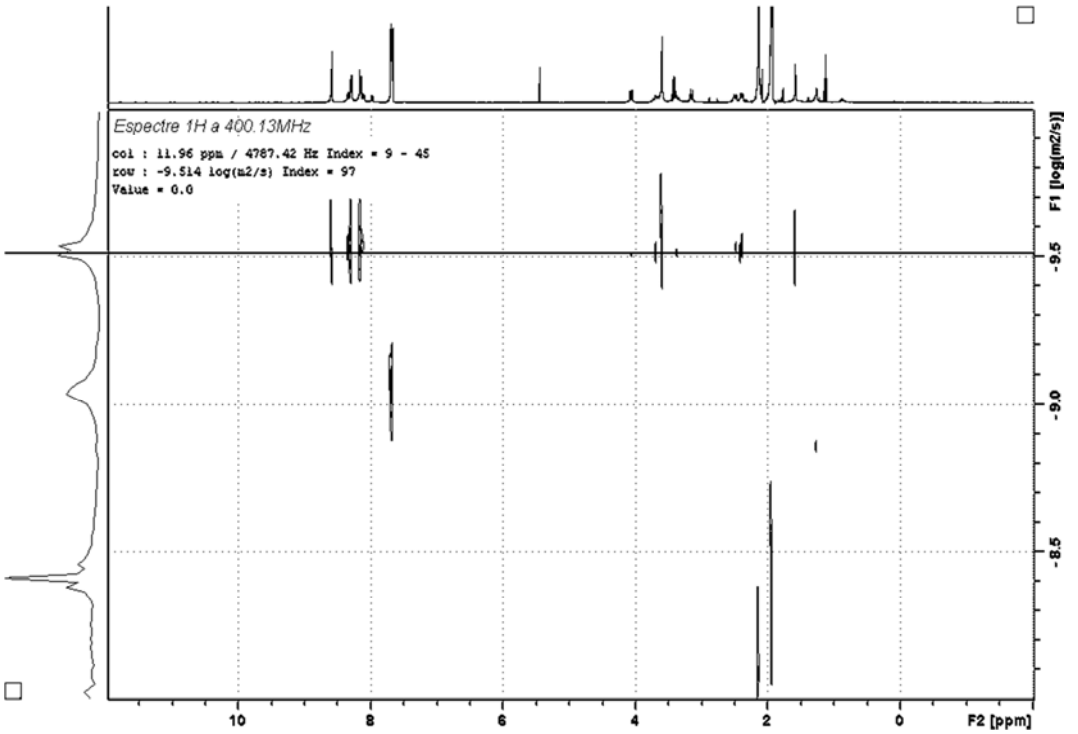

Supplementary Figure 63. DOSY NMR spectrum of nanocage C_{60}⊂4·$(BArF)_8$. Affording a diffusion coefficient (*D*) of $D=10^{-9.532}$ m^2 s^{-1} ($D_{CD3CN}= 10^{-8.443}$ m^2 s^{-1}).

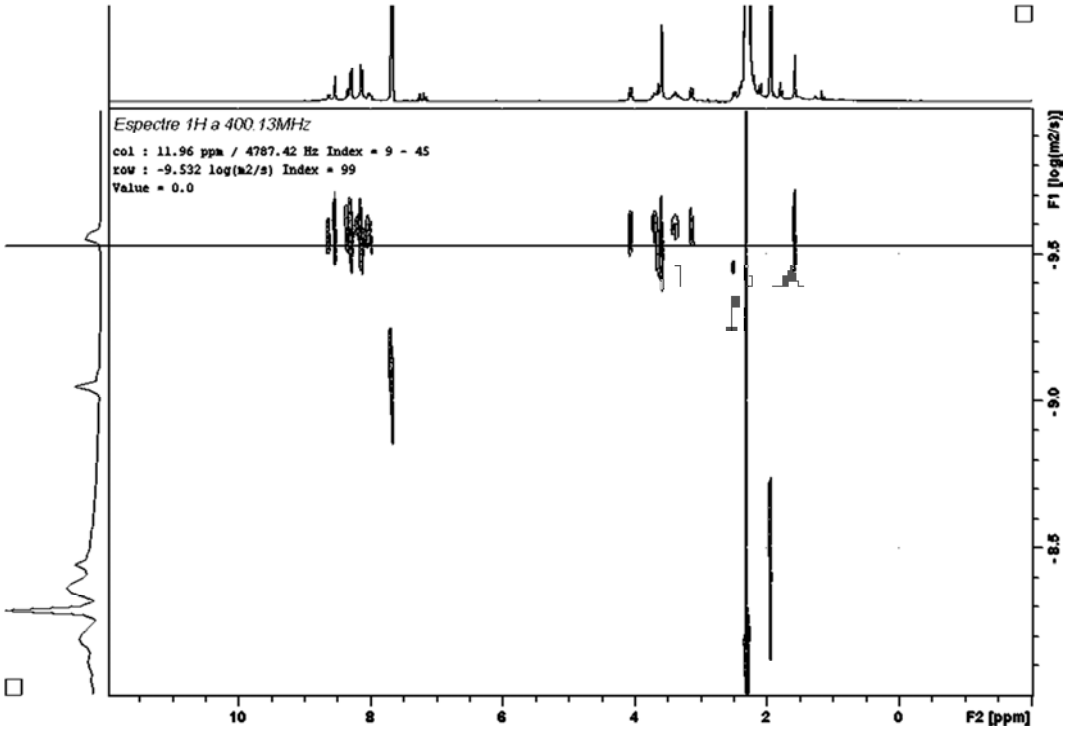

Supplementary Figure 64. DOSY NMR spectrum of nanocage C_{70}⊂**4**·$(BArF)_8$, affording a diffusion coefficient (*D*) of $D=10^{-9.525}$ m^2 s^{-1} ($D_{CD3CN}= 10^{-8.468}$ m^2 s^{-1}).

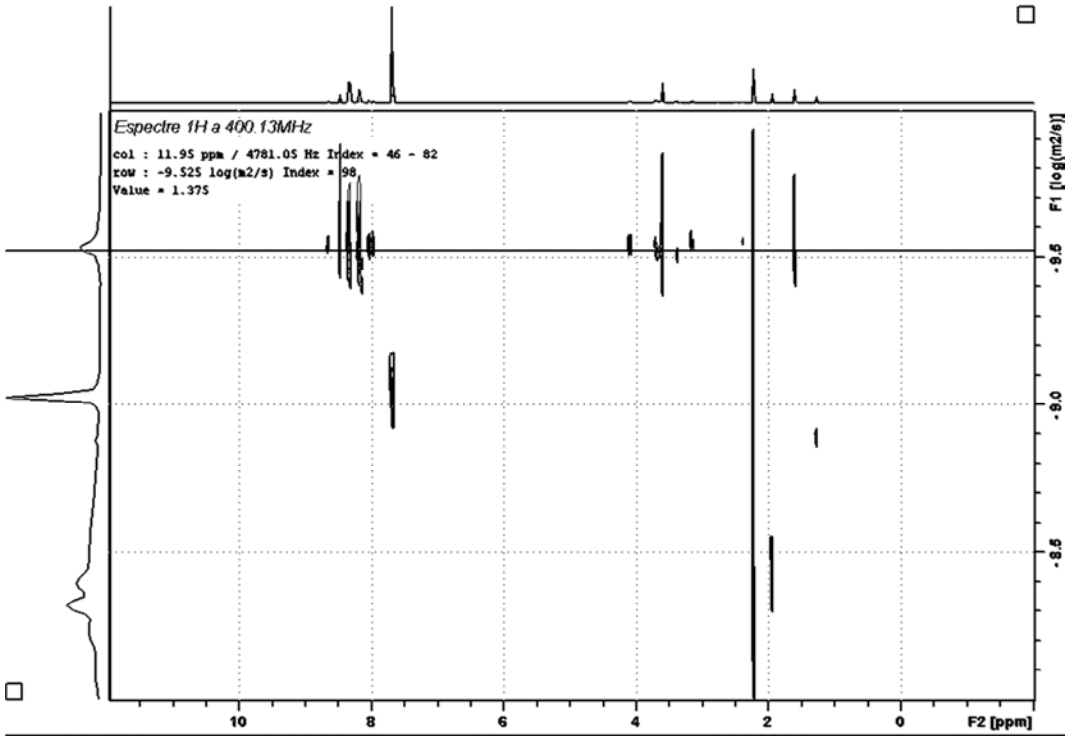

Supplementary Figure 65. Crystal structure of macrocyclic compound Pd-1b·$(AcO)_2(CF_3COO)_2$. H atoms and solvent molecules are omitted for clarity.Pd (II) presents a d^8 electronic configuration which enforce palladium ions to adopt a tetracoordinated square-planar geometry formed by three N atoms of the macrocyclic ligand **1b** and one O atom from the carboxylate group, which coordinates in a monodentate mode. As expected from previous studies with **Pd-1** complexes (C. García-Simón; M. Garcia-Borràs; Laura Gómez; I. Garcia-Bosch; S. Osuna; M. Swart; J.M. Luis; C. Rovira; M. Almeida; I. Imaz; D. Maspoch; M. Costas; X. Ribas, *Chem. Eu. J.* **2013**, *19*, *4*,1445-1456.), the coordination planes of the two Pd atoms are nearly parallel, oriented in the same direction. This arrangement creates a well-defined molecular “clip”, and therefore is susceptible to be used in rational building of supramolecular structures.

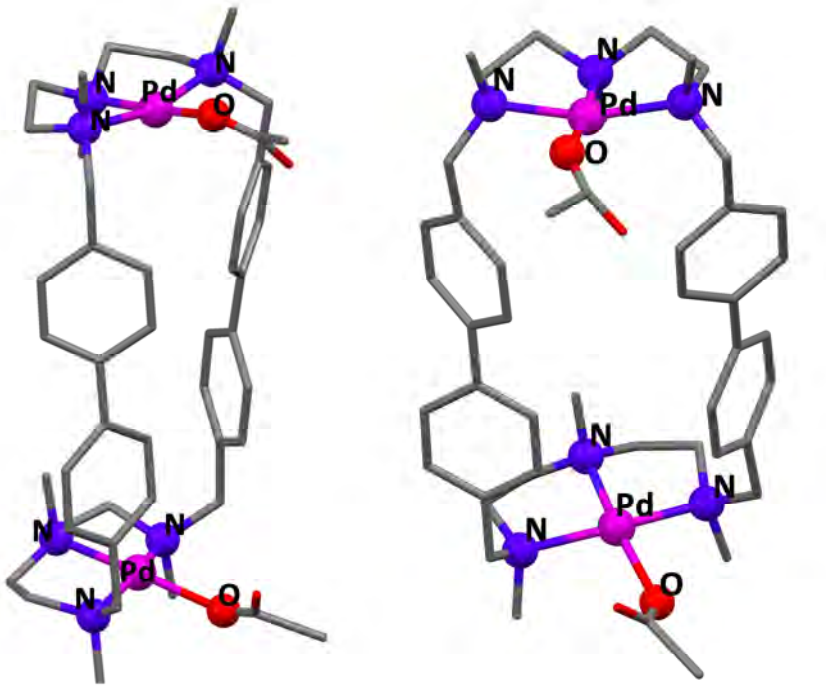

Supplementary Figure 66. XRD data of 4^{8+} nanocapsule. a) Space-filling representation of $\mathbf{4}^{8+}$. Note that a 5.5 Å-in-radius sphere (green ball; volume = 696 $Å^3$) can fit inside the cage. **b)** Illustration showing the packing of these cages along the 100 (left) and 001 (right) axes, which reveals the presence of channels with dimensions of ~ 10 Å x 20 Å. **c)** Figure illustrating the square planar geometry around the Pd(II) centers, which bear three tertiary amine and one carboxylate (from the Zn(II) porphyrin) moieties as coordinating groups. (purple: Zn, orange: Pd, grey: C, red: O, blue: N, and white: H).

a)

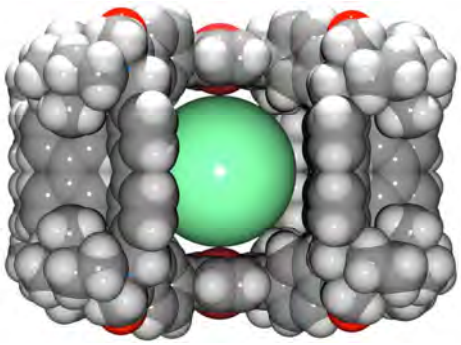

b)

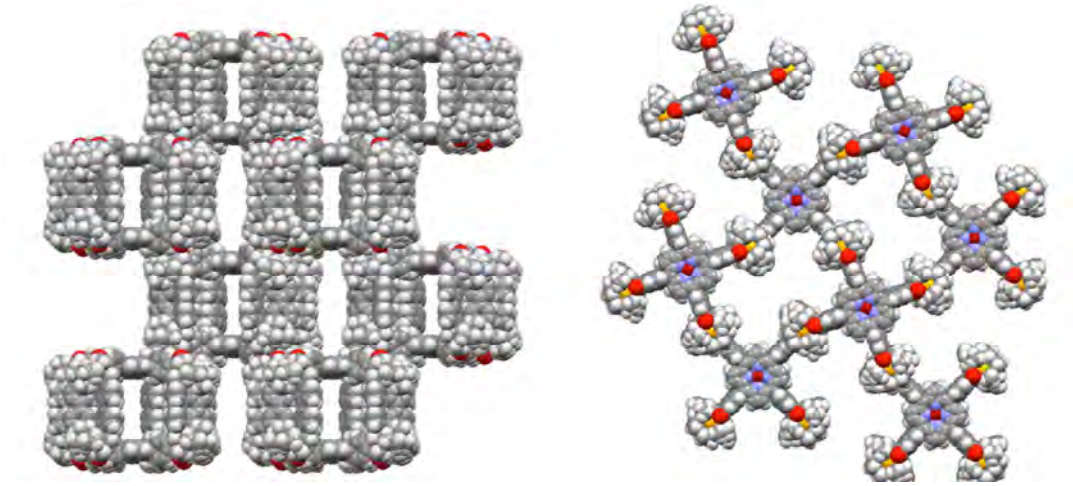

c)

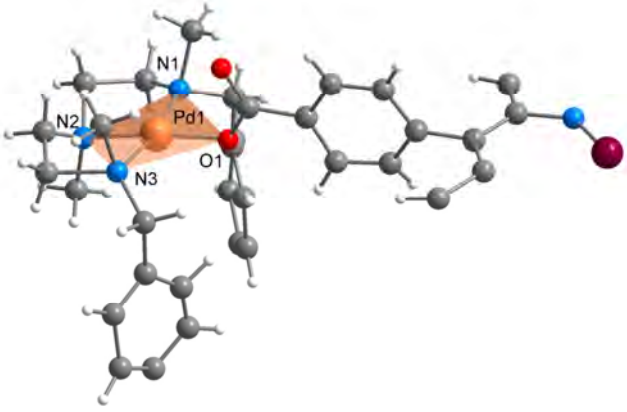

Supplementary Figure 67. Diffraction patterns of 4·(BArF)$_8$ (top), C_{60}⊂4·(BArF)$_8$ (middle) and C_{70}⊂4·(BArF)$_8$ (bottom). They show the degradation of the quality of the diffraction in terms of intensity and resolution after 266, 220 and 178 images, respectively.

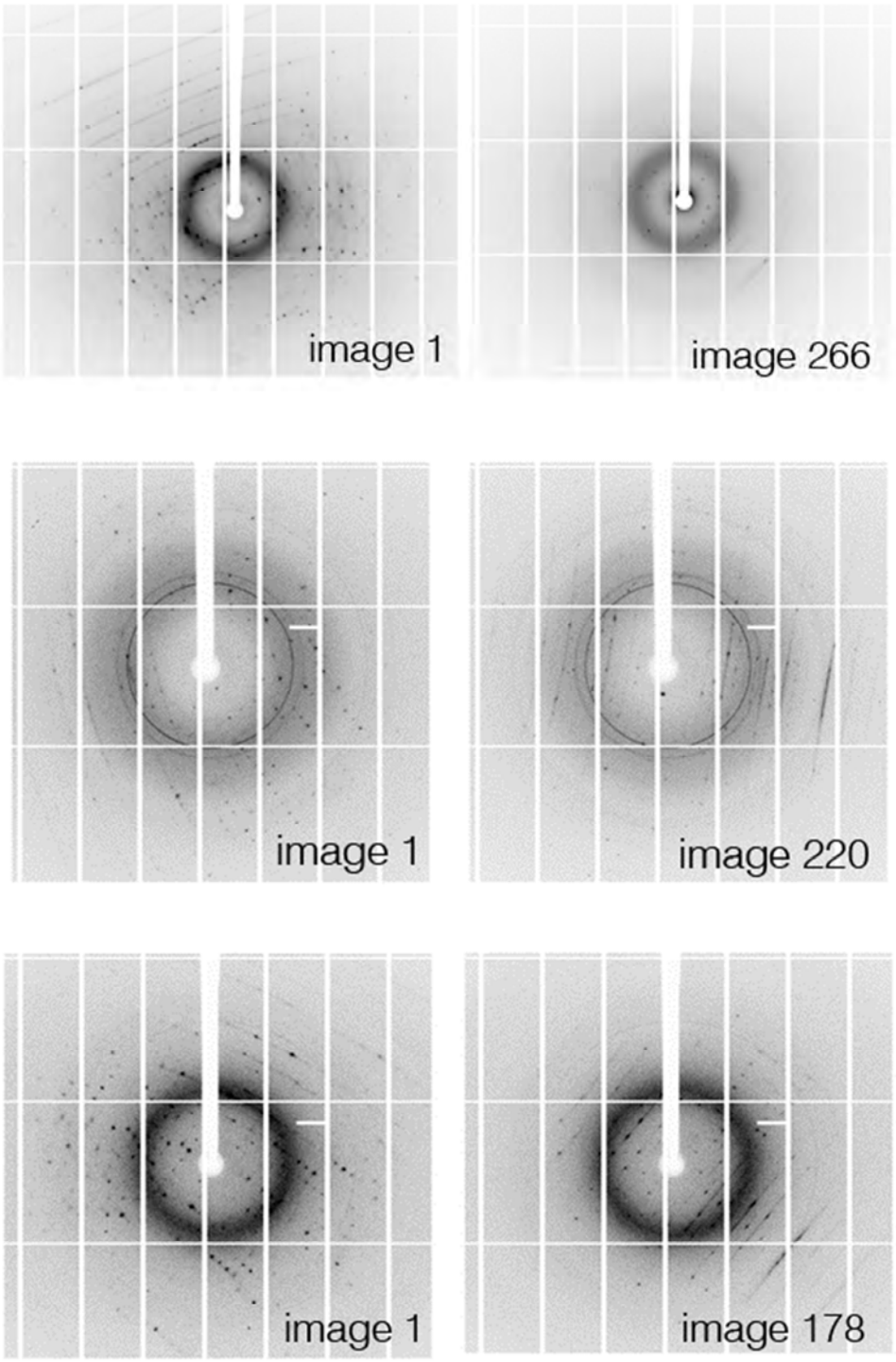

Supplementary Figure 68. Illustrations showing the packing oh the C_{60} and C_{70} host-guest adducts. Illustration showing the packing of $C_{60}\subset\mathbf{4}^{8+}$ (top) and $C_{70}\subset\mathbf{4}^{8+}$ (bottom) along the 100 (left) and 001 (right) axes. (purple: Zn, grey: C, red: O, blue: N, and white: H, pink C_n fullerene).

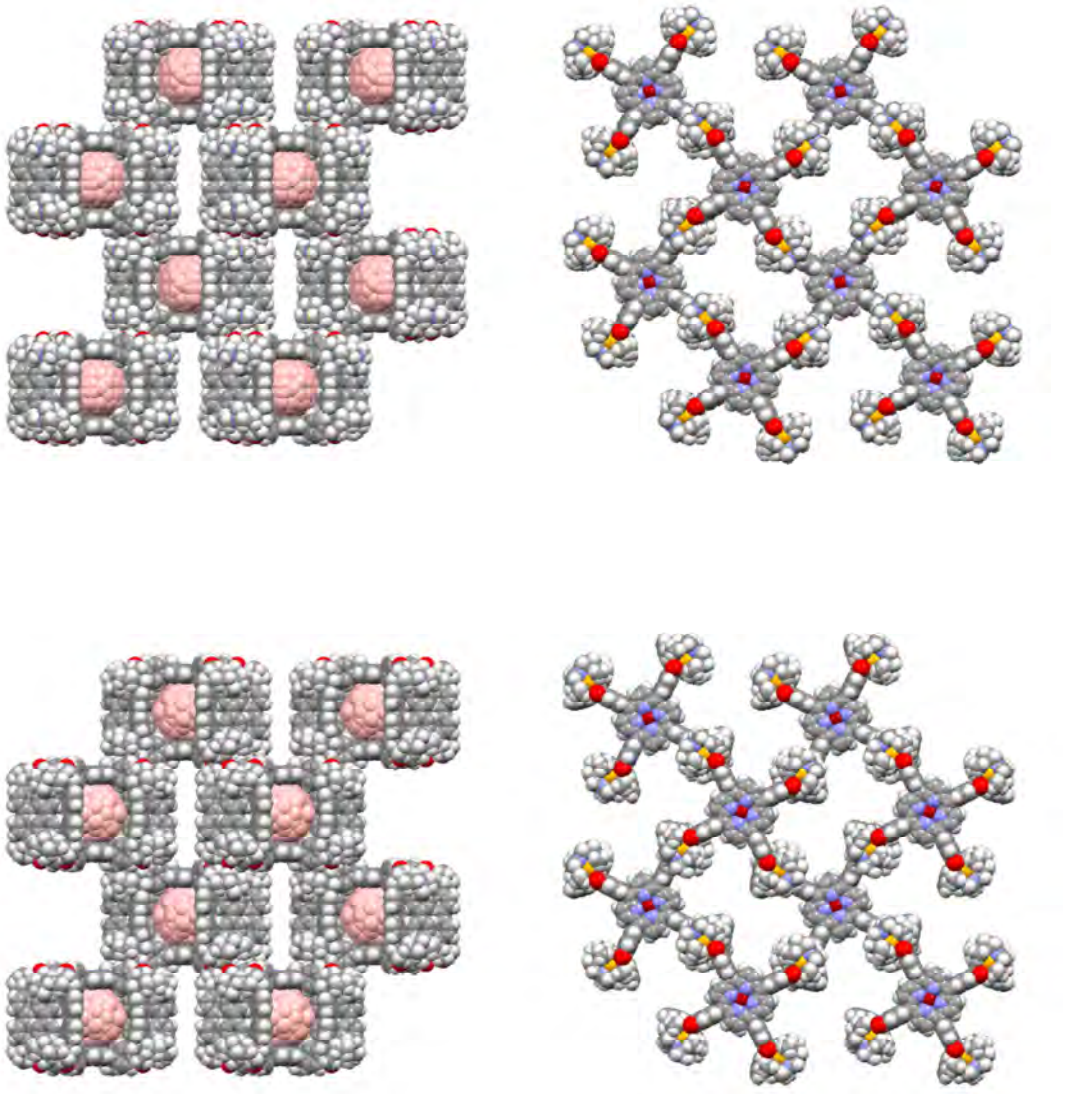

Supplementary Figure 69. Ball and stick illustration 4 nanocapsule and its host-guest adduct with C_{60} and C_{70}. $\mathbf{4}^{8+}$ (top), $C_{60}\subset\mathbf{4}^{8+}$ (middle) and $C_{70}\subset\mathbf{4}^{8+}$ (down), and selected distances. (central-red: Zn, orange: Pd, grey: C, red: O, blue: N, and white: H).

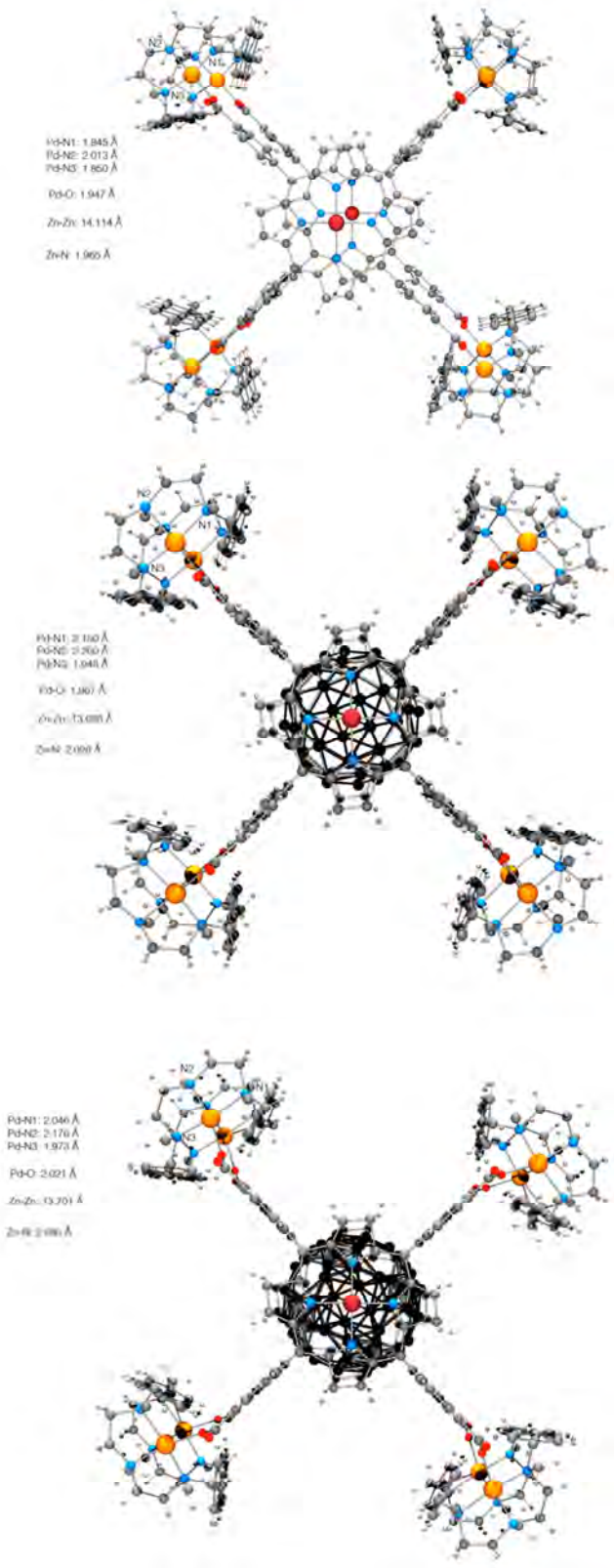

Supplementary Figure 70. 4·$(Cl)_8$ DFT optimized structure and superposition between X-Ray (purple) and DFT (grey) optimized structures. All distances are given in Å. Cl and H atoms are omitted for clarity.

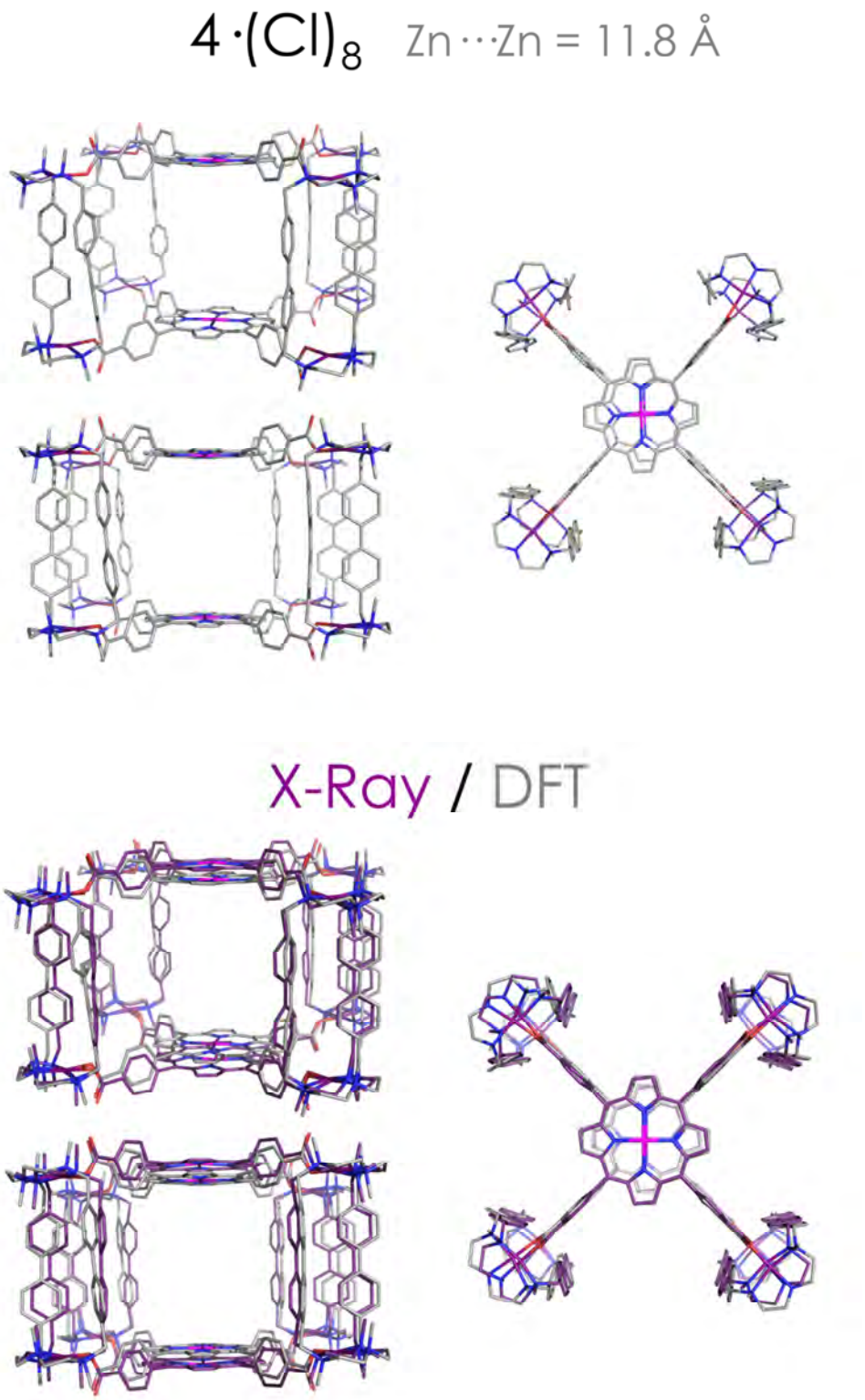

Supplementary Figure 71. $C_{60}\subset 4\cdot(Cl)_8$ DFT optimized structure and superposition between X-Ray (purple) and DFT (grey) optimized structures. All distances are given in Å. Cl and H atoms are omitted for clarity.

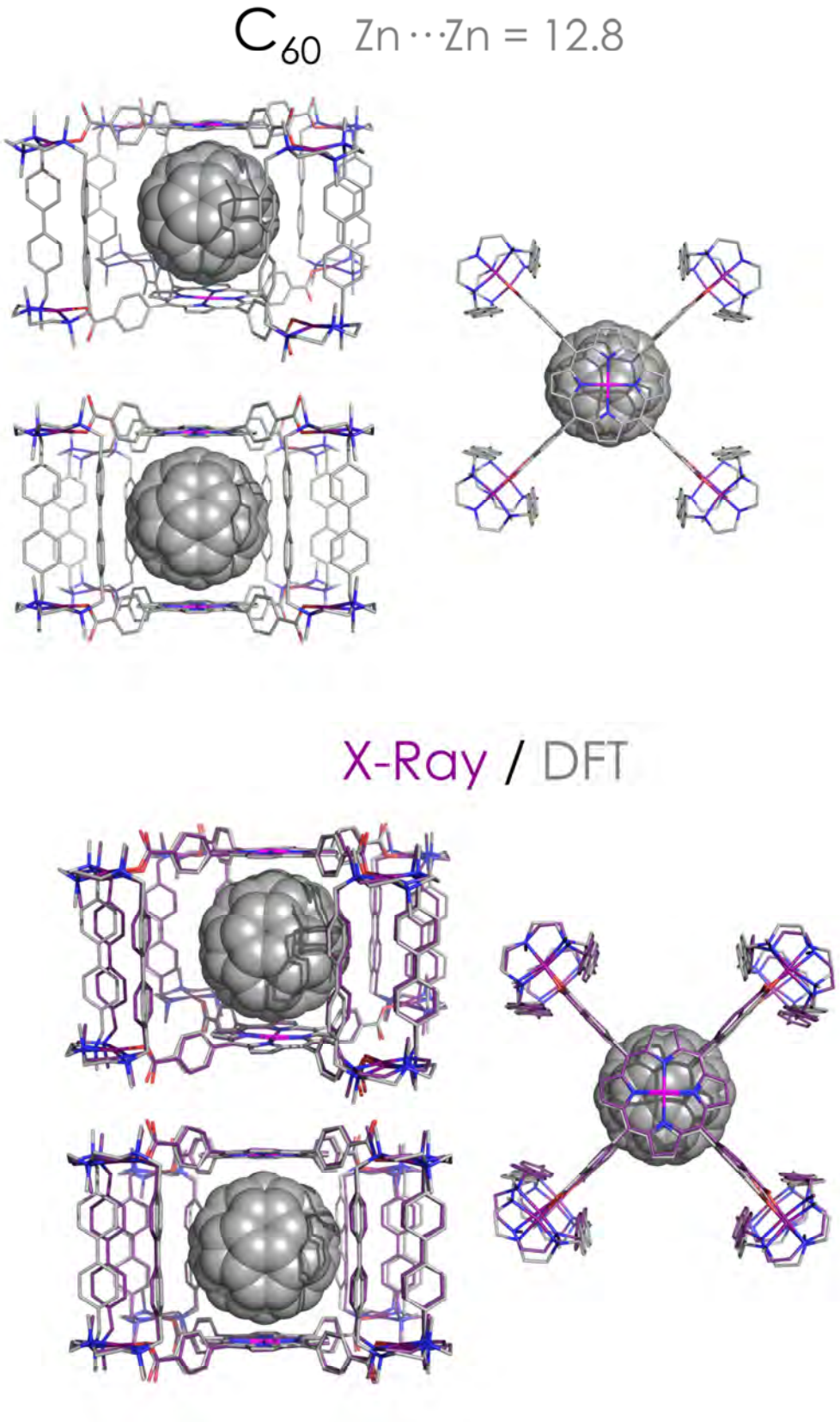

Supplementary Figure 72. $C_{70}\subset 4\cdot(Cl)_8$ DFT optimized structure and superposition between X-Ray (purple) and DFT (grey) optimized structures. All distances are given in Å. Cl and H atoms are omitted for clarity.

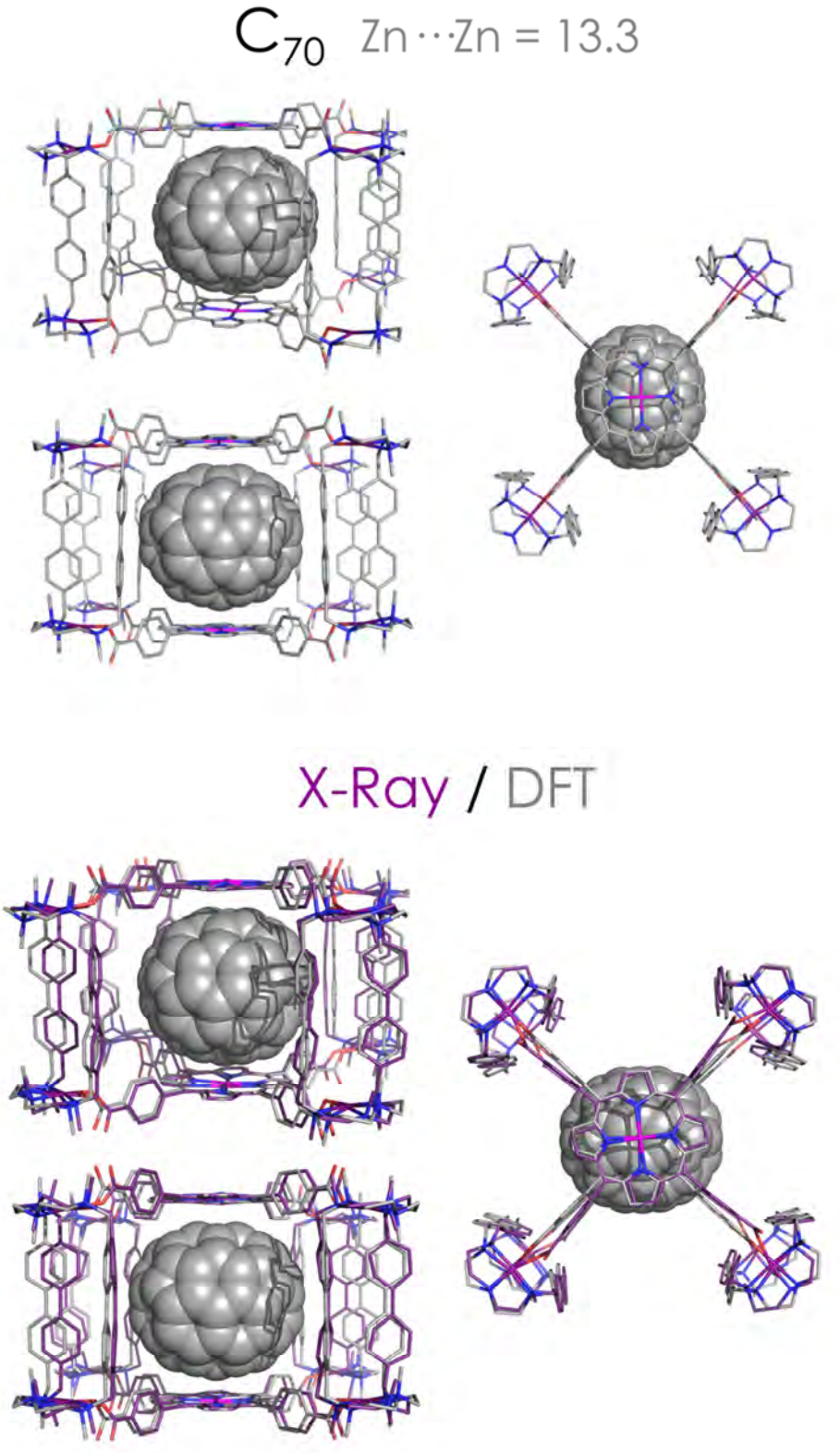

Supplementary Tables

Supplementary Table 1. Hydrodynamic ratios (r_H) values calculated from the diffusion coefficients (D) extracted from DOSY NMR experiments in CD_3CN as solvent (at 298 K).

	D ($m^2 s^{-1}$)	r_H (Å)	XRD radii (Å)*
Pd-1b	$7.31 \cdot 10^{-10}$	8.0	7.5
4·$(BArF)_8$	$3.06 \cdot 10^{-10}$	19.0	17.4
$\mathbf{C_{60}}\subset\mathbf{4}\cdot(BArF)_8$	$2.94 \cdot 10^{-10}$	19.8	17.4
$\mathbf{C_{70}}\subset\mathbf{4}\cdot(BArF)_8$	$2.99 \cdot 10^{-10}$	19.5	17.6

*Approximate values of radii have been obtained from XRD without taking in consideration any counteranion or solvent molecules.

Supplementary Table 2. DFT Porphyrin-C_{60} orientational analysis at BLYP-D3/TZP//BLYP/DZP level of theory.

Orientation	Zn···Zn (Å)	$\Delta E_{rel.}$ (kcal/mol)
C_{60} [6,6]_1	13.6	2.3
C_{60} [6,6]_2	**13.4**	**0.0**
C_{60} [5,6]_1	13.7	3.3
C_{60} [5,6]_2	13.4	0.2

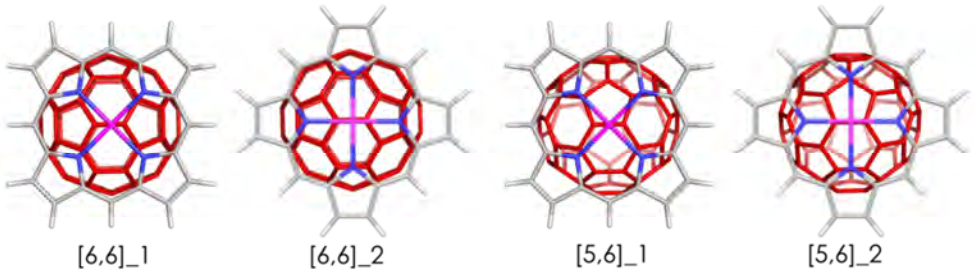

We have computationally analysed different orientations of the C_{60} molecule inside the nanocapsule by using a simple porphyrin dimer model (see Figure above). Analysing the optimal Zn···Zn distance for the most favoured orientation, C_{60} [6,6]_2 (13.4 Å), we can see that it only differs in 0.4 Å (Relative Deviation = 3.1%) with respect to the x-ray distance for the entire system. This observation indicates that the proposed model correctly describes the entire system, and more importantly, it shows that the main interaction between the C_{60} and the nanocage comes directly from the porphyrin – C_{60} moiety. The cage has the correct shape and size for maximizing this porphyrin – C_{60} interaction.

In addition, our results indicate that, although there exists a preference for one disposition of the C_{60} fullerene between both porphyrins, different orientations are accessible (energy differences around 2 kcal/mol), and thus, a dynamic $C_{60}\subset$**4** system is expected. This observation is in perfect agreement with the experimental observations and X-ray crystals, which suggested different possible arrangements for C_{60} inside the nanostructure.

Supplementary Table 3. DFT Porphyrin-C_{70} orientational analysis.

Orientation	Zn···Zn (Å)	$\Delta E_{rel.}$ (kcal/mol)
C_{70} 5MR	15.0	5.4
C_{70} diag	-*	-*
C_{70} [6,6]_1	13.8	0.1
C_{70} [6,6]_2	**13.7**	**0.0**

*The diag geometry optimizations lead to a very distorted system where the parallel disposition of both porphyrins is totally loss. This system was not further considered.

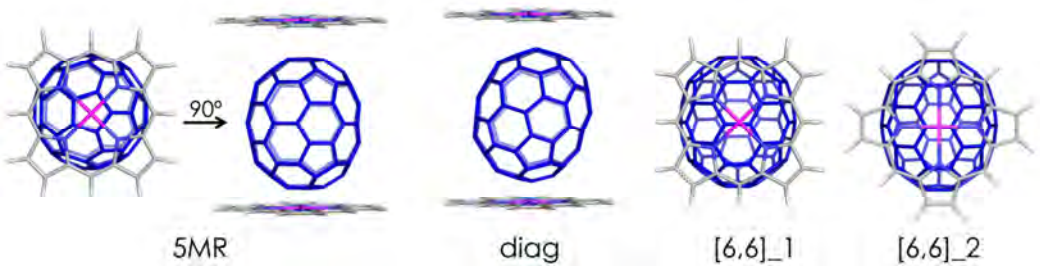

For the C_{70} system, the same conclusions described for the C_{60} case in Table **S3** are valid.

Analysing the optimal Zn···Zn distance for the most favoured orientation in C_{70} model [6,6]_2 (13.7 Å), we can see that it is in perfect agreement with the x-ray distance for the entire system (13.7 Å). Thus, the proposed model correctly describes the entire system and again indicates that the main interaction between the C_{70} and the nanocage comes directly from the porphyrin – C_{70} one.

We have explored the possibility of having the C_{70} molecule in two major positions: having the semi-major axis perpendicular to the porphyrin planes (C_{70} 5MR, see figure above) or having the semi-major axis parallel to the porphyrin planes (C_{70} [6,6]_1 and [6,6]_2, see figure above). Our calculations indicate that the orientation with the C_{70} molecule positioned with the semi-major axis parallel to the porphyrin planes is ca. 5.5 kcal/mol more favourable than the perpendicular orientation, being in agreement with the experimental X-ray observations. Moreover, if we analyse the Zn···Zn distances for both cases, we can observe that [6,6] orientations exhibit equivalent distances (13.7 Å) with respect to the X-ray structure (13.7 Å, Table 1 in the paper), while 5MR distances are longer (15.0 Å, 1.3 Å longer). These computational results also support that the parallel disposition of the C_{70} molecule between the porphyrins is the most favourable one. The perfect agreement between porphyrin dimer model

and X-ray C_{70}⊂**4** nanostructure indicates that the supramolecular cage has the correct shape and size for maximizing the porphyrin – C_{70} interaction.

Considering now only the semi-major axis parallel to the porphyrin planes dispositions ([6,6]_1 and [6,6]_2), our calculations point out that there exist different energetically accessible orientations of C_{70} molecules inside the supramolecular cage. Different possible arrangements of C_{70} in the C_{70}⊂**4** nanostructure are expected in agreement with the X-ray measurements and in the same line of the C_{60} case (see previous discussion).

Supplementary Table 4. DFT Porphyrin-Fullerene interaction analysis at BLYP-D3/TZP//BLYP/DZP level of theory.

Orientation	Zn···Zn (Å)	ΔE_R (kcal/mol)
C_{60} [6,6]_2	13.4	-28.4 (+1.6)
C_{70} [6,6]_2	12.7	-30.0 (0.0)

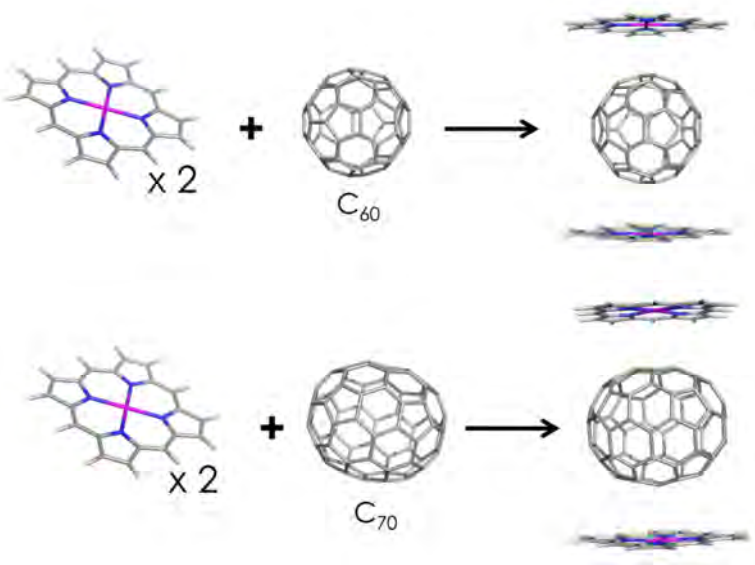

By comparing the stability of the most favourable orientation of the C_{60} and C_{70} porphyirin dimers (see Table S3 and S4), we can conclude that the porphyrin-C_{70} interaction is larger than the C_{60} one. This computational result is in agreement with the experimental observations that indicate a larger affinity of the supramolecular structure for C_{70} fullerenes.

Supplementary Table 5. Crystal Data and Structure Refinement Compounds Pd-1b·$(AcO)_2(CF_3SO_3)_2$, 4, C_{60}⊂4 and C_{70}⊂4.

	Pd-1b·$(AcO)_2(CF_3SO_3)_2$	$\mathbf{4^{8+}}$	$\mathbf{C_{60}}$⊂$\mathbf{4^{8+}}$	$\mathbf{C_{70}}$⊂$\mathbf{4^{8+}}$
Formula	$C_{46}H_{64}F_6N_6O_{10}Pd_2S_2$	$C_{264}H_{280}N_{32}O_{16}Pd_8Zn_2$	$C_{264}H_{280}N_{32}O_{16}Pd_8Zn_2,C_{76}$	$C_{264}H_{280}N_{32}O_{16}Pd_8Zn_2,C_{116}$
fw	1275.97	5139.44	6051.94	6532.43
cryst system	Monoclinic	Tetragonal	Tetragonal	Tetragonal
space group	C2/c	P4/mnc	P4/mnc	P4/mnc
a (Å)	18.686(7)	32.760(4)	32.160(4)	32.202(4)
b (Å)	14.993(6)	32.760(4)	32.160(4)	32.202(5)
c (Å)	23.283(9)	35.290(4)	34.850(4)	34.970(5)
α (deg)	90.00	90	90	90
β (deg)	107.387(6)	90	90	90
Y (deg)	90.00	90	90	90
V ($Å^3$)	6286(4)	37873 (3)	36044(4)	36258(4)
Z	4	2	2	2
*D*c (Mg m-3)	1.384	0.449	0.558	0.602
T (K)	300(2)	100 K(2)	100 K(2)	100 K(2)
-*λ* (Mo KR) (Å)	0.71073	0.82656	0.98482	0.82656
μ (mm-1)	0.708	0.268	0.288	0.290
2*Θ* max (deg)	28.69	22.0	22.1	23.8
reflns collected	43301	221439	115405	218018
indep. reflns	7669 (0.0950)	10719	8936	11379
params	338	142	160	154
GOF on F^2	0.900	3.84	2.63	2.92
$R_{indices}$ (all data)	R1=0.075, wR2=0.1959	R1=0.248, wR2=0.459	R1=0.267, wR2=0.486	R1=0.301, wR2=0.497

Supplementary Methods

DFT calculations

All Density Functional Theory (DFT) calculations were performed with the Amsterdam Density Functional (ADF 2010) program.[1] The molecular orbitals (MOs) were expanded in an uncontracted set of Slater type orbitals (STOs) of double-ζ (DZ), and double-ζ (DZP) and triple-ζ (TZP) quality containing diffuse functions and one set of polarization functions. In order to reduce the computational time needed to carry out the calculations, the frozen core approximation has been used.[2] In this approximation, the core density is obtained and included explicitly, albeit with core orbitals that are kept frozen during the SCF procedure. It was shown that the frozen core approximation has a negligible effect on the optimized equilibrium geometries.[3] Thus, in this work, core electrons (1s for second period (C, N, O); 1s2s2p for third and fourth periods (Cl, Zn); and 1s2s2p3s3p4s3d for fifth period (Pd)) were kept frozen during the calculations. Scalar relativistic corrections have been included self-consistently using the Zeroth Order Regular Approximation (ZORA).[4] An auxiliary set of *s*, *p*, *d*, *f*, and *g* STOs was used to fit the molecular density and to represent the Coulomb and exchange potentials accurately for each SCF cycle.[5] Energies and gradients were calculated using the local density approximation (Slater exchange) with non-local corrections for exchange (Becke88)[6] and correlation (Lee-Yang-Parr)[7] included self-consistently (i.e. the BLYP functional). BLYP (and BLYP-D) were found to accurately reproduce CCSD(T) structural and energy data of stacked as well as hydrogen- bonded and van der Waals complexes.[8]

All geometries reported in this work related to the supramolecular nanocage were optimized at the DFT level with the DZ basis set (i.e. BLYP/DZ). Although these systems contain a large number of atoms (for example, 670 atoms for the smallest $C_{60}\subset 4\cdot Cl_8$ system, being 10 of them transition metals, 8 Pd and 2 Zn), we could treat them at DFT level by using the well parallelized ADF and QUILD codes on MareNostrum supercomputer architecture at the Barcelona Supercomputing Centre (BSC-CNS). We have demonstrated that $BArF^-$ anions do not have any relevant role in the event of fullerene encapsulation. On the other hand, each of the eight $BArF^-$ anions is constituted by 69 atoms ($C_{32}H_{12}BF_{24}^-$, $C_{32}H_{12}BF_{24}^-$, 552 atoms in total for the eight anions), thus their inclusion in the computational DFT calculation would be impossible in terms of computing time. Therefore, we selected Cl^- monoatomic anions to perform the calculation as the lighter of the halogen atoms (excluding F^- for its implications as strong base) and aiming at compensating the positive charge of cage $\mathbf{4}^{8+}$. The eight Cl^- anions were introduced in the calculation input in the vicinity of the Pd^{2+} cations of the macrocyclic building blocks, where the charge was built-in. In this way, the computed cage $\mathbf{4}\cdot(Cl)_8$ reliably reproduced the neutrality and geometrical aspects of $\mathbf{4}\cdot(BArF)_8$ with the minimum computational costs. Because of the large flexibility of the supramolecular systems, the high number of degrees of freedom and the flat PES, the convergence thresholds during the optimization procedure were set to 10^{-3} a.u. For the present optimizations using QUILD program and ADF computational package, it has been

considered the Gradient (forces) root-mean-square and maximum values given in atomic units (a.u.). No symmetry requirements have been imposed during any optimization.

In the present study, energy dispersion corrections were not introduced by using empirical methods such are Grimme's methodology[9,10] (D2 or D3) implemented in commercial quantum chemistry codes during the optimizations. It is well documented the overbinding tendency of DFT-D2 and DFT-D3 methods when large carbon systems or porphyrin dimers are considered.[10] In our case, we have performed several tests including D2 and D3 empirical dispersion corrections during the optimization procedures, observing strange torsions and folding of the supramolecular nanosystems due to these overestimations of the interaction energies between porphyrins and fullerene carbon structures. Moreover, our results clearly indicate that geometries optimized at DFT level without dispersion corrections are in perfect agreement with the X-Ray structures, whereas DFT-D2 and DFT-D3 predicted substantially shorter inter-porphyrin distances.

All energies reported related to the porphyrin dimer model were obtained with the TZP basis in single-point energy calculations including Grimme's D3[10] dispersion corrections at geometries that were optimized with the DZP basis (i.e., BLYP-D3/TZP//BLYP/DZP). It is well known that dispersion corrections on DFT (GGA functionals) energy values are essential to correctly reproduce the experimental trends (see for instance ref. "Dispersion Corrections Are Essential for the Study of Chemical Reactivity in Fullerenes"*, J. Phys. Chem. A*, **2011**, *115*, 3491), but they were not included during the optimization procedure (see discussion above).

The actual geometry optimizations were performed with the QUILD[11] (QUantum-regions Interconnected by Local Descriptions) program, which functions as a wrapper around the ADF program. The QUILD program constructs all input files for ADF, runs ADF, and collects all data; ADF is used only for the generation of the energy and gradients. Furthermore, the QUILD program uses improved geometry optimization techniques, such as adapted delocalized coordinates[12] and specially constructed model Hessians with the appropriate number of eigenvalues.[12]

Non-Covalent Interaction (NCI) analyses were performed with the NCIPLOT program[13,14] on the BLYP/DZP optimized porphyrin dimer C_{60} and C_{70} models. We used the promolecular densities, defined as the sum of atomic contributions. Although promolecular density does not consider the relaxation due to the SCF procedure, it has been shown that results obtained from relaxed density and promolecular ones are qualitatively equivalent. The NCI analysis is based on 2D plot of the reduced density gradient, *s*, and the electron density, ρ (Supplementary Equation 1)[14]:

$$s = \frac{1}{2(3\pi^2)^{1/3}} \frac{|\nabla\rho|}{\rho^{4/3}} \qquad \text{(Equation1)}$$

A change in the reduced density gradient between the interacting atoms takes place when a weak inter- or intramolecular interaction is present, appearing density critical points between interacting fragments.[9] The density and reduced density gradient are computed at a number of grid points around the atoms. Dispersion interactions appear at very low density values ($\rho > 0.01$ a.u.), while stronger interactions such hydrogen bonds appear at higher density values ($0.01 < \rho < 0.05$ a.u.). The sign of the second eigenvalue (λ_2) of the electron-density Hessian matrix is used as a tool for distinguishing between bonded (attractive interaction, $\lambda_2 < 0$) or nonbonded (repulsive interaction, $\lambda_2 > 0$) interactions. Consequently, the gradient is plotted against the product of the sign (λ_2) and the electron-density function. For the isosurface representation (isosurface s value 0.3 a.u.), a RGB (red-blue-green) scale was used: red is used to represent repulsive interactions, blue for attractive interactions and green for weak van der Waals interactions. For further explanations regarding to NCI and NCIPLOT representations see refs. 13, 14, and 15.

Supplementary Discussion 1

Additional comments to X-ray diffraction data

The experiments with these crystals were performed in two different beamlines of two different synchrotrons, the I19 beamline of DIAMOND synchrotron in Didcot, UK (MT 8477 Visit May 2nd, 2013) dedicated to small molecules, and XALOC beamline of ALBA-CELLS synchrotron in Barcelona dedicated to proteins crystallography (in-house project IH-BL13-2013-iimaz). XALOC beamline, although being initially designed as a protein beamline, meets all requirements to solve the structures of our crystals. The beamline is equipped with a large-area, background noise-free pixel detector (Pilatus 6M, Dectris), which can be placed at only 123mm from the sample. This fact, together with the relatively high energy achievable (22 keV), allows the beamline to collect up to 0.65 Å resolution routinely, which higher than the resolution obtained from the crystals. As a matter of fact, the sensitivity of the detector, the resolution at low angles (were our compounds diffract) and the fast data collection offered by the XALOC protein beamline gave us better data.

Another issue is the use of cryogeny to obtain better diffraction data. We tested flash cooling the crystals at 100 K by mounting them in a capillar with cryoprotectants. However, this procedure did not provide better crystallographic data than that collected with the crystals mounted in a capillary, observing a low initial diffraction and a faster degradation of the crystallinity for all measured crystals. For this reason, to ensure the preservation of the crystals, we decided to mount the crystals on a capillary, not in the initial mother liquor, but in mother liquor saturated with diethyl ether. The crystallographic data collected with this procedure is below of the typical quality for MOF compounds, but we honestly believe it is the best that can be extracted with current X-ray diffraction technologies, and most importantly the solutions of the structures, albeit of low resolution, are reliable and provide a suitable structural support to all the conclusions of the manuscript.

Since precise location of BArF anions within these structures has not been possible, a tentative residual void space can only be given by considering the volume of a BArF molecule: 349 $Å^3$ (calculated from crystallographic data using Discovery Studio Viewer Pro[17]. From this value, the estimated volume that occupies all BArF molecules in $C_{60}⊂$**4**$\cdot(BArF)_8$ is 5584 $Å^3$, corresponding to 16 BArF molecules per unit cell. The total solvent-accessible void space of $C_{60}⊂$**4**$\cdot(BArF)_8$ is 25646 $Å^3$ (71 % of the total volume in unit cell; Spek, A. L. PLATON, *A Multiporpose Crystallographic Tool*, Utrecht University, Utrecht, **1998.**). Therefore, taking into account the inclusion of fullerenes and the presence of 16 BArF molecules per unit cell, it still remains a residual void space of 20062 $Å^3$ (~78 % of the total solvent-accessible void space). In other words, BArF anions only occupy ~22 % of the total solvent-accessible void space in unit cell, confirming that there is enough space for accommodating them after the solid-state inclusion of fullerenes.

Supplementary References

(1) Baerends, E.J., Ziegler. T., Autschbach, J., Bashford, D., Bérces, A., Bickelhaupt, F.M., Bo, C., Boerrigter, P.M., Cavallo, L., Chong, D.P., Deng, L., Dickson, R.M., Ellis, D.E., Faassen, Mv., Fan, L, Fischer, T.H., Fonseca Guerra, C, Ghysels, A., Giammona, A., Gisbergen, S. J. A. van., Götz, A. W., Groeneveld, J. A., Gritsenko, O. V., Grüning, M., Gusarov, S., Harris, F.E., Hoek, P. van den., Jacob, C.R., Jacobsen, H., Jensen, L., Kaminski, J.W., Kessel, G. van, Kootstra, F., Kovalenko, A., Krykunov, M.W., Lenthe, E. van, McCormack, D.A., Michalak, A., Mitoraj, M., Neugebauer, J., Nicu, V.P., Noodleman, L., Osinga, V.P., Patchkovskii, S., Philipsen, P. H. T., Post, D., Pye, C.C., Ravenek, W., Rodríguez, J.I., Ros, P., Schipper, P. R. T., Schreckenbach, G., Seldenthuis, J. S., Seth, M., Snijders, J. G., Solà, M., Swart, M., Swerhone, D., Velde, G. te, Vernooijs, P., Versluis, L., Visscher, L., Visser, O., Wang, F., Wesolowski, T.A., Wezenbeek, E. M. van, Wiesenekker, G., Wolff, S. K., Woo, T. K., and Yakovlev, A.L., *ADF2010*, SCM, Amsterdam (2010).

(2) Velde, G. te, Bickelhaupt, F. M., Baerends, E. J., Fonseca Guerra, C., Gisbergen, S. J. A. van, Snijders, J. G., and Ziegler, T., Chemistry with ADF, *J. Comput. Chem.*, **22**, 931-967 (2001).

(3) Swart, M., and Snijders, J. G., Accuracy of geometries: Influence of basis set, exchange-correlation potential, inclusion of core electrons, and relativistic cor rections, *Theor. Chem. Acc.*, **110**, 34-41 (2003).

(4) Lenthe, E. van, Baerends, E. J., and Snijders, J. G*., Relativistic regular two-component Hamiltonians,* J. Chem. Phys*.,* 99, 4597-4610 (1993)*.*

(5) Baerends, E. J., Ellis, D. E., and Ros, P., Self-consistent molecular Hartree—Fock—Slater calculations I. The computational procedure, *Chem. Phys.*, **2**, 41-51 (1973).

(6) Becke, A.D., Density-functional exchange-energy approximation with correct asymptotic behavior, *Phys. Rev. A*, **38**, 3098-3100 (1988).

(7) Lee, C., Yang, W. and Parr, R.G., Development of the Colle-Salvetti correlation-energy formula into a functional of the electron density, *Phys. Rev. B*, **37**, 785-789 (1988).

(8) Wijst, T. van der, Fonseca Guerra, C, Swart, M., Bickelhaupt, F.M., Lippert, B., A Ditopic Ion-Pair Receptor Based on Stacked Nucleobase Quartets, *Angew. Chem. Int. Ed.*, **48**, 3285 – 3287 (2009).

(9) Grimme, S., Semiempirical GGA-type density functional constructed with a long-range dispersion correction, *J. Comput. Chem.*, **27**, 1787–1799 (2006).

(10) Grimme, S., Antony, J., Ehrlich, S., and Krieg, H., A consistent and accurate *ab initio* parametrization of density functional dispersion correction (DFT-D) for the 94 elements H-Pu, *J. Chem. Phys.*, **132**, 154104 (2010).

(11) Swart, M., and Bickelhaupt, F.M., QUILD: QUantum-regions interconnected by local descriptions, *J. Comput. Chem.*, **29**, 724-734 (2008).

(12) Swart, M. and Bickelhaupt, F.M., Optimization of strong and weak coordinates, *Int. J. Quant. Chem.*, **106**, 2536-2544 (2006).

(13) Contreras-García, J., Johnson, E.R., Keinan, S., Chaudret, R., Piquemal, J-P., Beratan, D.N., Yang, W., NCIPLOT: A Program for Plotting Noncovalent Interaction Regions**,** *J. Chem. Theory Comput*., **7**, 625-632 (2001).

(14) Johnson, E.R., Keinan, S., Mori-Sánchez, P., Contreras-García, J., Cohen, A.J., Yang, W., Revealing Noncovalent Interactions, *J. Am. Chem. Soc*., **132**, 6498-6506 (T. van der).

(15) Chaudret, R., Courcy, B. de, Contreras-García, J., Gloaguen, E., Zehnacker-Rentien, A., Mons, M., Piquemal, J-P., Unraveling non-covalent interactions within flexible biomolecules: from electron density topology to gas phase spectroscopy, *Phys. Chem. Chem. Phys*., **16**, 9876-9891 (2014).

(16) Alonso, M., Woller, T., Martín-Martínez, F.J., Contreras-García, J., Geerlings, P., Proft, F. De., Understanding the Fundamental Role of π/π, σ/σ, and σ/π Dispersion Interactions in Shaping Carbon-Based Materials, *Chem. Eur. J.*, **20**, 4931-3941 (2014).

(17) Hannant, M.H., Wright, J.A., Lancaster, S.J., Hughes, D.L., Horton, P.N., Bochmann, M., The synthesis of new weakly coordinating diborate anions: anion stability as a function of linker structure and steric bulk, *Dalton Trans*., 2415-2426 (2006).

Supporting Information Chapter V

ENANTIOSELECTIVE HYDROFORMYLATION BY A Rh-CATALYST ENTRAPPED IN A SUPRAMOLECULAR METALLOCAGE

Table of contents

1. Supplementary methods

1.1. Materials and methods

Unles indicated otherwise, reagents and solvents used were commercially available reagent quality and reactions were carried out under an atmosphere of nitrogen using standard Schlenk techniques. Ligands **α**[1], **β**[2] and molecular cage **4**·$(BArF)_8$[3] were synthesized following previously reported procedures.

1.2. Instrumentation

NMR spectra (^1H, ^{31}P and ^{13}C) were measured on a Bruker DRX 400 MHz, Bruker AVANCE 500 MHz, Bruker AVANCE 600 MHz and Varian Inova 500 MHz; $CDCl_3$, CD_3CN or Toluene-d_8 were used as solvents, if not further indicated. High resolution mass spectra (HRMS) were obtained on a Bruker MicroTOF-Q-II, using acetonitrile as the mobile phase. UV-Vis spectroscopy was performed on an Agilent 8452 UV-vis spectrophotometer with 1 cm quartz cell. IR experiments were performed at r.t. into a Nicolet 510 FTIR spectrometer. Gas chromatographic analyses were runed on a Shidmandu GC-17A apparatus (split/splitless injector, J&W 30 m column, film thickness 3.0 µm, carrier gas 70kPa He, FID Detector). Chiral GC separations were conducted on the Iterscience HR GC with a Supelco β-dex 225 capillary column. Molecular Modeling calculations were performed using PM3-Spartan molecular modeling program.

1.3. Synthesis of ligands γ and δ

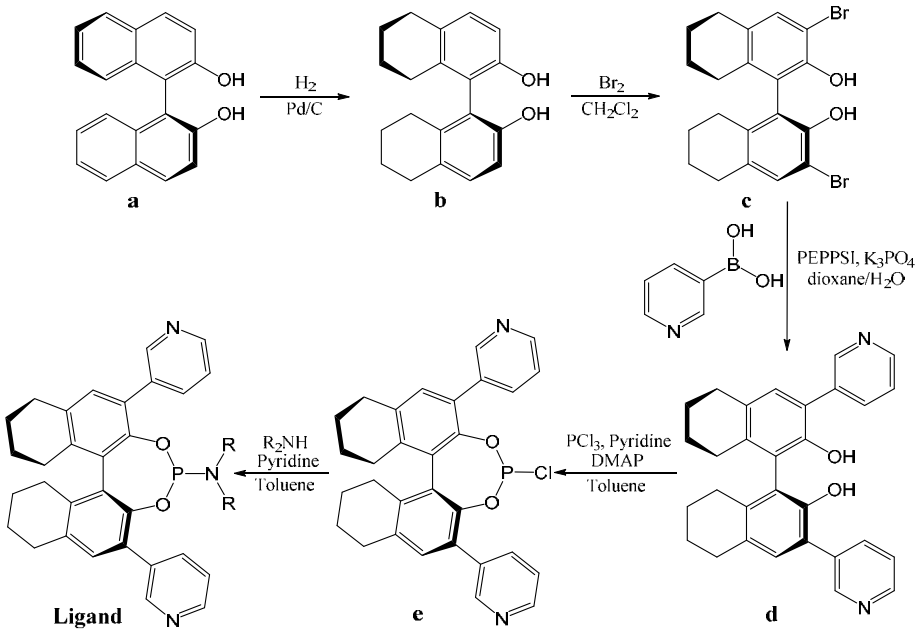

Compound **d** and ligand **α** (ligand precursor) were synthesized following the procedure reported in the literature.[1-2]

Synthesis of the Ligands α, γ, δ: In a flame dried Schlenk 200 mg (0.44 mmol) **d**, pyridine (0.068 mL, 0.88 mmol) and DMAP (10 mol%) were suspended in dry toluene (4.4 mL, 0.1 M). The solution was cooled to 0 ℃ and distilled PCl_3 (0.080 mL, 0.88 mmol) was added dropwise over 10 min. The mixture was warmed up to room temperature and then refluxed overnight. The reaction mixture was cooled to room temperature and the formation of product was checked by ^{31}P-NMR. The solvent and the residual PCl_3 were removed in vacuum. The resulting solid was used for the next step without any further purification.

In a flame dried Schlenk the dialkylamine (0.44 mmol) and pyridine (0.040 mL, 0.48 mmol) were dissolved in dry toluene (1 mL). The solution was added drop wise to a cooled (0 ℃) mixture of **e** (225.7 mg, 0.44 mmol) in dry toluene (5 mL). The mixture was warmed up to room temperature and stirred overnight at room temperature. The precipitate formed was filtered over a pad of Celite under argon, and then solvent was evaporated in vacuum to obtain **α**, **γ**, **δ**.

Ligand **γ**: Yield: 81 % (white foam); ^{1}H NMR (400 MHz, $CDCl_3$): δ = 8.85 (m, 2H) 8.54 (dd, 2H), 7.96 (dt, 1H), 7.90 (dt, 1H), 7.28 (m, 2H), 7.16 (s, 1H), 7.14 (s, 1H), 2.90 (m, 4H), 2.54 (m, 2H), 2.35 (m, 4H), 1.87 (m, 8H), 0.51-0.59 (t, 6H); ^{13}C NMR: 150.2, 149.1, 147.2, 138.0, 136.2, 130.2, 129.1, 128.4, 122.5, 122.1, 34.2, 30.2, 29.1, 28.3, 27.8, 23.1, 22.2; ^{31}P NMR: δ= 140.85 ppm.

Ligand **δ**: Yield: 52 % (white foam); ^{1}H NMR (400 MHz, Toluene): δ = 8.99-9.07 (dd, 2H) 8.43 (d, 2H), 7.84 (dt, 1H), 7.73 (dt, 1H), 7.01 (m, 2H), 6.97 (s, 1H), 6.71 (s, 1H), 2.68 (m, 6H), 2.44 (m, 2H), 1.79 (m, 2H), 1.59 (m, 8H), 0.87 (4*d, 12H); ^{13}C NMR: 153.2, 152.7,150.2, 14.1, 139.2, 138.0, 135.2, 130.2, 129.1, 128.6, 122.1, 47.5, 46.6, 35.6, 34.2, 31.1, 28.3, 12.8, 12.1, 11.2; ^{31}P NMR: δ= 139.89 ppm.

1.4. Diffusion-Ordered NMR spectroscopy experiments

The DOSY spectrum of **4,4-bpy**⊂**4**·$(BArF)_8$ (see Figure S9) affords a diffusion coefficient for the cage protons of $D=10^{-9.532}$ m^2 s^{-1} that give a hydrodynamic ratio of 19.8Å after applying the Stokes-Einstein equation. Very importantly, the **4,4'-bpy** signal at 4.92 ppm also presents the same diffusion value than the cage and therefore the location of the bpy ligand into the cavity of the cage is fully confirmed. The simplicity pattern of the bpy signals also confirm that the original symmetry of the free ligand is maintained into the cavity, suggesting that the complex presents a symmetric coordination. Similar porphyrin structures with Rh and bpy have been previously described, as well as different cage-like systems which interact with **4,4-bpy**, all these precedents on the literature support our ^{1}H NMR data.[4-7]

1.5. Chiral GC data for hydroformylation producs.

The enantiomeric ratio was analyzed by Chiral GC (Supelco β-dex 225).[8]

- **Hydroformylation styrene.** Initial temperature= 100ºC for 5 min, then 4ºC/min to 160ºC. t_R (R)= 11.350 min, and t_R(S)= 11.518 min.
- **Hydroformylation 4-Chlorostyrene.** Initial temperature= 100ºC for 7 min, then 0.2ºC/min to 120ºC, and then 40ºC/min to 220 for 1 min. t_R (R)= 34.810 min, and t_R(S)= 34.910 min.
- **Hydroformylation 4-Methylstyrene.** Initial temperature= 100ºC for 7 min, then 0.2ºC/min to 120ºC, and then 40ºC/min to 220 for 1 min. t_R (R)= 24.821 min, and t_R(S)= 25.561 min.
- **Hydroformylation 4-Methoxystyrene.** Initial temperature= 100ºC for 7 min, then 0.2ºC/min to 120ºC, and then 40ºC/min to 220 for 1 min. t_R (R)= 34.800 min, and t_R(S)=34.898 min.
- **Hydroformylation 3-Methoxystyrene.** Initial temperature= 100ºC for 1 min, then 0.2ºC/min to 125ºC, and then 40ºC/min to 220 for 1 min. t_R (R)= 53.393 min, and t_R(S)=54.740 min.
- **Hydroformylation 2-Methoxystyrene.** Initial temperature= 100ºC for 0 min, then 0.1ºC/min to 120ºC, and then 40ºC/min to 220 for 1 min. t_R (R)= 73.093 min, and t_R(S)=73.105 min.
- **Hydroformylation 4-*tert*-Butylstyrene.** Initial temperature= 100ºC for 7 min, then 0.2ºC/min to 180ºC, and then 2.5ºC/min to 220 for 15 min. t_R (R)=64.810 min, and t_R(S)=65.670 min.

2. Supplementary Figures

Figure S1. HRMS spectra of **4,4'-bpy⊂4**·$(BArF)_8$ host-guest complex (green squares). Experimental conditions: 100 μM in Toluene/CH_3CN (4/1), registered with a Bruker MicroTOF-Q-II exact mass spectrometer.

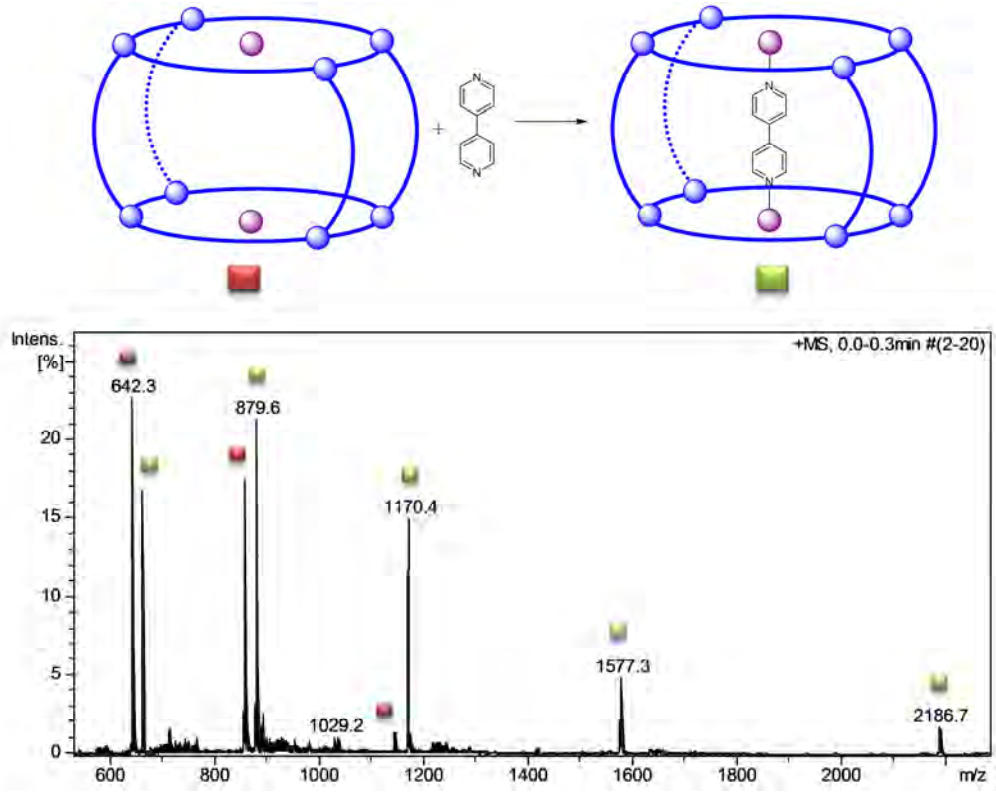

Figure S2. UV-Vis monitoring of the titration of **4**·$(BArF)_8$ nanocapsule with **4,4'-bpy**. Up to 14 eq. of **4,4'-bpy** were added to a $4.32 \cdot 10^{-7}$ M solution of **4**·$(BArF)_8$ in Toluene/CH_3CN (9/1).

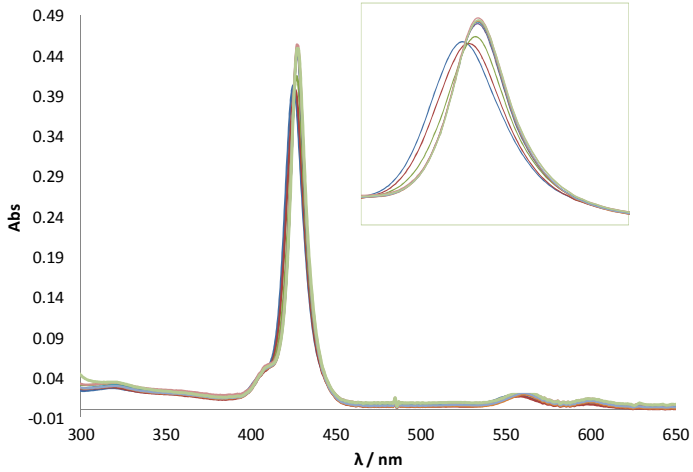

Figure S3. Job's plot, to obtain the stoichiometry for the host-guest complex between the nanocage **4**·$(BArF)_8$ and **4,4'-bpy**. X has a value arround 0.5, indicating that the host-guest complexe has 1:1 stoichiometry (n≈1).

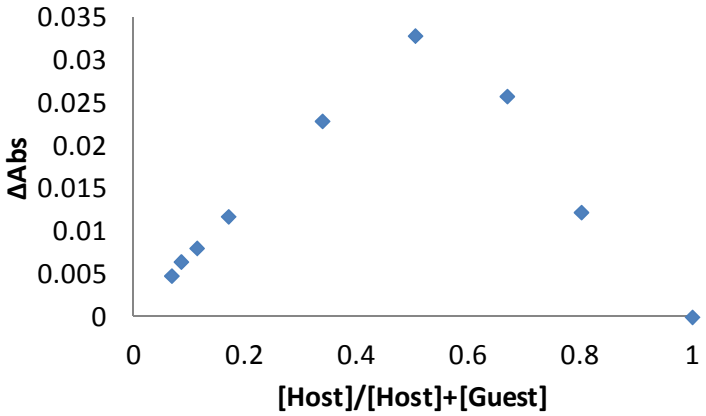

Figure S4. In green ^{1}H-NMR spectrum of free nanocage **4**·$(BArF)_8$ (bottom). In black ^{1}H-NMR spectrum of host-guest complex **4,4-bpy⊂4·(**$BArF)_8$ (top). a) From 7 to 9 ppm, and b) from 1.5 to 5.5 ppm (CD_3CN, 295 K, 400 MHz).

a)

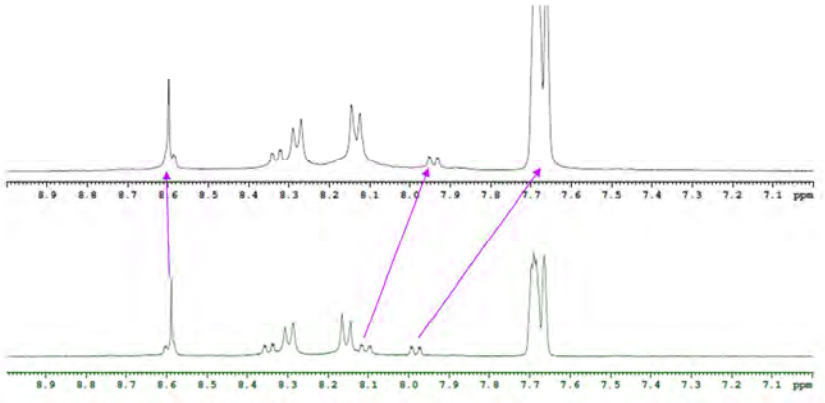

b)

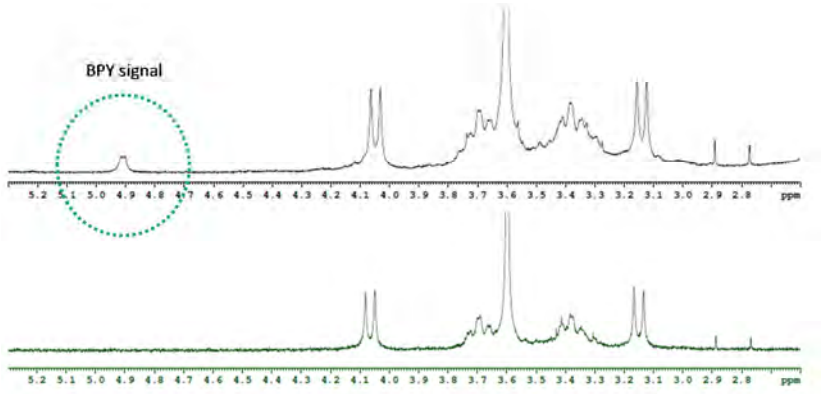

Figure S5. NMR spectrum of **4,4'-bpy⊂4**·$(BArF)_8$: a) ^{1}H-NMR (CD_3CN, 298 K, 500 MHz), b) COSY-NMR and c) Multiplicity-edited HSQC (CD_3CN, 298 K, 400 MHz).

a)

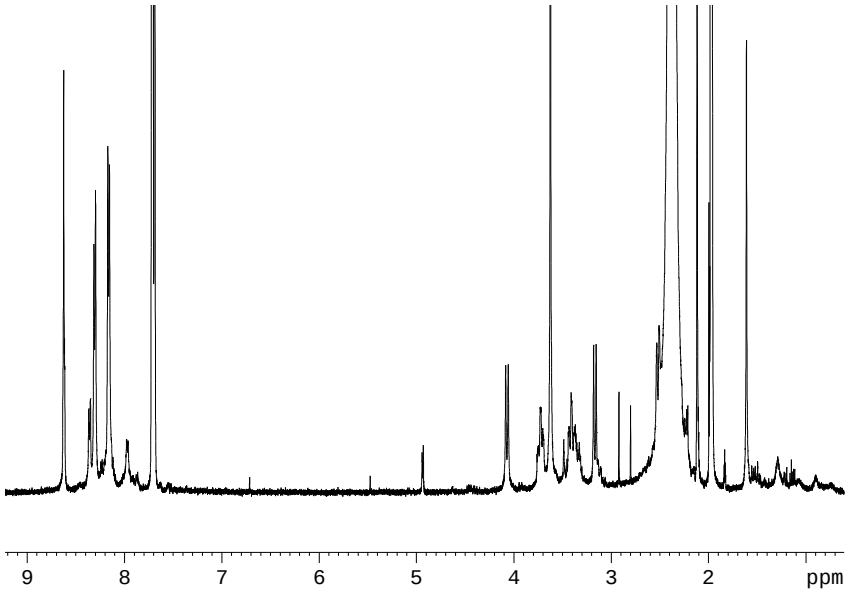

b)

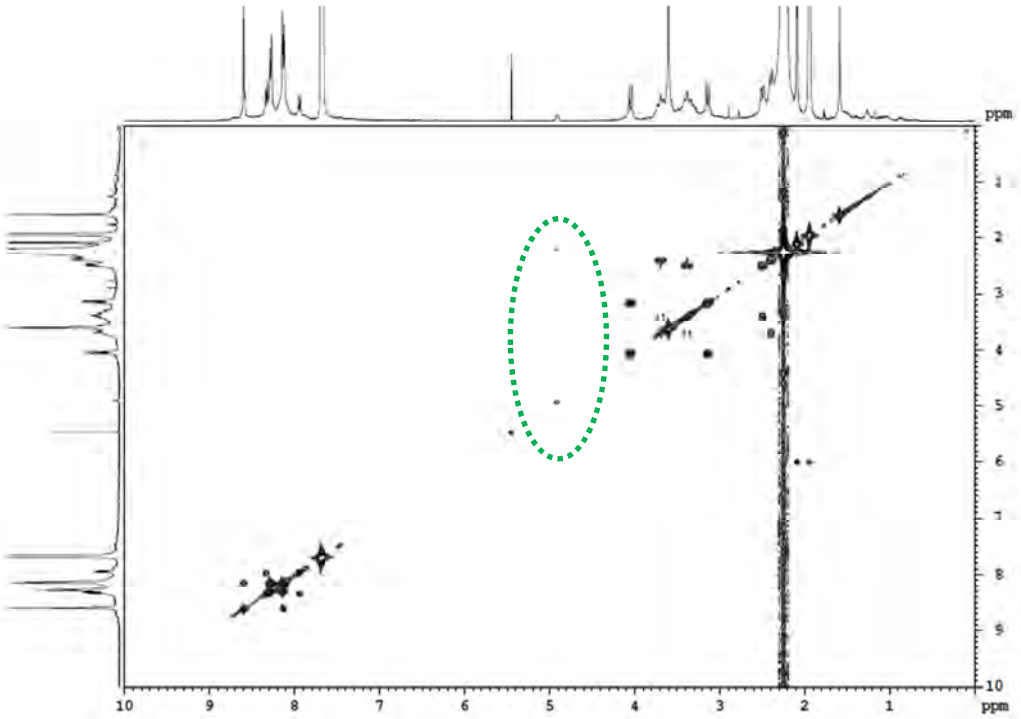

c)

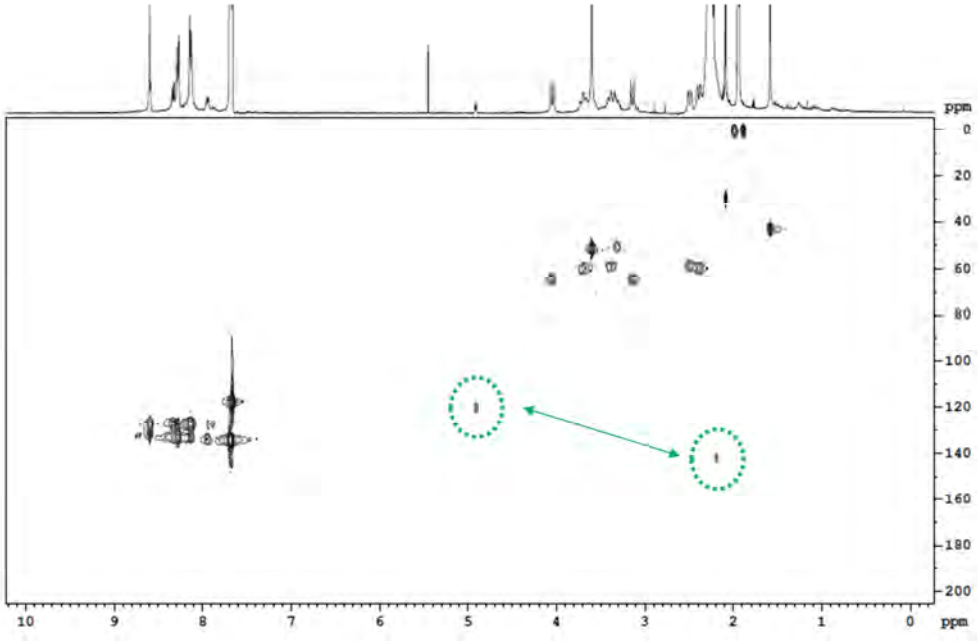

Figure S6. 2D ROESY of **4,4'-bpy⊂4**·$(BArF)_8$ with 400ms of mixing (CD_3CN, 298 K, 500MHz).

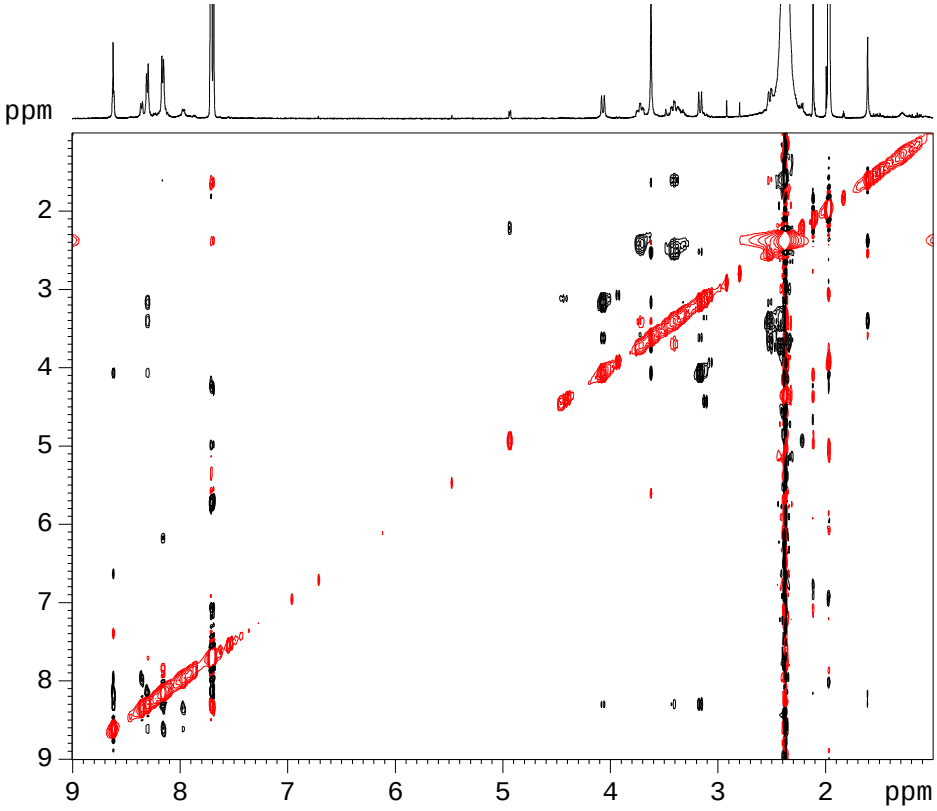

Figure S7. 2D ^{1}H-^{15}N HMBC of 4,4'-bpy in CD_3CN (used as an internal reference, $\delta(^{15}N)$ = 246.9 ppm, 298 K, 500MHz).

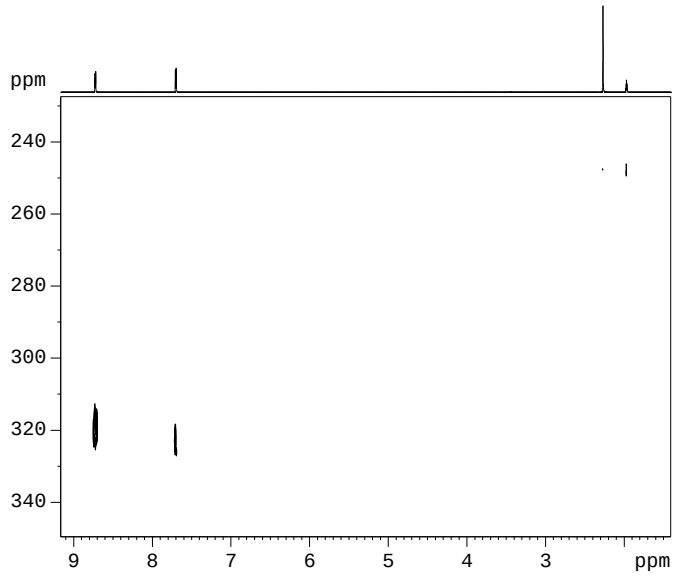

Figure S8. 2D ^{1}H-^{15}N HMBC of 4,4'-bpy⊂4·$(BArF)_8$ host-guest complex in CD_3CN (used as an internal reference, $\delta(^{15}N)$ = 246.9 ppm, 298 K, 500MHz) showing a cross-peak at 2.21/271.1 ppm corresponding to the bpy nitrogen.

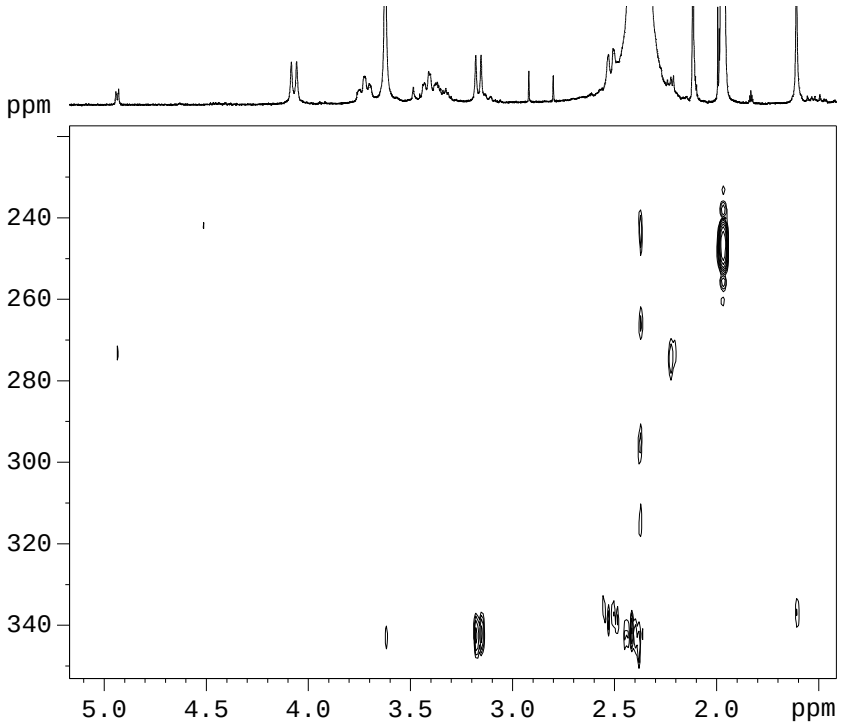

Figure S9. DOSY NMR experiments of nanocage **4,4-bpy⊂4**·$(BArF)_8$, affording a diffusion coefficient (*D*) of $D=10^{-9.532}$ m^2 s^{-1} ($D_{CD3CN}= 10^{-8.389}$ m^2 s^{-1}). The hyrodynamic ratio (r_H) obtained using SEq. 1 was 19.8 Å.

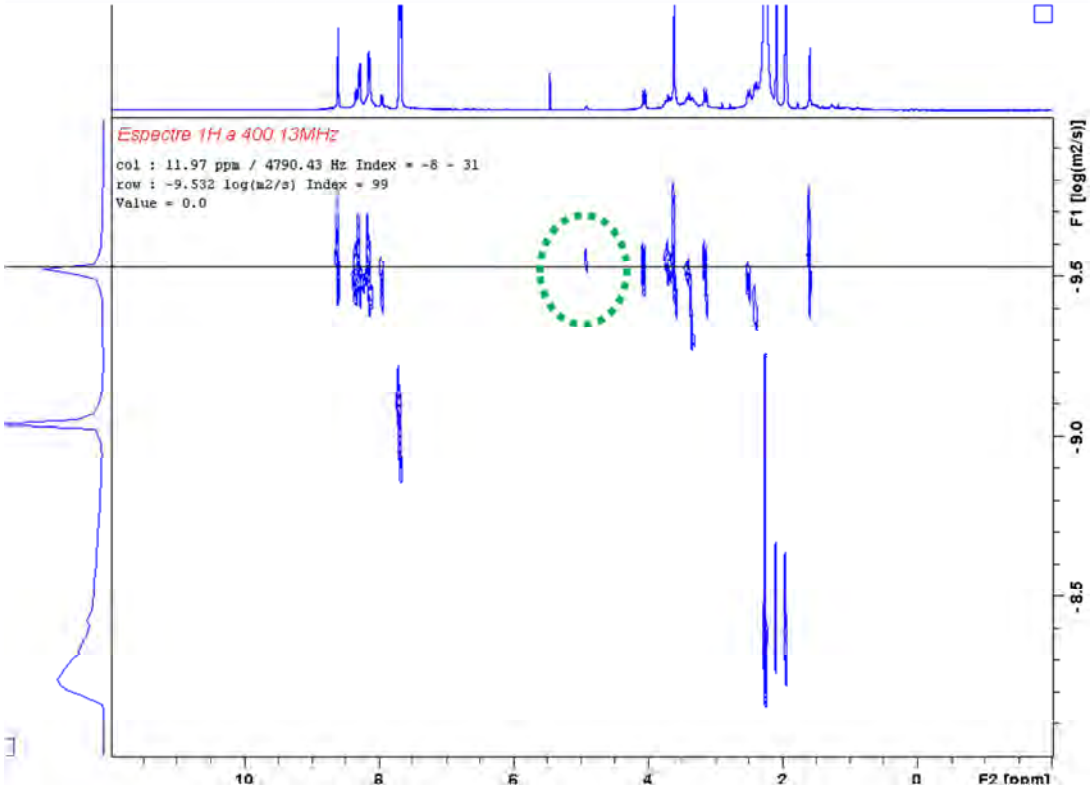

Figure S10. HRMS spectrum **α⊂4**·$(BArF)_8$ host-guest complex. Experimental conditions: 100 μM in CH_3CN, registered with a Bruker MicroTOF-Q-II exact mass spectrometer.

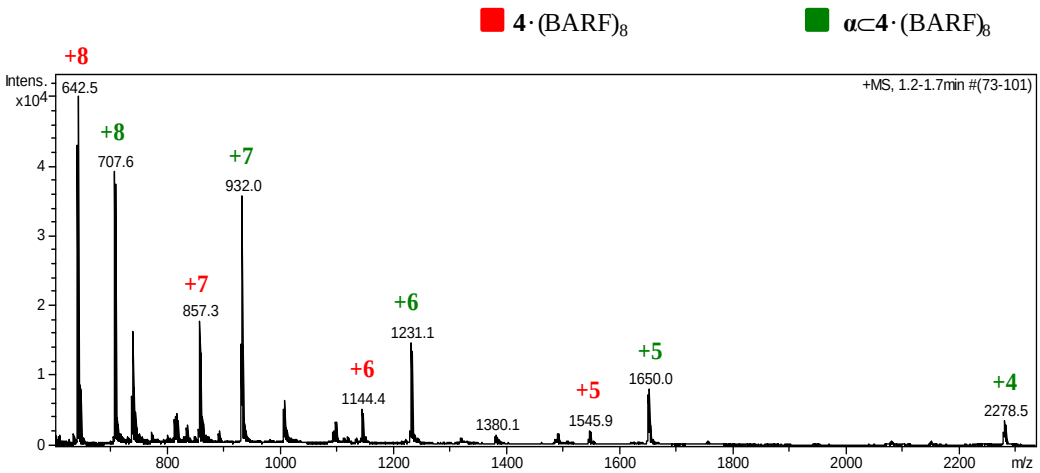

Figure S11. UV-Vis monitoring of the titration of **4**·$(BArF)_8$ nanocapsule with ligand **β,** at a fixed total concentration ($4.32 \cdot 10^{-7}$ M) of **4**·$(BArF)_8$ in Toluene/CH_3CN (9/1).

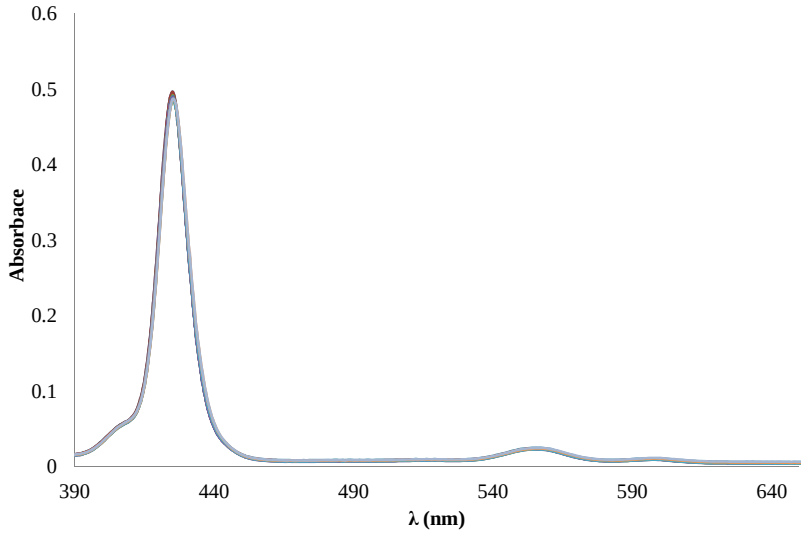

Figure S12. ^{1}H-NMR spectrum of nanocage **4**·$(BArF)_8$ (red, top) and complex **α⊂4**·$(BArF)_8$ (CD_3CN, 295 K, 400 MHz).

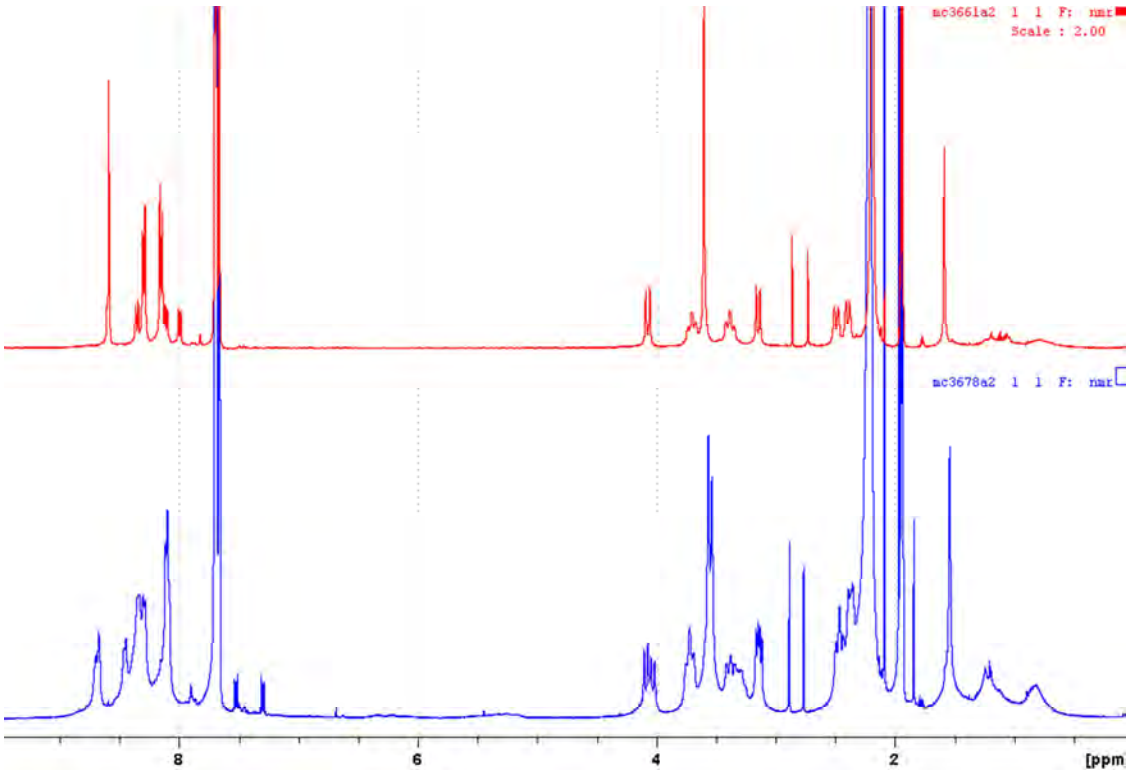

Figure S13. ^{1}H-NMR spectra of the **α⊂4**·$(BArF)_8$ host-guest complex in CD_3CN at 240 K (top) and in CD_3CN at 298 K (bottom) (600 MHz).

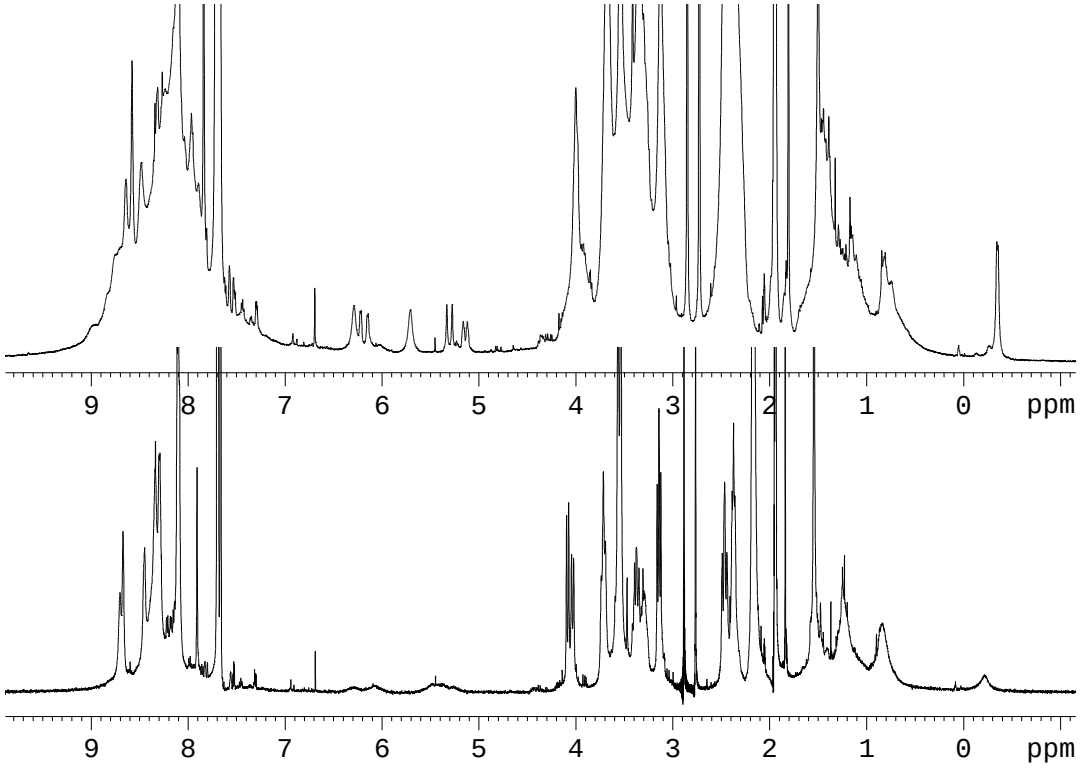

Figure S14. 2D COSY **α⊂4**·$(BArF)_8$ adduct at low temperature (CD_3CN, 240 K, 600 MHz)

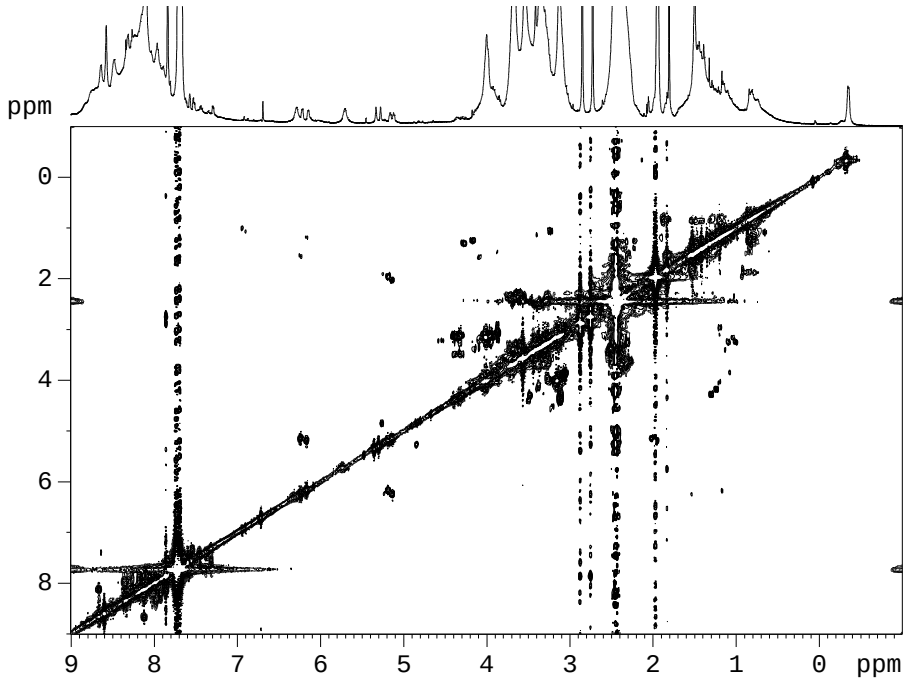

Figure S15. NMR characterization of the **α⊂4**·$(BArF)_8$ host-guest complex: a) esquematic representation of encapsulated ligand **α** and b) ^{1}H NMR of **α⊂4**·$(BArF)_8$ at low temperature (CD_3CN, 240 K, 500 MHz)

a)

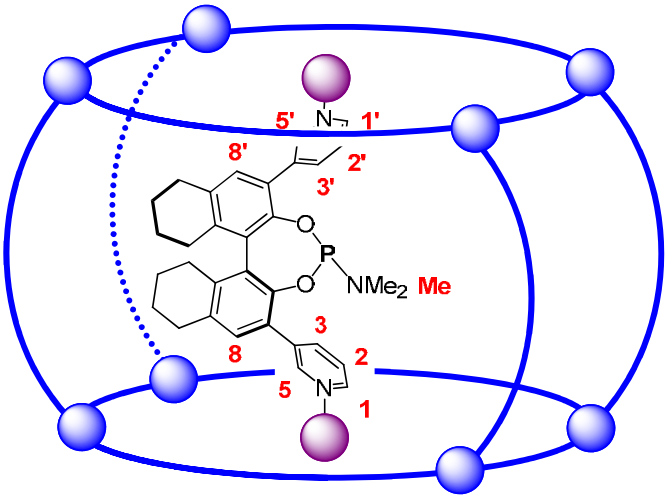

b)

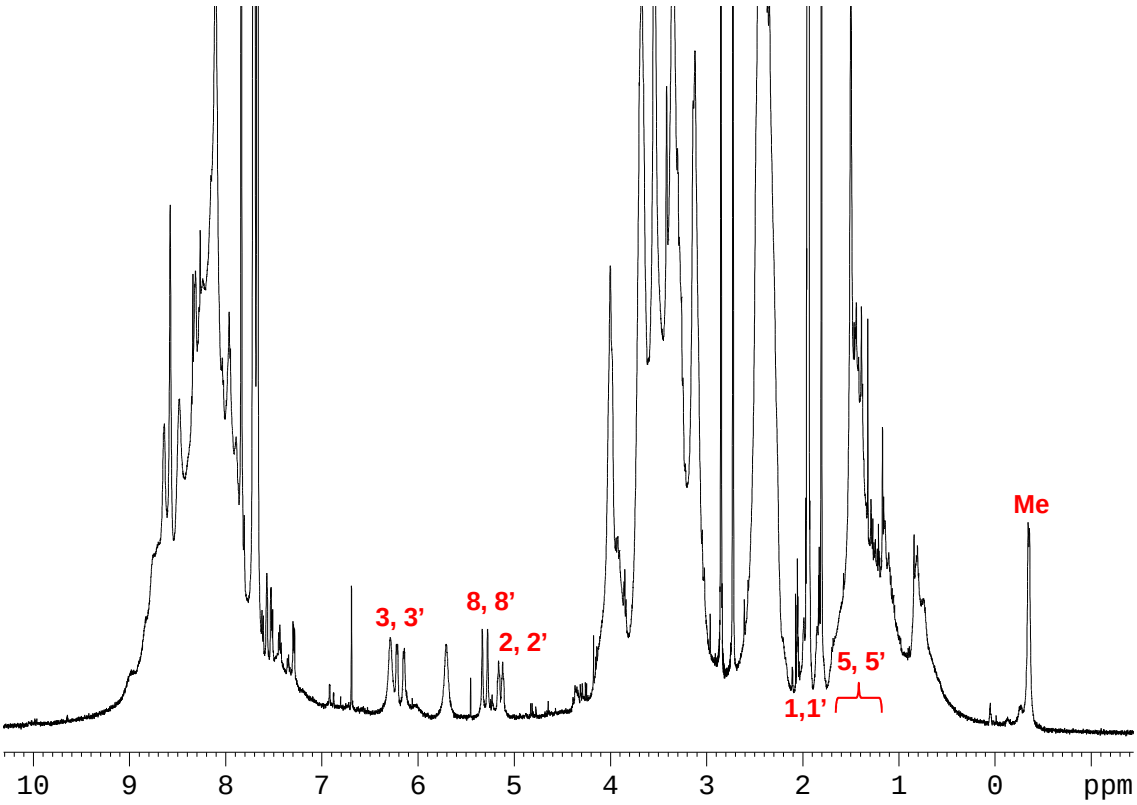

Figure S16. 2D NOESY spectrum: a) of **α⊂4**·$(BArF)_8$ host-guest complex and b) expanded plot centered at 4.5-5.5 ppm (CD_3CN, 243 K, 500 MHz).

a)

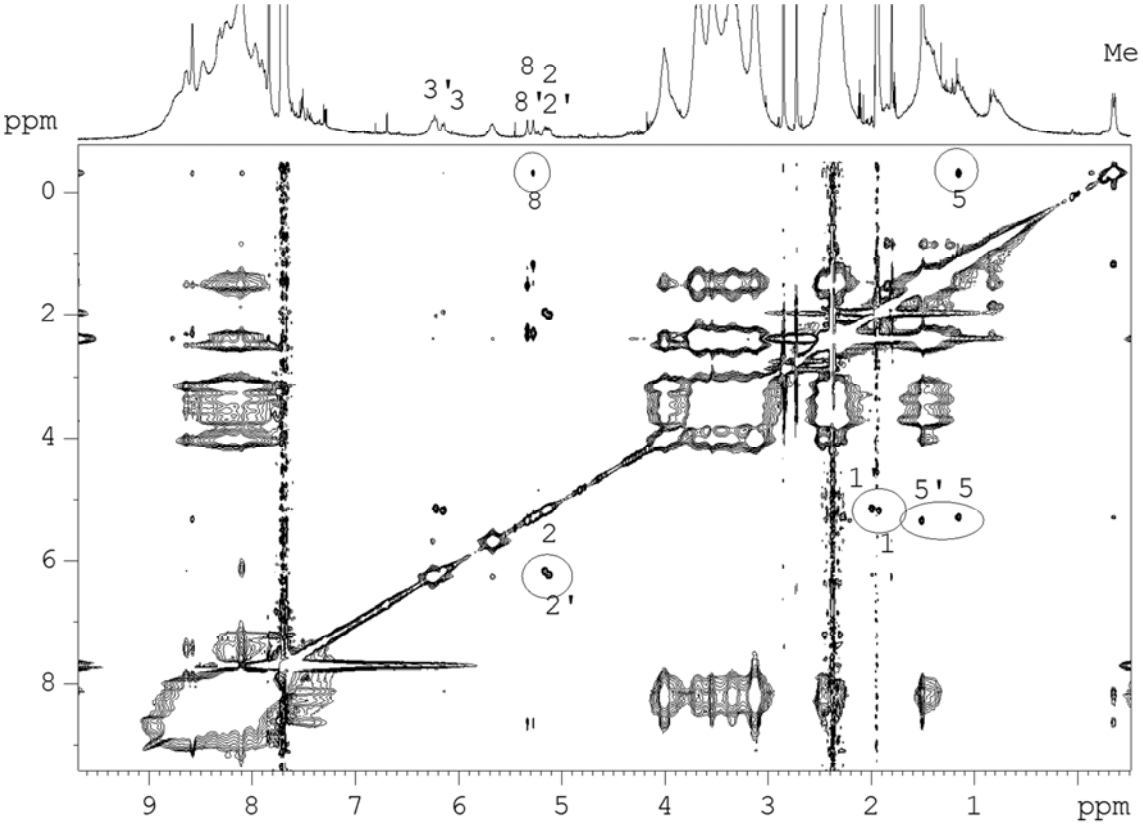

b)

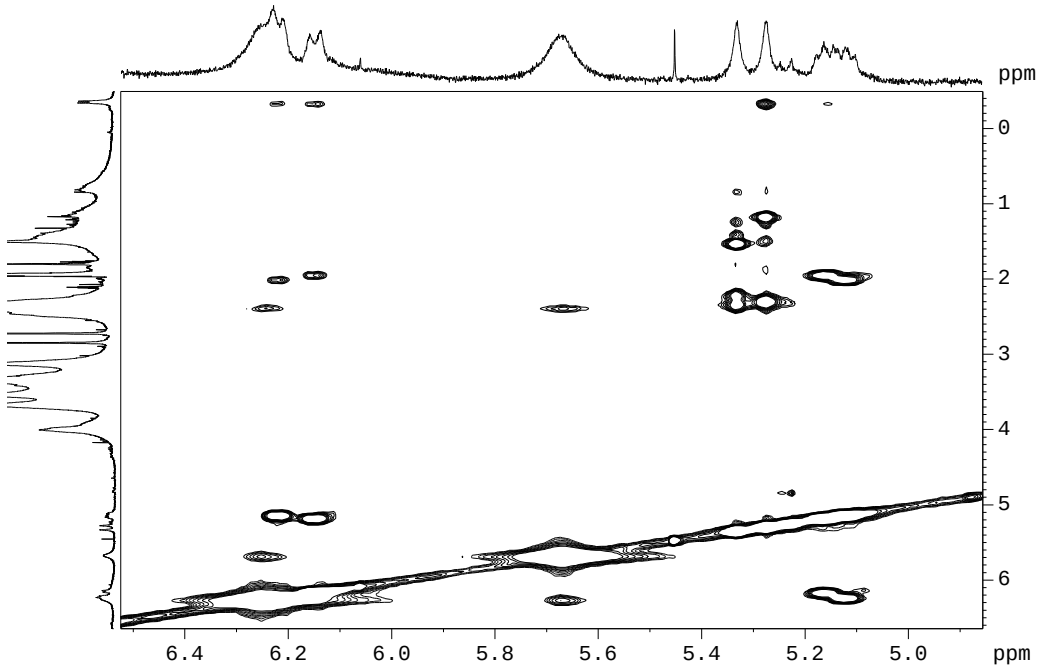

Figure S17. Expanded area corresponding to the 2D HSQC spectrum of **α⊂4**·$(BArF)_8$ host-guest complex at 243 K (CD_3CN, 500 MHz). Note the strong upfield ^1H chemical shifts effects observed for the aromatic protons of the ligand.

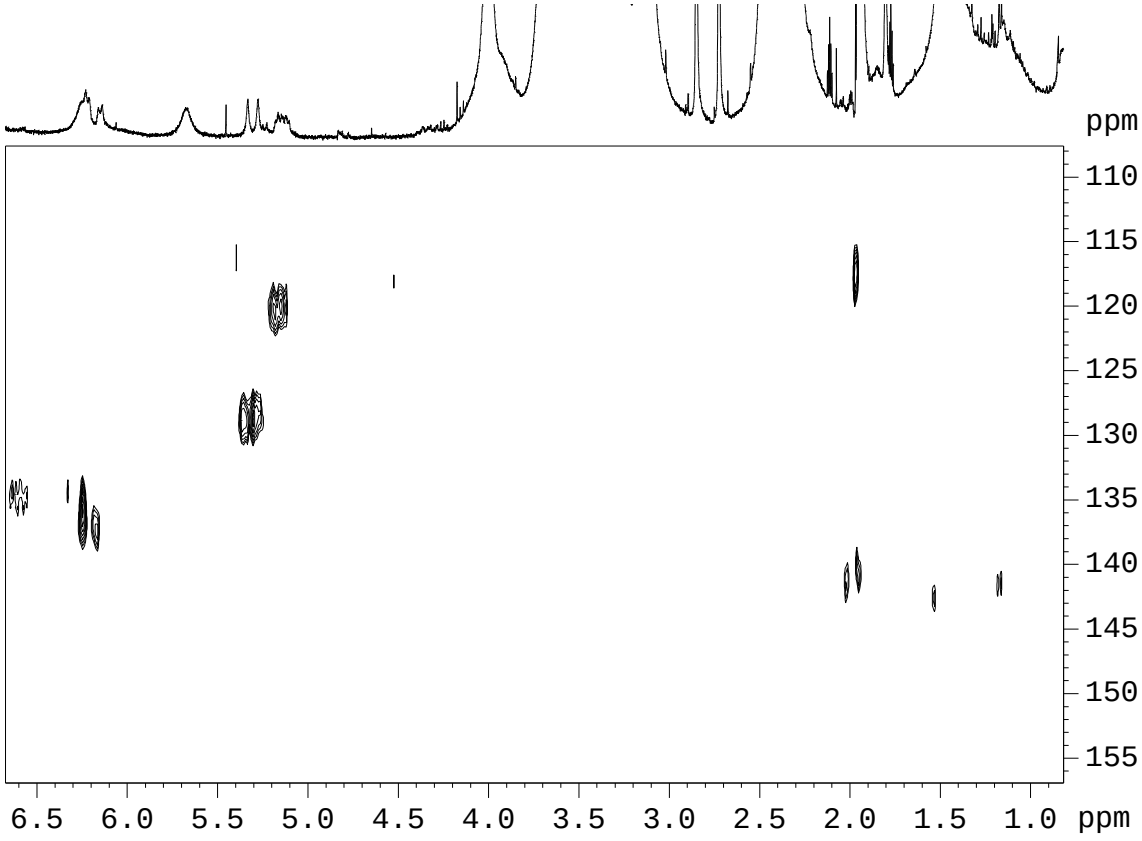

Figure S18. ^{31}P-NMR spectrum of complex **α⊂4**·$(BArF)_8$ (CD_3CN, 298 K, 400 MHz).

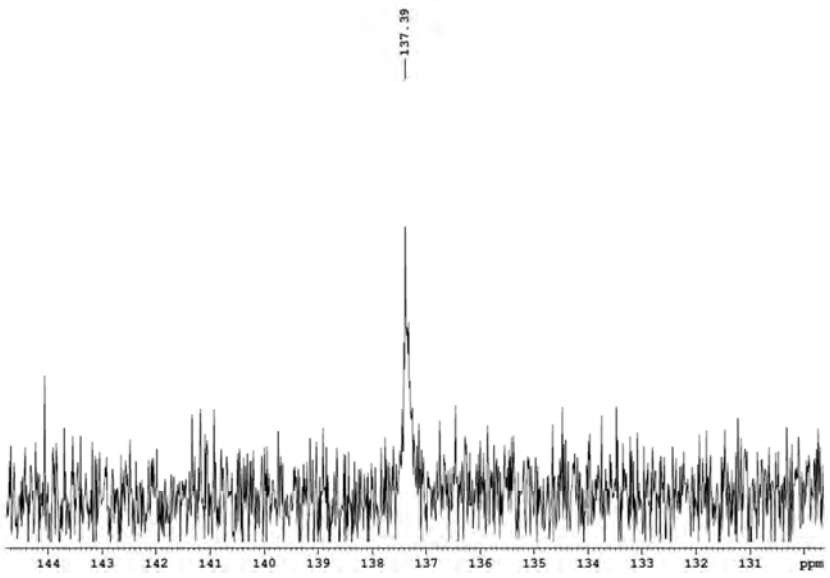

Figure S19: ^{1}H-NMR spectrum of complex **α⊂4**·$(BArF)_8$ (d8-Toluene/CD_3CN (4/1), 295 K, 500 MHz).

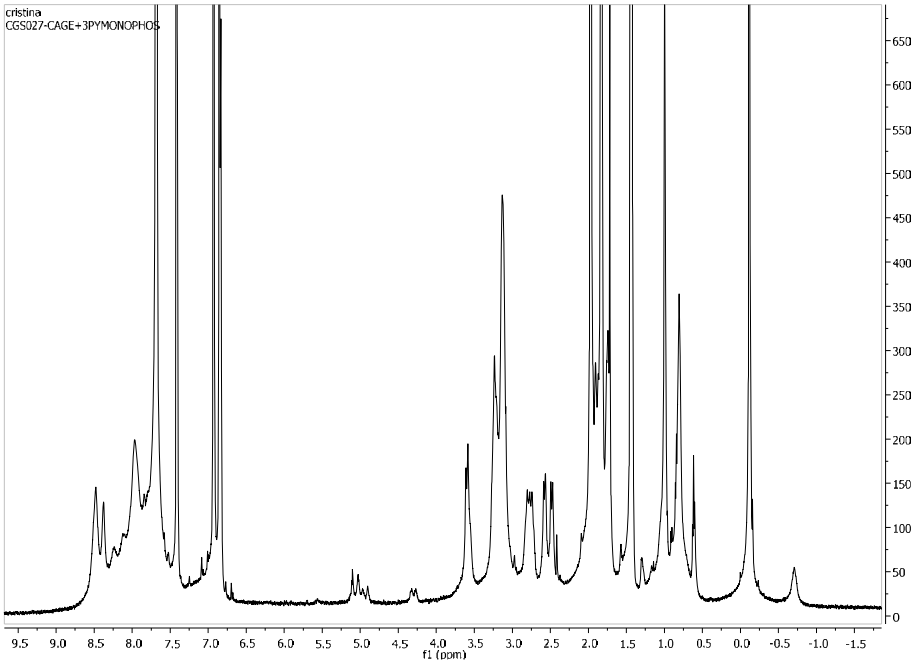

Figure S20. ^{1}H-NMR spectrum of complex [Rh(acac)CO-**α⊂4**·$(BArF)_8$] (d_8-Toluene/CD_3CN (4/1), 295 K, 500 MHz).

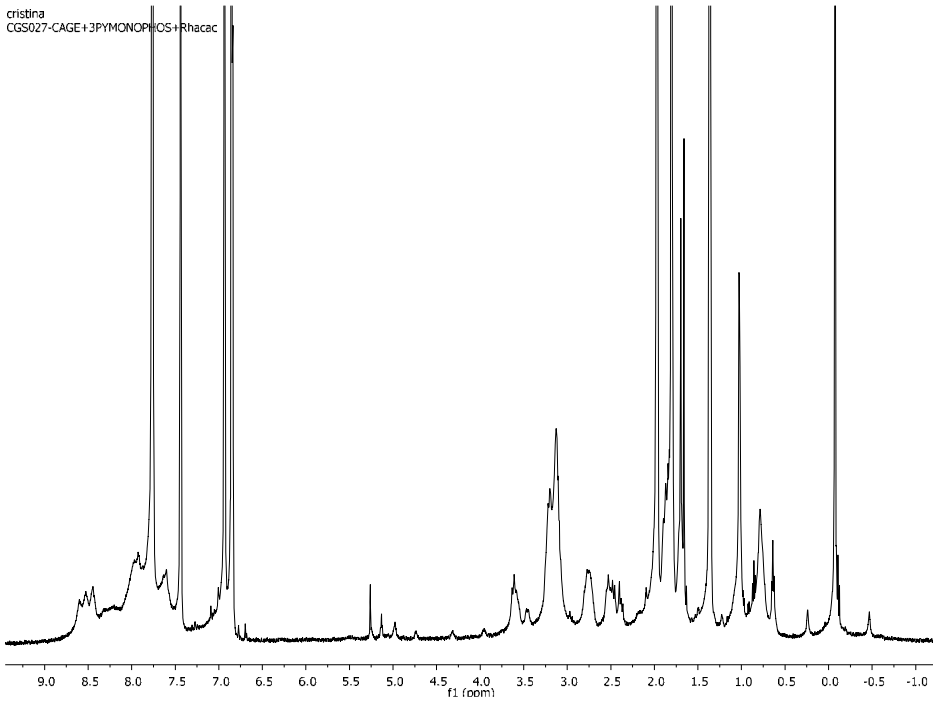

Figure S21. A 4 mM solution of [Rh(acac)$(CO)_2$] (red) and a 0.65 mM solution of [Rh(acac)CO-**α**⊂**4**·$(BArF)_8$] (blue) in toluene/acetonitrile (4/1), were transfered into an IR cell and the spectrum was recorded.

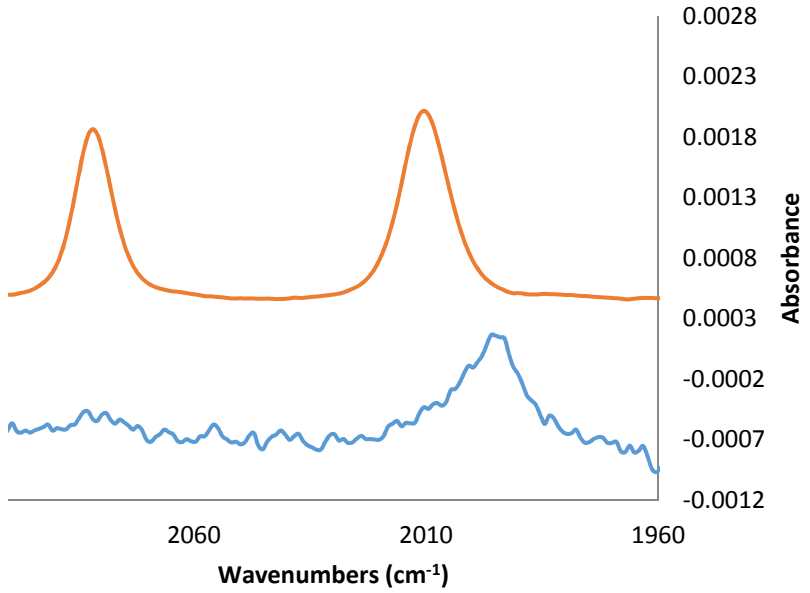

Figure S22. (HP) ^{1}H-NMR spectrum of complex [*trans*-Rh(H)$(CO)_3$-**α**⊂**4**·$(BArF)_8$]. a) 12-18.5 ppm spectrum region: the signal at 15.7 ppm belongs to the released acetylacetonate which appears upon pressurizing the rhodium precatalyst with syngas b) full spectrum (d_8-Toluene/CD_3CN (4/1), 295 K, 500 MHz, 5 bar H_2:CO).

a)

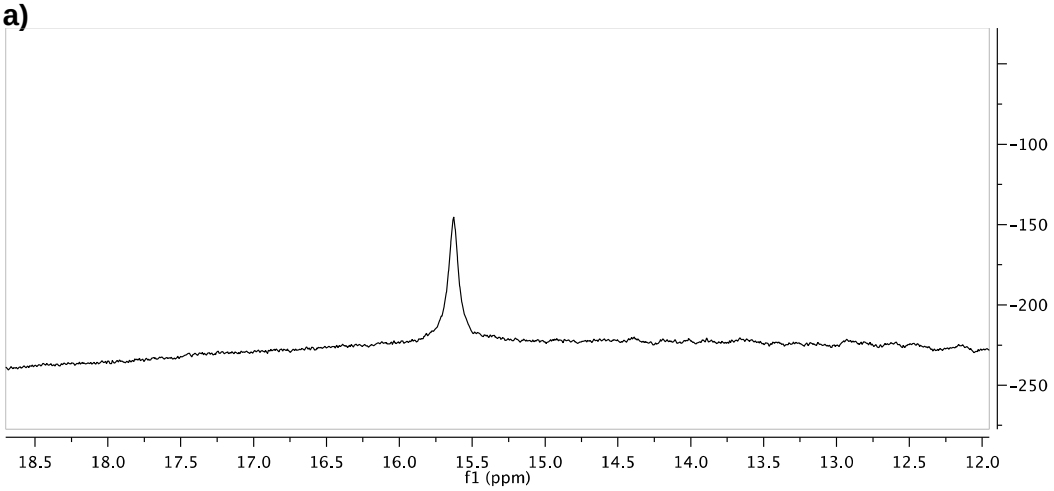

b)

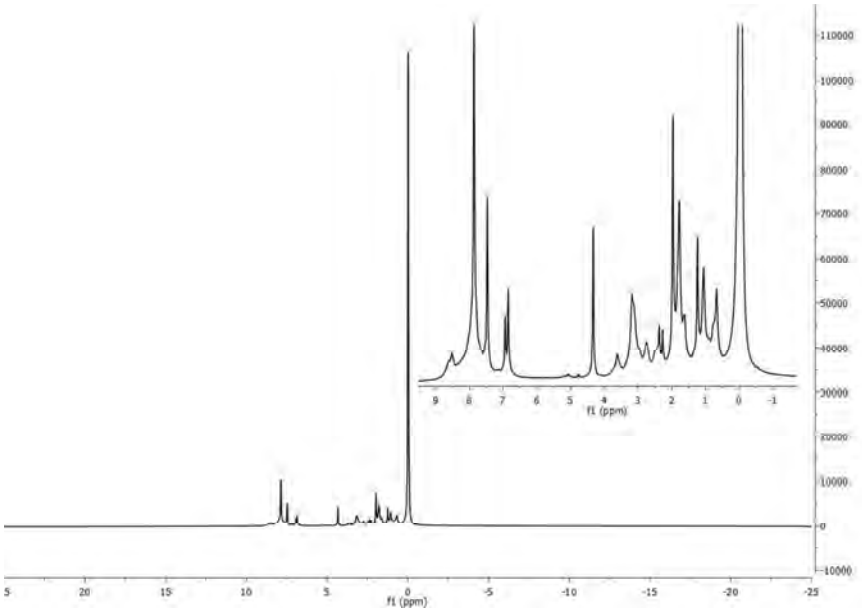

Figure S23. ^{1}H-{^{31}P}-NMR spectrum (σ= -11.87 ppm) corresponding to the complex [*trans*-Rh(H)(CO)$_3$-**α**⊂**4**·(BArF)$_8$] (d$_8$-Toluene/CD$_3$CN (4/1), 295 K, 500 MHz, 5 bar H$_2$:CO).

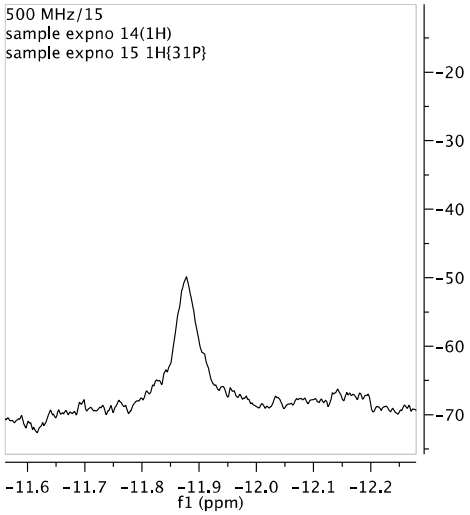

Figure S24. a) ^{1}H-NMR of **4**·$(BArF)_8$ (CD_2Cl_2, 298 K, 300 MHz). **b)** The previous **4**·$(BArF)_8$ solution was pressurized with 5 bar of syngas. A high pressure (HP) NMR was recorded at 298K. **c)** The sample was left at HP 2h at 333 K, afterwards the tub was cooled down to r.t. and the NMR recorded at 298K.

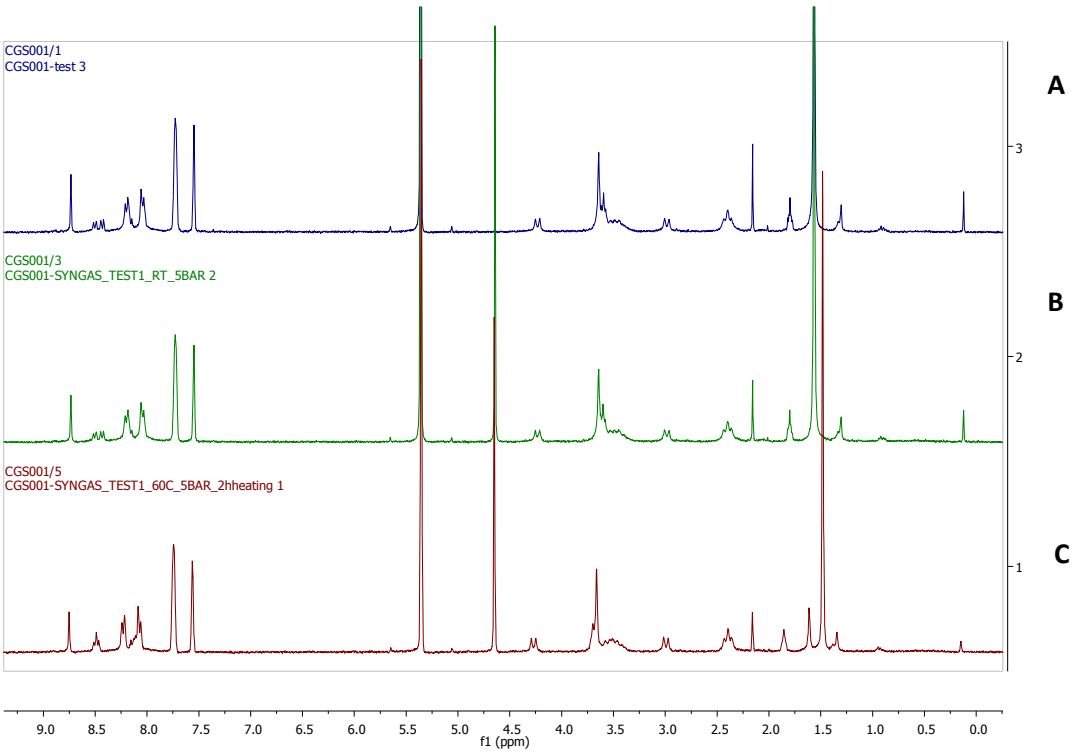

Figure S25. ^{1}H-NMR spectrum of complex the reaction crude obtained after a hydroformylation catalytic experiment (d_8-Toluene/CD_3CN (4/1), 295 K, 500 MHz).

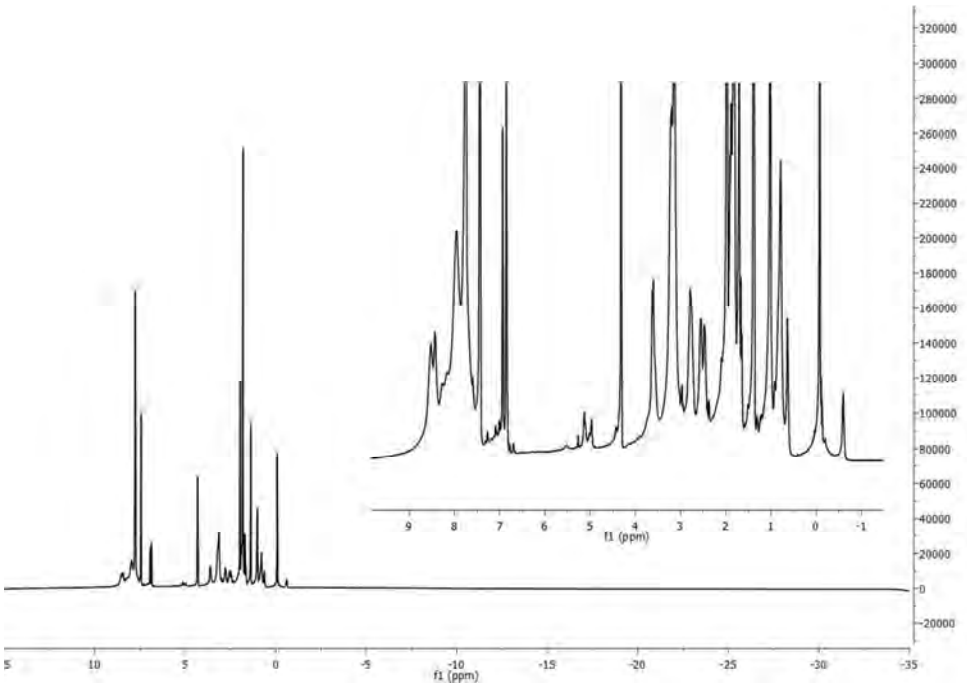

Figure S26. Molecular modelling picture of the active complex, showing clearly that at the two coordination sites in the equitorial plane (where CO is coordinated) there is sufficient space for the styrene to coordinate in many different ways (in fact at both sites it the alkene can coordinate in 4 manners, leading to 8 complexes).

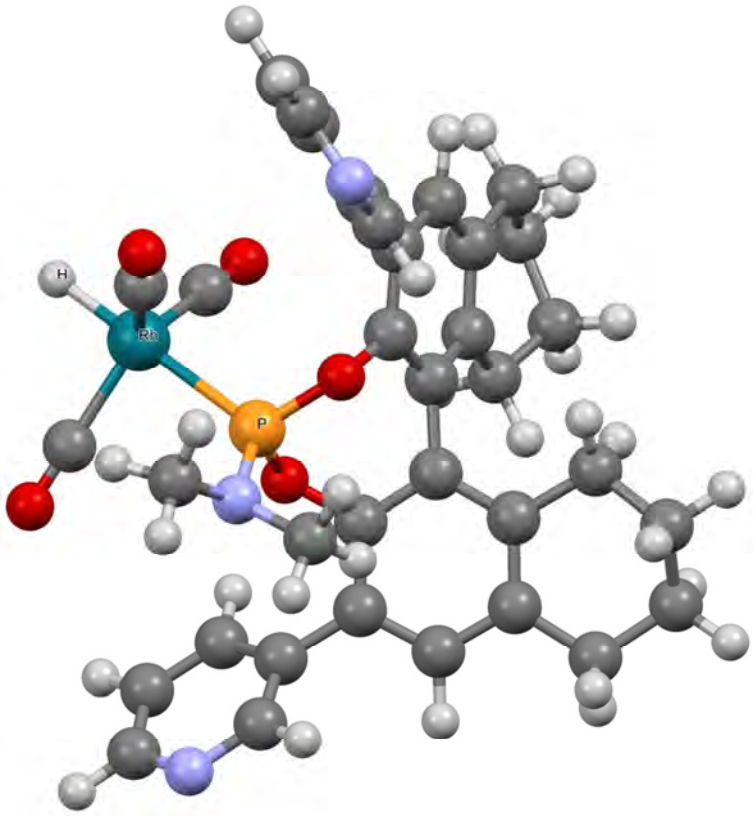

Figure S27. Molecular modelling picture of the active complex docked into the cage (3 different perspectives a-c), showing that there is limited space for styrene coordination, most like leading to a reduced number of alkene complexes that form during catalysis (oxygens are depicted in red, nitrogens in blue, phosphorous in orange, hydrogen in white and rhodium in green).

a)

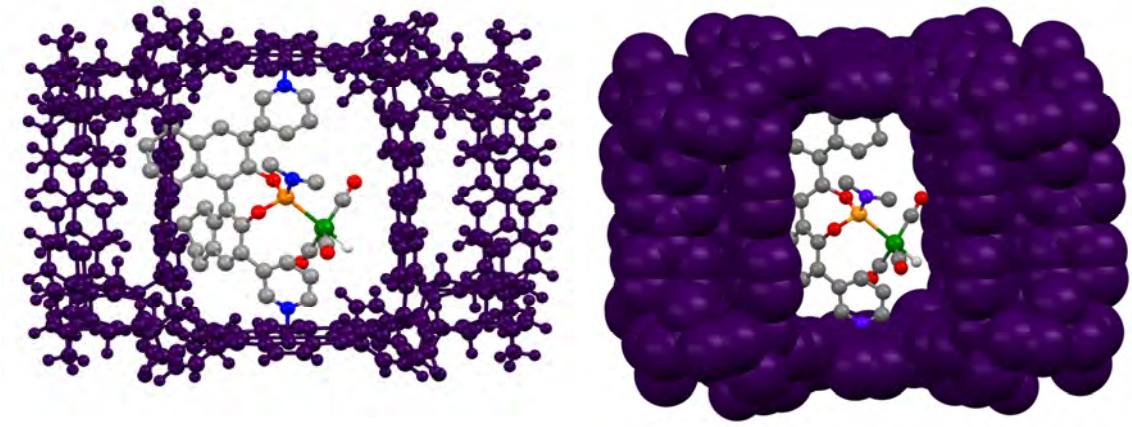

b)

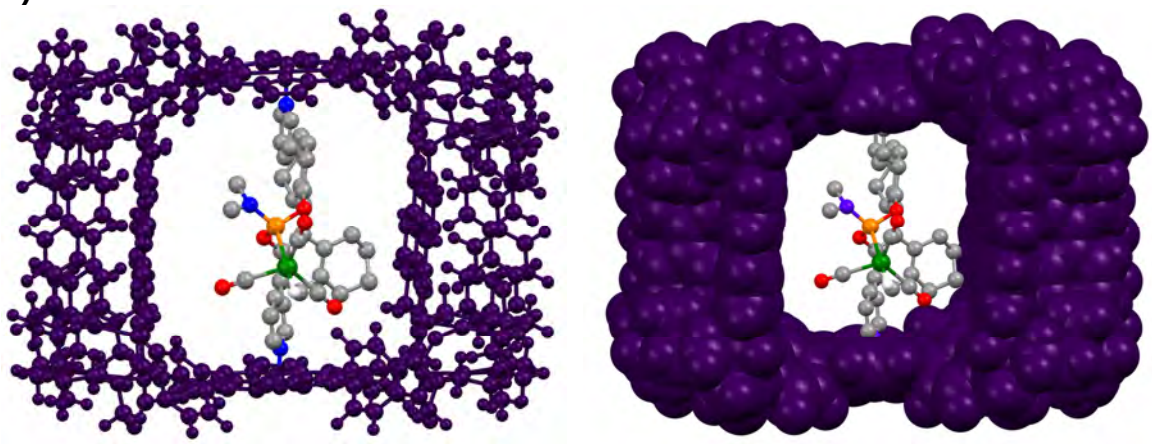

b)

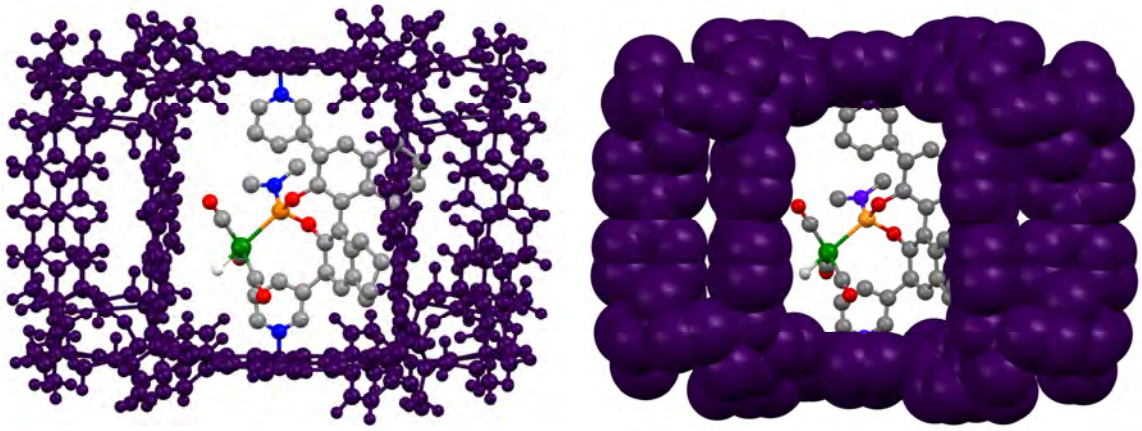

Figure S28. Representation of the four encapsulated rhodium-styrene coordination complexes proposed. The most preferred alkene coordination complexes that can be formed are depicted on the left. The styrene complexes of which the formation is sterically hindered by the capsule's structure are displayed on the right.

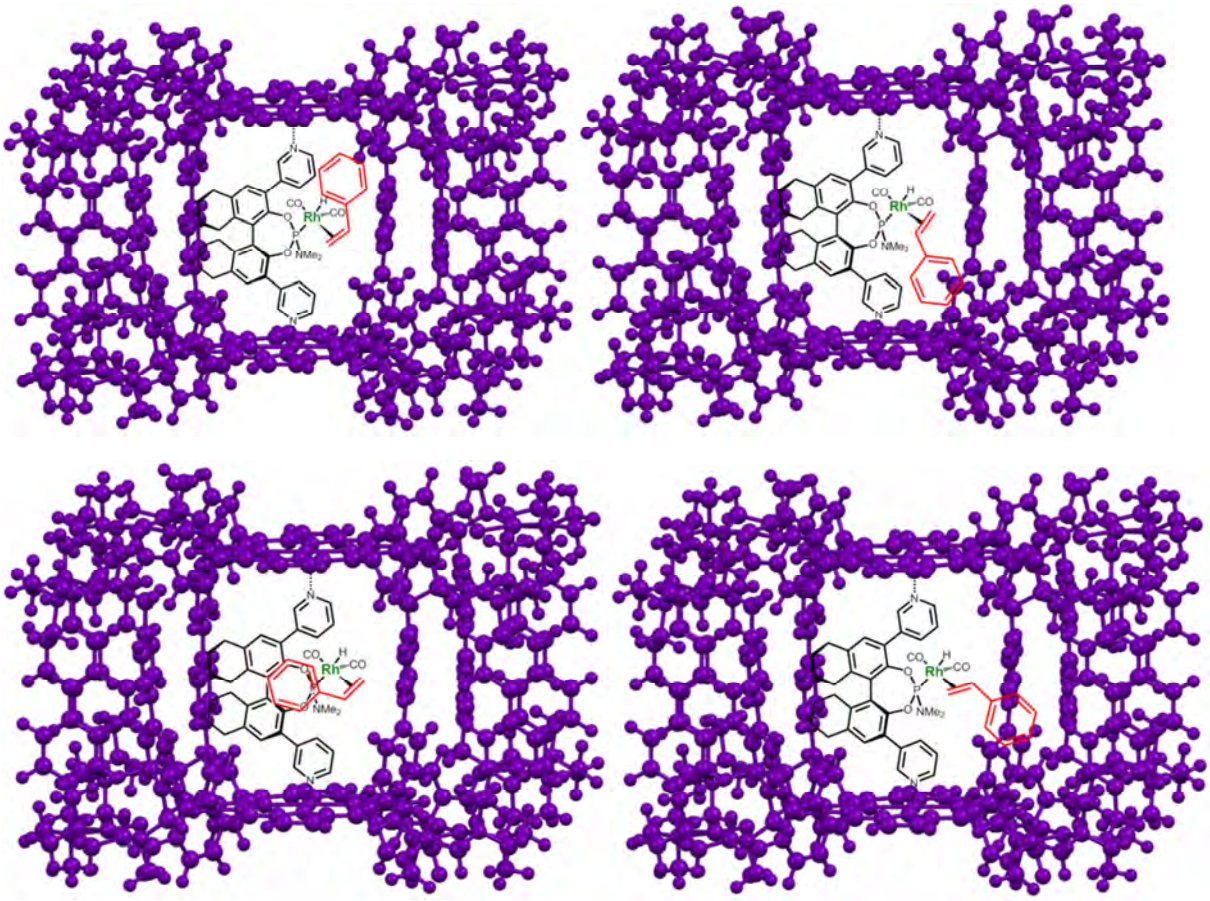

Figure S29. PM3 optimized structures of the two most preferred encapsulated rhodium-styrene complexes.

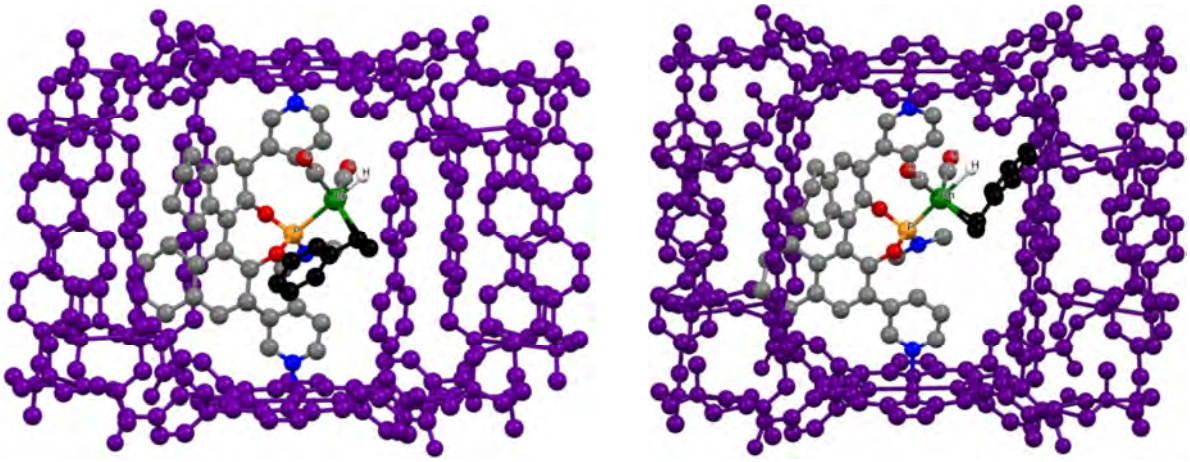

Figure S30. Plot of the convension values (%) versus the catalyst concentration for the AHF of styrene.

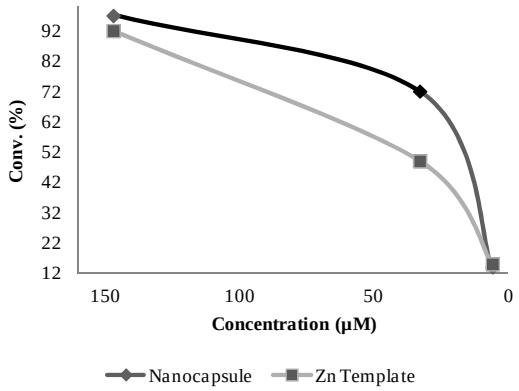

Figure S31. NMR spectrum of free ligand **γ** a) ^{1}H-NMR, b) ^{13}C-NMR and c) ^{31}P-NMR ($CDCl_3$, 298 K, 400 MHz).

a)

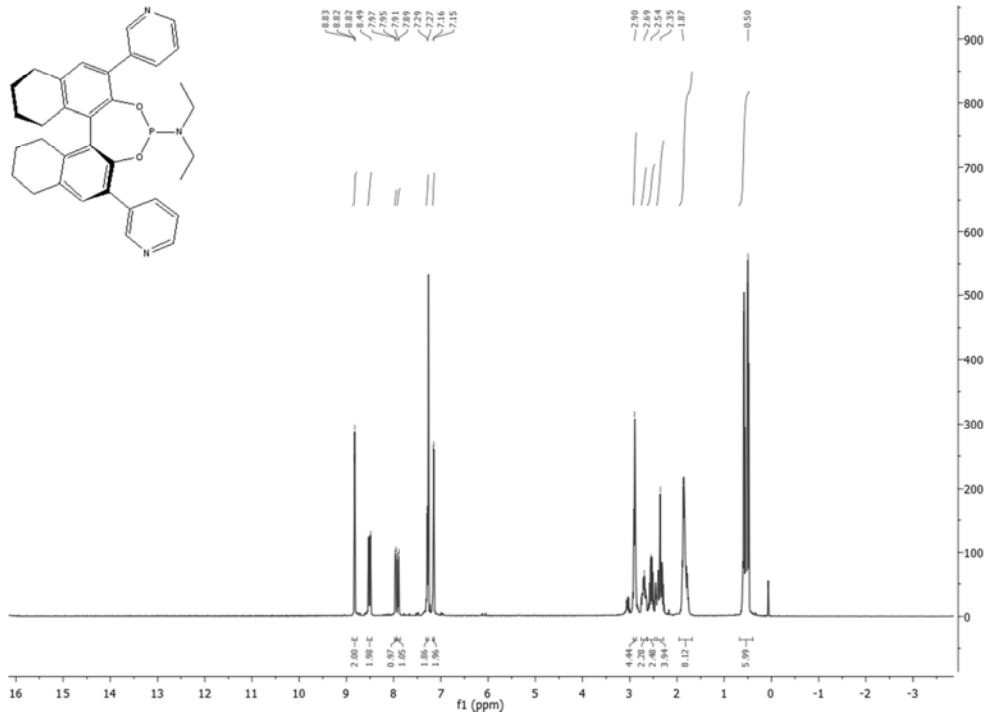

b)

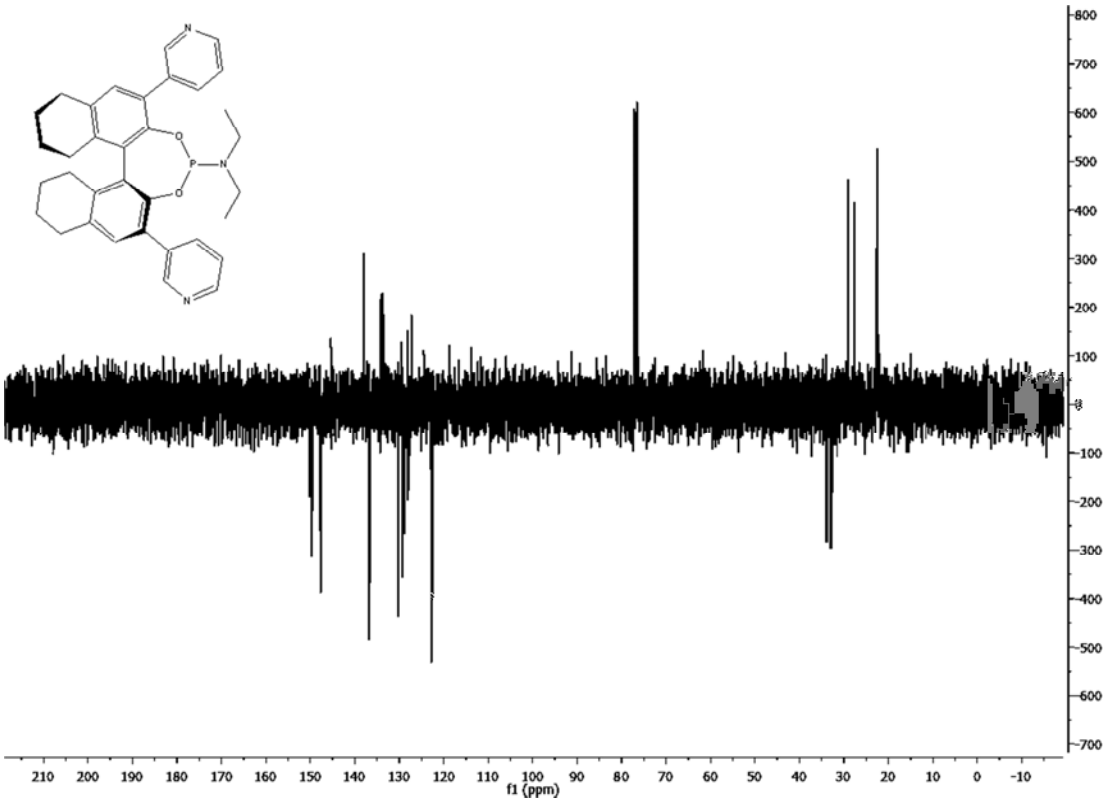

c)

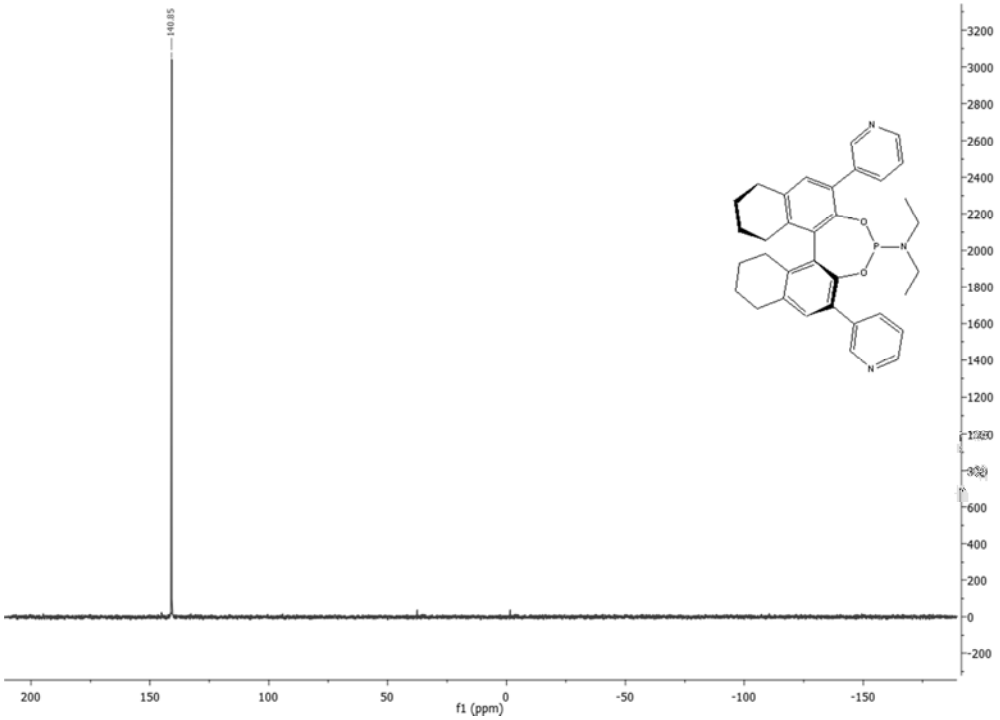

Figure S32. NMR spectrum of free ligand δ a) ^{1}H-NMR, b) ^{13}C-NMR and c) ^{31}P-NMR ($CDCl_3$, 298 K, 400 MHz).

a)

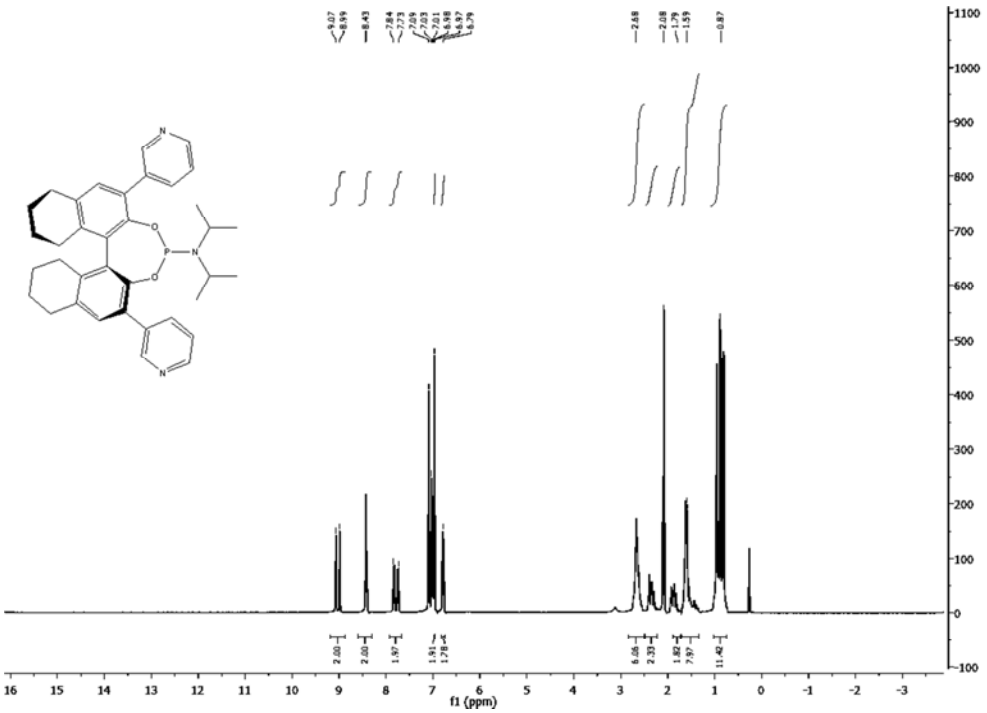

b)

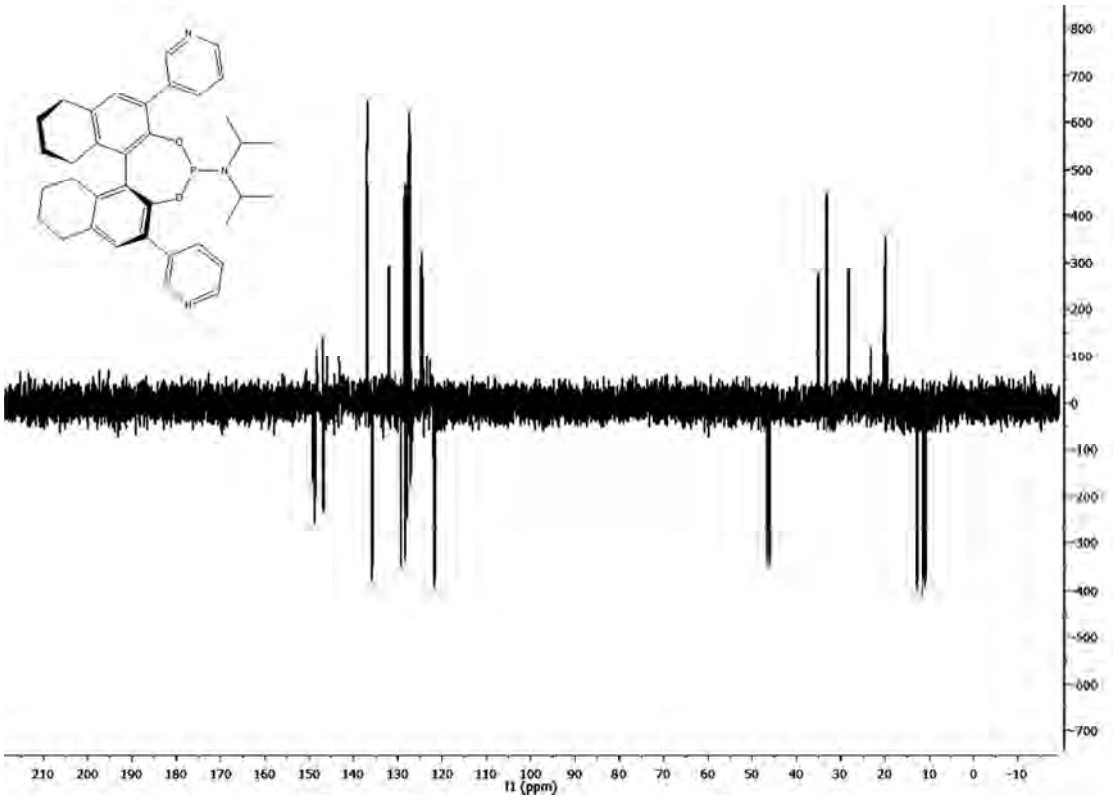

c)

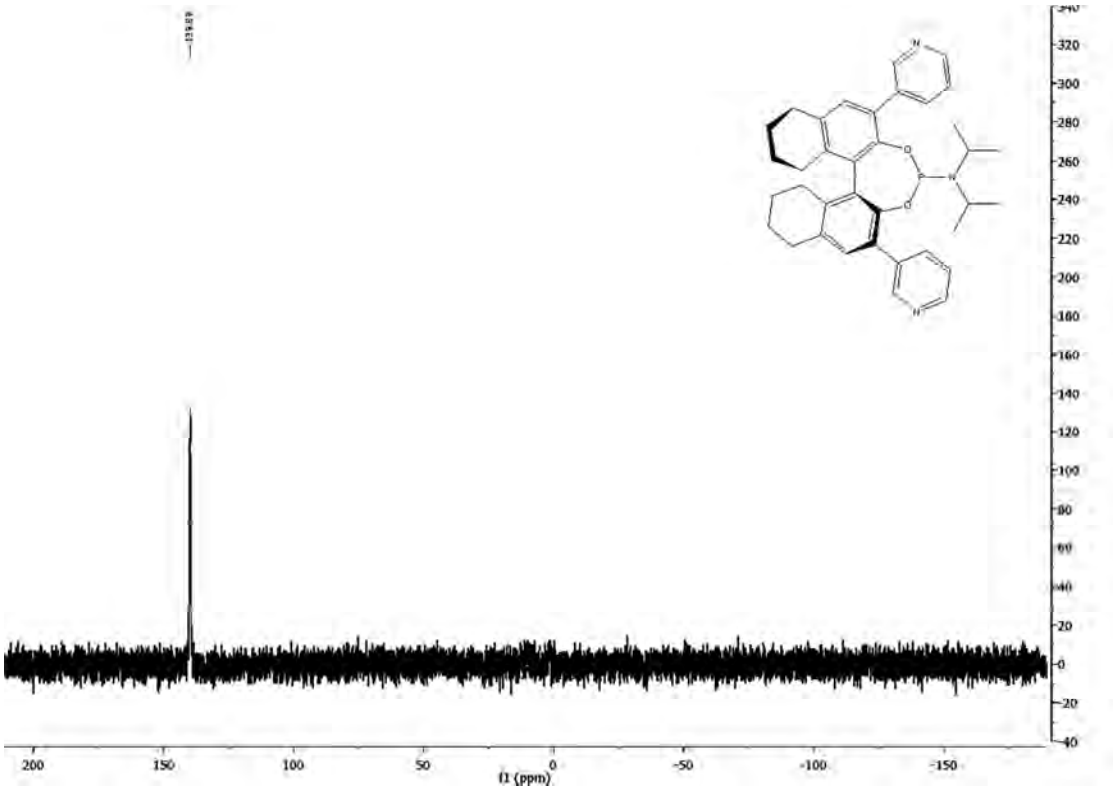

Figure S33. GC analysis for **α** ligand (manuscript: Table 1 entries 3 and 4).

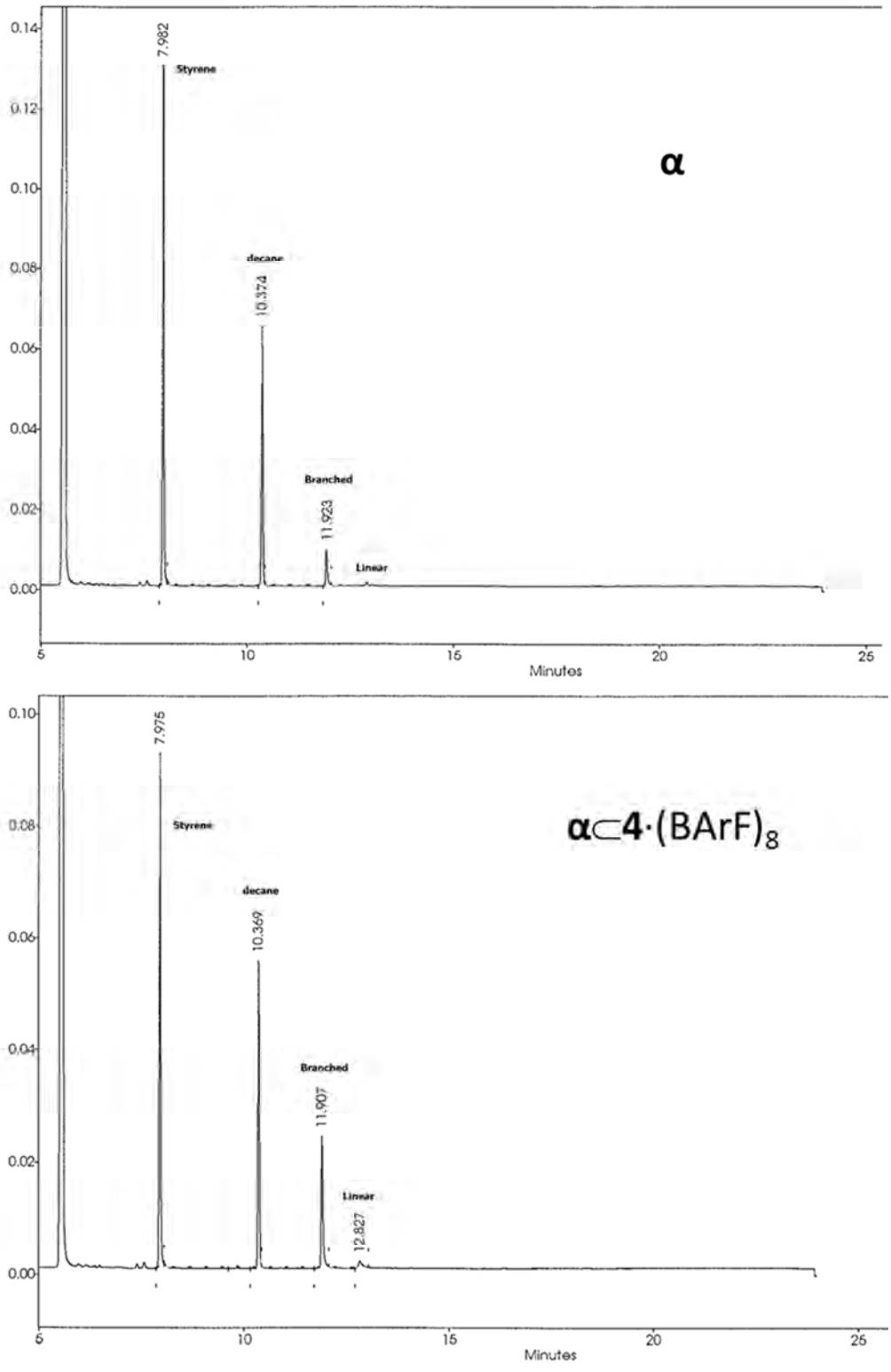

Figure S34. GC analysis for **γ** ligand (manuscript: Table 1 entries 11 and 12).

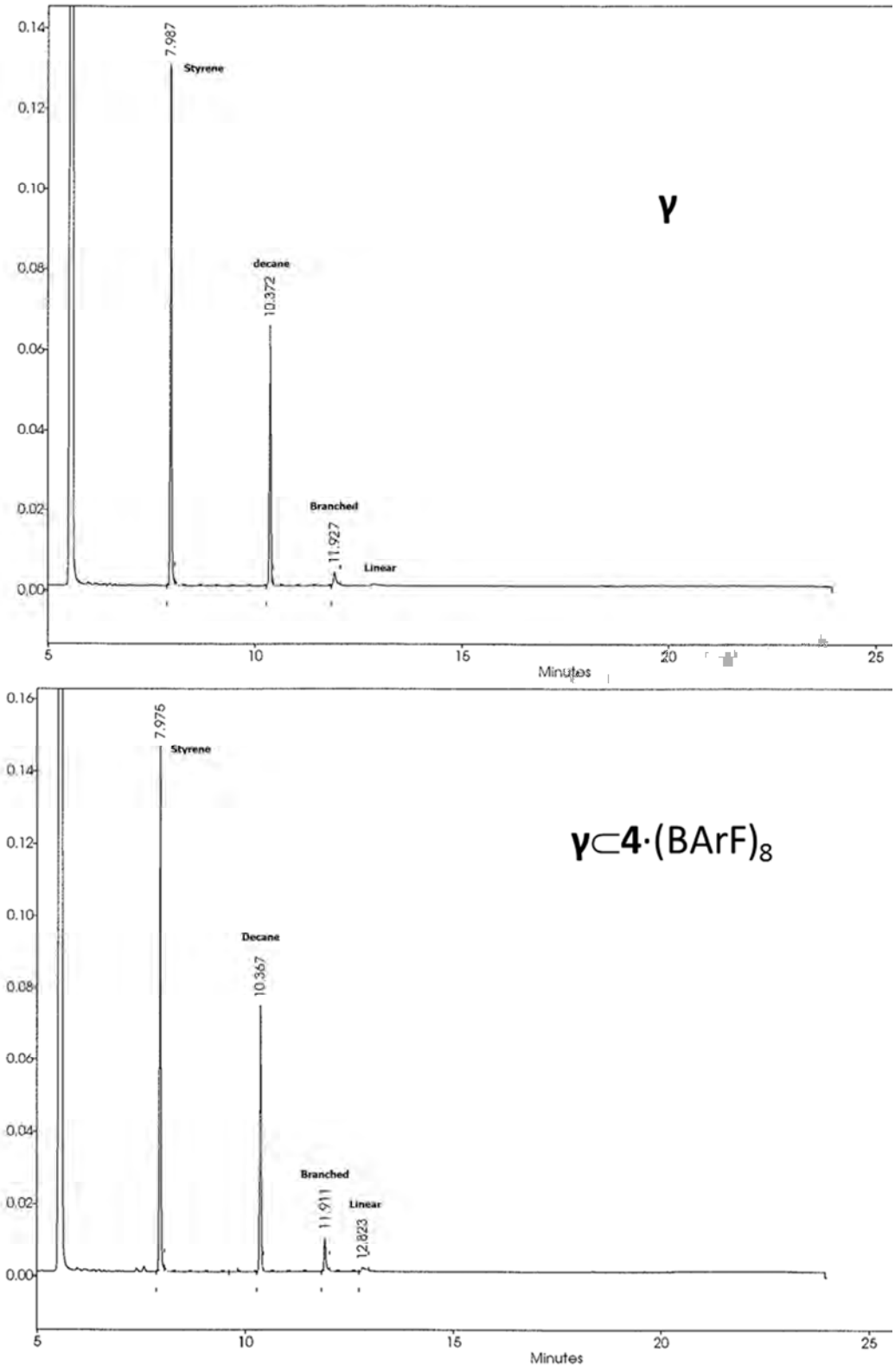

Figure S35. GC analysis for **δ** ligand (manuscript: Table 1 entries 13 and 14).

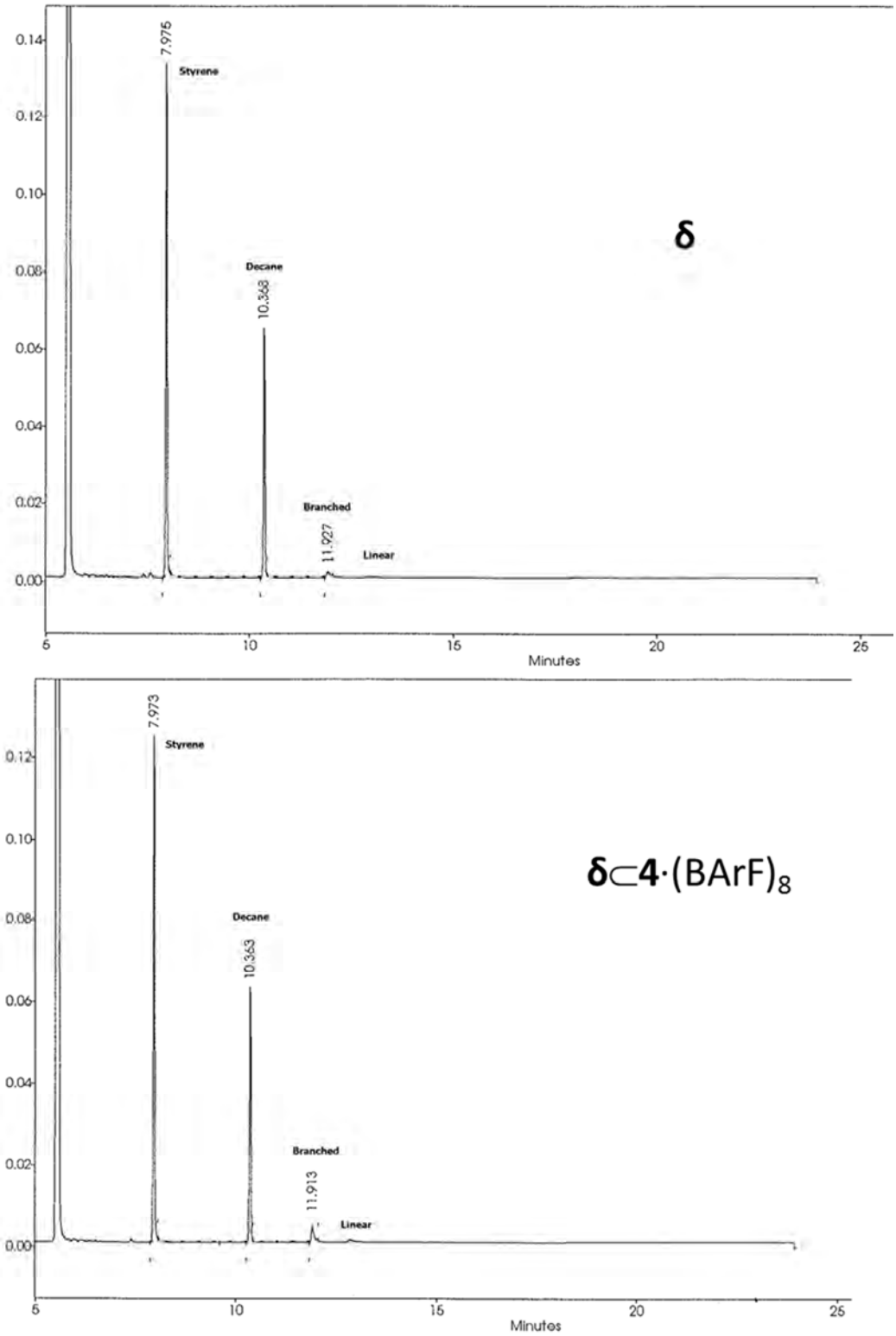

Figure S36. Chiral GC analysis for **α** (manuscript: Table 1 entries 3 and 4), **γ** (manuscript: Table 1 entries 11 and 12) and **δ** (manuscript: Table 1 entries 13 and 14) ligands.

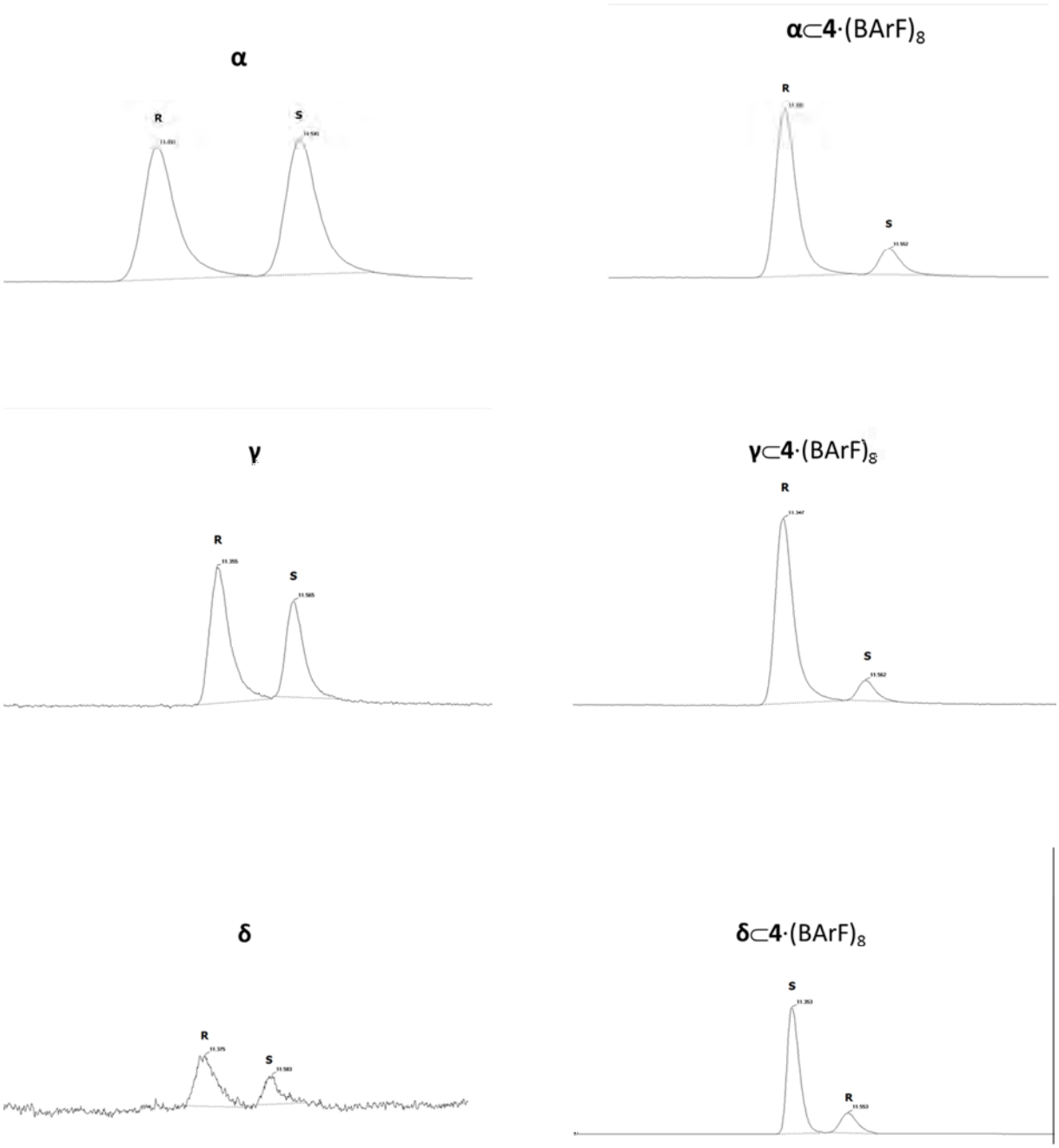

Figure S37. Typical chiral GC analysis for **α** ligand using vaious styrene derivatives as substrate (manuscript: Table 3).

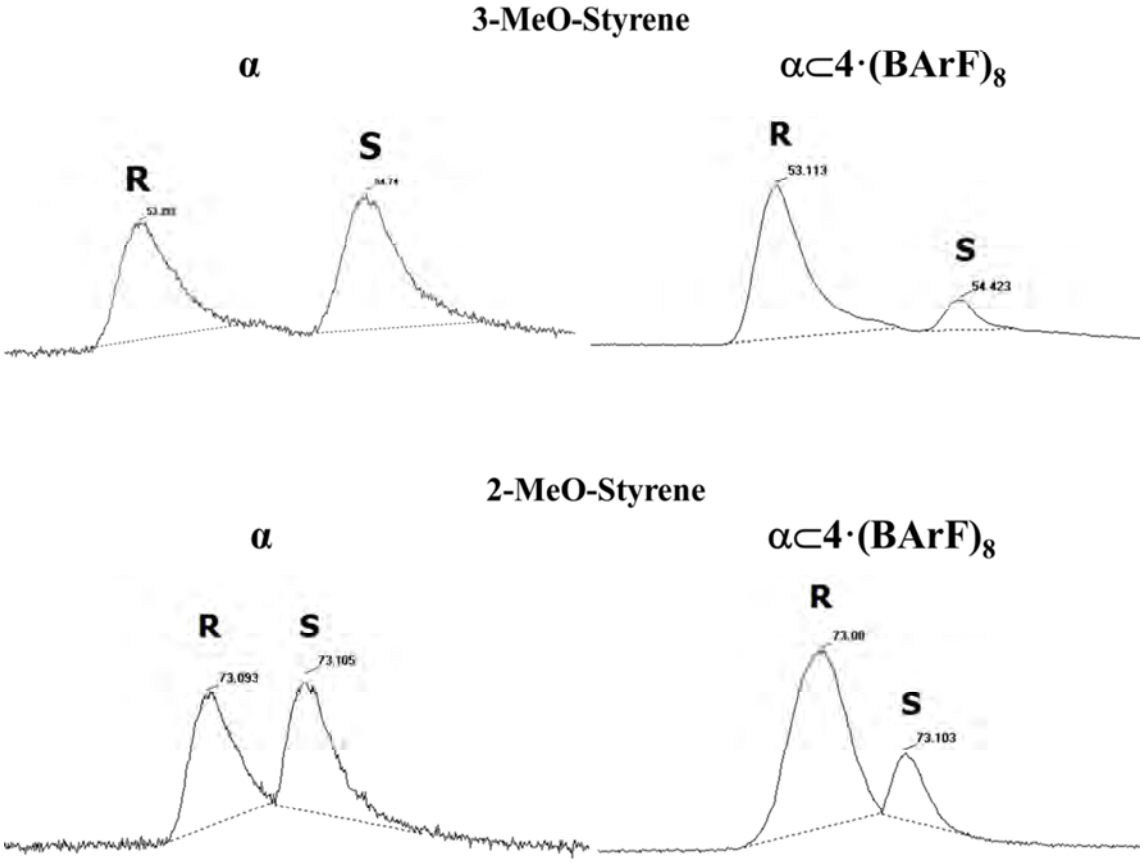

3. Supplementary References

(1) T. Gadzikwa, R. Bellini, H.L. Dekker, J.N.H. Reek., *J. Am. Chem. Soc*, **2012**, 134, 2860.

(2) R. Bellini, S.H. Chikkali, G. Berthon-Gelloz, J.N.H. Reek, *Angew. Chem. Int. Ed.*, **2011**, 50, 7342-7345.

(3) C. García-Simón, M. Garcia, L. Gómez, T. Parella, S. Osuna, I. Imaz, D. Maspoch, M. Costas, and X. Ribas. Nat. Commun. 2014, DOI: 10.1038/ncomms6557

(4) H.-J. Kim, J. E. Redman, M. Nakash, N. Feeder, J. K. M. Sanders, S. J. Teat, *Inorg. Chem.,* **1999**, 38, 5178.

(6) T. Sawada, M. Yoshizawa, S. Sato, M. Fujita, *Nat. Chem.*, **2009**, 1, 53.

(5) E. Stulz, Y-F. Ng, S. M. Scott and J. K. M. Sanders, Chem. Comm., **2002**, 524.

(7) L. H. Uppadine, J. M. Weeks and P. D. Beer , *J. Chem. Soc., Dalton Trans.*, **2001**, 3367-3372.

(8) Bellini, Rosalba, PhD thesis. Amsterdam: Universiteit van Amsterdam. *Chiral Supramolecular Ligands in Transition Metal Catalysis.* Chemistry Department, 2012.

.